



ICMATSE 2024

**INTERNATIONAL CONFERENCE ON ADVANCED MATERIALS
SCIENCE & ENGINEERING AND HIGH TECH DEVICE APPLICATIONS**

PROCEEDING BOOK



October 24 - 26 2024

Ankara / TURKEY

icmatse.org

ISBN: 978-625-97601-1-7

ICMATSE 2024

INTERNATIONAL CONFERENCE ON ADVANCED MATERIALS SCIENCE & ENGINEERING AND HIGH TECH DEVICE APPLICATIONS



TEKNOLOJİK SİSTEMLER A.Ş.
www.tetratek.com.tr

Seeing beyond



TEKNOGEM
X-ray Çözümleri



TEKNOPLAN



October 24 - 26 2024 Ankara / TURKEY

icmatse.org

International Conference on Advanced Materials Science and Engineering and High Tech Device Applications (ICMATSE 24)

October 24– 26 2024, Ankara/TURKEY

EDITORS

Prof. Dr. Hakan ATES/Gazi University

Assoc. Prof. Dr. Gokhan SURUCU/Gazi University

Assoc. Prof. Dr. Ersin BAHCECI/Iskenderun Technical University

EDITORIAL BOARD

Prof. Dr. Munir H. NAYFEH/University of Illinois at Urbana-Champaign

Prof. Dr. Bekir OZCELIK/Cukurova University

Prof. Dr. Ammar NAYFEH/Khalifa University, UAE

Prof. Dr. Necdet SAGLAM/Hacettepe University

Prof. Dr. Behcet GULENC/Gazi University

Prof. Dr. Irshad HUSSAIN/Lahore University, Pakistan

Prof. Dr. Dmitri GORIN/SCP& QM Skolkovo Inst. of Sci. and Tech., Russia

Assoc. Prof. Dr. Ozge SURUCU/Atilim University

Prof. Dr. Meena Laad/ Symbiosis International University, India

Assoc. Prof. Dr. Bilge IMER/Middle East Technical University

Dr. Mete Bakir/TAI / A. Yildirim Beyazid University

Dr. Osman Safa CIFTCI/ Bogazici University

ANKARA

NOVEMBER 2024

Proceeding Book

Online: ISBN: 978-625-97601-1-7

Contact Address

Gazi University, Faculty of Technology, Dept. of Metallurgy and Materials Engineering,
Yenimahalle/Ankara/TURKEY

icmatse.org, icmatse@gmail.com

International Conference on Advanced Materials Science and Engineering and High Tech Device Applications (ICMATSE 2024)

October 24 – 26 2024, Ankara/TURKEY

CHAIRMAN

Munir H. NAYFEH (Prof. Dr)/University of Illinois

Hakan ATES (Prof. Dr)/ Gazi University

SCIENTIFIC COMMITTEES

Prof. Dr. Ayhan EROL/Afyon Kocatepe University

Prof. Dr. Ahmad I. AYESH/Qatar University, Qatar

Prof. Dr. Ali GUNGOR/Karabük University

**Assoc. Prof. Dr. Aisha IHSAN/National Inst. Of
Biotech and Eng, Pakistan**

Prof. Dr. Md. A. Ali/ Chittagong University

Prof. Dr. Alpay OZER/Gazi University

Prof. Dr. N. Alper TAPAN/ Gazi University

Prof. Dr. Ammar NAYFEH/Khalifa University, UAE

Assoc. Prof. Dr. Ayhan ORHAN/Firat University

**Prof. Dr. Andrei Kovalevsky/ University of Aveiro /
PT**

Assoc. Prof. Dr. Gokhan SURUCU/Gazi University

**Assoc. Prof. Dr. Ersin BAHCECI/Iskenderun Technical
University**

**Assoc. Prof. Dr. Abdullah CANDAN/ Kirsehir Ahi
Evrans University**

Prof. Dr. Aytunç ATES/A. Yildirimbeyazit University

Assoc. Prof. Dr. Aytac ERKISI/Pamukkale University

**Assoc. Prof. Dr. Babek ERDEBILLI/A. Yıldırım Beyazıt
University**

Assoc. Prof. Dr. Battal DOGAN/ Gazi University

Prof. Dr. Bekir OZCELIK/Cukurova University

**Assoc. Prof. Dr. Bilge IMER/Middle East Technical
University**

**Prof. Dr. Bulent YESILATA/A. Yildirim Beyazıt
University**

Prof. Dr. S. Bora LİSESİVDİN/ Gazi University

**Prof. Dr. C. SURYANARAYANA/University of Central
Florida, Orlando, USA**

**Prof. Dr. Canan VARLIKLI/Izmir Institute of
Technology**

**Prof. Dr. Dmitri GORIN/SCP& QM Skolkovo Inst. of
Sci. and Tech., Russia**

Prof. Dr. Emine ALDIRMAZ/ Amasya University

**Prof. Dr. Guven CANKAYA/A. Yıldırım Beyazıt
University / Roketsan**

**Assoc. Prof. Dr. Fatih CALISKAN/Sakarya University
of Applied Sciences**

**Prof. Dr. Feza KORKUSUZ/Hacettepe University /
TUBITAK**

**Prof. Dr. Francesco COTTONE/Perugia University,
Italy**

**Assoc. Prof. Dr. Gokhan KUCUKTURK/Gazi
University**

**Prof. Dr. Haitham Abu-RUB/Texas A&M University,
Qatar**

**Prof. Dr. C. Hakan GUR/Middle East Technical
University**

Dr. Hasan M. NAYFEH/IBM, USA

**Prof. Dr. Husnu Emrah UNALAN/Middle East
Technical University**

Prof. Dr. Hakan GURUN/Gazi University

Prof. Dr. Ahmet DURGUTLU/Gazi University

Prof. Dr. Hacı OZISIK/ Aksaray University

**Prof. Dr. Hanan Issa MALKAWI/Yarmouk
University, Jordan**

**Prof. Dr. Hussein MOHAMED/Helwan University
Cairo, Egypt**

**Prof. Dr. H. HADIYANTOI/Diponegoro University,
Indonesia**

Prof. Dr. Ilyas UYGUR/Duzce University

**Assoc. Prof. Dr. Ihsan TOKTAS/A. Yildirimbeyazıt
University**

**Prof. Dr. Irshad HUSSAIN/Lahore University,
Pakistan**

**Prof. Dr. Idris AKYUZ/Eskisehir Osmangazi
University**

Assoc. Prof. Dr. Idris CANDAN/ Kocaeli University

Prof. Dr. Irfan AR/Gazi University

Prof. Dr. Kadir KOCATEPE/Gazi University

**Prof. Dr. Madjid FATHI/Inst. For Knowledge Based
Sys., Germany**

**Prof. Dr. Laila H. Abu Hassan/University of Jordan,
Jordan**

**Prof. Dr. Liviu Brandusan (Retired)/Technical
University Cluj-Napoca, Romania**

Prof. Dr. Muhammad Faizal Bin A. Gani/University of Malaya, Malaysia
Assoc. Prof. Dr. Melika OZER/Gazi University
Prof. Dr. Mehmet EROĞLU/Firat University
Prof. Dr. Metin BEDİR/Gaziantep University
Prof. Dr. Meryem EVECEN/ Amasya Univeristy
Prof. Dr. Mustafa ACARER/Selcuk University
Prof. Dr. Meena LAAD/Symbiosis International University, India
Prof. Dr. M. Ishaque KHAN/Illinois Institute of Technology, USA
Prof. Dr. N. Fazil YILMAZ/Gaziantep University
Prof. Dr. Nurettin KOROZLU/ Burdur Mehmet Akif University
Prof. Dr. Noha ELHALAWANI/NRC, Cairo, Egypt
Prof. Dr. Oguzhan YILMAZ/Gazi University
Prof. Dr. Olena S. Melnyk/Oleksandr D Dovzhenko HNP University, Ukraine
Dr. Osman Safa CIFTCI/ Bogazici University
Prof. Dr. Rabah KHENATA/ Mascara University
Prof. Dr. Rahmi UNAL/Gazi University
Prof. Dr. Ramazan KACAR/Karabuk University
Prof. Dr. Rasid Ahmad/Kashmeer University, Pakistan

Prof. Dr. Raul MITRA/Indian Institue of Technology, India
Assoc. Prof. Dr. Recep ZAN/N. Omer Halis Demir University
Prof. Dr. Rached HABIB/ Hassiba Benbouali University of Chlef
Prof. Dr. Saffa RIFFAT/University of Nottingham, UK
Prof. Dr. Shadia IKHMAYIES/Al Isra University, Jordan
Prof. Dr. Salim ARSLANLAR/Sakarya University of Applied Sciences
Prof. Dr. Serdar SALMAN/Marmara University
Prof. Dr. Semra IDE/Hacettepe University
Assoc. Prof. Dr. Sekip Esat HAYBER/ Bursa Uludag University
Prof. Dr. Suleyman GUNDUZ/Karabuk University
Assoc. Prof. Dr. Tarik ASAR/Gazi University
Prof. Dr. Takashige OMATSU/Chiba University, Japan
Prof. Dr. Tolga DEPCI/Iskenderun Technical University
Assoc. Prof. Dr. Volkan KILICLI/Gazi University
Prof. Dr. Zakaria BOUMERZOUG/University of Biskra / DZ



ORGANIZING COMMITTEE

Prof. Dr. Hakan ATEŞ -/Gazi University
Prof. Dr. Munir H. NAYFEH/University of Illinois at Urbana-Champaign, USA
Assoc. Prof. Dr. Ersin BAHCECI/Iskenderun Technical University
Assoc. Prof. Dr. Gokhan SURUCU/Gazi University
Prof. Dr. Bekir OZCELIK/Cukurova University
Prof. Dr. Ammar NAYFEH/Khalifeh University, UAE
Prof. Dr. Behcet GULENC/Gazi University
Dr. H. M. NAYFEH/IBM, USA
Assoc. Prof. Dr. Bilge IMER/Middle East Technical University
Prof. Dr. Alpay ÖZER/ Gazi University
Prof. Dr. Olena S. Melnyk/Summy University, Ukraine
Prof. Dr. Dmitri GORIN/SCP& QM Skolkovo Inst. of Sci. and Tech., Russia
Prof. Dr. C. Hakan GUR/Middle East Technical University
Dr. Osman Safa CIFTCI/ Bogazici University
Prof. Dr. Ahmet KARAASLAN/Yildiz Technical University
Prof. Dr. Canan VARLIKLI/Izmir Institute of Technology
Assoc. Prof. Dr. Memduh KURTULMUS/ Marmara University

Assoc. Prof. Dr. Zuhai ER/Istanbul Technical University
Prof. Dr. Liviu Brandusan/Technical University Cluj-Napoca, Romania
Prof. Dr. Mehmet OZALP/Karabuk University
Prof. Dr. Necdet SAGLAM/Hacettepe University
Dr. Sahin COSKUN/Eskisehir Osmangazi University
Prof. Dr. Niyazi OZDEMIR/Firat University
Dr. Mete BAKIR/ TAI / A. Yildirim Beyazid University
Prof. Dr. Sinan AKGOL/Ege University
Prof. Dr. Yusuf Z. MENCELOGLU/Sabanci University
Prof. Dr. Rabah KHENATA/ Mascara University
Prof. Dr. Zafer TATLI/Sakarya University of Applied Sciences
Assoc. Prof. Dr. Yunus OZEN/
Assoc. Prof. Dr. Melika OZER/Gazi University
Prof. Dr. Irfan AR/Gazi University
Dr. Halil İbrahim EFKERE/ Gazi University
Assoc. Prof. Dr. Sedat SURDEM/ Gazi University
Assoc. Prof. Dr. H. Huseyin GULLU/ Aselsan
Assoc. Prof. Dr. Umut AYDEMİR/ Bursa Uludag University
Dr. Pelin TOREN OZGUN/ Ostim Technical University

TECHNICAL COMMITTEE

Prof. Dr. Munir H. NAYFEH/University of Illinois at Urbana-Champaign
Assoc. Prof. Dr. Gokhan SURUCU/Gazi University
Assoc. Prof. Dr. Ersin BAHCECI/Iskenderun Technical University

Assoc. Prof. Yunus OZEN/Gazi University
Dr. Bugra YILDIZ/ Hacettepe University

PUBLICATION COMMITTEE

Prof. Dr. S. Bora LİSESİVDİN/Gazi University
Assoc. Prof. Dr. Gokhan SURUCU/Gazi University
Assoc. Prof. Dr. Zuhall ER/Istanbul Technical University

Assoc. Prof. Dr. Ersin BAHCECI/Iskenderun Technical University
Dr. Mete BAKIR/A. Yıldırım Beyazid University
Dr. Erdem MERMER/TAI

SPONSORSHIP AND EXHIBITION COMMITTEE

Assoc. Prof. Dr. Zuhall ER/Istanbul Technical University
Assoc. Prof. Dr. Ersin BAHCECI/Iskenderun Technical University

Halil İ. EFKERE/Gazi University
Erdem MERMER/TAI

EVENTS AND ACTIVITIES COMMITTEE

Assoc. Prof. Dr. Ayhan ORHAN/Firat University
Assoc. Prof. Dr. Zuhall ER/Istanbul Technical University
Dr. Halil İ. EFKERE/Gazi University

Erdem MERMER TAI
Tolga YILMAZ/Gazi University
Burak NALCACI/Gazi University

MEDIA AND INTERNATIONAL RELATIONS COMMITTEE

Assoc. Prof. Dr. Zuhall ER/Istanbul Technical University
Dr. Halil İ. EFKERE/Hacettepe University
Erdem MERMER/TAI

Gizem C. DELİBALTA/Mugla Sıtkı Kocman University
Berkcan ERENLER/Gazi University

Notice: The conference has attended by academics about 24 different countries. 57% of conference participants are foreign authors and / or his work with researchers in Turkiye of these authors. Publications selected from the ICMATSE 2024 conference to the journals will not be included in the papers in the proceedings book. All responsibility for references, text and citations belong to the authors.

PREFACE

As organizing this event of ICMATSE in 2024, we are excited and proud to have a magnificent scientific program, publish the main developments in the field in the form of 34 keynote/invited talks, a distinguished of 12 session presentations with recent advances. This book presents the papers / abstracts of material science focused on advanced materials and nanotechnology having in energy conversion and storage and LED lighting, optoelectronics, biomedical, agricultural and food and mechanical and thermal applications as well as commercialization issues. In addition to these, powder metallurgy, additive manufacturing, advanced manufacturing and joining techniques are also included. A committee discussed and determined the conference topics that constituted of renowned representatives of academia from Turkiye, several European Asian and African countries and the USA.

Our world-renowned and top-ranked institutions enriched our conference by opening exhibitions. They deserve all the thanks.

Due to the COVID - 19 outbreak, one – on - one contact events were carried out through online platforms at icmatse2020. Although we missed the face – to - face activities and there was a distance between them for public health, virtual meetings have been considered to be used. The virtual meeting took place between 2–4 October 2020. Remote/virtual presentations sessions were allowed for live interaction. But, icmatse 2022 and 2024 were held as hybrid format. The longing for face-to-face conferences is evident from the participation of a large number of audiences. We are proud to be able to achieve this.

See you at icmatse 2026; Wishing you a healthy and successful life. All this has been possible thanks to your participation, to our institutions' supports, and to our colleagues' involvement.

We would like to thank to keynote/invited speakers, participants and all sporters.

Hakan ATES
(Prof. Dr.)

Ersin BAHCECI
(Assoc. Prof. Dr.)

Gokhan SURUCU
(Assoc. Prof. Dr.)

On behalf of the organizing Committee

CONTENTS

2D Modelling of Pentacene based TGTC OTFTs	12
Nora Amele Abdeslam	
Mustapha Charef Eddine Yagoub	
Louiza Arab	
Nouredine Sengouga	
Microstructural and Mechanical Analysis of Hardfaced Surfaces Using a Novel Self-Shielded Flux-Cored Arc Welding Wire	17
Feyza Sari	
Can Yılmaz	
Halil Altındal	
Uğur Özdemir	
Investigation of the performance of an ejector refrigeration system operating in critical mode	22
Abbaci Wissem Eddine	
Boumaraf Latra	
The Effect of Bi[(Ti_{0.9}Zr_{0.1})_{0.5}Zn_{0.5}]O₃ Doping on the Structural, Dielectric, and Optical Properties of BiFeO₃	27
Nihed Ben Salah	
Najmeddine Abdelmoula	
Gas Metal Arc Weldability of Strenx 700MC Steel with Flux Cored Filler Metal	32
Serhat AKSOY	
Ramazan KAÇAR	
Samet NOHUTÇU	
Hayriye Ertek EMRE	
Microstructure and the mechanical properties of homogenized and hot rolled Mg-3Zn-0.2Ca-0.3Mn alloy	35
Laith M. Al MASHHADANI	
Ali GÜNGÖR	
Synthesis and Characterization of N-doped Carbon Black Supported Fe, Zn and Mo Based Catalysts for Oxygen Reduction Reaction.....	39
Ali Tambwe AMİR	
Çiğdem GÜLDÜR	
Silver GÜNEŞ	
Technical innovations in the service of architectural history continuity	42
Natia Kochladze	
Nino Imnadze	
Tinatin Chigogidze	
Bella Tinikashvili	
David Bostanashvili	

Ketevan Saluqvadze

Designing Efficient Solar-Powered Desalination Systems in Arid Region47

Nour sabira

Daoudi mebarka

Wind Energy application for Small-Scale Irrigation for Semiarid Region51

Hadja GUEDAOURIA

Mebarka DAOUDI

Abdelhak MAAZOUZI

Karim TALHI

Ahmed BENNIA

**Prospects of laser processing of Ta-substituted TiO₂
for designing thermoelectric materials58**

Diogo Lopes

Nuno Ferreira

Andrei Kovalevsky

**Bulk Nanostructured Bainitic Steels: Superior Engineering Properties with Considerable
Mechanical and Thermal stability60**

Behzad Avishan

Effect of PbS Quantum Dot Nanoparticles on The Dielectric Properties of Nematic Liquid Crystals64

Doğan Burak Aydın

Leyla Taştan

Mahpeyker Kocakoç Toprakoğlu

Mouna El Abboubi

İdris Candan

Sait Eren San

The Use of Hydrogels in Femoral Head Necrosis Research68

Zeynep Bal

Nobuyuki Takakura

**Tolerances and Mechanical Properties Comparison As-built Hole vs. Drilled Hole of Polymer
Additive Manufacturing70**

Abdulcelil Bayar

Umit Aytar

Erdem Mermer

Mete Bakir

**The Importance of Representative Sampling and Homogenization in
Designing the Reference Material Production Processes76**

Berna YUKSEL

Aysel BERKKAN

Hakan ATES

Fatma Cigdem GULDUR

Dual-Doped NCZ-AZ Cathode Material for Lithium-Ion Batteries	82
Duygu CANDEMIR	
Oncu AKYILDIZ	
Hakan ATES	
Acoustic-Based Evaluation of Laser Micromachining for Enhanced Ceramic Processing	85
Can Ozcelik	
José Ramón Beltrán	
Hippolyte Amaveda	
Elena Martínez	
German F. de la Fuente	
Luis Alberto Angurel	
Characterization Of Pomegranate Peel, Activated Carbon And Hard Carbon Derived From Pomegranate Peel.....	87
Mesut KARTA	
Tolga DEPCI	
Energy as a Dual Use Item under European Union Law	90
Natalia Charalampidou	
Mixed-Variable Bayesian Optimization for Solar Selective Absorbers	95
Azra Arslan	
Osman Safa Cifci	
Development and Performance Evaluation of Radiation-Resistant Secondary Emission Ionization Calorimeters for High-Energy Physics Experiments.....	99
Nejdet Paran	
Saleh Abubakar	
Burak Tekgun	
Emrah Tiras	
Nilüfer Kul	
WAAM Properties of Mild and Carbon Steels.....	103
Ezgi DOGAN	
Mustafa AY	
Memduh KURTULMUS	
Ahmet Irfan YUKLER	
Wall Dimensions of MIG based Mild Steel WAAM Parts	107
Ezgi DOGAN	
Mustafa AY	
Memduh KURTULMUS	
Ahmet Irfan YUKLER	
Investigation of the effect of composite layer thickness on low-velocity impact behaviour in fibre metal laminate materials	111
Mustafa Dündar	

İlyas Uygur

Ergün Ekici

Cihat Taşçıoğlu

Employment of black phosphorous in nematic liquid crystals for enhancing their dielectric properties.....117

Mouna El Abboubi

Mahpeyker Kocakoç Toprakoğlu

Doğan Burak Aydın

Leyla Taştan

İdris Candan

Sait Eren San

The Effect of WC Content in Ni Based WC Reinforced Laser Surface Cladding.....121

Aysenur Elci

Hakan Ates

Mehmet Eroglu

A Case Study on Ultrasonic Atomization of Stainless-Steel Powder for Additive Manufacturing126

Anil EMIRALIOGLU

Rahmi UNAL

Ab Initio Computational Materials Science130

Engin Deligöz

Opening the Third Dimension on SEM: FIB-SEM and Laser FIB133

Volkan Erkut

Examination of Electroless Nickel Coated Silicon Nitride Ceramics by Ultrasonic Pulse Echo Method136

Vildan ÖZKAN BİLİCİ

Ahmet YONETKEN

Ayhan EROL

Multiphase Fiber Reinforced Composites and CNT Wires for Aerospace and Defense Industries140

Abdulhammed K. Hamzat

Md Shafinur Murad

Ramazan Asmatulu

An assessment of the potential of the conversion of pomegranate membrane into value-added products145

Emine Yalman

Tolga Depci

Yunus Onal

Enhancement of HER Catalysts for PEM Electrolyzers: Investigating the Effects of Boron and Phosphorus on Ruthenium-Based Catalysts Supported by Active Carbon in Acidic Media.....149

Gökalp Dilmen

Fatma Çigdem Guldur

Silver Gunes

Investigation Of Thermal And Crystallographic Properties Of Copper Filaments Used In Metal 3d Printers.....	153
Gözde ALTUNTAS	
Bulent BOSTAN	
Removal of Boron and Boron Compounds from Waste Waters.....	158
Ipek CELEBI GURSOY	
İrfan AR	
Investigation of structural, electronic, and optical properties of KSiI₃ cubic perovskite using first-principles methods	162
Gulcin CORBACI	
Yasemin Oztekin CIFTCI	
Scaling up Superconducting Quantum Processors: Materials and Fabrication Challenges	166
Hasan M. Nayfeh	
Illumination Effects on Capacitance-Voltage Characteristics and Negative Capacitance Behavior in Au/n-GaAs (MS) And Au/Si₃N₄/n-GaAs (MIS) Type Structures	168
Mahmut Bucurgat	
Effect of WC Addition on Fe-B/WC Laser Composite Coating	171
Mehmet Eroglu	
Laser-induced structural modifications and surface functionalization of metallic oxide thin films: HfO₂, ZnO and Cu₂O	175
Alejandro Frechilla	
Luis A. Angurel	
David Muñoz-Rojas	
José Ángel Pardo	
Germán F. de la Fuente	
The rise of 212 MAX phase borides with enhanced thermo-mechanical properties	177
Md. Ashraf Ali	
Biocompatibility Issues for the Tissue Engineered Products for Commercialization	181
Gilson Khang	
Harnessing Rosa damascena Residue for Green Synthesis of Zinc Oxide Nanoparticles: Response Surface Methodology Optimization	183
Imane Adraoui	
Nabil Saffaj	
Rachid Mamouni	
Si Mohamed Jadoualia	
Femtosecond Laser-FIB-SEM Triple Beam for Sample Preparation and Large Volume Analysis.....	185
Daniel Phifer	
Interplay between laser induced surface nanostructures and superconductivity on Nb thin films	186
Luis A. Angurel	
Javier Frechilla	
Luis Porta-Velilla	

Elena Martínez

Germán F. de la Fuente

Nicolas Lejeune

Emile Fourneau

Alejandro V. Silhanek

Jörn Bonse

A. Badía-Majós

The effect of Li doping In₂O₃ thin films on structural and optical properties deposited by ultrasonic spray188

Bourhefir Ranida

Saidi Hanane

Hamani Nedjette

Attaf Abdellah

Okba ben khetta

Development of a Non-Toxic CuSbSe₂/Zn_xSn_(1-x)O Thin-Film Solar Cell with Optimized Multilayer Architecture189

Rawshan Tareq M.Nadhaif Mohammednadhaif

Aysenur Gencer

Ozge Surucu

Integration of Electrospinning and Additive Processing for Harvesting Energy in IoTs.....191

Ashok Vaseashta

Green Hydrogen Generation Using Innovative MXene/Ni-functionalised Composite Electrodes192

Andrei V. Kovalevsky

Sergii A. Sergiienko

Daniela V. Lopes

AI-Driven Optimization of Hydrogen Storage in TiO₂/CNTs Nanocomposites-Under Simple Conditions.....196

Isabel Capela

Behrouz Nemati

Mohammadreza Kamali

Shahed Rasekh

M. Elisabete V. Costa

Structural, magnetic, and blood compatibility studies of Nickel-Copper nanoferrites produced by laser ablation technique201

Can Özçelik

Sezen Özçelik

Bestenur Yalçın

Lütfi Arda

Luis A. Angurel

Bekir Özçelik

Third Generation Single Crystal Superalloys-A Short Review	204
Cemre ATALAY	
Volkan KILICLI	
Preparation and characterization of ZnO- based Schottky diode prepared with sol-gel method.....	208
Arab Louiza	
Sengouga Nouredine	
Abdeslam Nora Amel	
Chenni Chaima	
Latif Aya	
Design Application Against Temperature and Magnetic Noise in Adjustable Constant Current DC LED Drivers Under 50 Volts.....	213
Bariş GÖKÇE	
Mehmet BİNGÜL	
Salih Metin YURTER	
Zuhal ER	
Effects of Shot Peening Parameters on Low Cycle Fatigue Life of 17-4 PH H1150 Steel	218
Ramazan Meral	
Ahmet Özdemir	
Considerations on surface roughness for additively manufactured structures using non-explosible AlSi10Mg feedstock on a medium-wattage L-PBF machine.....	225
Fatma Nur Depboylu	
Andrei-Alexandru Popa	
Quantum Computational Discovery of Novel High-Entropy Alloys	217
Houlong Zhuang	
Payden Brown	
Lemon peel incorporated PVA/chitosan composites for advanced bioactive food packaging : Physico-chemical properties and interfacial dynamics.....	229
Oumaima Fakraoui	
Isabelle Royaud	
Mourad Arous	
Zoubir Ayadi	
Machine Learning-Based Optimization of the Synthesis of TiO₂/CNTs Composites via Genetic Algorithms (GA).....	234
Sara Zandi	
Behrouz Nemati	
Mohammadreza Kamali	
Shahed Rasekh	
M. Elisabete V. Costa	
Isabel Capela	
Fabrication of Thermoelectric Legs and Their Integration Into A Prototype Thermoelectric Generator	239
Sotelo, Andres	

Amirkhizi, Parisa	
Hedayati, Mehdi	
Madre, Maria A.	
Torres, Miguel A.	
Kovalevsky, Andrei	
Rasekh, Shahed	
Surface Treatment Application of Bulk Amorphous Steel	244
Amdulla O. MEKHRABOV	
Hafize CAKMAK ALPASLAN	
M. Vedat AKDENIZ	
A5356 Material Production and Characterization by Waam Technique.....	251
Berfin GURSU	
Murat KAYAALP	
Hakan ATES	
Thermo-Calc Investigation of the Ga-As Binary System	257
Shadia J. Ikhmayies	
Phase Diagram and Thermodynamic Properties of the Fe-Cu Binary System	262
Shadia J. Ikhmayies	
The Importance of Surface Topography	267
Marek Jemelka	
Investigating the Solidification Temperature Range of High Strength Low Alloy Steels Using the Scheil Solidification Model with CALPHAD Methodology	268
Adem KAYADELEN	
Oguzhan YILMAZ	
Hakan ATES	
Thermoluminescence of hydrothermally grown ZnO nanorods	276
Mohammed Khenfouch	
Issam Derkaoui	
Mohammed Hamzah	
Issam Boukhoubza	
Mohamed Achehboune	
Rhizlane Hatel	
Dumisani Mlotswa	
Bakang Moses Mothudi	
Extending Synchrotron X-ray Microscopy to the Laboratory – X-Ray Microscopy as a correlative imaging technique	280
Mohsen Samadi Khoshkhoo	
Self-Healing Metals versus Microcrack Healing of Metals	281
Volkan Kilicli	
Amorphous Matrix Nanocomposites in Three-component Manganese-containing Borate Systems	284

Marina Kapanadze	
Maia Mshvildadze	
Tamar Loladze	
Nino Keadze	
Zurab Sabashvili	
Plasma Cutting of High-Strength Non-Metallic Fiber Composite Materials	288
Zurab Sabashvili	
Tamar Loladze	
Gela Otarashvili	
Nino Kenchiashvili	
Marina Kapanadze	
Silica Nanoparticles and CVD Graphene for Hydrophobic Modified Surfaces	292
Majid S. Al-Ruqeishi	
Balqis Al-Yaqoubi	
Electrochemical synthesis of Oleic Acid coated Magnetite nanoparticles from water/ethanol media	297
Nino Makhaldiani	
Marine Donadze	
Investigation of The Life Time of The Coating Applied on The Steam Turbine Blade In Terms of Corrosion And Erosion	302
Mehmet Seyrek	
Murat Kayaalp	
Hasan Hasirci	
Hakan ATES	
Enhancing Desalination Rates of Saltwater using Superhydrophobic Nanomembranes and Machine Learning Approaches	307
Nikhil Paranjpe	
Shruti R. Kshirsagar	
Ramazan Asmatulu	
Development of biodegradable Mg-Zn-Ca alloys to be used in bone fracture treatments	310
Jameel Fadhil Hassan Al – Ogaidi	
Ali Güngör	
The Effects of Ni-SiC Electrocomposite Coating on the Mechanical Properties of Aviation Piston Engine Cylinders	314
Mehmetcan OKSUZ	
Ugur KARAHAN	
Guven CANKAYA	
Friction Welding of Dissimilar Steels	317
Zakaria Boumerzoug	
Rare Earth Fluorescent Nanomaterials for Enhanced Development of Latent Fingerprints in Forensic Sciences	322

Hanen DOURI

Ramzi MAALEJ

Towards High Temperature Thermoelectrics: Effect of simultaneous doping and defect chemistry engineering on perovskite materials.....326

Shahed Rasekh

Parisa Amirkhizi

Mehdi Hedayati

Maria A. Madre

Andres Sotelo

Miguel A. Torres

Andrei Kovalevsky

Photocatalytic activity under sunlight by copper Oxide Thin Films.....331

Nour elhouda Redjough

Nedjette Belhamra

Research and Development of Gd-doped Al/Gd/Y2O3/Si/Al MOS-based Nuclear Radiation Detectors332

Canan Kaliber

Saleh Abubakar

Emrah Tiras

Ni-Co based metallic foams for hydrogen production via electrochemical water splitting335

Sadia Ata

Anila Tabassum

Advances and Challenges in Solid State Electrolytes and Processing Technology for Energy

Storage Devices337

Sajid Hussain Siyal

Synthesis, Structure and Magnetic Properties of (Co/Ce) co-doped ZnO Nanoparticles339

Merve Mine Seker Perez

Cihat Boyraz

Lutfi Arda

Investigation Of The Springback Behavior Of Double-Phase Steel Sheets In The V Bending Process341

Eda Nur Düzenli

Hakan Gürün

Quality Control Analysis in the Steel Industry with Simulation Techniques348

İsmail Taşçı

İlhami Muharrem Orak

4D Printing of Shape Memory Polymer with Digital Light Processing354

Nurdan TATLISU

Oğuzhan YILMAZ

A Study on Production and Characterization of AlSi10Mg Alloy Using SLM Technique.....359

Zehra TEKKAYA

Alpay OZER

Hakan ATES

Zinc foams made by a cold sintering process.....361

Thalmaier Gyorgy

Sechel Niculina Argentina

Nasui Mircea

Simon Alexandra

Constantinescu Horia

Ioan Vida-Simiti

Development of Nickel-Based Bimetallic Anode Catalysts for Direct Ethanol Fuel Cells366

Fatma Nur Tiren

Yavuz Yağızatlı

İrfan Ar

**The Effect of Temperature on the Tensile Behavior of Additively Manufactured IN 718 for
As-Built and Direct-Aged Conditions.....370**

Tuğçe Kaleli Alay

Cemil Hakan Gür

Next generation drug delivery nanosystems374

Tanveer Tabish

Open Hole Tension Test And Finite Element Method Simulation In Polymer Matrix Composite

Materials: Experimental And Analytical Comparison.....376

Mete Bakir

Utku Dogan

Sefa Sahin

Enes Karakus

Residual Stresses and Distortion in WAAM381

Ahmet İrfan YÜKLER

2D Modelling of Pentacene based TGTC OTFTs

Nora Amele Abdeslam

*Laboratory of Semiconducting and Metallic Materials (LMSM), Biskra University, 07000 Biskra, Algeria,
noura.abdeslam@univ-biskra.dz,
ORCID: 0009-0007-6495-8313*

Mustapha Charef Eddine Yagoub

*School of Electrical Engineering and Computer Science, University of Ottawa, Ottawa, ON, Canada, K1N 6N5,
myagoub@uottawa.ca ,
ORCID: 0000-0002-8763-7738*

Louiza Arab

*Laboratory of Semiconducting and Metallic Materials (LMSM), Biskra University, 07000 Biskra, Algeria,
louiza.arab@univ-biskra.dz ,
ORCID: 0009-0003-9695-3374*

Nouredine Sengouga

*Laboratory of Semiconducting and Metallic Materials (LMSM), Biskra University, 07000 Biskra, Algeria,
n.sengouga@univ-biskra.dz ,
ORCID: 0000-0002-4437-0869*

Cite this paper as: Abdeslam, NA, Yagoub, M.C.E, Arab, L, Sengouga, N. 2D Modelling of Pentacene based TGTC OTFTs. Int. Conf. Advanced. Mater. Sci.& Eng. HiTech.and Device Appl.Oct. 24-26 2024, Ankara, Turkiye

Abstract: Nowadays, modern electronics have been shifting towards organic materials based on their specific electroactivity. From the spectrum of technologies involved, Pentacene (C₁₄H₂₂) molecule is widely used as p-type semiconductor channel in thin-film transistors (TFTs) and has high mobility. In this study, a 2-dimensional modelling was performed. Since, the TFT behaves like MOSFET, we simulated a high-k (ϵ_r) dielectric material between the gate and organic semiconductor (OSC) which helps to control the transfer of charge carriers and increase their accumulation inside the channel leading to estimable OTFT performance. Thus, from our results, the Al₂O₃ shows the best OTFT characteristics and parameters compared to SiO₂, PMMA and HFO₂. We simulated also the Poly(3-hexylthiophene) (P3HT) based OTFT since the P3HT is a p-type organic semiconductor with interesting properties. P3HT based OTFT exhibits a rapid response at low gate voltage compared to that based on Pentacene under the same conditions (length, width and topology) but its low mobility still limits considerably all its characteristics.

Keywords— Pentacene-OTFT, P3HT, Al₂O₃ dielectric, high k dielectric, Silvaco Modelling.

© 2024 Published by ICMATSE

1. Introduction

Recently, electronic organic devices have emerged as a suitable alternative to standard components. They are mainly based on electroactive organic materials, such as nanomaterials-based carbon and conjugated polymers. Pentacene (C₁₄H₂₂) as organic material is extensively used as organic p-type-semiconductor channel between the gate and the dielectric (oxide) in Thin Film Transistors (TFTs) (1). Usually, pentacene is used in TFTs because of its small model molecule with one of the highest field effects mobilities reported so far (2–4). Pentacene-based OTFTs have several applications due to their high specific

sensitivity to toxic and dangerous gases to humans such as ammonia (NH₃). Significant changes in current (I_{on}), intrinsic mobility (μ), and threshold voltage (V_{th}) were observed with respect to the change in ammonia concentration. Pentacene-based OTFTs have also been studied as a transducer for biochemical detection in aqueous media: when exposed to humidity, their saturation current decreases. This decrease has been shown to be reversible and can therefore be used to measure the amount of relative humidity in the surrounding environment. It has been found that the sensitivity depends on the thickness of the pentacene layer.

Indeed, the deposition of pentacene on the appropriate dielectrics is essential in order to control the morphology of the films and thus, to reduce the interface traps that help the transport of charge carriers, and finally allowing obtaining the ultimate performance of the OTFT. In fact, p-type organic semiconductors such as poly (3-hexylthiophene) (P3HT) stand out as large sensitive competitive devices for humidity levels and NH_3 (1). Despite its low mobility, P3HT shows outstanding solubility, making it suitable for transistors dedicated to non-invasive disease diagnosis and environmental monitoring through the detection of gaseous analytes such as methanol, acetone and chloroform(5). Basically, OTFT works similar to a capacitor by producing an electric field for p/n type organic semiconductors (OSCs) inside the dielectric (insulator between the OSC and the gate) at negative/positive gate-source voltages (V_{gs}). The OTFTs can be driven at lower supply voltages (less than 5 V) for a large capacitor (C_i), which helps to accumulate more charge carriers. So, among strategies to increase the C_i is to use high- $k(\epsilon_r)$ dielectric materials, such as PMMA, SiO_2 , Al_2O_3 , HfO_2 (4). Therefore, particular care has been given in this work to materials for OSC channel and dielectric by considering a two-dimensional model (2DM), involving the length (l) and thickness(d). This modeling was performed under the commercial Software Silvaco. Such an approach is advantageous since it can also allow to specify the third dimension (width). Fortunately, the OTF current is directly proportional to channel width, so it permits Silvaco to simulate a device with a default width (1 μm) and multiply the results by the measured width (w) to obtain the correct current-voltage characteristics (6).

2.Results and discussion

The simulated material parameters are summarized in Tables 1, 2, and 3. Initially, a top contact top gate (TCTG) OTFT pentacene was explored where the inorganic dielectric materials Al_2O_3 and SiO_2 (inorganic) were compared to PMMA (organic). As

The acronyms in Table.1,2 and 3 are N_c (N_v) is the effective density of states in the conduction (valence) band, E_g is the energy gap, χ is electron affinity, μ_n (μ_p) is electron(hole) Mobility and N_A is the acceptor concentration. The subscripts T stands for tail, G stands for Gaussian, A stands for acceptor and D stands for donor, NTA and NTD denote edge intercept densities of valence and conduction band with exponential tail distribution. Its characteristic decay energy is WTA and WTD. NGA and NGD denote total

density of state with Gaussian distribution and its peak energy distributions are EGA and EGD, respectively. Its characteristic decay energy is WGA and WGD. HA(HD) is the acceptor (donor) traps density of states, TCA (TCD) is the acceptor (donor) traps characteristic temperature, σ_{gae} (σ_{gah}) Specifies the electron (hole) capture cross-section for acceptor traps, σ_{gde} (σ_{gdh}) Specifies the electron (hole) capture cross-section for donor traps and n_{md} (n_{md}) specifies the number of discrete levels used in continuous distribution of acceptor (donor)states. In the hopping mobility equation (3), V_{0n-hop} is the frequency at which an electron attempts to jump into the conduction band, β_{n-hop} is the percolation, and γ_{n-hop} is 1/carrier locus radius. While for pool Frenkel mobility equation, the δ_{p-pf} , δ_{n-pf} are activation energy for holes and electrons. β_{n-pf} and β_{p-pf} denote the factor for electron and hole, respectively and γ_{n-pf} (γ_{p-pf}) is fitting parameter.

As Fig. 1 shows, the Al_2O_3 presents the best features for either $I_{ds}-V_{ds}$ or $I_{ds}-V_{gs}$ characteristics. The Al_2O_3 allows better performance for the OTFT because of its high dielectric constant ($\epsilon_r = 9.3$), and since SiO_2 and PMMA have close dielectric constant value, they give the same results despite their difference in material type (inorganic/organic).

Table.1: Materials and physical parameters under consideration

	Pentacene	P3HT	SiO_2	PMMA	Al_2O_3	HfO_2
d (μm)	0.05	0.05	0.3	0.3	0.3	0.3
E_g (eV)	1.08	1.9	9.1	3.6	6.75	5.45
χ (eV)	4.17	3.4				
ϵ_r	11.8	3.0	3.9	3.6	9.3	22.0
N_c (cm^{-3})	2.8×10^{19}	2×10^{21}				
N_v (cm^{-3})	1.04×10^{19}	2×10^{21}				
μ_n/V_{nsat} (cm/V)	$-/10^6$	1×10^{-4}				
μ_p/V_{psat} (cm/V)	$-/10^6$	5×10^{-4}				
N_A (cm^{-3})	2×10^{16}	2×10^{17}				
ref	(6)	(3)			(6)	

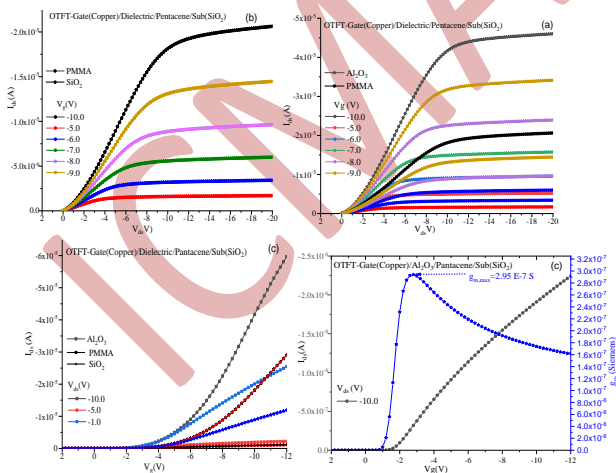
Table.2 Traps parameters for Pentacene and P3HT organic material

Parameters	Pentacene	Parameters	P3HT
HD (cm ⁻³)	4.75x10 ¹⁷ , 9.25x10 ¹⁶	N _{TA} (cm ⁻³ /eV)	1x10 ¹²
		N _{TD} (cm ⁻³ /eV)	1x10 ¹²
TCD (K)	4.409x10 ² , 4.293x10 ³	N _{GA} (cm ⁻³ /eV)	1x10 ¹⁶
		N _{GD} (cm ⁻³ /eV)	1x10 ¹²
numd	128, 128	E _{GA} (eV)	0.5
Sigde & sigdh	1x10 ⁻²⁰ , 1x10 ⁻²⁰	E _{GD} (eV)	0.7
HA (cm ⁻³)	4.75x10 ¹⁷ , 9.25x10 ¹⁶	W _{TA} (eV)	0.5
TCA (K)	4.409x10 ² , 4.293x10 ³	W _{TD} (eV)	0.7
numa	128, 128	W _{GA} (eV)	0.4
Sigae & sigah	1x10 ⁻²⁰ , 1x10 ⁻²⁰	W _{GD} (eV)	0.1
Ref	(7)	(3)	

Table.3: Mobility models for Pentacene and P3HT (Pool Frenkel and hopping) (references (3,7))

Hopping Model		Poole-Frenkel Model	
Parameters	OSC	Parameters	OSC
β _{n-hop}	1.6	δ _{n-pf} (eV)	6.524x10 ⁻⁵
γ _{n-hop} (cm ⁻¹)	2x10 ⁸	β _{n-pf} eV(cm/V) ^{1/2}	1.243 x10 ⁻²
v _{0n-hop} (Hz)	4x10 ¹¹	γ _{n-pf} (cm/V) ^{1/2}	1.545x10 ⁻⁵
β _{p-hop}	1.7	δ _{p-pf} (eV)	1.792 x10 ⁻²
γ _{p-hop} (cm ⁻¹)	9x10 ⁸	β _{p-pf} eV(cm/V) ^{1/2}	7.758 x10 ⁻⁵
v _{0p-hop} (Hz)	1x10 ¹²¹	γ _{p-pf} (cm/V) ^{1/2}	1.807 x10 ⁻⁵
Interface charge 1 x 10 ¹⁰ (cm ⁻²)			

Since, HfO₂ has been applied and studied extensively in MOS technology (8) due to its high k value of 22, it is compared here to Al₂O₃.


Figure 1: I_{ds} - V_{ds} Characteristics and transfer Characteristics of OTFT for different dielectric materials.

Indeed, as shown in Fig. 2a, 2b, and 2c, HfO₂ offers better performance by increasing the OTFT I_{ds} , especially for high gate voltages (V_g). As for the maximum transconductance, it is quite interesting with $g_{m,max}=13.89 \mu S$ for $V_g=-10 V$ for Hafnia (HfO₂) compared to $9.97 \mu S$ for Al₂O₃. But, HfO₂ shifts the threshold voltage (V_{th}) towards less negative values, which is a disadvantage because it requires more gate voltage. Moreover, HfO₂ has a smaller band gap of 5.45 eV (9), since the gate dielectric band gap (E_g) must be large to ensure an adequate band discontinuity in MOS structures. Also, the conduction band shift (ΔE_c) and valence band shift (ΔE_v) relative to those of the OSC must be large enough to keep the hot carrier injection below the levels specified for gate current (I_g) and dielectric reliability requirements. Al₂O₃, with a considerably larger band gap of 6.75 eV (10) than other high-k dielectrics, gives higher energy band shifts with OSCs, resulting in reduced gate leakage currents for the same thickness as other high-k dielectrics. For this, the following work will be based on Al₂O₃ as gate dielectric.

The charge carrier mobility (μ) is the average charge carrier drift velocity (V_{drift}) per unit electric field along the channel:

$$\mu = v_{drift}/E_{ds} \quad \text{Eq.1}$$

with E_{ds} the field (V_g/x). μ reflects the measure of the moving efficiency of the charge carriers along the conducting channel; it is directly related to g_m , (Fig.1.d) or Fig.2.b at $|V_{ds}| \ll |V_g - V_{th}|$ according to Eq.2 (1,4)

$$\mu = \left(\frac{L}{W}\right) \left(\frac{g_m}{C_i V_{ds}}\right) = \frac{\mu_0}{[1+\theta(V_g - V_{th})]^2} \quad \text{Eq.2}$$

with θ the mobility attenuation factor. Furthermore, μ is not necessarily constant, so these slopes will not be either. This is one of the reasons why, in most cases, a linear fit of the I_{ds} (V_{ds}) curve is performed to extract an average mobility value; $g_{m,max}$ being calculated to provide a maximum mobility value.

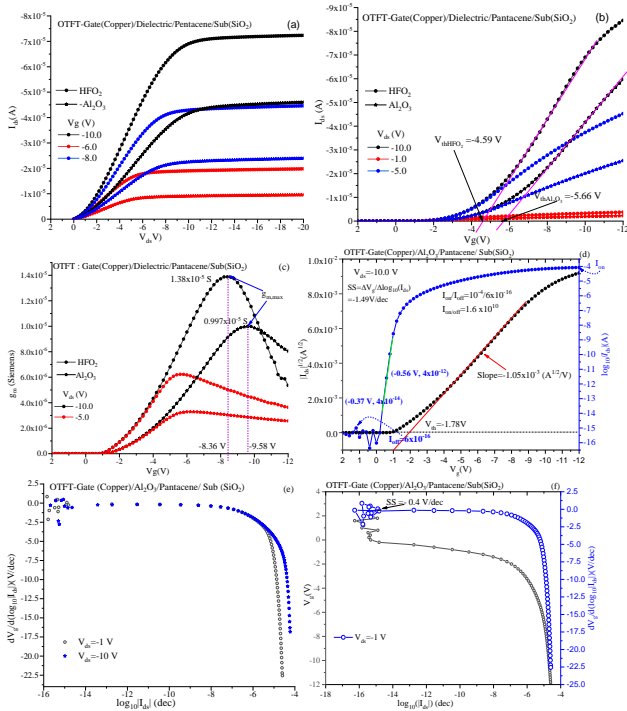


Figure.2: The influence of dielectric type (Al_2O_3 and HfO_2): a) on I_{ds} - V_{ds} characteristics, b) on transfer characteristics and c) on g_m transconductance (V_g) (Extraction of V_{th} and $g_{m, max}$ in the linear region), d) $\sqrt{I_{ds}}(V_g)$ for $V_{ds} = -10$ V to illustrate the linear fit for calculating mobility (μ) and V_{th} in saturation region. Right axis: $I_{ds}(V_g)$ in logarithmic scale to extract I_{on} and I_{off} and calculate an approximate value for the subthreshold slope (SS) (which is the variation of V_g to produce one-decade change in I_{ds}), e) Plot of V_g versus $\log_{10}|I_{ds}|$ and its first derivative to illustrate the SS calculation (method described in (1))

It is also worth mentioning that thinner dielectrics, lower gate length values, and larger μ values, are related to higher switching speeds in digital circuits, but not necessarily to faster sensing responses and improved sensitivity (11). A similar phenomenon occurs as V_g approaches V_{th} (Fig.2.a). Since there is a region of the channel near the drain contact that is devoid of carriers, it is not advisable to relate this slope to μ . However, a rough estimate is obtained by a linear fit from the plot $\sqrt{I_{ds}}(V_g)$ as in Fig. 2d, according to Eq.3 (1,4).

$$\mu_{sat} = \left(\frac{2L}{C_i W} \right) \left(\frac{\partial \sqrt{I_{ds}}}{\partial V_g} \right)^2 \quad \text{Eq.3}$$

V_{th} , which is the minimum gate-source voltage required to accumulate charge carriers at the semiconductor/dielectric interface and form a conductive path between the source and drain electrodes, is also an important parameter of OTFT to consider (Figs. 2a and 2d). V_{th} can be related to a current level, depending on the structure technology (i.e. conductivity and dimensions of the channel

semiconductor), or more precisely, on the minimum of the second derivative of I_{ds} with respect to V_g (Fig. 2d). Known as the ratio of current in the accumulation and depletion modes, I_{on}/I_{off} is a key parameter as well. The I_{off} is related to the channel dimensions and conductivity (σ_s) and for a device transitioning from cutoff to saturation, the I_{on}/I_{off} ratio can be extracted graphically from the $\log_{10}(I_{ds}(V_g))$ plots (Fig. 2d). As a high k and a thin dielectric film are required to increase C_i , this can increase the leakage current density of the gate electrode as well, thus impacting I_{off} . However, the other key factors to generate large current modulation are thin and lightly doped semiconductor films. For the subthreshold slope (SS), a graphical estimation was done from the plots $|I_{ds}|(V_g)$ in logarithmic scale (Fig. 2b). A more precise calculation is to plot V_g versus $\log_{10}|I_{ds}|$ and its first derivative (Fig. 2a and 2b). SS is the minimum of $\partial V_g / \partial \log_{10}(I_{ds})$ in absolute values for $V_g > V_{th}$. It depends on the impurity concentration, interface state, and trap density, as for V_{th} and I_{on}/I_{off} . The exponential increase in the channel current in absolute values, Fig. 2d, is a direct consequence of the transition from depletion to accumulation of charge carriers. In an OTFT, SS is closely related to the mobility enhancement for carrier hopping.

The OSC material in TFT largely impacts the quality of the device in terms of performance and its use as a specific detector. P3HT based OTFT was then simulated to compare it to Pentacene OTFT with same structure topology and dimensions. Indeed, the P3HT-OTFT current I_{ds} (Figs. 3a and 3b) is low compared to that of Pentacene due to its low mobility which impact the current. Also, the drain-source voltage V_{ds} needed to switch to the saturation zone is (-14 V), the same for the shift in V_{th} to 1.72 V and the slope implying g_m (7.24×10^{-10} S) for $V_{ds} = -10$ V. However, the P3HT based TFT is faster in terms of response at low V_g values.

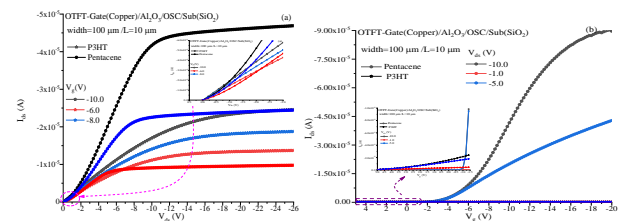


Figure 3: Comparison of OTFT characteristics according to the type of p-type OSC material (P3HT/Pentacene).

Conclusion

Even extensively explored, Pentacene based OTFT still constitute a hot research topic to enhance its performance. In this aim, a two-dimensional modelling under Silvaco software was done to simulate TGTC TFT based Pentacene semiconductor. First, Al_2O_3 dielectric allowed the best OTFT

performances compared to SiO_2 , PMMA and HfO_2 due to its high k and band energy concur with gate and OSC (channel). Pentacene based OTFT also was compared to that on P3HT, where it stands more high-performing because to its high mobility value while P3HT based OTFT showed a rapid response at low V_g .

References

1. Cavallari MR, Pastrana LM, Sosa CDF, Marquina AMR, Izquierdo JEE, Fonseca FJ, et al. Organic Thin-Film Transistors as Gas Sensors: A Review. *Materials*. 2020 Dec 22;14(1):3.
2. Feng T, Li Q, Hu X, Yang Y, Xu H, Zhu H, et al. TIPS-pentacene organic field-effect transistor for optoelectronic neuromorphic simulation. *Jpn J Appl Phys*. 2024 Mar 1;63(3):031008.
3. Dadhich S, Dwivedi ADD, Singh AK. Fabrication, characterization, numerical simulation and compact modeling of P3HT based organic thin film transistors. *Journal of Semiconductors*. 2021 Jul 1;42(7):074102.
4. Kumar B, Kaushik BK, Negi YS. Organic Thin Film Transistors: Structures, Models, Materials, Fabrication, and Applications: A Review. *Polymer Reviews*. 2014 Jan 2;54(1):33–111.
5. Cavallari M, Izquierdo J, Braga G, Dirani E, Pereira-da-Silva M, Rodríguez E, et al. Enhanced Sensitivity of Gas Sensor Based on Poly (3-hexyl thiophene) Thin-Film Transistors for Disease Diagnosis and Environment Monitoring. *Sensors*. 2015 Apr 22;15(4):9592–609.
6. Atlas user manual device simulation software. 2019.
7. Ioanna Dimkou. Simulation of organic TFT with TCAD tools. Aristotle University of Thessaloniki; 2018.
8. Chang YC, Huang ML, Chang YH, Lee YJ, Chiu HC, Kwo J, et al. Atomic-layer-deposited Al_2O_3 and HfO_2 on GaN: A comparative study on interfaces and electrical characteristics. *Microelectron Eng*. 2011 Jul;88(7):1207–10.
9. Hong M, Kwo J, Lin TD, Huang ML. InGaAs Metal Oxide Semiconductor Devices with $\text{Ga}_2\text{O}_3(\text{Gd}_2\text{O}_3)$ High- κ Dielectrics for Science and Technology beyond Si CMOS. *MRS Bull*. 2009;34(7):514–21.
10. Huang ML, Chang YC, Chang YH, Lin TD, Kwo J, Hong M. Energy-band parameters of atomic layer deposited Al_2O_3 and HfO_2 on $\text{In}_x\text{Ga}_{1-x}\text{As}$. *Appl Phys Lett*. 2009 Feb 2;94(5).
11. Gold H, Haase A, Fian A, Prietl C, Striedinger B, Zanella F, et al. Self-aligned flexible organic thin film transistors with gates patterned by nano-imprint lithography. *Org Electron*. 2015 Jul;22:1406.

Microstructural and Mechanical Analysis of Hardfaced Surfaces Using a Novel Self-Shielded Flux-Cored Arc Welding Wire

Feyza Sari

*Gedik Welding Inc. – R&D Center, 54300, Sakarya, Turkey,
can.yilmaz@gedik.com.tr
ORCID: 0009-0006-1845-9401*

Can Yilmaz

*Gedik Welding Inc. – R&D Center, 54300, Sakarya, Turkey,
can.yilmaz@gedik.com.tr
ORCID: 0000-0002-2249-9274*

Halil Altındal

*Gedik Welding Inc. – R&D Center, 54300, Sakarya, Turkey,
can.yilmaz@gedik.com.tr
ORCID: 0009-0000-2335-5603*

Uğur Özdemir

*Gazi University, Faculty of Technology, Metallurgical and Materials Engineering Dpt., 06560, Ankara,
Turkey, uozdemir@gazi.edu.tr
ORCID: 0000-0003-0521-4617*

Cite this paper as: Sari, F., Yilmaz, C., Altındal, H., Ozdemir, U., Microstructural and Mechanical Analysis of Hardfaced Surfaces Using a Novel Self-Shielded Flux-Cored Arc Welding Wire .Int. Conf. Advanced. Mater. Sci.& Eng. HiTech.and Device Appl.Oct. 24-26 2024, Ankara, Turkiye

Abstract. In this study, self-shielded flux-cored arc welding (FCAW-S) was performed using a newly developed hardfacing wire with a 2.4 mm diameter that meets the DIN 8555: MF 10 GF 60 G standard without any protective gas. Three-pass welding were applied on S355JR plates at low (320 A) and high (400 A) amperages. Beside the welding performance and the visual tests (VT) of the beads, the resulting samples underwent microstructural examinations, wear and hardness tests.

Microstructural examinations were conducted to determine the homogeneity of the coating surface and the microstructural characteristics of the welded region. Wear tests were carried out to evaluate the mechanical strength and surface wear resistance of the coatings. Hardness tests were performed to compare the hardness values of the coating and the base metal regions. The study provides important insights into the performance of hardfacing coatings produced by FCAW-S, highlighting the effectiveness of the newly developed welding wire in achieving desirable microstructural and mechanical properties.

Keywords: FCAW-S, self-shielded, hardfacing, wear, hardness
© 2024 Published by ICMATSE

1.Introduction

While over 50% of the total failure is wear induced, 20% of the wear failures are caused by abrasion [1]. Hardfacing stands as a cost-effective method for depositing hard metal layers onto a comparatively

more resilient and softer substrate, aiming to enhance its wear resistance or restore deteriorated surfaces [2,3]. Welding is the most widely used hardfacing technique due to its low setup cost, wide availability, and suitability for on-site applications. The most frequently employed welding methods for

hardfacing include gas tungsten arc welding (GMAW, GTAW), oxyacetylene welding (OAW), plasma transferred arc welding (PTAW), submerged arc welding (SAW), and shielded metal arc welding (SMAW) [4].

In the realm of hardfacing applications, self-shielded flux-cored wires have gained prominence, particularly for the repair and maintenance of critical engineering components compromised by wear. These wires are ingeniously designed based on advanced principles of second and third generation self-shielding alloy configurations, incorporating significant alloying elements such as carbon, chromium, niobium and molybdenum [5]. Among cobalt and nickel-based alloys, iron-based Fe-Cr-C and Fe-C-B hardfacing alloys are regarded as the most economical and appropriate options for industries such as iron and steel, mining and construction, cement production, and thermal power plants [6-9].

In this present work, weldments were fabricated using a innovatively developed self-shielded hard cored wire underwent rigorous visual, mechanical, and microstructural analyses.

2. Experimental Procedures

The base metal used in this study is a standard hot-rolled low-carbon structural steel, classified as S355JR. The welding processes were carried out using a self-shielded flux-cored wire with 2.4 mm diameter, innovatively designed by the R&D center of Gedik Welding Inc., with a typical chemical composition of C: 0.05, Si: 0.015, Mn: 0.013, Cr: 0.027, Fe: Balance, corresponding to the DIN 8555: MF 10 GF 60 G standard. 3-pass overlay welding procedure were carried out at 300 A (Specimen A) and 400 A (Specimen B) on S355JR substrates with a 25×15×100 mm. dimensions. The interpass temperatures during welding were kept below 150°C. Following the welding process, the top layers of the samples were machined down by 0.6 mm to create a flat surface for the hardness and wear tests. Samples are sectioned by water cooled bandsaw for grinding, polishing, and later selectively etched by %2 Nital solution (HNO₃ + Ethanol) for the base metal and Aqua Regia (3x HCl + 1x HNO₃) for the weld metal. ZEISS MERLIN model scanning electron microscope (SEM) used cross-section microstructure observations. Vickers hardness tests were performed on EMCOTEST DURASCAN G5 universal hardness test device with 1kgf load on the cross-section from surface to the base metal and the results are converted into Hardness Rockwell C

(HRC) scale. 5 to 8 indentations were taken with at least 2 mm distance between them. A linear reciprocating wear test was performed using a UTS 10/20 Tribometer, following the ASTM G133-05 standard. The samples were subjected to tests under a nominal load of 20 N and a sliding speed of 200 mm/s. The test duration for each condition was set to 20.8 minutes, corresponding to a sliding distance of 250 m.

3. Results and Discussions

3.1 Wire Production and Welding Performance

The FCAW-S wire were produced with DC03 class low-alloy sheet with %44 flux ratio. During the production process, no issues such as sheet breakage, failure to form into a tubular shape, or flux spillage were encountered with the wire, and no problems were observed in its welding performance or weld seam. Transverse cracks, which are commonly seen in hardfacing welds and allow stress relief in the weld metal according to AWS A5.21 [10], were observed (Figure 1).

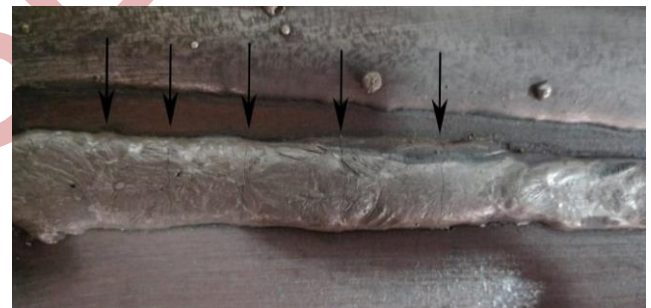


Figure 1. Transverse cracks on the weld bead.

3.1 Microstructures

The SEM microstructure of hardfacing layers is shown in Figure 2.

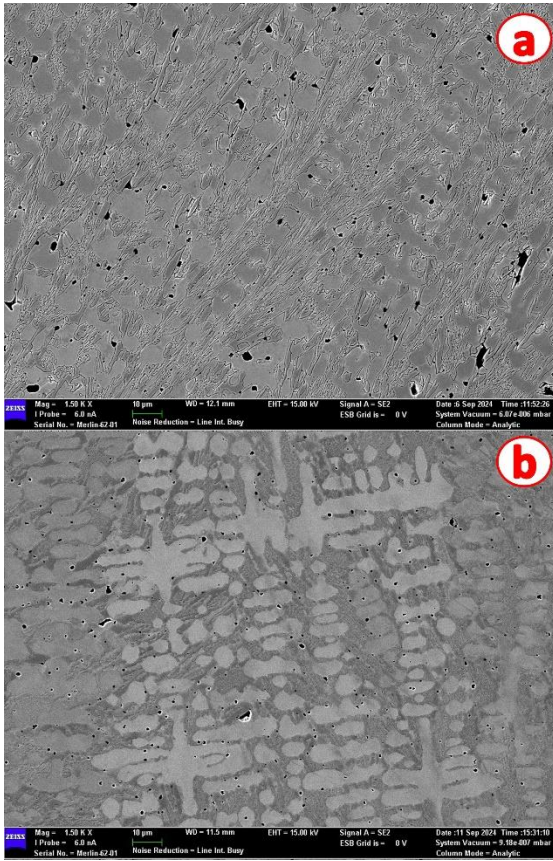


Figure 2. SEM images of a) sample A and b) sample B.

In the A specimen welded with 300 Amps, due to the relatively lower heat input and rapid cooling, fine dendritic formations have been observed. The light-colored phases predominantly consist of M_7C_3 carbides, with a small amount of $M_{23}C_6$ carbides also present. The dark-colored matrix is austenite, while martensite was also expected to be observed due to the rapid cooling. Further investigation with XRD is needed for presence of martensite and distribution of the other phases. The carbide network seems more continuous, providing potential wear resistance but possibly indicating some brittleness.

The dendritic and carbide formations are visibly more spaced out in specimen B, and the carbides seem more scattered, suggesting less uniform distribution. The larger dendrites could lead to reduced hardness, making the layer slightly more ductile but less wear-resistant. The slower cooling rate due to the higher heat input likely promoted the formation of coarser M_7C_3 carbides and much less amount of $M_{23}C_6$ carbides along the grain boundaries, with more retained austenite in the matrix.

3.3 Hardness Test

Cross-section hardness graphs are given in Figure 3. Mean hardness value of the base metal was found 185 HV1 which is equivalent to 13 HRC. Gradual decrease from surface to the base metal is visible in both specimens. This is due to massive hardness difference between highly alloyed weld metal and low-alloyed ductile base metal and the dilution occurred during welding.

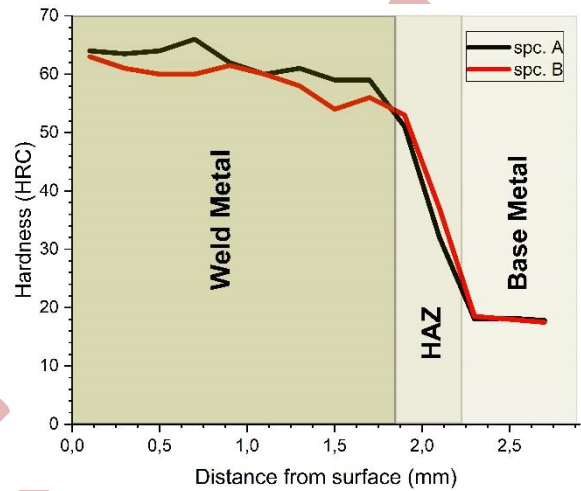


Figure 3. Cross-section hardness graph of the samples.

As predicted from the microstructure evaluations specimen A showed higher hardness values throughout the cross-section indentations due to the finer and well distributed carbide formation.

3.4 Wear Test

Figure 4 illustrates the coefficient of friction (COF) values in relation to the sliding distance of the hardfacing deposits.

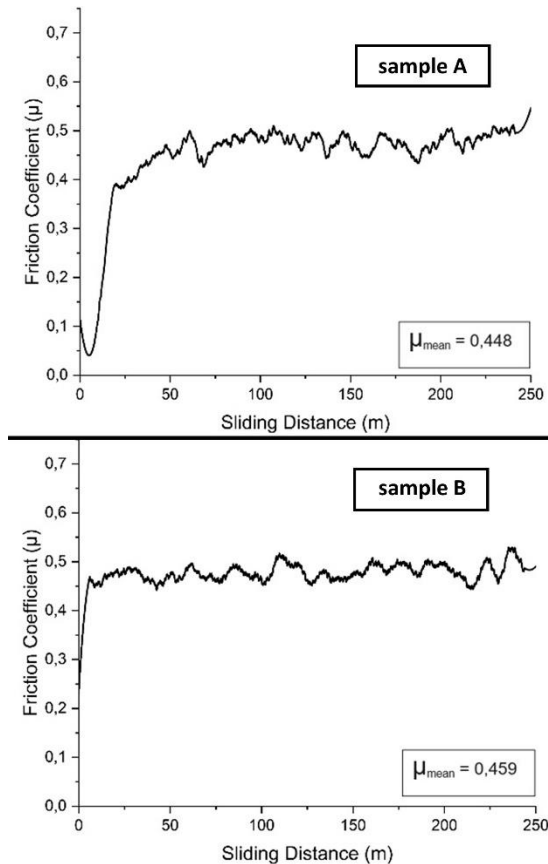


Figure 4. COF graphs of the samples.

Since the wear specimens were too heavy and was not possible to section smaller, weight loss could not be calculated. The coefficient of friction can indicate the accumulation patterns of wear debris. Although it is not possible to directly dictate a rule regarding the relationship between the coefficient of friction and wear resistance, materials with high wear resistance are generally expected to have a low coefficient of friction. Considering that the wear test was conducted under the same conditions, it can be

References

1. D. H. A. Jeffrey, R. Wilson, R. D. Daniel, and M. T. Kiser, *Abrasive Wear Failures*, vol. 11 (2002), Ohio, United States, ASM International.
2. Ugur Ozdemir, Mustafa Sozeri, Tayfun Findik, Volkan Kilicli, Effect of buttering on the wear behavior of the SMA welded hardfacing layer in a low-carbon steel, *Materials Testing*, 65 4 (2023), pp. 494-504. <https://doi.org/10.1515/mt-2022-0438>
3. Mustafa Sozeri, Ugur Ozdemir, Tayfun Findik, Halil Karakoc, Comparative Study of Hardfacing Applications on Structural Steel Surfaces to Improve Ballistic Properties, *Materials Today Communications*, 38 (2024), 107733, doi:10.1016/j.mtcomm.2023.107733.
4. M. Kirchgaßner, E. Badisch, and F. Franek, Behaviour of iron-based hardfacing alloys under abrasion and impact, *Wear*, 265 5-6 (2008), pp. 772–779. <https://doi.org/10.1016/j.wear.2008.01.004>.
5. M. Dumovic, D. Dunne, J. Norrish, H. Li, B.J. Monaghan, Effect of cooling rate on microstructural evolution and hardness of self-shielded arc weld deposits containing 1 wt% aluminium, *Welding in the World*, 62 (2018), pp. 685–697 <https://doi.org/10.1007/s40194-018-0568-8>.
6. S. Pawar, A. K. Jha, and G. Mukhopadhyay, Effect of different carbides on the wear resistance of Fe-based hardfacing alloys, *Int. J. Refract. Metals Hard Mater.*, 78 (2019), pp. 288–295, <https://doi.org/10.1016/j.ijrmhm.2018.10.014>.

said that the wear resistance of sample A is higher than that of sample B.

4. Conclusion

This study evaluated a novel self-shielded flux-cored arc welding (FCAW-S) wire for hardfacing applications on S355JR steel. Specimen A, welded at 300 A, displayed finer microstructures with better carbide distribution, resulting in higher hardness and improved wear resistance compared to specimen B, welded at 400 A, which showed coarser grains and reduced wear resistance.

Hardness tests confirmed a gradual decrease from the surface to the base metal, with specimen A maintaining higher hardness due to the finer carbide network. The wear test results aligned with this, showing lower friction and better wear performance for specimen A.

In summary, the novel FCAW-S wire proved effective in producing durable, wear-resistant coatings, particularly at lower amperages. These findings suggest that FCAW-S wires offer a viable alternative to conventional FCAW wires, providing effective hardfacing performance without the need for external shielding gases. Future work should focus on refining process parameters to enhance performance further.

Acknowledgements

The authors would like to thank The Scientific and Technological Research Council of Türkiye - TÜBİTAK (Project Number: 123M034) for the financial support of the study.

7. N. Yüksel and S. Şahin, Wear behavior–hardness–microstructure relation of Fe–Cr–C and Fe–Cr–C–B based hardfacing alloys, *Mater. Des.*, 58 (2014), pp. 491–498, <https://doi.org/10.1016/j.matdes.2014.02.032>.
8. Y. Wang, J. Gou, R. Chu, D. Zhen, and S. Liu, The effect of nanoadditives containing rare earth oxides on sliding wear behavior of high chromium cast iron hardfacing alloys, *Tribol. Int.*, 103 (2016), pp. 102–11, <https://doi.org/10.1016/j.triboint.2016.06.041>.
9. H. Durmuş, N. Çömez, C. Gül, M. Yurddaşkal, Yurddaskal M. Wear performance of Fe-Cr-C-B hardfacing coatings: dry sand/rubber wheel test and ball-on-disc test, *Int. J. Refract. Metals Hard Mater.*, 77 (2018), pp. 37–43, <https://doi.org/10.1016/j.ijrmhm.2018.07.006>.
10. AWS A5.21, Specification for Bare Electrodes and Rods for Surfacing, (2011), American Welding Society, Miami, USA.

ICMATSE 2024

Investigation of the performance of an ejector refrigeration system operating in critical mode

Abbaci Wissem Eddine

*Badji Mokhtar University- Mechanical Engineering Department, Phd student, Annaba, Algeria,
abbaci.w2209@yahoo.com.
ORCID: 0009-0009-5559-9587*

Boumaraf Latra

*Badji Mokhtar University- Mechanical Engineering Department, Professor, Annaba, Algeria,
l_boumaraf@yahoo.fr
ORCID: 0000-0002-8386-7413*

Cite this article: Wissem eddine, AB, Latra, B. Investigation of the performance of an ejector refrigeration system operating in critical mode. Int. Conf. Advanced. Mater. Sci. & Eng. HiTech. and Device Appl. Oct. 24-26 2024, Ankara, Turkiye

Abstract. The heat-powered ejector refrigeration machine is a favorable alternative to the compression refrigeration system in terms of minimizing energy use due to the use of a free energy source and helping in the reduction of CO₂ emissions in the atmosphere. As it's known, the performance of this system is related to the performance of its ejector. Indeed, the entrainment ratio of this device is often low and influenced by several parameters such as the nature of the used refrigerant, operational conditions (generator, evaporator and condenser temperatures) and geometrical parameters. In order to investigate the effects of the above mentioned parameters on ejector performance in critical mode, a thermodynamic model based on one-dimensional theory is established and simulated by the most commonly used software engineering equation solver (EES). The studied fluids are: R141b (reference fluid), R600, R600a, R290, R1270, R236fa, R245fa, R717, R134a, R1234yf and R1234ze. For fixed operational conditions, the simulation results showed that R717 is the best fluid followed by R1270, then R290.

Keywords: *refrigeration system; ejector; performance; modeling, EES software*
© 2024 Published by ICMATSE

Introduction

In order to fulfill the population's need for greater well-being, the use of refrigeration systems has expanded in modern times. In today's world, air-conditioning systems have brought about innovative changes in the rhythm that characterizes human lifestyles [1]. In view of this need, many researchers have analyzed a thermodynamic model in order to investigate the effect of fluid nature and the operational conditions on ejector refrigeration system performance [2].

In recent years, a lot of numerical and experimental research has been conducted on ejector refrigeration systems in order to improve their performances. Konstantinos Braimakis(2020) [3], Chen et al (2015) [4] presented the most comprehensive review on the state of the art of

ejector technology presenting The main aspects of design, operation and performance of ejector devices and The main research trends dealing with all ejector cooling cycles mentioned in the literature, while Besagni et al (2016) [5] reviewed the ejector technology, These studies provided all the detailed information on the ejector operating principle, working fluid selection and ejector technology. In this study, a one-dimensional mathematical model based on the real gas properties were conducted in order to evaluate both ejector and system performance in critical mode using several working fluids.

Materials and method

the investigated refrigeration system as it presented in figure 1 is composed from an: ejector, generator, condenser, evaporator, throttling device and pump.

The commonest working principle of this system is briefly explained as follows. The primary flow is the high-pressure flow emitted by the generator and enters the supersonic nozzle where it attracts the low-pressure flows coming from the evaporator, called secondary flow. The two flows are mixed at constant mixing chamber and leave the ejector after a pressure recovery in the diffuser. The mixed flow is then carried to the condenser. The resulting flow is divided into two streams. One goes through the expansion device to the evaporator. The remaining part is pumped back to the generator and completes the cycle.

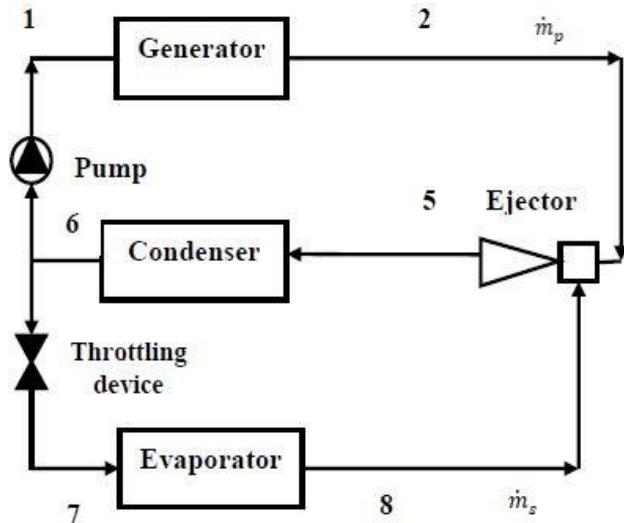


Figure 1. schematic diagram of ERS

a thermodynamic model was conducted by applying the mass balance, energy balance and momentum balance equations at several key point of the ejector (figure2) in order to identify the entrainment ratio U , coefficient of performance COP and the geometric parameter Φ . The above mentioned equation and performance characteristics are presented respectively by the following equations:

$$\dot{m} = \rho * V * A \quad (1)$$

$$h_i + \frac{v_i^2}{2} = h_o + \frac{v_o^2}{2} \quad (2)$$

$$P_i * A_i + \dot{m}_i * V_i = P_o * A_o + \dot{m}_o * V_o \quad (3)$$

$$U = \frac{\dot{m}_s}{\dot{m}_p} \quad (4)$$

$$COP = \frac{\dot{Q}_{Evap}}{\dot{Q}_{Gen} + \dot{W}_{Pump}} = U * \frac{\Delta h_{Evap}}{\Delta h_{Gen} + \dot{W}_{Pump}} \quad (5)$$

$$\Phi = \frac{A_{mixing\ chamber}}{A_{col}} \quad (6)$$

Where, “i” and “o” indicate respectively the inlet and the outlet.

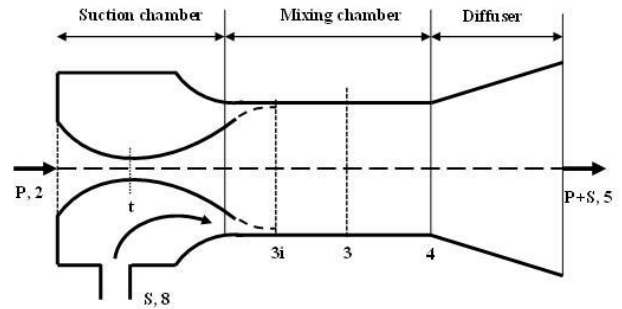


Figure 2. configuration of the ejector

Results and discussion

Model validation:

The experimental results of Huang [6] using R141b were employed in order to validate the accuracy of the developed 1_D model based on the real gas properties in a critical mode. In this part the experimental operational conditions were employed and generated the same as in the mentioned literature in order to obtain both the geometric parameter Φ and the entrainment ratio U . Then the obtained theoretical results were compared with the experimental results.

Validation with Huang results:

The Following figure3 (a & b) illustrate the comparison of the calculated theoretical results with the experimental data obtained from Huang studies. This comparison clearly shows that, in terms of geometric parameters Φ , the developed model achieves satisfactory results compared to the results obtained from Huang experiments. An average error of 5,3% for the tested cases for $Te=8$ as its showed in figure3(a). In the other hand, the calculated results of entrainment ratio U were in good agreement with Huang experimental U , an average error of 10% was recorded for $Te=8$ as its presented in figure3(b).

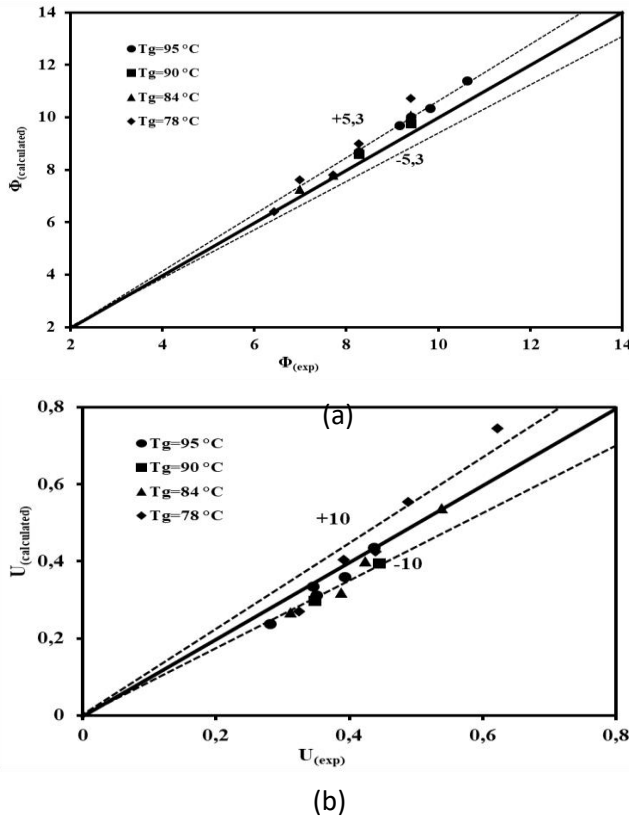


Figure3 (a-b). Comparison of the calculated Φ (a) and U (b) with Huang experimental results for $T_e=8$

The fluid nature effect:

For a fixed cooling capacity of 5kW, generator, condenser and evaporator temperatures equal to 85, 30 and 5°C, respectively. the simulation results showed that R717 is the best fluid followed by R1270, then R290 in term of COP, meanwhile, in term of entrainment ratio U , the R290 give the better result followed by R1270 then R600a. figure4 gives a better presentation of the fluid nature effect for the rest of the tested fluid.

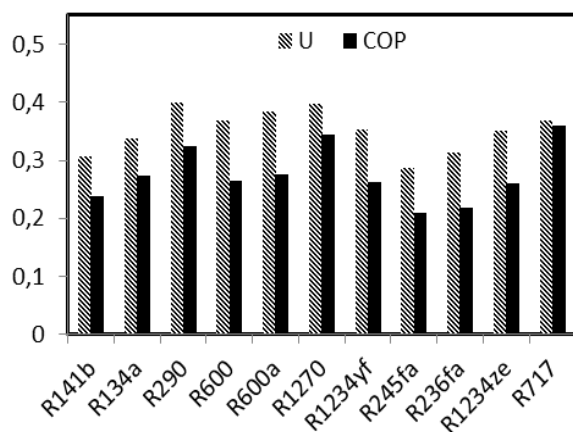


Figure 4. entrainment ratio U and COP comparison

Figure5 showed the difference between the critical geometric parameter Φ needed to generate 5kW of cooling capacity for the tested fluids

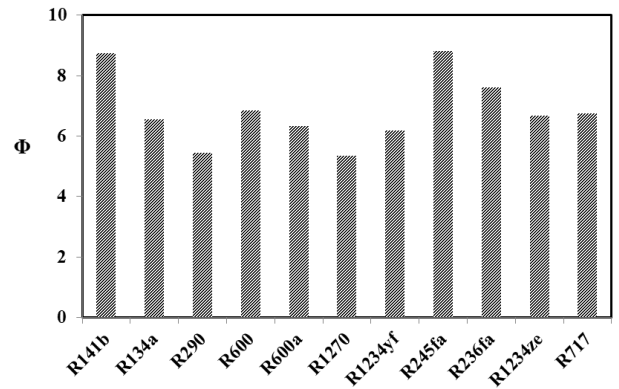


Figure 5. Geometric parameter Φ comparison

Where, R290 and R1270 need a small geometry to generate the desired cooling capacity, meanwhile, R245fa and R141b need a biggest geometry as its showed.

Operational parameters effect:

In this part, we focused in the investigation of the influence of the operational conditions for the best tested fluids.

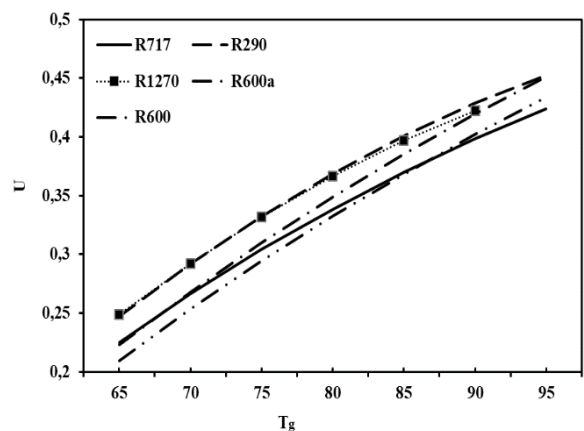


Figure 6. Variation of the entrainment ratio U with T_g

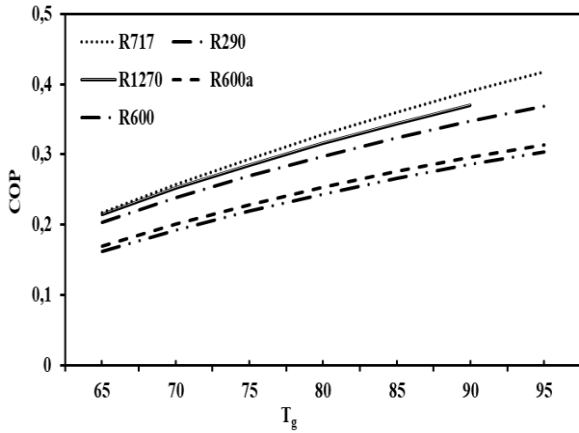


Figure 7. Variation of the COP with T_g

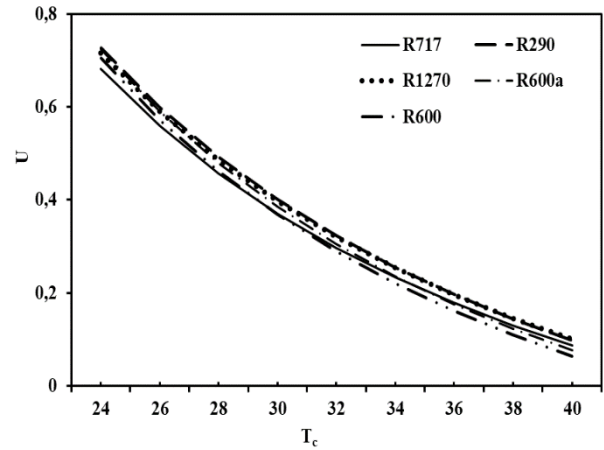


Figure 9. Variation of the entrainment ratio U with T_c

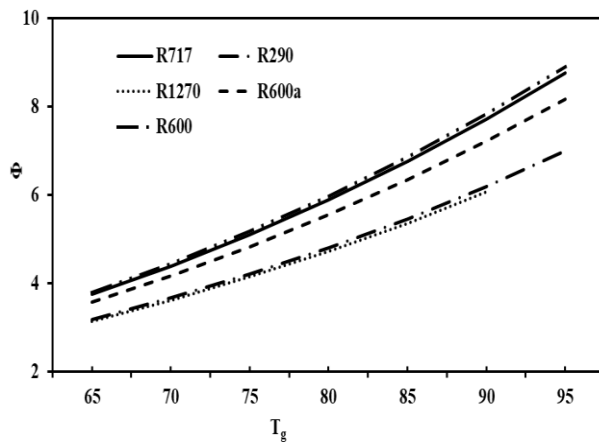


Figure 8. Variation of geometric parameter Φ with T_g

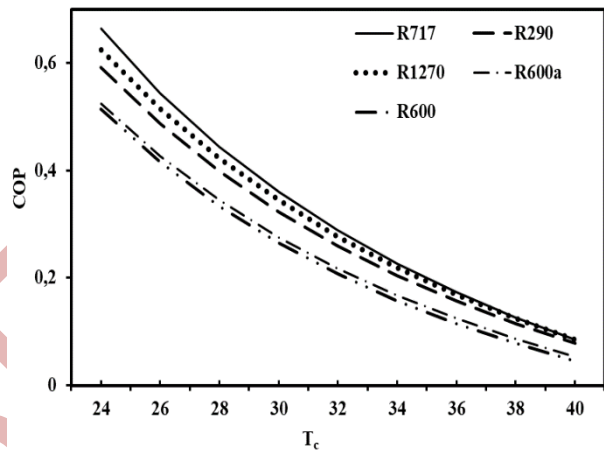


Figure 10. Variation of the COP with T_c

Figure 6 represent the variation of the critical entrainment ratio U with the generator temperature at a fixed cooling capacity of 5kW, $T_e=5^\circ\text{C}$ and $T_c=30^\circ\text{C}$, it's noticed that the entrainment ratio increase with the increase in the generator temperature, it's also noticed that for R600a the pattern of U become closer to the higher pattern of R290 at higher generator temperature. Meanwhile, when the generator temperature is above the critical temperature that causes the dysfunction of the system (R1270 case at 95°C). The same trend of evolution of COP is noticed in figure 7, where, R717 has the biggest value of COP. The effect of specific latent heat is remarked in this part (R717 has the biggest value of latent heat).

Figure 8 depicts the variation of the critical Φ with the generator temperature, it's showed that Φ increase with the increase of T_g , where, R1290 and R290 have the smallest values.

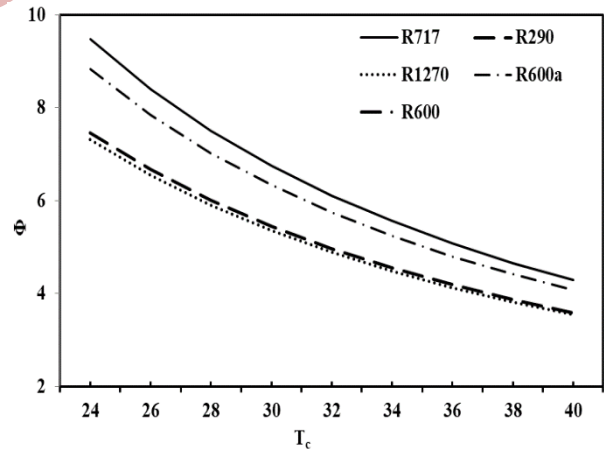


Figure 11. Variation of geometric parameter Φ with T_c

The previous figures (9,10 and 11) showed that the U , COP and Φ decrease with the increase of the condenser temperature. What can explain the decrease in U with the increase in T_c , is that the increase in the condenser temperature is followed by a large increase in the mixing pressure P_3 , which leads to a considerable reduction in the difference between the secondary flow pressure P_e and the mixing pressure P_3 , while the evaporator pressure

remains constant. As a result, there is less secondary flow to be entrained in the ejector. As it's mentioned below, the COP is related to U so, the pattern of variation for the tested fluid follow the same trend of variation of the entrainment ratio U

As a conclusion, the obtained result showed that the system COP, the entrainment ratio and the main geometrical parameter of ejector increase with generator and evaporator temperatures and decrease with condenser temperature in operating critical mode.

References

1. Anand S, Gupta A, Tyagi SK. Solar cooling systems for climate change mitigation: a review. *Renew Sustain Energy Rev* 2015;41:143–61.
2. Arvind Kumar, Surendra Kumar Yadav, Virendra Kumar, Abhishek Kulkarni. A comprehensive exploration of ejector design, operational factors, performance metrics and practical applications. *J of the Braz Soc of Mech Sci and Engi* (2024) 46:39, doi.org/10.1007/s40430-023-04618-8
4. Braimakis K, Solar ejector cooling systems: A review, *Renewable Energy*.2020; 164:566-602.
5. J. Chen, S. Jarall, H. Havtun, B. Palm, A review on versatile ejector applications in refrigeration systems, *Renew. Sust. Energ. Rev.* 2015;49: 67–90.
6. Giorgio Besagni, Riccardo Mereu, Fabio Inzoli. Ejector refrigeration: A comprehensive review. *Renewable and Sustainable Energy Reviews*. 2016;53:373–407.

The Effect of Bi[(Ti_{0.9}Zr_{0.1})_{0.5}Zn_{0.5}]O₃ Doping on the Structural, Dielectric, and Optical Properties of BiFeO₃

Nihed Ben Salah

Laboratory of Multifunctional Materials and Applications (LaMMA), Faculty of Sciences of Sfax, University of Sfax, BP 1171, 3000 Sfax, Tunisia.

Najmeddine Abdelmoula

Laboratory of Multifunctional Materials and Applications (LaMMA), Faculty of Sciences of Sfax, University of Sfax, BP 1171, 3000 Sfax, Tunisia.

Abstract. The multiferroic material BiFe_{1-x}[(Ti_{0.9}Zr_{0.1})_{0.5}Zn_{0.5}]_xO₃, with various substitution rates including $x = 0$ and $x = 0.1$, was synthesized using the solid-state reaction technique. All compositions exhibited a distorted rhombohedral structure with R3c space group, as confirmed by XRD. A significant impurity phase (Bi₂₅FeO₄₀) was observed in both pure and doped BFO samples. UV-vis spectroscopy indicated that the optical band gap decreased with substitution. The smallest band gap, $E_g = 1.80$ eV, was observed for BiFe_{1-x}[(Ti_{0.9}Zr_{0.1})_{0.5}Zn_{0.5}]_xO₃. Highlighting the potential of doped BFO for applications in the visible spectrum, making it suitable for photocatalytic and solar cell applications.

I. Introduction

Multiferroics are a unique category of materials that exhibit both ferroelectric and ferromagnetic properties simultaneously. They have garnered significant attention in recent years due to their potential for various important technological applications [1]. The Bismuth Ferrite is the most studied multiferroic as it exhibits ferroelectric ($T_C \sim 1100$ K) and antiferromagnetic ($T_N \sim 643$ K) ordering at room temperature. While the ferroelectric order in BiFeO₃ emanates from the stereochemical activity of 6s² lone pair of Bi³⁺, the antiferromagnetic order originates from the spin canting structure giving spiral modulation with a long cycloid periodicity of 62 nm [2]. BFO crystal exhibits rhombohedral distorted perovskite structure with R3c space group ($a_r = 3.96$ Å and $\alpha_r = 0.6^\circ$) [3]. Furthermore, synthesizing a single-phase BFO is challenging due to factors such as oxygen vacancies, mixed valence states of Fe ions, and the presence of impurity phases like Bi₂₅FeO₄₀. These issues can enhance electrical conductivity, which presents significant drawbacks for device applications. To address these challenges and minimize leakage currents, various strategies have been employed, including the adoption of different processing techniques [4], substituting different atoms at either the A or B sites, or at both, has proven to be an effective strategy for modifying the aforementioned properties. However, despite significant advancements in BFO research, creating a low-

temperature synthesis method that avoids the formation of intermediate impurity phases remains a challenge [5]. On the other hand, BFO is notable as a promising lead-free ferroelectric material due to its remarkable intrinsic polarization, which exceeds 100 mC cm⁻² [6]. Doping at site A or B enhances the multiferroic properties of BFO [7]. This work aims to improve the multiferroic properties of BFO. Additionally, substituting Fe³⁺ with Ti⁴⁺ and Zr⁴⁺ has been shown to enhance the electrical properties of BFO [8]. Furthermore, the incorporation of divalent ions like Zn²⁺ into BFO thin films has led to a significant reduction in leakage current and an improvement in ferroelectric properties [9].

II. Methods

The BiFeO₃ and BiFe_{1-x}[(Ti_{0.9}Zr_{0.1})_{0.5}Zn_{0.5}]_xO₃ ceramics were synthesized using the standard solid-state reaction method. The substitution rates of interest in this study are $x = 0.00$ and $x = 0.1$.

The oxide powders (Bi₂O₃; Fe₂O₃; TiO₂; ZrO₂; and ZnO) are dried in an oven maintained at 180°C for 1 hour. These oxides in powder form are weighed in stoichiometric proportions: $\frac{1}{2}$ Bi₂O₃ + $(\frac{1-x}{2})$ Fe₂O₃ + (0,45.x)TiO₂ + (0,05.x)ZrO₂ + (0,5.x)ZnO \Rightarrow BiFe_{0.9}[(Ti_{0.9}Zr_{0.1})_{0.5}Zn_{0.5}]_{0.1}O₃

The powder was finely ground in an agate mortar for 2 hours to ensure a homogeneous mixture. The milled powder was compacted into pellets measuring 13 mm in diameter and 10 mm in

thickness under a uniaxial load of 100 MPa for 5 minutes at room temperature. The pellet was initially calcined at 650 °C for 2 hours. Afterward, it was ground again for 2 hours before undergoing a second calcination at 750 °C for 2 hours to promote the desired phase formation. Following this process, the resulting powder was ground for an additional 2 hours and then pressed under 100 MPa into disks with a diameter of 8 mm and a thickness of approximately 1 mm. Finally, the pellets were sintered at 850°C for 2 hours, followed by furnace cooling.

The phase purity of the synthesized samples was evaluated using an X-ray diffractometer equipped with CuK α radiation ($\lambda = 1.5405 \text{ \AA}$).

Raman spectra of the sintered samples were obtained at room temperature using the HORIBA Jobin-Yvon Labram, HR 4600 h 800 equipped with a diode laser emitting a green line ($\lambda = 532 \text{ nm}$).

UV-visible diffuse reflectance spectra of the powder samples were measured using a LAMBDA 365 UV/Vis Spectrophotometer.

Impedance measurements were carried out on metallized pellets using a broadband dielectric spectrometer.

III. Results and discussions

1. Structural characterization

To examine the influence of coding (Zr, Ti, Zn) on the crystal structure of BFO, X-ray diffraction (XRD) measurements were carried out at room temperature. Figure 1 shows the XRD patterns of the doped Bfo samples. The high-intensity peaks observed indicate the phase purity and good crystallinity of the prepared ceramic. However, traces of a secondary phase, specifically the selenite-type Bi₂₅FeO₄₀, were detected in the doped sample, a common finding in the solid-state synthesis of BFO-based materials, as noted in various studies.

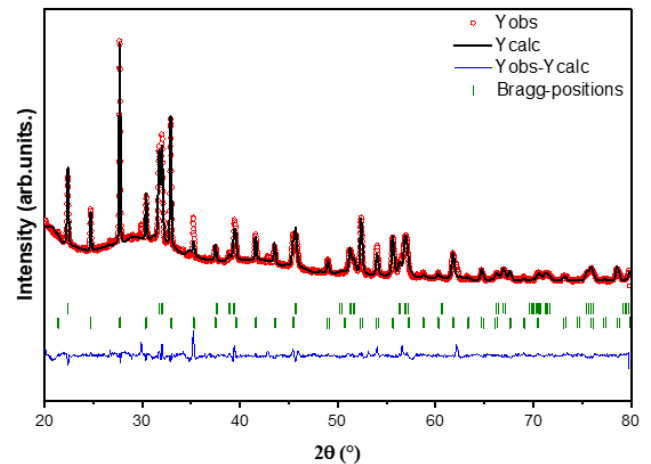


Figure 1. X-ray diffractogram of the compound $\text{BiFe}_{0.9}[(\text{Ti}_{0.9}\text{Zr}_{0.1})_{0.5}\text{Zn}_{0.5}]_{0.1}\text{O}_3$.

The identified diffraction peaks correspond to the R3c space group of a rhombohedral structure [10]. A shift in peak position towards lower 2θ values is observed with increasing zn^{2+} , Ti^{4+} and zr^{4+} content. This shift can probably be attributed to the increase in network parameters. To further examine the X-ray diffraction data, a Rietveld refinement of the doped BFO diagrams was performed using the FullProf program to provide detailed crystal structure parameters [11]. Here, two-phase refinements were used to identify the amounts of BFO phase and Bi₂₅FeO₄₀ phase impurity in the prepared sample.

2. Vibrational analysis

Raman spectroscopy is a powerful technique for investigating short-range ordered structures and local symmetries in various materials. This method leverages the scattering of monochromatic light to provide insights into molecular vibrations, which are indicative of structural characteristics. Figure 3 presents the Raman scattering spectra of both undoped and doped BFO ceramics, obtained at room temperature using an excitation wavelength of 532 nm. According to group theory, the BiFeO₃ compound with rhombohedral structure and space group R 3 c exhibits 13 phonon modes active in Raman spectroscopy: $G = 4 A_1 + 9 E$ [12]. In our spectrum (Fig.2) we observe 10 phonon modes in the range 50 to 800 cm^{-1} instead of the expected 13.

To better understand the changes observed, we have divided the spectra into three regions:

* Region 1 between 50 and 235 cm^{-1} : Four bands are observed: E_1 , A_{1-1} , A_{1-2} and A_{1-3} , at room temperature. Variations in the low-frequency A_1 modes of the $\text{BiFe}_{0.9}[(\text{Ti}_{0.9}\text{Zr}_{0.1})_{0.5}\text{Zn}_{0.5}]_{0.1}\text{O}_3$

compound are associated with changes in the occupancy of Bi atoms in the perovskite unit.

The A_{1-2} and A_{1-3} modes, associated with the Fe atoms responsible for magnetism, showed displacements.

This shift is attributed to the incorporation of Ti, Zr and Zn, leading to an increase in disorder.

*Region 2 between 235 and 400 cm^{-1} : The E modes observed in this region are referred to in the literature as corresponding to the vibrations of Fe-O bonds. There is a high-frequency shift in the modes compared with the undoped compound. This shift can be attributed to modifications of the Fe-O bonds following the substitution of Ti, Zr and Zn on the Fe sites.

*Region 3 between 400 and 800 cm^{-1} : The bands observed towards higher frequencies, mainly in the area between 400 and 800 cm^{-1} , are attributed to vibrations of oxygen atoms. Moreover, the bands in this frequency range are broadening.

This reflects the increase in substitution-induced disorder.

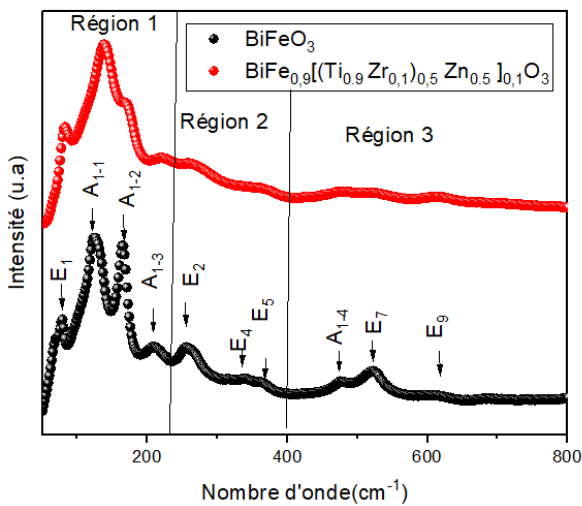


Figure 2. The Raman spectra in the range of 50-800 cm^{-1} of BiFeO_3 and $\text{BiFe}_{0.9}[(\text{Ti}_{0.9}\text{Zr}_{0.1})_{0.5}\text{Zn}_{0.5}]_{0.1}\text{O}_3$ ceramics at room temperature.

3. Dielectric measurements

Dielectric properties of BFO are of significant interest due to its multiferroic nature, exhibiting both ferroelectric and magnetic ordering.

For BFO (Fig.3), we observed an anomaly at a temperature $T_m = 450$ K close to the Néel

temperature. BiFeO_3 exhibits two main transitions: a structural phase transition at Curie temperature $T_c = 1103$ K and a magnetic transition at Néel temperature $T_N = 640$ K

[13].

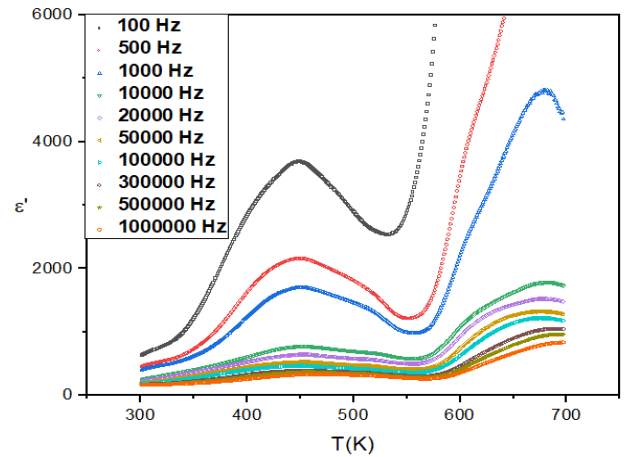


Figure 3. Variation of ϵ' of BiFeO_3 compounds as a function of temperature and for different frequencies.

At $T_m = 450$ K, the permittivity ϵ' associated with this maximum decreases rapidly from 1700 (1kHz) to 770 (10kHz) as the frequency increases, with no change in temperature T_m , suggesting that this transition can be attributed to dipolar relaxation. A second anomaly is observed at a temperature $T_N = 675$ K for a frequency of 1 kHz. The dielectric permittivity ϵ' related to temperature T_N decreases from 4800 (1kHz) to 1769 (10 kHz) with increasing frequency. We also note that the Néel temperature and dielectric permittivity ϵ'_{max} associated with T_N shift slightly towards higher temperatures, demonstrating the diffuse nature of this transition. Figure 4 shows the variation in ϵ' of our second compound $\text{BiFe}_{0.9}[(\text{Ti}_{0.9}\text{Zr}_{0.1})_{0.5}\text{Zn}_{0.5}]_{0.1}\text{O}_3$ as a function of temperature and for different frequencies. This result shows the significant effect of Fe substitution by the 3 elements Ti / Zr / Zn. Indeed, we note that the temperature T_m shifts towards higher temperatures compared with the temperature ($T_m = 450$ K) of pure BFO, at around 512K. On the other hand, the temperature is lower than that of pure BFO at $T_N = 636$ K. The effect of substitution can also be seen in the lower T_c of BFO at 703K. This closeness of the T_N and T_c transition temperatures in our substituted compound may favor increased magnetoelectric coupling in this material. We also note that as frequency increases, the temperature $T_m = 512$ K shifts, while T_N and T_c remain unchanged.

Furthermore, the dielectric permittivity ϵ' of the $\text{BiFe}_{0.9}[(\text{Ti}_{0.9}\text{Zr}_{0.1})_{0.5}\text{Zn}_{0.5}]_{0.1}\text{O}_3$ compound decreases as a function of frequency from 900 (1kHz) to 321(10

kHZ), describing the phenomenon of dielectric dipolar relaxation.

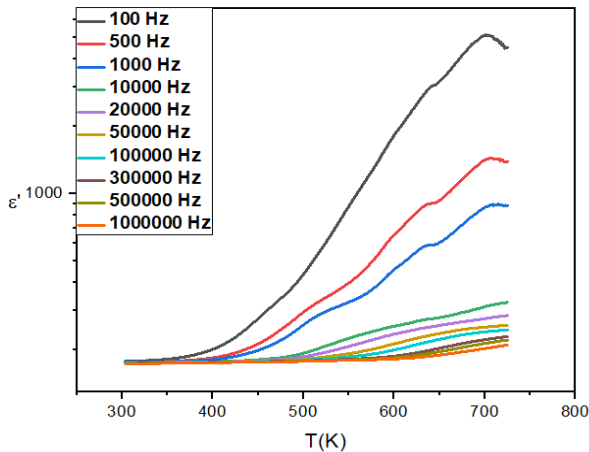


Figure 4. Variation of ϵ'_r of $\text{BiFe}_{0.9}[(\text{Ti}_{0.9}\text{Zr}_{0.1})_{0.5}\text{Zn}_{0.5}]_{0.1}\text{O}_3$ compounds as a function of temperature and for different frequencies.

4. Optical properties

To investigate the optical properties of bismuth ferrite (BFO), UV-Vis spectroscopy measurements were performed, providing valuable insights into its light absorption characteristics and band gap energy.

Fig. 5 displays the results of these measurements taken at RT.

We recorded reflectance spectra in the UV-visible range, from 200 to 800 nm, at room temperature, as shown in Figure 5.

BiFeO_3 exhibits quite low reflectance in the visible spectrum range (400-700 nm), suggesting that it absorbs much of the incident visible light in this wavelength range. Furthermore, in the near infrared (700 nm), the reflectance of BiFeO_3 gradually increases, reaching higher values. This increase in reflectance is linked to the decrease in absorption in this region of the spectrum. The reflectance of $\text{BiFe}_{0.9}[(\text{Ti}_{0.9}\text{Zr}_{0.1})_{0.5}\text{Zn}_{0.5}]_{0.1}\text{O}_3$ decreases compared to that of the undoped compound which is explained by the doping with elements such as Ti, Zr and Zn in the material.

We conclude that doping with Ti, Zr and Zn improves absorption.

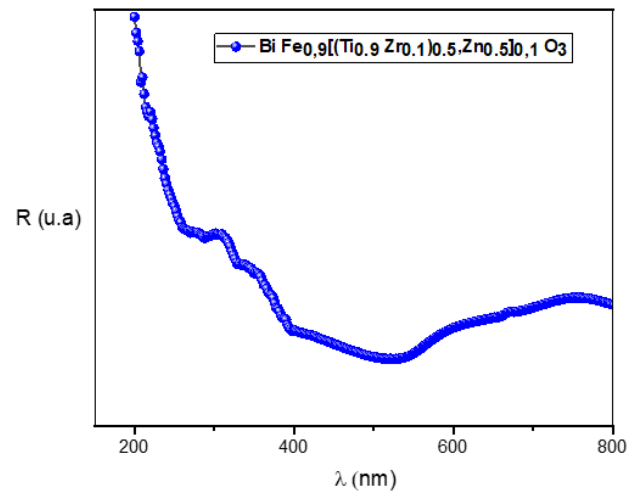


Figure 5. the reflectance spectra of the compounds $\text{BiFe}_{0.9}[(\text{Ti}_{0.9}\text{Zr}_{0.1})_{0.5}\text{Zn}_{0.5}]_{0.1}\text{O}_3$, at room temperature.

4.1. Energy Gap:

The band gap energy is essential in determining the electrical properties of the material. The transfer of electrons can only occur when the energy of the incident radiation $h\nu$ is equal to or greater than the energy of this band gap.

The Kubelka-Munk method is used to analyze the reflection spectra of scattered light:

$$F(R) = \frac{(1-R)^2}{2R} \quad [14]$$

The band gap is determined by extrapolating the linear part of the optical absorption curve up to the axis $h\nu = 0$.

For the compound BiFeO_3 , the energy gap $E_g = 2.10$ eV [15], typical of a direct transition semiconductor. For the doped compound (Fig.6), the energy gap $E_g = 1.80$ eV. This value indicates a slightly lower bandgap than that of BiFeO_3 , likely due to substitution and associated effects on the electronic structure of the material. Energy gap values are crucial for determining the optical properties of materials.

Doping with Ti, Zr and Zn reduces the gap energy, indicating a better ability to absorb visible light.

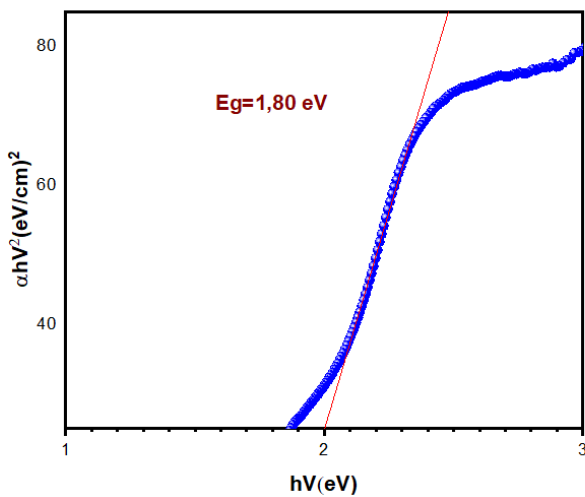


Figure 6. The evolution of $(ahV)^2$ as a function of the energy (hV) of the compound.

IV. Conclusion

In this paper, $\text{BiFe}_{0.9}[(\text{Ti}_{0.9}\text{Zr}_{0.1})_{0.5}\text{Zn}_{0.5}]_{0.1}\text{O}_3$ and BFO were successfully prepared using a solid-solid method. The addition of X-ray diffraction analysis showed that the substitution by Ti/Zr/Zn in the Fe site did not affect the symmetry of BiFeO_3 . Dielectric studies show dielectric properties due to the existence of three interesting transitions at different temperatures (T_m , T_N and T_c). Raman spectroscopy analysis confirms the correlation between vibrational and structural properties and we can classify these compounds among the family of semiconductors.

References

1. Srivastava, A., Singh, A. K., Srivastava, O. N., Tewari, H. S., Masood, K. B., & Singh, J. Magnetic and dielectric properties of La and Ni Co-substituted BiFeO_3 nanoceramics. *Frontiers in Physics*, 8, 282. (2020). <https://doi.org/10.3389/fphy.2020.00282>
2. Gadhoumi, F., Lahmar, A., Abdelmoula, N., El Marssi, M., & Khemakhem, H. The effects of N_2 atmosphere annealing on the physical properties of $\text{BiFe}_{0.5}\text{Mn}_{0.5}\text{O}_3$ ceramic. *Journal of Alloys and Compounds* 877 (2021): 160323. (2021). <https://doi.org/10.1016/j.jallcom.2021.160323>
3. Kubel F, Schmid H. Structure of a ferroelectric and ferroelastic monodomain crystal of the perovskite BiFeO_3 . *Acta Crystallogr B Struct Sci. B.* (1990) 46:698–702. doi: 10.1107/S0108768190006887
4. Adineh, Zahra, and Ahmad Gholizadeh. "Hydrothermal synthesis of Ce/Zr co-substituted BiFeO_3 : R 3 c-to-P 4 mm phase transition and enhanced room temperature ferromagnetism." *Journal of Materials Science: Materials in Electronics* 32.22 (2021): 26929-26943. <https://doi.org/10.21203/rs.3.rs-304914/v1>
5. Kumar M, Yadav KL. Study of room temperature magnetoelectric coupling in Ti substituted bismuth ferrite system. *J Appl Phys.* (2006) 100:074111. doi: 10.1063/1.2349491.
6. Lebeugle, Delphine, et al. "Very large spontaneous electric polarization in BiFeO_3 single crystals at room temperature and its evolution under cycling fields." *Applied Physics Letters* 91.2 (2007). <https://doi.org/10.1063/1.2753390>.
7. Prasad, N. P., Rohnke, M., Verheijen, M. A., Sturm, J. M., Hofmann, J. P., Hensen, E. J., & Bieberle-Hütter, A. Role of Excess Bi on the Properties and Performance of BiFeO_3 Thin-Film Photocathodes. *ACS Applied Energy Materials*, 6(24), (2023)12237-12248. <https://doi.org/10.1021/acsaem.3c01926>.
8. Sati, P. C., Kumar, M., Arora, M., Tomar, M., & Gupta, V. Effect of Zr substitution on structural, magnetic, and optical properties of $\text{Bi}_{0.9}\text{Dy}_{0.1}\text{Fe}_{1-x}\text{Zr}_x\text{O}_3$ multiferroic ceramics prepared by rapid liquid phase sintering method. *Ceramics International*, 43(6) (2017): 4904-4909. <https://doi.org/10.1016/j.ceramint.2016.12.141>.
9. Yang, S., Zhang, F., Xie, X., Guo, X., Zhang, L., & Fan, S. Effects of transition metal (Cu, Zn, Mn) doped on leakage current and ferroelectric properties of BiFeO_3 thin films. *Journal of Materials Science: Materials in Electronics*, 28 (2017):14944-14948.
10. Ouertani, A., Abdelkafi, Z., Khemakhem, H., & Randrianantoandro, N. Investigating the influence of Cu and Ti substitution on the structural, optical, and dielectric properties of BiFeO_3 . *RSC advances*, 14(20) (2024): 14080-14090. DOI: [10.1039/D4RA01850H](https://doi.org/10.1039/D4RA01850H).
11. Yacoubi, A. E., Massit, A., Moutaouik, S. E., Rezzouk, A., & Idrissi, B. C. E. Rietveld refinement of the crystal structure of hydroxyapatite using X-ray Powder Diffraction. *American Journal of Materials Science and Engineering* 5.1(2017): 1-5. DOI: 10.12691/ajmse-5-1-1.
12. Cazayous, M., Malka, D., Lebeugle, D., & Colson, D. Electric field effect on BiFeO_3 single crystal investigated by Raman spectroscopy. *Applied physics letters*, 2007, vol. 91, no 7. <https://doi.org/10.1063/1.2771380>.
13. Fischer, P., Polomska, M., Sosnowska, I., & Szymanski, M. Temperature dependence of the crystal and magnetic structures of BiFeO_3 . *Journal of Physics C: Solid State Physics*, 1980, vol. 13, no 10, p. 1931. DOI 10.1088/0022-3719/13/10/012.
14. Yakuphanoglu, Fahrettin. "Electrical characterization and device characterization of ZnO microring shaped films by sol-gel method." *Journal of Alloys and Compounds* 507.1 (2010): 184-189. <https://doi.org/10.1016/j.jallcom.2010.07.151>
15. MCDONNELL, Kevin A., WADNERKAR, Nitin, ENGLISH, Niall J., et al. Photo-active and optical properties of bismuth ferrite (BiFeO_3): An experimental and theoretical study. *Chemical Physics Letters*, 2013, vol. 572, p. 78-84. <https://doi.org/10.1016/j.cplett.2013.04.024>.

Gas Metal Arc Weldability of Strenx 700MC Steel with Flux Cored Filler Metal

Serhat AKSOY

Safety Respect, 41455, Kocaeli, Türkiye,
serhat-aksoy@outlook.com.tr
ORCID: 0009-0008-5689-9330

Ramazan KAÇAR

Karabük Üniversitesi, Metallurgy and Materials Engineering, 78050, Karabük, Türkiye,
rkacar@karabuk.edu.tr
ORCID: 0000-0002-3903-1838

Samet NOHUTÇU

Karabük Üniversitesi- Mechanical Engineering, 78050, Karabük, Türkiye,
sametnohutcu@karabuk.edu.tr
ORCID: 0000-0002-2600-3993

Hayriye Ertek EMRE

Karabük Üniversitesi, Metallurgy and Materials Engineering, 78050, Karabük, Türkiye,
hayriyeertek@karabuk.edu.tr
ORCID: 0000-0002-8218-037X

Cite this paper as: Aksoy, S, Kaçar, R, Nohutçu, S, Ertek Emre, H. Gas Metal Arc Weldability of Strenx 700MC Steel with Flux Cored Filler Metal. Int. Conf. Advanced. Mater. Sci.& Eng. HiTech.and Device Appl.Oct. 24-26 2024, Ankara, Turkiye

Abstract. The weldability of Strenx 700MC steel is very important, as it is preferred in the manufacture of transport vehicles, cranes, mining vehicles and machinery because it reduces costs. The joining process uses the traditional fusion welding method, the GMAW method with solid filler wire. The main disadvantage of this method is that the loss of alloying elements cannot be amortised in GMAW applications with solid filler metal. Flux-cored gas metal arc welding (FCGMAW) is a welding process that uses filler metal in the form of a mineral-filled tube to amortise the loss of alloying elements. The advantages of this method include the production of high-quality weld metal, smooth appearance of welds, reduced need for pre-cleaning, reduced distortion and residual stress, and the weldability in all positions. For this purpose, the FCGMAW capability of Strenx 700MC steel was investigated in this study. The mechanical properties of the weldment were determined by tensile testing and hardness measurement, and its formability was determined by a three-point bend test. In addition, the microstructure of the weldment and the fracture surfaces of the test specimens were examined. The results showed that the strength and formability of the Strenx 700MC-Strenx 700MC joint were within acceptable limits.

Keywords: Strenx 700MC steel, FCGMAW method, Weldability, Mechanical properties and microstructure
© 2024 Published by ICMATSE

The main problem in the welding of HSLA steels is the loss of superior mechanical properties of the base metal due to localized softening due to thermal cycling. For this reason, research on the welding of these steels has been concentrated in this field [1]. It is a subject that needs to be determined and investigated whether local softening occurs in the

joints made with cored wire [2]. In this context, FCGMAW welding capability of commercially available Strenx 700MC steel was investigated in this study [3–5]. The mechanical properties of the joint were determined by tensile test and hardness measurement, and the formability was determined by three-point bending test. Strenx 700MC steel

plate, the chemical composition of which is given in Table 1, was prepared in dimensions of 100 x 500 x 5 mm³.

Table 1. Chemical composition of the steels used in the study (% weight).

Strenx 700MC	C	Si	Mn	P	S	Cr	Ni	Mo	Cu	Ti
	0,067	0,036	1,85	0,019	0,002	0,038	0,049	0,019	0,021	0,126
Filler metal	Al	V	Co	W	Nb	Pb	Sn	Zn	Se	Fe
	0,037	0,006	0,006	0,034	0,056	0,005	0,002	0,002	0,008	97,6
Filler metal	C	Si	Mn	P	S					
	0,08	0,5	1,30	0,015	0,015					

60° V weld groove was opened on Strenx 700MC steel plate. SAF-PRO DIGIWAVE 3 520-R COOLER 3PW/Water cooled GMAK machine was used in the welding process. Ø1.2 mm flux cored filler metal in accordance with EN ISO 17632-A standard was used for joining. Three three-point bending test specimens were prepared based on EN910 standard. Hardness was measured using a Vickers FV-700 SHIMADZU microhardness tester which covered the weld metal, HAZ and base metal. For metallographic examination, microstructure images were taken after 5s etching with 2% nital on the sample prepared by classical metallography method. In the study, XRD measurements were taken after the fracture zones of the tensile specimens were powderised by mechanical grinding.

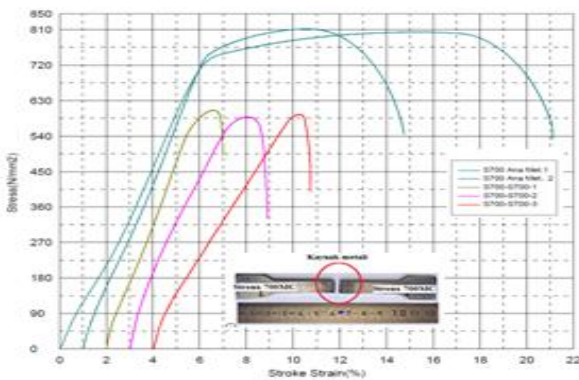


Figure 1. Weldment and base material stress-strain curves and weldment fracture zone.

The strength of the specimen welded by FCGMAW method was found to be more than two thirds of

References

1. Satoh, T., A. S., N. T. L. and H. Y., "The fatigue life of the spot welded joint under a repeated load of R = -1. Comparison of mild steel and high strength steel: Welding in the World (1996) 37 (1), 12–15", *International Journal of Fatigue*, 19 (8–9): 659 (1997).
2. Nový, F., Petrů, M., Trško, L., Jambor, M., Bokůvka, O., and Lago, J., "Fatigue properties of welded Strenx 700 MC HSLA steel after ultrasonic impact treatment application", *Materials Today: Proceedings*, 32: 174–178 (2019).
3. Trško, L., Lago, J., Jambor, M., Nový, F., Bokůvka, O., and Florková, Z., "Microstructure and residual stress analysis of Strenx 700 MC welded joint", *Production Engineering Archives*, 26 (2): 41–44 (2020).
4. Köçük Fatih, "Östenitik paslanmaz çeliklerin kaynağında kaynak yönteminin ısı tesiri altında kalan bölgeye etkisinin incelenmesi", Yüksek Lisans Tezi, *Gazi Üniversitesi Fen Bilimleri Enstitüsü*, Ankara, 14-49, (2000).

the strength of the base metal but lower than the minimum required YS and UTS of the base metal (Fig. 1).

Macro views of the test specimens folded 180° during the test process are shown in Fig. 2.

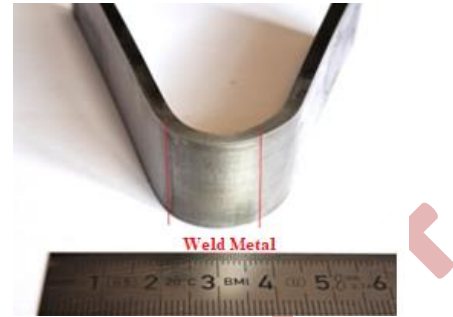


Figure 2. Macro view of the weldment after bending test.

As a result of the test, no crack formation was observed on the weld cap, weld bead surfaces and weld root.

- Depending on the cooling rate regime, the weld metal microstructure is mainly composed of phases such as acicular ferrite and bainite.
- The strength of the joint was more than two thirds of the strength of the base metal and within the acceptable range. The %EL of the joint was lower than that of the base metal and the filler metal.
- In the weldment, the hardness of the base metal averaged 267HV_{0.1}, while the hardness, which increased slightly in the HAZ transition, reached 290HV_{0.5} and then decreased as it progressed towards the weld metal and decreased to 240HV_{0.5}.
- In the bending test, no crack formation was observed on the weld cap and root as well as on the weld bead surfaces. The fact that the weldment, whose elongation decreased compared to the base metal, was not damaged during the test indicates that the formability is acceptable.

5.Huilin, Z., Changjiang, W., Xuemei, Y., Xinsheng, W., and Ran, L., "Automatic welding technologies for long-distance pipelines by use of all-position self-shielded flux cored wires", *Natural Gas Industry B*, 1 (1): 113–118 (2014).

ICMATSE 2024

Microstructure and the mechanical properties of homogenized and hot rolled Mg-3Zn-0.2Ca-0.3Mn alloy

Laith M. Al MASHHADANI

Iraqi Council of Representatives, Baghdad, Iraq
Metallurgical and Materials Engineering, Karabuk University, Karabuk, Turkey
laithimm75@gmail.com

Ali GUNGOR

Metallurgical and Materials Engineering, Karabuk University, 78050 Karabuk, Turkey
agungor@karabuk.edu.tr

Abstract. The investigation was carried out to evaluate how hot rolling process affects the microstructure and mechanical properties of an Mg-3Zn-0.2Ca-0.3Mn alloy produced via gravity die-casting. After casting, homogenization heat treatment (12 h at 400 °C) and hot rolling (30 % deformation at 250 °C) were applied to the alloy. Optical microscopy, X-ray diffraction (XRD), field emission scanning electron microscopy with energy-dispersive X-ray spectroscopy (SEM-EDS), microhardness, and tensile test and measurements were used to characterize the alloy. The results showed that hot rolling resulted in lower grain size, formation of twins, and higher yield and tensile strength, hardness. However, the ductility of the alloy decreased after hot rolling.

Key Words: Hot Rolling, Microstructure, Mechanical Properties.
© 2024 Published by ICMATSE

Introduction

Magnesium (Mg) is a lightweight material that exhibits mechanical properties and biocompatibility similar to natural bone[1]. Nevertheless, Mg and its alloys corrode uncontrollably in body fluid, leading to possible implant failure before tissue regeneration[2]. Therefore, one of the important challenges in front of the Mg-based implants is to be able to control the corrosion rate. On the other hand, Mg and its alloys face significant challenges when it comes to their ductility and strength, which limits their use in various applications[3]. Therefore, it is crucial to regulate the mechanical and corrosion properties of Mg alloys to address these issues and ensure their safe and effective use[4]. Over time, various methods have been attempted to reduce the rapid degradation of magnesium, such as high purification, alloying, thermomechanical processing, heat treatment, and surface modification treatments. However, a definite solution to this challenge remains elusive[5].

Magnesium alloys have gained significant attention of the researchers due to their potential applications in various fields. It should be noted that Alper Incesu

and Ali Gungor employed hot rolling after homogenization and alloying processes to enhance the mechanical properties of the magnesium alloys. Their research revealed that increasing the levels of zinc and calcium in magnesium resulted in a decrease in grain size and an increase in hardness [5]. Dae Hyun Cho et al. evaluated the microstructure, mechanical properties, and corrosion behavior of squeeze-cast Mg-4Zn-0.5Ca-xMn alloys, where x ranged from 0 to 0.8 wt%. Their findings revealed that an increased Mn content led to enhancements in the homogeneity and refinement of the dendritic microstructure, as well as improvements in the corrosion resistance and mechanical properties of the alloys[6]. In this regard, Viacheslav et al. conducted a study on four variants of the Mg-Zn-Ca-(Mn) alloy. The study showed that lower temperatures of hot extrusion resulted in increased ultimate tensile strength and yield strength, but reduced elongation, while the opposite trend was observed for higher temperatures[7].

The aim of this study is to examine the effects of hot rolling on the microstructure and mechanical properties of Mg-3Zn-0.2Ca-0.3Mn alloy. The alloy was produced by gravity casting using high purity Ar

gas in the melting zone and 0.8 vol.% SF₆+CO₂ gas mixture in the casting zone of the furnace. Then, the alloy was homogenized and hot-rolled. Homogenization heat treatment was applied at 400 °C for 12 hours. Hot rolling process was carried out at 250 °C and 30% deformation was applied in three-pass.

Results and Discussions

Chemical composition of the alloy measured using the XRF method is given in Table 1. The result shows that the targeted composition was closely obtained.

Table 1. Nominal and measured composition of the alloy after homogenization.

Nominal Composition				Measured Composition			
Mg	Zn	Ca	Mn	Mg	Zn	Ca	Mn
96.5	3.0	0.2	0.3	96.57	2.91	0.21	0.29

Optical microscope images of the homogenized and hot rolled alloys are shown in Fig.1. The figure shows that secondary phase (Ca₂Mg₆Zn₃) is present along the grain boundaries and within the grains.

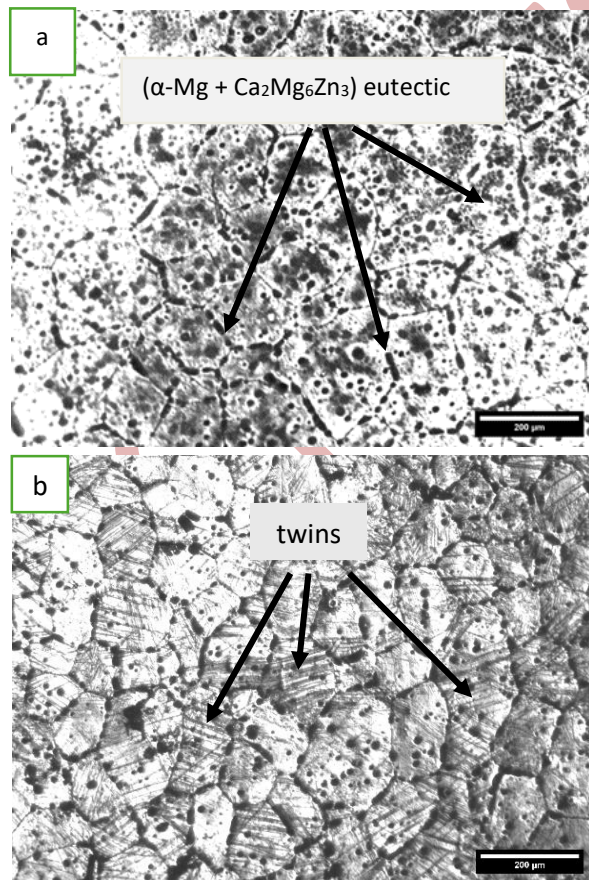


Figure 1. Optical microscope images of a homogenized alloy (a) and hot-rolled alloy (b).

In addition, the images given in Fig.1 show that the initial coarse-grained microstructure in the homogenized sample (Fig.1 a) transformed into relatively fine elongated grains, and deformation twins appeared when the cross-section was reduced by 30% using hot rolling (Fig.1 b). The increased grain boundary area resulting from grain refinement and twin boundaries are expected to restrict the movement of dislocations on the slip planes, leading to higher strength but lower ductility. Fig. 2 presents SEM images illustrating the microstructure of the homogenized and hot rolled samples. The images reveal a secondary phase uniformly distributed as lamellar eutectic phase along the grain boundaries and in disc shape within the grains. Additionally, the alloy exhibits a predominantly coarse-grained microstructure. The presence of coarse grains in the homogenized alloy can be attributed to the grain growth and coarsening phenomena that occur during the homogenization heat treatment.

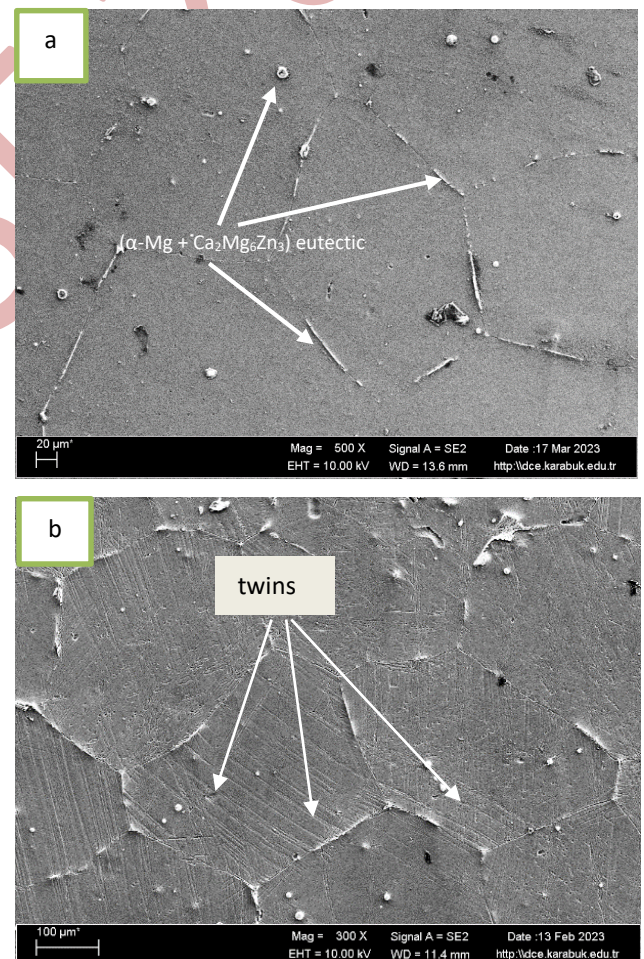


Figure 2. SEM images of the homogenized (a) and hot rolled (b) alloys.

The XRD patterns provide insight into the alloy's microstructural features. Fig.3 shows XRD patterns of the homogenized and hot rolled alloys. The intensities of the peaks observed in XRD patterns provide information about the alignment of crystals along specific axes. The presence of all of the crystallographic planes in Fig. 3 indicates random orientation occurred in homogenized alloy, and a preferred texture was not developed during the homogenization heat treatment process. However, after hot rolling, a transition from random to preferred orientation occurs as evidenced from the diminishing intensity of some reflections such as (100), (101), (200) etc. accompanying strong reflections from some crystallographic planes such as (002), (102), and (103).

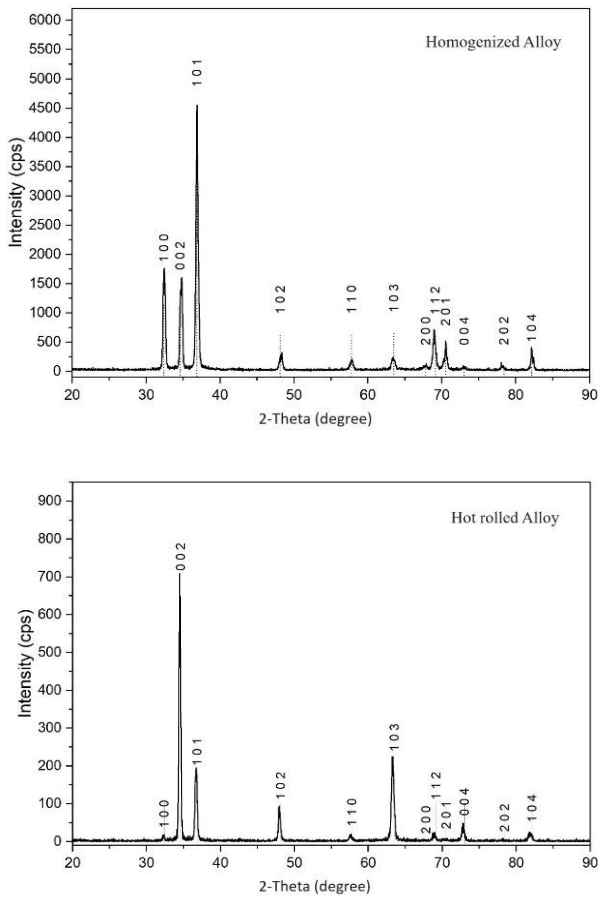


Figure 3. XRD patterns of the homogenized and hot rolled alloys, respectively.

This means that more grains with a preferential orientation formed during hot rolling. Texture development during hot rolling can be explained with the rotation and alignment of crystals with rolling direction. At the same time, dynamic recrystallization process that formed during hot rolling provides randomly oriented grains. Therefore, texture

development is a trade-off between the alignment of crystals and the degree of dynamic recrystallization process that takes place during hot rolling. Coarse $\text{Ca}_2\text{Mg}_6\text{Zn}_3$ particles along the grain boundaries and inside the grains are crushed into fine particles during hot rolling. Dislocation density increases around the fine particles and clustering occurs. The increased dislocation density provides driving force for the dynamic recrystallization process. Therefore, it can be said that particle induced recrystallization occurs. It's worth noting that Jiang et al. determined that larger isolated particles exceeding $1 \mu\text{m}$ can also act as nucleation sites during hot deformation, a process known as particle-induced nucleation [5]. The X-ray diffraction analyses of homogenized and hot-rolled alloys revealed the presence of peaks corresponding to the $\alpha\text{-Mg}$ and $\text{Ca}_2\text{Mg}_6\text{Zn}_3$ phases. The XRD results are consistent with the findings of the previous study[8].

The tensile properties and hardness of the alloys after homogenization and hot rolling are given in Table 2 and Fig. 4. it is seen from the table and figure, hot rolling results in much higher yield and tensile strength and hardness. However, strain at fracture that is a measure of ductility is much lower. The fact that homogenized alloy has larger grain size as well as higher ductility than hot rolled alloy can be explained with the precipitate coarsening that occurs during the homogenization heat treatment because finely dispersed secondary phase after hot rolling limits the dislocation movements and pins the grain boundaries. As a result, strength of the alloy increases and its ductility decreases.

Table 2. Results of the tensile test and Vickers hardness.

Sample	Yield Strength (MPa)	Tensile Strength (MPa)	Elongation (%)	Hardness HV0.5
Homogenous	43.96	148.6	8.78	52.8
Hot rolled	133.50	204.6	1.89	67.7

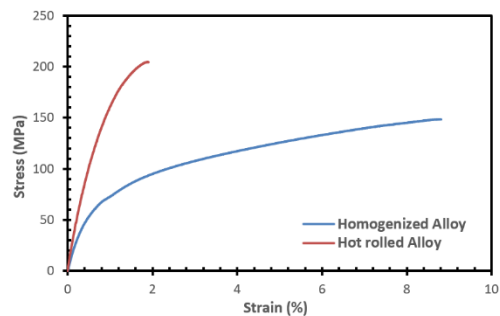


Figure 4. The stress-strain graphics of the homogenized and hot rolled alloys.

Conclusions

SEM-EDS and XRD analyses showed that the alloy is composed of α -Mg matrix and $\text{Ca}_2\text{Mg}_6\text{Zn}_3$ s phases. Hot rolling decreased the grain size and resulted in twin formation.

The hot rolling enhanced the alloy's strength and hardness but lowered the ductility.

Acknowledgement: This research was supported by the Scientific Research Projects Coordination Unit of Karabuk University with KBUBAP-22-YL-119 project number.

References

- 1.U. C. Nwaogu, C. Blawert, N. Scharnagl, W. Dietzel, and K. U. Kainer, "Influence of inorganic acid pickling on the corrosion resistance of magnesium alloy AZ31 sheet," *Corros. Sci.*, vol. 51, no. 11, pp. 2544–2556, 2009, doi: 10.1016/j.corsci.2009.06.045.
- 2.Z. Zou, J. Chen, H. Yan, B. Su, and X. Gong, "Microstructure, Bio-corrosion Behavior, and Corrosion Residual Strength of High Strain Rate Rolled Mg-4Zn Alloy Sheet," *J. Mater. Eng. Perform.*, vol. 25, no. 5, pp. 1974–1985, 2016, doi: 10.1007/s11665-016-2041-4.
- 3.B. JIANG, Z. hua DONG, A. ZHANG, J. feng SONG, and F. sheng PAN, "Recent advances in micro-alloyed wrought magnesium alloys: Theory and design," *Trans. Nonferrous Met. Soc. China (English Ed.)*, vol. 32, no. 6, pp. 1741–1780, 2022, doi: 10.1016/S1003-6326(22)65907-7.
- 4.J. Fu *et al.*, "Effect of the $\text{Ca}_2\text{Mg}_6\text{Zn}_3$ Phase on the Corrosion Behavior of Biodegradable Mg-4.0Zn-0.2Mn-xCa Alloys in Hank's Solution," *Materials (Basel)*, vol. 15, no. 6, 2022, doi: 10.3390/ma15062079.
- 5.A. Incesu and A. Gungor, "Mechanical properties and biodegradability of Mg–Zn–Ca alloys: homogenization heat treatment and hot rolling," *J. Mater. Sci. Mater. Med.*, vol. 31, no. 12, 2020, doi: 10.1007/s10856-020-06468-5.
- 6.D. H. Cho, T. Avey, K. H. Nam, D. Dean, and A. A. Luo, "In vitro and in vivo assessment of squeeze-cast Mg-Zn-Ca-Mn alloys for biomedical applications," *Acta Biomater.*, vol. 150, pp. 442–455, 2022, doi: 10.1016/j.actbio.2022.07.040.
- 7.J. K. Viacheslav BAZHENOV, Anna LI, Andrey KOLTYGIN, Alexander KOMISSAROV, Stanislav TAVOLZHANSKII, Denis TEN, Yury GAMIN, "MICROSTRUCTURE AND MECHANICAL PROPERTIES OF THE Mg-Zn-Ca AND Mg-Zn-Ca-Mn BIODEGRADABLE MAGNESIUM ALLOYS AFTER HOT EXTRUSION," *Met. 2019*, pp. 211–235.
- 8.A. Gungor and A. Incesu, "Effects of alloying elements and thermomechanical process on the mechanical and corrosion properties of biodegradable Mg alloys," *J. Magnes. Alloy.*, vol. 9, no. 1, pp. 241–253, 2021, doi: 10.1016/j.jma.2020.09.009.

Synthesis and Characterization of N-doped Carbon Black Supported Fe, Zn and Mo Based Catalysts for Oxygen Reduction Reaction

Ali Tambwe AMİR

Gazi University, Graduate School of Natural and Applied Sciences, Chemical Engineering Department,
Ankara, Turkey,
amirtambwe97@gmail.com
ORCID: 0000-0003-1035-5342

Çiğdem GÜLDÜR

Gazi University, Engineering Faculty, Chemical Engineering Department, 06570, Maltepe, Ankara,
Turkey,
cguldur@gazi.edu.tr
ORCID: 0000-0002-4404-6882

Silver GÜNEŞ

Gazi University, Graduate School of Natural and Applied Sciences, 06500, Beşevler, Ankara, Turkey,
silver@gazi.edu.tr
ORCID: 0000-0001-7608-3779

Cite this paper as: Amir, AT, Güldür, Ç, Güneş, S.. Synthesis and Characterization of N-doped Carbon Black Supported Fe, Zn and Mo Based Catalysts for Oxygen Reduction Reaction,. Int. Conf. Advanced. Mater. Sci.& Eng. HiTech.and Device Appl.Oct. 24-26 2024, Ankara, Turkiye

Abstract. Nitrogen-doped carbon black supported Fe, Zn and Mo catalysts were synthesized for being used as oxygen reduction electrocatalysts in fuel cells. Doping of carbon black was achieved by pyrolysis using melamine as nitrogen source. Metallic catalysts were prepared by polyol method where ethylene glycol was used as the reducing agent. The as-prepared catalysts were physically characterized by X-ray photoelectron spectroscopy (XPS) and X-ray diffraction (XRD) analyses. Cyclic voltammetry analysis was performed in an alkaline electrolyte environment to examine the oxygen reduction activities of the catalysts. According to the results, the nitrogen was successfully doped on carbon black with a percentage of 2.49% (wt). Physical and electrochemical characterization, the prepared Zn-CN sample was found to be the best catalyst in terms of metal distribution and oxygen reduction activity. According to cyclic voltammetry measurements, the Zn-CN catalyst gave an OR peak current of -1.04 mA around -0.4 V potential.

Keywords: Carbon black, Nitrogen doping, Oxygen reduction reaction
© 2024 Published by ICMATSE

1. INTRODUCTION

Fuel cells are devices that convert chemical energy into electrical energy. Among different cell designs, PEM (polymer electrolyte membrane) fuel cell stands out with its advantages such as low operating temperature, corrosion resistance and high-power density. However, the performance of PEM fuel cells is limited by the low reaction rate at the cathode and the need for the use of high-cost platinum catalysts. Therefore, there is a need to develop active and inexpensive catalysts that do not contain platinum

group metals for the electrocatalysis of the oxygen reduction reaction (ORR). To solve this problem, different approaches have been taken including the alloying of platinum with other transition metals [1] and developing new carbon supports [2]. However, very little progress have been made regarding alternatives for platinum so far.

Recently, the heteroatom doping of carbon has been extensively studied due to its considerable ORR activity [3]. Although not as active as platinum, they can help increase the activity of inexpensive non-

noble catalysts. Especially, the nitrogen-doped carbon supported non-noble catalysts have been reported to possess significant ORR activities [4]. Thanks to its similar size with the carbon atoms, the nitrogen atoms can be easily doped into the carbon framework and modify the electronic distribution on the surface [5]. Iron is one of the most extensively studied transition metal combined with nitrogen doped carbons. Sibul et al., obtained significant ORR activity using N-doped graphene based iron catalysts [6]. Adabi et. Al, also used Fe-N-C catalysts as anion exchange membrane fuel cell cathode and obtained peak power densities over 2 W/cm^2 [7]. Next to iron-based catalysts, cobalt is also a commonly studied metal in nitrogen doped electrocatalysts. Cobalt based catalysts supported by nitrogen doped carbon nanotubes provided excellent performance in anion exchange membrane fuel cells [8]. Other transition metals such as Mn and Cu have also been studied and shown to be promising as oxygen reduction electrocatalysts [9,10]. Here in this study, nitrogen-doped carbon black supported Fe, Zn and Mo catalysts were synthesized and characterized for their oxygen reduction activities.

2. EXPERIMENTAL

Doping of nitrogen on carbon black was achieved with pyrolysis at $650 \text{ }^\circ\text{C}$ using melamine as the nitrogen source. The metals were deposited on N-doped carbon black by polyol method where ethylene glycol (EG) was employed as reducing agent. As metal precursors, $\text{Fe}(\text{NO}_3)_3$, $\text{Zn}(\text{NO}_3)_2$ and $(\text{NH}_4)_6\text{Mo}_7\text{O}_{24}$ were added to the EG solution in appropriate amounts corresponding to a 20% metal content (w/w). Chemical reduction was carried out at $120 \text{ }^\circ\text{C}$ under argon flow. Catalysts were then filtered, washed and dried before characterization.

Catalysts were physically characterized by X-ray diffraction (XRD) and X-ray photoelectron spectroscopy (XPS). Oxygen reduction activities were tested by cyclic voltammetry in 0.1 M KOH electrolyte. CV measurements were conducted in a three electrode cell consisting of Ag/AgCl reference electrode, Pt counter electrode and a glassy carbon working electrode. The working electrode was prepared by applying a mixture of the catalyst and nafion solution on the glassy carbon disk. Scans were obtained in range between $-0,1$ and $0,2 \text{ V}$.

3. RESULTS AND DISCUSSION

X-ray photoelectron spectroscopy confirmed that nitrogen was successfully doped on the carbon black with 2.49% incorporation percentage (wt).

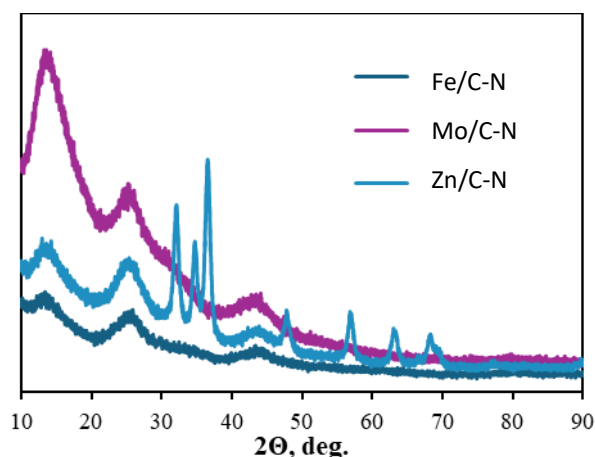


Figure 1. XRD spectra of Fe, Zn and Mo catalysts supported by N-doped carbon black.

According to X-ray diffraction studies, Mo and Fe were mostly in amorphous state, with weak peaks at 13° corresponding to Mo_2C and MoO_3 and at 43° corresponding to Fe_5C_2 , Fe_3C . Graphitic carbon (002) was apparent in all catalysts. On the other side, Zn nanoparticles gave discernible peaks at 32° , 35° , 38° , 48° , 57° and 63° , corresponding to the characteristic peaks of ZnO. This showed that the polyol method was more successful in deposition of Zn nanoparticles on carbon black.

According to the cyclic voltammetry results, the highest oxygen reduction activity was obtained from the Zn/C-N catalyst with -1.04 mA peak current around -0.4 V (vs. Ag/AgCl) potential. The catalyst metal-free C-N catalyst also gave a discernible ORR peak and a considerable peak current of -0.88 mA , which shows that the doped nitrogen is a major contributor to the overall activity. ORR activity was lower Fe/C-N and Mo/C-N, possibly due to poor metal distribution on the surface.

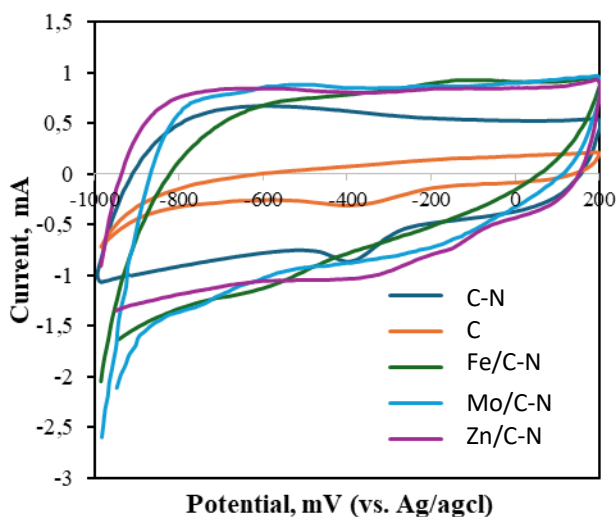


Figure 2. Cyclic voltammograms of the catalysts

4. CONCLUSIONS

Nitrogen-doped carbon black supported Fe, Mo and Zn catalysts were prepared and tested for their ORR activities. A nitrogen-doping of 2.49% (wt) was obtained by pyrolysis of melamine on carbon black. XRD analysis showed that ZnO nanoparticles were successfully deposited on C-N by the polyol method, while Fe and Mo presence on the surface was poor. Cyclic voltammetry results were in accordance with the physical characterization, as Zn/C-N catalyst provided the highest ORR activity with -1.04 mA current at -0.4 V potential. Results show that the Zn/C-N catalyst is promising as a cathode catalyst in low-temperature fuel cells.

ACKNOWLEDGMENTS

This study was supported by Gazi University Scientific Projects Unit through project number FGA-2024-9130.

References

1. Wang, C., Markovic, N. M., Stamenkovic, V. R. (2012) Advanced Platinum Alloy Electrocatalysts for the Oxygen Reduction Reaction, *ACS Catalysis*, 2, ACS Catal. 2012, 2, 5, 891–898.
2. Wang, D. W., Su, D. (2014) Heterogeneous nanocarbon materials for oxygen reduction reaction, *Energy Environmental Science*, 7, 576-591.
3. Woo, J., Lim, J.S., Kim, J.H., Joo, S.H. (2021) Heteroatom-doped carbon-based oxygen reduction electrocatalysts with tailored four-electron and two-electron selectivity, *Chemical Communications*, 57, 7350-7361.
4. Singh, S.K., Takeyasu, K., Nakamura, J. (2019) *Advanced Materials*, 31: 1804297.
5. Lv, Q., Si, W., He, J., Sun, L., Zhang, C., Wang, N., Yang, Z., Li, X., Wang, X., Deng, W., Long, Y., Huang, C., Li, Y. (2018) *Nature Communications*, 9: 3376.
6. Sibul, R., Kibena-Poldsepp, E., Ratso, S., Kook, M., Sougrati M.T. et al. (2020) Iron- and Nitrogen-Doped Graphene-Based Catalysts for Fuel Cell Applications, *ChemElectroChem*, 7: 1739–1747.
7. Adabi, H., Shakouri, A., Hassan, N., Varcoe, J.R., Zulevi B. et al. (2021) High-performing commercial Fe-N-C cathode electrocatalyst for anion-exchange membrane fuel cells, *Nat. Energy* 6: 834–843.
8. Lilloja, J., Kibena-Poldsepp, E., Sarapuu, A., Kodali, M., Chen Y. et al. (2020) Cathode Catalysts Based on Cobalt and Nitrogen-Doped Nanocarbon Composites for Anion Exchange Membrane Fuel Cells, *ACS Appl. Energy Mater.* 3: 5375–5384.
9. Akula, S., Mooste, M., Kozlova, J., Maike, K., Treshchalov A. et al. (2023) Transition metal (Fe, Co, Mn, Cu) containing nitrogen-doped porous carbon as efficient oxygen reduction electrocatalysts for anion exchange membrane fuel cells, *Chemical Engineering Journal*, 458, 141468.
10. Bai, J., Fu, Y., Zhou, P., Xu, P., Wang, L., Zhang, J. et al. (2022) Synergies of atomically dispersed Mn/Fe single atoms and Fe nanoparticles on N-doped carbon toward high-activity electrocatalysis for oxygen reduction, *ACS Appl. Mater. Interfaces* 14: 29986–29992.

Technical innovations in the service of architectural history continuity

Natia Kochladze

Georgian Technical University- Faculty of Architecture, Urban Planning and Design, 0175, Tbilisi,
Georgia, qochladzenatia06@gtu.ge
ORCID: 0009-0008-5922-2982

Nino Imnadze

Georgian Technical University- Faculty of Architecture, Urban Planning and Design, 0175, Tbilisi,
Georgia, n.imnadze@gtu.ge
ORCID: 0000-0003-1235-5354

Tinatin Chigogidze

Georgian Technical University- Faculty of Architecture, Urban Planning and Design, 0175, Tbilisi,
Georgia,
t.chigogidze@gtu.ge
ORCID: 0009-0002-5794-3053

Bella Tinikashvili

Georgian Technical University- Faculty of Architecture, Urban Planning and Design, 0175, Tbilisi,
Georgia, b.tinikashvili@gtu.ge
ORCID: 0009-0002-7497-7626

David Bostanashvili

Georgian Technical University- Faculty of Architecture, Urban Planning and Design, 0175, Tbilisi,
Georgia, d.bostanashvili@gtu.ge
ORCID: 0009-0007-9574-3980

Ketevan Saluqvadze

Georgian Technical University- Faculty of Architecture, Urban Planning and Design, 0175, Tbilisi,
Georgia, saluqvadzeqetevani06@gtu.ge
ORCID: 0009-0009-0633-8823

Cite this paper as: Kochladze, N., Imnadze, N., Chigogidze, T., Tinikashvili, B., Bostanashvili, D., Saluqvadze, K., Technical innovations in the service of architectural history continuity, Int. Conf. Advanced. Mater. Sci.& Eng. HiTech.and Device Appl.Oct. 24-26 2024, Ankara, Turkiye

Abstract. Modern technologies are developing at lightning speed and apart of using the new materials, modern architecture also includes the virtual world and digital technologies. New virtual “realities” themselves lead to the changes in people’s behavior and attitude towards the environment. The issue of preserving the historical and cultural heritage and transferring it to future generations becomes particularly relevant. In this regard, we would like to discuss few examples: Vernacular wooden houses were spread all over Georgia and do not lose their relevance even today thanks to projects carried out in the 21st century. The Tbilisi Opera and Ballet Theater meets modern requirements thanks to the large-scale renovation works carried out in 2010-2016. The use of clay pots characteristic of folk crafts as a cooling system on the facade of the Museum’s modern building (Telavi) and the graffiti drawing of a khachapuri baker grandmother in Kutaisi express the continuity of cultural heritage. In our opinion, the examples discussed in the article are evidence of the combination of the historical and the new, the rethinking (expansion) of cultural heritage, which is carried out using the latest technologies and materials and puts technical innovations at the service of the continuity of history.

Keywords: heritage, technologies, materials, architecture, modern

© 2024 Published by ICMATSE

Introduction

In the modern world, technologies are developing at lightning speed, and if historically the emergence of new inventions and techniques in architecture meant the formation of new styles and the use of new materials, then modern architecture also includes the virtual world and digital technologies. New virtual "realities" themselves lead to changes in human behavior and attitudes towards the environment. Along with the many advantages that new technologies provide in architecture, due to the abundance of information and the simplicity of visual implementation, there is a danger of homogenization of design. In this situation, the issue of preserving the historical and cultural heritage and passing it on to future generations is particularly relevant; this task is often performed by new technologies. In this context, we would like to discuss several examples:

Results and Discussion

Wooden houses in various variations were widespread throughout Georgia. It acquired its final classical appearance in the 19th century, when sawmills, construction glass, and urban living conditions were created in Georgia. Wooden houses were especially widespread in Western Georgia, where the warm climate, humidity, and the development of new living conditions determined the leading role of the wide balcony in residential architecture (1). It was a wooden house with windows, a wooden balcony, wooden ceiling and floor. For the roof where used tiles or shingles. The houses were standing on stone or wooden poles. At the end of the 19th century, some houses had their first floors built of stone (2). This type of housing is quite diverse in its layout and volumetric-spatial solution. Three fundamental types can be distinguished, where a more complex space develops from a simple space (one room). The balcony acquired the most important significance in the architectural and artistic solution. The columns of the balconies were decorated with beautiful carving. Over time, hand carving was replaced by ornaments made with a saw. It is worth noting the excellent technique of disassembling and assembling a wooden house. Already built houses were transported on carts from one village to another. Many wooden houses

have been given the status of immovable cultural monument. With the emergence of many new materials and technologies, wooden houses do not lose their relevance and keep up with modernity. For example, Latvian architect, founder of the architectural studio "Goodpattern" Guntis Zingis after a trip to Georgia created a prefabricated wooden house, which, according to the author, allows you to integrate with nature and lead a harmonious life, since the wide verandas and terraces characteristic of them are a kind of continuation of the internal living space and a transition zone to the environment. The name of the project is "Veranda". Three models were developed. Wooden frame-panel houses are produced in transportable sizes in the form of modules with a faced facade, windows and a roof. A house of this type is placed on a concrete block foundation, and as for the interior decoration, this part of the work is performed by a builder hired by the customer. The building has triple-glazed windows. Heat and wind insulation is also used on the walls and roof, which allows for virtually zero energy consumption. The wooden frame construction uses standard length wooden beams to avoid unwanted loss (3).



Figure 1. House "Veranda", model V102

Source - <https://shorturl.at/rSMhN>

In the north-eastern part of Western Georgia, in Racha, you can find centuries-old wooden carved houses in many places. Some of them are still preserved in their original form, while others need restoration. An interesting project is underway called "Write the History of Racha's wooden houses", where modern Internet technologies are at the service of cultural heritage. The goal of this project is the photodocumentation of wooden houses, finding their stories and placing them on a single bilingual platform, which will contribute to the creation of a new tourist route in Racha. The authors of the project hope, that the arrival of a tourist will stop the migration from Racha's

villages, will develop this beautiful region and will stop the destruction of wooden houses (4).



Figure 2. Wooden house in Racha
Source -<https://shorturl.at/4hwWV>



Theater of Tbilisi Source -
<https://shorturl.at/A7Tch>

The Tbilisi Opera and Ballet Theatre, located on the main street of Tbilisi – Rustaveli Avenue, is a striking example of the use of modern technologies in the reconstruction of a historical building in Georgia. The appearance of the building is determined by the combination of elements characteristic of Islamic architecture. Its construction was completed in 1896 (architect V. Shreter). The territory is a historic district, and the building itself is a monument of cultural heritage. After the fire in 1973, it was reconstructed (architects L. Medzmariashvili, M. Chachanidze), and in 2010-2015, large-scale renovation works were carried out in the theater building (architect L. Medzmariashvili). The main building, the hall,

the auxiliary buildings, all wings and levels, as well as the external territory have been completely renovated and reconstructed. Objects and areas with new functions were added to the theater (5). The stage as well as all necessary communications were equipped with the latest centralized and computerized management system. About the technical arrangement of the theater building Mr. I. Kavsadze (People's Artist of Georgia) and A. Ananiashvili (head of the staging department) talked to us. It was especially noted that the audio-video and lighting system was computerized and updated, and so-called "Safes" were introduced - mobile shelves for storing scenery, arranged under the stage floor (author A. Ananiashvili). The stage is separated from the hall by a curtain lined with fire-resistant material on both sides of the stage portal. An iconic stage curtain destroyed by fire in the 1970s has been restored in Germany and hang behind the main curtain. The railing separating the parterre and the orchestra space and the floor of the orchestra space are movable, which allows to reorganize and increase the stage space. A video projector was considered for modern opera productions, and a subtitle LED screen was also installed. An air conditioning system is provided throughout the building. As a result of the mentioned technical arrangement, the opera theater is a comfortable working space for the employees, and it does not lose its popularity and prestige for the audience.



Figure 4. The Georgian National Opera and Ballet Theater of Tbilisi- stage

In the Kakheti region, the Batoni Castle Museum Complex, located in Telavi, is one of the most important monuments of Georgian secular architecture of the late feudal era. In 2012-2018, the complex was rehabilitated (6), during which two buildings with an exhibition function, built in the 1930s, were dismantled and a new museum building was built, taking into account modern standards, equipped with a modern heating-

cooling-ventilation system. The use of clay pots typical for folk crafts as a cooling system on the facade of the modern museum building can be seen as an act of respect for cultural heritage.



Figure 5. Telavi historical museum

The three-story Green Architecture and Engineering Technology Demonstration Center building (architect Gvantsa Kheladze) built in the village of Bazaleti, Dusheti district, 60 kilometers from Tbilisi, has been certified by the Green Construction Council of Georgia and has been awarded gold status. This 21st century building uses the latest technologies to absorb heat/electrical energy generated from the sun, wind, and agricultural waste. The entire energy storage and transmission system is registered with a special software package purchased from the American company Honeywell (7). During the planning, the inner yard, historically characteristic of a Tbilisi house, is preserved, on which the buildings come out with balconies. The solution of the balconies, on which the greenery is arranged, is also interesting, and it evokes the association of houses with a terrace common in Georgia.



Figure 6. Green building in Bazaleti

Source -<https://archiaward.com/ge/work/3166>

Modern street painting, which originates from graffiti (and graffiti is widely believed to have appeared during World War II), does not have a long history in Georgia, but it has recently become very popular and many beautiful examples have been created in the cities of Georgia. Techniques and materials for street painting, aerosol spray paint, marker pens, fire extinguishers, etching tools, represent an innovation. Ukrainian artist Sasha Korban's painting of the Khachapuri baker grandmother on the facade of a residential house in Kutaisi, "Khorumi" painting on the wall of a multi-storey house in Tbilisi by the street art movement "Niko" use technical innovation and are an expression of the continuity of history, respect and love for it.

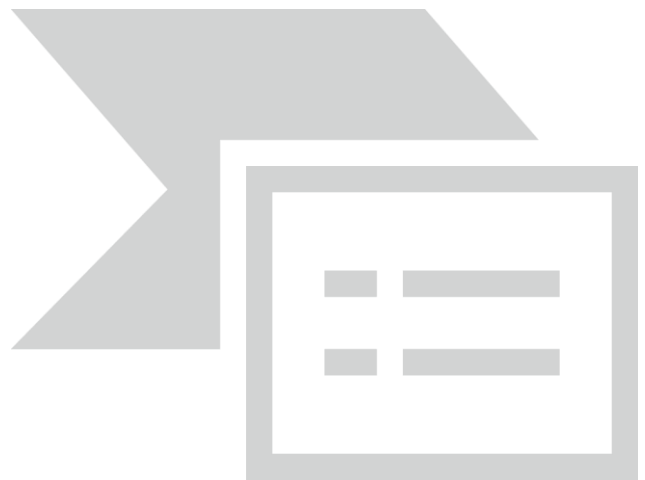


Figure 7. "With love" - Street art

Source - <https://rb.gy/lycl0c>

Conclusion and References

The title of the painting made in Kutaisi by Sasha Korban is "With love", the artist took a photo of one of the elderly women living in Imereti as inspiration. This work has become a business card of Kutaisi. We would like to mention that khachapuri, a dish made from dough and cheese, is included in the list of intangible cultural monuments of Georgia. In the work of "Niko" - "Khorumi" - a shot of the dance performed by the Georgian national ensemble "Sukhishvili" is presented. "Khorumi" is an ancient Georgian folk dance of martial content and has been granted the status of a monument of intangible culture (8).

In our opinion, the examples discussed in the article are evidence of connecting the historical and the new, rethinking (extending) the cultural heritage, which is carried out using the latest technologies and materials, and puts technical innovation at the service of the continuity of history.



Figure 8. "Khorumi" - Street art

References

1. L.Sumbadze, Wood carving in Georgian architecture, J A friend of a monument, 12 (1967), pp.61-62
2. Wikipedia, Western Georgia, <https://shorturl.at/VmyPL>
3. Home is, Prefab wooden houses inspired by Georgian architecture from a Latvian designer, (2022) <https://rb.gy/76jh79>
4. Histori of Racha's wooden houses (2020) <https://csogeorgia.org/ge/post/rachuli-odebis-istoria>
5. Wikipedia, Georgian National Opera Theater, <https://shorturl.at/QyDCS>
6. The renovated Batoni Castle Museum was opened in Telavi (2018) <https://www.kakheti.gov.ge/geo/news/show/7/297>
7. Archieward, Green house, (2022), <https://archiaward.com/ge/work/3166>
8. Wikipedia, Intangible cultural heritage of Georgia, https://en.wikipedia.org/wiki/Intangible_cultural_heritage_of_Georgia

Designing Efficient Solar-Powered Desalination Systems in Arid Region

Nour sabira

*Higher normal school of Bechar- Department of physics, 08000, Bechar, Algeria,
Laboratory of Semiconductor devices physics-Tahri Mohamed University,08000, Bechar, Algeria,
nour.sabira@ensbechar.dz
ORCID:0000-0001-8606-3894*

Daoudi mebarka

*Laboratory of Semiconductor devices physics-Tahri Mohamed University,08000, Bechar, Algeria,
daoudi.mebarka@univ-bechar.dz
ORCID: 0000-0003-0140-7921*

Cite this paper as: Sabira, N., Mebarka, D., Designing Efficient Solar-Powered Desalination Systems in Arid Region, Int. Conf. Advanced. Mater. Sci.& Eng. HiTech.and Device Appl.Oct. 24-26 2024, Ankara, Turkiye

Abstract. in its arid regions such Algeria has abundant solar resources, faces the dual challenge of increasing electricity and freshwater demands. This study investigates the feasibility of integrating solar desalination systems to address these challenges, we were focusing on the Bechar region. The research proposes studied brackish well water desalination station using reverse osmosis (RO) technology powered by photovoltaic (PV) panels and grid-connected. This innovative approach examines the optimal design of desalination plant, considering factors such as configuration and sizing of the RO system, integration of a grid-connected PV system for maximum solar radiation energy captured and product electrical energy, studied impact of factors like angle tilt of fixed solar modules, soiling, and temperature on the efficiency of both the energy so on water systems. The study aims to demonstrate the technical of solar desalination in arid regions, providing a comprehensive design framework and quantifying the impact of environmental factors on system performance. This research contributes to advancing sustainable water access and environmental conservation in arid regions, aligning with the global need for innovative solutions to water scarcity and promoting renewable energy utilization.

Keywords:

Arid Region, Solar Energy, Well Brackish, Desalination, Reverse Osmosis

© 2024 Published by ICMATSE

Introduction

It is difficult to find enough drinkable water in semi-arid and dry regions, such as Algeria, a semi-arid country with irregular rainfall. Due to the region's year-round abundance of solar energy, desalination processes, particularly reverse osmosis (RO) [1], which requires a lot of electrical energy to operate well, may be powered by solar energy[2]. In this work, we presented a study of how to implement a desalination station using brackish well water in the software TORAY DS. in order to better understand the station and calculate how much electrical energy is required to operate it. In the second stage,

we designed a PV system connected to the grid in PVsyst. based on the station's specifications. This work investigated the incoming radiation and product electrical energy, as well as the number of solar modules required, and we investigated some factors that reduce electrical energy product, resulting in reduced flow water product, and we proposed how alleviated losses cross-reduced the effect of some factors such as angle tilt, soiling and temperature. First, we created a Brackish Water RO system that was used in the TORAY DS2 program. It has a recovery rate of 45% and generates 21 m³/day of drinkable and culturable water. We use 42 m³/day of feed flow, pH 7, a brackish surface, 25°C,

and 5000 mg/L of NaCl as inputs for feeding. The recommended design station requires 1,318 kwh/m³ of electricity. The flow schematic for the desalination station is shown in (Fig. 1).

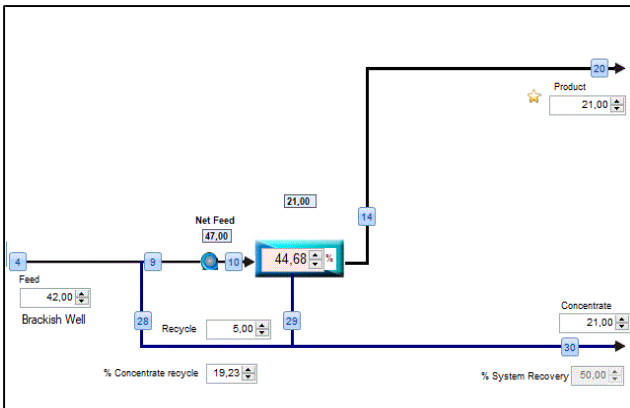


Figure 01 show the flow diagram

Our recommendation is to construct a grid-connected photovoltaic system to supply solar energy to the investigated desalination facility facilities. We want to carry out our investigation in the dry Bechar region of Algeria, specifically at latitude 31,6066° and longitude 2,2382°. Our design allows us to capture 2323 kw of incoming radiation for the PV system used in PVsyst. With seven bifacial solar modules fixed at an annual tilt angle of 31° and an azimuth of 0°, we are able to produce 4259 kw of electricity annually on a 12 m² surface with a performance rate of 83,02% and system losses of 16%. (Fig. 2) system on grid.

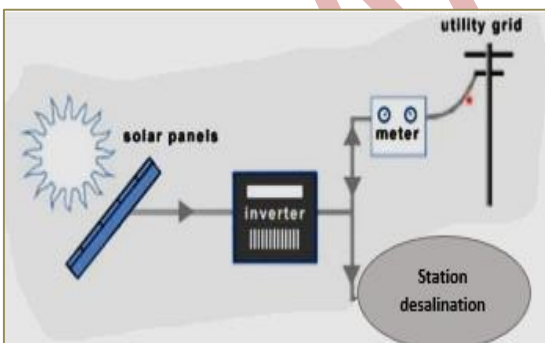


Figure 2 show design powered energy electric on grid

Results and Discussion

1- Output the calculate

The simulation in PV sys provides a wealth of information in terms of input and output; we concentrated our efforts on the loss aspects

that reduce the performance of our system. (Fig. 3) shows the loss diagram for our approach. With a global energy radiation intake of 2061 kw/m³, our system collects 2323 kw/m³ and produces 4259 kw of electricity for the desalination unit. We can observe that temperature is the most significant contributor to loss, accounting for an estimated 10.51%. This makes sense because rising solar cell temperatures heat up all of the system's components due to electron movement (product current), reducing the system's energy, performance, and efficiency. In this study, we look at the aspects that have an impact on performance in order to mitigate these features and improve the design.

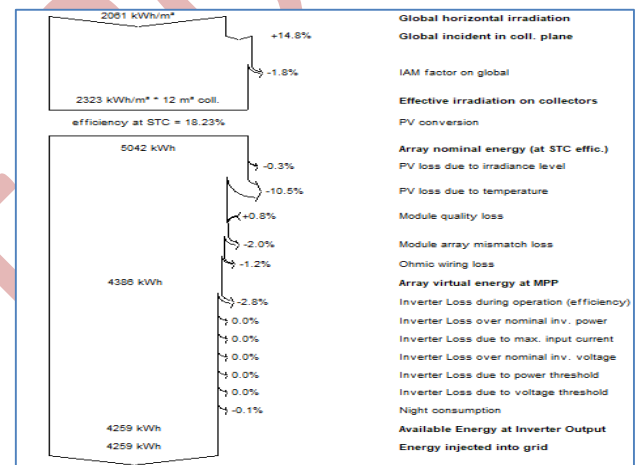


Figure 3 show the losses diagram

2- Effect the plane tilt

to investigate how fixed solar panel tilt angles affect the amount of electrical energy that enters and leaves the system while reducing radiation losses. Our study concentrated on tilting fixe solar modules in our region, which is above the equator in Bechar, Algeria, in the direction of the equator. To ascertain the impact of altering the tilt angle on fixed solar modules on system performance, we varied the tilt angle of the fixed solar panels as indicated in (Table 1). a and compared the simulation results (Table 1). b show varied the tilt angle of the fixed solar panels twice in year. The relationship for calculating the tilt angle in Algeria above the line that runs from latitude 25° to latitude 50° is [3]: $tilt\ angle = (latitude * 0.76) + 3$ Eq. [1]

Table 1. a

Angle tilt	Effective irradiation on collector (kwh/m ²)	electrical energy	System Losses	PERF RATION
0°	2002	3698	0.14	0.827
5°	2092	3857	0.14	0.828
10°	2168	3990	0.15	0.829
15°	2229	4096	0.15	0.829
20°	2276	4177	0.16	0.829
30°	2323	4259	0.16	0.830
40°	2307	4236	0.16	0.831
50°	2229	4111	0.16	0.833
60°	2093	3886	0.15	0.835

Table 1. b

Angle tilt	Effective irradiation on collector (kwh/m ²)	electrical energy	System Losses	PERF RATION
Summer 20° and Winter 50°	2433	4446	0.17	0.829

3- Effect soiling

The second aspect of our research is soiling, which decreases the efficacy of design [4]. Our area has a lot of dust and dirt, as evidenced by this. This can be found in (Table 2): Soiling's Effect on System Performance.

Table 02 effect the soiling on system

Soiling	Effective irradiation on collector plane (kwh/m ²)	Produced energy electric	System Losses	Performance ration
0%	2323	4259	0.16	0.830
5%	2207	4071	0,15	0.793
10%	2090	3880	0,15	0,756

The effect of soiling forward diminishes irradiance, which is collected and converted directly into electrical energy. We see that 5% soiling reduces 4.9% of incoming radiation and 4.4% of product electrical energy, while 10% soiling reduces 8.8% of incoming radiation and 10% of product electrical energy, implying that all factors are lowered in accordance with the presence of soiling. In our location, we utilize 5% soiling [5]. To avoid soiling in

solar modules, we may always cleanliness monitor our solar modules, however we are cautious of the hot components in our design and dusty days.

4- Effect temperature

Understanding temperature losses is critical for improving design [6]. The PV system uses a balance to mimic and account for all incoming and outgoing energy flows in the array; we investigate the influence of temperature and how we may enhance our design. To calculate the cell temperature, use the relationship below.

$$T_{cell} = T_{ambient} + \frac{1}{U} * (\alpha * G_{irradiance} * (1 - E_{efficiency})) \quad \text{Eq. [2]}$$

Alongside:

The heat loss factor [W/m²·k] is denoted by U. α is the solar irradiance absorption coefficient. (Table 3) includes this effect.

The coefficient of heat loss factor is the major input parameter used throughout the simulation to evaluate the performance of the design. We can lessen the influence of temperature and alleviate thermal losses using the approaches outlined below:

- Open-rack systems with air circulation around collectors have a heat loss coefficient of U=29 w/ (m² k°),
- while an air duct below the collectors has a heat loss value of U=20 w/ (m² k°).
- Domes: U=27 w/ (m² k°)
- Fully insulated backside: U=15 w/ (m² k°), Only one side contributes to heat exchange.

we summarize above in (Table 3).

Table 03 effect thermal losses

Temperature	Produced energy electric	System Losses	Performance ration
Free-with air circulation	4413	0.17	0.860
Domes	4389	0.17	0.855
with air duct below the collectors	4259	0.16	0.830
Fully insulated backside	4087	0.15	0.796

We saw an effect of reducing heat losses in our design by enhancing all energy results while using open-rack systems[6].

Conclusion

To summarize everything mentioned above, we studied the design of a brackish well station in Bachar, Algeria, with the goal of helping to sustainably develop our dry region in the future. We proposed using solar energy in particular to desalinate brackish water. We simulated our ideas

using the PVsystem and TORAY DS applications. We suggested tilting fixed solar modules 30 degrees each year to collect incoming radiation and produce electrical energy in order to explore how to improve performance and decrease losses. However, by manually changing the modules twice a year, we were able to maximize both incoming and outgoing energy. It's also crucial to clean solar modules in advance to lessen the impact of soiling. and lastly affect the temperature. The methods we employed to update our design were crucial, particularly in a dry area.

References

- [1] Z. Tigrine *et al.*, "Feasibility Study of a Reverse Osmosis Desalination Unit Powered by Photovoltaic Panels for a Sustainable Water Supply in Algeria," *Sustainability (Switzerland)*, vol. 15, no. 19, Oct. 2023, doi: 10.3390/su151914189.
- [2] B. Bouchekima, "Solar desalination plant for small size use in remote arid areas of South Algeria for the production of drinking water," *Desalination*, vol. 156, no. 1–3, pp. 353–354, Aug. 2003, doi: 10.1016/S0011-9164(03)00367-9.
- [3] T. Sarver, A. Al-Qaraghuli, and L. L. Kazmerski, "A comprehensive review of the impact of dust on the use of solar energy: History, investigations, results, literature, and mitigation approaches," 2013. doi: 10.1016/j.rser.2012.12.065.
- [4] J. Miura, "Support vector path planning," *IEEE International Conference on Intelligent Robots and Systems*, pp. 2894–2899, 2006, doi: 10.1109/IROS.2006.282140.
- [5] E. Skoplaki and J. A. Palyvos, "On the temperature dependence of photovoltaic module electrical performance: A review of efficiency/power correlations," *Solar Energy*, vol. 83, no. 5, pp. 614–624, May 2009, doi: 10.1016/j.solener.2008.10.008.
- [6] S. Nour, A. Merabti, H. Issani, R. Abdeldjebar, and A. Djatout, "Optimization the Characteristics of Solar Cell based on InGaN," 2023.

Wind Energy application for Small-Scale Irrigation for Semiarid Region

Hadja GUEDAOURIA

*Laboratory of physics Semiconductor Devices (LPDS), University of Bechar, P.O. Box 417, Bechar (08000),
Algeria,
hadja.guedaoria@univ-bechar.dz
ORCID: <https://orcid.org/0000-0003-3544-0770>*

Mebarka DAOUDI

*Laboratory of physics Semiconductor Devices (LPDS), University of Bechar, P.O. Box 417, Bechar (08000),
Algeria,
daoudi.mebarka@univ-bechar.dz
ORCID: <https://orcid.org/0000-0003-0140-7921>*

Abdelhak MAAZOUZI

*Laboratory of Chemistry and Environmental Sciences (LCSE), University of Bechar, P.O. Box 417, Bechar (08000),
Algeria, maazouzi.abdelhak@univ-bechar.dz*

Karim TALHI

*Laboratory of Laboratory of Environmental and Energy Systems (LSEE), Institute of Science and
Technology, University Center Ali KAFI Tindouf, Algeria,
karim.talhi@gmail.com*

Ahmed BENNIA

*Laboratory of Laboratory of Environmental and Energy Systems (LSEE), Institute of Science and
Technology, University Center Ali KAFI Tindouf, Algeria
Agence Spatiale Algérienne, Centre des Techniques Spatiales, Arzew, Algérie,
redabennia@gmail.com*

*Cite this paper as: GUEDAOURIA, H, DAOUDI, M, MAAZOUZI, A, TALHI, K, BENNIA, A. Wind Energy application
for Small-Scale Irrigation for Semiarid Region. Int. Conf. Advanced. Mater. Sci. & Eng. HiTech. and Device
Appl. Oct. 24-26 2024, Ankara, Turkiye*

Abstract. This work evaluates the feasibility and effectiveness of wind power in the Bechar–Algeria region to sizing and design an off-grid wind farm. We sized the wind system as a stand-alone system to provide energy for irrigating an area of 300 m². In previous studies, authors [1,2] have determined the required energy by detailing the steps of sizing and designing the irrigation network. Power requirement equals 1100 W (1.5 H). Researchers conduct a metrological study to determine wind data. Researchers use wind roses and histograms of wind speed frequencies to analyze and illustrate this data, to assess the wind potential energy. The study proved that the Bechar–Algeria region has suitable potential for wind energy projects with moderate wind resources, so we can use this renewable energy for small-scale irrigation. As a result, we designed an off-grid wind farm. The sizing explores that to provide the needed energy, the wind system must contain 2 turbine, 4 batteries.

Keywords: wind energy, irrigation, Weibull distribution, Bechar -Algeria region.

© 2024 Published by ICMATSE

1. Introduction

Bechar region is located the southern region of Algeria between longitudes -2.22000 and latitudes 31.60778, hyper arid climate with mild winters and hot sunny summers characterizes it [4]; it is a significant city of the Algerian Sahara covering around 5 0000 km². Unfortunately, it is still depending on the power grid and electrogen group for providing needed energy for irrigation. These sources of energy affect the environment and make irrigation systems costly. This is one reason that led our city lacs of green spaces. There is thus a need for alternative energy source renewable and eco-friendly [5]. Wind energy is a renewable energy not degraded, geographically diffuse. It is one of the cleanest and most sustainable sources of power [6,7]. In this context, the study aim is to determine the requirement power of an off grid wind farm in order to irrigate an area of green space that is around 300 m².

2. Materials and methods

To carry out this study, we collect data on wind direction and speed at a depth of 10 meters in the soil for ten years (from 01/01/2013 to 31/12/2023) for three hours per day. We get this data from the POWER Data Access Viewer, which is affiliated with the NASA power agency, and the Bechar meteorological station (airport) located 5 kilometers north-west of the city.

The wind roses are the basic curves for determining the prevailing directions of the wind, and the histograms show the frequency of each speed. To determine the dominant directions of the wind and define the best wind field for this site, researchers conduct an annual and seasonal study of all wind directions during the study period, identifying changes between seasons.

After determining the prevailing directions of the wind, we study the seasonal and annual variation wind speed frequencies [10] that allowed it possible to determine the average wind speed V_{avr} , scale factor c and shape factor k , these parameters allow direct access to the characteristics wind potential [11,12]. three wind turbines with distinct designs studied for the same nominal power 2kw (vertical axis wind turbine generator EN-2KW-H, spiral blades vertical axis small wind turbine EN-XL-2KW and small horizontal axis wind turbine EN-2KW-L) in order to choose the most efficient [13], according to them

power curves the wind turbine EN-2KW-H is the most suitable for study region [14].

The productivity of a selected wind turbine is calculated using the Pallabazzer and Weibull distribution models and REETSscreen software.

After studying wind potential of the region, analyzing wind data and selection the wind turbine model that best match the site's wind conditions, then calculation its productivity, dimensioning a stand-alone wind farm becomes clear.

An off-grid wind system is an energy solution that uses wind turbines to generate electricity independently of the public utility grid. For isolated areas where grid electricity is either nonexistent, unstable, or too expensive to connect to, this kind of system is perfect. The following are the essential elements for Dimensioning a stand-alone wind system element [15,16]:

- Estimating energy consumption
- Determination of the optimal wind turbines number and their layout
- Total storage capacity of batteries bank
- Sizing charge controller
- Sizing the inverter

3. Results and Discussion

The area to be irrigated has palm trees, grass, flowers, and aromatic plants, the irrigation network combines both sprinkler and drip irrigation systems, for more details about hydraulic sizing, the references [1,2] provide information of the model used to estimate the energy required, the simple layout of the green area is illustrated in figure 1:

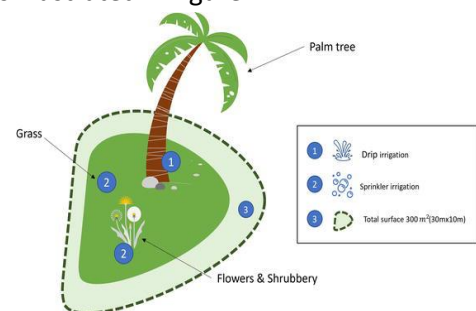


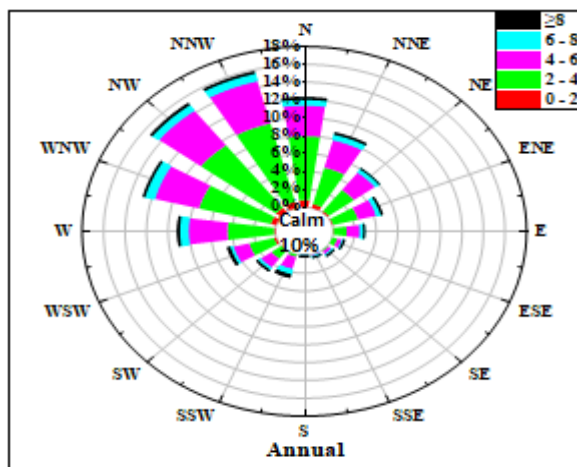
Figure 1. Layout of green space and different irrigation systems used [2].

The data shown in table (1) present some properties of the green space:

Table 1. Green space specification [1,2].

Type of soil	sandy loam
Root Depth Zone RDZ (mm)	0.7 (Palm tree) 0.5 (Grass)
Evapotranspiration at peak demand (mm/day)	7.4 (Palm tree) 8 (Grass)
Moisture FC-PWP (mm/m)	90
Pump power requirement	1100

Figure 2 presents the simulation of wind speed and direction data results in the annual wind rose and figure 4 illustrates wind rose for each season.


Figure 2. Annual wind rose in Bechar in period of study 2013-2023.

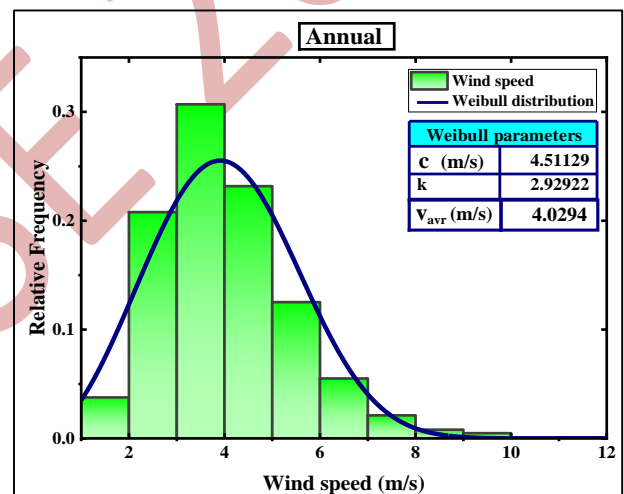
The annual wind rose illustrated reveals that the prevailing winds in Bechar during this period predominantly blow towards the northwest (NW). In fact, the three spokes representing the northwest direction (WNW, NW, and NNW) account for 44% (The summing the frequencies of each of these directions) of all hourly wind directions. In addition, it shows that southeast winds are infrequent. The wind rose also provide speed details from different directions. It shows that approximately 1% of the time (40.18 days of study period) the wind blows from the northwest at speeds between 0 and 2 meter per second (represented by the red color in the legend). Similarly, on this spoke, winds blow to the same direction at speeds between 2 and 4 m/s (green color) about 9% of the time (361 days), between 4 and 6 m/s (pink color) about 5% of the time (200.9 days), and between 6 and 8 m/s (blue color) about 1% of the time (40.18 days). Higher wind speeds are less frequent, where the speeds exceeding 8m/s (black color) being rare.

From the annual analysis, we can conclude that the Bechar region has two dominant directions, 15%

northwest wind and 16% (NN- towards W) (the longest spoke). The more frequent wind speeds between 2 and 4 m/s which represents 9% of the time or 361 days of the study period.

Based on the analysis of the wind rose for each season, we observe that the prevailing winds from the north-northwest (NN-O) in winter and autumn can reach 13%. While spring and summer have high frequencies towards (NN-O) in spring and on side (N-O) for summer at the respective rates of 16% and 20% where the winds look stronger compared with the other seasons (between 4 and 6 m/s about 8% of the time). In autumn and winter, the more frequent winds ranging from 2 to 4 m/s (8% in winter and 11% autumn).

Figures 3 and 5 show graphs of annual and seasonal histograms of wind speeds frequencies adjusted by the Weibull distribution.


Figure 3. The annual histogram of wind speeds at 10 m of the Bechar region adjusted by the Weibull distribution (2013-2023).

From results shown in figure (2), wind speeds cover a range of variation up to 10 m/s, large frequencies on the range from 2m/s to 5m/s during the period of study, where they attain their pic (30%) between 3 m/s and 4m/s, this confirms what the Weibull model is the suitable with speeds between 4 m/s and 10 m/s. The shape parameter k has a value of about 2.93. This suggests that the distribution has a relatively balanced spread between lower and higher wind speeds, but there is still some skewness towards higher wind speeds compared to a perfectly symmetric distribution. K presents the wind stability, where higher values represent a narrower distribution with more high-speed winds, while lower

values suggest a larger distribution with more low-speed winds [17].

In addition, the average wind speed attains 4.0294m/s and the value of scale parameter C equals 4.51129 m/s, it means that this site is moderately

windy, and the distribution has significant probability mass at both lower and higher wind speeds, making it potentially suitable for wind energy generation, because of the higher value of parameter c signify the more wind energy resources [11].

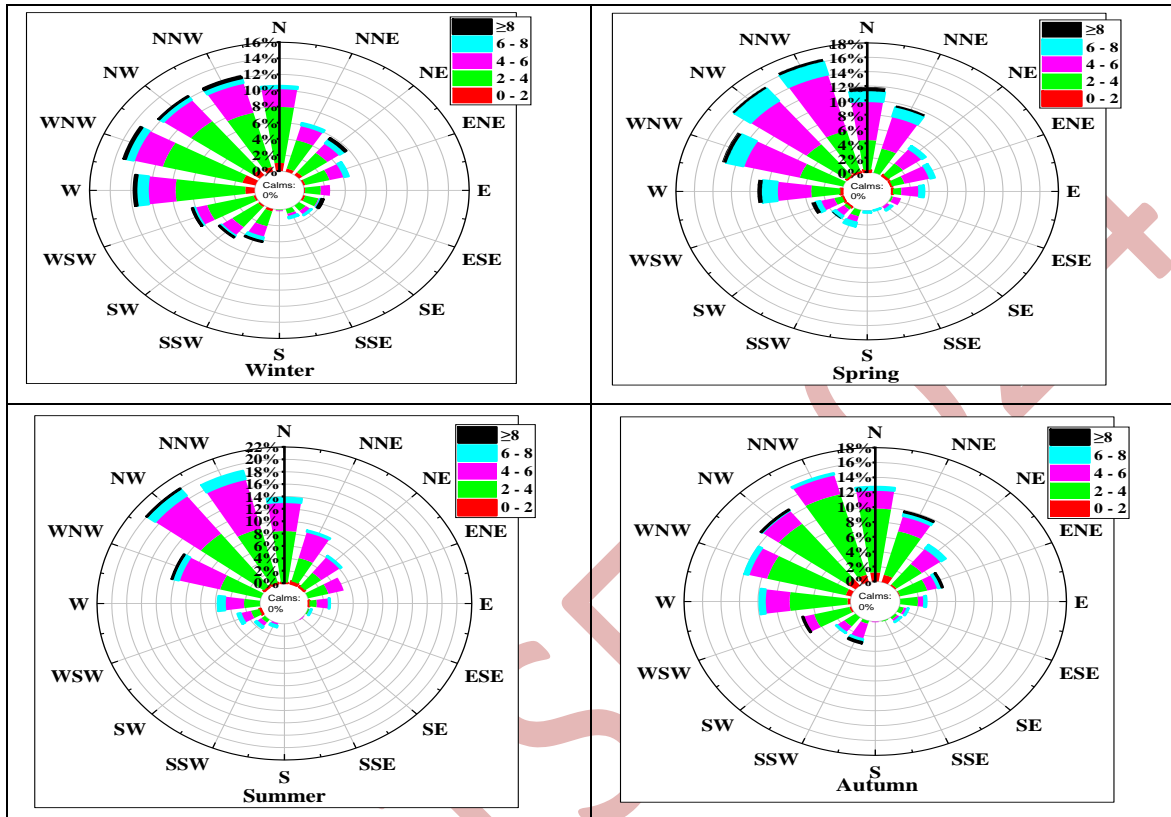
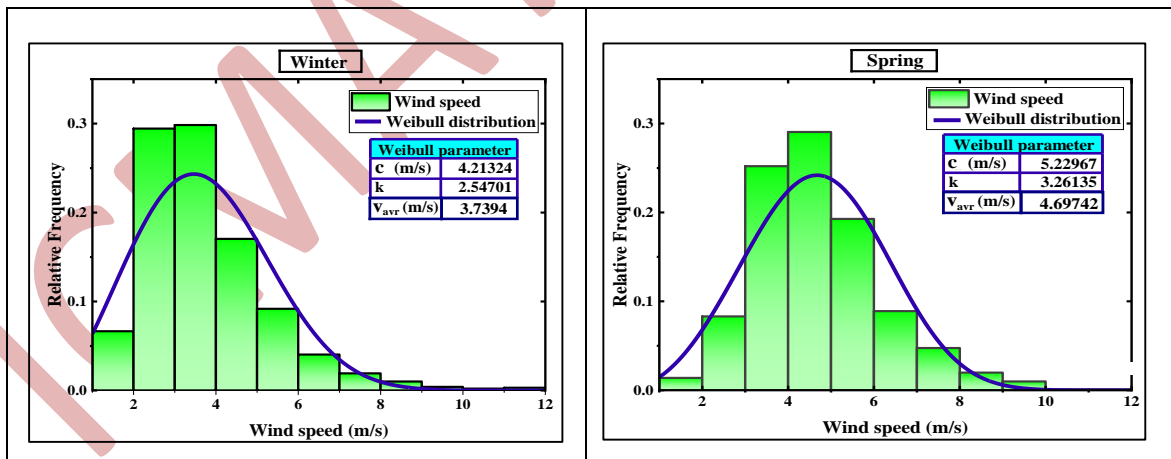


Figure 4. Seasonal wind rose in Bechar in period of study 2013/2023.



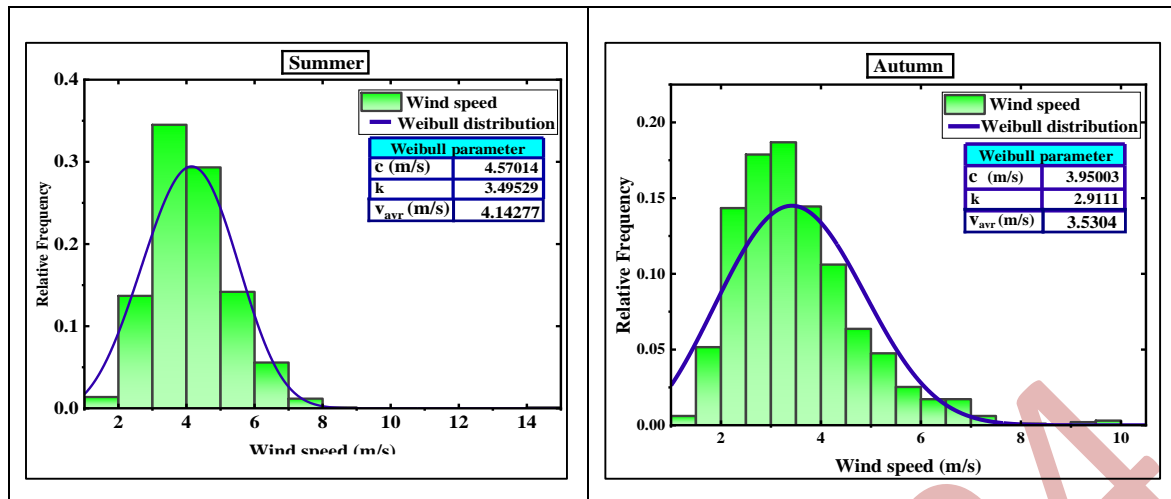


Figure 5. Seasonal histograms of wind speeds at 10 m of the Bechar region adjusted by the Weibull distribution (2013-2023).

It shows from the Figure 5, summer season has the highest frequencies that exceed 35% for a speed of 3 m/s to 4 m/s and 23% for 4m/s to 5m/s with a wind speed variation range that can reach 8 m/s. While the autumn season has a wide frequency range maximum which equals 19% with stability for speed values between 2 m/s and 4 m/s, and the variation of the wind speed can reach 8 m/s. spring has almost the same characteristics of summer but the high frequency does not exceed 30%. In winter, wind speeds between 2m/s and 4m/s are the most frequent (30%). In addition, the graphs present how well the Weibull distribution fits the data of wind speed throughout all seasons. The average wind speed and Weibull parameters values are converge in spring and summer: The range of the parameter k is from 3.26 to 3.49, between 5.22m/s and 4.57 the parameter c is the fluctuated, the mean wind speed varies between 4.69m/s and 4.16m/s. Winter and autumn also have a close values of Weibull parameters and average wind speed (k ranges from 2.54 to 2.91, c from 4.21 m/s to 3.95 m/s, and v_{avr} from 3.73 m/s to 3.53 m/s).

These results present that spring and summer are the windiest period in the year, where the distribution has a higher probability of extreme wind speeds compared with other seasons.

According seasonal analyzes, it mentioned that the study site gives a stability of data in all seasons, significant frequencies over almost the same range from 2m/s to 6m/s throughout the year, The Weibull distribution offers a well-fitting with data of wind speed in the four seasons. In result, spring and summer season are the windiest period in the year.

Considering that the Bachar region has moderate wind resources, which is recommended for

investment, where using a small-scale wind turbine is preferable. In this context, three wind turbines with distinct designs studied for the same nominal power 2kw (vertical axis wind turbine generator EN-2KW-H, spiral blades vertical axis small wind turbine EN-XL-2KW and small horizontal axis wind turbine EN-2KW-L) in order to choose the most efficient [13], according to them power curves the wind turbine EN-2KW-H is the most suitable for study region [14]. Table (2) presents technical specifications of the selected wind turbine.

Table 2. The technical data of wind turbine selected.

Turbine diameter	2,55m
Rotor type	vertical straight blades
Blade material	Strong glass fiber
Peak output	2000w at 12m/s
Cut in speed (v_d)	2 m/s
Rated speed (v_n)	12 m/s
Cut out speed (v_m)	40 m/s
Wheel height	3m
Rated voltage	48v
Generator type	Permanent magnet generator

Using Weibull distribution and Pallabazzer models and REETScreen software, the productivity of selected wind turbine is determined, figure 6 presents the annual productivity [18]:

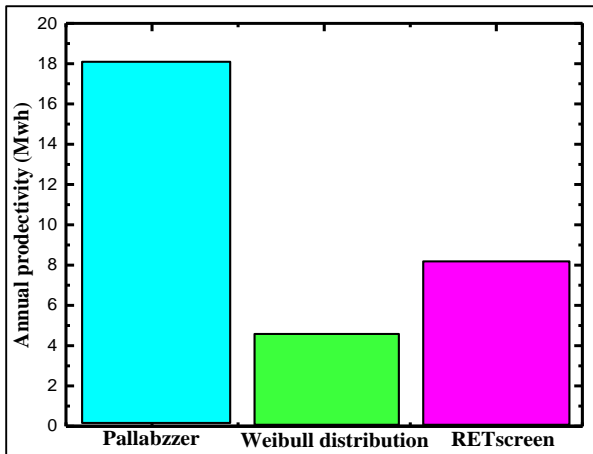


Figure 6. The annual wind energy output by wind turbine model EN-2KW-H.

As graph illustrated in figure 4 shows there is variation in annual productivity estimates between the Pallabazzar model, the Weibull model and RETScreen software (18 Mwh by Pallabazzar model, 4.5 Mwh by Weibull distribution and 8 Mwh by RETScreen software), this caused by the differences in approach and basic assumptions between them.

The Pallabazzar is simpler and rely on technical characteristics of wind turbine as capacity factor, cut in speed, while Weibull distribution model is more mathematically rigorous and detailed, it provides a more precise estimation by Integrate wind turbine's power curve with wind speed distribution. In the other hand RETScreen combines detailed climate data, turbine specifications, and various models in order to estimate energy production, it is considered tool that offers the most comprehensive and precise analysis, making it appropriate for expert feasibility assessments and detailed project planning. Therefore, each method has advantages and best use cases of its own. The choice depends on the specific needs and data for the wind energy project.

Acknowledgements

The General Direction of Scientific Research and Technology (DGRSDT) of the Algerian Ministry of Higher Education and Research support this social-economical project **2021/2024, N°2: protection de l'environnement et le développement durable au site de Béchar: traitement de l'eau usée par phytoépuration couplé à un système hybride PV-éolien** and PRFU project N°BOOL02UN080120220004: Smart irrigation system for green space in semiarid region of Algeria powered by solar energy.

We are grateful to **Miss. Fouzia Mehdi** for his significant contribution to finish this paper.

References

1. Hadja Guedaouria, Mebarka Daoudi, Youcef Benmoussa, Abdelhak Maazouzi; Irrigation Network Requirements for Watering Urban Green Space in Semiarid Region, 2022 IOP Conf. Ser.: Earth Environ. Sci. 973 012013.
2. Mebarka Daoudi, Hadja Guedaouria, Youcef Benmoussa, Abdelhak Maazouzi, Karima Seddiki, Fouzia Mehdi, Hanane Maammeri and Asma Belaid, Hydraulic Sizing for Watering Green Space Application in Bechar-Algeria'. Urban Horticulture - Sustainable Gardening in Cities, IntechOpen, 17 July 2023. Crossref, doi:10.5772/intechopen.1001914.

The results of sizing an autonomy wind system illustrated in table (3):

Table 3. Elements of autonomy wind system sizing.

Wind turbine model	Vertical Axis Wind Turbine Generator EN-2KW-H
Number of wind turbine	2 turbines
Battery number & model	4 batteries & Victron Energy Lithium Smart battery with Bluetooth
Wind controller model	TriStar C60
Wind inverter model	EEJG-2000W

4. Conclusion

To realize an off-grid wind farm for irrigation, we need the efficiency method of calculation and sizing. This study concludes from the annual and seasonal analysis of wind data that there are two dominant wind directions in the Bechar region: northwest (NW) and north (NN-W), with wind speeds that are the more frequent (between 2 and 4 m/s). Here, the Weibull distribution model is more suitable at speeds varying from 4 m/s to 10 m/s. parameters k (4.5) and c (2.9 m/s) provide valuable insights into the wind speed characteristics of the location and are essential for wind resource assessment and wind energy project planning, recommend that Bechar region has suitable potential for wind energy projects with moderate wind resources. We made this effort to draw the attention of the persons responsible in the energy sector to use wind energy in the Bechar region. This can contribute to reducing the costs of irrigation systems and encourage the creation of green spaces.

3. Tony Burton, David Sharpe, Nick Jenkins, Ervin Bossanyi, WIND ENERGY HANDBOOK, (2001) by John Wiley & Sons, Ltd Baffins Lane, Chichester West Sussex, PO19 1UD, England ISBN: 978-0-470-69975-1.
4. Abdesselem Kabour, Azedine Hani, Lynda Chebbah; Impact Des Rejets Urbains Sur Laqualite Des Eaux Souterraines De La Ville De Bechar (SW ALGEIEN), second international conference on applied energetics and pollution. (ICAEP) 2014 Constantine, Algeria.
5. Preface of the First International Conference on Physics of Semiconductor Devices, Renewable Energies, and Environment M Daoudi, S Kadri, Y Himri, M Bensafi, A Talhi Physical Sciences Forum 6 (1), 9, 2023.
6. Vaughn Nelson, Kenneth Starcher, Wind Energy: Renewable Energy and the Environment. 3rd Edition (2019).
7. Bangga, G. Progress and Outlook in Wind Energy Research. *Energies* 2022, 15, 6527. <https://doi.org/10.3390/en15186527>.
8. Genç, M. S. Determination of the Most Appropriate Site Selection of Wind Power Plants Based Geographic Information System and Multi-Criteria Decision-Making Approach in Develi, Turkey. *IJSEPM* 2021, 30.
9. Hakim Merarda, Mohamed Toumi, Azzedine Boutelhig, Analysis of heliostat fatigue: Impact of wind speed distribution, studied over six regions of Algeria, *Solar Energy*, Volume 278, 2024, 112776, ISSN 0038-092X, <https://doi.org/10.1016/j.solener.2024.112776>.
10. Li, Z.; Xu, B.; Shen, X.; Xiao, H.; Hu, Z.; Cai, X. Performance Analysis of Ultra-Scale Downwind Wind Turbine Based on Rotor Cone Angle Control. *Energies* 2022, 15, 6830. <https://doi.org/10.3390/en15186830>.
11. A, Marshli and all, Statistical Analysis of Wind Speed Distribution Based on Five Weibull Methods for Wind Power Evaluation in Maan, Jordan, *Journal of Energy Technologies and Policy*, SSN 2224-3232 (Paper) ISSN 2225-0573 (Online), Vol.11, No.4, 2021.
12. Guenoukpati, A., Salami, Kodjo, M.K., and Napo, K, Estimating Weibull Parameters for Wind Energy Applications Using Seven Numerical Methods: Case studies of Three Coastal Sites in West Africa. *International Journal of Renewable Energy Development* (2020), 9(2), 217-226.
13. Alcayde, A.; Hernandez-Escobedo, Q.; Muñoz-Rodríguez, D.; Perea-Moreno, A.-J. Worldwide Research Trends on Optimizing Wind Turbine Efficiency. *Energies* 2022, 15, 6559. <https://doi.org/10.3390/en15186559>.
14. Chitura, A.G.; Mukumba, P.; Lethole, N. Enhancing the Performance of Savonius Wind Turbines: A Review of Advances Using Multiple Parameters. *Energies* 2024, 17, 3708. <https://doi.org/10.3390/en1715370>.
15. Stand-Alone Wind Energy system A Buyer's Guide, Marbek Resource Consultants and SGA Consulting for the Renewable and Electrical Energy Division, (2003) Energy Resources Branch of Natural Resources Canada (NRCAN).
16. Matt Little, Wind Turbine Electrical System Design Guide, 1 (2008) pp11-44.
17. Azada, A. K and all, Analysis of wind energy conversion system using Weibull distribution, 10th International Conference on Mechanical Engineering, ICME 2013, *Procedia Engineering* 90 (2014) 725 – 732 ELSEVIER. Statistical Analysis of Corrosion Data Luciano Lazzari, in *Engineering Tools for Corrosion*, 2017.
18. Sameh Alsaqoor¹, Abdullah Marshli, Reem At-Tawarah, Gabriel Borowski, Ali Alahmer, Nader Aljabarin, Nabil Beithou; Evaluation of Wind Energy Potential in View of the Wind Speed Parameters – A Case Study for the Southern Jordan. *Advances in Science and Technology Research Journal* 2022, 16(6), pp 275–285.

Prospects of laser processing of Ta-substituted TiO₂ for designing thermoelectric materials

Diogo Lopes

*CICECO – Aveiro Institute of Materials, Department of Materials and Ceramic Engineering,
University of Aveiro, 3810-193, Aveiro, Portugal, djlopes@ua.pt
ORCID: 0000-0002-1087-9990*

Nuno Ferreira

*i3N – Physics Department, University of Aveiro, 3810-193, Aveiro, Portugal, nmferreira@ua.pt
ORCID: 0000-0002-4398-9256*

Andrei Kovalevsky

*CICECO – Aveiro Institute of Materials, Department of Materials and Ceramic Engineering,
University of Aveiro, 3810-193, Aveiro, Portugal, akavaleuski@ua.pt
ORCID: 0000-0001-5814-9797*

Cite this paper as: Lopes, Diogo, Ferreira, Nuno, Kovalevsky, Andrei. Prospects of laser processing of Ta substituted TiO₂ for designing thermoelectric materials. Int. Conf. Advanced. Mater. Sci. & Eng. HiTech. and Device Appl. Oct. 24-26 2024, Ankara, Turkiye

Abstract. The potential of Ta-substituted titanium dioxide (TiO₂) for thermoelectric applications was investigated using the Laser Floating Zone (LFZ) method under varying growth atmospheres: air and H₂/N₂. Samples were also post-annealed in H₂/N₂ following LFZ growth in air to further analyze the effects of processing conditions. X-ray diffraction (XRD) revealed rutile as the dominant phase, with phase composition influenced by the atmosphere. While oxidizing conditions led to TiTa₂O₇, reducing conditions favored the formation of Magnéli phases, particularly in samples with lower tantalum content. Thermogravimetric analysis confirmed that LFZ processing in a hydrogen atmosphere promotes titanium reduction and oxygen vacancies, improving electrical properties. The Seebeck coefficient and electrical conductivity were measured at high temperatures to evaluate thermoelectric performance. A maximum power factor of 735 μW/(m·K²) was achieved at 1120 K, one of the highest values reported for similar materials. This study demonstrates the effectiveness of LFZ processing, particularly in reducing atmospheres, for enhancing the thermoelectric performance of Ta-substituted TiO₂.

Keywords: Thermoelectric oxide; Rutile; Laser Floating Zone technique; electrical performance; power factor.

© 2024 Published by ICMATSE

The need for sustainable energy and efficient technologies has driven the exploration of thermoelectric (TE) materials, which convert thermal gradients into electrical energy, thus recovering waste heat from industrial processes [1]. The efficiency of this conversion is expressed by the dimensionless figure of merit, ZT:

$$ZT = \frac{\alpha^2 \sigma}{\kappa} \times T \quad \text{Eq. [1]}$$

Where α is the Seebeck coefficient, σ electrical conductivity, κ thermal conductivity, and T is the operating temperature, achieving high ZT values requires optimizing these properties [2]. While

effective, traditional thermoelectric materials like PbTe and Bi₂Te₃ face limitations due to toxicity and instability at high temperatures [3]. Alternatively, TiO₂-based materials are abundant, stable, and non-toxic, making them promising candidates for high-temperature applications [4].

This study focuses on using the Laser Floating Zone (LFZ), figure 1, to process Ta-substituted TiO₂ under air and H₂/N₂ atmospheres. Samples were also post-annealed in a reducing atmosphere to study its effects on microstructure and thermoelectric performance. Structural characterization was done via X-ray diffraction (XRD), while thermoelectric properties, including the Seebeck coefficient and electrical conductivity, were measured at high

temperatures. XRD revealed that rutile was the dominant phase across all samples, and the growth atmosphere significantly influences phase composition, with TiTa_2O_7 forming under oxidizing conditions and Magnéli phases appearing in reducing conditions, especially in samples with lower Ta content.

Thermogravimetric analysis confirmed that LFZ processing in a hydrogen-containing atmosphere

promoted the reduction of titanium cations and induced oxygen vacancies, enhancing electrical conductivity. A maximum power factor of $735 \mu\text{W}/(\text{m}\cdot\text{K}^2)$ was achieved at 1120 K. The results indicate that LFZ processing can significantly improve the thermoelectric properties of Ta-substituted TiO_2 , making it a promising candidate for high-temperature thermoelectric applications.

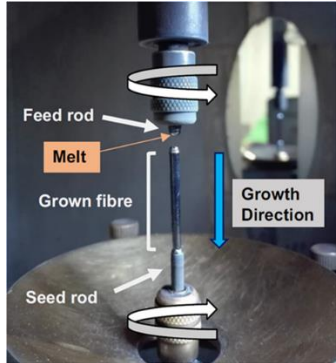


Figure 1. Schematic representation of the LFZ growth process.

References

1. J. He, Y. Liu, and R. Funahashi, "Oxide thermoelectrics: The challenges, progress, and outlook," *J. Mater. Res.*, vol. 26, no. 15, pp. 1762–1772, 2011, doi: 10.1557/jmr.2011.108.
2. A. V. Kovalevsky et al., "Designing strontium titanate-based thermoelectrics: insight into defect chemistry mechanisms," *J. Mater. Chem. A*, vol. 5, no. 8, pp. 3909–3922, 2017, doi: 10.1039/C6TA09860F.
3. F. P. Carreira, N. M. Ferreira, and A. V. Kovalevsky, "Laser processing as a tool for designing donor-substituted calcium manganite-based thermoelectrics," *J. Alloys Compd.*, vol. 829, p. 154466, 2020, doi: 10.1016/j.jallcom.2020.154466
4. H. Lee, S. J. Han, R. Chidambaram Seshadri, and S. Sampath, "Thermoelectric properties of in-situ plasma spray synthesized substoichiometry TiO_{2-x} ," *Sci. Rep.*, vol. 6, no. 1, p. 36581, Nov. 2016, doi: 10.1038/srep36581

Bulk Nanostructured Bainitic Steels: Superior Engineering Properties with Considerable Mechanical and Thermal stability

Behzad Avishan

Azərbaycan Şahid Mədani Universiteti, Mühəndislik Fakültəsi, Material Mühəndisliyi Departamenti, Tabriz, İran

Başkent Üniversitesi, Mühəndislik Fakültəsi, Mexanika Mühəndisliyi Departamenti, Ankara, Türkiyə

bavishan@baskent.edu.tr

ORCID: 0000-0001-7852-4478

Cite this paper as: B. Avishan, Bulk Nanostructured Bainitic Steels: Superior Engineering Properties with Considerable Mechanical and Thermal stability, Int. Conf. Advanced. Mater. Sci.& Eng. HiTech.and Device Appl.Oct. 24-26 2024, Ankara, Turkiye

Abstract. Bulk nanostructured bainitic steels represent a breakthrough in advanced high-strength steels (AHSS), offering exceptional mechanical properties due to their nanoscale microstructures. With ultimate tensile strengths ranging from 1.6 to 2.5 GPa and elongation rates of 10-30%, these materials are strong contenders for various industrial applications. This article introduces these cutting-edge materials, emphasizing their microstructural characteristics and the resulting mechanical properties. The role of the TRIP effect and the factors influencing it are thoroughly examined, highlighting its contribution to the material's enhanced performance. Additionally, the thermal stability of the nanostructured microstructure is discussed, with a focus on its remarkable tempering resistance, essential for applications requiring high-temperature durability. Key microstructural parameters such as size, morphology, and volume fraction, along with the heat treatment process, are identified as critical factors affecting the material's properties. Furthermore, it is demonstrated that these steels maintain their mechanical integrity at temperatures up to 400 °C, showcasing their suitability for high-temperature applications. By highlighting these advantages, bulk nanostructured bainitic steels are presented as a superior alternative to conventional AHSS, offering unmatched potential for high-performance applications that demand exceptional strength, toughness, and reliability.

Keywords: Nanobainite, Microstructure, Mechanical Performance, Mechanical Stability, Thermal Stability

© 2024 Published by ICMATSE

Introduction: Advanced high-strength steels (AHSS) offer superior mechanical properties compared to conventional steels, including enhanced strength, ductility, and toughness. They are crucial in modern manufacturing technology and engineering and are extensively used in the automotive industry, construction, machinery, and other sectors where material performance is critical. Among their different types, TRIP-assisted steels, metastable austenitic steels, medium-Mn TRIP steels, Q&P steels, and nanostructured bainitic steels provide an interesting strength-ductility combination, thanks to the austenite phase present in their microstructure and the corresponding TRIP effect phenomenon [1]. Nanostructured low-temperature bainitic steels consist of nanoscale bainitic ferrite, high-carbon retained austenite films, and austenite microblocks. While bainitic ferrites are responsible for the strength properties, austenite morphology and content are critical factors in ductility performance.

Additionally, the austenite phase adds to the strength of the engineering part due to the TRIP phenomenon [2]. On the other hand, high-carbon retained austenite present within the microstructure is susceptible to decomposition to ferrite and cementite at high temperatures, which can restrict component usage in high-temperature applications. Accordingly, both mechanical and thermal stability of the austenite must be considered to achieve the desired material with the required mechanical performance. The aim of the present work is to track the microstructural characteristics and the resulting mechanical properties in these high-performance steels. Moreover, the importance of the TRIP effect is examined, and the thermal stability of the high-carbon retained austenite is discussed, which is essential for high-temperature applications. Primary steel with a chemical composition of 0.9C, 1.63Si, 1.84Mn, 0.23Mo, 1.21Cr, 1.4Co, and 0.58Al (all in

weight percent) was received in sheet form after casting, homogenization, and hot rolling in 15 mm sheet shape. Nanostructured bainite was obtained after austenitizing at 900 °C for 30 min, followed by isothermal austempering at 200 and 300 °C for the optimum heat treatment time. The thermal stability of the microstructure has been studied after reheating the samples to the temperature range of 400-650 °C for 1 h. Microstructural evaluations were performed using a field emission gun scanning electron microscope (FEG-SEM) and X-ray diffraction methods. The hardness of the materials was determined, and tensile and Charpy impact tests were carried out at room temperature.

Results and discussion: Fig. 1 shows the microstructural characteristics of bainite obtained after isothermal transformation at 200 and 300 °C. The microstructure consists of bainitic sheaves separated by austenite microblocks, with each sheaf comprising alternating layers of nanoscale bainitic ferrites (bainite subunits) and austenite films. It is evident that bainitic ferrites and austenite films, with thicknesses of less than 70 nm, were achieved, being thinner at the lower transformation temperature.

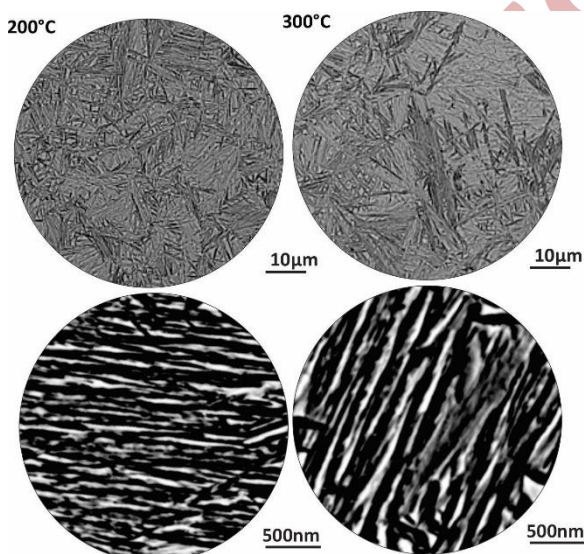


Figure 1. *Microstructure of original nanostructured bainite*

Bainite transformation starts with paraequilibrium nucleation of bainitic ferrites from primary austenite grain boundaries and progresses by their shear growth mechanism. The strength of the parent austenite from which bainite forms is a critical factor for the thickness of the bainitic subunits. Stronger austenite restricts the motion of the glissile interface of austenite/ferrite, resulting in finer bainitic subunits. In this study, bainitic subunits of 68 and 27 nm, and austenite films of similar thicknesses were

achieved at the end of the 300 and 200 °C transformations, respectively. Unlike martensite, which forms by shear transformation, bainite transformation is a paraequilibrium process, during which carbon partitioning from bainitic ferrite into the surrounding austenite occurs due to the higher transformation temperature, increasing the carbon content in solid solution in austenite. Carbon in solid solution stabilizes austenite, and it has been shown that almost 1 wt% of carbon is sufficient to stabilize the austenite phase. Accordingly, different tempering behavior is expected for bainite compared to that of martensite, which is well discussed elsewhere [3]. Generally, austenite is present in two morphologies—filmy and blocky—in nanobainite. Austenite microblocks are thermally and mechanically less stable compared to austenite films, and it is necessary to replace austenite blocks with austenite films as much as possible if enhanced mechanical properties are desired. Decreasing the primary austenite grain size, applying step austempering processes, and ausforming can be beneficial in this regard. Fig. 2 illustrates the XRD profiles of the heat-treated samples, and the corresponding refinements indicated that approximately 30% and 43% of austenite were attained in samples austempered at 200 and 300 °C, respectively. It is logical to obtain a higher volume fraction of bainite and, therefore, lower austenite content at lower transformation temperatures, according to the bainite transformation theory.

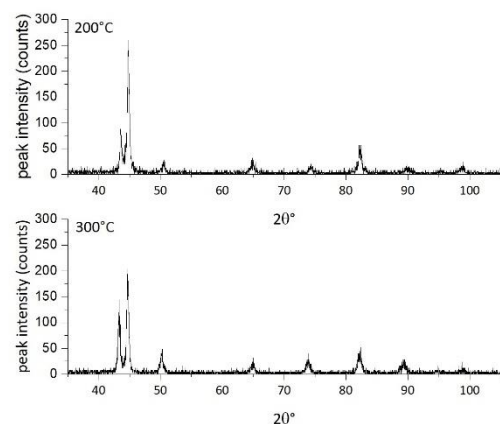


Figure 2. *XRD profiles for nanobainite obtained at two different temperatures*

Microstructural characteristics are directly responsible for the mechanical properties achieved in nanostructured bainite. Table 1 summarizes the resultant mechanical properties of steels heat-treated at two different temperatures in this study. Generally, different parameters control the strength-ductility combination in nanobainite. It is important

to note that while the volume fraction and thickness of the bainitic ferrites are critical factors for strength properties, austenite content and its morphology influence ductility. A higher volume fraction of thinner bainite is necessary for increased hardness and strength values. This is why stronger nanostructured bainitic steel is obtained at 200 °C. The dislocation density in nanobainite is also a crucial factor to consider when analyzing strength properties. A high number of dislocations are introduced within the microstructure of the material due to the shear transformation phenomenon, which can increase strength and hardness. Decreasing the transformation temperature and consequently stronger austenite, from which bainite forms, results in a higher number of dislocations in nanobainite. Examples of these dislocations can be found in Fig. 3.

Table 1. *Hardness (HV30), Yields strength (YS), Ultimate tensile strength (UTS), Elongation (El) and Impact toughness energy (IE) of the heat-treated materials*

Mechanical properties	200 °C	300 °C
HV30	544±10	430±10
YS (Mpa)	1500±11	1166±14
UTS (Mpa)	2340±20	1620±16
El (%)	14±2	30±3
IE (J)	10±3	18±3

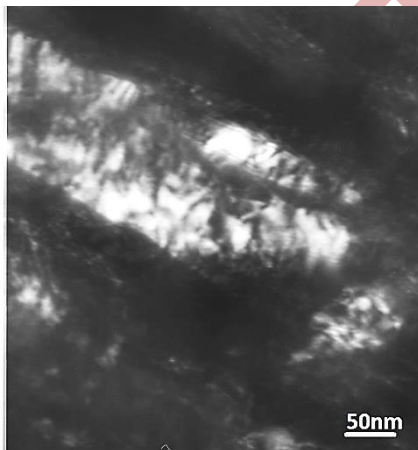


Figure 3. *dislocations introduced within the nanobainite achieved at 200 °C due to the shear transformation*

Although the austenite phase controls the ductility properties, its transformation to martensite during straining (TRIP effect) boosts both strength and ductility [2,4,5]. This is why the mechanical stability of austenite is a crucial factor that must be carefully considered. Moderate mechanical stability is essential to maximize the positive effect of the TRIP phenomenon, as it delays the austenite-to-martensite transformation, allowing for greater energy absorption and enhanced mechanical

performance [6]. Generally, austenite films are mechanically more stable compared to those with a blocky morphology. Austenite blocks are poorer in carbon, especially at their centers, making them prone to transform into martensite at earlier stages of deformation. As a result, replacing austenite blocks with austenite films and decreasing the size of the blocks can be beneficial for enhancing mechanical properties. Given the higher volume fraction of austenite in nanobainite obtained at higher transformation temperatures, it is logical to achieve higher toughness and elongation values, even if refined austenite blocks at an identical transformation temperature may further increase ductility. Besides the mechanical stability of austenite, its thermal stability is also of great importance, especially for high-temperature applications of nanostructured bainitic engineering parts. The question is: how does the tempering behavior of nanostructured bainite differ from that of martensitic steels? This can be addressed by examining the microstructural characteristics and mechanical performance of nanostructured bainite at high temperatures, by reheating the samples after the completion of the bainite reaction. As shown in Fig. 4, microstructural analysis confirms no significant change after reheating the sample up to 400 °C, indicating excellent resistance to microstructural decomposition. It can be concluded that, unlike martensite, the super bainite microstructure has significant thermal stability. Increasing the reheating temperature and corresponding microstructural studies indicated different behavior in microstructural changes. Cementite precipitations occurred at 500 °C, becoming more significant at higher temperatures. Moreover, austenite microblocks began to decompose into pearlite at 550 °C.

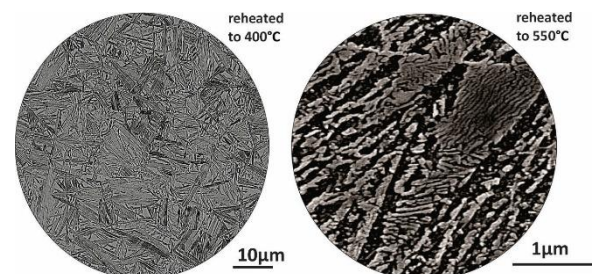


Figure 3. *Microstructure of reheated nanostructured bainite*

The results indicate that nanostructured bainite exhibits high thermal stability of its microstructure at elevated temperatures up to 400 °C, making it suitable for high-temperature applications if its mechanical properties remain consistent. The

hardness changes in nanostructured bainitic steels were compared with those in high-carbon steel with a martensitic microstructure after reheating to various temperatures for 1 hour. The findings showed significant differences in the tempering behavior between nanostructured bainite and martensite. In steels with martensite, hardness began to decrease upon reheating to 300 °C, with further reductions as the temperature increased. Conversely, the hardness of nanostructured bainitic steel remained stable even at 400 °C (see Table 2) and matched the values achieved under optimal austempering conditions. At 500 and 550 °C, not only did the hardness not decrease, but it slightly increased, reaching a peak before declining when reheated to 600 °C and above. Therefore, it can be concluded that, unlike martensitic steel, nanostructured bainitic steel exhibits excellent tempering resistance up to approximately 400–450 °C.

Table 2. Hardness (HV30), Yields strength (YS), Ultimate tensile strength (UTS), Elongation (El) and Impact toughness energy (IE) of the heat-treated materials

Mechanical properties	400 °C	500 °C	550 °C
HV30	430±10	500±10	520±110
YS (Mpa)	1125±15	1740±14	1545±10
UTS (Mpa)	1514±20	2006±15	1797±15
El (%)	29.1±2	5±1	5.3±3
IE (J)	19±2	8±3	-

Table 2 also summarizes the mechanical properties of the nanostructured bainite obtained at the end of austempering at 300 °C after reheating to higher temperatures. The sample reheated to 400 °C exhibited strength and ductility properties similar to

the initially formed super bainite, as they shared nearly identical microstructural characteristics, as previously discussed. The minor reduction in yield strength (YS) and ultimate tensile strength (UTS) is likely due to dislocation recovery at 400 °C. An increase in reheating temperature to 500 °C led to cementite precipitation, which enhanced strength properties. However, at 550 °C, austenite decomposition and pearlite formation caused a decrease in strength, which became more pronounced at 600 and 650 °C due to severe austenite decomposition and cementite spheroidization. Spheroidized cementite within the ferrite matrix at these temperatures resulted in the lowest strength levels. Changes in elongation can be linked to microstructural transformations. The similar elongation of the original super bainite and the sample reheated to 400 °C can be attributed to their similar austenite content and microstructural morphology. A reduction in austenite content by nearly 50% in the specimen reheated to 500 °C led to decreased elongation. Nonetheless, pearlite formation, more extensive austenite decomposition, and cementite spheroidization at higher temperatures increased elongation compared to the initially obtained nanobainite.

Conclusion: Nanostructured bainite is stable against any microstructural variations up to reheating at 400 °C, and nearly identical hardness and strength-ductility properties can be achieved compared to the base material. According to the results, large austenite blocks are susceptible to decomposition into pearlite, whereas austenite films are thermally more stable.

References

1. M. Soleimani, A. Kalhor, H. Mirzadeh, Transformation-induced plasticity (TRIP) in advanced steels: A review, *Mat Sci Eng A*, 795 (2020) 140023, 10.1016/j.msea.2020.140023
2. B. Avishan, Transformation induced plasticity effect under tensile and compression stresses in nanostructured bainite, *Mat Sci Eng A*, 729 (2018), pp. 362-369, 10.1016/j.msea.2018.05.085
3. P. R. Oskouei, B. Avishan, Thermal stability of microstructure and corresponding hardness variations in two high-carbon nanostructured bainitic steels, *Mater. Today Commun*, 37 (2023), 107153, 10.1016/j.mtcomm.2023.107153
4. C. Garcia-Mateo, F.G. Caballero, T. Sourmail, M. Kuntz, J. Cornide, V. Smanio, R. Elvira, Tensile behaviour of a nanocrystalline bainitic steel containing 3 wt% silicon, *Mat Sci Eng A*, 549 (2012), pp. 185-192, 10.1016/j.msea.2012.04.031
5. J. Hyun Ryu, D. I. Kim, H. Seop Kim, H.K.D.H. Bhadeshia, D. W. Suh, Strain partitioning and mechanical stability of retained austenite, *Scrip Mater*, 63 (2010), pp. 297-299, 10.1016/j.scriptamat.2010.04.020
6. B. Avishan, S. Yazdani, F. G. Caballero, T. S. Wang, C. Garcia-Mateo, Characterisation of microstructure and mechanical properties in two different nanostructured bainitic steels, *Mater Sci Tech*, 31 (2015), pp. 1508-1520, 10.1179/1743284714Y.0000000745

Effect of PbS Quantum Dot Nanoparticles on The Dielectric Properties of Nematic Liquid Crystals

Doğan Burak Aydın

Department of Physics; Kocaeli University; 41001, İzmit, Türkiye,
235131012@kocaeli.edu.tr
ORCID: 0000-0003-0563-9439

Leyla Taştan

Department of Physics; Kocaeli University; 41001, İzmit, Türkiye,
235131011@kocaeli.edu.tr
ORCID: 0009-0008-0968-2825

Mahpeyker Kocakoç Toprakoğlu

Department of Computer Technologies; Çukurova University; 01130, Adana, Türkiye,
mkocakoc@cu.edu.tr
ORCID: 0000-0001-7966-1482

Mouna El Abboubi

Department of Physics; Kocaeli University; 41001, İzmit, Türkiye,
186131006@kocaeli.edu.tr
ORCID :0000-0001-5745-0633

İdris Candan

Department of Physics; Kocaeli University; 41001, İzmit, Türkiye,
idris.candan@kocaeli.edu.tr
ORCID: 0000-0002-9950-713X

Sait Eren San

Department of Physics; Kocaeli University; 41001, İzmit, Türkiye,
saiteren.san@kocaeli.edu.tr
ORCID: 0000-0001-5042-4555

Cite this paper as: Aydın, DB, et al., Effect of PbS Quantum Dot Nanoparticles on The Dielectric Properties of Nematic Liquid Crystals., Int. Conf. Advanced. Mater. Sci.& Eng. HiTech.and Device Appl.Oct. 24-26 2024, Ankara, Turkiye

Abstract. In this study, different ratios of PbS quantum dots were doped to Nematic Liquid Crystals (NLCs) Dielectric Spectroscopy technique and capacitance-voltage (C-V) measurements using a LCR meter and a Source Meter were carried out to detailed investigation of the electrical properties of the samples. The optical characteristics of the samples were examined using UV-Vis spectroscopy. Moderate conductivity values and enhanced electrical behavior were noted when PbS QDs nanoparticles were doped into nanoparticles. The transmittance measurement showed that the doping of PbS QDs decreased the wave amplitude and, consequently, the nonlinear effects.

Keywords: Nematic Liquid Crystals; Dielectric Spectroscopy; PbS nanoparticles; Conductivity
© 2024 Published by ICMATSE

1.Introduction

Advances in nanoscience and nanotechnology bring about several application possibilities. Artificially designed materials are critical for applications in these areas. One material that is widely used in this application is liquid crystal (LC), which is a crucial

material with a nonlinear nature that offers amazing application possibilities. Due to their self-assembly properties and spatial control capabilities, they provide a variety of designs and usage possibilities in a wide variety of display devices such as televisions, clocks, viewfinders, computer monitors, laptop screens, digital displays, billboards, and navigation

systems. Each display pixel is made up of a configuration of liquid crystals that are guided by its own electromagnetic field [1]. The capacity for self-assembly and the simplicity with which their properties can be altered in response to external electric or magnetic fields make nematic liquid crystals (NLCs) unique among LCs. Recent advancements in nanotechnology have enabled the integration of nanoparticles, such as quantum dots, into LCs, which has opened up possibilities for modifying and enhancing their dielectric and conductive properties [2]. Lead sulfide semiconductor quantum dots (PbS QDs), with their adjustable bandgap and near-infrared emission, present promising opportunities for such modifications [3]. PbS QDs have excellent optical properties, suitable band width and near infrared emission wavelength range of 900 nm and 1600 nm. By controlling their size, they can easily extend the absorption wavelength of the primary exciton into the near infrared region. The calculated Bohr exciton radius for PbS semiconductors is approximately 20 nm, and the energy range can be tuned between 0.7 eV and 2.1 eV depending on the particle size.[4]

In this study, the effect of doping PbS QDs into NLCs on their dielectric and optic properties were investigated. We examined the effects of the variation in PbS QDS doping concentration on the conductivity and dielectric response of NLCs using dielectric spectroscopy and current-voltage (I-V) measurements.

2. Experimental

ITO cells were filled with commercially purchased liquid crystals. To examine the effects of adding PbS QDs, three separate liquid crystal cells were prepared. PbS QDs were added to the other two in varying ratios, leaving one of them without adding QDs as a reference. Before measurements, each sample was kept for one hour at 70 °C on a hot plate.

Optic characterizations of the samples were carried out by transmittance measurements using Agilent 8453 UV-Vis spectrophotometer in the wavelength region 300-1100 nm. For the electrical characterization, the capacitance-voltage (C-V) measurements were performed by using using a HIOKI 3522-50 LCR HiTester in the 0-5 V bias voltage range at constant frequencies for pure and PbS QDs added NLC samples.

3. Results and Discussion

In this section, we present the results of our study on the enhancement of the electrical and optical properties of liquid crystals doped with quantum dots. The following calculations and studies show how the dielectric characteristics, overall electrical and optical performance, and overall behavior of liquid crystals are affected by the addition of PbS quantum dots. These findings offer insights into the ways in which the quantum dot doping changes the electrical and optical properties of the liquid crystal cells as well as the dielectric constants.

3.1. Electrical Characterization

The study was focused on two samples: pure and PbS QDs doped NLC. The electrical response of these samples was evaluated by measuring the capacitance (C_p) and dielectric loss (D) over the applied fixed frequency and variable voltages. These parameters were then used to calculate the dielectric properties, specifically the real dielectric constant (ϵ'), imaginary dielectric constant (ϵ''), and the conductivity (σ) using the following relations:

$$\epsilon' = \frac{C_p \cdot d}{\epsilon_0 \cdot A} \quad (1)$$

$$\epsilon'' = \epsilon' \cdot D \quad (2)$$

$$\sigma = \frac{F \cdot C_p \cdot D \cdot A}{d} \quad (3)$$

where:

F is the applied frequency signal of 5 kHz, C_p is the parallel capacitance, D is the dielectric loss factor, A is the ITO electrode surface area of $1.6 \times 10^{-11} \text{ m}^2$, and d is the thickness of the cell, which is $5 \times 10^{-6} \text{ m}$. To understand the effect of quantum dot doping on the electrical behavior of NLC composites, the changes in conductivity depending on the PbS QD concentration were analyzed.

Figure 1 shows the conductivity – voltage (σ -V) graph of pure and PbS QDs added nematic liquid crystals samples. The calculated real dielectric constant (ϵ') and the imaginary dielectric constant (ϵ'') are given in Figure 2 (a) and (b), respectively.

The dielectric constant of the doped liquid crystal (LC) samples was significantly elevated in comparison to that of the undoped nematic liquid crystal (NLC) cells. This increase in the dielectric constant suggests an enhanced polarizability within the doped material,

likely due to the influence of quantum dots on the alignment and orientation of the LC molecules[5]. Additionally, a marked reduction in electrical conductivity was observed upon doping. This decline can be explained by the quantum dots acting as localized charge traps or scattering centers, which impede the mobility of charge carriers and thus contribute to decreased conductivity.

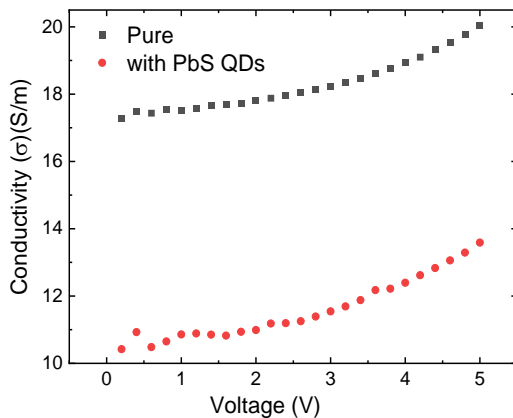


Figure 1. Conductivity – voltage (σ -V) graphs of pure and PbS QDs added nematic liquid crystals samples.

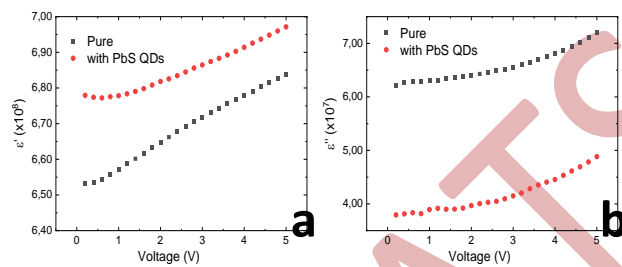


Figure 2. (a) The real; **(b)** the imaginary dielectric constant - voltage graphs of the pure and PbS QDs added nematic liquid crystals samples.

3.2. Optical Characterization

The measurements were conducted within ITO-coated cells. To ensure accuracy, the baseline transmission spectrum of the ITO layer was subtracted from the overall transmittance data, accounting for the ITO layer's contribution and isolating the intrinsic optical properties of the doped

NLC samples. Figure 3 shows transmittance – wavelength graphs of the pure and PbS QDs added nematic liquid crystals samples.

The results show a general decrease in transmittance for the doped samples across a broad wavelength in between 600-1000 nm as seen in Fig. 3. The measurement of transmittance indicated that the doping of PbS QDs reduced the amplitude of the wave and, as a result, the nonlinear effects.

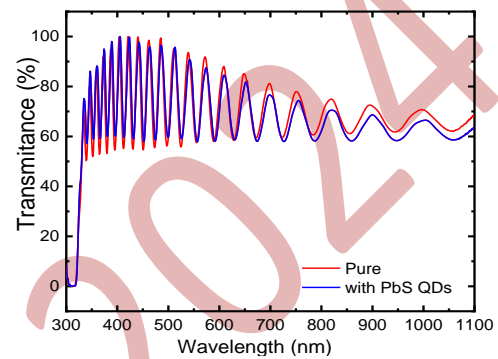


Figure 3. Transmission spectra for pure and PbS QDs doped NLC.

4. Conclusions

In this study, the impacts of PbS QDs nanoparticles doping into liquid crystals were investigated. The results of C-V and transmittance measurements shown that incorporating PbS quantum dots into NLC systems significantly alters their dielectric and conductive properties. These findings also present a possibility for applications requiring regulated electrical behavior. The results provide insight into the potential for innovative use of these nanocomposites in plasmonic and optoelectronic devices.

Acknowledges

This study was supported by Kocaeli University Scientific Research Projects (BAP) Coordination Unit (Project No: FBA-2024-3938).

References

- [1] Ö. T. Özmen, K. Goksen, A. Demir, M. Durmuş, and O. Köysal, "Investigation of photoinduced change of dielectric and electrical properties of indium (III) phthalocyanine and fullerene doped nematic liquid crystal," *Synth Met*, vol. 162, no. 24, pp. 2188–2192, 2012, doi: 10.1016/j.synthmet.2012.10.013.
- [2] F Simoni and O Francescangeli, "Effects of light on molecular orientation of liquid crystals," *Journal of Physics: Condensed Matter*, vol. 11, no. 41, p. R439, 1999, doi: 10.1088/0953-8984/11/41/201.
- [3] İ. Candan, "PbS Kuantum Nokta İnce Filmlerin Üretilmesi ve Karakterizasyonu," *Gazi University Journal of Science Part C: Design and Technology*, vol. 8, no. 4, pp. 1021–1033, 2020, doi: 10.29109/gujsc.825327.

- [4] İ. Candan, M. Parlak, and Ç. Erçelebi, "PbS quantum dot enhanced p-CIGS/n-Si heterojunction diode," *Journal of Materials Science: Materials in Electronics*, vol. 30, no. 3, pp. 2127–2135, 2019, doi: 10.1007/s10854-018-0484-0.
- [5] O. Köysal, M. Okutan, S. E. San, T. Nyokong, and M. Durmuş, "Diffraction efficiency and I-V characteristics of metal-free phthalocyanine doped nematic liquid crystals," *Mater Chem Phys*, vol. 114, no. 2–3, pp. 815–820, Apr. 2009, doi: 10.1016/j.matchemphys.2008.10.056.
- [6] B. Yang *et al.*, "Liquid crystal behaviors of micron and submicron-sized black phosphorus nanosheets," *J Lumin*, vol. 251, p. 119172, 2022, doi: <https://doi.org/10.1016/j.jlumin.2022.119172>.
- [7] B. A. Naqvi *et al.*, "Visualizing Degradation of Black Phosphorus Using Liquid Crystals," *Sci Rep*, vol. 8, no. 1, p. 12966, 2018, doi: 10.1038/s41598-018-31067-4.
- [8] S. Balwadkar, A. Sutar, S. Doke, Y. Jadhav, S. Kulkarni, and S. Kahane, "CdSe quantum dots enhancing blue emission of nematic liquid crystals," *J Phys Conf Ser*, vol. 2426, p. 12048, Sep. 2023, doi: 10.1088/1742-6596/2426/1/012048.

The Use of Hydrogels in Femoral Head Necrosis Research

Zeynep Bal

*Osaka University, WPI Immunology Frontier Research Center (IFReC) & Research Institute of Microbial Diseases (RIMD)- Department of Signal Transduction, P565-0871, Yamadaoka 3-1, Suita, Osaka, Japan, zeynepbal@gmail.com
ORCID: 0000-0003-1563-5036*

Nobuyuki Takakura

*Osaka University, Research Institute of Microbial Diseases (RIMD) & WPI Immunology Frontier Research Center (IFReC) - Department of Signal Transduction, P565-0871, Yamadaoka 3-1, Suita, Osaka, Japan, ntakaku@biken.osaka-u.ac.jp
ORCID: 0000-0003-0397-8605*

Cite this paper as: Bal, Z., Takakura, N. The use of hydrogels in femoral head necrosis research. Int. Conf. Advanced. Mater. Sci. & Eng. HiTech. and Device Appl. Oct. 24-26 2024, Ankara, Turkiye

Abstract. Osteonecrosis of the Femoral Head (ONFH) is an osteonecrotic condition originated from the inadequate blood supply to bone. Although it has a high rate of disability, because there is no clear ethiology of the disease, there is still no certain treatment for. Since it is characterized by a functional disability in microcirculation, the treatment is expected to include both vascular structure and bone regeneration. Hydrogels are networks of hydrophilic polymer chains which are capable of retaining large amount of water and also are promising solution for ONFH treatment because of their desirable chemical and physical properties as well as having a similar structure to extracellular matrix which may also give the advantage of the capability of regenerating different tissues such as bone and vascular structure, at the same time. Here, in this lecture there will be a brief information about ONFH, vascularisation and the use of hydrogels in treatment of ONFH.

Keywords: Osteonecrosis, Vascularization, Bone Regeneration, Hydrogels

© 2024 Published by ICMATSE

Introduction

Bone is the second largest transplant tissue in the world following the blood. In bone grafting autografts are the gold standard yet the donor side morbidity and the limited graft material are the main problems. Following autograft, allografts are the second popular because it decreases the surgical burden on the patient as well as the blood loss yet the disease transmission possibilities and the lack of allograft banking are the problems. On the other hand, composite grafts are getting more attention every day because of their adjustable properties based on the required conditions (Figure 1). Extracellular matrix provides a base for cell attachment and is also responsible for cell-to-cell signaling, cell migration, differentiation and proliferation. Therefore, throughout composite materials, because of their similarity to extracellular matrices (ECM), hydrogels have recently become more and more popular.

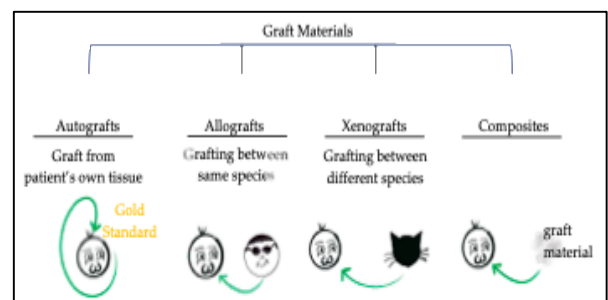


Figure 1: Graft material classification

Femoral head necrosis (FHN, aka osteonecrosis of the femoral head (ONFH), avascular necrosis (AN)) is a vascular disease and based on the etiology it can be mainly divided into two as traumatic femoral head necrosis or non-traumatic femoral head necrosis (Figure 2).

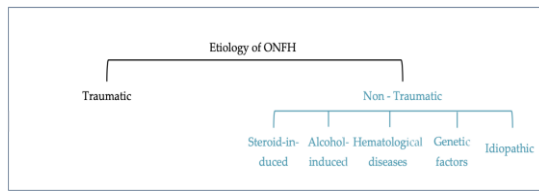


Figure 2. Etiology of FHN

Traumatic FHN is the most common type and steroid- and alcohol-induced FHN are the most frequently seen non-traumatic FHN types. Although the etiology can be divided into as such, the molecular reasons leading to FHN are not well described and well-known which causes many “early” treatment strategies for FHN not being successful. Hence, total hip arthroplasty (THA) is generally the last resort for treatment. However, in the case of early necrosis, which in clinics is defined as the state just before collapse, throughout the minimally invasive surgery techniques, core decompression surgery is chosen as the first solution before THA (Figure 3).

References

1. H-G. Kopp, S.Y AVECILLA, A.T. Hooper, S. Raffii. The bone marrow vascular niche: Home of HSC differentiation and mobilization. *Int. Union. Physiol. Sci/Am. Physiol. Soc.* 2005, 20, 349–356
2. J. Liu, L. Yang, K. Liu, F. Gao. Hydrogel scaffolds in bone regeneration: Their promising roles in angiogenesis. *Front. Pharmacol.* 2023, 14, 1050954
3. Z. Bal, T. Kaito, F. Korkusuz, H. Yoshikawa. Bone regeneration with hydroxyapatite-based materials. *Emergent Mater.* 2020, 3, 521-544
4. Z. Bal, N. Takakura. Hydrogel use in osteonecrosis of the femoral head. *Gels.* 2024, 10, 544
5. Y. Bian, T. Hu, Z. Lv, Y. Xu, Y. Wang, H. Wang, B. Feng, R. Liang. Bone tissue engineering for treating osteonecrosis of the femoral head. *Exploration* 2023, 3, 20210105.
6. Z. Fu, Y. Lai, Y. Zhuang, F. Lin. Injectable heat sensitive nanocomposite hydrogel for regulating gene expression in the treatment of alcohol-induced osteonecrosis of the femoral head. *APL Bioeng.* 2023, 7, 016107.

Femoral Head-Preserving Surgeries		Total Hip Arthroplasty (THA)
Core Decompression*	Bone Grafting Surgery	Last Resort
<ul style="list-style-type: none"> ✓ Removal of the necrotic tissue. ✓ Decreased inner pressure of femoral head. ✓ Stimulated bone cell growth. ✓ Improved microcirculation. 	<ul style="list-style-type: none"> ✗ Shifting or fallen bone flaps after surgery. 	
<ul style="list-style-type: none"> ✗ Disruption of mechanical support and structure of femoral head in the case of large diameter decompression holes. ✗ Possibility of iatrogenic complications**. 	<p align="center">Osteotomy</p> <ul style="list-style-type: none"> ✗ Decreased possibility of having hip replacement surgery due to a large trauma area and changed normal anatomical structures if osteotomy fails. 	

Figure 3. Surgical treatment techniques of FHN

Conclusion

Thus, in this study we aimed to explain the relation between osteogenesis and angiogenesis on FHN and how it can be treated with the use of hydrogels especially in case of core decompression surgery before FHN leads to physical disabilities.

Tolerances and Mechanical Properties Comparison As-built Hole vs. Drilled Hole of Polymer Additive Manufacturing

Abdulcelil Bayar

Turkish Aerospace- Material Engineering, 06980, Ankara, Turkiye,
abdulcelil.bayar@tai.com.tr
ORCID: 0000-0002-5759-4773

Umit Aytar

Turkish Aerospace- Material Engineering, 06980, Ankara, Turkiye,
uaytar@tai.com.tr
ORCID: 0009-0003-7636-4898

Erdem Mermer

Turkish Aerospace- Material Engineering, 06980, Ankara, Turkiye,
erdem.mermer@tai.com.tr
ORCID: 0000-0002-2540-1586

Mete Bakir

Turkish Aerospace- Material Engineering, 06980, Ankara, Turkiye,
mete.bakir@tai.com.tr
ORCID: 0000-0002-5044-3104

Cite this paper as: Bayar, A, Aytar, U, Mermer, E, Bakir, M. Tolerances and mechanical properties comparasion as-built hole vs. drilled hole of polymer Additive manufacturing. Int. Conf. Advanced. Mater. Sci.& Eng. HiTech.and Device Appl.Oct. 24-26 2024, Ankara, Turkiye

Abstract. This study investigates the comparative effects of as-built and drilled holes on the mechanical properties, defects, and tolerances of ULTEM® 9085 and Onyx materials using polymer additive manufacturing. Utilizing Stratasys Fused Deposition Modeling (FDM) 900 MC Printer and Markforged, we explore the variances in tensile strength, failure strain, and modulus across identical dogbone test samples with different hole types. The analysis shows a significant variation in mechanical strength between the FDM parts and comparable injection-molded parts, with a notable increase in the coefficient of variation as layer orientation deviates from the primary load direction. Microscopic examinations relate these variations to the macrostructure and mechanical response of the materials. Hole quality, material integrity, accuracy, tolerances, time efficiency, and cost considerations between additive manufacturing and conventional drilling are also discussed, highlighting the trade-offs and operational efficiencies unique to each technique. This comparative analysis provides valuable insights into the optimized use of additive manufacturing for engineering applications requiring precise hole dimensions and mechanical robustness.

Keywords: Additive manufacturing, ULTEM® 9085, Onyx, mechanical properties, hole
© 2024 Published by ICMATSE

Introduction

The broadening range of applications suggests the feasibility of utilizing three-dimensional (3D) printed parts in assemblies that include metal or other material components [1-3]. This situation presents

challenges related to dimensional and geometric quality; areas that have not been fully explored by the scientific community. Due to its considerable importance to industry, this study focuses on examining parts made of Ultem 9085 (PEI, Ultem) using fused deposition modeling (FDM), which may

be used in conjunction with other components. The research aims to provide critical insights into surface quality, dimensional precision, and the key distinctions between creating final 3D printed parts versus those that are printed and then machined using traditional manufacturing techniques [4,5].

The advancement and industrial adoption of Additive Manufacturing (AM) depend on its ability to meet defined quality standards for material and dimensional properties while maintaining cost competitiveness. This requires confirming the intended properties through proper methods, selecting suitable materials, optimizing production processes, and aligning with environmental standards to transition AM from rapid prototyping to industrial-scale manufacturing. However, this shift necessitates thorough research and validation of all associated AM processes [6-8].

Current research in Additive Manufacturing (AM) identifies surface quality as a critical issue in 3D printing. Studies consistently show that the quality of parts produced by AM significantly depends on the precise control of printing parameters [9,10]. These issues are generally categorized into four areas: optimization of build orientation, layer thickness, fabrication parameters, and post-treatment processes. The parameters of build orientation and layer thickness are particularly emphasized in scientific literature as crucial factors influencing the surface quality of specimens [11]. Furthermore, achieving an optimal configuration of manufacturing parameters to enhance surface finish could potentially affect the structural integrity of the printed objects. Many studies have delved into how printing parameters, especially the printing angle which is often crucial for determining surface quality, impact mechanical properties [12-14].

In recent years, various methods like steam smoothing, chemical treatments, and sandpaper polishing, finding that chemical treatments resulted in the lowest surface roughness have been explored to enhance the finish of 3D printed surfaces [15].

Dimensional accuracy remains a critical issue and a limitation for the industrial expansion of additive manufacturing (AM) Technologies [16,17]. Therefore, this research addresses the dimensional accuracy of parts produced by fused deposition modeling (FDM), comparing two methods: printing or drilling the through-holes on FDM parts. The

study explores both alternatives in detail to provide appropriate recommendations.

Materials and Method

The 3D Accuracy parameter impacts the surface finish (tessellation) of the STL file (input file for the printer). We used the value 0.01 as resolution in the option box of CATIA.

The STLs were processed using single contour and +45/-45 solid rasters, which are typical default settings. After the samples were sliced, and support and toolpaths were generated, seam control was used to ensure the seams were on the corners of the specimen out of the areas of concern for testing. Produced specimen definitions are presented in Table 1.

Table 1. Specimen Definitions

Specimen	Material	Number of Specimens	Direction
Without Hole	ULTEM 9085	3	XY
Drilled Hole	ULTEM 9085	3	XY
As-built Hole	ULTEM 9085	3	XY
Without Hole	Onyx	3	XY
Drilled Hole	Onyx	3	XY
As-built Hole	Onyx	3	XY

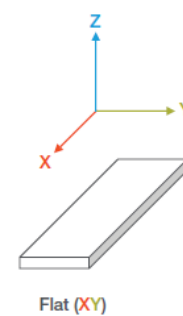


Figure 1. XY Orientation

The ASTM D638 Type 1 specimens were fabricated using Ultem 9085 and Onyx materials from the same CAD model. Some of the specimens were processed with holes drilled using a drill to achieve the final dimensions. The produced hole-free, drilled-hole, and as-built hole specimens were subjected to a study involving microstructure examination, measurements, and tensile testing.

The materials have been tested for tensile strength, defects and the tolerances of the samples. Tensile strength has been measured in accordance with ASTM D638.

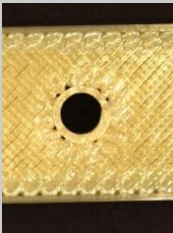

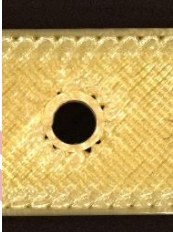
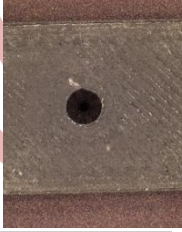
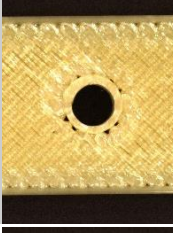



All specimens with holes have been examined with Zeiss Smartzoom 5 Digital Microscope. All specimens with hole diameters have been measured with Zeiss Smartzoom 5 Digital Microscope.

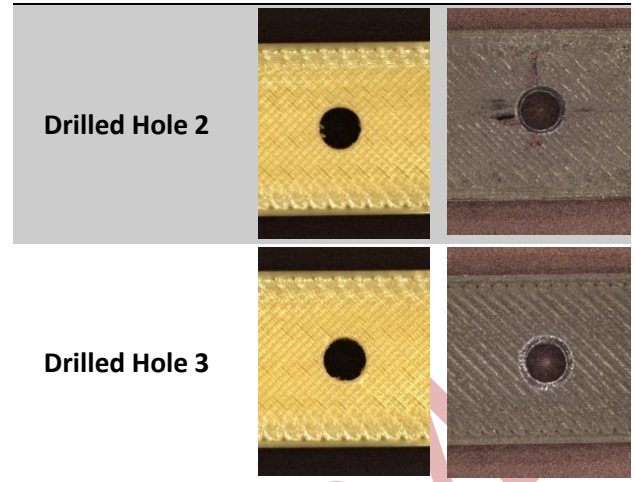
Tensile mechanical tests were performed to ASTM D638 Type I samples, thickness = 3.3 mm (0.130 in.) tested with a cross-head speed of 0.2 in./min. All samples were conditioned for a minimum of 40 hours at 23 ± 2 °C (73 ± 3.6 °F) and $50 \pm 10\%$ RH prior to testing.

Results and Discussion

Microscopic examinations revealed porosities around the hole. No errors were encountered when the hole was drilled. Microscopic examination of specimen holes are presented in Table 2.

Table 2. Microscopic Examination

Specimen	ULTEM 9085	ONYX
As-built Hole 1		
As-built Hole 2		
As-built Hole 3		
Drilled Hole 1		



The hole measurements were taken twice with a microscope, once from top of the hole and once from bottom. Besides, all measurements were taken at 0 and 90 degrees to also examine the roundness. The hole measurements of ULTEM 9085 and ONYX specimens are presented in Table 3 and Table 4.

Table 3. ULTEM 9085 Hole Measurement

Specimen and Location	Measured Diameter	
	0-degree (mm)	90-degree (mm)
As-built Hole 1 Top	2.90	2.94
As-built Hole 1 Bottom	2.50	2.64
As-built Hole 2 Top	2.90	3.08
As-built Hole 2 Bottom	2.50	2.65
As-built Hole 3 Top	2.90	2.96
As-built Hole 3 Bottom	2.70	2.78
Drilled Hole 1 Top	2.88	2.90
Drilled Hole 1 Bottom	3.05	3.10
Drilled Hole 2 Top	2.91	2.91
Drilled Hole 2 Bottom	2.90	2.99
Drilled Hole 3 Top	3.12	2.90
Drilled Hole 3 Bottom	3.26	2.99

Table 4. ONYX Hole Measurement

Specimen and Location	Measured Diameter	
	0-degree (mm)	90-degree (mm)
As-built Hole 1 Top	2.99	2.97
As-built Hole 1 Bottom	2.95	2.79
As-built Hole 2 Top	2.79	2.79
As-built Hole 2 Bottom	2.79	2.79
As-built Hole 3 Top	2.97	2.79
As-built Hole 3 Bottom	2.90	2.86
Drilled Hole 1 Top	3.12	2.92
Drilled Hole 1 Bottom	3.19	2.88
Drilled Hole 2 Top	3.10	2.82
Drilled Hole 2 Bottom	2.90	2.97
Drilled Hole 3 Top	3.12	3.13
Drilled Hole 3 Bottom	3.02	3.05

Drilled holes achieved 20% better precision compared to holes produced by additive manufacturing.

Ultimate tensile strength results of tensile test are presented in Figure 2 and Figure 3.

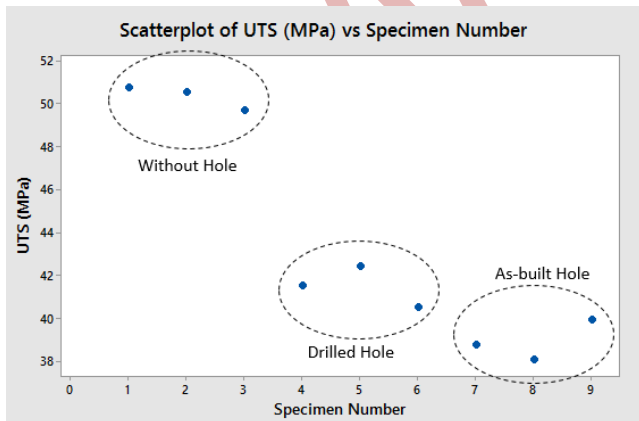


Figure 2. ULTEM 9085 Ultimate Tensile Strength

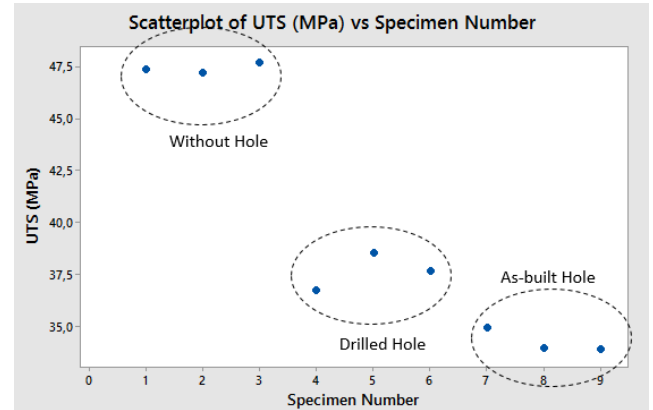


Figure 3. ONYX Ultimate Tensile Strength

The opening of a 3 mm hole in tensile test specimens resulted in a 27% reduction for both materials. Drilling the holes provided 12% higher tensile strength compared to creating the holes through additive manufacturing.

Additive manufactured holes had some material deformation around the hole edges. The defects impact mechanical properties worstly [8].

Stress-strain curves of tensile test are presented in Figure 4 and Figure 5.

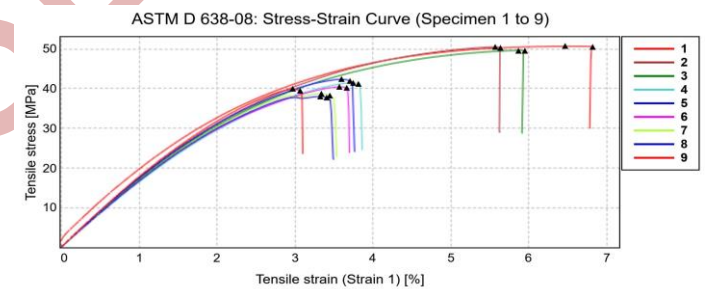


Figure 4. ULTEM 9085 Stress-Strain Curves

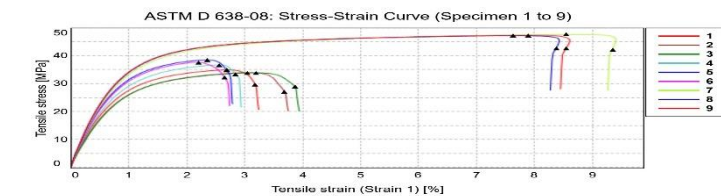


Figure 5. ONYX Stress-Strain Curves

The results are presented in a compiled format in which without hole, drilled hole and as-built hole specimens considered are plotted on the same graph for ease of visual comparison. The plots shown in Figure 4 and Figure 5 indicate the repeatability of the three specimens tested at each hole condition.

Conclusion

As a result of the study, various differences were observed between additive manufacturing-produced holes and conventionally drilled holes for fasteners. The detailed results are provided below:

- **Hole Quality:** The conventionally drilled holes showed improved surface finish and uniformity compared to additive manufacturing-produced holes. The conventionally drilling process allowed for better control over hole dimensions and reduced surface irregularities.
- **Material Integrity:** Holes created through drilling process exhibited better material integrity and strength. On the other hand, additive manufacturing-produced holes had some material deformation around the hole edges.
- **Accuracy and Tolerance:** Drilling allowed for achieving higher accuracy and tighter tolerances in hole dimensions, leading to better fit and alignment of fasteners. Additive manufacturing-produced holes had slightly looser tolerances and showed minor deviations from the target dimensions.
- **Time and Efficiency:** The additive manufacturing process demonstrated higher efficiency for producing holes, especially in complex geometries, as it eliminated the need for secondary machining operations. Conventional drilling required additional setup and machining time.
- **Cost Considerations:** The initial setup and equipment costs for drilling might be higher. Additive manufacturing holes in the overall cost per hole can be competitive due to lower labor costs for complex geometries.
- **Post-Processing Requirements:** Conventionally drilled holes often required deburring and surface finishing, adding extra post-processing steps. In contrast, additive manufacturing-generated holes usually required minimal post-processing.

Overall, the study showed that drilling can offer significant advantages in producing holes for fasteners, especially in terms of hole quality, accuracy, and material integrity. However, the choice between the two methods should consider factors such as geometrical complexity, production volume, and cost constraints.

References

1. Gibson I, Rosen DW, Stucker B. Additive manufacturing technologies: 3D printing, rapid prototyping, and direct digital manufacturing. New York: Springer; 2014.
2. Ford, S. and Despeisse, M. (2016), "Additive manufacturing and sustainability: an exploratory study of the advantages and challenges", *Journal of Cleaner Production*, Vol. 137, pp. 1573-1587.
3. Vasudevarao, B., Natarajan, D. P. and Henderson, M. (2000), "Sensitivity of Rp surface finish to process parameter variation", *Solid Freeform Fabrication Proceedings*, pp. 251-258.
4. Anitha, R., Arunachalam, S. and Radhakrishnan, P. (2001), "Critical parameters influencing the quality of prototypes in fused deposition modelling", *Journal of Materials Processing Technology*, Vol. 118 Nos 1/3, pp. 385-388.
5. Vijay, P., Danaiah, P. and Rajesh, K.V.D. (2011), "Critical parameters effecting the rapid prototyping surface finish", *Journal of Mechanical Engineering and Automation*, Vol. 1 No. 1, pp. 17-20.
6. Nidagundi, V., Keshavamurthy, R. and Prakash, C. (2015), "Studies on parametric optimization for fused deposition modelling process", *Materials Today: Proceedings*, 4th International Conference on Materials Processing and Characterization, Vol. 2 Nos 4/5, pp. 1691-1699.
7. Sood, A., Ohdar, R. and Mahapatra, S. (2010), "Parametric appraisal of mechanical property of fused deposition modelling processed parts", *Materials & Design*, Vol.31 No. 1, pp. 287-295.
8. Forés-Garriga, A., Pérez, M.A., Gomez-Gras, G. And Reyes-Pozo, G. (2020), " Role of infill parameters on the mechanical performance and weight reduction of PEI ultem processed by FFF", *Mater. Des.*, Vol.193.
9. Fernandez-Vicente, M., Calle, W., Ferrandiz, S. and Conejero, A. (2016), "Effect of infill parameters on tensile mechanical behavior in desktop 3D printing", *3D Printing and Additive Manufacturing*, Vol. 3 No. 3, pp. 183-192.
10. Pandey, P.M., Reddy, N.V. and Dhande, S.G. (2003a), "Improvement of surface finish by staircase machining in fused deposition modeling", *Journal of Materials Processing Technology*, Vol. 132 Nos 1/3, pp. 323-331.
11. Singh, R., Singh, S., Singh, I. P., Fabbrocino, F. and Fraternali, F. (2017), "Investigation for surface finish improvement of fdm parts by vapor smoothing process", *Composites Part B : Engineering*, Vol. 111, pp. 228-234.
12. Tiwary, V.K., Arunkumar, P., Deshpande, A.S. and Rangaswamy, N. (2019), "Surface enhancement of fdm patterns to be used in rapid investment casting for making medical implants", *Rapid Prototyping Journal*, Vol.25No.5, pp. 904-914.

13. Del Sol, I., Domínguez Calvo, Á., Piñero, D., Salguero, J. and Batista, M. (2019), "Study of the fdm parameters of the abs parts in the surface quality after machining operations", *Key Engineering Materials*, Vol. 813, pp. 203-208.
14. Christiyan KJ, Chandrasekhar U, Venkateswarlu K. A study on the influence of process parameters on the mechanical properties of 3D printed ABS composite. In *IOP Conference Series: Mater Sci Eng*, 2016 114(1) 1-8.
15. Chacón JM, Caminero MA, García-Plaza E, Núñez PJ. Additive manufacturing of PLA structures using fused deposition modelling: Effect of process parameters on mechanical properties and their optimal selection. *Mater Des*, 2017 124 143-157.
16. Ziemian C, Sharma M, Ziemian S. Anisotropic mechanical properties of ABS parts fabricated by fused deposition modelling. In: Gokcek M, editor. *Mechanical engineering*, InTech, 2012 159–180.
17. Durgun I, Ertan R. Experimental investigation of FDM process for improvement of mechanical properties and production cost. *Rapid Prototyping J*, 2014 20(3) 228-235.

ICMATSE 2024

The Importance of Representative Sampling and Homogenization in Designing the Reference Material Production Processes

Berna YUKSEL

*Gazi University-Faculty of Engineering-Department of Chemical Engineering, 06570, Ankara, TÜRKİYE,
bernayuksel85@gmail.com*

*^bTENMAK-Boron Research Institute, 06530, Ankara, TÜRKİYE,
berna.yuksel@tenmak.gov.tr
ORCID: 0000-0001-7506-9609*

Aysel BERKKAN

*Gazi University-Faculty of Pharmacy-Division of Basic Pharmaceutical Sciences-Department of
Analytical Chemistry, 06330, Ankara, TÜRKİYE,
ayselberkkan@gmail.com
ORCID: 0000-0003-4669-5496*

Hakan ATES

*^dGazi University-Faculty of Technology-Department of Metallurgy and Materials Engineering, 06560,
Ankara, TÜRKİYE,
hates@gazi.edu.tr
ORCID: 0000-0002-5132-4107*

Fatma Cigdem GULDUR

*Gazi University-Faculty of Engineering-Department of Chemical Engineering, 06570, Ankara, TÜRKİYE,
cguldur@gazi.edu.tr
ORCID: 0000-0002-4404-6882*

Cite this paper as: Yüksel, B, Berkkan, A, Ates, H, Güldür, F. C., The Importance of Representative Sampling and Homogenization in Designing the Reference Material Production Processes. Int. Conf. Advanced. Mater. Sci. & Eng. HiTech.and Device Appl.Oct. 24-26 2024, Ankara, Turkiye

Abstract. Rare earth elements (REE); constitutes the most important raw materials in renewable energy, aviation industry, electronics, defense industry and many other advanced technology fields. Today, the demand for REEs is increasing regardless of the supply security and diversity problem in USA and EU [1-3]. During and after the coal combustion (CC) in thermal power plants, huge amounts of by-products are released. These coal by-products contain a significant amount of REEs. For this reason, it is recommended to develop sustainable recycling technologies for the recovery of metals and REEs. While developing these technologies, accurate and precise analysis results in analytical chemical methods of REEs are required at every stage [4-7].The use of reference materials (RM) is a key activity to develop and maintain a consistent measurement system in the world. RM is used for various purposes such as deviation evaluation, calibration, method validation, etc. It has been emphasized that the use of CRM/RM is very important in order to ensure the quality and continuity of analysis in laboratories in a series of published all over the world and in EU [8-10].RM production process is a process that includes some major multiple steps but the most important ones are **Representative Sampling (RS)** and assurance of **Homogeneity (H)** and **Stability (S)** of the sample. Also, this is a production process that needs to be designed with different algorithms for each different matrix. Hence it is inevitable to evaluate the by-products generated by the CC in terms of REE recycling. While conducting RM production activities, it is determined that RS and H have a crucial importance on the process. It is concluded that these two important parts of the production are must be designed carefully in accordance with the specific matrix. Therefore, in this study, it is aimed to design the best RS and H processes for the production of RM that can be used in recovery of REE from coal ash.

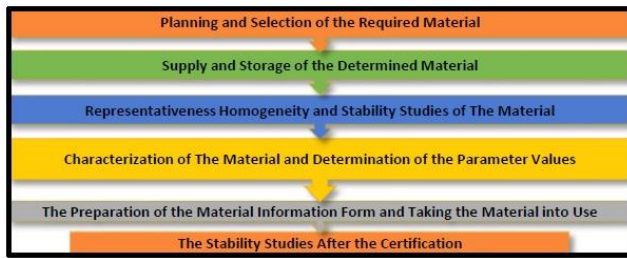


Figure 1. Reference Material Production Flow Chart

Keywords: reference material production, recovery of rare earth elements, coal ash, homogeneity, statistical data analysis

© 2024 Published by ICMATSE

Introduction

Rare Earth Elements (REEs) are a group of transition metals including lanthanides, scandium, and yttrium. There has been an increasing demand for REEs due to their wide range of applications, including phosphors, catalysts, ceramic and glass, metal alloys, polishing, permanent magnets, batteries, defense, and healthcare industries as well as clean energy technologies. Economic and environmental issues, as well as permitting and trade restrictions have raised concerns regarding the **mining and availability of REEs**. Hence, there has been **significant interest in the recovery of these elements from secondary sources including coal and coal combustion by-products** (e.g., Coal Fly Ash [CFA]) [2]. Recovering valuable elements from these waste streams is well aligned with the Waste to Value concept and enhances the sustainability of the current disposal practices. This also contributes European Green Deal Goals and Circular Economy Action Plan totally.

Since coal is one of the indispensable resources used in electricity generation both in our country and in the world, it is important to evaluate economically and environmentally their byproducts which contain a significant amount of REE. Rare earth elements are needed as raw materials in most of the advanced technological applications that will be increasingly used in the next century. However, rare earths are included in the critical raw materials classification in both the USA and the EU in terms of supply security and diversity. Therefore, recovery from secondary sources other than mining has become very important. It is a globally accepted idea that the recovery of rare earth elements from coal ash is a promising practice.

In this regard, there are many different recovery process designs in the literature. While designing these processes, accurate and precise analysis results

in analytical chemical methods of REEs are required at every stage. However, feasibility analysis of recovery process designs made with accurate, precise and high-quality analysis results (compliant with ISO / IEC-17025 [11] criteria) will be useful in industrial applications. **At this point, accurate, precise and high-quality analysis results can be obtained by using fully matrix-matched standard reference material or reference material, as it is accepted all over the world and Europe.**

The use of reference materials (RM) is a key activity to develop and maintain a consistent measurement system (like analysis/test laboratory) in the world. RM is used for various purposes such as deviation evaluation, calibration, assigning value to other materials and measuring device performance evaluation, method validation, demonstrating system adequacy. It has been emphasized that **the use of CRM/RM is very important in order to ensure the quality and continuity of analysis in laboratories** in a series of regulations and legal regulations published all over the world and in EU [10].

Reference material production process is a process that includes some major multiple steps which are shown in Figure 1. Also, this is a production process that needs to be designed with different algorithms for each different matrix.

Hence it is inevitable to evaluate the waste and residues (fly ash, bottom ash, etc.) generated by the coal combustion in terms of REE recycling. In Turkey and EU, there is no much study on the production of RM for REE in coal waste and residues (ash, etc.).

There are lots of certificated reference materials of different matrixes for various applications which are especially produced by geological survey foundations of different countries or some metrological institutions. However, there are still certain need for production of new reference materials of different

matrixes for different applications with a broaden research and development disciplines from food, environment, mining, health and medicine. The innovation in this reference material production topic **depends on different matrixes for different parameters.** For instance, there are some coal ash certificated reference materials available today but they had produced for different purposes before thus now they do not include the required parameters (REE) for that matrix. Therefore, in our study, it is aimed to produce a RM that can be used in recovery of REE from coal ash and to design a production process that meets all the requirements stated in international sources for the RM production for the specified specific matrix (coal ash) and parameter/s (REE) [10-19]. While conducting RM production activities, it is determined that representative sampling and homogenization have a crucial importance on the process. Thus, in this study it is aimed to show the importance of representative sampling and homogenization in designing the reference material production processes.

Results and Discussion

In this study, it is planned to make representative sampling of fly ash from a coal thermal power plant which is actively used in the production of electricity in Turkey with designed sampling methods. **One of the most important and critical points of the study is the representative sampling of coal fly ash.**

Homogenization of the representative sample is another key activity in order to determine the composition of coal fly ash taken from the power plant correctly in future chemical analyzes. With the homogeneity study, it is shown that the concentration of each element is the same throughout the representative sample. The "Representativeness" and "Homogeneity" studies mentioned here also appear as the conditions that must be met in the reference material production process in international standards, and each of them must be designed separately for each different matrix.

In the literature, a comparison of the REE content in coal fly ash from different regions in the world has been made, and according to this, the REE content in coal fly ash in Turkey appears to be above the world average [60]. When the studies conducted for Türkiye [61] are examined in detail; for some power plants in Turkey (Soma, Tunçbilek, Çatalağzı, Yatağan), it is determined that the REE content in coal fly ash is significantly above the world average [61].

Considering that the samples with the highest REE content in coal ash will be taken into consideration in studies on REE recovery from coal fly ash, it is thought that the production of suitable matrix RM especially for coal fly ashes with high REE content will be a higher priority. This issue was taken into consideration in the coal fly ash sampling to be carried out from the field, and therefore field studies were planned by selecting the Manisa-Soma region.

Very good planning is required before taking samples from the field. The importance of this issue is also highlighted in the UK Environment Agency's Technical Guidance Note (Monitoring) (2016) titled Ash Sampling and Analysis (TGN M4) [62]. There is even a sampling methodology proposal presented in the relevant document that takes into account the event holistically and from different aspects. It was thought that a similar method should be followed in representative coal ash sampling from the field in this study, and an original sampling plan was determined for this study. All details in the relevant Technical Guidance Note were taken into consideration when determining the sampling plan. The determined sampling plan is presented in Annex-1.

Based on the assumption that coal ash waste is kept in a pile before going to the field, representative sampling processes are discussed theoretically, and different methods and factors that may affect the process are evaluated. However, in the studies carried out in the field, it was determined that the coal ash waste areas were almost the size of more than ten football fields for the power plant and that all kinds of waste from the power plant were stored together in these waste dams. For this reason, in order to purify the scientific research to be carried out specific to coal ash from unknown and other variables that may affect the results, fresh coal fly ash from freshly burned coal in power plants is collected from the point where the fly ash itself is formed and transferred from the systems to the waste pools, without contacting any material other than the point where it will be transferred from the systems to the waste pools, and by preventing possible contamination. It was determined that taking it hot would be the most appropriate method. Due to the high temperature of the coal fly ash produced, it was evaluated that it would be more accurate to sample it with a steel container instead of plastic barrels in order to prevent possible chemical reactions that may occur between the sample container and the hot fly ash. As a result, it was decided to sample the coal fly ash freshly, conjugated with the feed coals, in steel containers

using the shift-based deposition method, without contacting any other materials.

On the other hand, representative sampling of coal fly ash fresh from the power plant, obtained under more ideal conditions, which is considered appropriate as a starting point in scientific research, cannot fully represent the coal fly ash waste that has been waiting in coal ash waste pools for years, so representative sampling methods can also be taken from coal ash waste pools waiting in the following stages. It is thought that it should be determined and research should be done.

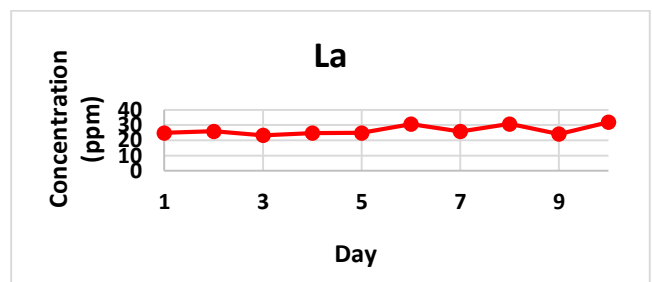
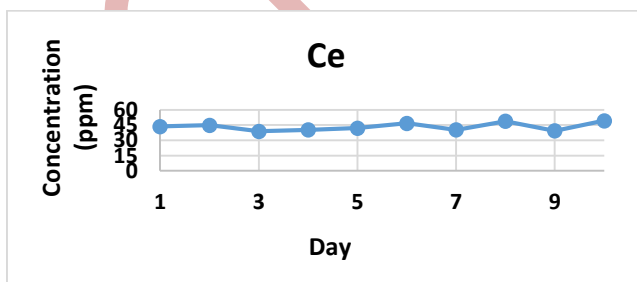
In the context of ensuring the high representativeness targeted in the representative sampling process, in order to minimize the effects of possible changes in the structure of the coal fed in 10-day periods on the composition of the sampled coal fly ash, it was determined that coal ash should be sampled as the highest amount (100 kilograms) by mass was collected for each fixed shift determined for each day within the 10-day period. Thus, it was envisaged that the coal fly ash sample to be collected for 10 days would represent the coal fly ash waste generated during the routine operations of the power plant, including the effect of all variables that could affect the composition of the waste. In accordance with the designed plan, a total of one ton of samples, 100 kilograms each, were taken from the same designated point of the process on the same shift for ten consecutive days. The samples taken for each day were coded and collected in separate containers. Afterwards, the samples taken for each separate day were manually mixed and quartered, and subsamples were made to represent each separate day. Finally, samples taken in equal amounts from each separate day were blended. All fly ash materials were mixed

manually, dried at 80°C for 24 hours, and 75% of the samples by mass were ground to below 75µm particle size.

All representatively sampled fly ash materials were dissolved with two different dissolution methods (3 acids and 4 acids) and chemical analysis of rare earth elements was performed with the ICP-MS device. The results are presented in Table-1. Here, with the prediction that the most daily change can be seen in the elements with the highest concentration, it is seen that the contents of the 4 elements with the highest concentration values (Ce, La, Nd and Y) in the waste fly ash on different days show undeniable changes and are not constant (Figure-2a and 2b).). Likewise, when making a representative sampling plan at the beginning of the study, the opinion that sampling should be done by daily accumulation in a 10-day period was to create a plan that would allow representative sampling to include the change in daily waste concentration that may result from daily changing feed coal. These data are an indication of how realistic the representative sampling plan determined at the beginning of the study was.

All the materials were mixed again and divided into 128 equal amounts by mass in an 8-compartment automatic sample divider. After the randomly determined samples are dissolved with the most appropriate dissolving method, REE analysis results will be conducted with the ICP-MS device and the homogeneity of the material will be shown by statistical data analysis.

In addition, unlike the design of the RM production process, the total REE concentration of Manisa-Soma Fly Ash as a waste were determined to be approximately 133 ppm.



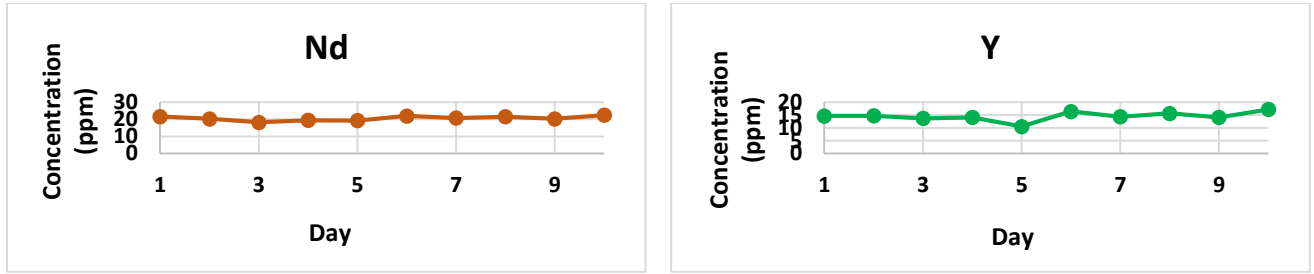


Figure 2a. Sample No. 1-10 Manisa-Soma Fly Ash Change of REE analysis results in 10 days by dissolving the samples taken separately from Day 1 to Day 10 with 3 acids

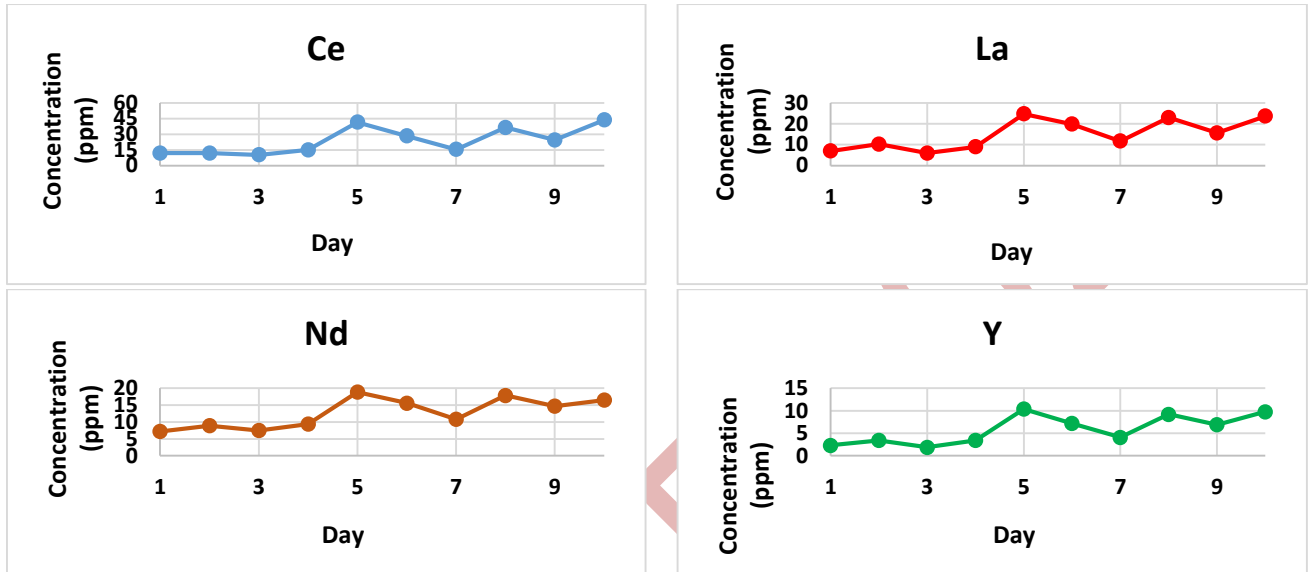


Figure 2b Sample No. 1-10 Manisa-Soma Fly Ash Change of REE analysis results in 10 days by dissolving the samples taken separately from Day 1 to Day 10 with 4 acids

Table 1. REE Analysis Results of Coal Fly Ash Samples with Different Dissolution Methods and on Different Days

Sample No	Ce	Dy	Er	Eu	Gd	Ho	La	Lu	Nd	Pr	Sc	Sm	Tb	Tm	Y	Yb	Sample List
1	43,6	2,7	1,4	0,9	3,1	0,5	24,9	0,3	21,6	4,6	7,6	2,9	0,6	0,3	14,6	1,8	3A-1
1	11,8	0,6	1,2	0,4	0,9	0,3	6,9	0,1	7,2	1,2	4,5	0,8	0,3	0,2	2,3	1,1	4A-1
2	44,8	2,8	1,4	0,8	3,2	0,5	25,9	0,3	20,3	4,7	7,8	2,9	0,6	0,3	14,7	1,7	3A-2
2	11,9	0,7	1,4	0,5	0,9	0,3	10,2	0,1	8,9	1,3	4,5	1,8	0,3	0,2	3,4	1,1	4A-2
3	38,9	2,7	1,5	0,7	2,8	0,5	23,3	0,3	18,2	4,1	7,1	3,5	0,5	0,3	13,7	1,9	3A-3
3	10,2	0,6	1,3	0,3	0,7	0,2	5,9	0,1	7,5	1,1	4,2	1,2	0,3	0,2	1,9	0,9	4A-3
4	40,3	2,6	1,7	0,7	2,9	0,5	24,8	0,3	19,4	4,2	7,8	3,6	0,5	0,3	14,1	1,9	3A-4
4	14,9	0,9	1,2	0,5	1,1	0,3	8,9	0,2	9,4	1,6	4,2	1,8	0,3	0,2	3,4	1,1	4A-4
5	42,1	1,9	2,4	0,9	2,8	0,5	24,9	0,3	19,2	4,4	4,8	4,6	0,5	0,3	10,5	1,9	3A-5
5	41,4	1,9	2,3	0,9	2,8	0,4	24,7	0,3	18,9	4,3	4,8	4,6	0,5	0,3	10,4	1,8	4A-5
6	46,7	2,8	1,8	0,8	3,4	0,5	30,6	0,3	21,9	4,9	8,4	4,4	0,6	0,3	16,4	2,1	3A-6
6	28,2	1,5	1,9	0,7	1,9	0,4	19,8	0,2	15,6	2,9	5,8	3,6	0,4	0,3	7,2	1,6	4A-6
7	40,3	2,7	1,7	0,9	2,9	0,5	25,8	0,3	20,7	4,2	7,9	3,7	0,5	0,3	14,3	1,9	3A-7
7	15,4	0,9	1,5	0,5	1,1	0,3	11,7	0,2	10,8	1,6	4,1	2,4	0,3	0,2	4,1	1,2	4A-7
8	48,8	2,9	1,9	1,1	3,5	0,5	30,7	0,3	21,5	5,1	8,8	4,2	0,6	0,3	15,6	1,9	3A-8
8	36,4	1,6	2,1	0,8	2,6	0,4	22,9	0,2	17,9	3,8	5,6	3,9	0,5	0,3	9,2	1,7	4A-8
9	39,4	2,6	1,7	0,9	2,9	0,5	24,1	0,3	20,3	4,2	8,4	3,8	0,5	0,3	14,1	1,9	3A-9
9	24,5	1,3	1,8	0,6	1,8	0,4	15,6	0,2	14,7	2,6	5,3	3,1	0,4	0,2	6,9	1,4	4A-9
10	49,3	3,1	1,5	1,1	3,6	0,5	31,9	0,3	22,4	5,2	8,3	4,7	0,6	0,3	17,2	2,2	3A-10
10	43,6	1,8	2,4	0,9	3,1	0,4	23,6	0,2	16,5	4,6	2,9	4,2	0,5	0,3	9,8	1,7	4A-10

References

1.Jyothi, R. K., Thenepalli, T., Ahn, J. W., Parhi, P. K., Chung, K. W., Lee, Jin-Y., "Review of rare earth elements recovery from secondary resources for clean energy technologies: Grand opportunities to create wealth from waste", Journal of Cleaner Production 267 (2020) 122048, 1-26.

2. Pan, J., Hassas, B. V., Rezaee, M., Zhou, C., Pisupati, S. V., "Recovery of rare earth elements from coal fly ash through sequential chemical roasting, water leaching, and acid leaching processes", *Journal of Cleaner Production* 284 (2021) 124725, 1-9.
3. Zhang, W., Rezaee, M., Bhagavatula, A., Li, Y., Groppo, J., Honaker, R., "A review of the occurrence and promising recovery methods of rare earth elements from coal and coal by-products", *Int. J. Coal Prep. Util.* 35, (2015) 295-330.
4. Dong, Y., Sun, X., Wang, Y., Huang, C., Zhao, Z., "The sustainable and efficient liquid-type saponification strategy for rare earth separation processing", *ACS Sustain. Chem. Eng.* 4, (2016) 1573-1580.
5. Lin, R., Howard, B.H., Roth, E.A., et al., "Enrichment of rare earth elements from coal and coal by-products by physical separations", *Fuel* 200, (2017) 506-520.
6. Huang, Z., Fan, M., Tiand, H., "Coal and coal byproducts: a large and developable unconventional resource for critical materials - rare earth elements", *J. Rare Earths* 36, (2018) 337-338.
7. Taggart, R.K., Hower, J.C., Dwyer, G.S., Hsu-Kim, H., "Trends in the rare earth element content of US based coal combustion fly ashes", *Environ. Sci. Technol.* 50 (2016) (11), 5919–5926.
8. I.R.B. Olivares, G.B. Souza, A.R.A. Nogueira, G.T.K. Toledo, D.C. Marcki, "Trends in developments of certified reference materials for chemical analysis - Focus on food, water, soil, and sediment matrices", *Trends in Analytical Chemistry* 100 (2018) 53-64.
9. Saito, T., Botha, A., "Guidance on the contents of accompanying documentation for reference materials (RMs)", *Accred Qual Assur* (2016) 21:239–241.
10. ISO Guide 30:2015 Reference Materials – Selected Terms and Definitions.
11. TS EN ISO/IEC 17025- General requirements for the competence of testing and calibration labs.
12. ISO Guide 31:2015 Reference Materials–Contents of certificates, labels and accompanying documentation.
13. ISO Guide 32:1997 Calibration in analytical chemistry and use of CRM.
14. ISO Guide 33:2015 Reference Materials – Good practice in using RM.
15. ISO Guide 34:2009 General requirements for the competence of RM producers.
16. ISO Guide 35:2017 Reference Materials – Guidance for characterization and assessment of homogeneity and stability.
17. ISO 17034:2016 Reference Material Producer Accreditation.
18. EA-4/14 INF:2003 The Selection and Use of Reference Material.s
19. ILAC-G12:2000 Guidelines for the Requirements for the Competence of RM Producers.
20. Shu, C., Volli, V., Gollakota, A.R.K., "Progressive utilisation prospects of coal fly ash: A review", *Science of the Total Environment* 672 (2019) 951–989.
21. Karayigit, A.I., Gayer, R.A., Querol, X., Onacak, T., "Contents of major and trace elements in feed coals from Turkish coal-fired power plants", *International Journal of Coal Geology* 44 (2000) 169–184.
22. Environment Agency of United Kingdom, *Guidelines for Ash Sampling and Analysis Technical Guidance Note (Monitoring) M4* (2016).

Dual-Doped NCZ-AZ Cathode Material for Lithium-Ion Batteries

Duygu CANDEMIR

Hitit University-Metallurgical and Materials Engineering, 19030, Corum, Turkiye,
duygukorsacilar@hitit.edu.tr
ORCID: 0000-0002-6186-0122

Oncu AKYILDIZ

Hitit University-Metallurgical and Materials Engineering, 19030, Corum, Turkiye,
oncukyildiz@hitit.edu.tr
ORCID: 0000-0002-0081-1642

Hakan ATES

Gazi University-Metallurgical and Materials Engineering, 06560, Ankara, Turkiye,
hates@gazi.edu.tr
ORCID: 0000-0002-5132-4107

Cite this paper as: Candemir, D, Akyildiz, O, Ates, H. Dual-Doped NCZ-AZ Cathode Material for Lithium-Ion Batteries. Int. Conf. Advanced. Mater. Sci. & Eng. HiTech. and Device Appl. Oct. 24-26 2024, Ankara, Turkiye

Abstract. Aluminum (Al) and zirconium (Zr) doping have been found to enhance the structural stability, thermal stability, and electrochemical performance of cathode materials, potentially improving their suitability for lithium-ion battery applications. Therefore, in this study, Al and Zr were incorporated into nickel-based hydroxide material ($\text{NiCoZn}(\text{OH})_2$, $\text{NCZ}(\text{OH})_2$) via sol-gel assisted solid-state doping synthesis to produce dual-doped $\text{Li}_{1.05}\text{Ni}_{0.8}[\text{Co}_{0.054}\text{Zn}_{0.046}]\text{Al}_{0.08}\text{Zr}_{0.02}\text{O}_2$ (NCZ-AZ) cathode material. Characterization was performed using SEM-EDS, X-ray diffraction (XRD) and Rietveld refinement analysis. As a result of the calcination process lasting 20 hours at 800 degrees, the ratio of $I_{(003)}/I_{(104)}$ peaks was found to be 1.2 and the c/a value was found to be 4.955. These structural parameters are critical indicators of the material's electrochemical stability and charge/discharge cycling performance. In conclusion, the dual-doped NCZ-AZ cathode materials synthesized in this study demonstrate promising characteristics for advanced lithium-ion battery applications. A systematic investigation of Al and Zr doping effects on the NCZ-AZ structure may provide valuable insights into the design and optimization of next-generation cathode materials with improved stability and performance.

Keywords: Lithium-ion battery, cathode material, energy storage

© 2024 Published by ICMATSE

Introduction

Numerous studies are being carried out to improve the performance of active materials through techniques such as doping and/or surface modification to prevent solid-electrolyte reactions,

crack formation, and degradation mechanisms in cathode materials. Research shows that doping of aluminum (Al), a transition element, reduces cation mixing and improves the structural and thermal stability of batteries [1], while zirconium (Zr) doping enhances cycling stability and increases specific capacity [2]. Moreover, co-doping with Al and Zr minimizes cation mixing and microcrack formation [3,4] by creating synergistic effects.

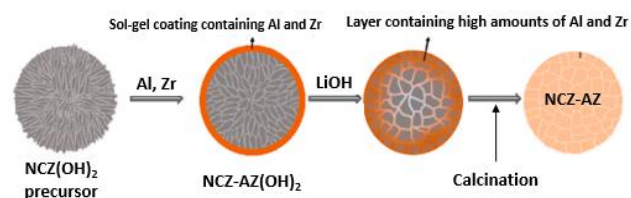


Figure 1. Schematic representation of the sol-gel assisted solid state doping method

In this study, we have synthesized cathode materials doped with aluminum and zirconium using a sol-gel assisted solid state doping method (Fig. 1). Following calcination at 800°C for duration

of 20 hours, the materials underwent analysis via SEM-EDS, X-ray diffraction (XRD) and Rietveld refinement.

Results and Discussion

The XRD spectrum of the NCZ-AZ cathode material (Fig. 2) confirms the successful incorporation of aluminum and zirconium (no impurity peaks or other undesirable peaks observed), demonstrating the effectiveness of the adopted doping approach.

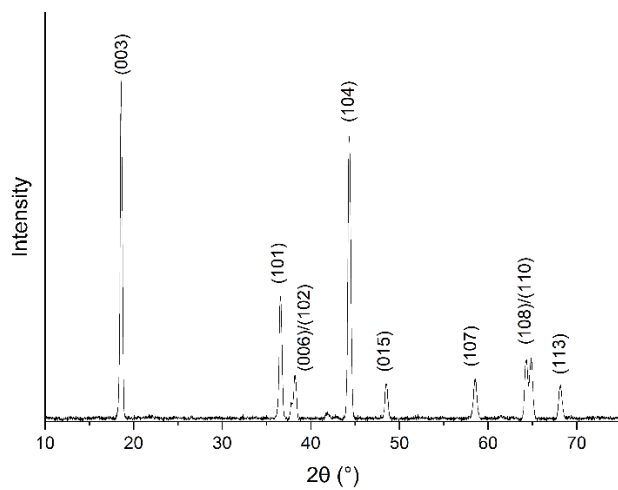


Figure 2. XRD spectrum of the synthesized NCZ-AZ

The c and a values are crystal lattice parameters and are obtained from Rietveld analysis (Fig. 3). In addition, the lithium layer gap (Li-gap) is also investigated.

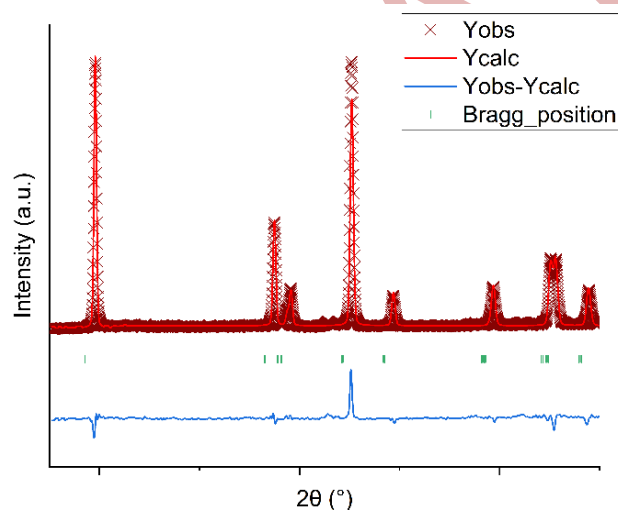


Figure 3. Rietveld spectrum of the NCZ-AZ

Table 1 includes an evaluation of the peak intensity ratio ($I_{(003)}/I_{(104)}$), which is considered as an indicator of cation mixing in our study, the c/a ratio, which reflects the cation order, and Li-gap value, which is important for facilitating Li^+ de/intercalation during charge/discharge cycles. When these values are

compared with related published studies, it was found that the results were in good agreement with the literature [2,5,6].

Table 1. Results of XRD and Rietveld refinement analysis

c/a	4.955
$I_{(003)}/I_{(104)}$	1.2
(Li-gap) (Å)	2.6182

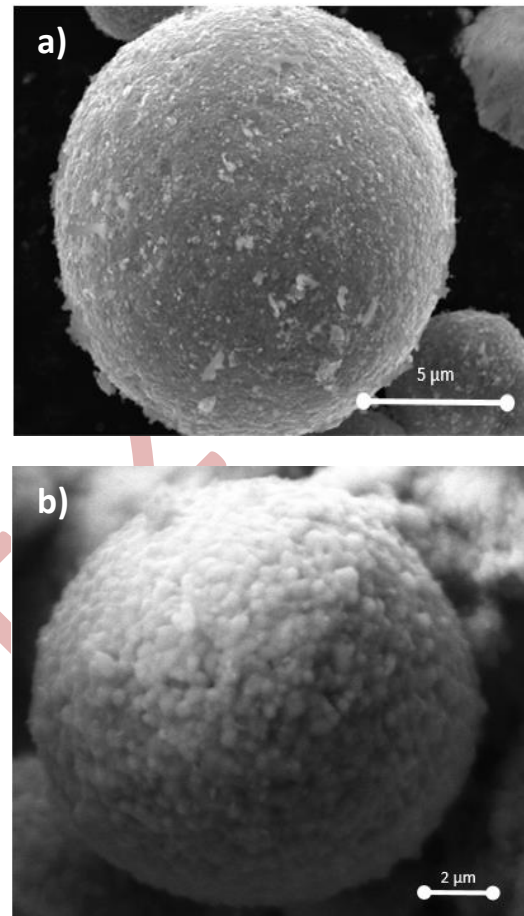


Figure 4. SEM images of a) Spherical $\text{NCZ}(\text{OH})_2$ powder and b) NCZ-AZ powders

SEM images of the starting material $\text{NCZ}(\text{OH})_2$ and NCZ-AZ are given in Figure 4. When the images are examined, it is clearly seen that the spherical form is

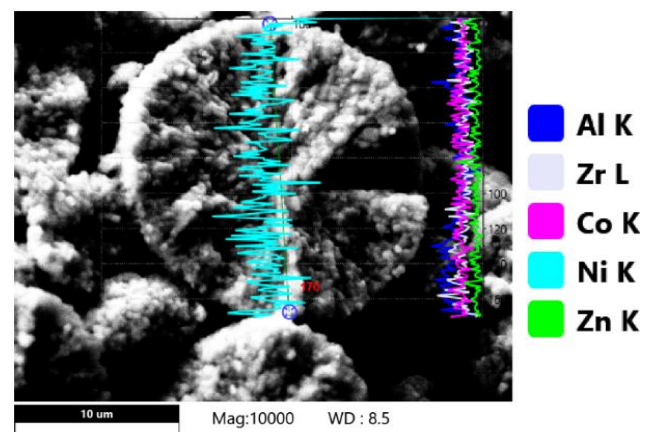


Figure 5. NCZ-AZ cross-section EDS linear scan profile

not distorted after the doping and calcination processes and that the NCZ-AZ cathode material consists of secondary particles surrounded by primary crystals at the nanometer scale (Figure 4b).

The cross-sectional linear element analysis of NCZ-AZ is shown in Figure 5. When the resulting spectrum is examined, it is clearly seen that Al and Zr elements are incorporated into the structure homogeneously throughout the particle after calcination at 800°C for 20 hours.

Conclusion

As a result, when the data obtained from the XRD spectrum and Rietveld analysis, the importance of

which has been emphasized in detail above, are evaluated; When we examine the $I_{(003)}/I_{(104)}$ ratio, which is an important indicator of the $\text{Li}^+/\text{Ni}^{2+}$ cation mixture, and the c/a values representing high cation ordering and low cation mixing, it was determined that the calcination process applied at 800 °C for 20 hours gave good results. In addition, it was determined that the lithium layer gap (Li-gap), which facilitates Li^+ de/intercalation during the charge/discharge process, also gave results compatible with the literature as a result of the 20-hour calcination process. In this study, which is carried out within the scope of the doctoral thesis subject, studies on the determination of different temperatures, different compositions and electrochemical properties are ongoing.

References

1. R. Venkatachalapathy et al., Solution combustion route for Ni and Al co-doped lithium ferrite nanoparticles: Synthesis, the effect of doping on the structural, morphological, optical, and magnetic properties, *Ceram. Int.*, 49-4 (2023) pp. 6594–6607, doi: 10.1016/j.ceramint.2022.10.212.
2. J. Ni et al., Cobalt-free nickel-rich layered $\text{LiNi}_0.9\text{Al}_0.1-x\text{Zr}_x\text{O}_2$ cathode for high energy density and stable lithium-ion batteries, *J. Taiwan Inst. Chem. Eng.*, 136 (2021), pp. 104421, doi: 10.1016/j.jtice.2022.104421.
3. Y. Ming et al., Dual Elements Coupling Effect Induced Modification from the Surface into the Bulk Lattice for Ni-Rich Cathodes with Suppressed Capacity and Voltage Decay, *ACS Appl. Mater. Interfaces*, 12-7 (2020), pp. 8146–8156, doi: 10.1021/acsami.9b18946.
4. X. Kong, et al., New insights in Al-doping effects on the LiNiO_2 positive electrode material by a sol-gel method, *Int. J. Energy Res.*, 45-7 (2021) pp. 10489–10499, doi: 10.1002/er.6536.
5. L. Li, et al. Effect of Zr doping and Al-Zr co-doping on $\text{LiNi}_0.5\text{Co}_0.25\text{Mn}_0.25\text{O}_2$ for lithium-ion batteries. *Solid State Ionics*, 346 (2020) pp. 115220, <https://doi.org/10.1016/j.ssi.2019.115220>.
6. X. Ou et al., Enabling high energy lithium metal batteries via single-crystal Ni-rich cathode material co-doping strategy. *Nature Communications*, 13 (2022), doi:10.1038/s41467-022-30020-4.

Acoustic-Based Evaluation of Laser Micromachining for Enhanced Ceramic Processing

Can Ozcelik

*Instituto de Nanociencia y Materiales de Aragón, INMA (CSIC-Universidad de Zaragoza), 50018
Zaragoza, Spain, ozcelik@unizar.es
ORCID: 0000-0002-8100-6417*

José Ramón Beltrán

*Instituto de Investigación en Ingeniería de Aragón, I3A, Universidad de Zaragoza, 50018 Zaragoza,
Spain, jrbelbla@unizar.es
ORCID: 0000-0002-7500-4650*

Hippolyte Amaveda

*Instituto de Nanociencia y Materiales de Aragón, INMA (CSIC-Universidad de Zaragoza), 50018
Zaragoza, Spain, hippo@unizar.es
ORCID: 0000-0003-2212-447X*

Elena Martínez

*Instituto de Nanociencia y Materiales de Aragón, INMA (CSIC-Universidad de Zaragoza), 50018
Zaragoza, Spain, elenamar@unizar.es
ORCID: 0000-0003-4839-5286*

German F. de la Fuente

*Instituto de Nanociencia y Materiales de Aragón, INMA (CSIC-Universidad de Zaragoza), 50018
Zaragoza, Spain, german.delafuente.leis@csic.es
ORCID: 0000-0002-0500-1745*

Luis Alberto Angurel

*Instituto de Nanociencia y Materiales de Aragón, INMA (CSIC-Universidad de Zaragoza), 50018
Zaragoza, Spain, angurel@unizar.es
ORCID: 0000-0001-5685-2366*

Cite this paper as: Ozcelik, C, Beltrán, JR, Amaveda, H, Martínez, E, de la Fuente, GF, Angurel, LA, Acoustic-Based Evaluation of Laser Micromachining for Enhanced Ceramic Processing, Int. Conf. Advanced. Mater. Sci. & Eng. HiTech.and Device Appl.Oct. 24-26 2024, Ankara, Turkiye

Abstract. This study investigates laser micromachining on complex ceramic substrates, including Al_2O_3 , Al_2O_3 - ZrO_2 eutectic, by employing a novel acoustic monitoring approach. Ceramics, with their inherent brittleness and high melting points, present significant challenges during laser processing, often leading to defects like cracking and uneven material removal. Traditional laser micromachining methods frequently lack effective, real-time monitoring capabilities, making it difficult to optimize machining parameters dynamically and prevent defect formation. To address this gap, our research integrates acoustic recording as a diagnostic tool, enabling real-time feedback on machining conditions and immediate identification of potential defects.

The methodology revolves around in-situ acoustic monitoring, where sound intensity is recorded during the laser machining process. By analyzing sound signals produced during ablation, we can establish correlations between acoustic patterns and the physical characteristics of machined regions, such as surface roughness, crack initiation, and machining depth. This

approach offers a non-invasive, real-time means of assessing machining quality, helping to determine optimal parameters for efficient material removal and minimized defect formation. Our research aims to contribute a reliable, responsive monitoring tool for laser micromachining, enhancing control over the process and ultimately improving the quality of machined ceramic surfaces.

In this study, we utilized a green femtosecond laser with a wavelength of 515 nm to conduct micromachining trials on Al_2O_3 and $\text{Al}_2\text{O}_3\text{-ZrO}_2$ eutectic plates. Parameters such as pulse energy, frequency, and scanning velocity were varied systematically to examine their effects on material ablation rates, crack formation, and surface morphology. Field emission scanning electron microscopy (FESEM) provided post-processing analysis, allowing for precise observation of crack initiation points, surface morphology, and the impact of machining parameters on each material. Comparative analysis between Al_2O_3 and $\text{Al}_2\text{O}_3\text{-ZrO}_2$ eutectic substrates revealed significant differences in machining behavior, attributed to the distinct thermal and mechanical properties of each material. For instance, the $\text{Al}_2\text{O}_3\text{-ZrO}_2$ eutectic displayed more complex crack propagation patterns under identical laser parameters, underscoring the need for customized parameter adjustments depending on the ceramic composition.

The integration of acoustic monitoring proved effective in capturing real-time changes in machining quality, especially during multi-step laser treatment processes. In multi-pass treatments, each successive laser scan impacts surface integrity incrementally, which can be challenging to monitor visually. Acoustic signals provided continuous feedback on efficiency and surface quality, with the temporal evolution of sound pressure revealing insights into how repeated laser exposure affects crack formation and overall surface morphology. This acoustic data enables a more refined optimization of laser processing sequences, providing a comprehensive understanding of how each laser pass influences machining outcomes.

The findings demonstrate that acoustic monitoring is a valuable addition to ceramic laser micromachining, providing a non-destructive, real-time diagnostic tool that enhances control and adaptability. By monitoring sound intensity variations, operators can detect changes in machining conditions, allowing for on-the-fly adjustments that minimize defect formation without compromising ablation efficiency. This technique holds promise for applications requiring high precision and defect-free surfaces, such as in microelectronics, biomedical devices, and high-performance ceramics.

In conclusion, this research establishes a robust framework for optimizing laser micromachining of ceramics, introducing acoustic monitoring as a powerful tool for process control. The study highlights the critical role of material properties in machining outcomes and offers a practical, non-invasive method for assessing surface integrity in real time. This approach paves the way for more precise, efficient laser processing of brittle materials, with broad applicability across various high-precision manufacturing fields.

Acknowledgments: Authors are grateful for funding from the Spanish MCIN/AEI/10.13039/501100011033 (project PID2020-113034RB-I00), and from the Government of Aragon (Research Group T54_23R). The authors also thank to the University of Zaragoza the use of the Servicio General de Apoyo a la Investigación - SAI.

Keywords: Laser machining, Ceramic materials, Acoustic monitoring, Femtosecond laser, Green Laser, UV laser, Surface morphology, Sound Analysis, Confocal Analysis.

References

1. Miloš, M., Marin, G., Dragan, R., Miroslav, R. Coteata Margareta, "Mathematical Modelling of the CO2 Laser Cutting Process Using Genetic Programming", *Facta Univ. Ser. Mech. Eng. (FU Mech. Eng.)* 2022, 20, 665–676.
2. Madic, M., Kovacevic, M., Radovanovic, M., Blagojevic, V., "Software Tool for the Laser Cutting Process Control—Solving Real Industrial Case Studies", *Facta Univ. Ser. Mech. Eng.* 2016, 14, 135–145.
3. Liu, C., Sun, J., Li, G., Li, B., Gong, F., "Fabrication, mechanical properties and fracture behaviors of the laminated $\text{Al}_2\text{O}_3\text{-ZrB}_2\text{-MgO}/\text{Al}_2\text{O}_3\text{-TiN-MgO}$ ceramic composite", *Ceram. Int.* 2020, 46, 857–865.
4. Gopal, P. M., Kavimani, V., Gupta, K., & Marinkovic, D. (2023). Laser-Based Manufacturing of Ceramics: A Review. *Micromachines*, 14(8), 1564. <https://doi.org/10.3390/mi14081564>

Characterization Of Pomegranate Peel, Activated Carbon And Hard Carbon Derived From Pomegranate Peel

Mesut KARTA

Iskenderun Technical University- İskenderun Vocational School, Metallurgy Program, 31200, Hatay, Türkiye, mesut.karta@iste.edu.tr
ORCID: 0000-0001-8009-5158

Tolga DEPCI

Iskenderun Technical University, Faculty of Engineering and Natural Sciences, Petroleum and Natural Gas Engineering, 31200, Hatay, Türkiye, tolga.depci@iste.edu.tr
ORCID: 0000-0001-9562-8068

Cite this paper as: Karta, M, Depci, T. Characterization of pomegranate peel, activated carbon and hard carbon derived from pomegranate peel. Int. Conf. Advanced. Mater. Sci. & Eng. HiTech. and Device Appl. Oct. 24-26 2024, Ankara, Turkiye

Abstract. In this study, high value added products were produced from pomegranate peel, which was determined as a starting sample, and activated carbon (AC) and hard carbon (HC) products were obtained. The usability of the obtained activated carbons as electrodes in supercapacitors and hard carbons as anode materials in Na/Li ion batteries were demonstrated by characterization studies.

The characterization studies of pomegranate peels were examined through proximate analysis and their structural-functional properties were investigated with lignocellulosic material analysis. Then, comparative characterization studies of pomegranate peel, active carbon, and hard carbon were performed using BET, FTIR, and SEM analyses. As a result of the studies, SEM images of active carbon showed porous volumes, and according to BET analysis results, a surface area of 692.08 m²/g was detected. Moreover, BET surface area of hard carbon was found to be 55.03 m²/g, consistent with the literature, and due to the absence of an activating agent, no porous structures were observed in SEM images. As a result of these studies, it was concluded that activated carbon is suitable for use as an electrode in supercapacitors, and hard carbon could be used as an anode material in Na/Li-ion batteries.

Keywords: Pomegranate Peel, Activated Carbon, Hard Carbon
© 2024 Published by ICMATSE

Introduction

Nowadays, with the spread of electric vehicles and electronic devices, the importance of large capacity and long-lasting energy storage systems is increasing [1]. The development of high-performance energy storage devices stands out as an important factor supporting the growth of the new energy sector. As one of the most mature energy storage technologies today, lithium-ion batteries are widely used in electric vehicles, electronic devices and many other fields [2]. Given the uneven distribution of global lithium resources and the limited availability of lithium reserves worldwide, widespread use of lithium-ion batteries (LIBs) in areas that do not require energy density is not a logical choice [3]. Sodium-ion batteries (SIBs) hold significant potential due to their

excellent safety performance, ability to function well in both high and low temperatures, the abundance of sodium resources, and their cost-effectiveness. The development of materials for SIBs is therefore of great importance [4, 5]. Hard carbons are among the promising anode materials for sodium-ion batteries due to their high specific capacities, strong conductivities, low costs and environmentally friendly properties [6].

In this study, since pomegranate fruit grows in Hatay region and pomegranate peel is obtained as waste, activated carbon and hard carbon products with high added value were produced. Characterization studies of the obtained AC and HC products were carried out and their usability in energy storage was investigated.

Materials and methods

In this study, activated carbon from pomegranate peel was obtained by impregnating it with 1/4 KOH by mass at 800 °C under experimental conditions. Hard carbon studies obtained from pomegranate peel were carried out at 1200 °C in an argon gas environment.

Result and discussion

The literature research conducted shows the different textural, surface and functional group properties of various biomasses used to prepare AC and HC by physical or chemical methods. The cellulose, hemicellulose and lignin percentages of the samples are given in Table 1 below.

Table 1. Pomegranate peel approximate composition analysis (m/m%)

Sample	Hemicellulose	Cellulose	Lignin
Pomegranate peel	2,92	12,24	6,20

Proximate analysis of the samples are given in Table 2 below. Proximate analysis of the samples is given in Table 2 below. Low ash content of pomegranate peel was found as 2.78%.

Table 2. Proximate analysis of the samples

Sample	Moisture%	Ash %	Volatile %	Fixed Carbon*
Pomegranate Peel	17,47	2,78	61,73	18,02

*= 100- Calculated from the difference

BET analysis of pomegranate peel and activated carbon and hard carbon obtained from pomegranate peel are given in Table 3 below.

Table 3. BET analysis of the samples

Sample	BET% (m ² /g)
Pomegranate Peel	0,1923

AC	692,08
HC	55,03

In Figure 1, it can be said that two broad peaks are observed in the raw sample pomegranate peel and these represent C-CH₂ bonds, respectively [7]. FTIR spectrum of (AC) band at 3432 cm⁻¹ is attributed to OH stretching and the band at 2924 cm⁻¹ is probably related to methyl and C-H vibrations [8]. Finally, FTIR of (HC) sample contains the bending vibration of -CH₂- at 1695 cm⁻¹ [9].

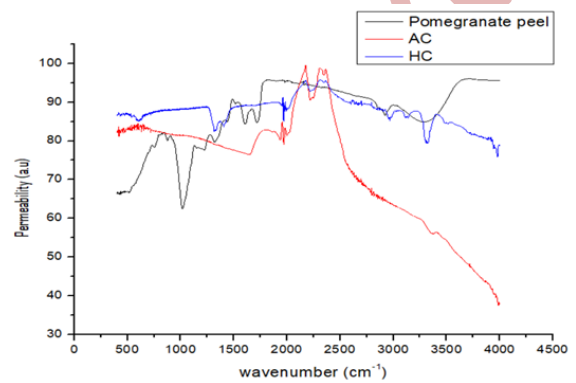


Figure 1. Pomegranate peel, Activated carbon and Hard carbon FTIR analysis

When Figure 2 SEM images were examined, rough structures were observed in the raw pomegranate peel, and pores of different sizes were detected in the activated carbon samples. When hard carbon samples were examined, non-porous structures were detected due to the absence of any pore-forming activator in the environment [10].

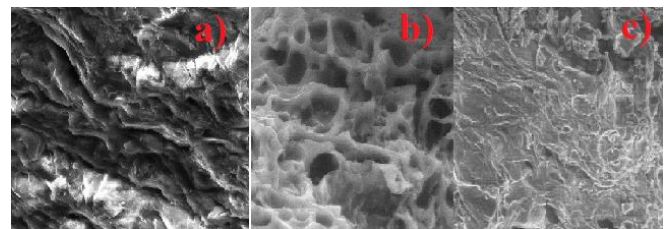


Figure 2. a) Pomegranate peel, b) Activated carbon c) Hard carbon SEM images

Conclusion

It was determined that the raw sample pomegranate peel had low moisture, low ash and volatile matter percentage. The amount of fixed carbon was found to be close to the literature. It was determined that the activated carbon produced from pomegranate peel

showed porous structures under the influence of KOH and the BET surface area was 692.08 m²/gr. When the hard carbon BET surface analysis was examined, it was found to be

55.03 m²/gr. According to these results, it can be said that activated carbon samples can be used in supercapacitors and hard carbon samples can be used in Na-ion batteries.

References

- [1] J. Jin, X. Geng, Q. Chen, and T. L. Ren, "A Better Zn-Ion Storage Device: Recent Progress for Zn-Ion Hybrid Supercapacitors," *Nano-Micro Lett.* 2022 141, vol. 14, no. 1, pp. 1–49, Feb. 2022, doi: 10.1007/S40820-022-00793-W.
- [2] H. Su, S. Jaffer, and H. Yu, "Transition metal oxides for sodium-ion batteries," *Energy Storage Mater.*, vol. 5, pp. 116–131, Oct. 2016, doi: 10.1016/J.ENSM.2016.06.005.
- [3] Y. Wang, M. Li, Y. Zhang, and N. Zhang, "Defect-rich hard carbon designed by heteroatom escape assists sodium storage performance for sodium-ion batteries," *Chem. Eng. J.*, vol. 499, p. 156115, Nov. 2024, doi: 10.1016/J.CEJ.2024.156115.
- [4] X. Chen *et al.*, "Understanding of the sodium storage mechanism in hard carbon anodes," *Carbon Energy*, vol. 4, no. 6, pp. 1133–1150, Nov. 2022, doi: 10.1002/CEY2.196.
- [5] M. Liu *et al.*, "Advances in Carbon Materials for Sodium and Potassium Storage," *Adv. Funct. Mater.*, vol. 32, no. 31, p. 2203117, Aug. 2022, doi: 10.1002/ADFM.202203117.
- [6] T. Zhao *et al.*, "The latest research progress on closed pore hard carbon for sodium-ion batteries," *J. Energy Storage*, vol. 102, p. 114209, Nov. 2024, doi: 10.1016/J.EST.2024.114209.
- [7] A. Neslihan Dundar *et al.*, "Characterization of pomegranate peel extract loaded nanophytosomes and the enhancement of bio-accessibility and storage stability," *Food Chem.*, vol. 398, p. 133921, Jan. 2023, doi: 10.1016/J.FOODCHEM.2022.133921.
- [8] C. S. Umpierrez *et al.*, "Microwave-activated carbons from tucumã (*Astrocaryum aculeatum*) seed for efficient removal of 2-nitrophenol from aqueous solutions," *Environ. Technol. (United Kingdom)*, vol. 39, no. 9, pp. 1173–1187, May 2018, doi: 10.1080/09593330.2017.1323957.
- [9] L. Shi *et al.*, "Tailoring the microstructure and solid electrolyte interface of hard carbon to realize high-initial-coulombic-efficiency and high-rate sodium storage," *Electrochim. Acta*, vol. 459, p. 142557, Aug. 2023, doi: 10.1016/J.ELECTACTA.2023.142557.
- [10] J. Serafin, B. Dziejarski, O. F. Cruz Junior, and J. Sreńscek-Nazzal, "Design of highly microporous activated carbons based on walnut shell biomass for H₂ and CO₂ storage," *Carbon N. Y.*, vol. 201, pp. 633–647, Jan. 2023, doi: 10.1016/J.CARBON.2022.09.013.

Energy as a Dual Use Item under European Union Law

Natalia Charalampidou

*Democritus University of Thrace – Faculty of Law, Department of International Relations,
GR-69100 Komotini, Greece, natalia.charalampidou@gmail.com
ORCID: 0000-0001-9792-0222*

Cite this paper as: Charalampidou, Natalia, Energy as a Dual Use Item under European Union Law, Int. Conf. Advanced. Mater. Sci. & Eng. HiTech. and Device Appl. Oct. 24-26 2024, Ankara, Turkiye

Abstract. It is herewith aspired to portray the regulatory measures on energy under the legislation of the European Union that relates to dual use items. To this end, it is first attempted to see how the legislators in Brussels understand the concept of energy in general, including under the rules for the internal market for electricity [1]. Then it is examined, under what circumstances energy qualifies as a *dual use item* according to the Dual Use Regulation [2]. Should these circumstances be met, the Dual Use Regulation comes into play and therewith the imposition of restrictions and curtailments. Yet, dual use items also fall within the scope of some – not all – sanctions regimes of the European Union, such as the ones targeting North Korea [3], Iran [4], and Syria [5]. Consequently energy, as a dual use item, faces further restrictions under the apposite legislation. Additionally, some sanctions regimes of the European Union, such as the ones targeting North Korea [3], Libya [6] and Russia [7], restrict energy *per se* alongside the aforementioned restrictions related to dual use items. These energy restrictions are also outlined. Conclusively, this paper illuminates the regulatory obstacles that energy as a dual use item faces under the law of the European Union.

Keywords: energy, dual use items, EU law, sanctions, restrictive measures
© 2024 Published by ICMATSE

I. Introduction

The seed that initiated the research for this paper was the news report from a conflict, where an electricity generating station was bombed and the reporter commented that this now destroyed station had been providing electricity to a hospital and to the military nearby. This is one of the most tangible examples of a dual use item, that being an item that has the capacity to be used for peaceful purposes and to be put into military use. From the perspective of law, and more specifically the law of the European Union qualifying as a dual use item can have significant consequences as it triggers the application of specific legislation. These issues are examined in the present paper.

II. The Statutory Definitions under EU Law

In pursuit of the meaning of *energy* under EU law, it is noted that Brussels regulates energy via a matrix of legislation setting out rules for matters such as the internal market for electricity [1], the natural gas market [8], the search for hydrocarbons [9], the use of renewable energy sources [10] and the trans-European energy infrastructure [11]. Public

procurement in the energy sector is also regulated, albeit in a different legal instrument [12].

Still, it is here suggested to search for the meaning of energy in tax related legislation, that being the framework for the taxation of energy products and electricity [13], as taxation tends to be very specific and less theoretical. Indeed the legislator resorts to standardization for specifying the terms ‘energy products’ and ‘electricity’, therefore opting for a definition with objective criteria. As ‘energy product’ qualifies any product falling under CN codes 2701 (coal, briquettes and ovoids), 2702 (lignite, excluding jet) and 2704 to 2715 (coke, coal gas, tar, products of the distillation of high temperature coal tar, pitch, petroleum oils, petroleum gases, petroleum jelly, petroleum coke, bitumen and asphalt and bituminous mixtures based on natural asphalt), 2901 and 2902 (acyclic hydrocarbons and cyclic hydrocarbons), 3403 (lubricating preparations), 3811 (anti-knock preparations), 3817 (mixed alkylbenzenes and mixed alkylnaphthalenes). As such also qualify products falling within CN codes 1507 to 1518 (soya-bean oil, ground-nut oil, olive oil and other oils, palm oil, sunflower-seed, safflower or cotton-seed oil, coconut (copra), palm kernel or babassu oil, rape,

colza or mustard oil, other fixed vegetable fats and oils, animal or vegetable fats and oils and margarine), 2905 11 00 (methanol (methyl alcohol)) and certain chemical products, including biodiesel (3824 99 86, 3824 99 92, 3824 99 93, 3824 99 96, 3826 00 10 and 3826 00 90), but for some exceptions, as long as they are intended for use as heating fuel or motor fuel [13, Article 2(1)]. Similarly 'electricity' is specified via correlation to products falling within CN code 2716 [13, Article 2(2)] that stands for electrical energy [14, Annex]. All references to codes of the combined nomenclature are to those of the Regulation on Statistical Nomenclature [14].

Nonetheless the legislator allowed for an abstract legal definition of these terms focusing on the human intention of items alongside the aforementioned standardization, thus introducing a parallel subjective definition. Accordingly other products may qualify as 'energy products', when they are intended for use, offered for sale or used as heating fuel or motor fuel or as an additive or extender in motor fuels. The same applies to hydrocarbons, with the exception of peat, when the intended or performed use or sale is for heating purposes [13, Article 2(3)].

Brussels defines the term *dual use item* in a similar manner, that being by adopting simultaneously a subjective and an objective approach. 'Dual use items' stands for items, including software and technology that can be used for civil and military purposes and includes items with non-explosive uses as well as items assisting in the manufacture of nuclear weapons and other nuclear explosive devices [2, Article 2(1)]. This definition could be characterized as a 'cycle definition' in view of the fact that it does very little to specify the word *item* and instead it focuses on elaborating the notion of *dual use*. Regardless, *items* is far from a blur term, in view of the list contained in the same legal instrument that contains nuclear and special materials, materials processing, electronics, computers, telecommunications and information security, sensors and lasers, navigation and avionics, marine and aerospace and propulsion [2, Annex I Parts 1 to 9]. This list implements international texts agreed by the Australia Group, the Missile Technology Control Regime, the Nuclear Suppliers Group and the Wassenaar Arrangement, those being non governmental organizations made by corporations that set standards for export controls of certain items and material.

III. Energy as a Dual Use Item

Comparing the notion of *energy*, as explained above, with the detailed description of the term *dual use items*, one can note the – partial – tautology among them and thus establish that energy constitutes, at least in certain instances, a dual use item. As an example of such tautology, which can be identified by ordinary persons without the expertise of science, would be lubricating materials (2, Annex I, 1C006). It is highly probable that experts on the energy science who do possess the knowhow of building and operating power grids and electricity generating facilities, along with pipelines and natural gas facilities, shall be able to identify more, especially in view of the subjective approaches to the statutory definitions of 'energy' and 'dual use item'.

IV. Consequences of Energy Being a Dual Use Item

The first obvious consequence for cases where energy qualifies as a dual use item is the application of the Dual Use Regulation, meaning that an authorization is necessary for their export [2, Article 3].

The legislator has opted for approaching the need for authorization in a way that reflects the objective and subjective approach to the term 'dual use item'. Thus, the Dual Use Regulation differentiates between items listed in the law as dual use items [2, Article 3(1)] and items not listed in the law as such [2, Article 3(2)]. In the latter case, an authorization is necessary, only with regard to export to certain destinations, as long as the competent authority of a Member State has decided that the item in question is or may be intended for use in chemical, biological or nuclear weapons, or means of delivery of such weapons and explosive devices [2, Article 4(1)(a)]. This also applies to items intended for military end-use, where the country of destination is subject to an arms embargo [2, Article 4(1)(b)]. Arms embargo, in the sense of prohibiting the export of arms and related materiel or items on the EU Common Military List [15] is currently imposed on Sudan [16, Article 2(a)], Lebanon [17, 2(a)], South Sudan [18, Article 2(1)], Myanmar/Burma [19, Article 3(1)(a)], Zimbabwe [20, Article 2(a)], Yemen [21, Article 1a(a)], Congo [22, Article 1a(1)&(2)], North Korea [3, Articles 5(1)(a) & 7(a)], Somalia [23, Article 8(1)(a)], Iran [4, Article 5(a)], Libya [6, Article 3(1)(a)], the Central African Republic [24, Article

2(a)], Venezuela [25, Article 2(1)(a)], Syria [5, Article 3a(a)], Russia [7, Article 4(1)(a)&(b)] and Belarus [26, Article 1b(1)(a) & (c)]. An authorization is finally necessary for items not listed in the Dual Use Regulation intended for use as parts or components of military items listed in a national military list, when these have been exported without authorization or in violation of an issued authorization [2, Article 4(a)(c)].

In the aforementioned cases, an export authorization is necessary that can be either individual, when it is granted to one specific exporter for a single end-user in a third country and covers one or more dual-use items [2, Articles 12(1)(a) & 2(12)], or global, when it is granted to one specific exporter for one or more end-users or in one or more specified third countries and covers a type or category of dual-use items [2, Articles 12(1)(b) & 2(13)]. Such authorizations are issued by the national authorities, where the exporter is resident or established [2, Article 12(2)]. Export authorizations may further have the form of national general export authorizations, as long as they are defined by national law or practice [2, Articles 12(1)(c) & (6) and 2(16)], and Union general export authorizations [2, Articles 12(1)(d), 2(15) and Annex II, Sections A to H].

A separate consequence of energy qualifying as a dual use item, is the application of sanctions regimes that restrict the use of dual use items. The regimes that provide for such restrictions are the ones with regard to North Korea [3, Article 3(1)(a) & (c) and Annex II Part I], Iran [4, Article 3a(1)(a) & (e) and Annex II], Myanmar/Burma [19, Article 3a(1)] and Syria [5, Article 2a(1)(a)]. Thus, the authorizations requested in these statutes are necessary parallel and in addition to the aforementioned export authorizations.

V. Energy *per se* and Sanctions

At this point it is noteworthy that certain sanctions regimes target energy as such; thus, an item qualifying as energy may well require further authorizations or face additional restrictions. Export, transfer and supply of coal, crude oil and aviation fuel is prohibited with regard to North Korea [3, Articles 3(1)(e), 16f & 3(1)(f)]. In relation to Libya, loading, transporting and discharging petroleum on

certain designated vessels is prohibited [6, Article 15(1)]. In regard to Syria, Syrian persons engaged in exploration, production and refining of crude oil may not be granted financial loan or credit [5, Article 13(1)].

Turning to electricity, supply, transfer and export of items and technology that shall be used for the construction and installation of new electricity power plants in Syria is prohibited [5, Article 12(1)(a) and Annex VII].

Finally, with regard to nuclear energy and Iran, an authorization is necessary for goods and technology that could contribute to Iran's reprocessing- or enrichment-related or heavy water-related activities that are inconsistent with the Joint Comprehensive Plan of Action of 14 July 2015 [4, Article 3a(2)]. Goods and technology that could contribute to North Korea's nuclear-related programmes are prohibited [3, Article 3(1)(a) & (c) and Annex II Part II].

VI. Conclusions

In conclusion, one single item or technology can be subject to one or more restrictions or even prohibitions depending both on its nature and on the country of destination, or even the conception of national authorities. Thus, one specific item may be eligible for supply, transfer and export to one country, but not to another one, depending on the imposed sanctions regimes. Circumventing such prohibitions and restrictions is equally prohibited not just by the general rule of acting in good faith, but by explicit relevant prohibitions of circumvention in the relevant statutes as well.

Conclusively, as the example of energy as a dual use item demonstrates, an item that appears to have a solid structure and to be thoroughly understood from the perspective of science and technology, could give rise to discussions and arguments on the application of several sets of legislation leading up to the necessity of authorizations or even outright prohibition. To this complexity, one could add the element of time, whereby an item may be set under such restrictive measures over night, not due to its nature or its actual use, but due to violence that erupted in some part of the world and obliged states to impose sanctions.

References

1. Directive (EU) 2019/944 of the European Parliament and of the Council of 5 June 2019 on common rules for the internal market for electricity and amending Directive 2012/27/EU OJ L 158, 14.6.2019, p. 125.
2. Regulation (EU) 2021/821 of the European Parliament and of the Council of 20 May 2021 setting up a Union regime for the control of exports, brokering, technical assistance, transit and transfer of dual-use items, OJ L 206, 11.6.2021, p. 1.
3. Council Decision (CFSP) 2016/849 of 27 May 2016 concerning restrictive measures against the Democratic People's Republic of Korea and repealing Decision 2013/183/CFSP, OJ L 141, 28.5.2016, p. 79, and Council Regulation (EU) 2017/1509 of 30 August 2017 concerning restrictive measures against the Democratic People's Republic of Korea and repealing Regulation (EC) No 329/2007, OJ L 224, 31.8.2017, p. 1.
4. 2010/413/CFSP: Council Decision of 26 July 2010 concerning restrictive measures against Iran and repealing Common Position 2007/140/CFSP, OJ L 195, 27.7.2010, p. 39, and Council Regulation (EU) No 267/2012 of 23 March 2012 concerning restrictive measures against Iran and repealing Regulation (EU) No 961/2010, OJ L 88, 24.3.2012, p. 1.
5. Council Regulation (EU) No 36/2012 of 18 January 2012 concerning restrictive measures in view of the situation in Syria and repealing Regulation (EU) No 442/2011, OJ L 16, 19.1.2012, p. 1, and Council Decision 2013/255/CFSP of 31 May 2013 concerning restrictive measures against Syria, OJ L 147, 1.6.2013, p. 14.
6. Council Decision (CFSP) 2015/1333 of 31 July 2015 concerning restrictive measures in view of the situation in Libya, and repealing Decision 2011/137/CFSP, OJ L 206, 1.8.2015, p. 34, and Council Regulation (EU) 2016/44 of 18 January 2016 concerning restrictive measures in view of the situation in Libya and repealing Regulation (EU) No 204/2011, OJ L 12, 19.1.2016, p. 1.
7. Council Decision 2014/512/CFSP of 31 July 2014 concerning restrictive measures in view of Russia's actions destabilising the situation in Ukraine, OJ L 229, 31.7.2014, p. 13, and Council Regulation (EU) No 833/2014 of 31 July 2014 concerning restrictive measures in view of Russia's actions destabilising the situation in Ukraine, OJ L 229, 31.7.2014, p. 1.
8. Directive (EU) 2024/1788 of the European Parliament and of the Council of 13 June 2024 on common rules for the internal markets for renewable gas, natural gas and hydrogen, amending Directive (EU) 2023/1791 and repealing Directive 2009/73/EC, digital OJ L, 15.7.2024.
9. Directive 2013/30/EU of the European Parliament and of the Council of 12 June 2013 on safety of offshore oil and gas operations and amending Directive 2004/35/EC Text with EEA relevance, OJ L 178, 28.6.2013, p. 66.
10. Directive (EU) 2018/2001 of the European Parliament and of the Council of 11 December 2018 on the promotion of the use of energy from renewable sources, OJ L 328, 21.12.2018, p. 82.
11. Regulation (EU) 2022/869 of the European Parliament and of the Council of 30 May 2022 on guidelines for trans-European energy infrastructure, amending Regulations (EC) No 715/2009, (EU) 2019/942 and (EU) 2019/943 and Directives 2009/73/EC and (EU) 2019/944, and repealing Regulation (EU) No 347/2013, OJ L 152, 3.6.2022, p. 45.
12. Directive 2014/25/EU of the European Parliament and of the Council of 26 February 2014 on procurement by entities operating in the water, energy, transport and postal services sectors and repealing Directive 2004/17/EC Text with EEA relevance, OJ L 94, 28.3.2014, p. 243.
13. Council Directive 2003/96/EC of 27 October 2003 restructuring the Community framework for the taxation of energy products and electricity, OJ L 283, 31.10.2003, p. 51.
14. Council Regulation (EEC) No 2658/87 of 23 July 1987 on the tariff and statistical nomenclature and on the Common Customs Tariff, OJ L 256, 07/09/1987, p. 1.
15. Council, Common Military List of the EU adopted by the Council on 17 Feb. 2022, OJ C 100, 1.3.2022, p. 3.
16. Council Regulation (EU) No 747/2014 of 10 July 2014 concerning restrictive measures in view of the situation in Sudan and repealing Regulations (EC) No 131/2004 and (EC) No 1184/2005, OJ L 203, 11.7.2014, p. 1.
17. Council Regulation (EC) No 1412/2006 of 25 September 2006 concerning certain restrictive measures in respect of Lebanon, OJ L 267, 27.9.2006, p. 2.
18. Council Regulation (EU) 2015/735 of 7 May 2015 concerning restrictive measures in respect of the situation in South Sudan, and repealing Regulation (EU) No 748/2014, OJ L 117, 8.5.2015, p. 13.
19. Council Regulation (EU) No 401/2013 of 2 May 2013 concerning restrictive measures in respect of Myanmar/Burma and repealing Regulation (EC) No 194/2008, OJ L 121, 3.5.2013, p. 1.
20. Council Regulation (EU) No 401/2013 of 2 May 2013 concerning restrictive measures in respect of Myanmar/Burma and repealing Regulation (EC) No 194/2008, OJ L 121, 3.5.2013, p. 1.
21. Council Regulation (EU) No 1352/2014 of 18 December 2014 concerning restrictive measures in view of the situation in Yemen, OJ L 365, 19.12.2014, p. 60.
22. Council Regulation (EC) No 1183/2005 of 18 July 2005 imposing certain specific restrictive measures directed against persons acting in violation of the arms embargo with regard to the Democratic Republic of the Congo, OJ L 193, 23.7.2005, p. 1.
23. Council Regulation (EU) No 356/2010 of 26 April 2010 imposing certain specific restrictive measures directed against certain natural or legal persons, entities or bodies, in view of the situation in Somalia, OJ L 105, 27.4.2010, p. 1.
24. Council Regulation (EU) No 224/2014 of 10 March 2014 concerning restrictive measures in view of the situation in the Central African Republic, OJ L 70, 11.3.2014, p. 1.

25. Council Regulation (EU) 2017/2063 of 13 November 2017 concerning restrictive measures in view of the situation in Venezuela, OJ L 295, 14.11.2017, p. 21.
26. Council Regulation (EC) No 765/2006 of 18 May 2006 concerning restrictive measures against President Lukashenko and certain officials of Belarus, OJ L 134, 20.5.2006, p. 1.

ICMATSE 2024

Mixed-Variable Bayesian Optimization for Solar Selective Absorbers

Azra Arslan

*Istanbul Technical University, Department of Metallurgical and Materials Engineering, 34469,
Istanbul, TURKIYE
arslanaz22@itu.edu.tr
ORCID: 0009-0007-3477-7239*

Osman Safa Cifci

*Boğaziçi University, Department of Mechanical Engineering, 34342 Istanbul, TURKIYE
osmansafa.cifci@bogazici.edu.tr
ORCID: 0000-0003-4431-0783*

Cite this paper as: Arslan, Azra, Çifçi, Osman S. Mixed-Variable Bayesian Optimization for Solar Selective Absorbers. Int. Conf. Advanced. Mater. Sci. & Eng. HiTech. and Device Appl. Oct. 24-26 2024, Ankara, Turkiye

Abstract. One of the most widely used global optimization algorithms in materials science is Bayesian optimization, which produces a statistical model of the objective function whose minima or maxima are to be found. New, potentially promising parameters are derived through Bayesian inference by taking the previous parameter samples into account and have been shown to work well for various materials optimization tasks. However, most Bayesian optimization implementations have focused on continuous variables only, such as optimization of topology parameters, while there is a need to co-optimize continuous variables with categorical ones, such as materials selection. Various strategies for incorporating mixed variables in Bayesian optimization have been proposed recently. Among them, reparametrizing the discrete random variables into continuous parameters for a more efficient acquisition function optimization has recently shown remarkable performance in non-material domains. This work demonstrates the potential of mixed-variable Bayesian optimization by probabilistic reparametrization by designing a solar selective absorber that absorbs well in the 0.3-2.5 μm range and poorly in the 2.5-25 μm range. Such a coating design can find applications in photothermal conversion.

Keywords: Bayesian optimization, mixed-variable, multi-layer structures, solar selective absorber

© 2024 Published by ICMATSE

Introduction

Numerical optimization, such as optical device design, is essential in various scientific and industrial settings. With the development of advanced deposition and processing technologies, structures on the order of micro- and nanometers are being fabricated accurately and flexibly. Numerical simulation and screening of chosen parameters can provide essential information, but simultaneous numerical optimization of all parameters (shape, thickness, material, etc.) is required for optimal structures. Such an optimization can take a prohibitively long time and requires an extensive computing infrastructure and efficient numerical optimization methods.

It is possible to divide regularly applied optimization algorithms into three categories: local optimization, global stochastic optimization, and global model-based optimization [1]. Local optimization methods

that do not necessarily find the global minimum explore the neighborhood of the current best position. The second category of optimization algorithms relies on random variables. They include particle swarm optimization and differential evolution, which require many function evaluations to converge [1]. The final category is model-based optimization methods, which build a model of the objective function to explore new sets of promising parameters. Bayesian optimization (**Fig. 1**) is an example of a model-based optimization method.

Bayesian optimization (BO) has been mostly used on only continuous parameters [2]. However, many problems that need to be optimized have categorical and continuous parameters. Thus, in recent years, researchers have proposed novel ideas to extend BO. For example, the algorithm COMBO produces the acquisition function's graph representation [3]. Another model named BODi uses dictionary-based embedding to achieve high performance [4]. Finally,

Daulton and colleagues propose reparametrizing the discrete random variables into continuous parameters for a more efficient acquisition function [5]. Co-optimizing categorical, continuous, or discrete variables can enable materials design for various scientific problems, including solar selective absorber design.

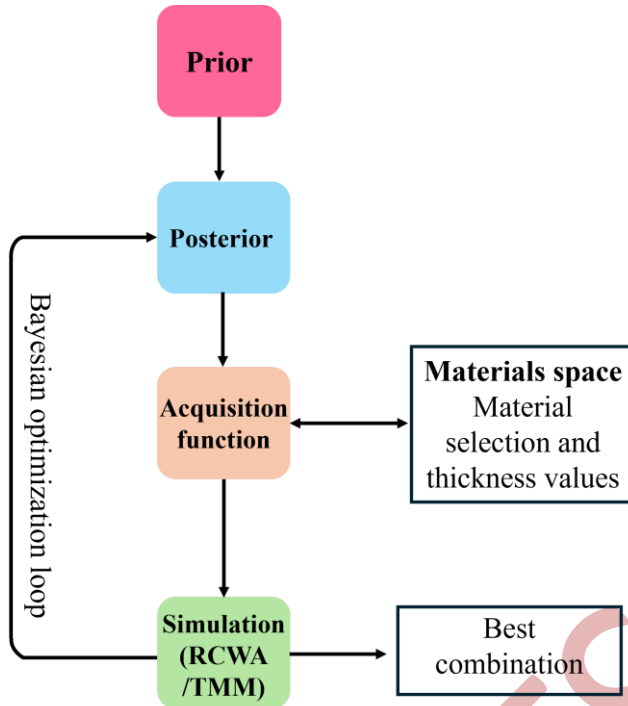


Figure 1. Bayesian optimization loop to find the best combination of materials and their thicknesses.

Solar selective absorbers are critical components in the solar energy domain [6]. An ideal solar selective absorber has high sunlight absorption (hence low reflectance) in the wavelength range of 300–2500 nm and low emissivity (hence high reflectance) in the range 2.5–25 μm wavelength range. Such a material design would have the best characteristics for the photothermal conversion process. Applications of solar selective absorbers include solar desalination, thermophotovoltaics, personal thermal management, photothermal catalysis, photothermal sterilization, and solar-driven soft robots.

When designing solar selective absorbers, it is essential to realize that the spectral irradiance is not constant and peaks around 550 nm [7]. Any irradiance below ~ 300 nm can be neglected as it is absorbed by the ozone layer. The irradiance starts to dip after around 600 nm and is nonexistent above 2.5 μm (Fig. 2).

Results and Discussion

A Bayesian optimization algorithm capable of co-optimizing categorical and numerical parameters minimizes reflectance in the 300–2500 nm range and maximizes reflectance between the 2500–25000 nm range. We focus on copper substrates with five layers with different thickness ranges (Table 1). The sample in the study has a metallic substrate, so the transmittance is zero. Only the sample's reflectance is studied as the sum of reflectance and emissivity (or absorptance) equals unity. The reflectance values are calculated using rigorous coupled-wave analysis, Torcwa library [8], and transfer-matrix method [9].

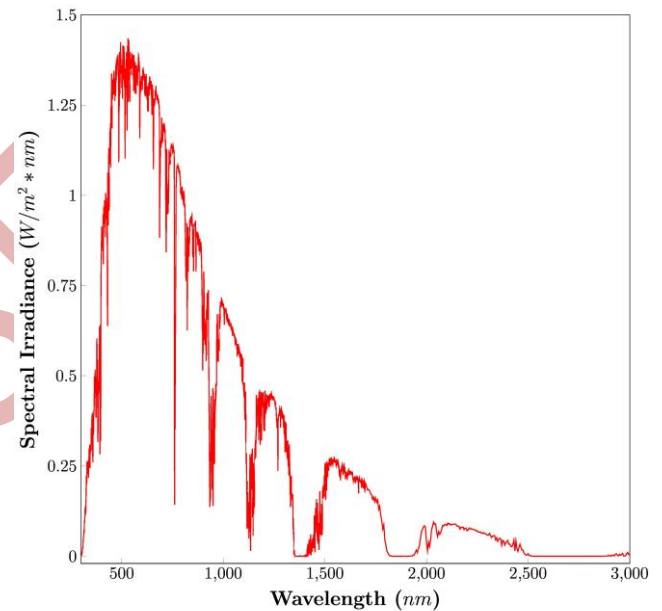


Figure 2. Solar spectral irradiance spectrum with an absolute air mass of 1.5 [7].

In the study, we begin by constructing a database of materials with reported refractive index values. Some materials do not have reported refractive index values beyond 14 μm . Based on this constraint, the optimization problem maximized absorbance between 300 and 2500 nm while minimizing absorbance between 2500 and 14000 nm. The materials we selected to include in our database are Al_2O_3 , BaF_2 , SiO_2 , Cu , TiO_2 , Ti , Si , ZnO , Fe_2O_3 , and Ge . Our selection of materials focused on the available data and ease of manufacture as they are among the most commonly used materials in thin coating. We chose five coating layers. It is important to note that the performance of the optimized solar selective absorber can increase with the number of layers.

Table 1. Multi-layer configuration used in the study

Layer No	Thickness Range (nm)
1	0-75
2	0-50
3	0-50
4	0-50
5	0-200

When constructing an optimization problem, the thickness ranges for each layer are specified and tabulated in **Table 1**. Each layer can have a thickness between 0 and 50 to 200 nm, depending on the layer number (**Fig. 3**). Furthermore, in the program, thickness values of multiples of 5 are chosen to construct each layer.

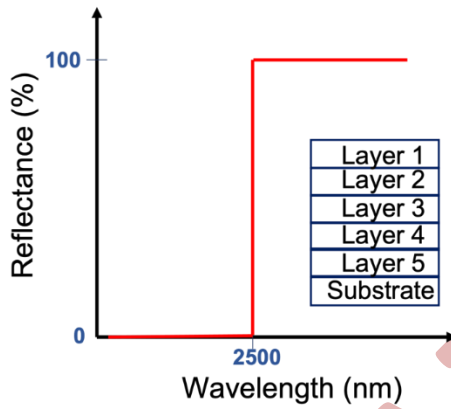


Figure 3. The ideal reflectance curve of a solar selective absorber and layer stack was used in the study. The red profile illustrates the reflectance characteristic of an ideal solar selective absorber.

This study covered two different problem settings, which required using two different objective functions in the mixed-space Bayesian optimization. The first study used the arithmetic average of the absorbance in the wavelength range of 300 to 2500 nm, subtracted by the arithmetic average of emissivity in the wavelength range of 2.5 to 14 μm . The second study used the solar irradiance weighted absorbance values instead of the arithmetic average of absorbance values subtracted by the arithmetic average of emissivity, which is given in Eqs. [1,2].

$$\text{Objective function 1} = \frac{1}{n} \sum_{i=1}^n \text{absorbance}_i - \frac{1}{m} \sum_{i=1}^m \text{emissivity}_i \quad (1)$$

$$\text{Objective function 2} = \frac{1}{n} \sum_{i=1}^n \text{absorbance}_i * \text{irradiance}_i - \frac{1}{m} \sum_{i=1}^m \text{emissivity}_i \quad (2)$$

The first optimization resulted in a structure with 70 nm of TiO₂, 30 nm of Ge, 40 nm of Ti, 25 nm of Si, and 195 nm of Cu, which has a mean absorbance of 0.827 and a mean emissivity of 0.092. In the second optimization, the optimized structure has 70 nm of ZnO, 40 nm of Fe₂O₃ (layers 2, 3, and 4 are of the same material), and 165 nm of Ge, which has a weighted absorbance of 0.803 and an emissivity mean of 0.044.

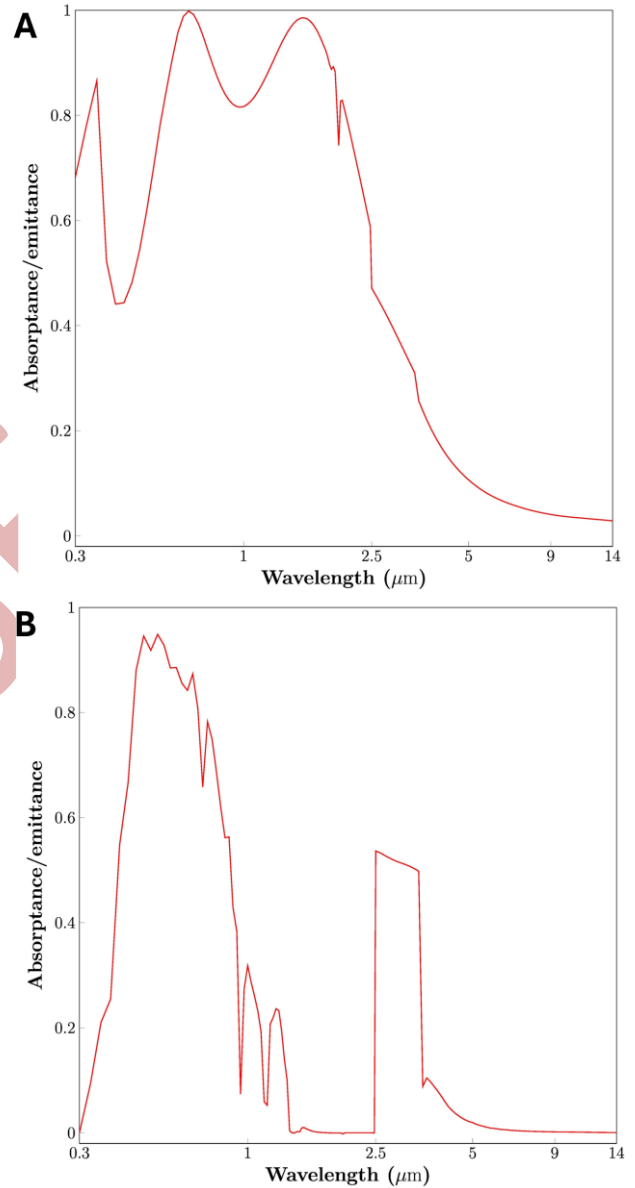


Figure 4. Absorbance/emittance graphs for optimized results with (a) average and (b) weighted absorbance values.

Conclusion

In this study, we use mixed-space Bayesian optimization to design a 5-layer coating that will perform as a solar selective absorber. Material selection and thickness optimization were simultaneously performed. An average absorbance above 80% between 300-2500 nm

and an average emissivity value below 10% between 2.5-14 μm were achieved. Better results can be obtained by increasing the amount of materials in the search space and the

number of layers. Such optimization solutions can be utilized in many materials-centric applications, such as solar energy utilization and energy storage.

References

1. Philipp-Immanuel Schneider, Xavier Garcia Santiago, Victor Soltwisch, Martin Hammerschmidt, Sven Burger, Carsten Rockstuhl, Benchmarking Five Global Optimization Approaches for Nano-optical Shape Optimization and Parameter Reconstruction, *ACS Photonics* 6 (2019), pp. 2726–2733.
2. Leonard Papenmeier, Luigi Nardi, Matthias Poloczek, Bounce: reliable high-dimensional Bayesian optimization for combinatorial and mixed spaces, *Advances in Neural Information Processing Systems* 36 (2023), pp. 1764-1793.
3. Changyong Oh, Jakub Tomczak, Efstratios Gavves, Max Welling, Combinatorial Bayesian Optimization using the Graph Cartesian Product, *Advances in Neural Information Processing Systems* 32 (2019).
4. Aryan Deshwal, Sebastian Ament, Maximilian Balandat, Eytan Bakshy, Janardhan Rao Doppa, David Eriksson, Bayesian Optimization over High-Dimensional Combinatorial Spaces via Dictionary-based Embeddings, *International Conference on Artificial Intelligence and Statistics* (2023), pp. 7021–7039.
5. Samuel Daulton, Xingchen Wan, David Eriksson, Maximilian Balandat, Michael A. Osborne, Eytan Bakshy, Bayesian optimization over discrete and mixed spaces via probabilistic reparameterization, *Advances in Neural Information Processing Systems* 35 (2022), pp. 12760-12774.
6. Jing Zhang, Chengbing Wang, Jing Shi, Dan Wei, Heng Zhao, Chuang Ma, Solar selective absorber for emerging sustainable applications, *Advanced Energy and Sustainability Research* 3 (2022), pp. 2100195.
7. Sarah R. Kurtz, Daryl Myers, Tim Townsend, Chuck Whitaker, Alex Maish, Roland Hulstrom, K. Emery, Outdoor Rating Conditions for Photovoltaic Modules and Systems, *Solar Energy Materials* 62 (2000), pp. 379–391.
8. Changyun Kim, ByoungHo Lee, TORCWA: GPU-accelerated Fourier modal method and gradient-based optimization for metasurface design, *Computer Physics Communications* 282 (2023), pp. 108552.
9. Steven J. Byrnes, Multilayer optical calculations, *arXiv preprint* (2016), 1603.02720.

Development and Performance Evaluation of Radiation-Resistant Secondary Emission Ionization Calorimeters for High-Energy Physics Experiments

Nejdet Paran

Erciyes University-Department of Physics, 38030, Kayseri, Türkiye,
nejdetparan@erciyes.edu.tr
ORCID: 0000-0003-0317-0438

Saleh Abubakar

Erciyes University-Department of Physics, 38030, Kayseri, Türkiye, salehbinabubakar@gmail.com
ORCID: 0000-0003-1511-2219

Burak Tekgun

Abdullah Gül University-Department of Electrical and Electronics Engineering, 38080, Kayseri, Türkiye,
burak.tekgun@agu.edu.tr
ORCID: 0000-0003-2720-8816

Emrah Tiras

Erciyes University-Department of Physics, 38030, Kayseri, Türkiye,
University of Iowa-Department of Physics & Astronomy, 52242, Iowa City, IA, USA,
etiras@fnal.gov
ORCID: 0000-0002-5628-7464

Nilüfer Kul

Erciyes University, Department of Physics, 38030, Kayseri, Türkiye,
nilfelek@gmail.com
ORCID: 0000-0003-XXXX-XXXX

Cite this paper as: Abubakar, S., Paran, N., Tekgun, B., Tiras, E., Development and Performance Evaluation of Radiation-Resistant Secondary Emission Ionization Calorimeters for High-Energy Physics Experiments. Int. Conf. Advanced. Mater. Sci. & Eng. HiTech. and Device Appl. Oct. 24-26 2024, Ankara, Türkiye

Abstract. Increasing the total collision energy and cumulative luminosity in particle accelerators enhances the importance of R&D efforts toward new detector systems resilient to higher radiation levels. In this context, the production of secondary emission ionization calorimeters (SE) resistant to high-radiation environments in clean-room facilities aims to develop, test, and analyze SE modules. This study focuses on the development, testing, and analysis of SE modules designed to replace traditional Hamamatsu R7761 Photomultiplier Tubes (PMTs) with more radiation-resistant alternatives. These modules replace traditional Hamamatsu single-anode R7761 Photomultiplier Tubes (PMTs). Specifically, three different voltage configurations integrating Gadolinium (Gd)-coated glass have been developed for each module, followed by comprehensive testing using cosmic, neutron, beta, and gamma radiation sources. Results indicate the functionality of all three modules and their sensitivity to neutron radiation. This study discusses the technical design, testing characteristics, and Gamma, Neutron, Beta, and cosmic radiation interaction results of the newly developed SE modules.

Keywords: Gadolinium (Gd), PMTs, Radiation, SE

© 2024 Published by ICMATSE

1. INTRODUCTION

In high-energy, particle, and nuclear physics, calorimetry is a widely used technique for measuring the momentum and energy of particles. Calorimeters operate by converting showers,

generated by primary particles, into light using materials like crystals, quartz, or plastic scintillators, which are then transformed into electrical signals by photodetectors. However, in high-energy radiation environments, calorimeters made of crystalline or plastic scintillators face challenges with maintaining long-term signal efficiency and calibration. The

materials also struggle to produce fast and narrowband signals, which are crucial for fast triggering and event selection algorithms. While quartz-based calorimeters produce a relatively low signal per charged particle [1-6]. To improve the performance of the PMTs in detecting gamma and neutron particles, we integrated gadolinium (Gd)-doped glass. Materials such as Gadolinium (Gd), Boron (B), and Lithium (Li) are commonly used elements for neutron detection. Notably, Gd has a significantly higher neutron capture cross-section for low-energy neutrons (<1 eV) than other elements. The benefits of this integration include increased efficiency in neutron detection due to the Gd's high neutron capture cross-section, improved overall sensitivity, and signal resolution of the PMTs, and enhanced resistance to high-radiation environments [6-11]. By examining their performance under cosmic, neutron, beta, and gamma radiation, this research aims to validate the effectiveness of these modules in high-radiation environments.

2. EXPERIMENTAL DETAILS

The SE modules were fabricated in clean-room facilities, where three distinct voltage configurations incorporating Gadolinium (Gd)-coated glass were developed for each module. We carried out the substrate preparation and gadolinium (Gd) thin film deposition process. Flat glass slides measuring 75 x 52 mm with a thickness of 1 mm were utilized as substrates for the deposition of Gd thin film layers. Before deposition, the substrates underwent a sequential ultrasonic bath treatment in acetone, isopropanol, and deionized water, followed by nitrogen gas drying to eliminate any impurities. Gadolinium thin films were deposited on the prepared glass substrates utilizing the Electron Beam Evaporation (E-beam) process. Gd thin film layers of two different thicknesses, 100nm and 500nm, were grown. In the test process, two 500nm Gd-coated glasses were used for 1000nm measurements, and three 500nm Gd-coated glasses were used for 1500nm measurements. The E-beam deposition technique was performed at a base pressure of 10^{-7} Pa in a high vacuum chamber to reduce oxidation and contamination during deposition. Initially, the prepared glass substrates were positioned within the E-beam chamber, which was then evacuated to a pressure of 5×10^{-7} Pascal (Pa). Upon the beginning of the procedure, an electric current was applied to a conductive filament, resulting in its heating and subsequent

electron emission. A voltage of approximately 6 kilovolts was subsequently supplied between the center and filament to propel the electrons toward the granular Gd designated for deposition. A robust magnetic field channels these electrons into beams, subsequently directing them toward the deposition material. Upon collision, the high-energy electrons induced the evaporation of the substance, which then deposited onto the glass substrates. The thicknesses of the formed Gd film layers were measured in situ during deposition utilizing a crystal microbalance (QCM) incorporated into the E-beam deposition chamber. This real-time monitoring facilitated accurate regulation of the film's thickness [3,6,11]. The fabrication procedures for the Glass-Gd are illustrated in Figure 1.

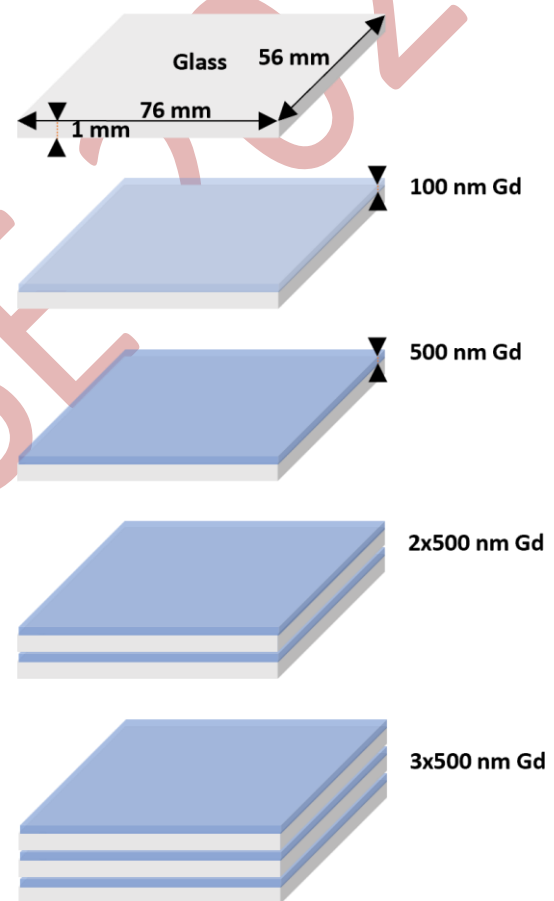


Figure 1. *Fabrication of Gadolinium (Gd) Thin Film Layers on Glass Substrates by E-beam Deposition Techniques.*

3. RESULTS AND DISCUSSION

To evaluate their radiation resistance and functionality, a series of tests were conducted using various radiation sources, including cosmic, neutron, beta, and gamma radiation. Table 1 illustrates the signal sizes generated by neutron rays for the three modules.

Table 1. The approximate signal sizes of Mode 1, 2, and 3 with a Gd-coated sample mounted on the PMT due to neutron irradiation

GdnThickness (nm)	Mode1 (mV)	Mode2 (mV)	Mode3 (mV)
100	88.68	39.67	37.05
500	87.23	39.81	36.94
1000	86.97	38.88	35.09
1500	85.78	39.02	35.75

Table 1 presents the signal amplitudes generated by neutron irradiation for the three experimental modules. It provides approximate values of the signals obtained from measurements conducted with Gd-coated glass samples of varying thicknesses—100 nm, 500 nm, 1000 nm, and 1500 nm under neutron exposure from an Am-241/Be source (3.3 MBq) for Modes 1, 2, and 3. Figure 2 shows the signal sizes of all three modes obtained from measurements with Gd-coated glasses with thicknesses of 100nm, 500nm, 1000nm, and 1500nm for neutron irradiation. As seen in Figure 2, the highest signal size can be obtained in Mode 1. The signal sizes of Modes 2 and 3 are close to each other and approximately half the size of Mode 1. Mode 1 consistently produces the most distinct neutron signals, showcasing a significant enhancement attributed to the Gd coating.

From this, we can conclude that Mode1 is the most suitable mode for Gd-coated measurements even if Mode2 and Mode3 are also sensitive to the Gd-coated measurements. It is also observed that the Gd coating thickness for all modes does not significantly change the signal strength. Therefore, in the range we have studied, applying a certain Gd coating thickness is unnecessary to keep the signal strength at a certain level.

Figure 3 illustrates the signal sizes obtained for cosmic rays, gamma rays, neutron, and beta (Sr-90, 3.7 kBq) irradiation. All are obtained in Mode 1 using a 500 nm thick Gadolinium (Gd)-coated glass mounted on the PMT. As shown in Figure 3, the neutron signal is significantly larger compared to the signals from the other radiation sources. This heightened response to neutrons is attributed to Gadolinium’s high neutron capture cross-section, which enhances the detector’s sensitivity to neutrons. In contrast, the signals from cosmic rays, gamma rays, and beta radiation are identical in

magnitude, indicating a similar response to these forms of radiation. This uniformity suggests that the detector, while efficient at all sources mentioned above, has a particularly strong sensitivity to neutrons (as developed with Gd-coated materials) making it well-suited for applications that require precise neutron detection.

Figure 4.19 displays the pulse shape distributions of all three modes coupled with a 500 nm thick Gd-coated glass due to neutron irradiation. Mode 3 exhibits noticeable signal distortion, indicating reduced accuracy in neutron detection under these settings. Mode 2 also provides less pronounced signals compared to Mode 1, though without the severe distortions seen in Mode 3. The larger neutron signal observed in Mode 1 emphasizes its superior sensitivity and suitability for neutron measurements, as the Gd layer effectively amplifies the detector's response to neutrons.

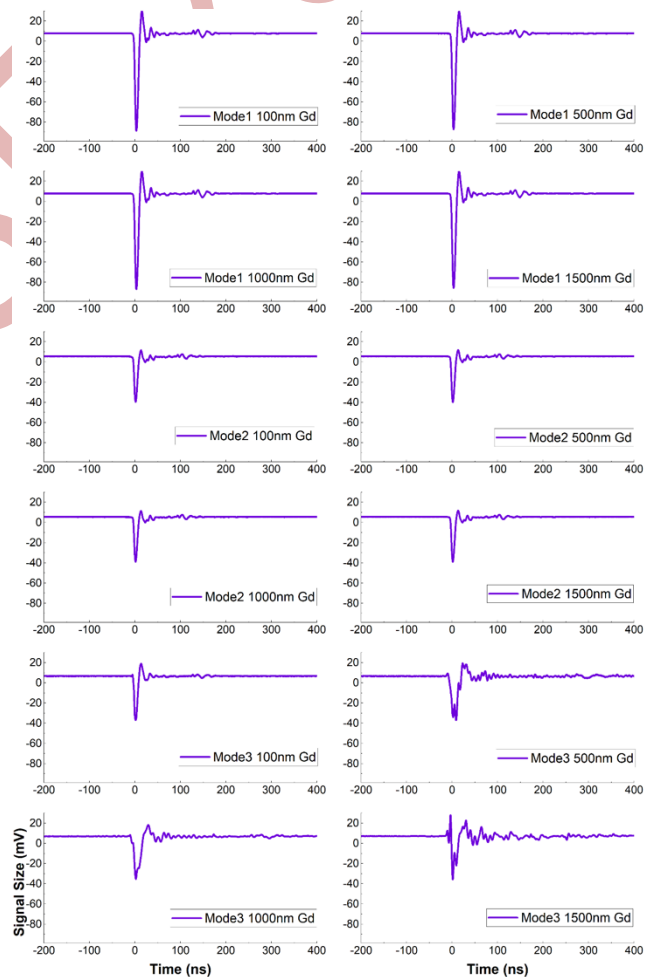


Figure 2. Pulse shapes of all three modes of the SE calorimetry module with Gd-coated glasses with thicknesses of 100nm, 500nm, 1000nm, and 1500nm due to neutron irradiation.

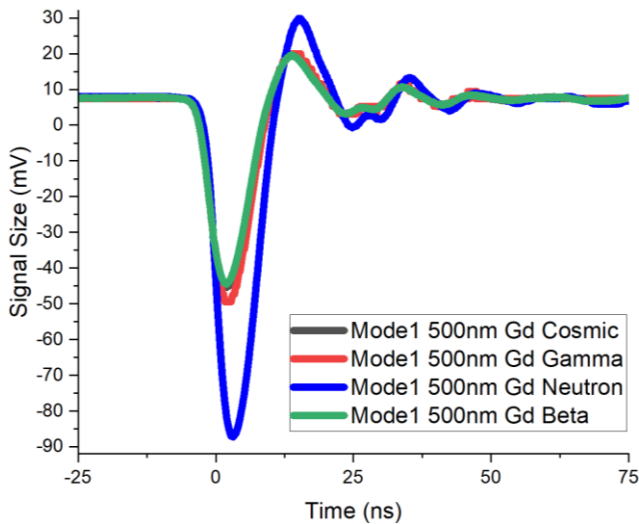


Figure 3. The pulse shape comparison of Mode 1 coupled with 500nm thick Gd-coated glass for Cosmic, Gamma, Neutron, and Beta irradiation.

This comparison highlights the critical role of mode selection in ensuring accurate and reliable neutron detection. Mode 1 emerges as the optimal choice, while Modes 2 and 3 are less effective, particularly for precise measurements, emphasizing the importance of careful calibration and configuration when using Gd-coated detectors. The double-pulse shape of Mode 3 is believed to be due to the afterpulse interaction of the delayed gammas produced by Gd atoms due to the capture of the neutrons. Both Mode 2 and Mode 3 would be

References

1. P.W. Nicholson, Nuclear electronics, (1974).
2. D.R. Winn, Y. Onel, Secondary Emission Calorimeter Sensor Development, J Phys Conf Ser 404 (2012) 012021.
3. L. Cerrito, Radiation and Detectors: Introduction to the Physics of Radiation and Detection Devices, 1st ed., Springer, 2017.
4. J. Sharpe, Nuclear Radiation Detectors, Methuen & Co, Ltd., London, UK (1964).
5. W.J. Price, Nuclear radiation detection, (1958).
6. G.F. Knoll, Radiation Detection and Measurement, Proceedings of the IEEE 69 (2010) 830.
7. A. Albayrak-Yetkin, B. Bilki, J. Corso, P. Debbins, G. Jennings, V. Khristenko, A. Mestvirivilli, Y. Onel, I. Schmidt, C. Sanzeni, D. Southwick, D.R. Winn, T. Yetkin, Secondary Emission Calorimetry: Fast and Radiation-Hard, (2013).
8. B. Bilki, K. Dilsiz, H. Ogul, Y. Onel, D. Southwick, E. Tiras, J. Wetzal, D.R. Winn, Secondary Emission Calorimetry, Instruments 6 (2022) 48. <https://doi.org/10.3390/INSTRUMENTS6040048>.
9. E. Tiras, Beam test results of Secondary Emission Ionization Calorimetry modules at Fermilab, Nucl Instrum Methods Phys Res A 1049 (2023) 168083. <https://doi.org/10.1016/J.NIMA.2023.168083>.
10. G.F. Knoll, Radiation Detection and Measurement, Proceedings of the IEEE 69 (2010) 830.
11. J. Dumazert, R. Coulon, Q. Lecomte, G.H.V. Bertrand, M. Hamel; Gadolinium for neutron detection in current nuclear instrumentation research: A review, Nuclear Inst. and Methods in Physics Research, A 882 (2018) 53–68.

developed as a sensitive mode to neutrons after careful optimization studies.

4. CONCLUSION

The development and testing of SE modules represent a significant advancement in the pursuit of radiation-resistant detection systems, crucial for particle detection. By integrating traditional Hamamatsu R7761 PMTs with gadolinium (Gd)-coated glass, we have shown the potential to improve neutron detection and resilience in a high-energy radiation environment. The neutron signals have significantly larger amplitudes compared to those produced by cosmic, gamma, and beta radiation, highlighting the superior neutron detection capability of the modules.

CONFLICTS OF INTEREST

No conflict of interest was declared by the authors.

ACKNOWLEDGEMENT

This work was supported by the Erciyes University Scientific Research Projects Coordination Unit (BAP) through the projects coded FBA-2022-12207, FBG-2022-11499, and FDS-2021-11525, as well as by a project awarded to Associate Professor Dr. Emrah TIRAŞ within the scope of the Outstanding Young Scientists Award Program (GEBİP) of the Turkish Academy of Sciences (TÜBA). We thank the Erciyes University BAP unit and TÜBA for their support.

WAAM Properties of Mild and Carbon Steels

Ezgi DOGAN

Marmara University- Mechanical Engineering Department, 34854, Istanbul, Türkiye,
ezgi.dogan@marun.edu.tr
ORCID: 0000-0003-0207-7178

Mustafa AY

Marmara University- Mechanical Engineering Department, 34854, Istanbul, Türkiye,
muay@marmara.edu.tr
ORCID: ORCID: 0000-0002-7672-1846

Memduh KURTULMUS

Marmara University- Applied Sciences Department, 34865, Istanbul, Türkiye,
memduhk@marmara.edu.tr
ORCID: 0000-0001-6525-232X

Ahmet İrfan YUKLER

Nişantaşı University- Mechanical Engineering Department, 34398, Istanbul, Türkiye,
irfan.yukler@nisantasi.edu.tr
ORCID: 0000-0001-8146-8665

Cite this paper as: Doğan, E, Ay, M, Kurtulmuş, M, Yüklér, Aİ. WAAM Properties of Mild and Carbon Steels. Int. Conf. Advanced. Mater. Sci.& Eng. HiTech.and Device Appl.Oct. 24-26 2024, Ankara, Turkiye.

Abstract. Wire arc additive manufacturing (WAAM) is becoming increasingly popular since it offers flexibility to produce complex designs with minimum material at shorter production times. The mild steel WAAM process has been investigated in this study. The influence of process parameters on bead geometry, microstructure, and mechanical properties were summarized. Although WAAM is recognized to have some advantages, the drawbacks of this technique, such as high heat input, result in serious thermal accumulation, which can significantly influence the microstructure and the mechanical properties, leading to anisotropy. The anisotropic phenomenon in WAAM is a serious problem.

Keywords: Wire arc additive manufacturing (WAAM), Mild steels, WAAM mild steel, Welding microstructure
© 2024 Published by ICMATSE

1.Introduction

The manufacturing of products by melting a raw material in the form of wire with an electric arc used as a heat source and depositing it layer upon layer is called wire arc additive manufacturing (WAAM) [1]. The process is schematically represented in Figure 1 [2]. The WAAM process reduces material waste and offers faster fabricating speeds than conventional manufacturing methods. [3].

The mild steel is cheap, malleable and ductile. The mild steel has a lower tensile strength than other

carbon steel types. It is machinable and weldable, which aids in its usefulness for most applications [4]. In mild steel WAAM applications especially GMAW machines are used [5]. The WAAM process has become an interesting alternative for the manufacturing of low-medium complexity large mild steel parts due to its high deposition rate [5]. The high temperature gradient, fast cooling rate, and sequential heating and cooling cycles experienced during WAAM effected the final microstructure, leading to a heterogeneous grain structure and anisotropic mechanical properties [17].

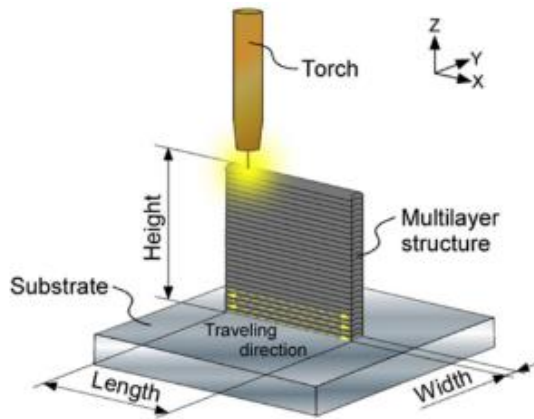


Figure 1. Schematic representation of the wire and the arc additive manufacturing (WAAM) process [6].

2. Results & Discussion

2.1. Mild Steel WAAM Wall Building

WAAM is a near-net shape technique, which means that the manufactured components are nearer to their actual designs but still require additional machining and surface finishing to get their final shape [1]. In GMAW processes the current is directly proportional to the wire feed speed [7]. The wire feed speed, welding speed and arc voltage determine the the heat input, the geometry and cooling rate of the weld [8]. These parameters must be properly chosen to produce smooth layers in the wall [1]. Duarte and his friends used GMAW continuous and pulsed wave welding modes to build WAAM steel walls [9]. The details of the welding parameters are given in Table 1. The results of width and height of each deposited layer measurements are shown in Figure 2 [9]. The results reveal the effects of the welding wave, wire feed speed and welding travel speed on the layer size. An increase in the travel speed leads to thinner deposited layers while the width is mostly controlled by the wire feed speed. It is possible to produce thinner samples with the pulsed wave than the continuous welding mode. The waviness of a WAAM wall decreases with the heat input. Less machining is needed for high heat input welding operations, because less waviness occur with high heat input [10].

Table 1. Process parameters of samples produced in GMAW pulsed and continuous wave modes [9].

Sample reference	Deposition rate, kg.h ⁻¹	Heat input, J.mm ⁻¹
PULSED WAVE MODE		
AP1	2.04	676.5
AP2	2.04	297.6
AP3	0.93	134.8
CONTINUOUS WAVE MODE		
AC1	1.11	521.8
AC2	1.85	209.5
AC3	1.11	155.0

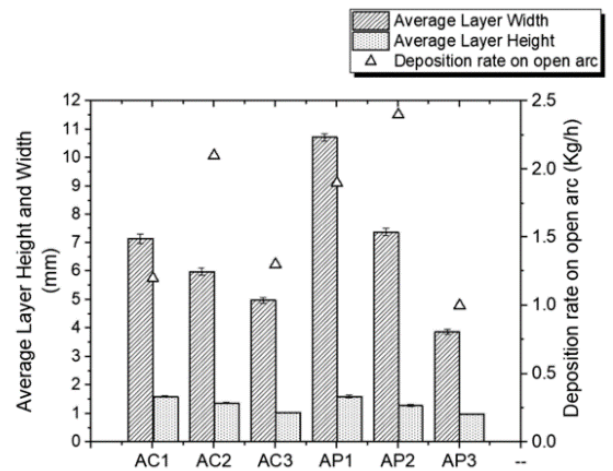


Figure 2. Average layer width and height of the as-built samples [9].

2.2. Microstructure of the Wall

The Figure 3 demonstrates the overall microstructure of the ER70S-6 steel wall at different regions [11]. The microstructure is fine polygonal ferrite as the primary phase and a low-volume fraction of the lamellar pearlite phase, which has primarily formed along the ferrite grain boundaries. The grain size is bigger in the top part compared to the lower part. This variation is a consequence of the different thermal history that the areas have undergone. Since the fusion boundaries experience a higher cooling rate during solidification process compared with the center of the melt pools, the formation of some acicular ferrite and bainite phases was detected adjacent to the fusion lines [12].

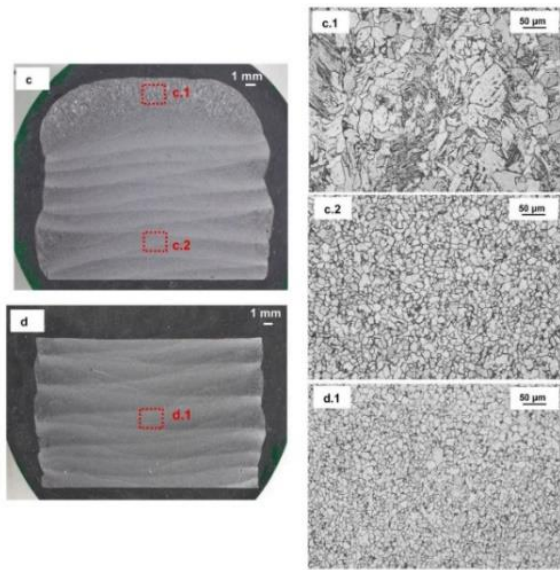


Figure 3. (left) Macrostructure of mild steel wall. (right) Microstructure of the wall. Note the microstructures are taken in the areas marked with the boxes in the macrographs [21].

2.3. Mechanical Properties of WAAM Parts

Sun and his friends investigated the mechanical properties of a steel component fabricated by WAAM [13]. They found the mechanical properties of transversal (horizontal) specimens are inferior to that of longitudinal (vertical) specimens, emerging anisotropic phenomenon as shown in Figure 4 [13]. The percentage of anisotropy (PA) was calculated. The anisotropic percentages of yield strength, ultimate tensile strength (UTS), and elongation was calculated as 10.1%, 4.2%, and 21.4%, respectively. The biggest difference happens in ductility.

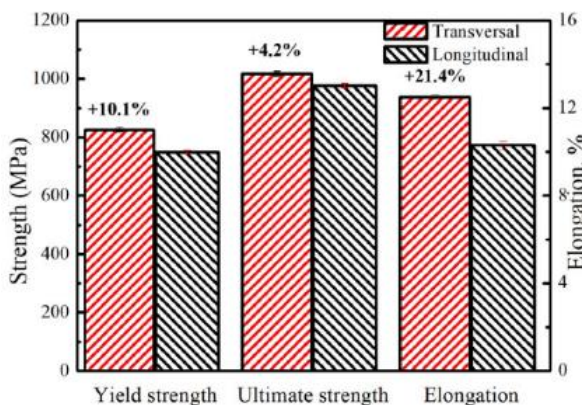


Figure 4. The anisotropic percentage of the mechanical properties low carbon high strength steels [25].

The hardness of mild steel WAAM weld beads are inversely proportional with the heat input [5]. Figure 5 illustrates the hardness variation in a mild steel

wall [14]. The upper region of the wall reveals the hardest average hardness value, while the middle region shows the smallest average hardness value. The hardness varies with the content and the grain size of the microstructure [14]. Acicular ferrite and bainite formation at the bottom and the top part of the Wall cause an increase in hardness.

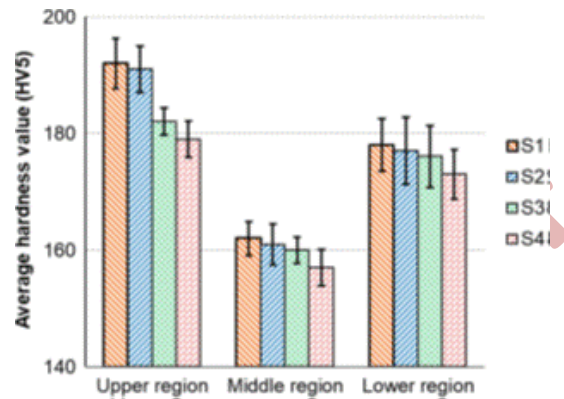


Figure 5. Hardness in mild steel WAAM wall [14].

The hardness values as well as tensile properties are related directly to the final microstructure. Figure 6 illustrates the influence of the heat input on tensile strength of deposited metal [9]. There is a sharp variation of the UTS for heat inputs around 200 J/mm, while above 300 J/mm there is almost no variation [9]. The deposited material goes through two important phase transformations, first from liquid to solid and then solid-state phase transformations that produce the final microstructure. The local composition and cooling rate determine the kinetics of those mentioned phase transformations, which in turn determine the final microstructure. Cooling occurs rapidly with lower heat input, because the weld bead is smaller compared with one with higher heat input. Hence, the cooling rate can be controlled by varying heat input. However, it should be noted that heat input is not the only parameter that controls the local cooling rate or the local microstructure.

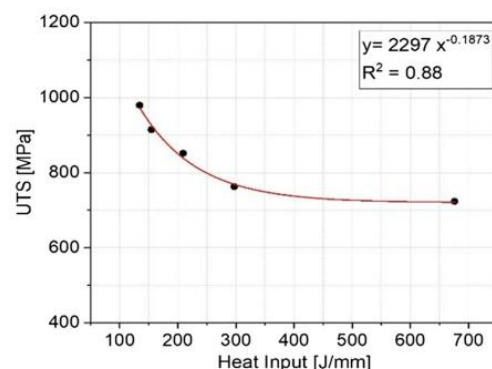


Figure 6. Influence of the heat input on the ultimate tensile strength of the mild steel WAAM part [9].

3. Conclusions

The following major conclusions can be drawn from the reviewed WAAM mild steel papers:

1. The dominant microstructure of the a WAAM mild steel component consists of polygonal ferrite grains along with a small volume fraction of lamellar pearlite formed at the ferrite grain boundaries.

2. There are fine grains at the bottom of the wall. At the top layer there are very coarse grains.

3. Hardness and the tensile strength of welds decrease with the increase in welding heat input.

4. The mechanical properties of the longitudinal tensile specimens are inferior to that of the transversal specimens, indicating anisotropy.

References

1. B. Saleh, et al., Fundamentals and advances of wire arc additive manufacturing: materials, process parameters, potential applications, and future trends, *Archives of Civil and Mechanical Engineering*, 23(2023), pp. 96, 10.1007/s43452-023-00633-7.
2. T.A. Rodrigues et al., Current Status and Perspectives on Wire and Arc Additive Manufacturing (WAAM), *Materials*, 12(2019), pp. 1121, 10.3390/ma12071121.
3. S.R. Singh, P. Khanna, Wire arc additive manufacturing (WAAM): A new process to shape engineering materials, *Materials Today: Proc*, 44(2021), pp. 118-128, 10.1016/j.matpr.2020.08.030.
4. Service Steel (2024, June, 20). Carbon steel vs. Mild steel: What's the difference?. <https://www.servicesteel.org/resources/carbon-vs-mild-steel>
5. A.S. Yildiz, et al., Wire arc additive manufacturing of high-strength low alloy steels: study of process parameters and their influence on the bead geometry and mechanical characteristics, *The Int J Adv Manf Tech*, 108(2020), pp. 3391–3404, 10.1007/s00170-020-05482-9.
6. D. Yang, C. He, G. Zhang, Forming characteristics of thin-wall steel parts by double electrode GMAW based additive manufacturing, *J Mats Proc Tech*, 227(2016), pp. 153–160, 10.1016/j.jmatprotec.2015.08.021.
7. H. Cary, S. Helzer, *Modern Welding Technology* (2004) 6th Edition, Pearson, New York.
8. M. Kurtulmus, Effects of Primary Welding Parameters on FCAW Steel Weld Form, *European Journal of Science and Technology*, 12, 1-5, 2018
9. V.R. Duarte, et al., Wire and Arc Additive Manufacturing of High-Strength Low-Alloy Steel: Microstructure and Mechanical Properties, *Adv Eng Mats*, 23(2021), pp. 2001036, 10.1002/adem.202001036.
10. T.A. Rodrigues, et al., Wire and arc additive manufacturing of HSLA steel: Effect of thermal cycles on microstructure and mechanical properties, *Add Manf*, 27(2019), pp. 440-450, 10.1016/j.addma.2019.03.029.
11. E. Aldalur, et al., High deposition wire arc additive manufacturing of mild steel: Strategies and heat input effect on microstructure and mechanical properties, *J Manf Proc*, 58(2020), pp. 615-626, 10.1016/j.jmapro.2020.08.060.
12. M. Ghaffari, et al., Effect of Solidification Defects and HAZ Softening on the Anisotropic Mechanical Properties of a Wire Arc Additive-Manufactured Low-Carbon Low-Alloy Steel Part, *The J The Mins, Met Mats Soc*, 71(2019), pp. 4215-4224, 10.1007/s11837-019-03773-5.
13. L. Sun, et al. Anisotropic mechanical properties and deformation behavior of low-carbon high-strength steel component fabricated by wire and arc additive manufacturing, *Mats Sci Eng A*, 787(2020), pp. 139514, 10.1016/j.msea.2020.139514.
14. V.T. Le, D.S. Mai, Q.H. Hoang, A study on wire and arc additive manufacturing of low-carbon steel components: process stability, microstructural and mechanical properties, *J Brazilian Soc Mech Sci Eng*, (2020), 42, pp. 480, 10.1007/s40430-020-02567-0.

Wall Dimensions of MIG based Mild Steel WAAM Parts

Ezgi DOGAN

Marmara University- Mechanical Engineering Department, 34854, Istanbul, Türkiye,
ezgi.dogan@marun.edu.tr
ORCID: 0000-0003-0207-7178

Mustafa AY

Marmara University- Mechanical Engineering Department, 34854, Istanbul, Türkiye,
muay@marmara.edu.tr
ORCID: ORCID: 0000-0002-7672-1846

Memduh KURTULMUS

Marmara University- Applied Sciences Department, 34865, Istanbul, Türkiye,
memduhk@marmara.edu.tr
ORCID: 0000-0001-6525-232X

Ahmet İrfan YUKLER

Nişantaşı University- Mechanical Engineering Department, 34398, Istanbul, Türkiye,
irfan.yukler@nisantasi.edu.tr
ORCID: 0000-0001-8146-8665

Cite this paper as: Doğan, E, Ay, M, Kurtulmuş, M, Yüklcr, Al. Wall Dimensions of MIG based Mild Steel WAAM Parts. Int. Conf. Advanced. Mater. Sci.& Eng. HiTech.and Device Appl.Oct. 24-26 2024, Ankara, Turkiye

Abstract. Wire and arc additive manufacturing (WAAM) can produce medium to large components economically because of its high-rate metal deposition and potentially unlimited build size. An optimized process planning that provides uniform, defect-free deposition is key for the production of WAAM parts. In this study, the effects of wire feeding speed, welding speed and arc voltage on the deposited wall dimensions in the WAAM process using gas welding process were investigated. The weld width increases with the arc voltage and the wire feeding rate. It decreases with the welding speed. The weld heightness decreases with the arc voltage and the welding speed, The wire feeding speed has the opposite effect on the bead height. The size of deposited metal wall increases with the layers number.

Keywords: Wire arc additive manufacturing, Primary welding parameters, Bead on plate welding
© 2024 Published by ICMATSE

1.Introduction

Wire and arc additive manufacturing (WAAM) method uses standard metal welding wires and arc welding equipment to produce builds layer-by-layer [1]. In particular, WAAM offers special benefits in the manufacture of near-net-shaped pieces including the ability to produce large structural components efficiently with modest complexity [2], and a high rate of production [3].

The WAAM technology produces steel, titanium, aluminum, nickel and magnesium components economically [3]. The WAAM process relies on the fundamental concepts of electric arc welding processes [1]. In mild steel WAAM applications especially GMAW machines are used, because high metal deposition rates are obtained with those machines [4]. The MIG based WAAM process is schematically represented in Figure 1 [5]. In order to provide dimensional accuracy on the wall and reduce the surface roughness, chip removal operation is applied after welding.

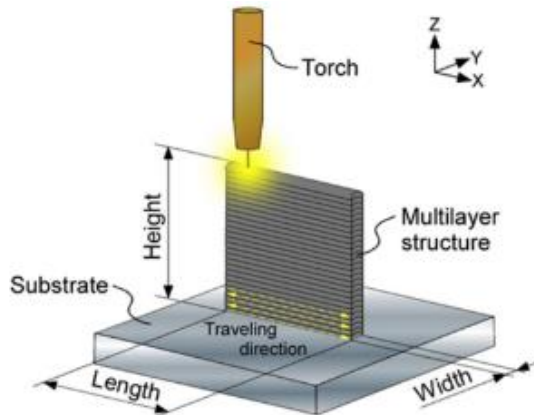


Figure 1. Schematic representation of the wire and the arc additive manufacturing (WAAM) process [6].

In GMAW process welding current, arc voltage and welding speed are called primary welding parameters [6]. These welding parameters directly determine the heat input energy and hence the weld geometry (bead width, height and penetration depth). In the case of MIG, the value is 0.8 [7]. Since the current varies with the wire feeding speed, it is possible to accept the wire feeding speed as the primary welding parameter [6]. The height of the WAAM wall depends on the number of layers. The wall dimensions are illustrated in Figure 2 [8]. Each dimension of the wall after chip removal is called as the effective dimension. For example, the wall width decreases to the effective width after machining. The amount of chips to be removed depends on the dimensions of the layers that make up the wall [9]. Metal losses and the production cost increase with the amount of chips removed from the wall [2]. The primary welding parameters are very effective on the geometry of bead on plate (BOP) welds [10].

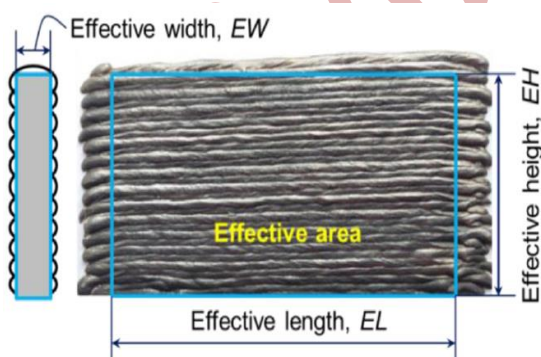


Figure 2. Schematic diagram illustrating the effective dimensions of the wall [8].

2. Results & Discussion

Mild steel (St37) plates with dimensions of $200 \times 200 \times 8$ mm were used as the substrates in the experiments. A Fronius TP400i GMAW machine was

used to deposit the material over the substrate. The welding machine's torch was connected vertically to a robot arm. The route of the torch was programmed before welding. In all welding processes, a constant oscillatory movement was given to the welding electrode. Direct current electrode negative mode was used for the metal deposition. The wire material (AWS ER70S-6) was a 1.2 mm diameter mild steel wire with a copper coating. During the welding process, a 93Ar/5% CO₂/2%O₂ gas was employed for the shielding purpose with a flow rate of 12 L/min. In every welding operation the free wire length was 7 mm and the arc length was 4 mm. The wire feeding speed was adjusted on the welding machine and the welding current in amperes was read on the welding machine screen during welding. No preheating was done before the first welding process. In multilayer welds, the weld area was allowed to cool by two minutes idle time after each pass. The welding process was designed so that the weld seam was obtained exactly in the middle of the plate. 200 mm long welds were obtained. The deposition directions of two adjacent layers were opposite. In multilayer welds, each new seam was started from the point where the previous seam ended. The workpiece was removed from the table when it was completely cooled to room temperature. The width and height of the seams were measured with a digital Vernier caliper. For each weld, 9 measurements were made at 200 mm intervals from the beginning and 200 mm from the end of the seam. The arithmetic mean of the measured results was calculated.

2.1. Effects of primary welding parameters on bead on plate weld geometry

The effects of primary welding parameters on bead on plate weld dimensions were illustrated in Figures 3, 4 and 5. First the effect of the arc voltage was investigated. The experiments performed with different arc voltage at a constant 3.5 m/min wire feeding speed and 3.33 mm/s welding speed. The results are shown in Figure 3. The welding heat input increased with the increasing of the arc voltage from 18 volts to 21 and 24 volts. The seam width increased and the seam height decreased with the arc voltage. The wire feeding speed or current intensity effect was illustrated in Figure 4. In those experiments constant 18 volt arc voltage and 3.33 mm/s welding speed were used. With the wire feed speed the deposited metal volume, bead width and bead height enlarged because of more heat input was performed. Figure 5 shows that there is a decrease in weld width and height with the welding

speed. The results of primary welding parameters are consistent with the results of other researchers [10-12].

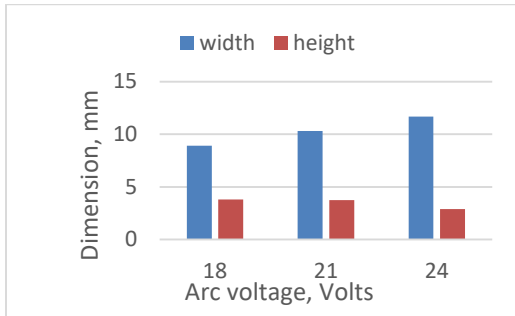


Figure 3. The variation of weld width and height with the arc voltage of the bead on plate welds.

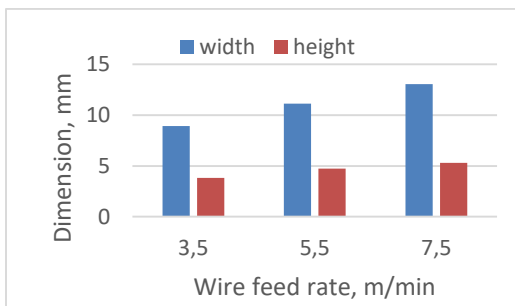


Figure 4. The variation of weld width and height with the wire feed rate of the bead on plate welds.

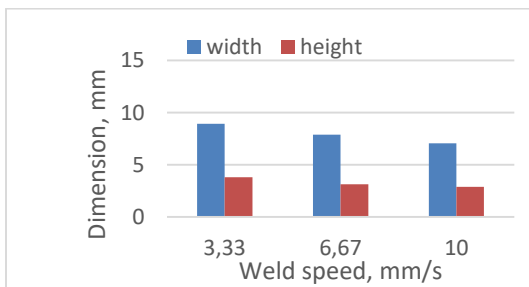


Figure 5. The variation of weld width and height with the welding speed of the bead on plate welds.

2.2. Effect of heat accumulation on wall dimensions of WAAM parts

The effect of the number of layers on WAAM wall dimensions is shown in Figure 6. In these experiments, 3.5 m/min wire feeding speed, 18 volt arc voltage and 3.33 mm/s welding speed were kept constant. The deposited metal volume increased with the weld layers number. As a natural result of the increase in metal volume, the wall height also increased. The wall width also expanded by layers. Growth rates in width and height were different. The

width expansion rate is significantly lower than the wall height increase rate.

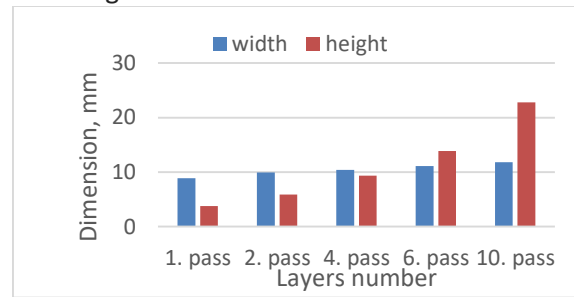


Figure 6. Wall dimensions of multi layered WAAM parts.

In GMAW based WAAM parts welding parameters, oscillations, and interpass temperature determine the arc conditions and the bead geometry [13]. During the process, the temperature of the substrate increases [14]. Higher weld heat input energy results in higher heat accumulation and interpass temperature [15]. The viscosity of the molten metal decreases with increasing temperature. Therefore, the melt pool will flow outward faster in higher layers and form a wider width and a shallow height [16].

In Figure 7, we see how welding heat input affects wall dimensions. In general, as heat input increases, wider and higher walls are obtained. However, it should not be forgotten that each welding parameter has a different effect on the width or height of the weld. The difference in wall width between the 1st pass and the 10th pass in experiment number 7 was 16%. This difference was 37% in experiment number 4. The wall height was 28.75 mm in experiment number 7. In experiment number 4 the wall height was only 20.26 mm. These results indicate that welding parameters of number 7 are more advantageous in terms of production economy.

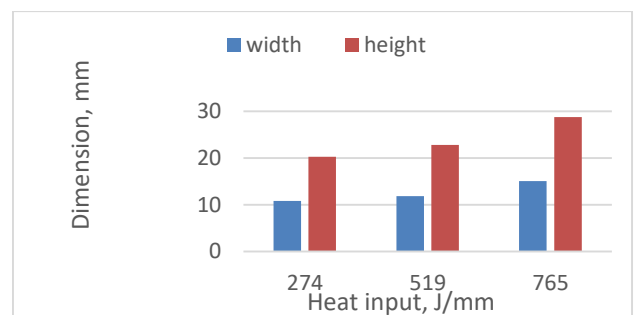


Figure 7. The variation of wall dimensions with welding heat input in 10 layered walls.

3. Conclusions

Below are the results obtained from the study investigating the effect of WAAM welding parameters of mild steels.

1. As the wire feeding speed increases, the weld cross-sectional area, width and height increase.
2. Weld cross-sectional area decreases with the welding speed.

3. The weld expands with arc voltage and its height decreases.

4. Heat accumulation in the welding area increases the weld width and reduces its height.

5. As the number of weld layers increases, wall dimensions increase

References

1. S.R. Singh, P. Khanna, Wire arc additive manufacturing (WAAM): A new process to shape engineering materials, *Materials Today: Proc*, 44(2021), pp. 118-128, 10.1016/j.matpr.2020.08.030.
2. M. Srivastava, Wire arc additive manufacturing of metals: A review on processes, materials and their behaviour, *Materials Chemistry and Physics*, 294(2023), pp.126988, 10.1016/j.matchemphys.2022.126988.
3. B. Saleh, et al., Fundamentals and advances of wire arc additive manufacturing: materials, process parameters, potential applications, and future trends, *Archives of Civil and Mechanical Engineering*, 23(2023), pp. 96, 10.1007/s43452-023-00633-7.
4. B.P. Nagasai, S. Malarvizhi, V. Balasubramanian, Effect of welding processes on mechanical and metallurgical characteristics of carbon steel cylindrical components made by wire arc additive manufacturing (WAAM) technique, *CIRP Journal of Manufacturing Science and Technology*, 36(2022), pp. 100-116, 10.1016/j.cirpj.2021.11.005.
5. M.Yamaguchi, Influence of metal transfer behavior under Ar and CO₂ shielding gases on geometry and surface roughness of single and multilayer structures in GMAW-based wire arc additive manufacturing of mild steel, *The International Journal of Advanced Manufacturing Technology*, 119(2022), pp. 911–926, 10.21203/rs.3.rs-657956/v1.
6. M. Kurtulmus, Effects of Primary Welding Parameters on FCAW Steel Weld Form, *European Journal of Science and Technology*, 12(2018), pp. 1-5.
7. L. Quintino, Heat input in full penetration welds in gas metal arc welding (GMAW), *International Journal of Advanced Manufacturing Technology*, 68(2013), pp. 2833–2840, 10.1007/s00170-013-4862-8.
8. V.T. Le, D.S. Mai, Q.H. Hoang, A study on wire and arc additive manufacturing of low-carbon steel components: process stability, microstructural and mechanical properties, *J Brazilian Soc Mech Sci Eng*, (2020), 42, pp. 480, 10.1007/s40430-020-02567-0.
9. B. Denkena, M. Wichmann, P. Pillkahn, Effect of process parameters during wire arc additive manufacturing (WAAM) and mechanical finishing on the surface zone properties, *Procedia CIRP*, 123(2024), pp. 262–267, 10.1016/j.procir.2024.05.047.
10. E. Doğan, Effects of welding parameters on the angular distortion of welded steel plates, *Open Chemistry*, 20(2022), pp. 417–423, 10.1515/chem-2022-0152.
11. B. Ma, Welding parameters effect and optimization on bead geometry during arc additive manufacturing, *Journal of Physics: Conference Series*, 1986(2021), pp. 012034, 10.1088/1742-6596/1986/1/012034.
12. D. Klobcar, M. Lindic, M. Basic, Wire arc additive manufacturing of mild steel, 65(2018), pp. 179–186, 10.2478/rmzmag-2018-0015.
13. P. Henckell, Reduction of Energy Input in Wire Arc Additive Manufacturing (WAAM) with Gas Metal Arc Welding (GMAW), *Materials*, 13(2020), pp. 2491, 10.3390/ma13112491.
14. D. R. Corradi, Effect of Magnetic Arc Oscillation on the geometry of single-pass multi-layerwalls and the process stability in wire and arc additive manufacturing, *Journal of Materials Processing Technology*, 283(2020), pp. 116723, 10.1016/j.jmatprotec.2020.116723.
15. T.A. Rodrigues et al., Current Status and Perspectives on Wire and Arc Additive Manufacturing (WAAM), *Materials*, 12(2019), pp. 1121, 10.3390/ma12071121.
16. B.P. Nagasai, S. Malarvizhi, V. Balasubramanian, Effect of interlayer delay on microstructure and bead geometry of wire arc additive manufactured low carbon steel components, *International Journal on Interactive Design and Manufacturing*, 17(2023), pp. 939–946, 10.1007/s12008-022-01009-6.

Investigation of the effect of composite layer thickness on low-velocity impact behaviour in fibre metal laminate materials

Mustafa Dündar

Düzce University - Institute of Graduate Education, Department of Mechanical Engineering, Düzce, Turkey

m.dundar@comu.edu.tr

ORCID : 0000-0002-3956-8088

İlyas Uygur

Düzce University - Faculty of Engineering, Department of Mechanical Engineering, Düzce, Turkey

ilyasuygur@duzce.edu.tr

ORCID :0000-0002-8744-5082

Ergün Ekici

Çanakkale Onsekiz Mart University, Faculty of Engineering, Department of Industrial Engineering, Çanakkale, Turkey

ergunekici@comu.edu.tr

ORCID :0000-0002-8744-5082

Cihat Taşçioğlu

Düzce University - Faculty of Forestry, Department of Forest Products Engineering, Düzce, Turkey

cihattascioglu@duzce.edu.tr

ORCID : 0000-0002-6770-8308

*Cite this paper as: Dündar, M, Uygur, İ, Ekici, E, Taşçioğlu, C. Numerical and statistical investigation of the effect of composite layer thickness on low-velocity impact behaviour in fibre metal laminate materials
Article title.Int. Conf. Advanced. Mater. Sci.& Eng. HiTech.and Device Appl.Oct. 24-26 2024, Ankara, Turkiye*

Abstract. In the field of aviation, reducing fuel costs by designing lighter vehicles and thus producing more environmentally friendly aircraft is one of the most important issues. This situation has led aircraft manufacturers to search for lighter and more durable materials. For this reason, Fibre Metal Laminate (FML) structures, which are used especially in the aerospace industry due to their superior fatigue and impact resistance properties, attract attention. Carbon fibre reinforced aluminium plates (CARALL), the most unique member of the FML hybrid structure family, has attracted the attention of researchers. In this study, the low velocity impact behaviour of CARALL FML structures with different composite layer thicknesses at different energy loading (8J-12J-18J) and different impactor types ($\varnothing 15$ and $\varnothing 20$) were statistically investigated. CARALL FML structures were modelled in 2/1 arrangement (Al-0°_[1]-Al, Al-0°_[3]-Al, Al-0°_[5]-Al) in LS-DYNA finite element programme. It is observed that the peak load Fmax increases with increasing energy loading. The increase in striker diameter decreased the amount of absorbed energy and increased the rebound.

Keywords: Fiber Metal Laminat, Low-velocity impact, composite, CFRP, FML, ANOVA

© 2024 Published by ICMATSE

1. Introduction

Fibre Metal Laminate materials (FMLs) are hybrid structures formed by combining thin metal layers with composite layers [1,2]. The most remarkable feature of FML materials is to combine the light weight of fibre reinforced polymer (FRP) materials with the good impact resistance of the metal layer [3]. FML materials were first developed in 1978 [4]. In the meantime, only Aramid fibre reinforced aluminium laminate and glass fibre reinforced

aluminium laminate (GLARE) product models have matured and started to be used in the aerospace industry. However, with the development of technology in the following years, carbon fibre reinforced aluminium laminates started to attract attention [5]. Carbon fibre reinforced composites have a large area of use due to their performance and light weight [6]. Due to these superior properties, studies have focused on CARALL FML materials. CARALL materials provide great advantages for the aerospace industry [7].

FML materials are mostly used in the aerospace industry. According to statistics, more than 13% of aviation accidents are caused by impact damage[8]. Impact damage can occur at high and low speeds. Impacts occurring at high speed can be visually recognised and intervened. However, unlike high speed, low speed impact can cause damage that is not visible to the eye [9]. Low velocity impact is usually dominated by in-plane stresses. This leads to the formation of different damage modes in the internal structure of the structure. It is impossible to determine this intuitively. This situation jeopardises the safety of the structure [10]. For these reasons, low velocity impact damage is one of the important damage conditions in FML materials. Therefore, it is an issue that needs to be investigated in detail at different energy loads and different impact properties of the structure to guide the design and development of the next generation CARALL FML materials. In their study, Sharma et al. [11] produced FML materials in 2/1, two different 3/2 and 4/3 formats by keeping the aluminium layer thickness constant. In the experiments, they observed that increasing the thickness of the structure decreases the degree of damage and increases the maximum peak load. Yaghoubi et al.[12] investigated the impact behaviour of 5 different GLARE types such as 2/1, 3/2, 4/3, 5/4 and 6/5. They reported that the critical behaviour of fibre and aluminium depends on the thickness of the panel. They stated that the threshold cracking energy varies parabolically with the thickness of the specimen. Fan et al. [14] observed that increasing both the number of metal layers and the thickness of the composite layer increased the puncture resistance.

It has been proved that the contact shape between the impactor and the structure has a significant effect on the impact response of general structures [17,18]. De Cicco et al. [19] investigated the low velocity impact behaviour of magnesium FMLs under impact forces of different sizes and shapes. Yao et al. [20] investigated the low velocity impact behaviour of FML materials under various impactor shapes and energy loads. At the end of the study, they stated that the impact behaviour of FMLs strongly depends on the striker shape, energy load and metal layer distribution.

In this study, we applied different composite layer thickness (0.5 mm) of different composite layer thickness (Al-0°_[1]-Al, Al-0°_[3]-Al, Al-0°_[5]-Al), The effect of different striker shapes (Ø15- Ø20) and

different energy loads (8J-12J-18J) on the impact behaviour at low speed was investigated numerically and statistically.

2. Material Method

FML structures are materials that are formed by the combination of metal and composite structure. In this study, Al2024-T3 material with a thickness of 0.5 mm obtained from AMAG Rolling company was preferred as the metal layer. Tensile test specimens were prepared in accordance with TS EN ISO 6892-1 standards in order to use engineering data in numerical analysis of Al2024-T3 material used in the study. The prepared tensile test specimens were carried out on a Zwick/Roell Z600 tensile testing machine. The tensile test data of Al2024-T3 material obtained as a result of the tensile test were added to the LS_DYNA related material card.

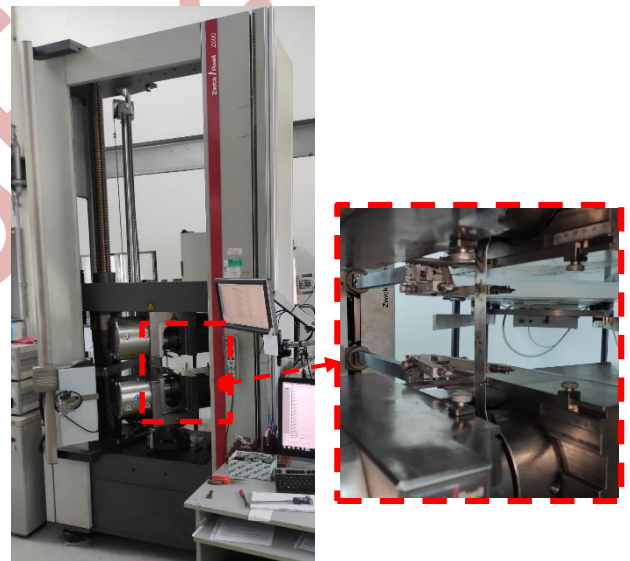


Figure 1. Tensile test of Al2024-T3 material

2.1. Multilayer Layer Design

The CARALL structure was modelled in 2/1 format to consist of 3 layers. The top and bottom plates consist of Al2024-T3 material, while the middle layer has a CFRP structure. All CARALL materials are in 2/1 format and modelled in LS_DYNA programme in such a way that only the composite layer thickness increases. The layer arrangement is shown in table 1. In all materials, the metal layer thickness is 1 mm in two layers. Each layer thickness of CFRP layers is 0.4 mm. Fibre orientations are modelled as 0° for all material groups. CARALL materials were modelled as multilayer shell elements with 3 different material codes. Material identification was made for

each layer. The test specimens were designed as $\varnothing 40$ mm diameter. Experiments were carried out with $\varnothing 20$ and $\varnothing 15$ mm striking tips with 8J, 12J and 18J values.

Table 1. CARALL deney numunelerinin plaka dizilimi

Material Code	Lay-up	Total Thickness
A	Al-0° _[1] -Al	1.4 mm
B	Al-0° _[3] -Al	2.2 mm
C	Al-0° _[5] -Al	3 mm

CARALL material The top and bottom plates consist of 0.5 m thick Al2024-T3 plates. In the middle layer there is a CFRP composite structure as shown in Table 1. All FML materials are stacked in 2/1 format. FML materials are modelled as shell elements in multiple layers. Material identification was made for each layer. Test specimens were designed in $\varnothing 40$ mm diameter. Experiments were carried out with $\varnothing 20$ and $\varnothing 15$ striking tips with 8J, 12J and 18J values (Figure 2.).

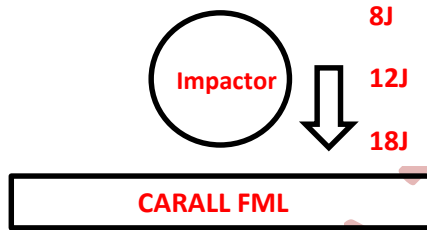


Figure 2. Schematic representation of the impact test

The Johnson-Cook material model was used to utilise the properties of the Al2024-T3 material used in the CARALL material. The Johnson-Cook material model best describes high strain rates and large deformation rates. It is widely used in researches due to its simplicity [21]. Johnson-Cook material model shows linear behaviour below the yield limit and plastic behaviour above the yield limit.

The experimentally obtained mechanical properties of Al2024-T3 material as described in section 2 are shown in table 2.

Table 2. Al2024-T3 malzemenin mekanik özellikleri

Mechanical properties	Units	Value
Modulus of Elasticity	E (GPa)	72
Poisson Ratio	ν	0.33
Yield Strength	σ_{Ak} (MPa)	358

The MAT054-055 material card is an improved version of the Chang-Chang composite damage model. This model is used for thin shells. The model is assumed to be elastic in the absence of damage. But when damage occurs, it is assumed to be nonlinear. MAT022 is an improved version of the material card.

The mechanical properties of the CFRP structure used in the composite layer were taken from the ANSYS material library. These constants were integrated into the MAT054-055 material card in Ls-Dyna. The engineering constants of the CFRP materials used are shared in Table 3.

Table 3. Mechanical Properties of CFRP Materials

Mechanical properties	Symbols and Units	Value
Density	gr/cm ³	1.54
1 direction Elasticity Modulus	E_1 (GPa)	123
2 direction Elasticity Modulus	E_2 (GPa)	9.87
Poisson Ratio	ν_{12}	0.27
1 direction tensile strength	X_T (MPa)	1979
1 direction tensile strength	Y_T (MPa)	26
1 direction compersion strength	X_C (MPa)	893
2 direction compersion strength	Y_C (MPa)	139
Shear strength	S_C (MPa)	100

In this experimental setup, it is assumed that the striker is not damaged and modelled rigidly using MAT020 board. The material properties of the striking tip using MAT20 are defined in Table 5.

Table 4. MAT20 steel material properties

Mechanical properties	Symbols and Units	Value
Modulus of Elasticity	E (GPa)	210
Poisson Ratio	ν	0.33
Yield Strength	gr/cm ³	7.85

3. Results and Discussion

The maximum peak load (F_{max}) is defined as the resistance of the specimen to the impact load in the low speed impact test. A high peak load means that the resistance of the material against impact is high. When the graphs of the maximum peak load in Figure 3 are examined, the increase in the thickness

of the composite layer led to an increase in the maximum peak load in all energy loads (8J-12J-18J) and in all samples. This situation shows that the increase in thickness is an effective factor in the load carrying capacity of the material. It shows that in specimens with low thickness, many damage modes occur in specimens where the peak load does not increase according to the energy load and the bearing capacity is lost [22]. It is seen in the figures that the striker diameter is another factor in peak loads. This shows that the contact area between the CARALL material and the striker is an important factor and is effective in the maximum peak load. It was found that as the contact area increases, the peak load increases [23].

3.1. Variance analysis (ANOVA)

Analysis of variance (ANOVA) at 95% confidence level was applied to determine the parameter effects and effect levels. The results of ANOVA at 95% confidence level for maximum peak load are presented in Table 5.

When the ANOVA table for maximum peak load is analysed, the interaction of striker diameter, material, impact energy and material impact energy (M*DE) is significant in terms of $P < 0.05$. When the contribution rates were analysed in terms of factors, the effective parameter was impact energy with a contribution rate of 49.2%, followed by material with a contribution rate of 37.16%. The contribution rate of the striker diameter remained below 3%. In terms of factor interactions, the material impact

energy (M*DE) interaction contributed 9.74%, while the other interactions had no significant (<1%) contribution. It is seen that the R^2 value is above 99.29% and the adjusted R^2 value is above 96.98%.

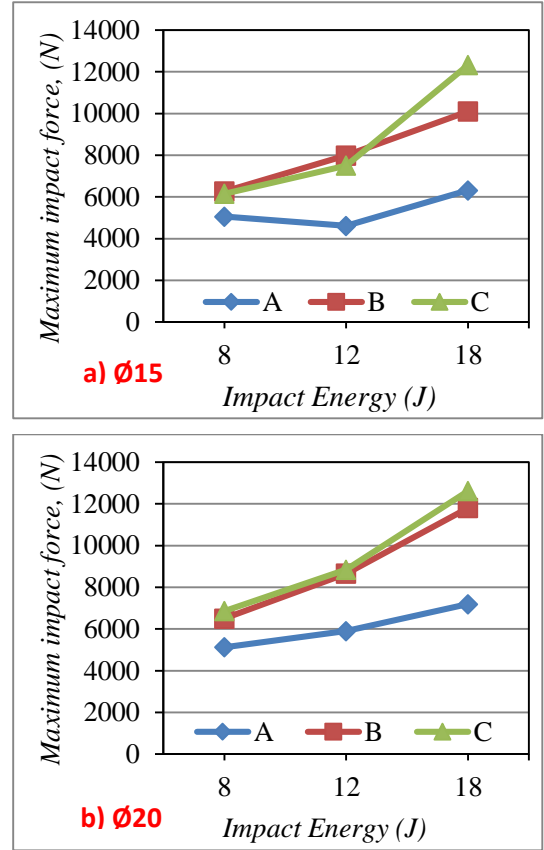


Figure 3. Maximum peak load obtained at different energy loads and different impactor diameters

Table 5. ANOVA results for maximum peak load

Maksimum tepe yükü, Fmax						
Ç	1	2858441	2858441	15.26	0.017*	2.708
M	2	39227079	19613540	104.7	0*	37.161
DE	2	51937373	25968687	138.63	0*	49.202
Ç*M	2	12249	6125	0.03	0.968	0.012
Ç*DE	2	489226	244613	1.31	0.366	0.463
M*DE	4	10285184	2571296	13.73	0.013*	9.744
Hata	4	749321	187330			0.710
Toplam	17	105558874				100
$R^2 = \%99.29$, $R^2_{(Düzeltilmiş)} = \%96.98$						
Kısaltmalar: Ç; Vurucu çapı, M; Malzeme, DE; Darbe enerjisi, F; Faktörler, SD; Serbestlik Derecesi, KT; Karalar toplamı, KO; Karalar ortalaması, %KO; Katkı oranı						
* ifadesi $P < 0.05$ olmak üzere anlamlı terimleri göstermektedir.						

4. Conclusion

1. Increasing the composite thickness increased the maximum peak load.
2. Reducing the diameter of the striker caused different damage mechanisms due to the lower contact area.
3. According to ANOVA results; impact energy is the most effective parameter for

- maximum peak load with 49.29% contribution rate, followed by material with 37.161% contribution rate. In terms of factor interactions, the material impact energy (M*DE) interaction contributed 9.74%, while the other interactions did not contribute significantly (<1%).
4. The work should be evaluated in terms of absorbed energy and maximum displacement.

References

- [1] Pang Y, Yan X, Yao H, Qu J, Wu L. Experimental study of basalt fiber/steel hybrid laminates under low-velocity impact. *Engineering Fracture Mechanics* 2022;259:108169. <https://doi.org/https://doi.org/10.1016/j.engfracmech.2021.108169>.
- [2] Bienias J, Jakubczak P, Dadej K. Low-velocity impact resistance of aluminium glass laminates – Experimental and numerical investigation. *Composite Structures* 2016;152:339–48. <https://doi.org/https://doi.org/10.1016/j.compstruct.2016.05.056>.
- [3] Hou W, Li M, Zhang X, Liu Z, Sang L. Design and optimization of the bumper beam with corrugated core structure of fiber metal laminate subjected to low-velocity impact. *Thin-Walled Structures* 2023;187:110746. <https://doi.org/https://doi.org/10.1016/j.tws.2023.110746>.
- [4] Sinmazçelik T, Avcu E, Bora MÖ, Çoban O. A review: Fibre metal laminates, background, bonding types and applied test methods. *Materials and Design* 2011;32:3671–85. <https://doi.org/10.1016/j.matdes.2011.03.011>.
- [5] Lu B, Zhang J, Zheng D, Xie J, Zhang L. Theoretical analysis on carbon fiber reinforced aluminum laminate under off-center impact. *International Journal of Mechanical Sciences* 2023;248:108247. <https://doi.org/https://doi.org/10.1016/j.ijmecsci.2023.108247>.
- [6] Hynes NRJ, Vignesh NJ, Jappes JTW, Velu PS, Barile C, Ali MA, et al. Effect of stacking sequence of fibre metal laminates with carbon fibre reinforced composites on mechanical attributes: Numerical simulations and experimental validation. *Composites Science and Technology* 2022;221:109303. <https://doi.org/https://doi.org/10.1016/j.compscitech.2022.109303>.
- [7] Song SH, Byun YS, Ku TW, Song WJ, Kim J, Kang BS. Experimental and Numerical Investigation on Impact Performance of Carbon Reinforced Aluminum Laminates. *JOURNAL OF MATERIALS SCIENCE & TECHNOLOGY* 2010;26:327–32. [https://doi.org/10.1016/S1005-0302\(10\)60053-9](https://doi.org/10.1016/S1005-0302(10)60053-9).
- [8] Wei S, Zhang X, Li Y, Wang T, Huang Q, Liu C, et al. Study of the dynamic response and damage evolution of carbon fiber/ultra-thin stainless-steel strip fiber metal laminates under low-velocity impact. *Composite Structures* 2024;330:117772. <https://doi.org/https://doi.org/10.1016/j.compstruct.2023.117772>.
- [9] Chai GB, Manikandan P. Low velocity impact response of fibre-metal laminates – A review. *Composite Structures* 2014;107:363–81. <https://doi.org/https://doi.org/10.1016/j.compstruct.2013.08.003>.
- [10] Xin H, Tao J, Xiaomin M, Xuefeng S, Xin L. Dynamic response of single curved fiber-metal hybrid lamina composites subject to low-velocity impact. *International Journal of Impact Engineering* 2022;164:104209. <https://doi.org/https://doi.org/10.1016/j.ijimpeng.2022.104209>.
- [11] Sharma AP, Khan SH, Kitey R, Parameswaran V. Effect of through thickness metal layer distribution on the low velocity impact response of fiber metal laminates. *Polymer Testing* 2018;65:301–12. <https://doi.org/https://doi.org/10.1016/j.polymertesting.2017.12.001>.
- [12] A. SY, Y. L, B. L. Low-Velocity Impact on GLARE 5 Fiber-Metal Laminates: Influences of Specimen Thickness and Impactor Mass. *Journal of Aerospace Engineering* 2012;25:409–20. [https://doi.org/10.1061/\(ASCE\)AS.1943-5525.0000134](https://doi.org/10.1061/(ASCE)AS.1943-5525.0000134).
- [13] Laliberté JF, Straznický P V, Poon C. Impact Damage in Fiber Metal Laminates, Part 1: Experiment. *AIAA Journal* 2005;43:2445–53. <https://doi.org/10.2514/1.15159>.
- [14] Fan J, Cantwell WJ, Guan ZW. The low-velocity impact response of fiber-metal laminates. *Journal of Reinforced Plastics and Composites* 2010;30:26–35. <https://doi.org/10.1177/0731684410386133>.
- [15] Atas C. An Experimental Investigation on the Impact Response of Fiberglass/Aluminum Composites. *Journal of Reinforced Plastics and Composites* 2007;26:1479–91. <https://doi.org/10.1177/0731684407079749>.
- [16] Sadighi M, Pärnänen T, Alderliesten RC, Sayeafabi M, Benedictus R. Experimental and numerical investigation of metal type and thickness effects on the impact resistance of fiber metal laminates. *Applied Composite Materials* 2012;19:545–59. <https://doi.org/10.1007/s10443-011-9235-6>.
- [17] Mohagheghian I, McShane GJ, Stronge WJ. Impact perforation of monolithic polyethylene plates: Projectile nose shape dependence. *International Journal of Impact Engineering* 2015;80:162–76.

- <https://doi.org/https://doi.org/10.1016/j.ijimpeng.2015.02.002>.
- [18] Ferrante L, Sarasini F, Tirillò J, Lampani L, Valente T, Gaudenzi P. Low velocity impact response of basalt-aluminium fibre metal laminates. *Materials & Design* 2016;98:98–107. <https://doi.org/https://doi.org/10.1016/j.matdes.2016.03.002>.
- [19] De Cicco D, Asae Z, Taheri F. Low-velocity impact damage response of fiberglass/magnesium fiber-metal laminates under different size and shape impactors. *Mechanics of Advanced Materials and Structures* 2017;24:545–55. <https://doi.org/10.1080/15376494.2016.1162343>.
- [20] Yao L, Wang C, He W, Lu S, Xie D. Influence of impactor shape on low-velocity impact behavior of fiber metal laminates combined numerical and experimental approaches. *Thin-Walled Structures* 2019;145:106399. <https://doi.org/https://doi.org/10.1016/j.tws.2019.106399>.
- [21] Hallquist JO. LS-DYNA® THEORY MANUAL. 2006. <https://doi.org/10.1002/ima.22028>.
- [22] Bieniaś J, Jakubczak P. Impact damage growth in carbon fibre aluminium laminates. *Composite Structures* 2017;172:147–54. <https://doi.org/10.1016/j.compstruct.2017.03.075>.
- [23] Sevkát E, Liaw B, Delale F. Drop-weight impact response of hybrid composites impacted by impactor of various geometries. *Materials & Design (1980-2015)* 2013;52:67–77. <https://doi.org/https://doi.org/10.1016/j.matdes.2013.05.016>.

ICMATSE 2024

Employment of black phosphorous in nematic liquid crystals for enhancing their dielectric properties

Mouna El Abboubi

Department of Physics; Kocaeli University; 41001, İzmit, Türkiye,
186131006@kocaeli.edu.tr
ORCID :0000-0001-5745-0633

Mahpeyker Kocakoç Toprakoğlu

Department of Computer Technologies; Çukurova University; 01130, Adana, Türkiye,
mkocakoc@cu.edu.tr
ORCID: 0000-0001-7966-1482

Doğan Burak Aydın

Department of Physics; Kocaeli University; 41001, İzmit, Türkiye,
235131012@kocaeli.edu.tr
ORCID: 0000-0003-0563-9439

Leyla Taştan

Department of Physics; Kocaeli University; 41001, İzmit, Türkiye,
235131011@kocaeli.edu.tr
ORCID: 0009-0008-0968-2825

İdris Candan

Department of Physics; Kocaeli University; 41001, İzmit, Türkiye,
idris.candan@kocaeli.edu.tr
ORCID: 0000-0002-9950-713X

Sait Eren San

Department of Physics; Kocaeli University; 41001, İzmit, Türkiye,
saiteren.san@kocaeli.edu.tr
ORCID: 0000-0001-5042-4555

Cite this paper as: EL Abboubi, M et al., Employment of black phosphorous in nematic liquid crystals for enhancing their dielectric properties., Int. Conf. Advanced. Mater. Sci.& Eng. HiTech.and Device Appl.Oct. 24-26 2024, Ankara, Turkiye

Abstract. The study of nanomaterials is increasingly significant in material science, unveiling new opportunities for diverse applications. Among these materials, nematic liquid crystals (NLCs) are particularly valuable due to their unique optical properties and ability to self-assemble, making them suitable for various electro-optic applications. This research investigates the effects of black phosphorus (BP) as a dopant in NLCs, focusing on different weight percentages. BP, a two-dimensional material known for its excellent electrical conductivity and anisotropic properties, is anticipated to enhance the dielectric properties of NLCs, including the dielectric constant and response time. By establishing a clear relationship between BP concentration and the dielectric performance of NLCs, this study aims to contribute to the development of tunable materials for devices such as displays, sensors, and photonic applications. Ultimately, this work seeks to advance understanding of BP-doped NLC systems and their potential to drive innovation in liquid crystal technology.

Keywords: Black Phosphorus, Nematic Liquid Crystals, Electro-optic Applications, Anisotropic Materials, Electrical Conductivity.

© 2024 Published by ICMATSE

1. Introduction

Nematic liquid crystals (NLCs) are widely recognized for their distinctive optical and electro-optical properties, making them crucial for applications such as displays, sensors, and photonic devices[1]. Their performance can be significantly enhanced by doping with nanoparticles, which improve dielectric properties, conductivity, and response times. In particular, recent research has focused on incorporating two-dimensional (2D) materials—similar to black phosphorus (BP)—such as graphene oxide, molybdenum disulfide (MoS_2), and other transition metal dichalcogenides (TMDs)[2], [3]. These materials introduce anisotropic interactions with NLCs, offering promising enhancements in electro-optical behavior, molecular alignment, and light manipulation. In parallel, the use of plasmonic nanoparticles within NLCs has shown considerable promise in enhancing optical responses. Localized surface plasmon resonance (LSPR), induced by nanoparticles like gold and silver, creates highly localized electromagnetic fields that can be exploited to dynamically control light within NLCs. 2D materials such as graphene oxide and MoS_2 have been observed to leverage these plasmonic effects, improving the overall alignment of liquid crystal molecules and enabling tunable photonic devices[4], [5]. The thermoplasmonic heating generated by these nanoparticles allows for reconfigurable optical properties, which are particularly advantageous for applications in optical switching and advanced displays.

Focusing on BP as a novel dopant, this study aims to explore its influence on the dielectric properties of NLCs. BP stands out due to its unique electronic and optical properties arising from its layered structure and high anisotropy, providing excellent electrical conductivity and substantial carrier mobility. When incorporated into NLCs, BP can enhance dielectric anisotropy and conductivity, leading to lower switching voltages and faster response times—key factors for efficient display technologies and optical devices[6]. Moreover, BP's ability to interact with electromagnetic fields can optimize the composite material's light absorption and tunable photonic characteristics. The impact of BP doping on NLCs will be investigated by examining dielectric parameters such as dielectric constant, loss tangent, and frequency response. This research aims to establish BP as a promising dopant for enhancing the electro-

optical properties of NLCs, providing a foundation for the development of advanced tunable displays, sensors, and flexible electronic devices. The integration of BP into liquid crystal technology highlights its potential to drive material science innovation and expand the possibilities of 2D materials in electro-optic applications.

3. Methods and Experimental Techniques

To investigate the effects of black phosphorus (BP) doping on the dielectric properties of nematic liquid crystals (NLCs), a comprehensive set of methods and experimental techniques will be employed:

3.1. Material Preparation

3.1.1. Synthesis of Black Phosphorus

High-energy ball milling was employed to reduce bulk black phosphorus into nanoscale particles, a mechanical grinding process that effectively breaks down the material while maintaining its chemical integrity. The synthesis of black phosphorus (BP) was conducted under an argon atmosphere in a glovebox to prevent oxidation. In this process, 200 mg of red phosphorus was combined with zirconium balls at a mass ratio of 1:10 and ground for 24 hours. This approach efficiently converted red phosphorus into high-purity black phosphorus, suitable for doping into nematic liquid crystals to investigate enhancements in dielectric properties.

3.1.2. Doping Process

Nematic liquid crystals (NLCs) were doped with varying concentrations of black phosphorus (BP) flakes, up to 1.0% by weight, to systematically study the impact of BP concentration on their dielectric properties

3.2. Dielectric Characterization

3.2.1. Impedance Spectroscopy

This technique was used to measure the dielectric constant and loss factor of the BP-doped NLCs over a range of frequencies (typically from 1 Hz to 1 MHz). This data will provide insight into the dielectric response of the composite materials.

3.2.2. Dielectric Relaxation Measurements

Using a HIOKI 3522-50 LCR HiTester analysis of the dielectric relaxation processes was conducted to understand how BP affects the dynamics of the liquid crystal molecules and their response to applied electric fields.

The study focused on comparing pure NLCs with those doped with BP. Capacitance (C_p) and dielectric loss (D) were measured at varying frequencies and a fixed voltage (0.1 V). These measurements were used to calculate the real dielectric constant (ϵ'), imaginary dielectric constant (ϵ''), and conductivity (σ) using the following equations:

$$\epsilon' = \frac{C_s \cdot d}{\epsilon_0 \cdot A} \quad (1) \quad \epsilon'' = \epsilon' \cdot D \quad (2) \quad \sigma = \frac{F \cdot C_p \cdot D \cdot A}{d} \quad (3)$$

where:

- F is the frequency of the applied signal .
- C_p is the parallel capacitance,
- D is the dielectric loss factor,
- A is the surface area of the ITO electrode ($1.6 \times 10^{-11} \text{ m}^2$),
- d is the thickness of the cell ($5 \times 10^{-6} \text{ m}$).

By analyzing how conductivity changes with varying BP doping, we aimed to understand its effect on the electrical behavior of NLCs and assess the potential for improved performance in various applications.

4. Results and Discussion

This section presents the electrical characterization of pure and BP-doped nematic liquid crystal (NLC) samples. The graphs provide a comparative analysis of the dielectric properties and overall electrical behavior of the NLCs, highlighting the impact of BP doping on their performance.

Electrical Characterization

Figure 1 illustrates the conductivity-voltage (σ -V) characteristics, revealing how the inclusion of BP nanoparticles affects the conductivity of the NLCs. The corresponding real (ϵ') and imaginary (ϵ'') components of the dielectric constant as a function of voltage are shown in Figures 2(a) and (b), respectively.

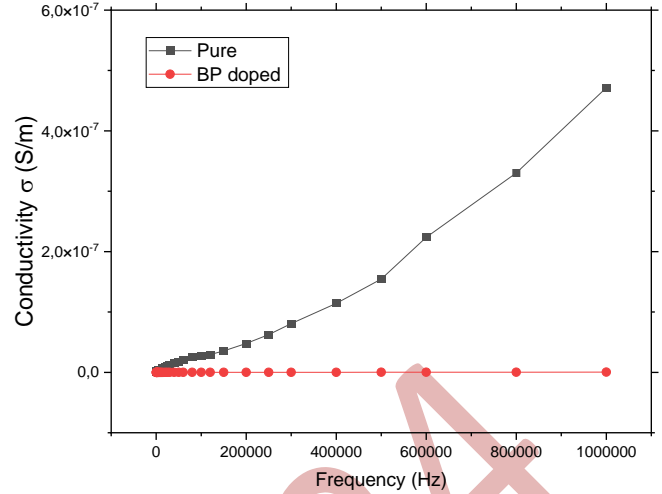


Figure 1. Conductivity – voltage (σ -V) graphs of pure and BP doped nematic liquid crystals samples.

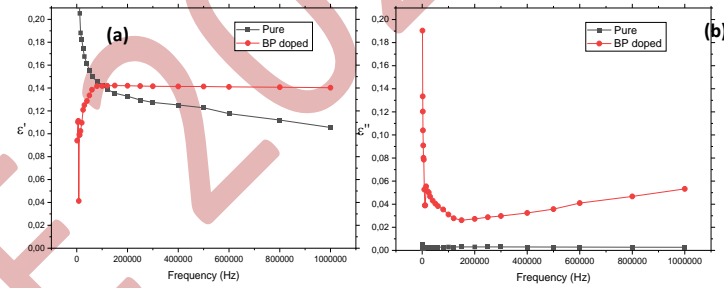


Figure 2. (a) The real; (b) the imaginary dielectric constant - voltage graphs of the pure and BP doped nematic liquid crystals samples.

The results demonstrate that doping NLC systems with BP nanoparticles significantly enhances the dielectric constant compared to pure NLC cells. This increase is attributed to the strong interaction between BP nanoparticles and LC molecules, which effectively enhances the overall polarizability of the composite material. BP's layered structure and high density of free charge carriers contribute to the formation of a localized electric field within the LC medium, facilitating greater distortion of the electron clouds of the LC molecules. Consequently, this leads to a marked increase in the dielectric response of the doped LCs.

Moreover, incorporating BP nanoparticles modifies the molecular alignment of the LCs under applied electric fields. BP's anisotropic nature promotes improved alignment and orientation of LC molecules, resulting in a higher order parameter and enhanced sensitivity to external stimuli. These changes stabilize molecular orientation and improve the overall dielectric properties of the material. Collectively, these findings highlight the promising potential of BP-doped liquid crystals for advanced applications in display technologies, tunable sensors, and responsive

optical devices, paving the way for innovative materials with tailored electro-optical functionalities.

Acknowledges

This study was supported by Kocaeli University Scientific Research Projects (BAP) Coordination Unit (Project No: FBA-2024-4063).

References .

- [1] M. Okutan, S. E. San, O. Köysal, and F. Yakuphanoglu, "Investigation of refractive index dispersion and electrical properties in carbon nano-balls' doped nematic liquid crystals," *Physica B Condens Matter*, vol. 362, no. 1–4, pp. 180–186, May 2005, doi: 10.1016/J.PHYSB.2005.02.009.
- [2] N. Dalir, S. Javadian, and Z. Dehghani, "High optical nonlinearity of nematic liquid crystal doped with graphen oxide," *J Mol Liq*, vol. 244, pp. 103–109, 2017, doi: <https://doi.org/10.1016/j.molliq.2017.08.123>.
- [3] Z. Dehghani and A. Madani, "Enhanced electro-optical properties of nematic liquid crystal doped with Nitrogen doped graphene quantum dots," *Optik (Stuttg)*, vol. 286, p. 171015, 2023, doi: <https://doi.org/10.1016/j.ijleo.2023.171015>.
- [4] J.-S. Yu, J.-J. Hwang, D.-H. Kim, and J.-H. Kim, "Anchoring strength of a nematic liquid crystal on 2D materials," *Liq Cryst*, vol. 50, no. 4, pp. 674–680, Mar. 2023, doi: 10.1080/02678292.2022.2157503.
- [5] O. V Kovalchuk *et al.*, "Dielectric and electrical properties of nematic liquid crystals 6CB doped with iron oxide nanoparticles. The combined effect of nanodopant concentration and cell thickness," *J Mol Liq*, vol. 366, p. 120305, 2022, doi: <https://doi.org/10.1016/j.molliq.2022.120305>.
- [6] B. Yang *et al.*, "Liquid crystal behaviors of micron and submicron-sized black phosphorus nanosheets," *J Lumin*, vol. 251, p. 119172, 2022, doi: <https://doi.org/10.1016/j.jlumin.2022.119172>.

The Effect of WC Content in Ni Based WC Reinforced Laser Surface Cladding

Aysenur Elci

*Gazi University, Dept of Metallurgical and Materials Engineering, 06530, Ankara, Turkiye,
aysenurelciii@gmail.com
ORCID: 0009-0000-2693-1530*

Hakan Ates

*Gazi University, Dept of Metallurgical and Materials Engineering, 06530, Ankara, Turkiye,
hates@gazi.edu.tr
ORCID: 0000-0002-5132-4107*

Mehmet Eroglu

*Firat University, Faculty of Engineering, Dept of Metallurgical and Materials Engineering, 23000, Elazig,
Turkiye
meroglu@firat.edu.tr
ORCID: 0000-0002-5097-1943*

Cite this paper as: Elci A., Ates H., Eroglu M. The Effect of WC Content in Ni Based WC Reinforced Laser Surface Cladding .Int. Conf. Advanced. Mater. Sci.& Eng. and HiTech. Device Appl. Oct. 24-26 2024, Ankara, Turkiye

Abstract. Laser surface treatments, which significantly increase resistance to wear and corrosion, have gained importance in recent years. Shallow penetration depth in laser coating enables the coating to occur without the parent material being affected by heat. In this study, a low carbon steel surface was coated by laser process by adding WC powder in different proportions to nickel-based powder. WC powder with the size of 106-44 microns was used in the coating at the rates of 20, 40, and 60%wt. The study also examined the effect of the second melting process. In the laser process, 3 mm/sec scanning speeds were used in the first melting process and 7 mm/sec in the second melting process. The energy input was the same for both speeds and was chosen as 1.6kW. After the coating process, microstructural characterization was made, hardness and wear tests were carried out. As a result, it was seen that double melting process was effective in terms of microstructure, hardness and wear resistance.

Keywords: Laser Cladding, Tungsten Carbide, Wear, Ni-based powder

© 2024 Published by ICMATSE

1.Introduction

Surface coating technologies, such as thermal spraying, electroplating, plasma transferred arc, and laser cladding, have gained widespread adoption in enhancing the surface hardness and wear resistance of components. This trend is driven by the continuous advancements in science and technology. These technologies are employed to create one or multiple layers of alloys or cermet coatings on the surface of

metallic materials, utilizing diverse techniques. Consequently, these metallic materials exhibit enhanced properties like high hardness, wear resistance, corrosion resistance, and other desirable features that they lack in their original state [1-8].

Laser cladding stands out as a novel surface modification technology that utilizes high-power lasers to melt alloy powders onto the surface of substrates. Compared to conventional surface modification techniques, laser cladding offers several advantages, including a lower dilution rate, stronger bonding

between the cladded layers and substrate, and reduced thermal deformation. The rapid heating and cooling rates inherent in the laser cladding process contribute to the formation of a fine microstructure during solidification. The rapid evolution of laser cladding technology has led to a surge in interest and development, particularly in the area of repair applications. Ni-based alloys exhibit good wettability, enabling them to adhere effectively to the substrate during the cladding process. These alloys demonstrate superior performance at elevated temperatures, making them ideal for applications operating in high-temperature environments. Compared to other high-performance materials, Ni-based alloys offer a relatively moderate price, making them cost-effective for industrial applications. These combined advantages contribute to the widespread use of Ni-based alloy powders in laser cladding [9].

Although laser coatings using Ni-based/WC powders are available in the literature, the number of studies on double melting is quite low. Therefore, in this study, the effect of double melting was studied experimentally.

2. Material and Method

In the study, low carbon steel specimens, the analysis of which is given in Table 1, was used. The samples with dimensions of 10 x 100 x 10 mm were coated with Ni-based and Ni-based powder/WC powder mixtures. The size range of Ni-based powder was between 53-150 microns. Chemical analysis of Ni-based powder is given in Table 2. WC powders were mixed with Ni-based powder at the rates of 20, 40 and 60 (wt.%). The size range of WC powders was between 105-44 microns. Sample coding is shown in Table 3. Prepared powder mixtures were bonded to the sample surface with PVA in 3 mm thickness and laser melting processes were performed. 3 mm/s laser scanning speed at first melting and 7 mm/s at second melting process with 1.6 kW laser power were used. In coated samples, samples were taken out for microstructure examination in the coating area and these were subjected to grinding and polishing processes. After necessary metallographic processing, the samples were etched in 3% nital solution. Images of the samples were taken with optical microscopy at different magnifications. In

addition, X-ray analyses, wear tests and microhardness measurements were performed. Hardness tests were conducted using a Qness branded microhardness tester, employing the Vickers microhardness method. In these tests, measurements were taken by indenting with a 200-gram load for 15 seconds. The wear resistance of the alloyed surfaces was assessed at room temperature using pin-on-disc wear tester. 60 mesh SiC abrasive papers were replaced after each test. A load of 20 N was applied to the specimens, and the sliding distance was set to 20 m.

Table 1. Chemical composition of low carbon steel (wt.%)

C	Mn	Si	P	S	Fe
0.14	0.48	0.21	0.02	0.02	Rest

Table 2. Chemical composition of Ni-based powder (wt.%)

C	Fe	Si	Cr	B	Ni
0.38	2.40	3.20	10.3	2	Rest

Table 3. Ni-based powder and WC powder ratios (wt.%)

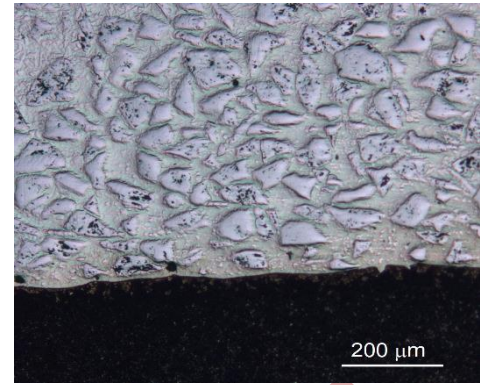
Specimen no	Ni-based powder	WC
S1 (SM)	100	-
S2 (DM)	100	-
S3 (SM)	80	20
S4 (DM)	80	20
S5 (SM)	60	40
S6 (DM)	60	40
S7 (SM)	40	60
S8 (DM)	40	60

SM: Single melting DM: Double melting

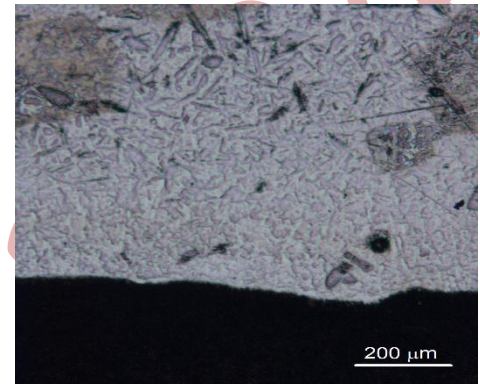
3. Results and Discussion

3.1. Microstructural Examinations

According to microstructural investigations, optical microscope images revealed that samples subjected to a single melting process exhibited a tendency for WC particles to agglomerate, leading to a non-homogeneous distribution. In contrast, the double melting process resulted in a more homogeneous structure on the coating surface and a more uniform distribution of WC particles. The second laser melting at a higher scanning speed showed that the WC carbides were fragmented and precipitated to smaller sizes. Representative images of samples S1, S2, S7 and S8 are given in Figure 1. In XRD analysis, it was observed that the microstructure in S1 and S2 samples main phases consisted of γ -Ni, CrB and Cr_{23}C_6 , while γ -Ni, CrB, Cr_7C_3 , WC, W_2C , W_2B phases appeared in WC added samples, S3-S8. WC powder added to nickel-based powder dissolves with laser beam and leads to the formation of new phases [8]. To illustrate this situation, the XRD graph of the S8 sample is given in Figure 2.

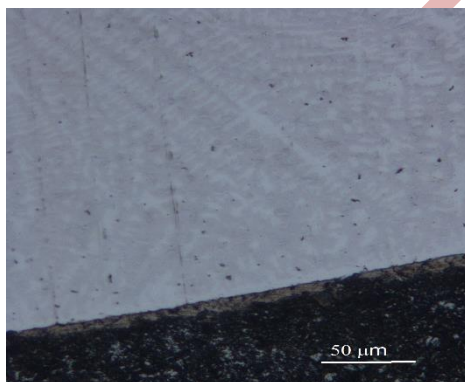


c)

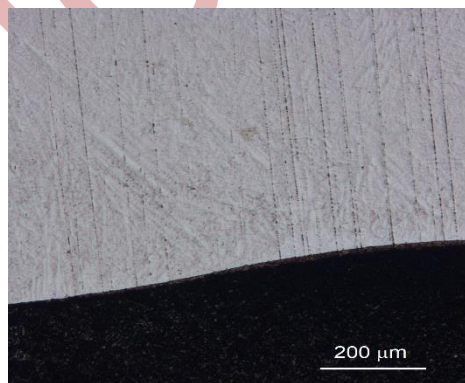


d)

Figure 1. Optical micrographs of a) S1, b) S2, c) S7 and d) S8 (Substrate + coating).



a)



b)

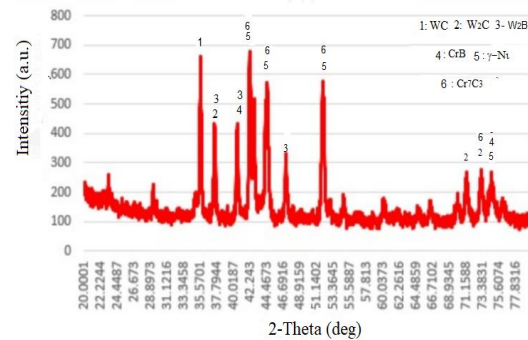


Figure 2. XRD diffraction patterns of S8

3.2. Hardness Test

As a result of microhardness measurements, the average hardness values taken from the samples are presented in Figure 3. As can be seen from this graph, the hardness values with Ni-based powder increased. However, the addition of WC powder to the Ni-based powder further increased the hardness. Considering that WC powder has a very high hardness, this result

is consistent with the literature [8]. When the effect of secondary melting is examined, it is shown that this melting causes an increase in hardness. This situation can be related to the fragmentation of WC particles during secondary melting and their dispersion into smaller sizes and also precipitation hardening [8].

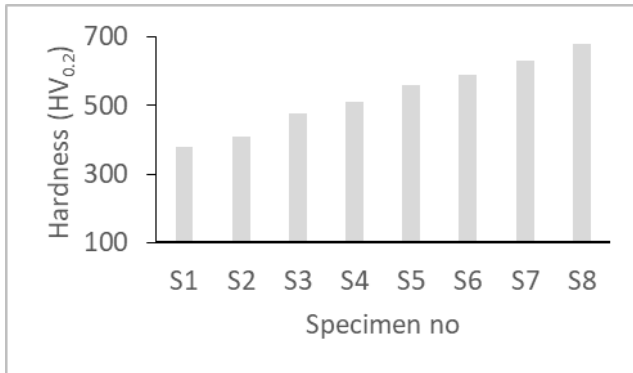


Figure 3. Average hardness values.

3.3 Wear Test

As a result of wear test, the mass loss values are given in Figure 4. As can be seen from this figure, laser coating with Ni-based powder and Ni-based/WC mixed powders protects the surface against wear. However, it is observed that adding WC powder to Ni-based powder and secondary melting are effective in terms of wear resistance. The increase in wear resistance in secondary melting is attributed to the carbides distributed more finely and widely in the matrix [8].

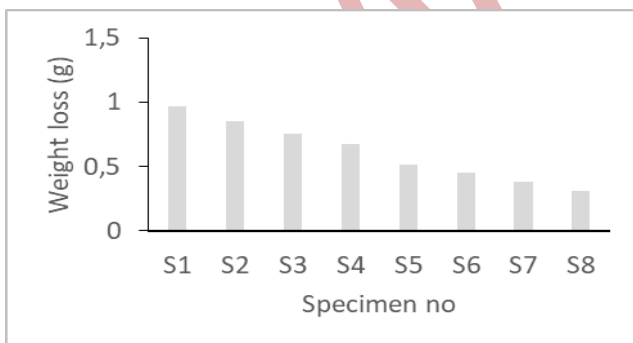


Figure 4. Mass loss values

References

1. J. Liu, Y. Li, P. He, N. Tan, Q. Li, G. Zhang, B. Lu, Microstructure and properties of ZrB₂-SiC continuous gradient coating prepared by high speed laser cladding, *Tribol. Int.*, 173 (2022), 107645.
2. X. Wen, X. Cui, G. Jin, Y. Liu, Y.e. Zhang, X. Zhang, E. Liu, H. Tian, Y. Fang, Corrosion and tribo-corrosion behaviors of nano-lamellar Ni_{1.5}CrCoFe_{0.5}Mo_{0.1}Nb_x eutectic high-entropy alloy coatings: The role of dual phase microstructure, *Corros. Sci.*, 201 (2022), 110305.

4. Conclusion

In this study, a low carbon steel surface was laser coated using Ni-based and Ni-based/WC mixed powders. Single and double melting processes were performed in the coating. The results obtained are generalized and given below.

- In the coating made by Ni- based powder, phases mainly consisted of γ -Ni, CrB and Cr₂₃C₆,
- In the coating made by Ni- based/WC powder mixture, phases mainly consisted of γ -Ni, CrB and Cr₇C₃, WC, W₂C and W₂B.
- Double melting process caused the WC particles to break up and precipitated in the matrix in finer sizes,
- Ni-based powder increased the surface hardness,
- Addition of WC to Ni-based powder provided a further increase in hardness,
- Hardness increased with double melting,
- Ni-based powder increased the surface wear resistance
- Addition of WC to Ni-based powder provided a further increase in wear resistance,
- Double melting increased the wear resistance.

Acknowledgements

This project was supported by Firat University Scientific Research Projects Management Unit (FÜBAB) under project number ADEP.23.15.

3. Y.-Y. Zhou, G.-Z. Ma, H.-D. Wang, G.-L. Li, S.-Y. Chen, H.-J. Wang, Ming-Liu, Fabrication and characterization of supersonic plasma sprayed Fe-based amorphous metallic coatings, *Mater. Des.*, 110 (2016), 332–339.
4. G. Ma, B. Xu, H. Wang, X. Wang, G. Li, S. Zhang, Research on the microstructure and space tribology properties of electric-brush plated Ni/MoS₂-C composite coating, *Surf. Coat. Technol.*, 221 (2013), 142–149.
5. A. Pascu, J.M. Rosca, E.M. Stanciu, Laser cladding: from experimental research to industrial applications, *Mater. Today Proc.*, 19 (2019), 1059–1065.
6. D. Bartkowski, A. Młynarczak, A. Piasecki, B. Dudziak, M. Gosciński, A. Bartkowska, Microstructure, microhardness and corrosion resistance of Stellite-6 coatings reinforced with WC particles using laser cladding, *Opt. Laser Technol.* 68, (2015), 191–201.
7. D. Bartkowski, A. Bartkowska, A. Piasecki, P. Jurćci, Influence of Laser Cladding Parameters on Microstructure, Microhardness, Chemical Composition, Wear and Corrosion Resistance of Fe–B Composite Coatings Reinforced with B₄C and Si Particles, *Coatings*, 10 (2020), 809.
8. H. Zeyu, L. Yang, L. Bingwen, T. Na, C. Lanrong, Y. Qingsong, Effect of WC content on microstructure and properties of high-speed laser cladding Ni-based coating, *Optics and Laser Technology*, 155 (2022), 108449.
9. W. Kaiming, C. Baohua, L. Yongping, F. Hanguang, L. Yinghua, Effect of cobalt on microstructure and wear resistance of Ni-based alloy coating fabricated by laser cladding, *Metals*, 7 (2017), 551

ICMATSE 2024

A Case Study on Ultrasonic Atomization of Stainless-Steel Powder for Additive Manufacturing

Anil EMIRALIOGLU

*Gazi University - Additive Manufacturing Technologies Application and Research Center (EKTAM), 06560, Ankara, TÜRKİYE,
anilemiralioglu@gazi.edu.tr
ORCID: 0000-0002-7505-5765*

Rahmi UNAL

*Gazi University - Department of Mechanical Engineering, 06570, Ankara, TÜRKİYE,
runal@gazi.edu.tr
ORCID: 0000-0001-5379-5159*

Cite this paper as: Emiralioğlu, A., Ünal, R., A Case Study on Ultrasonic Atomization of Stainless Steel Powder for Additive Manufacturing., Int. Conf. Advanced. Mater. Sci.& Eng. HiTech.and Device Appl.Oct. 24-26 2024, Ankara, Turkiye

Abstract. As a result of the interest in additive manufacturing methods, which have many advantages over conventional manufacturing methods, there has also been an increase in the number of studies on metal powders used as feedstock materials in these methods. It is observed that the powders obtained by the ultrasonic atomization method, which has been developing in recent years, have a narrower particle size distribution and higher sphericity than the powders obtained by the gas atomization method, one of the conventional powder production methods. In this study, a comparison was made between 316L powders produced using wire as feedstock material by ultrasonic atomization method and 316L powders purchased commercially and produced by gas atomization method in terms of particle size distribution and sphericity. Powder production was carried out at a fixed frequency with different electric current values, one of the parameters used in the ultrasonic atomization process. In addition to particle size distribution and shape analysis of the powders, non-destructive testing was carried out via Micro-CT. As a result, it is likely that the ultrasonic atomization method, which has impressive findings regarding sphericity and gas porosity, will become a crucial feedstock material production method for additive manufacturing in the coming years.

Keywords: Ultrasonic Atomization, 316L Stainless Steel, Powder Production, Sphericity

© 2024 Published by ICMATSE

Introduction

Due to their advantages, additive manufacturing (AM) methods have attracted the attention of many used as feedstock material. Therefore, the chemical and physical properties of the metal powders, such as particle size distribution (PSD), particle morphology, density, porosity, satellite formation, etc., become very important for a reliable final product [1]. Gas and plasma atomization methods produce many commercially used metal powders for additive manufacturing. These two methods are highly profitable, allow for producing large amounts of powder in a single process, and can be considered conventional [2,3]. Ultrasonic atomization (UA) has been developed recently and has brought significant innovations to powder

researchers, and as a result of the studies carried out, they have made rapid progress in recent years. In most metal AM methods, powder is

production on a laboratory scale. Compared to traditional powder production methods, it has great advantages in terms of sphericity and particle size distribution [4]. Powders produced with UA have narrower particle size distributions and much greater sphericity.

This paper summarizes the comparison of ultrasonically atomized and commercially available 316L stainless steel metal powder using wire-form raw material regarding PSD and sphericity.

Methods

Within the study's scope, stainless steel 316L material in wire form was powdered by ultrasonic atomization using different electric current values. Then, the produced powders were compared with the powders previously purchased and produced in ingot form by vacuum inert gas atomization (VIGA). In order to produce metal powders with the desired properties using the UA method, the working principle of the atomization device must be well understood (Figure 1). First, an electric arc is used to melt the raw material. This arc is created between the atomization platform at the top of the sonotrode and the non-consumable tungsten electrode. The working principle of the energy source is very similar to that of Tungsten inert gas (TIG) welding. After the arc is obtained, the ultrasonic vibrations obtained by the ultrasonic generator are transferred from the cold end of the sonotrode to the atomization platform via the sonotrode. After this stage, the raw material wire is continuously fed into the pressurized atomization chamber. The wire exposed to the electric arc melts as its temperature increases and forms a melt pool on the surface of the atomization platform. Due to the effect of surface tension, the liquid metal droplets take a spherical shape. They are thrown into the inert gas flow with the kinetic energy gained by the ultrasonic vibrations. The metal droplets formed cool and solidified in the atomization chamber through the convection and radiation processes. The solidified and powdered metal material accumulates in the powder chamber located at the bottom of the atomization chamber due to the effects of aerodynamic forces and gravity [5].

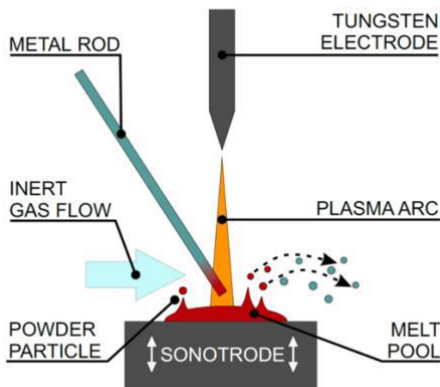


Figure 1. Schematic of Ultrasonic Atomization [6]

For the experiments carried out within the scope of the study, the ATO LAB Plus ultrasonic atomization

machine, which is in EKTAM's device infrastructure, was used. While the electric current from the process parameters was given values ranging from 120A to 160A, all other parameters (ultrasonic frequency= 20 kHz, amplitude= 70%, argon flow= 15l/min and wire diameter= 1.2 mm) were kept constant. Powders were produced using three different process parameter sets. In addition to the powders produced, powders produced by the VIGA method and purchased were named as given in Table 1.

Table 1. Analyzed powders and electric current values

Powders	Electrical Current (Amp)
Powder-120	120
Powder-140	140
Powder-160	160 -
Powder-VIGA	

Results Results and Discussions

The powders' particle size distribution and sphericity measurements were analyzed using laser diffraction and digital imaging on a Microtrac MRB Flowsync particle characterization machine. Particle size distributions of the powders used in the study are shown in Figure 2.

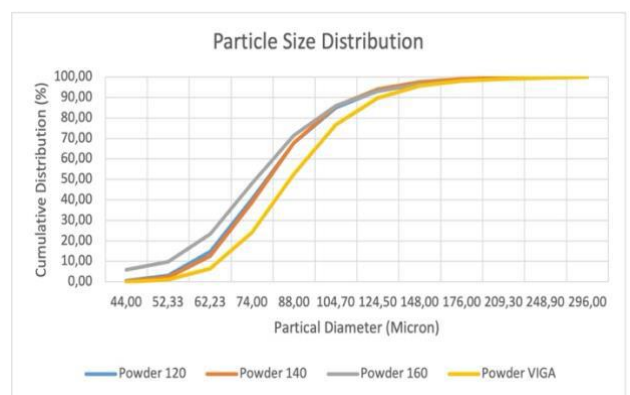


Figure 2. Particle Size Distribution

In Figure 2, the particle size distribution of the Powder-VIGA powder produced by the VIGA method has a wider range than that of the other powders produced by the ultrasonic atomization method. Although the difference seems to be negligible, this is a factor affecting the predictability of the AM process.

Table 2. D10, D50 and D90 values of the powders (Micrometers)

Powders	D10	D50	D90
Powder-120	59.05	78.37	114.10
Powder-140	60.48	78.95	112.30
Powder-160	52.53	75.02	113.60
Powder-VIGA	65.30	86.66	125.10

Table 2 shows the powders' D10, D50, and D90 values. The effect of the electric current used as a variable parameter in the production process is seen in this table. The fact that the Powder-160 powder produced with 160 Ampere contains more powder with a smaller diameter indicates that more small powder production than expected occurs due to the current exceeding a specific value. The D50 and D90 values of the three powders produced with UA are pretty close to each other. The powder produced with VIGA contains particles of a larger diameter.

Among the most frequently used AM methods, powder bed production technologies are at the forefront. One of the most essential elements of production made with this technology is laying the powder properly while creating the powder bed. Therefore, the more spherical the powder is, the more likely it is to obtain a uniform and smooth layer [7]. It can be seen in Figure 3 that the sphericity ratios of all powders produced by UA method are dramatically higher than those of powders produced by VIGA.



Figure 3. Sphericity of The Powders

Sphericity measurements were made by taking into account the number of particles. When a high sphericity ratio of 98% was determined as the threshold, 87% of Powder-120, 82% of Powder-140, 58% of Powder-160, and only 2% of Powder-VIGA were above the threshold. As the electric current increases during production, it is observed that the

sphericity decreases at high sphericity ratios. However, even these ratios are well above the powders sold commercially and produced by gas atomization methods.

As with other gas atomization methods, inert gas porosity is one of the most well-known disadvantages of the VIGA method. This phenomenon occurs when the viscosity of the liquid metal increases during solidification, closing on itself and trapping the gas inside the powder particles [8,9]. To investigate this situation, Powder-140 and Powder-VIGA powders produced with two different methods (UA and VIGA) were examined non-destructively with the Micro-Computer Tomography method. A Zeiss Xradia Versa 510 X-ray machine within EKTAM was used for the examination. As seen in Figure 4, while the powders produced with UA have no porosity, gas porosity is noticeable in the powders produced with VIGA. It was also determined that the powders produced with VIGA were worse in terms of sphericity and that there were satellites in some particles.

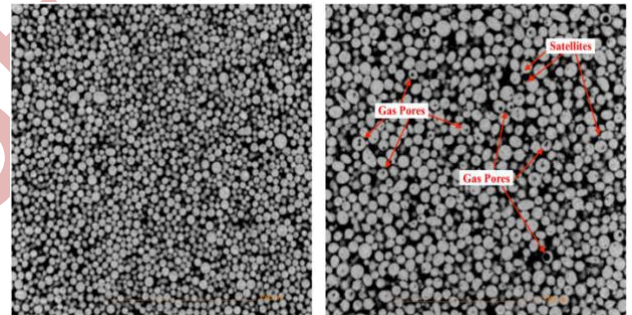


Figure 4. X-Ray Micro-CT images of the powders produced by ultrasonic atomization (left) and gas atomization (right)

Conclusions

This study discussed the effect of electric current on the powders produced by the ultrasonic atomization process and the comparison of the powders produced by ultrasonic atomization and the VIGA method. The summary of the results is as follows:

- 1) 316L powders produced by the UA method are dramatically better in terms of sphericity than those produced by the VIGA method.
- 2) When comparing Micro-CT images, the powders produced with UA showed almost no porosity and satellite formation. At the same time, these

problems were observed in those produced with the VIGA method.

3) The particle size distribution of powders produced with UA is narrower than those produced with VIGA, but this difference is not significant enough to be considered.

4) Increasing the electric current in powder production with UA does not significantly change at low currents. However, when currents can be considered high, such as 160 Amperes, deterioration in the sphericity of the particles may occur. In addition, the traditional proportion of particles smaller than its commercial expected increases.

References

- 1) P. Moghimian et al., Metal powders in additive manufacturing: A review on reusability and recyclability of common titanium, nickel and aluminum alloys, *Additive Manufacturing*, 43 (2021), doi.org/10.1016/j.addma.2021.102017.
- 2) O. Aydın and R. Ünal, Experimental and numerical modeling of the gas atomization nozzle for gas flow behavior, *Computers and Fluids*, 42 (2011), pp 37-43, doi.org/10.1016/j.compfluid.2010.10.013
- 3) L. Haferkamp *et al.*, The influence of particle shape, powder flowability, and powder layer density on part density in laser powder bed fusion, *Metals (Basel)*, 3 (2021), pp 1-15, doi.org/10.3390/met11030418.
- 4) S. H. Alavi and S. P. Harimkar, Ultrasonic vibration-assisted laser atomization of stainless steel, *Powder Technol*, 321 (2017), pp. 89–93, doi.org/10.1016/j.powtec.2017.08.007.
- 5) K. Grzelak et al., A Comparative Study on Laser Powder Bed Fusion of Differently Atomized 316L Stainless Steel, *Materials*, 15 (2022), doi.org/10.3390/ma15144938.
- 6) F. Hinrichs et al., Flexible powder production for additive manufacturing of refractory metal-based alloys, *Metals (Basel)*, 11 (2021), doi.org/10.3390/met11111723.
- 7) C. Monti, M. Turani, K. Papis, and M. Bambach, A new Al-Cu alloy for LPBF developed via ultrasonic atomization, *Mater Des*, 229 (2023), doi.org/10.1016/j.matdes.2023.111907.
- 8) I. E. Anderson, E. M. H. White, and R. Dehoff, Feedstock powder processing research needs for additive manufacturing development, *Current Opinion in Solid State and Materials Science*, 22 (2018), doi.org/10.1016/j.cossms.2018.01.002.
- 9) K. Kothari, R. Radhakrishnan, and N. M. Wereley, Advances in gamma titanium aluminides and their manufacturing techniques, *Progress in Aerospace Sciences*, 55 (2012), pp. 1–16, doi.org/10.1016/j.paerosci.2012.04.001.

5) The UA method has advantages in producing more spherical and denser powder compared to traditional methods. However, it has a slower production rate than traditional methods. Therefore, its commercial use is limited. With innovations and expansion of the material spectrum, it will be used more widely in the future.

Acknowledgements

This study is supported by The Scientific and Technological Research Council of Türkiye (TÜBİTAK) under the 1004 Program for the project number 20AG008.

Ab Initio Computational Materials Science

Engin Deligöz

Aksaray University- Department of Physics, 68100, Aksaray, Turkiye,
edeligoz@yahoo.com
ORCID:0000-0001-6289-9320

Cite this paper as: Deligoz E., Ab Initio Computational Materials Science, .Int. Conf. Advanced. Mater. Sci.& Eng. HiTech.and Device Appl.Oct. 24-26 2024, Ankara, Turkiye

Abstract. Ab initio ((Latin for “from the beginning”) computational materials science is play an important role in accelerating the development and optimization of new materials. It is widely used in materials science. The aim is to simulate the properties of materials in order to understand and complement experiments. Scientists use these methods in the discovery of new materials, materials design, catalysis and chemical reaction mechanisms. Ab initio method (often referred to as **first-principles** methods) contains no experimental input other than the fundamental physical constants, making it possible to analyze the properties of systems that are difficult to characterize experimentally, or to predict the physical properties of materials that have not yet been made. We present an overview of the capabilities of ab initio methods in the structural and mechanical properties, illustrated with an example for 2D orthorhombic β -GeSe compound using the VASP computer program.

Keywords: ab initio, first-principles, computational materials science

© 2024 Published by ICMATSE

Introduction

Ab initio computational materials science is a field that studies and simulates the structural, electronic, optical and mechanical properties of materials based purely on fundamental physical principles, without relying on experimental data. It is play an important role in accelerating the development and optimization of new materials [1]. This approach involves modelling and simulating the behavior of atoms and electrons using quantum mechanics, and is commonly carried out using methods such as Density Functional Theory (DFT). Unlike empirical methods that rely on experimental data, ab initio materials science operates solely based on the quantum mechanical interactions between atoms and electrons [2]. This is particularly useful for predicting the properties of unknown or newly designed materials before they have been synthesized.

Ab initio materials science aims to understand the behavior of atoms and electrons using quantum mechanical principles. The interactions between electrons and nuclei in materials are described by the Schrödinger equation, and solving this equation provides insight into the microscopic behavior of materials, which in turn explains their macroscopic properties. Quantum mechanical theories are used in materials simulations in two main ways. The

Schrödinger equation describes the wave function and energy of electrons in atoms or molecules. The Born-Oppenheimer approach makes calculations simple by separating the motion of the electrons from that of the nucleus [3], allowing the electronic structure of a material to be solved independently of the atomic positions.

A widely used method in ab initio materials science is Density Functional Theory (DFT) [4]. DFT calculates the total energy and electronic structures of a system by focusing on the electron density rather than tracking each electron individually. This greatly simplifies the solution of the quantum mechanical equations. The Kohn-Sham equations are the fundamental equations used in DFT to calculate the energy and structure of a material, taking into account the electron density. Exchange-correlation functional are mathematical approaches used in DFT to model interactions between electrons. Common functional include the Local Density Approximation (LDA) and the Generalized Gradient Approximation (GGA) [5]. Recent developments in hybrid functionals and beyond-DFT methods aim to increase the accuracy of predictions for more complex systems.

Results and Discussion

Ab initio methods can predict various properties of a material based on the interactions of its fundamental building blocks atoms and electrons. This

computational technique is widely used to understand new materials, design novel materials with desired properties (e.g., semiconductors, superconductors, or catalysts), and explore fundamental questions in materials science. Simulations extract physical, chemical, and mechanical properties that arise from the arrangement and movement of atoms.

Some of these properties are structural, electronic, elastic, optical and phonon. Electronic Structure estimates whether a material is a semiconductor, metal or insulator by calculating the energy levels of the electrons. Mechanical properties give the elastic modulus, hardness and tensile strength of materials. Optical properties model how materials interact with light. Phonon properties test stability, investigate heat transfer mechanisms and report thermodynamic properties that depend on temperature. Since first-principles calculations are highly complex and require vast amounts of data, powerful computing systems are essential. Supercomputers and parallel processors are often employed to simulate large material systems [2].

In this section, an overview of the capabilities of ab initio methods on structural and mechanical properties will be presented. For this, calculations for 2D β -GeSe compound using VASP code [6-8] are given as an example. Details about the calculations and other results can be found in Ref. [9]. The orthorhombic crystal structure of 2D β -GeSe is shown in Fig. 1.

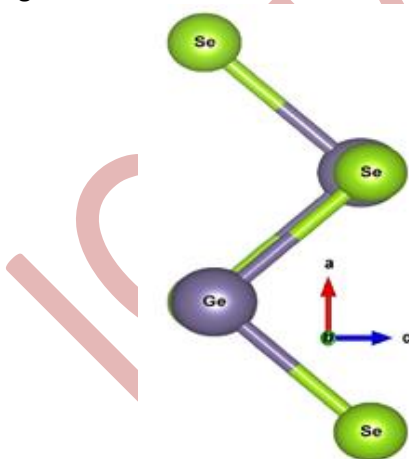


Figure 1. The orthorhombic crystal structure of 2D β -GeSe [9]

Structural properties are given in Table 1. The calculated structural characteristics are in good agreement with experimental data.

Table 1. The lattice constant (a , b , Å), bond length ($d1/Ge-Se$, $d2/Se-Ge$, Å), layer thickness (h , Å) and other study for β -GeSe.

a	b	d1	d2	h	Method	Refs.
3.66	5.90	2.54	2.72	1.86	GGA-PBE	Ref. [9]
3.83	5.80					Exp [10]

The elastic constants and mechanical properties are given in Tables 2 and 3.

Table 2. Elastic constants (C_{ij} , N/m), Young's modulus (E , N/m), Poisson ratio (ν), shear modulus (G , N/m) for β -GeSe.

C_{11}	C_{12}	C_{22}	C_{66}	Ref.
33.44	-0.36	33.17	7.88	[9]

The elastic constants meet the stability criteria, indicating its mechanical stability.

Table 3. Young's modulus (E , N/m), Poisson ratio (ν), shear modulus (G , N/m) for β -GeSe.

E_x	E_y	ν_x	ν_y	G	Ref.
33.43	33.16	-0.01	-0.01	7.88	[9]

2D β -GeSe compound are relatively flexible materials due to its low Young's modulus. Moreover, a negative Poisson's ratio indicates that the orthorhombic β -GeSe is an auxetic material [9]. It can be seen from Tables 1 and 2 that the structural and mechanical properties for β -GeSe have been successfully predicted by ab initio computational materials science.

Conclusion

Ab initio computational materials science has revolutionized the way we understand and design materials. By leveraging quantum mechanical principles, these methods allow the prediction of material properties from first principles, without the need for empirical data. This has opened up new avenues for the discovery of materials with tailored properties for applications in electronics, energy, catalysis, and beyond.

Despite their success, ab initio methods face several challenges, primarily related to computational cost

and accuracy. As system size increases, the computational effort grows exponentially, making large systems difficult to handle even with modern supercomputers. Additionally, the approximations

used in DFT, especially the exchange-correlation functionals, can lead to inaccuracies, particularly in materials with strong electron-electron interactions

References

1. Meng, Y. S., & Arroyo-de Dompablo, M. E. (2013). Recent advances in first principles computational research of cathode materials for lithium-ion batteries. *Accounts of chemical research*, 46(5), 1171-1180.
2. Pokluda, J., Černý, M., Šob, M., & Umeno, Y. (2015). Ab initio calculations of mechanical properties: Methods and applications. *Progress in Materials Science*, 73, 127-158.
3. Steihauser, M. O., & Hiermaier, S. (2009). A review of computational methods in materials science: examples from shock-wave and polymer physics. *International journal of molecular sciences*, 10(12), 5135-5216.
4. Neugebauer, J., & Hickel, T. (2013). Density functional theory in materials science. *Wiley Interdisciplinary Reviews: Computational Molecular Science*, 3(5), 438-448.
5. Hafner, J. (2008). Ab-initio simulations of materials using VASP: Density-functional theory and beyond. *Journal of computational chemistry*, 29(13), 2044-2078.ü
6. Kresse G., Hafner J, (1994) Ab initio molecular dynamics for liquid metals *Phys. Rev. B* 47 (1994) 558.
7. Kresse, G., & Furthmüller, J. (1996). Efficiency of ab-initio total energy calculations for metals and semiconductors using a plane-wave basis set. *Computational materials science*, 6(1), 15-50.
8. Le Page, Y., & Saxe, P. (2002). Symmetry-general least-squares extraction of elastic data for strained materials from ab initio calculations of stress. *Physical Review B*, 65(10), 104104.
9. Kutluca A., Deligoz E., Ozisik H. (2025) Impact of van der Waals corrected functionals on monolayer GeSe polymorphs: An in-depth exploration *Comm. Mater Sci.* (246) 113383
10. Von Rohr, F. O., Ji, H., Cevallos, F. A., Gao, T., Ong, N. P. and Cava, R. J., 2017. High-Pressure Synthesis and Characterization of β -GeSe—A Six-Membered-Ring Semiconductor in an Uncommon Boat Conformation. *J. Am. Chem. Soc.*, 139(7), 2771–2777.

Opening the Third Dimension on SEM: FIB-SEM and Laser FIB

Volkan Erkut

Carl Zeiss Technology Solutions Tic. Ltd. Şti.- Research Microscopy Solutions,
volkan.erkut@zeiss.com
ORCID: xxxx-xxxx-xxxx-xxxx

Cite this paper as: Erkut, Volkan. Opening the Third Dimension on SEM: FIB-SEM and Laser FIB. Int. Conf. Advanced. Mater. Sci.& Eng. HiTech.and Device Appl.Oct. 24-26 2024, Ankara, Turkiye

Abstract. A Focused Ion Beam Scanning Electron Microscope (FIB-SEM) is a combination of ion column and electron column in the same instrument. This system uses electron beam in order to get high resolution image while ion beam (mostly gallium ions) is used for doing modifications like milling, etching, deposition on a material. In material science, FIB-SEM usage is expanding day by day and it creates insights of third dimension in studies. Researchers can use FIB-SEM for cross section imaging, TEM sample preparation, I-beam lithography etc. These processes can take time due to hardness and physical properties of the material. In order to reduce the time of FIB-SEM workflow, Laser-FIB takes place as a solution as a ZEISS product. With laser you can do all FIB process within short time and very precisely.

Keywords: Ion, FIB, SEM, Laser, Cross section
© 2024 Published by ICMATSE

FIB-SEM is an integrated system with ion and electron beam and it can be used for cross section imaging, TEM lamella preparation, lithography etc. Reserachers who interested with material science sometimes need information from below the sample surface [1]. No matter if they are burried features or layers, they can be milled with ion beam on nanometric scale and precision [2]. Also with a Gas Injection System (GIS), there can be apply deposition on sample surface with a specific material like platinum. It protects the area for precise milling and after the workflow, the cross section can be seen very smoothly. With platinum deposition, researcher can do lithograpy to the sample surface [3]. Words or even images can be deposited or milled on the sample surface with FIB.

A LaserSEM is the combination of a fs-laser and a FE-SEM in one instrument (without FIB column) [4]. With LaserSEM you achieve high resolution and contrast imaging with the benefits of Zeiss Gemini optics and a new approach of rapid 3D-site-specific sample preparation with integrated fs-laser. Modern methods of sample preparation for high-resolution microscopy are achieved using conventional focused ion beam (FIB), Plasma-FIB (PFIB) or standalone laser. Each of them has its own advantages and disadvantages and preferable for certain applications. For example, the highest quality of preparation of thin lamellas for TEM is achieved using GaFIB. Large cross sections and

Large Trenches can be achieved by PFIB / laserFIB or Standalone laser. But in this case, the user meets the following challenges: limited sample size, cost prohibitive and time-consuming preparation process, contamination of the main PFIB chamber and limited opportunity of standalone laser preparation for air sensitive samples [5].

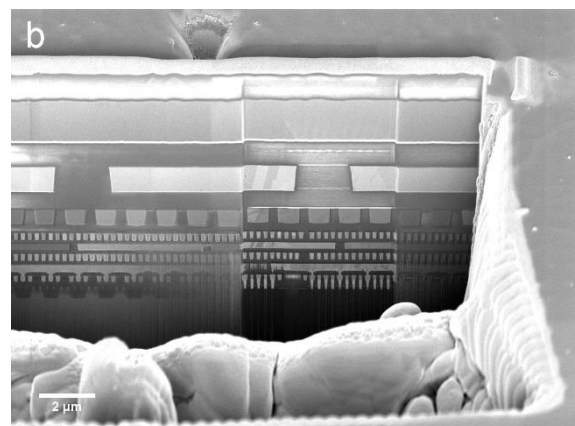
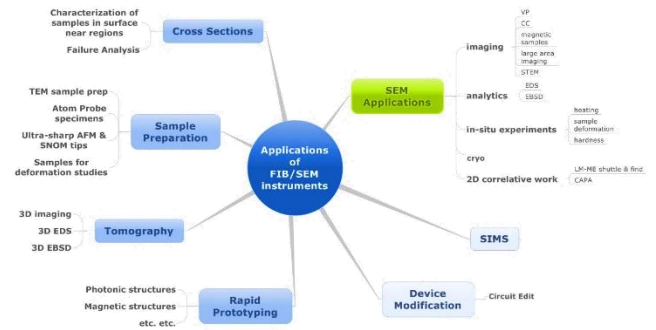
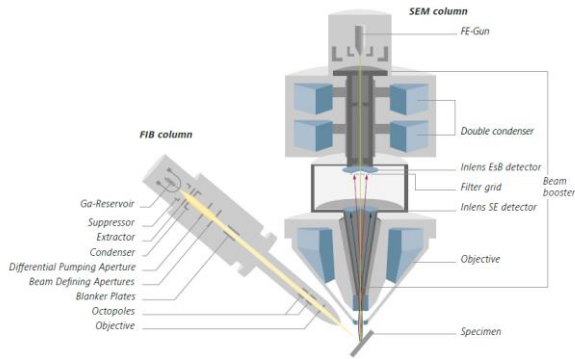
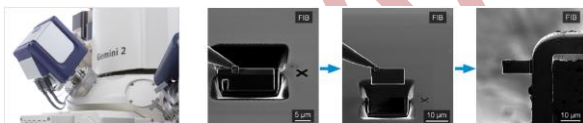
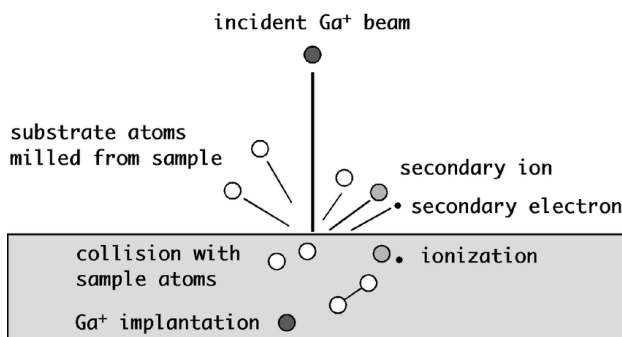


Figure 1. A cross section image of semiconductor sample

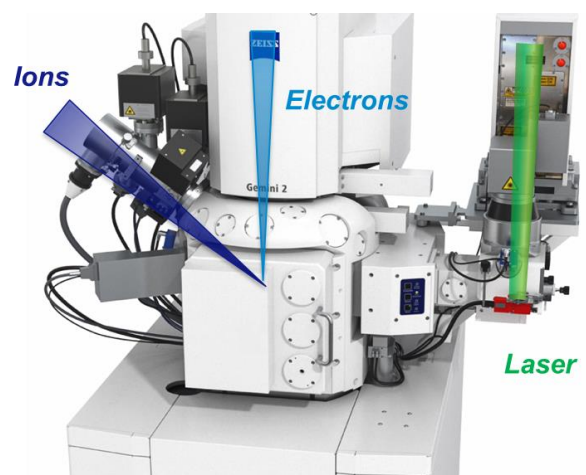


The column design gives you access to five orders of magnitude in beam current, from 1 pA up to 100 nA. The larger beam currents of up to 100 nA allow fast and precise material removal and milling processes. Meanwhile, at low currents you will achieve exceptionally high FIB resolution of less than 3 nm.

A Crossbeam is a very universal instrument. Of course, it covers all typical SEM Applications. However the FIB column adds the capability of removing material from the sample. Therefore, analysis of the sample is not limited to its surface. Cross sections can be prepared to study what is underneath the surface. Crossbeams can be used to prepare samples to serve other characterization methods: e.g. to prepare TEM lamellae, atom probe specimens, ultra-sharp tips for SPM or to machine samples for deformation studies in the microscale. Another important application is 3D FIB Tomography: serial cross sections are prepared by FIB milling and analyzed with the SEM, and others standard analytical methods like 3D EDS, 3D EBSD. FIB milling can be used for rapid prototyping of structures. In combination with a Gas Injection System it is also possible to deposit material from a precursor gas. This is a key component for Circuit Editing.



Micromanipulator is nothing but a needle. But this is really a sharp one. You have to use it while doing TEM lamella prep in order to detach your lamella from sample and attach to the lamella holder. It's really a sensitive process. Manipulator can be navigate with software. So you can control every direction. After attach your lamella to the holder, you can polish the sides with ion beam and thin the sample for TEM study.



With integrated FIB column to laser SEM you can benefit for TEM lamella preparation at atomic resolution or 3D tomography as potential future applications.

After laser prepared surface you need only few minutes of FIB polishing for high resol microscopy imaging and advanced analysis. Use your FIB for

final step of APT (atom probe tomography) and TEM lamella for atomic resolution sample prep.

References

1. L.A. Giannuzzi; F.A. Stevens. *Introduction to Focused Ion Beams: Instrumentation, Theory, Techniques and Practice*. Springer Press. (2004) ISBN 978-0-387-23116-7.
2. C.A. Volkert; A.M. Minor. "Focused Ion Beam: Microscopy and Micromachining" . *MRS Bulletin*. **32** (5): (2007) 389–399. doi:10.1557/mrs2007.62.
3. Smith, C. "Microscopy: Two microscopes are better than one". *Nature*. **492** (7428). (2012) 293–297. Bibcode:2012Natur.492..293S. doi:10.1038/492293a. PMID 23235883. S2CID 205075538.
4. *The Laser-Integrated FIB-SEM for Faster 3D Packages Characterization and Failure Analysis*, O Vertsanova, B Tordoff - Electrochemical Society Meeting ECS - Volume MA2023-02, D03: Advanced 3D Interconnect Technologies and Packaging 2 <https://iopscience.iop.org/article/10.1149/MA2023-02171191mtgabs/meta>.
5. *Femtosecond laser preparation of resin embedded samples for correlative microscopy workflows in life sciences*, Carles Bosch, Joerg Lindenau, Alexandra Pacureanu, Christopher J. Peddie, Marta Majkut, Andrew C. Douglas, Raffaella Carzaniga, Alexander Rack, Lucy Collinson, Andreas T. Schaefer, Heiko Stegmann; *Appl. Phys. Lett.* 3 April 2023; **122** (14):143701. <https://doi.org/10.1063/5.0142405>.

ICMATSE 2024

Examination of Electroless Nickel Coated Silicon Nitride Ceramics by Ultrasonic Pulse Echo Method

Vildan ÖZKAN BILICI

*Afyon Kocatepe University, Physics Dept., 03200, Afyonkarahisar, Turkey TURKEY,
vildanozkan@aku.edu.tr.*

ORCID: 0000-0002-3077-2103

Ahmet YONETKEN

*Afyon Kocatepe University, Engineering Faculty, Electrical Engineering Dept., ANS Campus 03200,
03200, Afyonkarahisar, TURKEY,
yonetken@aku.edu.tr*

ORCID: 0000-0003-1844-7233

Ayhan EROL

*Afyon Kocatepe University, Technology Faculty, Metallurgy and Materials Engineering, 03200
Afyonkarahisar, Turkey,
aerol@aku.edu.tr*

ORCID: 0000-0003-4215-9303

Cite this paper as: Bilici Ozkan, V, Yonetken, A, Erol A. Examination of Electroless Nickel Coated Silicon Nitride Ceramics by Ultrasonic Pulse Echo Method. Int. Conf. Advanced. Mater. Sci. & Eng. HiTech. and Device Appl. Oct. 24-26 2024, Ankara, Turkiye

Abstract. Silicon Nitride (Si_3N_4) is a superior ceramic material that generally surpasses other ceramic materials, exhibits excellent mechanical properties, and is preferred in high temperature and structural applications. Compared to other ceramics, silicon nitride offers a combination of high strength, exceptional hardness, low coefficient of friction, high thermal conductivity, toughness and reliability, making it a preferred option for many applications. At the same time, in addition to being a very hard material today, it also attracts attention with its biocompatibility in addition to these features with the development of rod-like beta (β) grains. In this study, it was aimed to determine the production parameters of Si_3N_4 ceramic obtained by electroless Ni plating and to characterize these products. The effects of secondary phases with high thermal conductivity such as SiC, parameters that change the internal structure such as amorphous or crystalline grain boundary phases, on both the ultrasonic method and thermal properties were investigated. As a result of the studies, it was determined that the sintering temperature, i.e. density and grain growth, increased the ultrasonic longitudinal wave velocity values.

Keywords: Elektroless Ni plating, Ultrasonik velocity, Sintering temperature, Silicon nitride
© 2024 Published by ICMATSE

1. Introduction

Silicon nitride ceramics have been widely used in aerospace, machining, automobile engines, bearings and other fields due to their high hardness, low density, high elastic modulus, high wear resistance, corrosion resistance and high fracture toughness as a self-reinforced material. In addition, the fact that they can maintain these properties at high temperatures is one of the main reasons why they are preferred in many fields [1-5]. It is a ceramic

material with wide application expectations. With the addition of the potential for use as a biomaterial to these application areas in recent years, studies on Si_3N_4 ceramics have increased again in recent years [6-11]. Various techniques have been used to measure the physical and mechanical properties of materials as well as elastic properties. The most preferred of these techniques is non-destructive testing (NDT), which is an assessment performed on an object of any type, size, shape or material, without changing the object in any way, to

determine the presence or absence of discontinuities or to examine other material properties. One of the commonly used NDT methods is the pulse echo method. In this non-destructive testing method, in order to detect discontinuities in the material to be examined, it is based on the principle that high frequency (0.1-20 MHz) ultrasound waves produced by the inspection probe propagate in the test material and are reflected back to the probe after hitting a discontinuity and thus detected by the probe. For sound waves in solids, liquids and gases, the vibrating bodies are the particles that make up the substance and the restoring forces are the elastic bonds that hold the substance together [12-15].

2. Materials and Methods

The starting powders used in the study were 99.8% purity Ni powders with a particle size smaller than 40 μm and 99.9% purity Si_3N_4 powders with a particle size smaller than 150 μm . Ni and Si_3N_4 powders were weighed so that the compositions of their powders at the given ratios of 0.85%Ni-0.15% Si_3N_4 were approximately 5g. After weighing, the mixture was mixed homogeneously in a mixer for 24 hours and then shaped by uniaxial cold hydraulic pressing using a high strength cylindrical steel mold. A pressure of 300 Bar was used for compaction of all powder mixtures. The cold pressed samples were sintered at 1000°C, 1050°C, 1100°C, 1150°C and 1200°C in a conventional tube furnace in an Argon gas atmosphere for 2 hours. After the sintering process, the samples were left to cool naturally in the oven and hardness measurements were performed using the METTEST-HT (Vickers) hardness tester. The volumetric changes of the prepared 0.85%Ni-0.15% Si_3N_4 composite material

after sintering were calculated using the formula ($d=m/V$).

In order to examine the ultrasonic properties, ultrasonic longitudinal wave velocities of the composite material obtained by the pulse echo method, which is one of the ultrasonic testing methods, were determined. Sonatest Sitiescan 150s (pulse-echo method, A-scan) was used for ultrasonic characterization of %0.85Ni-%0.15 Si_3N_4 composite samples. The center frequency of the transducer for longitudinal waves was 4 MHz (Sonatest SLH4-10) and this transducer was connected to the device to transmit ultrasonic waves to the sample. It was used to create a connector between the sample surface and the transducer. As a result of the ultrasonic signals of the samples examined with the transducer, the ultrasonic longitudinal wave velocities are determined by measuring the distance traveled between two back wall echoes, twice the 2d sample thickness, taking into account the propagation time (Δt) of the ultrasonic wave measurements.

$$V = (2xd)/t \quad (1)$$

where, d : thickness of the sample (mm), t : propagation time of the ultrasonic wave (ns) and V : velocity of the ultrasonic wave (m/s) [16-18].

3. Results and Discussions

The samples prepared and shaped in the study were sintered at different temperatures in a conventional tube furnace and made ready for physical, mechanical, metallographic and ultrasonic analyses.

Table 1. Sintering temperature, ultrasonic longitudinal velocity, hardness, porosity and density of 0.85%Ni-0.15% Si_3N_4 composite samples.

<i>Composite Samples</i>	<i>Sintering Temperature (°C)</i>	<i>V_L (m/s)</i>	<i>Hardness (HV)</i>	<i>Porosity (%)</i>	<i>Density (gr/cm³)</i>
%0.85Ni-%0.15 Si_3N_4	1000	2835±12.7	120.8	22.7	6.22
	1050	3037±12.0	128.4	12.1	7.08
	1100	3371±12.7	130.9	7.9	7.41
	1150	4001±14.1	139.8	14.4	6.89
	1200	4263±13.4	156.2	26.1	5.95

The sintering temperatures, ultrasonic longitudinal propagation velocity, hardness, bulk density and apparent porosity of the samples are listed in Table 1. The graph of sintering temperature, hardness,

porosity and density with ultrasonic longitudinal wave velocity is shown in Figure 1. When the results are examined, it is seen that the ultrasonic longitudinal wave velocity and hardness values

increase linearly as the sintering temperature increases. During sintering, the bonding of the powders with each other, the development of particle bonding due to point contact and the attraction of the molecules within the material to each other also increase the surface energy of the material. The gaps within the material decrease and accordingly the ultrasonic wave sent into the material is reflected back without loss. In Figure 1a, the linear relationship and dependence between the ultrasonic wave velocity and the sintering temperature with the correlation value of $R^2=0.95826$ is clearly seen. When the ultrasonic wave speed and hardness are examined in Figure 1b, there is a linear relationship between them. As the sintering temperature increases, the strength

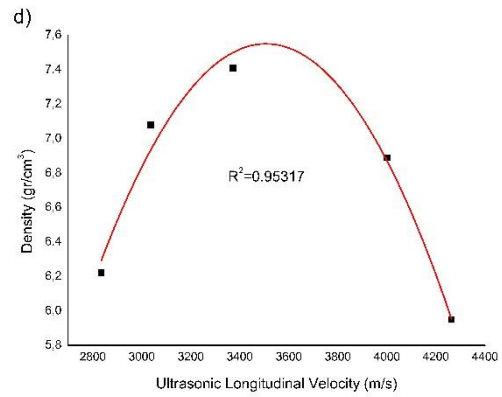
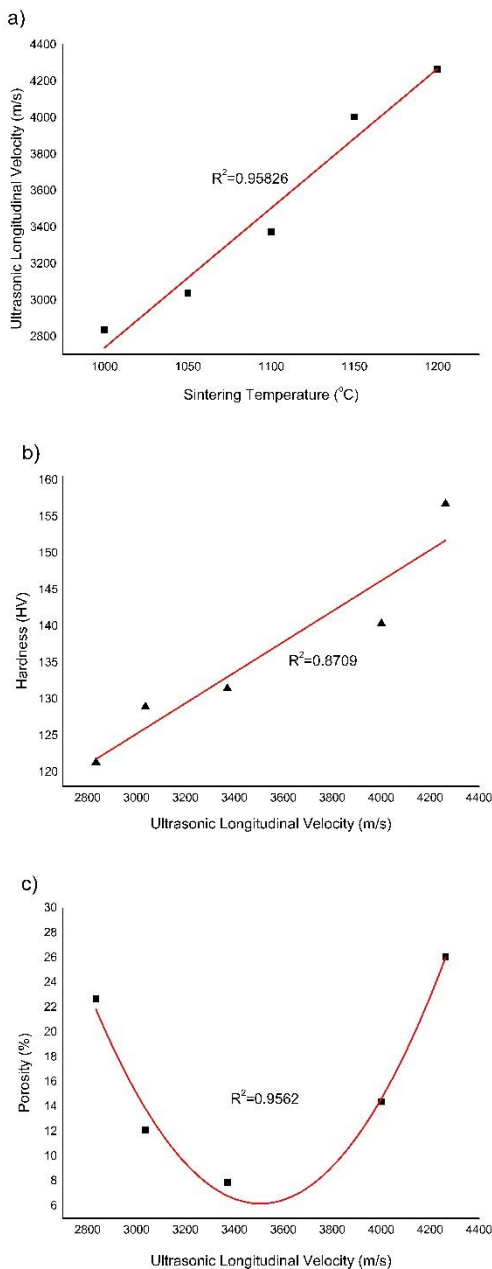


Figure 1. The graph of ultrasonic longitudinal wave velocity change with a) sintering temperature, b) hardness, c) porosity and d) density

becomes higher as the grains come into contact with each other more, the ultrasonic wave travels to the target in a shorter way and accordingly the porosity decreases, both the hardness (strength) and velocity increase. In Figure 1c, the porosity decreases as the ultrasonic wave speed increases. The 0.85%Ni-0.15%Si₃N₄ sample obtained at 1150°C is denser but its porosity is less. Since the ultrasonic sound wave cannot spend more time inside the structure, the ultrasonic wave velocity increases. In Figure 1d, it is seen that the ultrasonic wave speed also depends on the density of the medium. As the density in the material increases, the propagation velocity of the ultrasonic wave also increases. When the graphs in Figure 1c and Figure 1d are examined, there is a polynomial regression between them. This shows us how tightly the particles in the material are connected to each other, the phase transformations in the structure, and the increase in the sound velocity causes the nickel, which passes into the liquid phase with the electroless Ni coating, to wet the grains in the structure very well, thus eliminating the porosity in the structure.

4. Conclusion

Si₃N₄ ceramics with higher porosity were produced by electroless Ni coating method and their elastic properties were characterized by ultrasonic measurement. Ni coating is preferred because it facilitates the sintering of Si₃N₄ ceramic powders by providing a homogeneous coating and at the same time prevents oxidation. The relationship between ultrasonic sound wave velocity and sintering temperature, hardness, porosity and density was investigated. The obtained values and results showed good agreement with the literature values. The highest density in the composite made from

0.85%Ni-0.15%Si₃N₄ powders sintered at different temperatures was obtained as 1100 ° C. The highest density sample was found as 7.41 g/cm³ at 1100 ° C. The highest hardness in 0.85%Ni-0.15%Si₃N₄ composite samples produced using the powder

metallurgy method was found as 156.2 HV at 1200°C. It was also found that the composition of 0.85%Ni-0.15%Si₃N₄ showed the best properties at 1200°C.

References

- [1] S. Kankazi, M. E. Brito, M. C. Valecillos, K. Hirao, M. Toriyama, Microstructure Designing of Silicon Nitride, *J. Eur. Ceram. Soc.*, 17 (1997), pp. 1841-1847, [https://doi.org/10.1016/S0955-2219\(97\)00081-2](https://doi.org/10.1016/S0955-2219(97)00081-2)
- [2] W.M. Guoa, L. X. Wu, T. Ma, Y. You & H. T. Lin, Rapid fabrication of Si₃N₄ ceramics by reaction-bonding and pressureless sintering, *J. Eur. Ceram. Soc.*, 36 (2016), pp. 3919-3924, <https://doi.org/10.1016/j.jeurceramsoc.2016.06.007>
- [3] S. Hampshire, Silicon nitride ceramics—review of structure, processing and properties, *J. Achiev. Mater. Manuf. Eng.*, 24:1 (2007), pp. 43-50.
- [4] F. L. Riley, Silicon Nitride and Related Materials, *J. Am. Ceram. Soc.*, 83 (2000), pp. 245–265, <https://doi.org/10.1111/j.1151-2916.2000.tb01182.x>
- [5] A. M. Hadian, R. A. L. Drew, Strength and Microstructure of Silicon Nitride Ceramics Brazed with Nickel-Chromium-Silicon Alloys, *J. Am. Ceram. Soc.*, 79(3) (1996), pp. 659-665, <https://doi.org/10.1111/j.1151-2916.1996.tb07926.x>
- [6] R. Ş. Kuşhan Akın, Investigation of the Effect of Sintering Additive on the Microstructure and the Antibacterial Behavior of Reaction Bonded Silicon Nitride Ceramics, *UMAGD*, 13(2) (2021), pp. 375-381, <https://doi.org/10.29137/umagd.793123>
- [7] R. B. Heimann, Silicon Nitride Ceramics: Structure, Synthesis, Properties, and Biomedical Applications, *Materials*, 16(14) (2023), pp. 5142, <https://doi.org/10.3390/ma16145142>
- [8] L. Lan, J. Yu, Z. Yang, C. Li, Z. Ren, Q. Wang, Interfacial microstructure and mechanical characterization of silicon nitride/nickel-base superalloy joints by partial transient liquid phase bonding, *Ceram. Int.*, 42(1) (2016), 1633-1639, <https://doi.org/10.1016/j.ceramint.2015.09.115>
- [9] L. Esposito, A. Bellosi, G. Celotti, Silicon Nitride-Nickel Joints Through Diffusion Bonding, *Acta mater*, 45(12) (1997), pp. 5087-5097, [https://doi.org/10.1016/S1359-6454\(97\)00154-7](https://doi.org/10.1016/S1359-6454(97)00154-7)
- [10] F. Frajkorova, K. Bodisova, M. Bohac, E. Bartonickova, J. Sedlacek, Preparation and characterisation of porous composite biomaterials based on silicon nitride and bioglass, *Ceram. Int.*, 41(8) (2015), pp. 9770-9778, <https://doi.org/10.1016/j.ceramint.2015.04.049>
- [11] H. Ebrahimnezhad-Khaljiri, 15- Silicon nitride/carbide fibers: applications and composites, *Synthetic and Mineral Fibers, Their Composites and Applications*, Woodhead Publishing in Materials, (2024), pp. 407-432, <https://doi.org/10.1016/B978-0-443-13623-8.00015-0>
- [12] X. Zhang, S. Cui, S. Ma, W. Chen, Y. Ge, X. Zhao, H. Li, M. Lian, q. Tao, T. Cui, P. Zhu, Hardness, elastic modulus and their correlations in the transparent silicon nitrides, *Mater. Today Commun.*, 38 (2024), 108320, <https://doi.org/10.1016/j.mtcomm.2024.108320>
- [13] G. Topateş, E. Eren Gültekin, Sonic characterization of porous Si₃N₄ produced by various pore formers, *J. Achiev. Mater. Manuf. Eng.*, 63(1) (2014), pp. 13-18.
- [14] N. Kota, P. Jana, S. Roy, Elastic properties of porous silicon nitride fabricated via a low-temperature processing route, *Ceram. Int.*, 49(4) (2023), pp. 7066-7079, <https://doi.org/10.1016/j.ceramint.2022.10.178>
- [15] K. J. Singh, Y. Matsuda, K. Hattori, H. Nakano, S. Nagai, Non-contact sound velocities and attenuation measurements of several ceramics at elevated temperatures, *Ultrasonics*, 41(1) (2003), pp. 9-14, [https://doi.org/10.1016/S0041-624X\(02\)00392-X](https://doi.org/10.1016/S0041-624X(02)00392-X)
- [16] E. Kittinger, Correction for transducer influence on sound velocity measurements by the pulse echo method, *Ultrasonics*, 15(1) (1977), pp. 30-32, [https://doi.org/10.1016/0041-624X\(77\)90010-5](https://doi.org/10.1016/0041-624X(77)90010-5)

Multiphase Fiber Reinforced Composites and CNT Wires for Aerospace and Defense Industries

Abdulhammed K. Hamzat

*Department of Mechanical Engineering
Wichita State University, 1845 Fairmount, Wichita, KS 67260, USA
ORCID: 0000-0002-4063-9891*

Md Shafinur Murad

*Department of Mechanical Engineering
Wichita State University, 1845 Fairmount, Wichita, KS 67260, USA
ORCID: 0000-0002-5680-9859*

Ramazan Asmatulu

*Department of Mechanical Engineering
Wichita State University, 1845 Fairmount, Wichita, KS 67260, USA
ramazan.asmatulu@wichita.edu
ORCID: 0000-0001-8104-2285*

*Cite this paper as: Cite this paper as: Hamzat, Abdulhammed K., Murad, Md. Shafinur, and Asmatulu, Ramazan.
Multiphase Fiber Reinforced Composites and CNT Wires for Aerospace and Defense Industries. Int. Conf. Advanced. Mater.
Sci.& Eng. HiTech. and Device Appl. Oct. 24-26, 2024, Ankara, Turkiye.*

Abstract. The Multiphase fiber reinforced composites (MFRCs) and carbon nanotube (CNT) wires are highly innovative materials that have made important contributions to the field of materials science, namely in the aerospace and defense industries. MFRCs utilize a polymer matrix to incorporate several fiber types, including carbon, glass, and aramid, to improve mechanical characteristics such as strength, stiffness, and durability. These composite materials exhibit exceptional performance in harsh environments, making them well-suited for use in aircraft, drones, wind turbines, ships, spacecraft, and defense systems where reducing weight and maintaining structural integrity are of utmost importance. The integration of CNT wires in these sectors promises enhanced performance, reduced weight, and improved reliability of electronic and structural components. This study provides an extensive overview of the recent advancements in the manufacturing and characterization of FRCs and CNT wires, applications, and behaviors of these advanced materials under varied loadings and environmental conditions. The material's properties were found to be substantially enhanced with the incorporation of nanoparticles, nanomaterials, and hybrid reinforcement architectures within a polymer matrix. Also, findings from various numerical analyses are in close agreement with our numerous experimental studies. This research will help composite aircraft and wind energy businesses to build innovative and intriguing products based on fiber-reinforced nanocomposites and CNT wires.

Keywords: Fiber Reinforced Composites, CNT Wires, Physical Properties, Industrial Applications.

© 2024 Published by ICMATSE

1. Introduction

The aerospace and defense sectors are always pursuing new materials to increase system performance, efficiency, and functionality, while lowering weight and increasing durability [1]. Multiphase fiber reinforced composites and carbon nanotube (CNT) wires have emerged as viable candidates for fulfilling these requirements owing to

their distinctive properties and multifunctional capabilities [1], [2].

Multiphase fiber reinforced composites are materials comprising two or more distinct reinforcing phases embedded within a matrix material. Composites can be developed to demonstrate a mix of beneficial traits including high

strength, stiffness, toughness, and damage tolerance, by carefully selecting reinforcing phases and their distribution within the matrix. Reinforcing phases may consist of different fiber types, including carbon, glass, aramid, and basalt, in addition to nanomaterials such as carbon nanotubes and graphene [2].

CNT wires are macroscopic assemblies of aligned CNTs that demonstrate remarkable mechanical, electrical, and thermal properties [3]. Wires can be produced using several methods, including wet spinning, dry spinning, and direct spinning from CNT forests [4]. CNT wires may serve as substitutes for traditional metallic wires in aerospace and defense applications, providing notable weight reductions and enhanced performance during composite manufacturing.

The integration of multiphase fiber reinforced composites and CNT wires into aerospace and defense systems offers both opportunities and challenges. This research aims to provide an extensive overview of recent advancements in the development and application of these materials in the aerospace and military sectors, addressing the challenges and emphasizing potential solutions and future research paths..

2. Multiphase Fiber Reinforced Composites

2.1 Material Composition and Structure

Multiphase fiber-reinforced composites (MFRCs) are composed of two or more types of fibers that are embedded in a matrix material, which is typically a polymer. The fibers can include carbon, glass, aramid, and natural fibers, as well as nanostructured reinforcements like carbon nanotubes (CNTs) or graphene. The integration of various fiber types enables MFRCs to attain a diverse array of properties tailored for particular applications.

The matrix in MFRCs serves as a binder that holds the fibers together, providing shape and transferring load between the reinforcement phases. Typical matrix materials include thermosetting polymers like epoxy, polyester, or vinyl ester, and thermoplastics such as PEEK (polyether ether ketone) and PPS (polyphenylene sulfide). Thermosetting matrices are extensively utilized because of their outstanding

mechanical qualities and heat stability, whereas thermoplastics provide benefits in terms of toughness and impact resistance [3]–[6].

Carbon fibers, glass fibers, aramid fibers, nanoparticles (e.g., carbon nanotubes, graphene), and ceramic whiskers are the most often utilized reinforcing materials. The selection of these reinforcement materials depends on the desired properties and specific application requirements. For instance, carbon fibers provided high stiffness, strength, and low density and are desired for weight sensitive applications. Unlike carbon fiber, glass fiber are heavier and offer good strength and corrosion resistance. The exceptional impacty resistance and toughness exhibited by aramid fibers make them desirable for ballistic applications.

2.2 Material Composition and Structure

Several production methods such as resin transfer molding (RTM), autoclave processing, extrusion compound, filament winding, injection molding, hand layup, and compression molding has been explore in the literatures for the manufacturing of MFRCs. Fig. 1 illustates the various processes/techniques used in the manufacturing of multiphase composites. Here are brief explanation of some common methods:

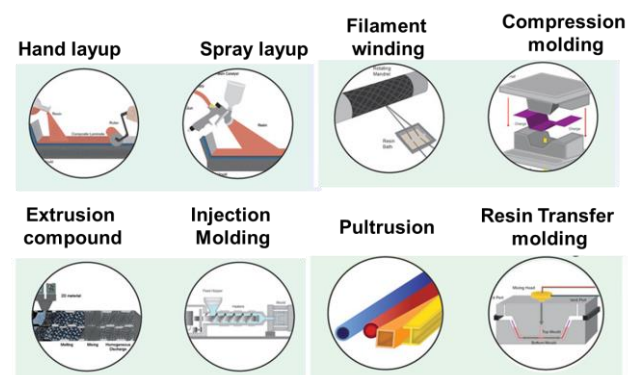


Fig. 1. Overview of various composites manufacturing techniques [7].

- Hand lay-up: This is a simple and widely used technique for producing multiphase fiber reinforced composites. It involves manually placing the reinforcing fibers or fabrics into a mold and then impregnating them with the matrix material. Then, appropriate curing

condition is used to cure the matrix to get the final composite.

- Resin transfer molding (RTM): In this process, the reinforcing fibers are placed in a closed mold, and the matrix material is injected under pressure, allowing for the production of complex-shaped composites with high fiber volume fractions.
- Filament winding: This technique is used to produce cylindrical or spherical composites by winding continuous fibers impregnated with the matrix material around a rotating mandrel.
- Powder impregnation: This method involves impregnating the reinforcing fibers with a powdered matrix material, followed by consolidation through hot pressing or sintering.
- 3D printing: Additive manufacturing techniques, such as fused deposition modeling (FDM) and stereolithography (SLA), can be used to produce multiphase fiber reinforced composites with complex geometries and tailored properties.

2.3 MFRC Application in Aerospace and Defense

Multiphase fiber reinforced composites find numerous applications in the aerospace and defense industries, owing to their exceptional properties and multifunctional capabilities. Some key applications include:

1. Structural components: Multiphase fiber reinforced composites are used in the production of lightweight and high-strength structural components, such as aircraft wings, fuselages, and satellite structures [8], [9].
2. Ballistic protection: Composites reinforced with high-strength fibers, such as aramid and ultra-high molecular weight polyethylene (UHMWPE), are used in the development of ballistic protection systems for personnel and vehicles.

3. Electromagnetic interference (EMI) shielding: Composites incorporating conductive fibers, such as carbon fibers and CNTs, can be used for EMI shielding in aerospace and defense electronic systems.
4. Thermal management: Multiphase composites with high thermal conductivity, achieved through the incorporation of materials like graphene and CNTs, can be used in the design of thermal management systems for spacecraft and high-performance electronics [8], [9].

3. CNT Wires

3.1 Overview and properties

Carbon nanotube (CNT) wires are macroscopic assemblies of aligned CNTs that exhibit exceptional mechanical, electrical, and thermal properties [7]. These unique nanostructures are composed of one or more layers of graphene, cylindrically wrapped to form tubes with diameters ranging from a few nanometers to tens of nanometers and lengths that can extend up to several centimeters [3], [10], [11]. The remarkable properties of CNTs, stemming from their unique structure, make them ideal building blocks for the development of high-performance wires and cables.

CNT wires possess a range of extraordinary properties that set them apart from conventional materials. Firstly, they demonstrate exceptional mechanical strength and stiffness, with tensile strengths up to 100 times higher than that of steel, along with high elastic moduli. This makes them particularly attractive for applications requiring lightweight and robust materials. Secondly, CNT wires exhibit excellent electrical conductivity, comparable to or even surpassing that of copper, rendering them suitable for a wide range of electrical and electronic applications [11]. Thirdly, these wires also boast high thermal conductivity, outperforming traditional materials like copper, which enables their use in efficient

thermal management systems. Lastly, CNT wires have a significantly lower density compared to metallic wires, offering substantial weight savings, which is of particular interest in the aerospace and defense industries [8].

3.2 Production Methods

To harness the exceptional properties of CNT wires, several production methods have been developed, each with its own advantages and challenges. One widely used technique is wet spinning, which involves dispersing CNTs in a solvent to form a spinnable solution. This solution is then extruded through a spinneret and undergoes coagulation in a non-solvent bath, resulting in the formation of CNT wires [26]. Another approach is dry spinning, where CNTs are directly drawn from a CNT forest or aerogel and twisted into a wire without the use of a solvent. This method offers a more straightforward and environmentally friendly process.

In addition to these methods, direct spinning has emerged as a promising technique for the continuous production of CNT wires. In this process, CNTs are grown in a chemical vapor deposition (CVD) reactor and simultaneously drawn into a wire, allowing for a seamless and efficient manufacturing process. Alternatively, dip coating involves coating a pre-existing fiber or wire with a CNT dispersion, followed by drying and consolidation, which can be used to enhance the properties of existing materials.

3.3 CNT Applications in Aerospace and Defense

The exceptional properties and multifunctional capabilities of CNT wires make them particularly well-suited for applications in the aerospace and defense industries. One of the most promising applications is in the development of lightweight electrical wiring. By replacing conventional metallic wires with CNT wires, significant weight savings can be achieved, along with improved electrical performance, which is crucial for reducing fuel consumption and enhancing the overall efficiency of aircraft and spacecraft [5].

Moreover, the high strength and low density of CNT wires make them ideal for the production of structural cables. These lightweight and durable

cables can be used in various aerospace applications, such as aircraft, satellites, and space tethers, where weight reduction is of paramount importance. CNT wires can also be employed as active elements in electromechanical actuators, exploiting their high strength and electrical conductivity to create compact and efficient actuation systems [12-14].

Another exciting application of CNT wires lies in the development of sensors and smart structures. By integrating CNT wires into composite materials, multifunctional structures with built-in sensing and structural health monitoring capabilities can be created. These smart materials can provide real-time information about the stress, strain, and damage states of aerospace components, enabling predictive maintenance and improved safety [4].

4. Challenges and Future Research Directions

Despite the immense potential of multiphase fiber reinforced composites and CNT wires in aerospace and defense applications, several challenges must be addressed to enable their widespread adoption. These challenges include scalability and cost, interfacial interactions, standardization and quality control, and long-term durability [8], [9]. To overcome these obstacles, researchers are exploring advanced manufacturing techniques, such as 3D printing and automated fiber placement, to reduce production costs and improve consistency. Additionally, surface modification and functionalization of reinforcing fibers and CNTs are being investigated to enhance interfacial interactions and mechanical properties. Multiscale modeling and simulation tools are also being employed to provide insights into structure-property relationships and guide material design [13,14]. Furthermore, in-situ characterization and monitoring techniques are being developed to assess the real-time performance and durability of these materials in aerospace and defense applications.

5. Conclusion

Multiphase fiber reinforced composites and CNT wires have emerged as potential materials for aerospace and military applications, having extraordinary characteristics and multifunctional

capabilities. This paper provides an extensive overview of current advances, characteristics, processing techniques, and significant uses of these materials in the aerospace and defense sectors. Despite challenges such as scalability, cost, interfacial interactions, and long-term durability, ongoing research efforts focusing on advanced manufacturing techniques,

functionalization, multiscale modeling, and in-situ characterization are expected to pave the way for the successful integration of these materials into next-generation aerospace and defense systems, revolutionising these industries and shaping the future of aerospace and defense technologies.

References

- [1] J. P. Immarigeon, R. T. Holt, A. K. Koul, L. Zhao, W. Wallace, and J. C. Beddoes, "Lightweight materials for aircraft applications," *Mater Charact*, vol. 35, no. 1, pp. 41–67, 1995.
- [2] P. K. Mallick, "Materials, manufacturing, and design," *Mech Eng (Marcel Dekker, Inc)*, vol. 83, pp. 74–81, 2007.
- [3] M. F. L. De Volder, S. H. Tawfick, R. H. Baughman, and A. J. Hart, "Carbon nanotubes: present and future commercial applications," *Science (80-)*, vol. 339, no. 6119, pp. 535–539, 2013.
- [4] N. Behabtu *et al.*, "Strong, light, multifunctional fibers of carbon nanotubes with ultrahigh conductivity," *Science (80-)*, vol. 339, no. 6116, pp. 182–186, 2013.
- [5] G. Koronis, A. Silva, and M. Fontul, "Green composites: A review of adequate materials for automotive applications," *Compos Part B Eng*, vol. 44, no. 1, pp. 120–127, 2013.
- [6] X. Wang, M. Jiang, Z. Zhou, J. Gou, and D. Hui, "3D printing of polymer matrix composites: A review and prospective," *Compos Part B Eng*, vol. 110, pp. 442–458, 2017.
- [7] S. Maiti, M. R. Islam, M. A. Uddin, S. Afroj, S. J. Eichhorn, and N. Karim, "Sustainable fiber-reinforced composites: a Review," *Adv Sustain Syst*, vol. 6, no. 11, p. 2200258, 2022.
- [8] B. De, M. Bera, D. Bhattacharjee, B. C. Ray, and S. Mukherjee, "A comprehensive review on fiber-reinforced polymer composites: Raw materials to applications, recycling, and waste management," *Prog Mater Sci*, p. 101326, 2024.
- [9] S. mahboubizadeh, A. Sadeq, Z. Arzaqi, O. Ashkani, and M. Samadoghli, "Advancements in fiber-reinforced polymer (FRP) composites: an extensive review," *Discov Mater*, vol. 4, no. 1, p. 22, 2024.
- [10] B. Vigolo *et al.*, "Macroscopic fibers and ribbons of oriented carbon nanotubes," *Science (80-)*, vol. 290, no. 5495, pp. 1331–1334, 2000.
- [11] P.-C. Ma, N. A. Siddiqui, G. Marom, and J.-K. Kim, "Dispersion and functionalization of carbon nanotubes for polymer-based nanocomposites: A review," *Compos Part A Appl Sci Manuf*, vol. 41, no. 10, pp. 1345–1367, 2010.
- [12] H. Xu, W. Jia, S. Ren, and J. Wang, "Novel and recyclable demulsifier of expanded perlite grafted by magnetic nanoparticles for oil separation from emulsified oil wastewaters," *Chem Eng J*, vol. 337, pp. 10–18, 2018.
- [13] M.S. Murad, E. Asmatulu, A. Nuraje, O. Er, M. Gursoy, E. Bahceci, M. Bakir, and R. Asmatulu.D. "Improved Mechanical and Fire-Retardant Properties of Fiber-Reinforced Composites Manufactured via Modified Resins and Metallic Thin Films," *International Journal of Advanced Manufacturing Technology*, Vol. 133, pp. 4715-4730, 2024.
- [14] D. Gurung, M.S. Murad, E. Asmatulu, M. Gursoy, E. Bahceci, M. Bakir, and R. Asmatulu "Enhancing the Thermal and Mechanical Properties of Sulfonated PEEK Fiber Composites with Reduced Smoke Density and Toxicity," *Journal of Applied Polymer Science*, Vol. 141(35), pp. e55886, 2024.

An assessment of the potential of the conversion of pomegranate membrane into value-added products

Emine Yalman

*Iskenderun Technical University - Department of Petroleum and Natural Gas Engineering, 31200,
Iskenderun-Hatay, Turkiye,
emine.avci@iste.edu.tr
ORCID: 0000-0002-1782-3543*

Tolga Depci

*Iskenderun Technical University - Department of Petroleum and Natural Gas Engineering, 31200,
Iskenderun-Hatay, Turkiye,
tolga.depci@iste.edu.tr
ORCID: 0000-0001-9562-8068*

Yunus Onal

*Inonu University - Department of Chemical Engineering, 44000, Malatya, Turkiye,
yunus.onal@inonu.edu.tr
ORCID: 0000-0001-6342-6816*

*Cite this paper as: Yalman, E, Depci, T, Onal, Y. An assessment of the potential of the conversion of pomegranate membrane into value-added products. *Int. Conf. Advanced. Mater. Sci. & Eng. HiTech. and Device Appl. Oct. 24-26 2024, Ankara, Turkiye**

Abstract. These days, energy consumption is constantly increasing due to urbanization and industrialization. Escalating energy need is met predominantly by fossil fuels. However, high cost of fossil resources, their limited availability and possibility of their depletion in the future are serious disadvantages. In addition, the use of fossil resources causes an increase in greenhouse gas emissions, which causes environmental problems such as climate change and pollution. Therefore, an alternative energy source is urgently needed. In this regard, a large attention is paid to biomass thanks to its valuable features that include renewable, environmentally friendly, economical and accessible. In the study, structural analysis of pomegranate membrane, one of the waste biomass sources, was examined and its conversion into a value-added product was evaluated. The study demonstrates that pomegranate membrane is a potential precursor can be employed as an energy resource and converted into value-added products, which will finally provide to come through energy crises to a degree.

Keywords: Biomass, energy, pomegranate, waste.

© 2024 Published by ICMATSE

1. Introduction

Today, due to the rapid increase in population and the increase in transportation, urbanization and industrialization, energy consumption is constantly increasing. Based on the International Energy Agency (IEA), it is expressed that energy consumption doubled between 1970-2000, and increased by 26% between 2000 and 2010 while there has been a large jump in energy production in recent years [1]. Although a significant part of this increase is due to renewable energy sources, 80% of

energy production is still provided by fossil resources [2]. However, consumption of fossil resources causes the release of greenhouse gases into the environment that has negative effects on the environment such as climate change and air pollution. In addition, cost of fossil resources is high and there may be a shortage of reserves, which poses a problem in terms of sustainability. Therefore, an alternative renewable, sustainable, and economical energy source to fossil fuels is of critical importance in meeting the escalating energy demand.

Biomass is generally a variety of by-products resulting from agricultural and industrial production and can be classified as lignocellulosic biomass and non-lignocellulosic biomass. Plants, agricultural wastes (corn stalks, straw, sugar cane bagasse) and forest wastes (paper and sawmill waste) are considered lignocellulosic biomass, while many industrial by-products such as fertilizer and industrial wastes, algae, and city sewage are considered non-lignocellulosic biomass. Hemicellulose, lignin and inorganic components are the main contents of lignocellulosic biomass [3]. On the other hand, lignocellulosic biomass has become a promising resource in terms of its evaluation due to its high yield, low-costness, abundance and easy access. In addition, the fact that lignocellulosic biomass can provide a number of uses with desired products as a sustainable and renewable carbon source increases its appeal. Therefore, lignocellulosic biomass attracts intense interest from researchers worldwide to accommodate world's increasing energy and material needs and as an alternative to traditional waste utilization methods.

To date, many biomass sources have been studied in the literature related to being an alternative to fossil fuels or to be converted into value-added products to be used in various applications [4], [5]. One of these is pomegranate waste. As pomegranate waste, researchers have mostly studied pomegranate peel and pomegranate seed [6], [7]. However, another pomegranate waste, the inner pomegranate membrane, has been overlooked and not focused on. In this study, the structural analysis of pomegranate membrane, an agricultural waste from lignocellulosic biomass sources, was used to investigate its potential to be transformed into energy and value-added products. To the best of the authors knowledge, the study is the first reported case in the literature and will fill the gap in this regard.

2. Material and Method

Firstly, pomegranate fruits were collected from Adana province in the Mediterranean region of Turkey for the supply of raw materials. The collected pomegranates were broken and the membrane were separated from the grains. The pomegranate membrane were dried in an oven at 100 °C for 3 hours. Then, it was grounded in an agate mortar in order to make them ready for analysis.

While the functional group and phase change of the pomegranate membrane were determined by FTIR (Jasco FT/IR 6700 spectrometers) and XRD (Malvern Panalytical EMPYREAN) respectively, its morphology and elemental composition were determined with devise of SEM and EDX Thermo Fisher Scientific Apreo S.

3. Results and Discussion

Fig. 1 demonstrates XRD pattern of agricultural waste biomass in the scanning range of 5 to 90 degrees. XRD measurement can provide information about the amorphous or crystalline structure of the material. From the structure, it is seen that the pomegranate membrane has both an amorphous and crystalline structure. The amorphous structure of the pomegranate membrane is consistent with the presence of hemicellulose and lignin in its content [8].

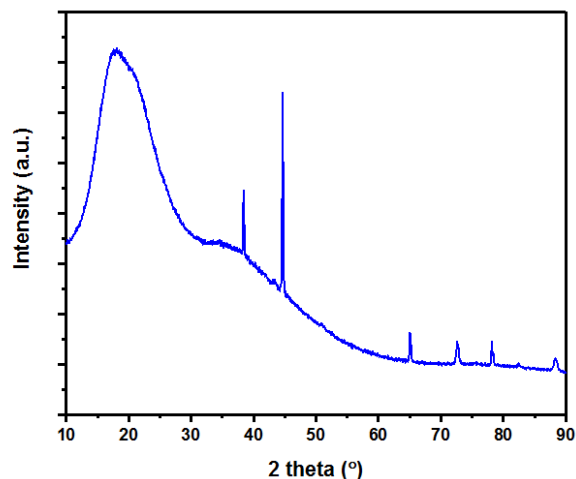


Figure 1. XRD pattern of pomegranate membrane

Structure of the pomegranate membrane was examined in more detail with FTIR analysis and the results were given in Fig. 2. FTIR results show that the pomegranate membrane contains cellulose, hemicellulose and lignin. Also, one of the most important points to be noticed in the spectrum from the figure is the existence of the peak at 2927 cm^{-1} and the -OH stretching vibration, which proves the cellulose, hemicellulose and lignin content [9]. In addition, 3286, 2927 and 865-1002 (cm^{-1}) bands in the structure show the presence of cellulose. Similarly, the peaks at 2927, 1713, 865-1002 (cm^{-1}) bands also prove the presence of hemicellulose. Regarding the lignin content, the 1713 and 1432-1597 (cm^{-1}) bands also reveal this [10]. The peak at 3286 cm^{-1} shows the -OH stretching of the carboxyl group in cellulose [10], [11]. The peak at 2927 cm^{-1} is due to the asymmetric stretching mode of C-H in cellulose [12]. The band between 1713 and 1651 cm^{-1}

1 is caused by the C=O stretching vibration of acetyl groups found in lignin and hemicellulose. The band between 1597 cm^{-1} and 1432 cm^{-1} represents the C=C aromatic skeleton vibration of lignin [13].

Surface properties of the pomegranate membrane were shown in Fig. 3, obtaining SEM analysis. From the SEM analysis, it is seen that the material consists of scattered and hollow bundles. At the same time, there are fractures and cracks on the cell surfaces. With this structure, it can be said that the material is suitable for energy storage by facilitating electron transfer [14].

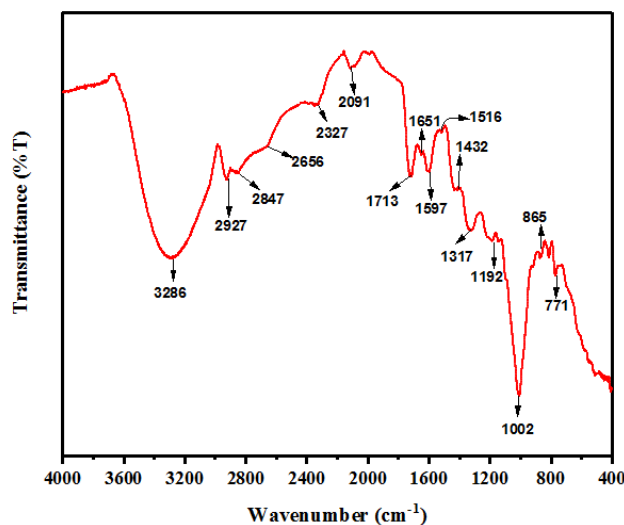


Figure 2. FTIR analysis of pomegranate membrane

Elemental analysis results of the pomegranate membrane obtained from EDX were presented in Fig. 4. The concentration of the elements in the material content is important in terms of obtaining energy from biomass or evaluating it as a raw material in various transformation methods to which it will be subjected for material production [15]. For example, Ca, Mg, K, P are elements that increase the amount of ash and can significantly affect the thermal power generation. In addition, The high atomic and weight numbers mean that the amount of volatile matter in the biomass fuel during combustion is low, and therefore it can be said that there is an inverse proportion between them. From the results, it is seen that the pomegranate membrane has a high oxygen content of 47.40%. The high oxygen content means that it can be easily burned in the production of energy from biomass, particularly in the case of gasification. Another point worth mentioning is that carbon content of 51.66% in the pomegranate membrane is higher than the oxygen content (47.40%) as a result of its cellulose and hemicellulose content.

On the other hand, inorganic content can also be seen from the figure and this content is known as the impurity of the material. The high inorganic content of the material negatively affects the efficiency of the conversion process to be applied [16]. From the analysis, it can be deduced that total inorganic atom content in the pomegranate peel is quite low (below 1%) and can be useful in obtaining bioenergy.

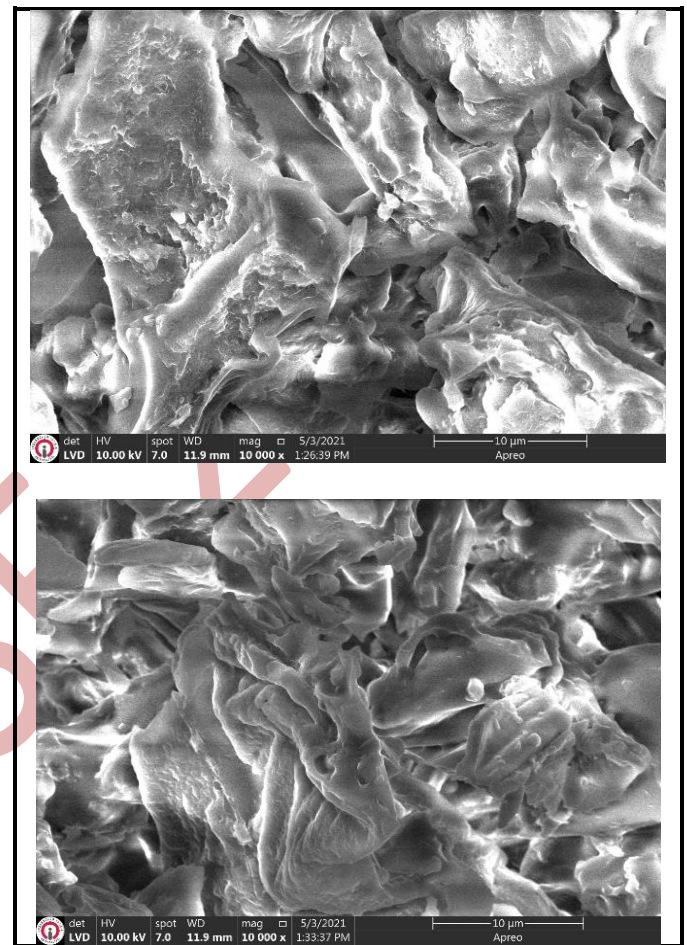


Figure 3. SEM images of pomegranate membrane

4. Conclusions

In the study, structural analysis of pomegranate membrane from agricultural biomass waste was revealed and its potential in conversion into a value-added product using various conversion methods and energy production was investigated. From the results, it was concluded that pomegranate membrane is a valuable material that should be evaluated in this regard due to its cellulose, hemicellulose and lignin content, amorphous structure, porous surface properties, high carbon and low inorganic matter content.

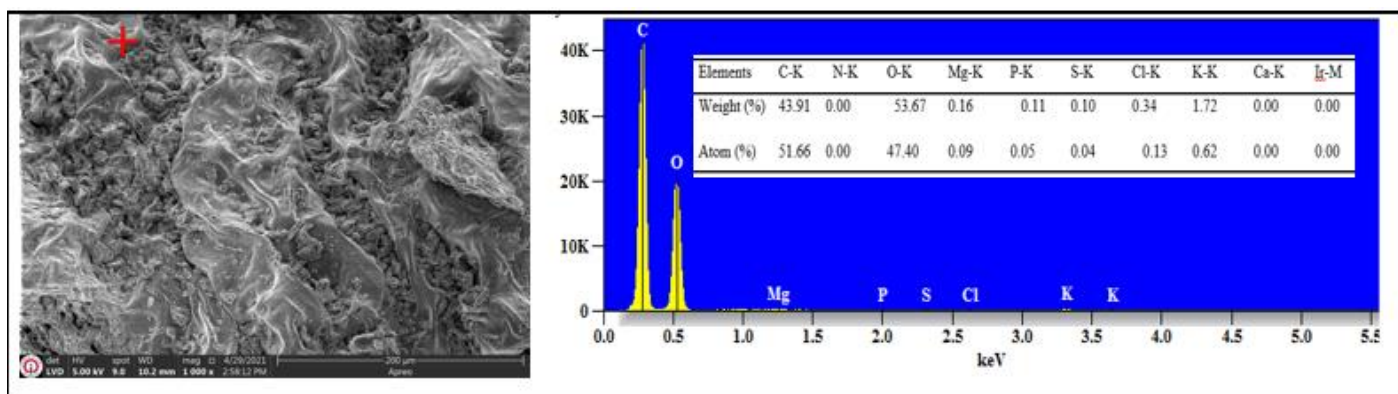


Figure 4. EDX analysis of pomegranate membrane

References

- Agrizzi, T., Oliveira, M. A., Faria, E. V., Santos, K. G., Xavier, T. P., & Lira, T. S. (2024). Assessing coconut shell pyrolysis: Biomass characterization, activation energy estimation, and statistical analysis of operating conditions. *Bioresource Technology Reports*, 26, 101831.
- Afraz, M., Muhammad, F., Nisar, J., Shah, A., Munir, S., Ali, G., & Ahmad, A. (2024). Production of value added products from biomass waste by pyrolysis: An updated review. *Waste Management Bulletin*, 1(4), 30-40.
- Begum, Y. A., Kumari, S., Jain, S. K., & Garg, M. C. (2024). A Review on Waste Biomass-to-Energy: Integrated Thermochemical and Biochemical Conversion for Resource Recovery. *Environmental Science: Advances*.
- Okolie, J. A., Epelle, E. I., Tabat, M. E., Orivri, U., Amenaghawon, A. N., Okoye, P. U., & Gunes, B. (2022). Waste biomass valorization for the production of biofuels and value-added products: A comprehensive review of thermochemical, biological and integrated processes. *Process Safety and Environmental Protection*, 159, 323-344.
- Ameh, V. I., Ayeleru, O. O., Nomngongo, P. N., & Ramatsa, I. M. (2024). Bio-oil production from waste plant seeds biomass as pyrolytic lignocellulosic feedstock and its improvement for energy potential: A review. *Waste Management Bulletin*.
- El Barnossi, A., Moussaid, F., & Housseini, A. I. (2021). Tangerine, banana and pomegranate peels valorisation for sustainable environment: A review. *Biotechnology Reports*, 29, e00574.
- Uçar, S., Erdem, M., Tay, T., & Karagöz, S. (2009). Preparation and characterization of activated carbon produced from pomegranate seeds by ZnCl₂ activation. *Applied Surface Science*, 255(21), 8890-8896.
- Rowell, R. M. (2005). *Handbook of wood chemistry and wood composites*. CRC press.
- George, O. S., Dennison, M. S., & Yusuf, A. A. (2023). Characterization and energy recovery from biomass wastes. *Sustainable Energy Technologies and Assessments*, 58, 103346.
- Méndez-Durazno, C., Carrillo, N. M. R., Ramírez, V., Chico-Proano, A., Debut, A., & Espinoza-Montero, P. J. (2024). Bioenergy potential from Ecuadorian lignocellulosic biomass: Physicochemical characterization, thermal analysis and pyrolysis kinetics. *Biomass and Bioenergy*, 190, 107381.
- Mayandi, K., Rajini, N., Pitchipoo, P., Jappes, J. W., & Rajulu, A. V. (2016). Extraction and characterization of new natural lignocellulosic fiber *Cyperus pangorei*. *International Journal of Polymer Analysis and Characterization*, 21(2), 175-183.
- Das, O., & Sarmah, A. K. (2015). Mechanism of waste biomass pyrolysis: Effect of physical and chemical pre-treatments. *Science of the Total Environment*, 537, 323-334.
- Wang, H., & Zhao, J. (2024). Characterization and optimization of waste *Cucurbita maxima moschata* lashes for biomass composite applications. *Materials Today Communications*, 40, 109996.
- Priya, D. S., Kennedy, L. J., & Anand, G. T. (2023). Emerging trends in biomass-derived porous carbon materials for energy storage application: A critical review. *Materials Today Sustainability*, 21, 100320.
- Kamruzzaman, M., Shahriyar, M., Bhuiyan, A. A., Bhattacharjya, D. K., Islam, M. K., & Alam, E. (2024). Energy potential of biomass from rice husks in bangladesh: An experimental study for thermochemical and physical characterization. *Energy Reports*, 11, 3450-3460.
- Sikarwar, V. S., Zhao, M., Fennell, P. S., Shah, N., & Anthony, E. J. (2017). Progress in biofuel production from gasification. *Progress in Energy and Combustion Science*, 61, 189-248.

Enhancement of HER Catalysts for PEM Electrolyzers: Investigating the Effects of Boron and Phosphorus on Ruthenium-Based Catalysts Supported by Active Carbon in Acidic Media

Gökalp Dilmen

Gazi University, Chemical Engineering Department, 06570, Ankara, Türkiye,
gokalp.dilmen@gazi.edu.tr
ORCID: 0009-0005-2311-9316

Fatma Çigdem Guldur

Gazi University, Chemical Engineering Department, 06570, Ankara, Türkiye,
cguldur@gazi.edu.tr
ORCID: 0000-0002-4404-6882

Silver Gunes

Gazi University, Graduate School of Natural and Applied Sciences, 06500, Ankara, Türkiye,
silver@gazi.edu.tr
ORCID: 0000-0001-7608-3779

Dilmen, G., Guldür, F. Ç., Güneş, S. Enhancement of HER catalysts for PEM electrolyzers: Investigating the effects of boron and phosphorus on ruthenium-based catalysts supported by active carbon in acidic media. Int. Conf. Advanced. Mater. Sci. & Eng. HiTech. and Device Appl. Oct. 24-26 2024, Ankara, Türkiye

Abstract. This study aimed to synthesize a more cost-effective and efficient catalyst than commercial platinum catalysts for the cathode side of Proton Exchange Membrane (PEM) electrolyzers, to support Turkey's green hydrogen production goals. Ruthenium (Ru) was chosen as a promising catalyst for hydrogen evolution reactions (HER) due to its low overpotential, low Tafel slope, high stability, and lower cost compared to platinum. Literature indicates that phosphorus (P) reduces catalyst activity but increases durability, while boron (B) enhances activity by lowering the free Gibbs energy of ruthenium. In this context, four catalysts were synthesized: Ru/AC, Ru-P/AC, Ru-B/AC, and Ru-B-P/AC. Electrochemical tests showed that the Ru-B-P/AC catalyst, with 8.5 wt% ruthenium, exhibited an overpotential of 174 mV and a Tafel slope of 99.9 mV dec⁻¹ in an acidic medium (0.5 M H₂SO₄), remaining stable after 50 cycles. Ru/AC, with 30 wt% ruthenium, displayed the highest activity. Despite having nearly half the ruthenium content, Ru-B/AC showed similar activity to Ru/AC, indicating boron's positive impact. Conversely, Ru-P/AC was less active due to lower ruthenium content and reduced conductivity caused by phosphorus. These findings suggest boron positively affects HER, while phosphorus has a negative impact. Future studies could focus on optimizing phosphorus content.

Keywords: Ruthenium-based catalysts, Hydrogen evolution, Electrocatalyst, Acidic media
© 2024 Published by ICMATSE

Introduction

Global energy demand is increasing with the growing population and rising living standards. Over 95% of this energy demand is met by fossil fuels [1]. However, the use of these fossil fuels contributes to global warming and environmental pollution by emitting high concentrations of greenhouse gases [2]. Efforts have begun to meet global energy demand in a sustainable and clean manner. In this context, the "Paris Agreement,"

framed and ratified by 196 parties at the 21st Conference of the Parties (COP 21) in 2015, aims to actively respond to global warming and keep the global temperature rise below 1.5°C [3]. Each participant has roughly indicated their target year for achieving net-zero emissions. Turkey's target is to reach net-zero emissions by 2053.

Considering Turkey's 2053 net-zero target, the Ministry of Energy and Natural Resources of the Republic of Turkey has published the "Turkey Hydrogen Technologies Strategy and Roadmap," which outlines the prioritization of hydrogen in the future of net-zero goals and sustainable energy by 2035 [4]. To meet Turkey's goals, efforts have been made to synthesize a more efficient and cost-effective catalyst than commercial platinum catalysts for use on the cathode side of proton exchange membrane (PEM) cells in green hydrogen production.

Experimental

To examine the effects of boron and phosphorus on the catalyst, four different catalysts were synthesized. The chemicals used in these catalysts are ruthenium (III) nitrosyl nitrate as ruthenium source, activated carbon, boric acid as boron source, and ammonium dihydrogen phosphate as phosphorus source. Schematic illustration of experimental procedure is given in Figure 1.

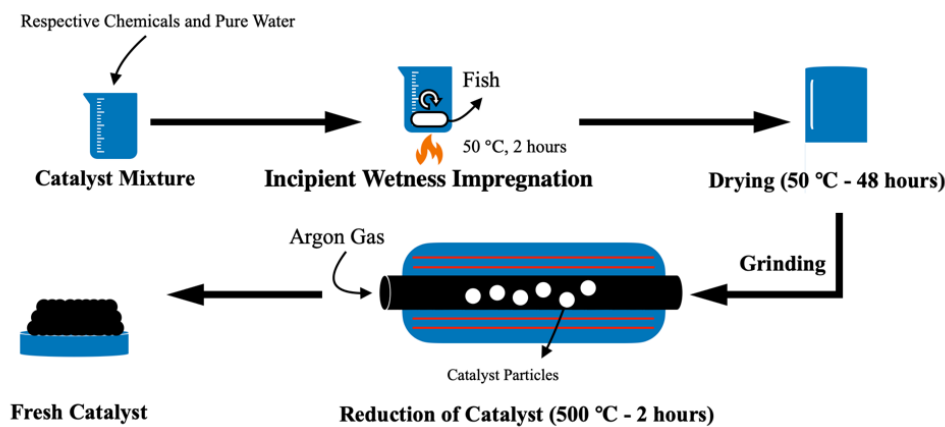


Figure 1. Schematic illustration of Experimental Procedure

Results and Discussions

XRD and XPS analyses were conducted to examine the structure of the catalysts. The XRD pattern of active carbon matched the JCPDS 00-056-0159 [5] reference, indicating successful synthesis with minimal impurities. The XRD pattern of Ru/AC matched the JCPDS 6-663 [6] reference, showing that ruthenium was synthesized in a single-phase nanocrystalline form. The absence of additional peaks beyond those from the active carbon support suggests the catalyst's purity, with peak widths supporting small ruthenium crystal sizes.

For Ru-B/AC, the XRD pattern conformed to the JCPDS 6-663 [6] reference but did not show new peaks indicating Ru-B bonds. This suggests that Ru-B bonds may be amorphous or too small to detect with XRD. Literature also supports the presence of amorphous RuB_x, as no new diffraction peaks specific to RuB_x were found.

The XRD pattern of Ru-P/AC matched the active carbon reference (JCPDS 00-056-0159) [7], but no peaks corresponding to a regular crystalline structure of ruthenium were observed. XPS confirmed the presence of Ru-P bonds, but the lack

of distinct peaks in the XRD pattern suggests these bonds may be amorphous. This indicates that the Ru-P/AC catalyst has an irregular structure, resulting in no prominent peaks in the XRD analysis.

The XRD patterns of the main Ru-B-P/AC catalyst are shown in Figure 2. The XRD pattern for Ru-B-P/AC reveals distinct diffraction peaks around 24.4°, 26.3°, 30°, 40°, 49°, and 63.2°, indicating the presence of BPO₄ crystals (XRD reference card code no. 96-101-0300) [9]. Additionally, peaks around 23° and 44° can be indexed to the (002) and (100) reflections of graphite (JCPDS 00-056-0159). However, characteristic peaks for ruthenium from the JCPDS 6-663 reference are absent, suggesting that ruthenium may be in an amorphous form.

XPS results support the chemical bonding of ruthenium to BPO₄ crystals. This finding indicates that ruthenium forms an amorphous structure with both boron and phosphorus contributions, co-existing with BPO₄ crystals on the catalyst surface, as also supported by XPS analysis (see Figure 3). The results confirm that the catalyst has a complex structure supported by active carbon, containing both carbon and BPO₄ phases. XPS spectra for Ru-B-P/AC are shown in Figure 3. From XPS data wt.

Percentage of Ru in Ru/AC, Ru-B/AC, Ru-P/AC and Ru-B-P/AC are found as 30.3%, 14.55%, 9.59% and 8.50% respectively. The electrocatalytic HER performance of Ru-B-P/AC and other catalysts was studied at 25°C in 0.5 M H₂SO₄ using a three-electrode electrochemical system with a scan rate of 5 mV s⁻¹. The HER activity was found to be in the order: Ru/AC > Ru-B/AC > Ru-B-P/AC > Ru-P/AC (see

Figure 13). Notably, the overpotential for Ru-B-P/AC was calculated to be only 400 mV vs. Ag/AgCl (to achieve a current density of 10 mA cm⁻², j₁₀). When converted to RHE, this overpotential is 174 mV, achieved with just 8.5 wt% ruthenium content. Catalytic performance comparison of prepared catalysts are given in Figure 4 and Table 1.

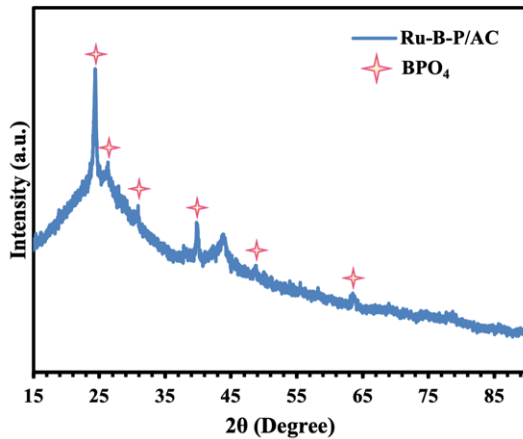


Figure 2. XRD Pattern of Prepared Ru-B-P/AC Catalyst

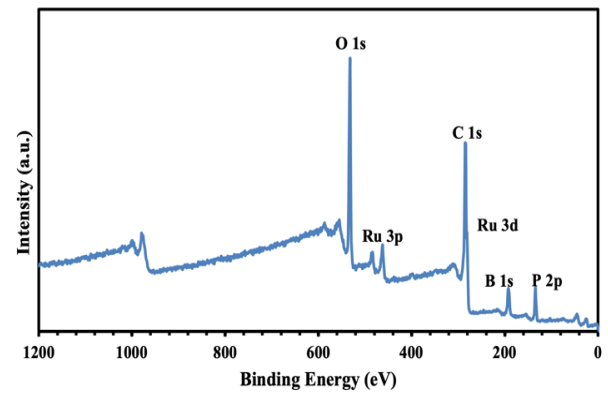


Figure 3. XPS Survey of Ru-B-P/AC

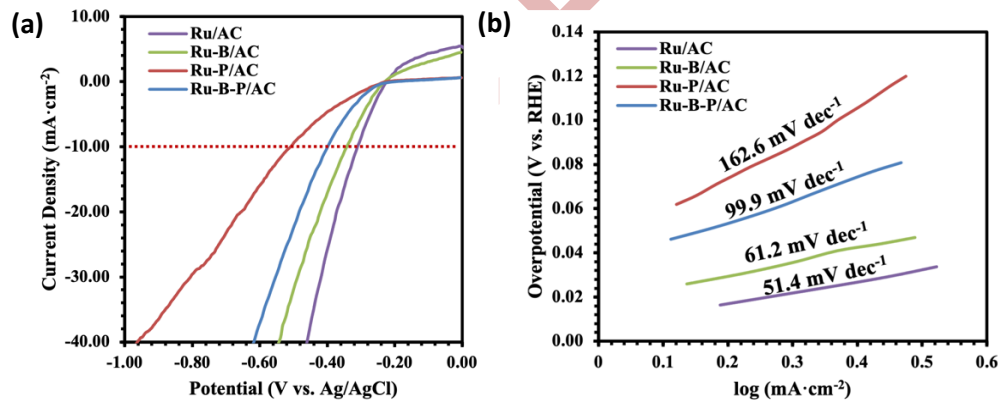


Figure 4. Comparative Activity of the Prepared Catalysts: (a) Overpotential (b) Tafel Curve

Table 1. Comparison of the Prepared Catalysts' Activities Based on Catalyst Content

Catalyst	Element	Element Ratio (wt.%)	Overpotential vs Ag/AgCl (mV)	Overpotential vs RHE (mV)	Tafel Slope (mV·dec ⁻¹)
Ru/AC	Ruthenium	30.3	310	84	51.4
	Carbon	69.70			
Ru-B/AC	Ruthenium	14.55	340	114	61.2
	Carbon	83.80			
	Boron	1.65			
Ru-P/AC	Ruthenium	9.59	510	284	162.6
	Carbon	65.21			
	Phosphorus	25.20			
Ru-B-P/AC	Ruthenium	8.50	400	174	99.9
	Carbon	47.04			
	Boron	12.71			
	Phosphorus	12.44			

Figure 4 and Table 1 show that the most active catalyst is Ru/AC, which is expected due to its highest ruthenium content among all catalysts. Comparing Ru/AC and Ru-B/AC, the latter, despite having nearly half the ruthenium content, shows similar activity, indicating that boron positively affects HER by lowering the free Gibbs energy of ruthenium. Conversely, Ru-P/AC is significantly less active than Ru/AC, likely due to lower ruthenium content and phosphorus reducing conductivity, which negatively impacts HER. Comparing Ru-P/AC with Ru-B-P/AC, the latter is notably more active despite similar ruthenium levels, due to the positive effect of boron and the negative impact of higher phosphorus content in Ru-P/AC. To assess durability, cyclic voltammetry

analyses of Ru-B/AC and Ru-B-P/AC are performed. Both catalysts remained stable over 50 cycles. Ru-B-P/AC showed good activity compared to other catalyst with phosphorus in literature with high ruthenium content, indicating that boron positively affects HER, whereas phosphorus has a negative impact. The 12.44% phosphorus in Ru-B-P/AC reduces activity but improves durability, suggesting that optimizing phosphorus levels could be beneficial in future studies.

Acknowledgments

This study was financially supported by Gazi University Scientific Projects unit through project number FLO-2024-9511.

References

- [1] Shiva Kumar, S., Lim, H. (2022). An overview of water electrolysis technologies for green hydrogen production. *Energy Reports*, 8, 13793-13813.
- [2] Sazali, N. (2020). Emerging technologies by hydrogen: A review. *International Journal of Hydrogen Energy*, 45(38), 18753-18771.
- [3] Jacquet, J., Jamieson, D. (2016). Soft but significant power in the Paris Agreement. *Nature Clim Change*, 6, 643–646.
- [4] Republic of Türkiye Ministry of Energy and Natural Resources. (2023). *Türkiye Hydrogen Technologies Strategy and Roadmap*. Accessed date: 13.01.2024. <https://enerji.gov.tr/announcements-detail?id=20349>
- [5] Keppetipola, N. M., Dissanayake, M., Dissanayake, P., Karunaratne, B., Dourges, M. A., Talaga, D., Servant, L., Olivier, C., Toupance, T., Uchida, S., Tennakone, K., Kumara, G. R. A., Cojocar, L. (2021). Graphite-type activated carbon from coconut shell: a natural source for eco-friendly non-volatile storage devices. *RSC Advances*, 11(5), 2854–2865.
- [6] Hilgendorff, M., Diesner, K., Schulenburg, H., Bogdanoff, P., Bron, M., Sebastian F. (2002). Preparation Strategies towards Selective Ru-Based Oxygen Reduction Catalysts for Direct Methanol Fuel Cells. *Journal of New Materials for Electrochemical Systems*. 5.
- [7] Tang, J., Wang, B., Zhang, Y., Zhang, X-H., Shen, Q., Qin, J., Xue, S., Guo, X., Du, C., Chen, J. (2022). One-step integration of amorphous RuBx and crystalline Ru nanoparticles into B/N-doped porous carbon polyhedrals for robust electrocatalytic activity towards HER in both acidic and basic media. *Journal of Materials Chemistry A*. 10.1039/D1TA08512C.
- [8] Schulze, G. Die Kristallstruktur von B P O⁴ und B As O⁴ Zeitschrift fuer Physikalische Chemie, Abteilung B: Chemie der Elementarprozesse, Aufbau der Materie, 1934, 24, 215-240
- [9] Vaitkus, A., Merkys, A., Sander, T., Quirós, M., Thiessen, P. A., Bolton, E. E., Gražulis, S. (2023). A workflow for deriving chemical entities from crystallographic data and its application to the Crystallography Open Database. *Journal of Cheminformatics*, 15.

Investigation Of Thermal And Crystallographic Properties Of Copper Filaments Used In Metal 3d Printers

Gözde ALTUNTAS

*Gazi University, Faculty of Technology, Department of Metallurgical and Materials Engineering,
Ankara, Turkey
gozdealtuntas@gazi.edu.tr
ORCID0000-0003-4504-0850*

Bulent BOSTAN

*Gazi University, Faculty of Technology, Department of Metallurgical and Materials Engineering,
Ankara, Turkey
bostan@gazi.edu.tr
ORCID: 0000-0002-6114-875X*

Cite this paper as: Altuntas, G., Bostan, B.. Investigation Of Thermal And Crystolographic Properties Of Copper Filaments Used In Metal 3d Printers. Int. Conf. Advanced. Mater. Sci.& Eng. HiTech.and Device Appl.Oct. 24-26 2024, Ankara, Turkiye

Abstract. The additive manufacturing sector, one of today's innovative production methods, continues to become widespread day by day. In this study, materials were produced with Cu filaments used in metal 3D printers, and the thermal and crystallographic properties of the material formed at each step were examined. Firstly, XRD, TGA and DTA analyzes of the raw material Cu filament were performed. Then, the material produced from the filament and the produced material were analyzed after the washing process. Finally, after washing, the material was sintered and turned into the final product, and XRD, TGA and DTA analyzes were completed. The results obtained showed that there was a mass loss in the materials until the sinter stage. This shows that there may be polymer-derived materials inside the copper filament. XRD analyzes showed that there was a main Cu peak in the materials at every stage. The presence of polymers in it could not be detected by XRD analysis. DTA and TGA analyzes detected similar results in the filament, the produced material and the materials washed after production. In the material, which is the final product after sintering, it was observed that the polymers were removed from the structure with the effect of sintering.

Keywords: Additive manufacturing, metal 3D printers, thermal analyzes

© 2024 Published by ICMATSE

Metal powders play a very important role in additive manufacturing processes [1]. Basically, powder and wire fed systems are used. Copper material can be used in electronic components, coolers and inductors through additive manufacturing due to its very high electrical and thermal properties [2]. In this study, the thermal and crystallographic properties of filaments used in metal 3D printers were examined at every step from the wire stage to the sinter stage.

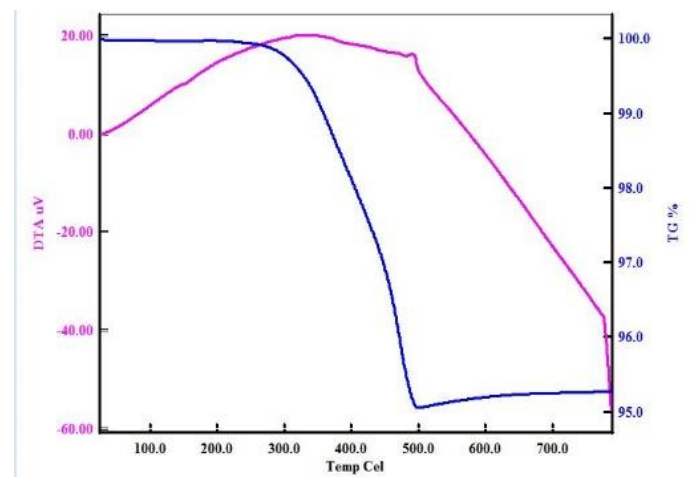


Figure 1. DTA and TGA analysis of copper filament

As a result of DTA and TGA analyzes performed to determine the thermal properties of the materials, it was observed that there was a mass loss in the materials until the sinter stage. This proved the existence of polymer-derived materials in the copper filament. However, the presence of polymers could not be detected by XRD analysis.

1. Introduction

Copper is one of the oldest metals used by humanity. With the industrial revolution, there was a tremendous increase in the production and consumption of copper and copper alloys. Today, copper remains the main metal in modern power generation facilities. Electrolytic copper is obtained after refining and purification by electrolysis in the production of metallic copper from copper ore. In this way, the quality of copper increases in terms of electrical conductivity. Since their workability increases, they can be easily turned into wire and sheet [3]. Copper and copper alloys are frequently used in industry due to their thermal and electrical properties [4]. Pure copper is widely preferred in aviation, automotive, and electrical fields, especially due to its high heat, electrical conductivity, and ease of machinability [5]. It is very difficult to process complex structures with traditional production methods. In recent years, additive manufacturing has become an alternative for the production of complex parts [6]. Previous studies have examined the structural and mechanical properties of pure copper parts produced by additive manufacturing with selective laser melting (SLM), selective electron beam melting (SEBM), powder bed fusion (PDF), laser metal deposition (LMD), and binder jetting (BJ) methods. In different studies, laser-based powder bed fusion (L-PBF) has attracted great attention by academic and industrial research aiming to meet the increasing demand for the efficiency of electrical and thermal management components [7]. The forming mechanism of ultrasonic additive manufacturing (UAM) additive manufacturing technology was examined in different studies. It is found that the

bonding mechanism of UAM additive manufacturing is the formation of severe shear deformation at the interface [8]. The aim of this study is to examine the thermal and crystallographic properties of copper material produced by the ADAM method using the commercial system available on the market, Markforged Metal X, by obtaining copper from copper filaments by diffusion. Copper filament and samples produced from the filament were characterized before and after washing and sintering.

2. Experimental Studies

The materials produced in experimental studies were obtained with the Markforged metal X – washing - sinter device. The washing step of the designed parts is done in chemical solvent to remove polymers. Drying was done to remove the remaining solvent in the raw piece. The raw parts, whose printing, washing and drying periods were completed, were loaded into the sinter furnace to be sintered. 2.6% H₂ and 87.4% Ar (Mix) gas were used for sintering. Thermal analysis of the prepared samples was carried out on the Hitachi STA7300 device at a speed of 10°C/min. Necessary calculations were made with the data obtained as a result of the analysis using the Bruker D8 Advance device for crystallographic analysis. Samples produced from the copper filament, washed after production, and finally sintered were characterized separately at each stage.

3. Result and Discussion

Figure 2(a) shows DTA and TGA analysis of copper filament. It was observed that there was a transformation at approximately 200, 300, 400 and 500 °C and a mass loss of 5% occurred. Figure 2 (b) shows that the material produced from filament shows approximately the same results. In Figure 2 (c), it was observed that after the washing process, although the transformation temperatures of the sample were the same as the other samples, their intensity decreased and the mass loss decreased by 2.5%. Figure 2 (d) shows that there are no

more transformations with the copper filament, which is sintered and the final product is obtained, and the mass loss decreases by 0.1% with temperature. This situation proves the presence of polymer material in the other three

samples except the sintered sample. While the polymer material causes more phase mass loss against temperature, it also shows endothermic transformation at certain temperatures.

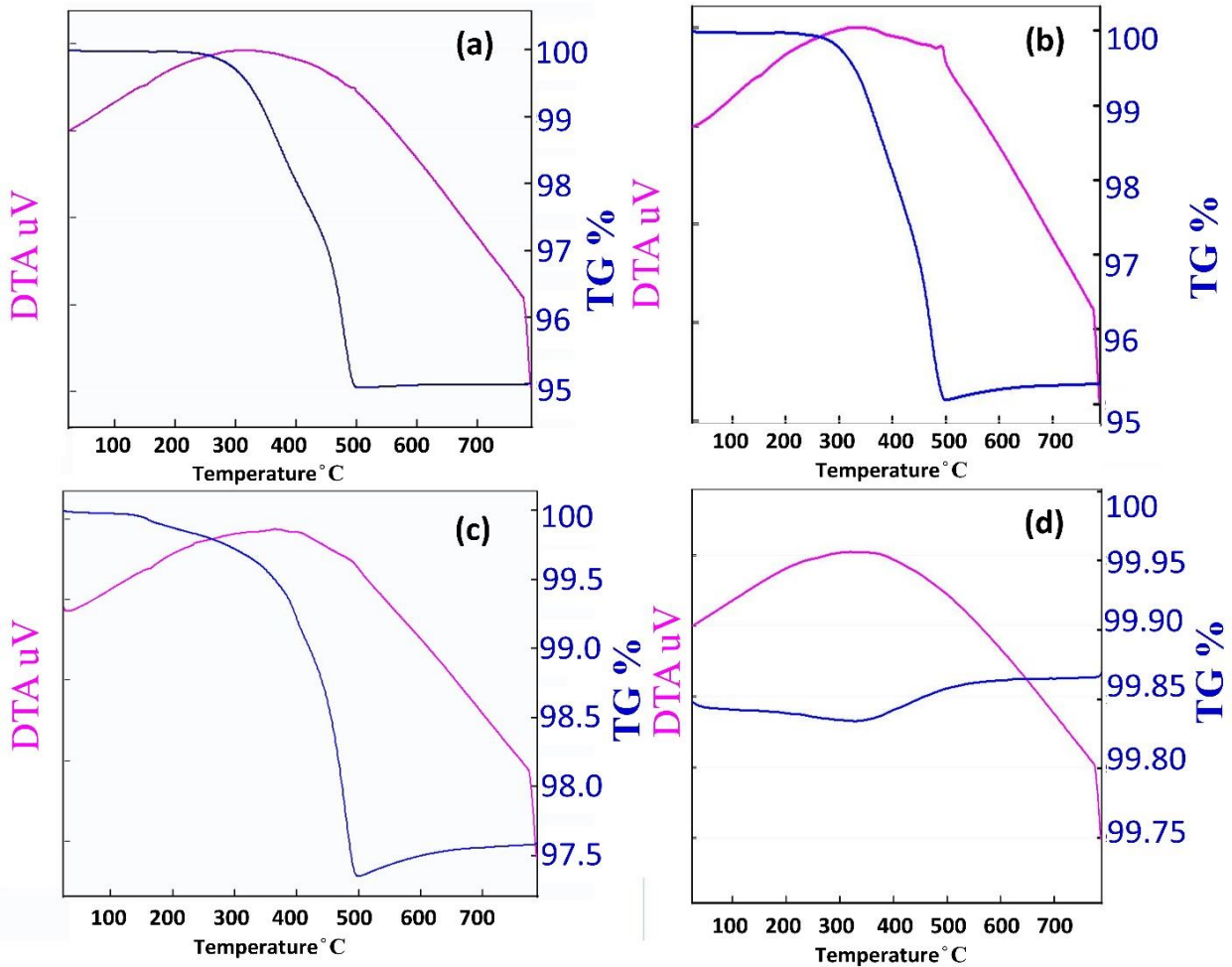


Figure 2. DTA and TG graphs of samples (a)copper filament (b) sample made from copper filament (c) washed sample (d) sintered sample

Figure 3 shows the XRD analysis of the whole material. In each sample, the main peaks were all found to be Cu. The presence of polymers could not be detected here. However, by XRD analysis, it was determined that there was a difference in the FWHM value of the diffraction peaks in the samples. Half-maximum full widths changed with each process in the production phase. This situation shows the hardness value, dislocation density, grain size, strain value, and texture effect of the material [9,10].

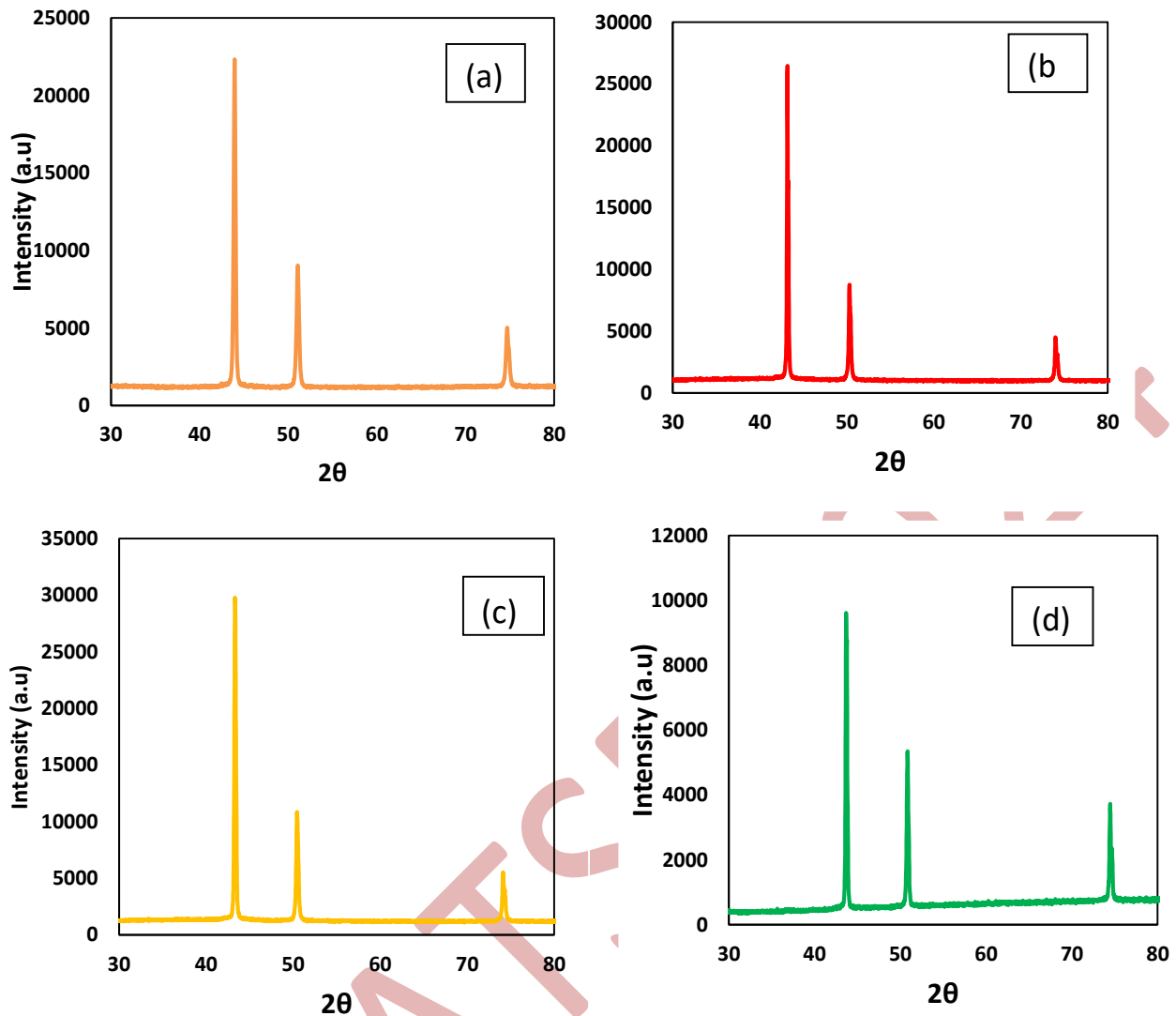


Figure 3. XRD patterns of samples (a) copper filament (b) sample made from copper filament (c) washed sample (d) sintered sample

References

- Constantin, L., Wu, Z., Li, N., Fan, L., Silvain, J. F., & Lu, Y. F. (2020). Laser 3D printing of complex copper structures. *Additive Manufacturing*, 35, 101268., 10.1016/j.addma.2020.101268
- Singer, F., Deisenroth, D. C., Hymas, D. M., & Ohadi, M. M. (2017, May). Additively manufactured copper components and composite structures for thermal management applications. In *2017 16th IEEE Intersociety Conference on Thermal and Thermomechanical Phenomena in Electronic Systems (ITherm)* (pp. 174-183). IEEE. 10.1109/ITHERM.2017.7992469
- Richardson, H. W. (1997). *Handbook of copper compounds and applications*. CRC Press.
- Ikeshoji, T.T.; Nakamura, K.; Yonehara, M.; Imai, K.; Kyogoku, H. Selective Laser Melting of Pure Copper. *JOM* 2018, 70, 396–400.
- Colopi, M.; Demir, A.G.; Caprio, L.; Previtali, B. Limits and solutions in processing pure Cu via selective laser melting using a high-power single-mode fiber laser. *Int. J. Adv. Manuf. Technol.* 2019, 104, 2473–2486.
- Gradl, P.R.; Protz, C.S.; Ellis, D.L.; Greene, S.E. Progress in additively manufactured copper-alloy GRCOP-84, GRCOP-42, and bimetallic combustion chambers for liquid rocket engines. *Proc. Int. Astronaut. Congr. IAC* 2019, 2019, 21–25
- Tran, T. Q., Chinnappan, A., Lee, J. K. Y., Loc, N. H., Tran, L. T., Wang, G., ... & Ramakrishna, S. (2019). 3D printing of highly pure copper. *Metals*, 9(7), 756.
- Sriraman, M.R.; Gonser, M.; Fujii, H.T.; Babu, S.S.; Bloss, M. Thermal transients during processing of materials by very high power ultrasonic additive manufacturing. *J. Mater. Process. Technol.* 2011, 211, 1650–1657.

9. Altuntaş, G., Özdemir, A. T., & Bostan, B. (2023). A survey of the effect of cryogenic treatment and natural ageing on structural changes and second-phase precipitation in Al–Zn–Mg–Cu alloy. *Journal of Thermal Analysis and Calorimetry*, 148(20), 10713-10725.
10. Warren, B. E. (1990). *X-ray Diffraction*. Courier Corporation.

ICMATSE 2024

Removal of Boron and Boron Compounds from Waste Waters

Ipek CELEBI GURSOY

*Eti Mine Works- Plant Construction and Engineering Department, 06530, Ankara, Turkiye,
icelebi@etimaden.gov.tr*

ORCID: 0000-0003-0830-1441

İrfan AR

*Gazi University-Chemical Engineering Department, 06570, Ankara, Turkiye,
irfanar@gazi.edu.tr*

ORCID: 0000-0002-6473-9205

Cite this paper as: ÇELEBİ GURSOY, İpek, AR, İrfan. Removal of Boron and Boron Compounds from Waste Waters. Int. Conf. Advanced. Mater. Sci.& Eng. Hi Tech. and Device Appl. Oct. 24-26 2024, Ankara, Turkiye

Abstract

Firstly, adsorption studies were carried out with the wastewater of Eti Mine Works with waste clays and zeolites taken from Eti Mine in a shaking, thermostat water bath. Modified walnut shells and waste corn cobs also with waste sunflower stems were used. The adsorption processes were insufficient to remove boron from wastewater because of high boron content. For this reason, chemical precipitation with lime as a preliminary process before adsorption was carried out. Secondly, it was aimed to eliminate high boron content in Espey Spring Water in the Espey Site to improve the quality of irrigation water within the framework of social responsibility. Then, the adsorption studies were carried out. Modified walnut shells and almond shells at different fractions and amounts were used at the same adsorption conditions as in the first part of this study, at the different pH values. Almond shell was found to be effective. Following studies, saw dust was soaked to Espey Spring Water, diluted with pure water at different ratios, at the same adsorption conditions. Also saw dust was found to be a promising adsorbent with its porous cellulosic structure and boron complexation with the hydroxylic, carboxylic and phenolic groups in the structure of it.

Keywords: boron removal, adsorption, waste waters

© 2024 Published by ICMATSE

Introduction

Boron, located in III A group of periodic table and shown as B, has semi-metallic and semi-conducting properties. Boron is never found free in nature [1]; it tends to bond with oxygen. It is found in nature as minerals bound to sodium, calcium and magnesium oxides and containing crystal water. The general name of boron-oxygen compounds is borate. Turkey has 73% of the world's boron reserves. Known boron deposits are located in Eskişehir- Kırka, Kütahya-Emet, Balıkesir-Bigadiç and Bursa-Kestelek [2,3]. The production, operation and marketing activities of boron mines in Turkiye were given to the Eti Mine Works. The impact of boron on the environment is to the air, soil and

water. The effect of boron on water is evaluated as its effect on drinking water and its effect on agricultural water. Waste waters generated during the operation of mines can cause soil and water pollution problems and reach to high levels if precautions are not taken. When the boron concentration in these wastes exceeds the limit values determined by the legislation, it harms aquatic creatures or plants if used in agricultural irrigation. And then they can be harmful to people who use them in their diet. Boron limit values vary depending on the receiving environment where the wastewater will be discharged. There is no simple method for removing boron from water and wastewater [4]. One of the methods used for this purpose has been adsorption due to its ease of application

[4]. Evaluating natural waste adsorbents is important from an environmental and economic perspective. Boron is an essential micronutrient for plants and animals. Although boron has important micronutrient properties, it has harmful effects when taken in high doses. As a result, although boron is necessary, too much of it has a poisonous effect for living things. So, the importance of keeping the amount of boron in various water resources under control and removing boron from wastewater becomes evident. In this study, it is aimed to conduct studies on the removal of boron in wastewaters and spring waters taken from Eti Mine Works to determine the best removal method using natural and modified adsorbents.

Results and Discussion

At the first part of this study, boron removal from wastewater taken from the Emet Boric Acid Factory Waste Dam belonging to the Emet Boron Operations Directorate, which has a high boron content was studied. This waste water had 5883 ppm boron value. Different adsorption studies were carried out with natural clays which exist in the site of Emet, Kirka, Bigadiç, Bandırma Boron Operations Directorate which belong to the Eti Mine Works and also with zeolite exists in the site of Bigadiç Boron Operations Directorate. All adsorption studies were carried out at 25 °C in a water bath with 170 rpm rapid shaking. 100 mL boron wastewater was used. These two adsorbents did not have sufficient capacity in terms of boron adsorption. Using clay, after adsorption there was an increase in the amount of boron in the water compared to the initial value. This increase in boron concentration can be explained by the release of boron during adsorption from clay minerals that extracted from the same mine and saturated with boron. So, being saturated with boron negatively effected adsorption for these two adsorbents. Different adsorption studies were carried out with natural adsorbents as modified walnutshells, modified waste sunflower stems and waste corn cobs. These adsorbents were found to be insufficient for the removal of boron from waste water too. An additional method was needed before adsorption since the adsorption process using environmentally friendly adsorbents were insufficient for removing boron from industrial wastewater with high boron content. It was thought that it would be more suitable to remove some boron from waste water by chemical precipitation then to continue to removal by adsorption using environmentally friendly adsorbents. In the second part of this study, it was decided to study removal of boron from Espey Spring Water which causes environmental problems due to its impact on

agricultural surface waters because of having high boron content. This water is located in the Espey Open Pit Site belonging to the Emet Boron Operations Directorate of Eti Mine Works. So it was thought to continue studies with this water in the scope of social responsibility. For boron removal, firstly chemical precipitation with lime was carried out in a temperature-controlled magnetic stirrer heater at a temperature of 25 °C and a rotation speed of 760 rpm for one hour. 1 hour working time, 1 hour waiting time were applied. Espey Spring Water's initial boron value was 4590 ppm. Three different amounts of lime were added (5, 10, 20 g) to 200 mL Espey Spring Water samples. The change in amount of lime did not have much effect on the removal of boron and at the same time, as the amount increased, the formation of process waste sludge increased according to the chemical reaction between boron and lime. So, it was decided that chemical precipitation with 5 g lime would be sufficient. The decrease from 4590 ppm to 424 ppm can be considered as a very good result in terms of purification. Afterwards, adsorption studies were carried out at 25 °C in a water bath with 170 rpm rapid shaking. 100 mL of Espey Spring Water was used. Adsorption studies were carried out using different amount of adsorbent, pH and particle size to determine the effects of these parameters on adsorption.. As the amount of adsorbent increased, the adsorption amount and efficiency increased slightly because of increased sites. Output results were 410 ppm for 2 g adsorbent, 401 ppm for 4 g adsorbent. Studies continued by adjusting the pH. In the study conducted by adjusting the pH to 9, more efficient results were obtained compared to study with pH 11.67, which was spring water's pH value after chemical treatment. The highest efficiency, 379 ppm, was obtained with 4 g of adsorbent at pH 9. The study continued using 0.1 M HCL treated walnut shells in the -63 µ fraction at different pH values. Optimum removal pH was found to be 9 with 346 ppm output boron value. It was concluded that as the degree of acidity or alkalinity increases, adsorption was negatively affected. Because walnut shell particles were modified with HCl to eliminate impurities. They had a surface with (+) charged. So in this situation, for effective adsorption, the molecule to be adsorbed should have (-) charge. And pH is an important parameter affecting the behaviour of boron in water. When the pH is less than 7, boron is present in water in the form of non-ionized boric acid, H_3BO_3 and at pH values greater than 10.5 behave as, (-) charged borate, $B(OH)_4^-$. So, in this conditions borate is more favourable for (+) charged surfaces. At higher pH's as 12, the reason for the decrease in boron adsorption is that the hydroxyl ion competes with the (-) ions on the surface of adsorbent. Because at higher pH's, (+) charged surfaces turns to (-) charge. When the studies carried out with different particle sizes of walnut shells, +500 µ and -63 µ fractions compared, it was

observed that when the particle size decreased, the adsorption efficiency would increase slightly because of increased surface area. Since efficient results could not be obtained, almond shells as different adsorbent were tried. Adsorption was carried out under the same conditions, using +500 fraction almond shells treated with 0.1 M HCl. At pH 9, output values of 330 ppm (2 g adsorbent) and 325 ppm (4 g adsorbent) were

Table 1. Adsorption Results of Espey Spring Water with 2 g Almond Shell Particles (Activated with HCl, (+500 μ) at 25 °C, at Different pHs

pH	B ₂ O ₃ [ppm]	B [ppm]
12,10	1117	347
9	1064	330
7	1134	353
4	1134	353

Table 3. Adsorption Results of Espey Spring Water with 2 g Almond Shell Particles (Activated with HCl, (-63 μ) at 25 °C, at Different pHs

pH	B ₂ O ₃ [ppm]	B [ppm]
12,10	1077	334
9	1042	324
7	1095	340
4	1112	345

Afterwards, it was decided to work with 0.1 M NaOH treated wood sawdust, and the adsorption process was carried out under the same conditions. The boron value of spring water decreased from 424 ppm to 404 ppm which was due to calcium borate precipitation formed at the bottom of Espey Spring water over time. As a result of the adsorption study performed without dilution at the same conditions, the amount of boron remaining in the wastewater was 383 ppm as seen from Table 4 above. The boron removal

obtained. Considering that the initial boron concentration was 424 ppm, approximately 100 ppm boron was removal. At pH 9 with -63 μ at the same adsorption conditions, output value was 324 ppm. When the particle size decreases, the adsorption efficiency increases when the -63 μ and + 500 μ fractions are compared. The results can be seen from Tables-1-3.

Table 2. Adsorption Results of Espey Spring Water with 4 g Almond Shell Particles (Activated with HCl, (+500 μ) at 25 °C, at Different pHs

pH	B ₂ O ₃ [ppm]	B [ppm]
12,10	1099	341
9	1046	325
7	1099	341
4	1117	347

Table 4: Adsorption Results of Espey Spring Water with 2 g of Saw Dust at 25 °C, at Different Dilution Rates

Dilution Rate	B ₂ O ₃ [ppm]	B [ppm]
0	1233	383
1/2	616	191
1/5	205	64
1/10	120	37

achieved was 21 pmm (5.2 %), which was much higher than the discharge upper limit value specified in the wastewater regulation of Turkiye. For this reason, it was decided to carry out adsorption studies by diluting the spring water. After adsorption using 1/2 diluted Espey Spring Water, the boron concentration remaining in the wastewater was found to be 191 ppm. With dilution, the initial waste boron concentration in wastewater, which was 202 ppm before adsorption, decreased to 191 ppm after

adsorption. In other words, 11 ppm (5,4 %) removal was achieved. Since it was observed that boron removal increased with dilution, it was decided to conduct adsorption studies by increasing the dilution rates. After adsorption with 1/5 diluted water, the boron concentration remaining in the wastewater was found to be 64 ppm. Considering that the initial boron concentration with dilution was 81 ppm, it could be seen that 17 ppm (26,6%) boron removal was achieved by adsorption. After adsorption with 1/10 diluted water, the remaining boron concentration in the wastewater was found to be 37 ppm. Considering that the concentration of wastewater before adsorption as a result of dilution was 40 ppm, 3 ppm (7,5%) boron removal was achieved with adsorption. When all results were evaluated for 2g adsorbent, boron removal was achieved. The reason for this can be explained as the fact that sawdust is a material with a porous cellulosic structure and complexation with the hydroxylic, carboxylic and phenolic groups in the structure of sawdust. In addition, it can be mentioned that treatment with NaOH has a positive contribution to adsorption in terms of removing impurities in the adsorbent and allowing easier access of boron to the pores. As explained in the literature, concentration is an important parameter affecting the behaviour of boron in water. The concentration constant (K) of boric acid increases with increasing concentration. It is known that if the total boron concentration in aqueous solution is less than 0.025 M (270 mg B/L), only H_3BO_3 and $B(OH)^4-$ ions are present in the environment. At higher concentrations (>0.025 M), conversion to polyborates occurs. At high concentrations, polyborate ions such as $B_3O_3(OH)^{4-}$, $B_4O_5(OH)^{4-}$ and $B_5O_6(OH)_4$ are formed. The reason for the positive effect of dilution on

adsorption is that as a result of dilution, H_3BO_3 and $B(OH)^4-$ ions present in water at low concentrations; This can be explained as easier adsorption compared to large molecules such as polyborate, which is thought to exist at a concentration of 404 ppm before dilution.

Conclusions

These results showed that, sawdust and almond shells showed effective performance in adsorption studies. For saw dust; there was an optimum dilution rate for boron removal of Espey Spring Water. Based on these results, it could be concluded that the active area of the adsorbent might be insufficient at high boron concentrations, in other words, since all active areas were occupied by boron, the adsorption phenomenon reached a dynamic balance and the amount of adsorbent was increased and the adsorption experiments were carried out with different dilution rates.

Adsorption experiments were repeated for different dilution rates and by increasing the amount of adsorbent. Also other natural adsorbents may be used for further studies. Within the framework of social responsibility, it will be determined whether the boron concentration in Espey Spring Waters can be lowered below the regulation limit values under the best adsorption conditions. In literature, generally, boron removal from synthetically prepared boron solutions were studied. From environmental and economic perspective, boron removal from waters which have high boron content with evaluating natural waste adsorbents in adsorption makes this study specific.

References

1. Baran P. (2014). Atık Sulardan Bor Gideriminde Modifiye Doğal Kil Minerallerinin Kullanılabilirliğinin Araştırılması, Doktora Tezi, İTÜ Fen Bilimleri Enstitüsü, İstanbul.
2. Yağmur Y. (2012). *Birlikte Çöktürme-Mineralizasyon Yöntemi ile Sulu Çözeltilerden Bor Kazanımı*, Yüksek Lisans Tezi, İTÜ Fen Bilimleri Enstitüsü, İstanbul.
3. Yiğitbaşıoğlu, H. (2004). *Türkiye İçin Önemli Bir Maden: Bor*. Ankara Üniversitesi Coğrafi Bilimler Dergisi, 2:13-25.
4. Zincir E. (2013). Modifiye Edilmiş Perlit ile Atık Sulardan Bor Giderimi, Yüksek Lisans Tezi, İTÜ Fen Bilimleri Enstitüsü, İstanbul

Investigation of structural, electronic, and optical properties of KSil_3 cubic perovskite using first-principles methods

Gulcin CORBACI

Gazi University- Faculty of Science, 06560, Ankara, Turkey,
gulcincorbaci1997@gmail.com
ORCID: 0000-0002-5900-5952

Yasemin Oztekin CIFTCI

Gazi University- Faculty of Science, 06560, Ankara, Turkey,
yasemin@gazi.edu.tr
ORCID: 0000-0003-1796-0270

Cite this paper as: Çorbacı Gülçin, Oztekin Ciftci Yasemin Investigation of structural, electronic, and optical properties of KSil_3 cubic perovskite using first-principles methods, Int. Conf. Advanced. Mater. Sci.& Eng. HiTech.and Device Appl.Oct. 24-26 2024, Ankara, Turkiye

Abstract. This study investigated the electronic, structural, elastic, and optical properties of KSil_3 perovskite using density-functional theory (DFT). Our calculations show that the material is mechanically stable. Electronic calculations suggest that KSil_3 has a metallic behavior. The results obtained from this study agree with previously published literature. This research explores the structural, electrical, elastic, and optical properties of KSil_3 , a promising lead-free alternative. To comprehend the electrical properties of a material, a thorough analysis of its solid-state optical properties is indispensable. Understanding the interaction between photons and matter requires a deep dive into optical characteristics. Consequently, a profound knowledge of the optical properties of materials used in light-driven applications, such as photocatalysis, is crucial for advancing this field.

Keywords: KSil_3 , perovskite, DFT, electronic structure, band gap, optical properties
© 2024 Published by ICMATSE

INTRODUCTION

The ABX_3 perovskite family, comprising a broad spectrum of ternary oxides, presents significant potential as a functional material for diverse applications. These applications extend across chemical engineering, thermal engines, hydrogen separation membranes, actuators, sensors, electrochemical systems, and solid oxide fuel cells [1]. Despite extensive research on the structural, elastic, dielectric, and piezoelectric properties of pristine ABO_3 perovskites and their alloys, further investigation is required to fully harness their potential. The tunable piezoelectric and dielectric responses observed in perovskite solid solutions make them particularly suitable for various technological advancements, including high-dielectric constant capacitors, ferroelectric thin-film memory devices, and transducers used in sensors, actuators, piezoelectric sonars, atomic force microscopes, ultrasonic generators, piezoelectric motors, inkjet printer nozzles, and fuel injectors [2]. The mechanical

response of a material to external macroscopic stress is quantified by its elastic constants. A strong correlation exists between interatomic bonding, mechanical stability, thermal relaxation, and internal strain within the material [3].

COMPUTATIONAL METHOD

Density Functional Theory (DFT) is a quantum mechanical computational method used to investigate the electronic structure of multi-electron systems. Instead of directly solving the Schrödinger equation, DFT calculates the system's energy and other properties based on the ground state electron density, $n(r)$. All computational tasks in this study were performed using the Vienna Ab initio Simulation Package (VASP). The Perdew-Zunger type generalized gradient approximation (GGA) functional was employed to model exchange-correlation effects within the electron-electron interactions. A plane wave basis set with a kinetic energy cutoff of 750 eV was utilized within the projector augmented wave (PAW)

method to describe electron-ion interactions. A 12x12x12 Monkhorst-Pack k-point mesh was adopted to sample the Brillouin zone. Elastic constants were determined through a stress-strain analysis.

STRUCTURAL AND ELASTIC CHARACTERISTICS

Initially, the lattice parameters corresponding to the energy minimum were determined through an optimization process using the VASP program with ISIF = 3, enabling the unit cell volume to relax. Subsequently, energy values were calculated for different lattice constants, and the bulk modulus and its pressure derivative were calculated using the Murnaghan equation of state (EOS).

Table 1. Structural and Elastic characteristics

Basınç (GPa)	a (Å)	B (GPa)	C ₁₁ (GPa)	C ₁₂ (GPa)	C ₄₄ (GPa)	G (GPa)	E (GPa)	ν	B/G
0	5.80	19.7	43.1	8.1	9.3	11.9	29.7	0.2485	1.655
KGeI3[5]		24.13	49.83	11.29	9.21	12.43	31.825	0.280	1.94

The calculated lattice parameters, bulk modulus, and elastic constants align well with those reported in previous studies. Based on the computed elastic constants, the KSiI₃ compound was determined to be mechanically stable. Poisson's ratio provides valuable information regarding the material's microstructure and interatomic bonding. Materials with a low Poisson's ratio tend to be more susceptible to brittle fracture, characterized by high hardness and low ductility. The B/G ratio is a parameter used to assess the tendency of a material to fail in a brittle or ductile manner. A B/G ratio below 1.75 suggests a more brittle material, which fails without significant plastic deformation.

Born mechanical stability conditions;

$$C_{11} > 0, C_{12} > 0, C_{44} > 0, C_{12} > C_{44}, \\ C_{11} + 2C_{12} > 0, C_{11} - C_{12} > 0$$

ELECTRONIC CHARACTERISTICS

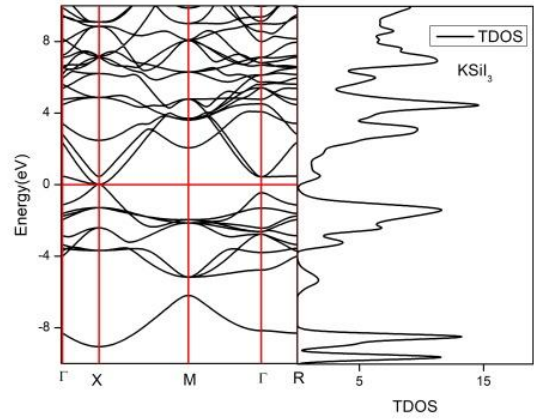


Figure 2. Electronic band structure graph

The electronic band structure is illustrated in Figure 2. For KSiI₃, the energy band gap E_g was calculated to be 0 eV, indicating a semimetal behavior of the compound. However, a previous study [2] reported E_g as 1.027 eV. Recalculations will be conducted using correction terms such as HSE06 or mBJ to address this discrepancy.

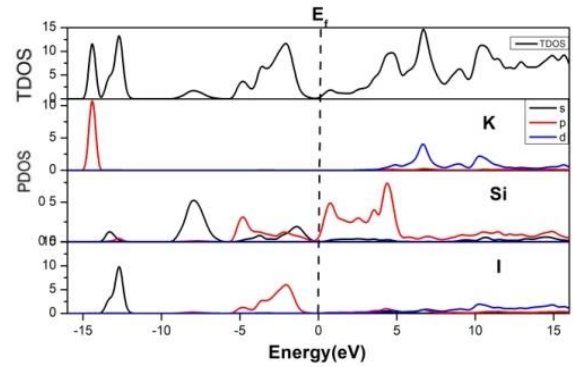


Figure 3. Total and projected density of states

When analyzing the total and partial densities of states, it is evident that the DOS graphs align with the band structure. Within the valence band, between -14 eV and 0 eV, the primary contributions originate from the s and p bands of I and Si atoms. Additionally, the p band of K atoms contributes to the valence band. Furthermore, Si atoms contribute to both the p and s bands near the Fermi level in the valence band. In the conduction band, contributions arise from the d band of K atoms and the p band of Si atoms. A small contribution is also observed from the d band of I atoms. The prominent peaks formed in the valence band near the Fermi energy are characteristic of materials suitable for thermoelectric applications.

OPTICAL CHARACTERISTICS

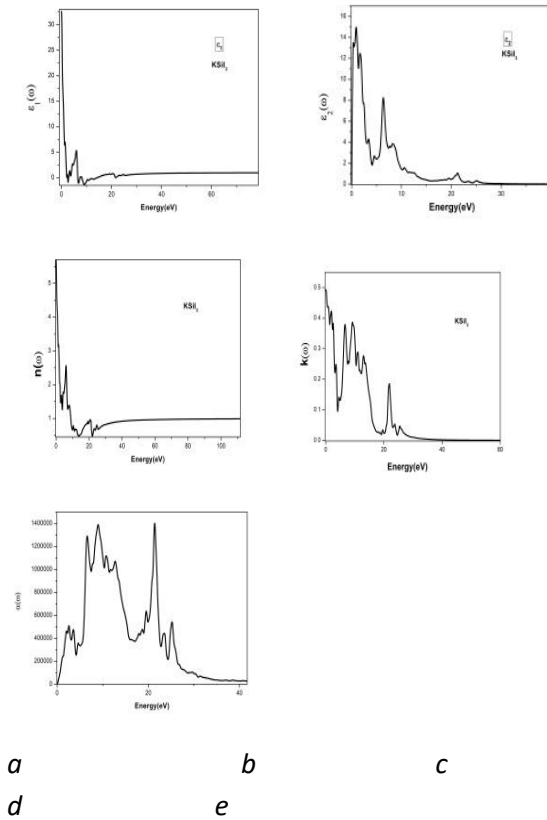


Figure 4. a.) Real Dielectric Constant, b.) Imaginary Dielectric Constant, c.) Refractive index, d.) extinction coefficient, e.) Absorption coefficient

The interaction of materials with electromagnetic radiation is characterized by their optical properties, including the dielectric constant, refractive index, and absorption coefficient. The bulk optical properties of solids in the linear regime are governed by the frequency-dependent dielectric function,

$$\epsilon(\omega) = \epsilon_1(\omega) + i\epsilon_2(\omega),$$

which is significantly influenced by the electronic structure. Optical functions provide valuable insights into the electronic band structure, revealing the fine structure of the electronic energy dispersion within both the valence and conduction bands. The imaginary component of the dielectric function, ϵ_2 , directly correlates the electronic structure with the occurrence of interband transitions. Additionally, the dielectric

function is crucial for studying light absorption, as elevated values of $\epsilon_2(\omega)$ indicate enhanced absorption at specific frequencies. As illustrated in Figure (a), the real part of the dielectric function, $\epsilon_1(\omega)$, exhibits a prominent peak centered at 4.1 eV with an amplitude of 7.78, originating from a constant background value of 6.1. Static dielectric constant $\epsilon_1(\omega) = 25.5$. The dielectric function, $\epsilon(\omega)$, quantifies the probability of electronic transitions between various energy states within a material. An examination of Figure (b) reveals a pronounced peak in $\epsilon_2(\omega)$ at approximately 5 eV, attributed to electronic transitions from the valence band maximum, specifically the 1-p state, to the conduction band minimum, characterized by the Si-p state. These findings align with the density of states (DOS) data. The most prominent peak in the spectrum resides in the ultraviolet range, with a peak energy falling between 5 and 10 eV.

The refractive index, n , signifies the extent to which light slows down and deviates from its original path as it traverses a material. Materials with elevated refractive indices are favored for applications such as lenses and optical fibers. The relatively large refractive index values observed in certain materials are often attributed to their small band gap. The refractive index at zero frequency, $n(0)$, is determined to be 5.5. The highest peaks of the refractive index are situated in the ultraviolet region, while a minimum value is observed around 10 eV. The extinction coefficient, $k(\omega)$, measures the degree to which an electromagnetic wave is attenuated as it propagates through a material and is directly related to the absorption of radiation. The energy-dependent behavior of $k(\omega)$ closely resembles that of the imaginary component of the dielectric function, $\epsilon_2(\omega)$. The maximum peak of $k(\omega)$ occurs at approximately 2 eV. The absorption coefficient, $\alpha(\omega)$, provides valuable information regarding a material's solar energy conversion efficiency and indicates the penetration depth of light at a specific frequency within the material. By analyzing $\alpha(\omega)$, it is possible to assess a material's sensitivity to sunlight, quantifying the number of photons captured within the relevant light range and, consequently, its ability to generate electron-hole pairs. A more in-depth analysis of the calculated absorption spectrum clearly reveals a continuous increase in $\alpha(\omega)$ with increasing energy, culminating in a prominent peak at approximately 10.2 eV. This peak corresponds to the

electronic transition between the valence band maximum and the conduction band minimum, as evidenced by the characteristic peak at 10.2 eV.

CONCLUSION

We have studied detailed physical properties such as structural, elastic, electronic, and optical for KSil_3 in cubic structure. KSil_3 is stable mechanically due to positive elastic constants. From electronic structure calculations, KSil_3 has a semi-metallic character. We have also investigated the optical properties of this material.

REFERENCES

1. S.-W. Baek, Jung Hyun Kim, J. Bae, *Characteristics of ABO₃ and A₂BO₄ (A:Sm, Sr; B:Co, Fe, Ni) samarium oxide system as cathode materials for intermediate temperature-operating solid oxide fuel cell*, Department of Mechanical Engineering, Korea Advanced Institute of Science and Technology, 373-1, Guseong-Dong, Yuseong-Gu, Daejeon, 305-701, Republic of Korea Received 15 July 2007; received in revised form 23 November 2007; accepted 5 December 2007, *Solid State Ionics*, vol. 179, pp. 1570, 2008.
2. W. Guyton Candy, *Piezoelectricity*, McGraw-Hill Book Company, New York, 1946
3. G. Rohrer, M. Affatigato, M. Backhaus, R. Bordia, K.S. Weil, *J. Am. Ceram. Soc.*, *Challenges in Ceramic Science: A Report from the Workshop on Emerging Research Areas in Ceramic Science*, Soc.vol. 95, pp. 3699, 2012.
4. Muhammad Khuram Shahzad, *ab Syed Taqveem Mujtaba, c Shoukat Hussain, ab Jalil Ur Rehman, ab Muhammad Umair Farooq, d Muhammad Aslam Khan, ab Muhammad Bilal Tahirab and Muhammad Ali Mahmoodef, *Zirconium-based cubic-perovskite materials for photocatalytic solar cell applications: a DFT study*
5. Md. Adnan Faisal Siddique a, Abu Sadat Md. Sayem Rahman b,*, *The SCAPS-1D simulation of non-toxic KGeCl₃ perovskite from DFT derived properties*, a Institute of Energy Technology (IET), Chittagong University of Engineering & Technology (CUET), Chittagong 4349, Bangladesh b Department of Materials Science and Engineering (MSE), Chittagong University of Engineering and Technology (CUET), Chittagong 4349, Bangladesh, *Materials Science and Engineering B* 303 (2024) 117268

Scaling up Superconducting Quantum Processors: Materials and Fabrication Challenges

Hasan M. Nayfeh

IBM T.J. Watson Research Center, Yorktown Heights, New York 10598

Abstract. Scaling up quantum processors based on superconducting qubits will require continued technology improvements in the areas of qubit quality, gate performance, and scalable microwave signal generation and delivery. In recent years at IBM, we have delivered improvements in gate-based superconducting processors that break the 100-qubit barrier, and we have demonstrated coherence time approaching 1 msec on individual qubits. We have demonstrated the capability of solving problems at a scale beyond brute force classical simulation using error mitigation, ushering in the era of quantum utility. Despite these positive developments, fabrication and design challenges need to be overcome to reduce noise and errors further to continue scaling towards the goal of eventual fault-tolerant computation, which requires the capability of running error correction protocols. A key challenge to realize high fidelity quantum circuits, which are the fundamental unit of quantum computation, is coherence stability and reproducibility. This is limited primarily by qubit interactions with two-level systems (TLS) attributed to defects in amorphous materials present at interfaces in the transmission line resonators and Josephson junction (JJ) tunnel barriers. Our hardware development roadmap outlines our plan to extend the utility era by reducing gate errors using a tunable gate architecture that results in faster gates with less crosstalk, improving qubit coherence with TLS mitigation, and increasing qubit count using a modular chip architecture enabled by inter-chip couplers. Finally, increasing qubit connectivity by integrating multi-qubit couplers will enable error correction protocols that can be implemented with a manageable number of qubits.

Keywords: quantum computing, superconducting qubits, interface science, material defects

© 2024 Published by ICMATSE

Illumination Effects on Capacitance-Voltage Characteristics and Negative Capacitance Behavior in Au/n-GaAs (MS) And Au/Si₃N₄/n-GaAs (MIS) Type Structures

Mahmut Bucurgat

*Gazi University Faculty of Science - Department of Physics, 06500, Ankara, Türkiye,
mahmut.bucurgat@gazi.edu.tr
ORCID: 0000-0002-6368-1945*

Bucurgat, M. Illumination Effects on Capacitance-Voltage Characteristics and Negative Capacitance Behavior in Au/n-GaAs (MS) And Au/Si₃N₄/n-GaAs (MIS) Type Structures. Int. Conf. Advanced. Mater. Sci. & Eng. HiTech. and Device Appl. Oct. 24-26 2024, Ankara, Turkiye

Abstract. The illumination effects on the capacitance-voltage (C-V) characteristics were investigated in the voltage range of $\pm 2V$ for 1 MHz both in dark and under 100 mW/cm² illumination-intensity on the Au/n-GaAs (MS) and Au/Si₃N₄/n-GaAs (MIS) structures. Experimental results show that the capacitance is a strong function of illumination in the reverse-bias region due to the strong electric field in this region; and hence, obstacles the recombination of illumination induced electron-hole pairs. The C-V plot of MIS type structure both in dark and under illumination shows an abnormal peak at almost 0.9 V; and then, it decreases rapidly after the peak value and tends to continue to negative values of capacitance at 1.9 V. On the other hand, the MS type structure has peaks close to 0.8 V in dark and 0.2 V under illumination; then, tends to decrease to negative values similar to MIS type structure. The effect of the surface states (N_{ss}) on C-V relation is analyzed with the dark-illumination capacitance ($C_{dark-C_{ill}}$) method. It is interpreted that the negative capacitance (NC) appearing on the C-V relation is the result of the existence of N_{ss} at interlayer/semiconductor interface, series resistance (R_s) of the structure, the loss of interface charge at occupied states due to impact ionization. The observation of NC was attributed to instrumental problems by some researchers; or, some others probably did not report to prevent any confusion. Some basic electrical parameters such as diffusion-potential (V_D), Fermi-energy (E_f), doping concentration of donor-atoms (N_D), and barrier-height ($\Phi_B(C-V)$) were also obtained from the intercept and slope reverse-bias C^{-2} -V plot.

Keywords: Illumination and voltage dependence of capacitance; Negative capacitance; Surface states and series resistance

© 2024 Published by ICMATSE

Introduction

Metal-semiconductor (MS) and metal-interlayer-semiconductor (MIS) type diodes, photodiodes, solar cells are used widely in electric and optoelectronic applications. Today, the main problem of these structures is to improve the performance of them and reduce the manufacturing costs. There are many factors affecting the performance and efficiency of these devices such as the interlayer between metal and semiconductor –and its thickness- and the value of dielectric constant, the nature of the barrier height at M/S interface, R_s , doping level of donor or acceptor atoms, temperature, frequency, illumination intensity, voltage, etc. [1-5]. When an interlayer is grown on M/S interface by using various techniques, MS type diodes converts to MIS type diodes or solar cells [6-9].

These devices must be fabricated under special conditions; otherwise, many surface states or traps can occur at interlayer/semiconductor interface, located in the forbidden bandgap of the semiconductor. They are usually originated from the doping donor and acceptor atoms into semiconductor, unsaturated dangling bonds, some disorders in the periodic lattice, some organic impurities in the laboratory conditions, and oxygen vacancies [1-4,6-7]. The other important electric parameters on the I-V and C-V measurements are the series resistance of the structure and it can be originated the formation of back-ohmic and front rectifier contacts, the resistivity of bulk semiconductor, and the used wires to get electric measurements. The use of high dielectric interlayer such as insulators, polymers, metal oxides can reduce the leakage current, R_s and N_{ss} [10-14]. Since, a photodiode or a solar cell

were exposed to light which its energy higher than the bandgap energy of semiconductor ($hc/q\lambda \geq Eg$), many electron hole pairs are created at M/S interface and then they move in different directions ($F = \pm qE$) under interior electric field at junction [15-17] which produce a photocurrent and this situation is known as photovoltaic event in the literature.

(Au:Ti)/n-GaAs (MS) and Au/Si₃N₄/n-GaAs (MIS) diodes were grown by Atomic Layer Deposition (ALD) technique onto n-GaAs wafer with $6.8 \times 10^{15} \text{ cm}^{-3}$ doping donor atoms. C-V measurements were taken at 1 MHz between $\pm 2\text{V}$ by 50 mV steps both in dark and under 100 mW/cm^2 at room temperature.

Results and Discussion

The value of the capacitance increases with increasing applied voltage until accumulation region and then goes to zero which is known as negative capacitance (NC) in the literature (Fig.1. (a)-(b)). NC in different electronic devices are usually different and, in general, is attributed to ohmic and rectifier contacts, surface states, series resistance and minority carrier injection. According to Champness et al. [18], NC means that material displays an inductive behavior while the value of conductance starts to increase, capacitance decreases. Gökçen et al. [19] have also explained the NC effect with the theory of injection and relaxation by minority carriers and surface states. On the other hand, according to Butcher et al. [20], Huang et al. [21], such NC or negative dielectric behavior is the result of instrumental problems. As can be seen in Fig. 1.(a)-(b), the tendency of the magnitude of NC decreases due to the Si₃N₄ interfacial insulator layer. Because, interfacial layer passivates N_{SS} and this improves the performance of the MS structure.

The voltage dependent profile of N_{SS} was obtained from ($C_{dark}-C_{ill}$) method for MS and MIS type diodes by using the following relation [1,2]:

$$qAN_{SS} = \left[\left(\frac{1}{C_{ill}} - \frac{1}{C_i} \right)^{-1} - \left(\frac{1}{C_{dark}} - \frac{1}{C_i} \right)^{-1} \right] \quad (1)$$

In Eq.(1), A is the rectifier contact area of the diode, q is the electronic charge, C_{dark} and C_{ill} are the measured capacitance in dark and under 100 mW/cm^2 illumination intensity at any bias voltage, and C_i is the interfacial layer capacitance. Voltage dependent N_{SS} shows a peak behavior in the forward/positive bias region for both MS and MIS type diodes (Fig.2 (a)-(b)). The observed shifts in the peak position can be attributed to a special density distribution of N_{SS} and

their life time/relaxation time and reordered/restructure under illumination and electric field [1,3,4,10]. It is clear that, the mean value of N_{SS} for MIS diode is almost one order lower than the MS diode's due to the interfacial layer effect.

Some important electrical parameters MS and MIS type diodes, both in dark and under 100 mW/cm^2 illumination intensity, were obtained by the use of the reverse bias C^2-V plots and given in Fig. 3.(a)-(b), respectively. These plots display convenient linear regions in wide range of applied bias voltage at 1 MHz and analyzed with the reverse bias C-V relations as follows [1, 3]:

$$C^{-2} = \left(\frac{2}{q\epsilon_s\epsilon_0 N_D A^2} \right) (V_0 + V) \quad (2)$$

In Eq.2, ϵ_s and ϵ_0 are the semiconductor and free space dielectric constants, respectively. According to Eq.2, N_D value can be obtained directly from the slope and intercept/ordinate point, the values of E_F , W_D , $\Phi_B(C-V)$, and W_D can be determined directly from the linear part of the C^2-V plots by using the following expressions [1,3,22,23] and given in Table 1.

$$E_F = \frac{kT}{q} \ln \left(\frac{N_C}{N_D} \right) \quad (3a)$$

$$W_D = \left(\frac{2\epsilon_s\epsilon_0 V_D}{qN_D} \right)^{0.5} \quad (3b)$$

$$\Phi(C - V) = c_2 V_0 + \frac{kT}{q} + E_F = V_D + E_F \quad (3c)$$

The existence of N_{SS} and an interlayer at M/S interface leads to a large intercept point in the C^2-V plot. However, this situation can easily be overcome by applying modification to Φ_B values with $c_2 (=N_{exp}/N_{theor} \cong 1/n)$ [1,3,4].

Conclusion

Basic electrical parameters obtained from the reverse bias C^2-V plot both in dark and under illumination may be different for MS and MIS type diodes as well as forward bias $\ln(I)-V$ characteristics due to the nature of the calculation method, a special energy density distribution of N_{SS} , R_s , barrier inhomogeneity and interfacial layer. In addition, it is seen that a high dielectric interlayer such as high dielectric Si₃N₄ usage leads to improve the performance of conventional MS type diode in respect of high barrier height and low surface states.

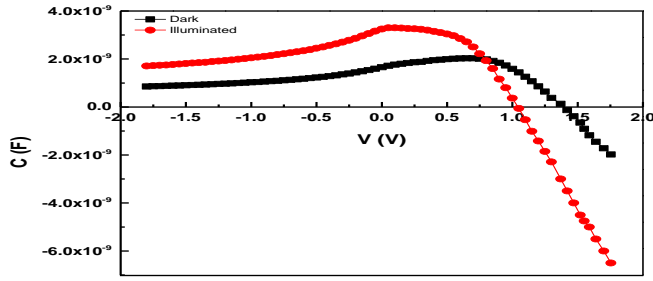


Figure 1.a. C-V graph of reference (Au:Ti)/n-GaAs (MS) type diode both in dark and under 100mW.cm⁻² illumination intensity.

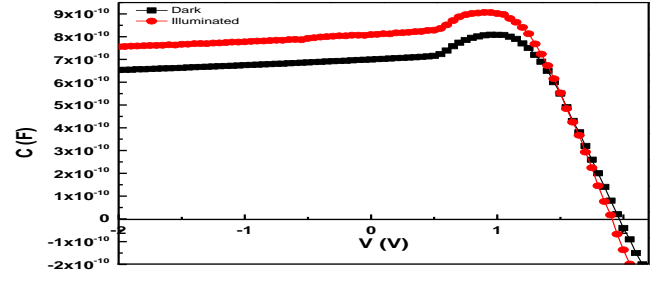


Figure 1.b. C-V graph of (Au:Ti)/Si₃N₄/n-GaAs (MIS) type diode both in dark and under 100 mW.cm⁻² illumination intensity.

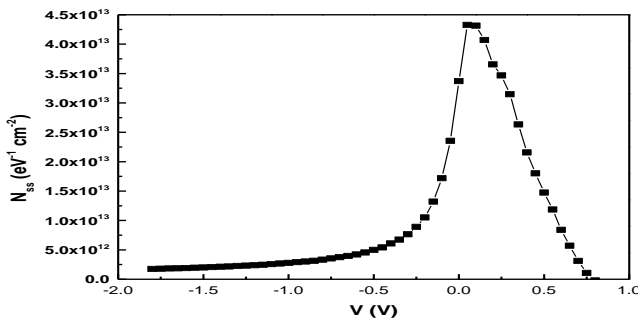


Figure 2.a. N_{ss} graph of reference (Au:Ti)/n-GaAs (MS) type diode.

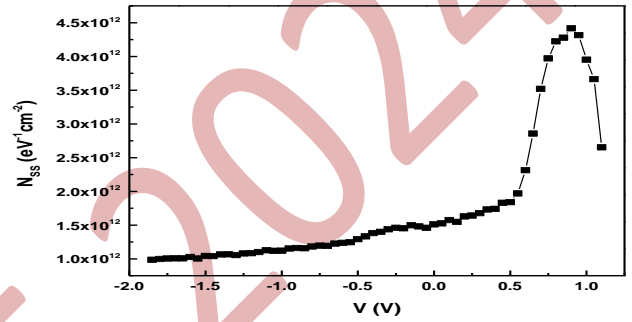


Figure 2.b. N_{ss} graph of (Au:Ti)/Si₃N₄/n-GaAs (MIS) type diode.

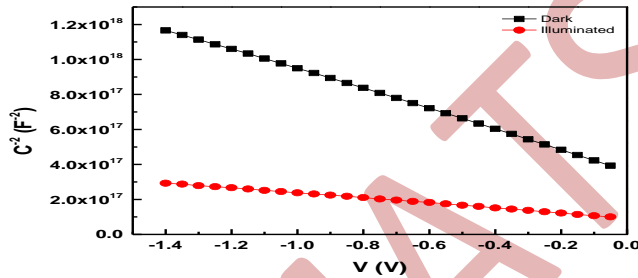


Figure 3.a. C²-V plots of reference (Au:Ti)/n-GaAs (MS) type diode both in dark and under 100 mW.cm⁻² illumination intensity.

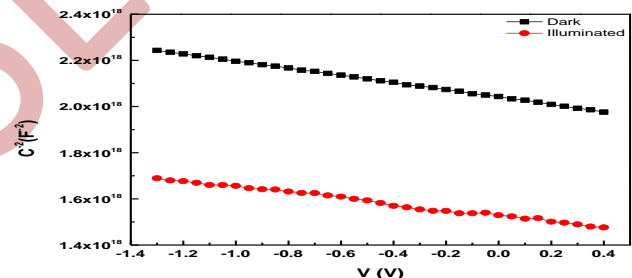


Figure 3.b. C²-V plots of (Au:Ti)/Si₃N₄/n-GaAs (MIS) type diode both in dark and under 100 mW.cm⁻² illumination intensity.

Table 1. Basic electrical parameters of (Au:Ti)/n-GaAs structure with/without Si₃Ni₄ interlayer in dark and under illumination of 100 mW/cm².

Parameters	(Au:Ti)/n-GaAs (MS)		(Au:Ti)/Si ₃ N ₄ /n-GaAs (MIS)	
	Dark	Illuminated	Dark	Illuminated
E_F (eV)	0.649	0.658	0.784	0.752
N_D (cm ⁻³)	2.02x10 ¹⁶	8.08x10 ¹⁶	7.43x10 ¹⁶	9.18x10 ¹⁶
$[\Phi_B(C-V)]$ (eV)	0.753	0.727	0.855	0.791
W_D (μm)	21.0	10.5	12.0	10.4

References

- [1] S. M. Sze and Kwok K. Ng, Physics of Semiconductor Devices, 3rd ed. 2007 New Jersey: John Wiley & Sons.
- [2] N. A. Al-Ahmadi, Metal oxide semiconductor-based Schottky diodes: A review of recent advances, Mater. Res. Express, 7 (2020) 032001.
- [3] B. L. Sharma, Metal-Semiconductor Schottky Barrier Junctions and Their Applications, 1984 Plenum Press New York.
- [4] H. C. Card, E. H. Roderick, Studies of tunnel MOS diodes I. Interface effects in silicon Schottky diodes, J. Phys. D: Appl. Phys., 4 (1971) 1589-1601

- [5] E. Özavcı, S. Demirezen, U. Aydemir, Ş. Altındal, A detailed study on current-voltage characteristics of Au/n-GaAs in wide temperature range, *Sens. Actuators A*, 194 (2013) 259–268.
- [6] M. M. Bülbül, S. Zeyrek, Ş. Altındal, H. Yüzer, On the profile of temperature dependent series resistance in Al/Si₃N₄/p-Si (MIS) Schottky diodes, *Microelectron. Eng.*, 83 (2006) 577–581.
- [7] D. S. Reddy, V. Janardhanam, V. R. Reddy, C. J. Choi, Modification of interface properties of Au/n-GaN Schottky junction by rare-earth oxide Nd₂O₃ as an interlayer and its microstructural characterization, *Vacuum*, 215 (2023) 112300.
- [8] V. R. Reddy, V. Manjunath, V. Janardhanam, Y. H. Kil, C. J. Choi, Electrical properties and current transport mechanisms of the Au/n-GaN Schottky structure with solution processed high-k BaTiO₃ interlayer, *J. Electron. Mater.*, 43 (2014) 3499–3507.
- [9] E. E. Tanrikulu, I. Taşçıoğlu, Variation of the surface states and series resistance depending on voltage, and their effects on the electrical features of a Schottky structure with CdZnO interface, *J. Electron Mater.*, 52 (2023) 2432-2440.
- [10] A. Tataroglu, Ş. Altındal, Analysis of electrical characteristics of Au/SiO₂/n-Si (MOS) capacitors using the high–low frequency capacitance and conductance methods, *Microelectronic Engineering*, 85 (2008) 2256–2260.
- [11] E. Yükseltürk, O. Surucu, M. Terlemezoglu, Illumination and voltage effects on the forward and reverse bias current–voltage (I-V) characteristics in In/In₂S₃/p-Si photodiodes, *Journal of Materials Science: Materials in Electronics*, 32 (2021) 21825–21836.
- [12] E. Yükseltürk, M. M. Bülbül, S. Zeyrek, The effects of illumination on electrical parameters of Au/P3HT/n-Si Schottky barrier diode, *AIP Conference Proceedings*, 1 (2016) 1722.
- [13] H. Elamen, Y. Badali, M. Ulusoy, Y. A. Kalandaragh, Ş. Altındal, M. T. Güneşer, The photoresponse behavior of a Schottky structure with a transition metal oxide-doped organic polymer (RuO₂:PVC) interface, *Polymer Bulletin*, 81 (2024) 403-422.
- [14] E. Orhan, A. Anter, M. Ulusoy, B. Polat, C. Okuyucu, M. Yıldız, Ş. Altındal, Effect of Gadolinium on electrical properties of polyethyleneimine functionalized and nitrogen-doped graphene quantum dot nanocomposite based diode, *Advanced Electronic Materials*, 9 (2023) 2300261.
- [15] S. Demirezen, M. Ulusoy, H. Durmuş, H. Cavusoglu, K. Yılmaz, Ş. Altındal, Electrical and photodetector characteristics of Schottky structures interlaid with P(EHA) and P(EHA-co-AA) functional polymers by the ICVD Method, *ACS Omega* 8 (2023) 46499-46512.
- [16] M. Saad, A. Kassis, Analysis of illumination-intensity-dependent j–V characteristics of ZnO/CdS/CuGaSe₂ single crystal solar cells, *Sol. Energy Mater. Sol. Cells*, 77 (2003) 415–422.
- [17] H. Elamen, Y. Badali, M. Ulusoy, Y. A. Kalandaragh, Ş. Altındal, M. T. Güneşer, The photoresponse behavior of a Schottky structure with a transition metal oxide-doped organic polymer (RuO₂: PVC) interface, *Polym. Bull.*, 81 (2024) 403-22.
- [18] C. H. Champness, W. R. Clark, Anomalous inductive effect in selenium Schottky diodes, *Applied Physics Letters*, 56 (1990) 1104.
- [19] H. G. Çetinkaya, D. E. Yıldız, Ş. Altındal, On the negative capacitance behavior in the forward bias of Au/n–4H–SiC (MS) and comparison between MS and Au/TiO₂/n–4H–SiC (MIS) type diodes both in dark and under 200 W illumination intensity, *International Journal of Modern Physics B*, 29 (2015) 1450237.
- [20] K. S. A. Butcher, T. L. Tansley, D. Alexiev, An instrumental solution to the phenomenon of negative capacitances in semiconductors, *Solid State Electronics*, 39 (1996) 333-336.
- [21] X. L. Huang, Y. G. Shin, K. Y. Lim, E. K. Suh, H. J. Lee, S. C. Shen, *Solid State Electronics*, 41 (1997) 845-850.
- [22] H. G. Cetinkaya, A. F. Vahid, N. Basman, S. Demirezen, Y. S. Asar, Ş. Altındal, On the wide range frequency and voltage dependence of electrical features and density of surface states of the Al/(Cu:DLC)/p-Si/Au Schottky diodes (SDs), *Journal of Materials Science: Materials in Electronics*, 34 (2023) 822.
- [23] Ç. Ş. Güçlü, A. F. Özdemir, A. Kökce and Ş. Altındal, Frequency and voltage-dependent dielectric properties and ac electrical conductivity of (Au/Ti)/Al₂O₃/n-GaAs with thin Al₂O₃ interfacial layer at room temperature. *Acta Physica Polonica A*, 129 (2016) 325-330.

Effect of WC Addition on Fe-B/WC Laser Composite Coating

Mehmet Eroglu

*Firat University, Faculty of Engineering, Department of Metallurgical and Materials Engineering, Elazig, Turkiye,
meroglu@firat.edu.tr*

ORCID: 0000-0002-5097-1943

Cite this paper as: Eroglu, M., Effect of WC Addition on Fe-B/WC Composit Coating, Int. Conf. Advanced. Mater. Sci.& Eng. HiTech.and Device Appl.Oct. 24-26 2024, Ankara, Turkiye

Abstract. In this study, Fe-B eutectic powders were produced by gas atomization and then mixed with WC powders with different ratios (5, 10, 20 wt.%). Laser coating processes were carried out using prepared mixed powders. After the coating process, microstructures in the coating area were examined, hardness values were measured and wear tests were performed. In the microstructural examinations, it was observed that the matrix phase generally consisted of primary (pearlite) and eutectic phases and WC particles partially dissolved and precipitated in the matrix phase. It was observed that the hardness and wear resistance increased with the increase in the WC ratio in the matrix phase. As a result, it was concluded that such an application can be used in the coating industry.

Keywords: Laser cladding, WC, Wear, Hardness, Boride

© 2024 Published by ICMATSE

Laser cladding (LC) is a sophisticated surface modification technology where a laser is used to melt both the filler material (powder or wire) and the substrate, creating a coating on the substrate's surface. This process enhances the substrate's wear and corrosion resistance. LC stands out due to its high efficiency, low pollution emissions, and capability to produce coatings with different thicknesses, offering significant advantages over traditional surface treatment methods. Additionally, the rapid cooling rate inherent to LC helps refine grain structures and stabilize the phase of the material. Furthermore, laser-clad coatings typically exhibit a low dilution rate and robust metallurgical bonding with the substrate. This characteristic has garnered significant attention, making laser cladding a prominent focus of contemporary research. Its applications are broad and impactful, extending to critical fields such as aerospace, metallurgy, and engineering machinery [1-5].

Laser cladding (LC) employs various types of powders, including self-fusing alloy powders, ceramic powders, and composite powders. Self-fusing alloy powders, such as Fe-based [6], Ni-based [7], and Co-based alloys [8], are designed to form a metallurgical bond with the substrate. Among these, Fe-based alloys are particularly compatible with steel substrates due to their similar composition, resulting in strong interfacial bonding. Additionally, Fe-based alloy powders are cost-effective, making them popular in LC applications. However, they generally exhibit

poorer self-melting properties and weaker corrosion resistance compared to Ni-based and Co-based alloys.

Ceramic powders, like WC (tungsten carbide), are known for their high hardness and excellent wear resistance, which can significantly enhance the wear properties of LC coatings. Composite powders, which combine ceramic and metal powders, are becoming increasingly popular in LC research. These powders aim to harness the benefits of both materials, offering improved performance in various applications [3-5]. This study aims to explore how the Fe-B based powder and Fe-B base powder with tungsten carbide (WC) affect the morphology, microstructure, and properties of laser coatings. Specifically, Fe-B based LC coatings with varying WC content were applied to St37 structural steel to enhance the wear resistance. The outcomes of this research are anticipated to offer valuable insights and technical support for the repair and manufacturing of wear resistance materials.

In the study, low carbon steel (St 37), the analysis of which is given in Table 1, was used. The samples with dimensions of 10 x 100 x 10 mm was coated with Fe-B based powder and Fe-B/WC powder mixtures. For this purpose, Fe-B based powders were first produced by gas atomization method and the size range was between 50-150 microns. The image of Fe-B based alloy powders is shown in Figure 1.

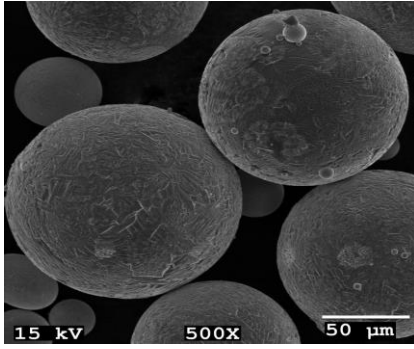


Figure 1. SEM micrograph of Fe-B alloy powder

Chemical analysis of Fe-B based powder is given in Table 2. WC powders were mixed with Fe-B powders at the rates of 5, 10, 20 wt.%. The size range of WC powders was between 75-44 microns. Sample coding is shown in Table 3. Prepared mixtures were bonded to the surface with PVA in 4 mm thickness and laser melting processes were performed. 3 mm/sec scanning speed and 1.6 kW laser power were used in laser melting process. From the coated St37 steels, samples were taken out for microstructure examination in the coating area and these were subjected to necessary grinding and polishing processes. The samples were last passed through 3 micron diamond paste and etched in 3% nital solution. Images of the samples were taken under SEM at different magnifications and micro analyses were performed with EDX. In addition, XRD analyses were performed. Micro-hardness measurements of the coatings were carried out at 200-micron intervals from the top of the coating to the substrate under a load of 200 g. Dry-sliding wear tests were carried out using a ball-on-disk dry-sliding wear tester using a WC ceramic ball with a diameter of 6 mm at room temperature. The tests were conducted under loads of 10N, 20N, and 30N at 8 mm/s for 1800 seconds. After the wear tests, the wear volume losses of the samples were determined using a 3D profilometer.

For X-ray and wear tests on the coatings, multi-pass coatings were applied side by side with 50% overlap on 20 mm x 20 mm x 10 mm samples and their surfaces were subjected to the necessary polishing process before the tests.

Table 1. Chemical composition of St 37 steel (wt.%)

C	Mn	Si	P	S	Fe
0.16	0.52	0.25	0.02	0.02	Rest

Table 2. Chemical composition of Fe-B based powder (wt.%)

C	Mn	Si	Cr	B	Fe
0.23	0.91	0.93	1.35	3.80	Rest

Table 3. Fe-B powder and WC powder ratios (wt.%)

	Fe-B	WC
S1	100	-
S2	95	5
S3	90	10
S4	80	20

SEM micrographs of samples are given in Figure 2.

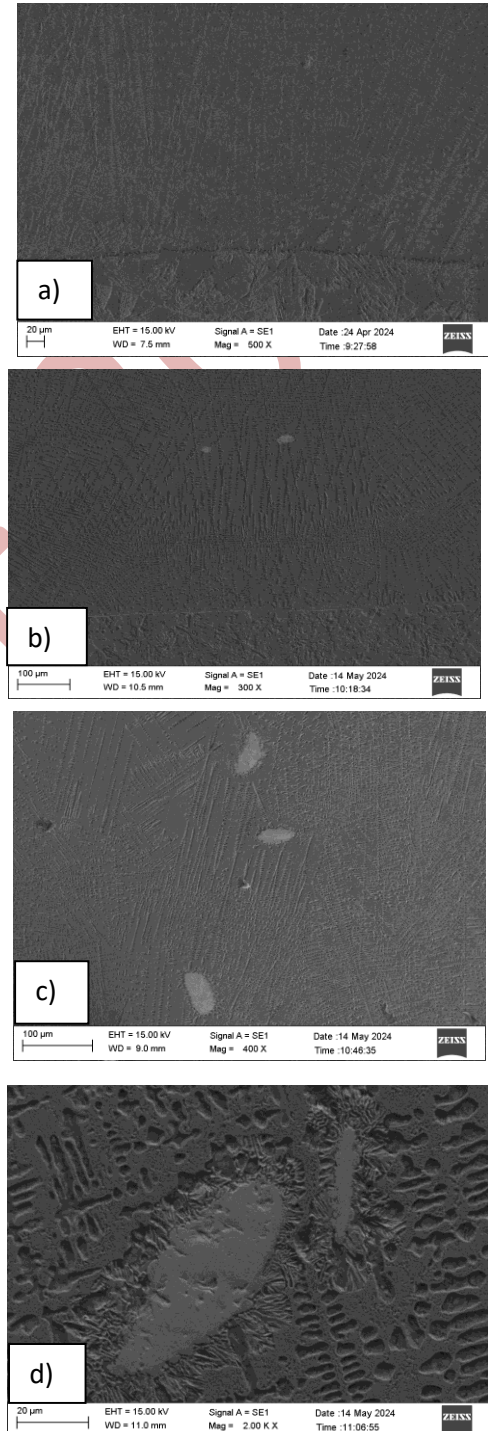


Figure 2. SEM micrographs of samples; a) S1 (substrate + coating), b) S2 (substrate + coating), c) S3 (coating), d) S4 (coating)

Microstructure of S1 exhibits a proeutectic structure, and the microstructure consists mostly of pearlite +eutectic(Fe₂B + ferrite/cementite/pearlite) structure. This situation can be explained as follows. Fe-B based powder, which has an approximately eutectic structure, melts with the laser beam and a certain amount of iron transfers from the substrate to the coating. Thus, the eutectic structure shifts towards the proeutectic structure. Samples S2, S3 and S4 also exhibited similar matrix microstructure as S1.

As can be seen from these microstructure images, WC powders passed into the coatings. The X-ray results are given for S1 and S4 in Figure 3, and as a representative example of the EDX analyses, the EDX results obtained from sample S4 are given in Figure 4, Table 4 and Table 5, respectively. The existing phases and compounds are quite consistent with these results. With the increase in the amount of WC in the mixed powder, the amount of WC passing into the coating naturally increases, and changes are also observed in the compounds formed depending on the increase in the ratio. When the microstructure images, EDX and XRD results are evaluated together, it is seen that WCs are dissolved slightly [9].

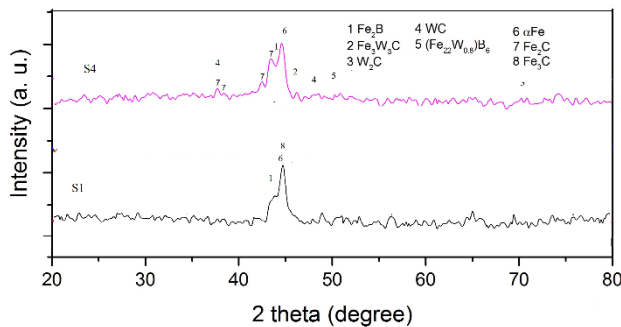


Figure 3. XRD graphs of S1 and S4.

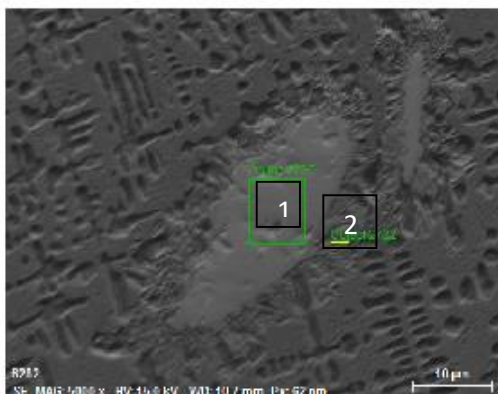


Figure 4. SEM micrograph of S4 showing EDX points.

Table 4. EDX results of Region 1

El	AN	Series	unn. C [wt.%]	norm. C [wt.%]	Atom. C [at.%]	Error (1 Sigma) [wt.%]
W	74	L-series	96.68	97.05	68.25	3.45
C	6	K-series	2.94	2.95	31.75	0.67
Total:			99.62	100.00	100.00	

Table 5. EDX results of Region 2

El	AN	Series	Net	unn. C [wt.%]	norm. C [wt.%]	Atom. C [at.%]	Error (1 Sigma) [wt.%]
W	74	L-series	11129	46.69	52.85	19.85	1.72
Fe	26	K-series	34728	36.22	40.99	50.69	1.11
C	6	K-series	2246	4.25	4.81	27.67	0.81
Cr	24	K-series	1803	1.19	1.35	1.79	0.07
Total:				88.36	100.00	100.00	

As a result of the microhardness measurements, the average hardness values obtained from the samples are presented in Table 6. As can be seen from these values, coating the surface of a low-carbon steel with Fe-B based powder using a laser increased the surface hardness. Additionally, the addition of WC powder to the Fe-B based powder further increased the hardness. Considering that the hardness of the coated low-carbon steel is 175 HV, the hardness increased approximately 3.6 times with the Fe-B alloy powder and up to 4 times with the addition of WC.

Table 6. Average hardness values of coatings (HV_{0.2})

S1	640
S2	653
S3	668
S4	710
St 37	175

These results are also consistent with the literature [3-9]. However, the Fe-B eutectic alloy powder was produced and used for the first time in this study. In this regard, these results have been contributed to the literature through this study.

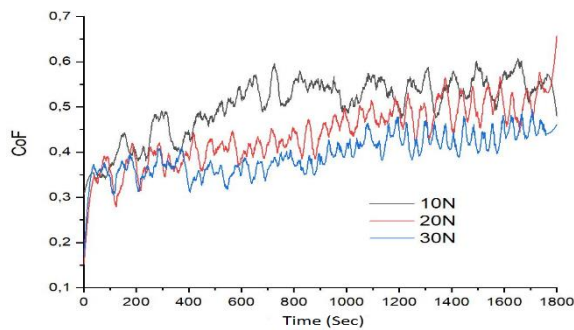
As a result of the wear test, the volume losses are presented in Table 7 and the friction coefficients (COFs) are presented in Table 8 for all specimens and in Figure 5 for the S4. As can be seen from these values, laser coating with Fe-B based powder protects the surface of low-carbon steel against wear. The Fe-B based powder is observed to be effective in terms of wear resistance, and the addition of WC powder further increases the wear resistance [5-9].

Table 7. Wear volume loose values of specimens

Load (N)	S1	S2	S3	S4
10	115.7	109.5	98.4	91.7
20	127,4	119.5	110.9	101.9
30	145.5	135.7	131.8	125.7

Table 8. Friction coefficient values of specimens

Load (N)	S1	S2	S3	S4
10	0.62	0.61	0.59	0.57
20	0.60	0.58	0.54	0.52
30	0.54	0.51	0.49	0.45


Figure 5. COF values of S4

In this study, Fe-B based powder was produced and a low carbon steel was coated with laser beam by adding WC powder to this powder at 5 wt.%, 10 wt.% and 20 wt.% ratios. As a result of the experimental study, the following conclusions were reached:

- Coating made with Fe-B based powder, the coating microstructure consisted of pearlite + eutectic structure.
- Coatings made with Fe-B/WC powder mixture, WC passed into the coating and these partially dissolved,
- Fe-B based powder increased hardness and wear resistance,
- Adding WC powder to Fe-B based powder further increased hardness and wear resistance,
- The maximum values of hardness and wear resistance were obtained at 20 wt.% WC ratio,
- Fe-B based powder and WC mixed powders can be effectively used in laser surface coating.

Acknowledgements

This project was supported by the Firat University Scientific Research Projects Management Unit (FÜBAB) under project number ADEP.23.15.

References

1. Z. Shengbin, J. Chenpeng, Y. Yuxue, W. Lixin, H. Yiming, Y. Lijun, Effects of laser remelting on microstructural characteristics of Ni-WC composite coatings produced by laser hot wire cladding, *J. Alloy. Compd.*, 908 (202), 164612.
2. S. Zhao, S. Xu, L. Yang, Y. Huang, WC-Fe metal-matrix composite coatings fabricated by laser wire cladding, *J. Mater. Process. Technol.*, 301 (2022), 117438.
3. J.M. Pelletier, M.C. Sahour, M. Pilloz, A.B. Vannes, Influence of processing conditions on geometrical features of laser claddings obtained by powder injection, *J. Mater. Sci.*, 28 (1993), pp. 5184–5188.
4. F. Meyer, J.F. Mathieu, D. Cesario, J.M. Pelletier, Production of Ti/TiC dispersoid coatings on titanium base alloys by laser treatment, *Lasers Eng.* 4 (1995), 263.
5. A. Hidouci, J.M. Pelletier, Microstructure and mechanical properties of MoSi₂ coatings produced by laser processing, *Mater. Sci. Eng. A.*, 252 (1998), pp. 17–26.
6. Q. Wang, R. Qian, J. Yang, W. Niu, L. Zhou, X. Pan, C. Su, Effect of high-speed powder feeding on microstructure and tribological properties of Fe-based coatings by laser cladding, *Coatings*, 11 (2021), 1456.
7. J. Ju, Z. Shen, M. Kang, J. Zhang, J. Wang, On the preferential grain boundary oxidation of a Ni-Co-based superalloy, *Corros. Sci.*, 199 (2022), 110203.
8. R. Liu, M. Zhang, J. Yu, Q. Yang, S. Gao, Microstructural transformation and high-temperature aluminum corrosion properties of Co-based alloy coating prepared by laser cladding, *Coatings*, 12 (2022), 603.
9. Z. Shengfeng, D. Xiaoqin, Z. Haizhong, Microstructure and wear resistance of Fe-based WC coating by multi-track overlapping laser induction hybrid rapid cladding, *optics and laser technol.*, 44 (2012), pp. 190-197.

Laser-induced structural modifications and surface functionalization of metallic oxide thin films: HfO₂, ZnO and Cu₂O

Alejandro Frechilla

*Instituto de Nanociencia y Materiales de Aragón, INMA (CSIC-Universidad de Zaragoza), 50018 Zaragoza, Spain,
afrechi@unizar.es
ORCID: 0009-0007-9057-3943*

Luis A. Angurel

*Instituto de Nanociencia y Materiales de Aragón, INMA (CSIC-Universidad de Zaragoza), 50018 Zaragoza, Spain,
angurel@unizar.es
ORCID: 0000-0001-5685-2366*

David Muñoz-Rojas

*Instituto de Nanociencia y Materiales de Aragón, INMA (CSIC-Universidad de Zaragoza), 50018 Zaragoza, Spain,
david.munoz-rojas@grenoble-inp.fr
ORCID: 0000-0003-1234-0814*

José Ángel Pardo

*Instituto de Nanociencia y Materiales de Aragón, INMA (CSIC-Universidad de Zaragoza), 50018 Zaragoza, Spain,
jpardo@unizar.es
ORCID: 0000-0002-0111-8284*

Germán F. de la Fuente

*Instituto de Nanociencia y Materiales de Aragón, INMA (CSIC-Universidad de Zaragoza), 50018 Zaragoza, Spain,
xerman@unizar.es
ORCID: 0000-0002-0500-1745*

Cite this paper as: Frechilla, A, Angurel, LA, Muñoz-Rojas, D, Pardo, J, de la Fuente, GF, A. Laser-induced structural modifications and surface functionalization of metallic oxide thin films: HfO₂, ZnO and Cu₂O, Int. Conf. Advanced. Mater. Sci. & Eng. HiTech. and Device Appl. Oct. 24-26 2024, Ankara, Turkiye

Abstract. Laser processing of thin films is a powerful technique for tailoring material properties with high precision, enabling advancements in various applications such as electronics, photonics, and functional coatings. In this study, we explore the effects of laser irradiation on the crystallization of thin films made from different metallic oxides: HfO₂, ZnO, and Cu₂O. Laser processing induces significant phase transformations and microstructural changes in these oxide coatings. Specifically, we observe the transition from amorphous to crystalline phases, along with corresponding modifications in grain size, crystallographic orientation, and surface morphology.

In addition to crystallization changes, we observe significant alterations in the intrinsic properties of the thin films, including changes in the electrical resistance of ZnO and Cu₂O films, as well as the emergence of ferroelectric behavior in laser-annealed HfO₂ films. The study provides insights into the underlying mechanisms driving these transformations and demonstrates the versatility of laser processing as a tool for engineering thin films with customized properties. These findings hold great potential for the development of advanced materials with specific optical, electronic, and surface functionalities, opening new pathways for innovative applications in high-tech industries.

Keywords: Laser-induced crystallization, Hafnium oxide, Zinc oxide, Copper oxide
© 2024 Published by ICMATSE

Acknowledgements

Work funded by EU project SPRINT (H2020-FETOPEN 801464), the Spanish MCIN/AEI/10.13039/501100011033 (projects PID2020-113034RB-I00 and PID2020-112914RB-I00) and by Gobierno de Aragón (research group T54_23R). Authors also would like to acknowledge the use of Servicio General de Apoyo a la Investigación-SAI and the Spanish National Facility ELECOMI ICTS, node Laboratorio de Microscopías Avanzadas (LMA) , Universidad de Zaragoza.

ICMATSE 2024

The rise of 212 MAX phase borides with enhanced thermo-mechanical properties

Md. Ashraf Ali

*Department of Physics, Chittagong University of Engineering and Technology (CUET), Chattogram-4349, Bangladesh,
ashrafphy31@cuet.ac.bd
ORCID: 0000-0003-4957-2192*

Cite this paper as: Ali, MA. The Rise of 212 MAX phase borides with enhanced thermo-mechanical properties. Int. Conf. Advanced. Mater. Sci. & Eng. HiTech. and Device Appl. Oct. 24-26 2024, Ankara, Turkiye (AM_01.)

Abstract. The 212 MAX phase borides, an expansion of the MAX phase, have attracted attention from researchers due to their enhanced thermo-mechanical properties in comparison with the 211 MAX phases. What causes the properties to be enhanced in the 212 phases? Even though the 212 and 211 phases are part of the same group of materials (MAX family), their structure is different. Both belong to the hexagonal system but are crystalized in different space groups (P-6m2 (No. 187) for 212 phases and P63/mmc (No.194) for 211 phases), as depicted in Figure 1, which resulted in different atomic bondings. A 2D layer of B atoms is formed within the 212 phase, which is absent in the 211 MAX phase. In addition, a strong covalent between M and X atoms and a comparatively weaker bond between M and A atoms are also formed, like in the 211 MAX phases. The main difference is the non-existence of covalent bonds among the X (C-C/B-B) atoms in the 211 phase. Thus, the enhancement of the thermo-mechanical properties is expected due to the existence of the 2D boron layer within the 212 MAX phase borides.

Keywords: 212 MAAX phases; DFT; Structural properties; Mechanical properties; Thermal properties
©2024 Published by ICMATSE

The MAX phases are layered ternary solids, well-known as ceramic metals, owing to the exceptional bridging of the properties of ceramics and metals [1–3]. The uncommon properties make them potential candidates for application in diverse fields, which are listed elsewhere [4–6]. For a long time, the X element of the MAX phases was limited to carbon and nitrogen from 1960 to 2014, and this has been expanded up to B, creating a new scope for the researchers who are interested in the MAX phase research [3]. The unique characteristics and properties of B and B-containing compounds ensured the promising prospects of the borides MAX phase, which replaces nitrogen and carbon with boron [7]. The materials containing boron are known as MAX phases. Scientists are also working on broadening the variety of MAX phases by making structural modifications, as shown by instances such as Cr₃AlB₄ (space group Immm), Cr₄AlB₆ (space group Cmmm), and Cr₄AlB₄, Cr₄AlB₄ [8–10]. Wang et al. [11] synthesized the first 212 MAX phase boride, which was then extended by different research groups such as Zr₂AB₂ (A = In, Tl) [12] and Hf₂AB₂ (A = In, Sn) [13], Ti₂InB₂ [14], Ti₂PB₂, Zr₂PbB₂, Nb₂PB₂, Nb₂SB₂ [15], Zr₂AB₂ (A = In, Tl) [16], M₂AB₂ (M = Mo, Ta; A = Ga, Ge) [17].

As reported in the literature, the 212 MAX phases exhibit enhanced thermo-mechanical properties compared to their other part, the 211 MAX phases, borides/carbides. These properties are better suited for their application in high-temperature technology, for instance, as thermal barrier coating materials. These prospects motivate the researchers to pay attention to this new class of MAX phases.

The Cambridge Serial Total Energy Package (CASTEP) code [18,19] was employed to calculate the physical properties of the herein-presented 212 MAX phases and 211 MAX phases. The CASTEP code incorporated the plane-wave pseudopotential-based DFT technique, utilizing the Perdew–Burke–Ernzerhof (PBE) generalized gradient approximation (GGA) to handle the exchange and correlation energy [20].

Fig. 1 shows the unit of the 212 MAX phase (Mo₂GaB₂) along with the unit cell of the 211 phase (Mo₂GaB) for comparison. Both cells have hexagonal structures but different space groups: P-6m2; No. 187 for 212 phases and P63/mmc; No.194 for 211 phases, as depicted in Figure 1 [21], which clearly demonstrates the differences in characteristics between these two groups. In 212 phases, the atoms occupy the following positions: M (Mo) at (1/3, 2/3, 0.6935), A at

($2/3, 1/3, 0.0$), and two B atoms positioned at ($2/3, 1/3, 0.5$) and ($0.0, 0.0, 0.5$). For 212 phases, there are two B (X) atoms, while there is only one X atom in the 211 phases. The X atoms occupy the ($0, 0, 0$) position in the unit cell in typical 211 MAX phases, whereas for 212 phases, the B atoms form a 2D layer sandwiched between two M layers. The existence of this 2D layer (forming B-B covalent bonds) results in enhanced stability of 212 phases compared with the conventional 211 MAX phases.

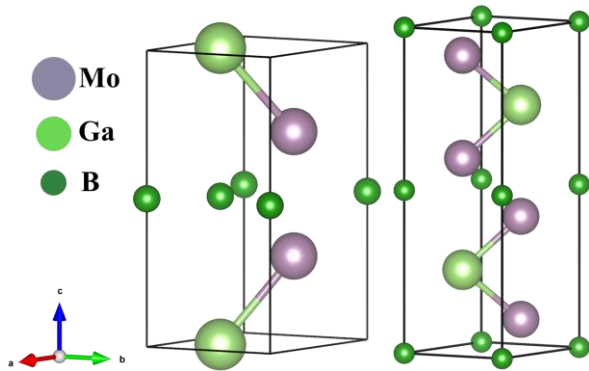


Figure 1. The schematic unit cell of (left) Mo_2GaB_2 and (right) Mo_2GaB compound.

Table 1 lists the elastic moduli and hardness parameters of some 212 and 211 phases to demonstrate the variation of the values due to changes in structure. As seen, the values of elastic moduli and hardness parameters of 212 MAX phases are significantly higher than those of 211 MAX phases (carbides/borides).

Table 1. Elastic moduli (GPa) and hardness parameters (GPa) of the 212 and 211 phases.

Phase	B	G	Y	H_{chen}	H_{miao}	Ref.
Ti_2PB_2	198	152	361	24.74	30.79	[15]
Ti_2PB	158	110	267	17.48	20.65	[15]
Ti_2PC	184	113	282	14.96	19.24	[15]
Zr_2PbB_2	138	95	232	15.55	17.73	[15]
Zr_2PbB	98	66	162	11.61	12.12	[15]
Zr_2PbC	116	78	191	13.08	14.28	[15]
Nb_2PB_2	241	179	430	26.36	35.49	[15]
Nb_2PB	207	146	355	21.53	27.82	[15]
Nb_2PC	225	144	355	18.72	25.24	[15]
Hf_2InB_2	154	114	274	19.46	22.56	[13]
Hf_2InC	152	105	256	16.75	19.65	[13]
Hf_2SnB_2	165	124	297	21.02	24.84	[13]
Hf_2SnC	145	87	218	12.00	14.50	[13]

The differences in mechanical properties are attributed to the structures of the 212 MAX and 211 MAX phases, as depicted in Fig. 1. In contrast to traditional MAX phases, the 212 phases feature a B layer (2D layer). The covalent bonding between B

atoms within the B layer is significantly stronger than the M-X bonding, which is the strong covalent bond for the 211 phases. As a result, the 212 MAX phases exhibit enhanced bonding strength compared to the 211 MAX phases, leading to the expectation of larger values for the mentioned parameters in the 212 phases.

Table 2. Debye temperature, Θ_D , minimum thermal conductivity, K_{min} , Grüneisen parameter, γ , and melting temperature, T_m of the 212 and 211 phases.

Phase	Θ_D (K)	K_{min} (W/mK)	γ	T_m (K)	Ref.
Ti_2PB_2	861	1.71	1.26	2033	[15]
Ti_2PB	704	2.43	1.35	1617	[15]
Ti_2PC	702	2.12	1.47	1731	[15]
Zr_2PbB_2	434	0.77	1.36	1613	[15]
Zr_2PbB	342	0.88	1.38	1338	[15]
Zr_2PbC	366	0.97	1.41	1223	[15]
Nb_2PB_2	745	1.45	1.29	2382	[15]
Nb_2PB	635	1.80	1.34	1997	[15]
Nb_2PC	627	1.85	1.44	2058	[15]
Nb_2SB_2	643	1.39	1.37	1965	[15]
Nb_2SB	594	1.14	1.36	1824	[15]
Nb_2SC	565	1.09	1.40	1790	[15]
Hf_2InB_2	431	0.77	1.29	1800	[13]
Hf_2InC	383	1.04	1.32	1691	[13]
Hf_2SnB_2	447	0.80	1.28	1872	[13]
Hf_2SnC	393	1.07	1.49	1746	[13]

Table 2 provides an in-depth analysis of the thermal properties characterizing parameters of both the 212 MAX and 211 MAX phases, offering a comprehensive understanding of their respective thermal behaviors. These parameters are crucial as the MAX phases represent promising candidates for use in high-temperature technology, such as thermal barrier coating materials. The equations used to calculate these parameters can be found elsewhere [13]. The data presented in Table 2 displays the Θ_D values for the compounds presented here. The Debye temperature measures how atoms vibrate in solids at various temperatures and indicates the strength of interatomic bonding. A higher Θ_D suggests stronger bonding and correlates with the hardness of the solids. It is expected that harder solids will have a higher Θ_D . The findings in Tables 1 and 2 support this, demonstrating that harder phases exhibit higher Θ_D values. One of the most important parameters required for designing a material for use as a thermal barrier coating is the minimum thermal conductivity

(K_{min}), which determines heat transfer at higher temperatures. Lower the K_{min} , better suitable the material. As seen in Table 2, the K_{min} of 212 MAX phases is lower than those of the corresponding carbides/borides counterparts, indicating the better suitability of the 212 phases for use as TBC materials. Another important parameter, the Grüneisen parameter (γ), has been computed and presented in Table 2. A higher γ value indicates more anharmonicity present within the crystal. The 212 MAX phases have lower γ values than those of the 211 MAX phases. One essential factor in the selection of materials for high-temperature applications is the melting point (T_m), which gives an indication of the temperature threshold for use. MAX phases, which possess both ceramic and metallic properties, are widely known as potential candidates for applications in elevated temperatures, such as TBC applications [22]. In the case of 212 MAX phases, T_m is notably higher compared to 211 carbides/borides discussed here. The melting temperature gives insight into bonding strength and is closely linked to Young's modulus. Generally, materials with a higher Young's modulus tend to possess a higher melting point, indicating robust atomic bonds and increased resistance to deformation at elevated temperatures. [23]. Understanding the link between melting temperature and Young's modulus is crucial for predicting material behavior. The higher melting temperature of 212 MAX phase borides is attributed to a significant increase in bonding strength compared to carbides.

From Tables 1 and 2, it is obvious that the thermo-mechanical properties of 212 phases have been improved compared to those of 211 phases. Why are these parameters enhanced? The difference can be attributed to the structure. Though both the 212 and 211 phases have layered structures and crystallize in a hexagonal system, their structures differ. The bonding characteristics within these two structures also vary. In the 212 phases, there are stronger covalent bonds among the B atoms, forming a 2c-2e type of bonding within the 2D B layer, as shown in Fig. 2 (a and b). Additionally, there is another strong covalent bonding between M and B atoms and a relatively weaker M-A covalent bond, similar to the 211 phases (wherein a strong M-X covalent bonding

is present). Conversely, there is no covalent bond among the C atoms in the 211 phase. Additionally, the 212 phases become more stable due to the presence of very strong B-B covalent bonding, resulting in significantly enhanced cohesive energy compared to the 211 phases.

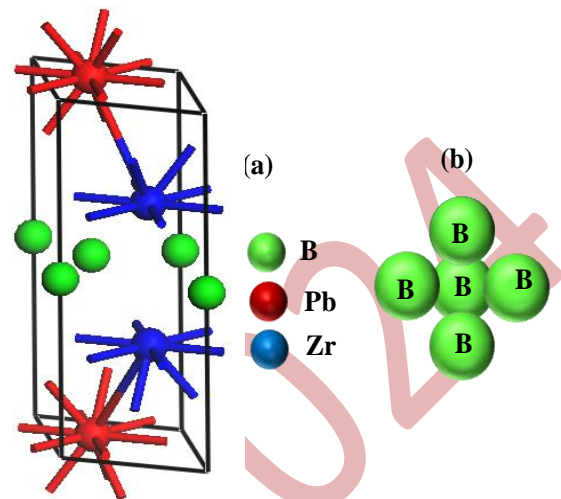


Figure 3. The unit cell of Zr_2PbB_2 (a) and formation of the B-B covalent bonding (b) within Zr_2PbB_2 .

The enhancement of mechanical properties can also be understood in terms of bond length and bond overlap population (BOP). As seen in the previous literature [12,13,15–17], the bond length of the strongest covalent bond, B-B, is lower than 1.9 Å, and the BOP is greater than 2.2 for 212 phases. In contrast, the bond length of the strongest bond in 211 phases is 2.2 Å, and the BOP is usually 1.1/1.2. The BOP is a measure of bonding strength, where a positive higher value indicates a stronger covalent bonding. Thus, due to the smaller bonding length of the primary covalent bond and higher BOP in 212 phases compared to 211 phases, the higher overall bonding strength, elastic moduli, and hardness values, as well as enhanced thermal properties, are expected for the 212 MAX phases.

In conclusion, we expect that the prospects discussed in this paper will inspire further research into the 212 MAX phases. These phases exhibit superior qualities for use in the thermo-mechanical sectors compared to many other traditional MAX phase nanolaminates.

References

- [1] M.W. Barsoum, MAX phases: Properties of machinable ternary carbides and nitrides, Wiley-VCH Verlag GmbH & Co. KGaA, Weinheim, Germany, 2013. <https://doi.org/10.1002/9783527654581>.
- [2] M. Khazaei, M. Arai, T. Sasaki, M. Estili, Y. Sakka, Trends in electronic structures and structural properties of MAX phases: a first-principles study on M_2AlC ($M = Sc, Ti, Cr, Zr, Nb, Mo, Hf, or Ta$), M_2AlN , and hypothetical M_2AlB

- phases, *J. Phys. Condens. Matter* 26 (2014) 505503. <https://doi.org/10.1088/0953-8984/26/50/505503>.
- [3] T. Rackl, L. Eisenburger, R. Niklaus, D. Johrendt, Syntheses and physical properties of the MAX phase boride Nb₂SB and the solid solutions Nb₂S_{B_x}C_{1-x}(x=0-1), *Phys. Rev. Mater.* 3 (2019) 054001. <https://doi.org/10.1103/PhysRevMaterials.3.054001>.
- [4] M. Sokol, V. Natu, S. Kota, M.W. Barsoum, On the Chemical Diversity of the MAX Phases, *Trends Chem.* 1 (2019) 210–223. <https://doi.org/10.1016/j.trechm.2019.02.016>.
- [5] M.A. Ali, Newly Synthesized Ta-Based MAX Phase (Ta_{1-x}Hf_x)₄AlC₃ and (Ta_{1-x}Hf_x)₄Al_{0.5}Sn_{0.5}C₃ (0 ≤ x ≤ 0.25) Solid Solutions: Unravelling the Mechanical, Electronic, and Thermodynamic Properties, *Phys. Status Solidi* 258 (2021) 2000307. <https://doi.org/10.1002/pssb.202000307>.
- [6] A.S. Ingason, M. Dahlqvist, J. Rosen, Magnetic MAX phases from theory and experiments; A review, *J. Phys. Condens. Matter* (2016). <https://doi.org/10.1088/0953-8984/28/43/433003>.
- [7] O.O. Kurakevych, Superhard phases of simple substances and binary compounds of the B-C-N-O system: from diamond to the latest results (a Review), *J. Superhard Mater.* 31 (2009) 139–157. <https://doi.org/10.3103/S1063457609030010>.
- [8] M. Sheikholeslami, D.D. Ganji, I. Nuclear, 50 + years of INIS, *Chem. Phys. Lett.* 7 (2017) 164–165.
- [9] M. Ade, H. Hillebrecht, Ternary Borides Cr₂AlB₂, Cr₃AlB₄, and Cr₄AlB₆: The First Members of the Series (CrB₂)_nCrAl with n = 1, 2, 3 and a Unifying Concept for Ternary Borides as MAB-Phases, *Inorg. Chem.* 54 (2015) 6122–6135. <https://doi.org/10.1021/acs.inorgchem.5b00049>.
- [10] H. Zhang, F. zhi Dai, H. Xiang, Z. Zhang, Y. Zhou, Crystal structure of Cr₄AlB₄: A new MAB phase compound discovered in Cr-Al-B system, *J. Mater. Sci. Technol.* 35 (2019) 530–534. <https://doi.org/10.1016/j.jmst.2018.10.006>.
- [11] J. Wang, T.N. Ye, Y. Gong, J. Wu, N. Miao, T. Tada, H. Hosono, Discovery of hexagonal ternary phase Ti₂InB₂ and its evolution to layered boride TiB, *Nat. Commun.* 10 (2019) 1–8. <https://doi.org/10.1038/s41467-019-10297-8>.
- [12] M.A. Ali, M.M. Hossain, M.M. Uddin, A.K.M.A. Islam, S.H. Naqib, Understanding the improvement of thermo-mechanical and optical properties of 212 MAX phase borides Zr₂AB₂ (A = In, Ti), *J. Mater. Res. Technol.* 15 (2021) 2227–2241. <https://doi.org/10.1016/j.jmrt.2021.09.042>.
- [13] M.A. Ali, M.M. Hossain, M.M. Uddin, A.K.M.A. Islam, D. Jana, S.H. Naqib, DFT insights into new B-containing 212 MAX phases: Hf₂AB₂ (A = In, Sn), *J. Alloys Compd.* 860 (2021) 158408. <https://doi.org/10.1016/j.jallcom.2020.158408>.
- [14] Y.X. Wang, Z.X. Yan, W. Liu, G.L. Zhou, Structure stability, mechanical properties and thermal conductivity of the new hexagonal ternary phase Ti₂InB₂ under pressure, *Philos. Mag.* 100 (2020) 2054–2067. <https://doi.org/10.1080/14786435.2020.1754485>.
- [15] M.A. Ali, M.M. Hossain, M.M. Uddin, A.K.M.A. Islam, S.H. Naqib, The Rise of 212 MAX Phase Borides: DFT Insights into the Physical Properties of Ti₂PB₂, Zr₂PbB₂, and Nb₂AB₂ [A = P, S] for Thermomechanical Applications, *ACS Omega* 8 (2023) 954–968. <https://doi.org/10.1021/acsomega.2c06331>.
- [16] M.N. Uddin, A.K. N. Ishtiaq, S. Islam, M.R. Rana, M.A. Ali, K. Hoque, Prediction of new 212 M₂AB₂ borides as a promising candidate for future engineering: DFT calculations, *Mater. Today Commun.* (2024) 108536. <https://doi.org/10.1016/j.mtcomm.2024.108536>.
- [17] A.K.M.N. Ishtiaq, M.N. Uddin, M.R. Rana, S. Islam, N. Afsary, K. Hoque, M.A. Ali, Exploration of new 212 MAB phases: M₂AB₂ (M=Mo, Ta; A=Ga, Ge) via DFT calculations, (2024). <http://arxiv.org/abs/2408.17160>.
- [18] M.D. Segall, P.J.D. Lindan, M.J. Probert, C.J. Pickard, P.J. Hasnip, S.J. Clark, M.C. Payne, First-principles simulation: ideas, illustrations and the CASTEP code, *J. Phys. Condens. Matter* 14 (2002) 2717–2744. <https://doi.org/10.1088/0953-8984/14/11/301>.
- [19] S.J. Clark, M.D. Segall, C.J. Pickard, P.J. Hasnip, M.I.J. Probert, K. Refson, M.C. Payne, First principles methods using CASTEP, *Zeitschrift Für Krist. - Cryst. Mater.* 220 (2005) 567–570. <https://doi.org/10.1524/zkri.220.5.567.65075>.
- [20] J.P. Perdew, K. Burke, M. Ernzerhof, Generalized Gradient Approximation Made Simple, *Phys. Rev. Lett.* 77 (1996) 3865–3868. <https://doi.org/10.1103/PhysRevLett.77.3865>.
- [21] N. Miao, J. Wang, Y. Gong, J. Wu, H. Niu, S. Wang, K. Li, A.R. Oganov, T. Tada, H. Hosono, Computational Prediction of Boron-Based MAX Phases and MXene Derivatives, *Chem. Mater.* 32 (2020) 6947–6957. <https://doi.org/10.1021/acs.chemmater.0c02139>.
- [22] J. Gonzalez-Julian, Processing of MAX phases: From synthesis to applications, *J. Am. Ceram. Soc.* 104 (2021) 659–690. <https://doi.org/10.1111/jace.17544>.
- [23] D. Salamon, *Advanced Ceramics*, in: *Adv. Ceram. Dent.*, Elsevier Inc., 2014: pp. 103–122. <https://doi.org/10.1016/B978-0-12-394619-5.00006-7>.

Biocompatibility Issues for the Tissue Engineered Products for Commercialization

Gilson Khang

*Department of Bionanotechnology and Bio-Convergence Engineering, Jeonbuk National University, Jeonju-si, Jeonbuk, Korea
gskhang@jbnu.ac.kr
ORCID: 0000-0002-6452-5653*

Abstract. Around 1992 as 20 years ago, Advance Tissue Science Co (USA), now merged to Smith & Nephew Co., USA, had been submitted to approve to USA FDA for first cartilage Tissue engineered products (TEMPs) as autologous chondrocyte/polyglycolic acid (PGA) nonwoven scaffold. At that time, no one had doubted to approve cartilage TEMP since PGA was already approved by FDA in human clinical trial and chondrocyte was used autologous primary cell. At last, this product has been still retarded up to approve FDA. Main reason might be in terms of safety. Implanted TEMPs have been reported to induce sequential events of immunologic reactions in response to injury caused by implantation procedures and result in acute inflammation marked by a dense infiltration of inflammation-mediating cells at the materials-tissue interface. Prolonged irritations provoked by implanted biomaterials advance acute inflammation into chronic adverse tissue response characterized by the accumulation of dense fibrotic tissue encapsulating the implants.

In this lecture, we will discuss (1) recent advances for the commercialization trends for the tissue engineered products (TEMPs) including regenerative medicinal products, (2) scaffolds in terms of biocompatibility and safety issue, (3) smart scaffold for the application of clinical trial including improved biocompatibility and the reduction of host response, and (4) biocompatibility issue for the natural and synthetic polymers.

Keywords: Biocompatibility, Tissue Engineered Products (TEMPs), Smart scaffold

© 2024 Published by ICMATSE

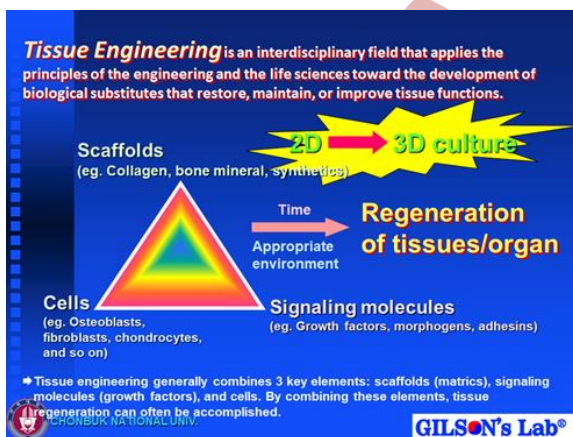


Figure 1. Concepts of Tissue engineering

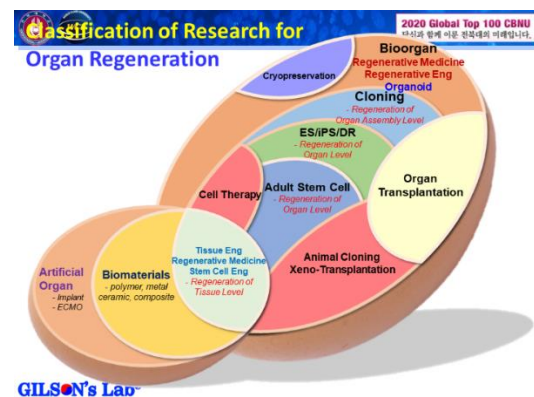


Figure 2. Classification of Research of Organ Regeneration

Results & Discussion

The first autologous chondrocytes/PGA (polyglycolic acid) nonwoven hybrid constructs were submitted for approval to the US FDA in 1992 by ATS. At that time, there was little doubt that these tissue-engineered medical products (TEMPs) would be approved.

However, the approval process for such products has been significantly delayed, even to this day.

This delay highlights the need to address critical issues related to both safety and efficacy. A key challenge arises from the immunologic responses triggered by implantation procedures, which initiate a cascade of events. The injury caused by the implantation induces an acute inflammatory response, characterized by the infiltration of inflammation-mediating cells at the material-tissue interface.

References

1. Langer, R. (1993). VacantiJP: Tissue engineering. *Science*, 260(5110), 920-926.
2. Silva, A. T. C. R., Cardoso, B. C. O., e Silva, M. E. S. R., Freitas, R. F. S., & Sousa, R. G. (2015). Synthesis, characterization, and study of PLGA copolymer in vitro degradation. *Journal of Biomaterials and Nanobiotechnology*, 6(01), 8.

If this irritation persists due to the implanted biomaterials, the acute inflammation can progress to a chronic adverse tissue response. This chronic stage is marked by the formation of dense fibrotic tissue, which encapsulates the implant, ultimately compromising its integration and function.

To overcome these challenges, it is essential to develop strategies that mitigate prolonged irritation and ensure biocompatibility, thus improving the long-term success of tissue-engineered products.

ICMATSE 2024

Harnessing *Rosa damascena* Residue for Green Synthesis of Zinc Oxide Nanoparticles: Response Surface Methodology Optimization

Imane Adraoui

*Team of Biotechnology, Materials and Environment, Faculty of Sciences Agadir, Ibn Zohr University,
Morocco Faculty of Applied Sciences-Ait Melloul, Ibn Zohr University, Morocco*

ORCID 0000-0002-9075-4855

Nabil Saffaj

*Team of Biotechnology, Materials and Environment, Faculty of Sciences Agadir, Ibn Zohr University,
Morocco*

ORCID 0000-0003-0844-0898

Rachid Mamouni

*Team of Biotechnology, Materials and Environment, Faculty of Sciences Agadir, Ibn Zohr University,
Morocco*

ORCID 0000-0001-5627-6426

Si Mohamed Jadoualia

*Team of Biotechnology, Materials and Environment, Faculty of Sciences Agadir, Ibn Zohr
University. Laboratory of Biotechnology, Bioresources and Bioinformatics, EST Khenifra, Sultan Moulay
Sliman University, Morocco*

*I Adraoui I, Saffaj N, Mamouni R, Jadoualia S M. Harnessing *Rosa damascena* Residue for Green Synthesis of Zinc
Oxide Nanoparticles: Response Surface Methodology Optimization. Conf. Advanced. Mater. Sci.& Eng.
HiTech.and Device Appl.Oct. 24-26 2024, Ankara, Turkiye*

Abstract. The fight against water pollution has received particular attention and is one of the most pressing environmental concerns, given that water is susceptible to pollution. Therefore, it is necessary to create new ecologically friendly technology for wastewater treatment. In the present study, the dry rose waste (*Rosa damascena*) extract was used for the first time to synthesize zinc oxide nanoparticles (ZnO NPs) as an alternative to environmentally and cost-effective chemical and physical procedures, and their application in wastewater treatment is examined. Various techniques including scanning electron microscopy (SEM), X-ray diffraction (XRD), and UV-visible spectroscopy were used to confirm the composition of ZnO NPs. However, the response surface methodology (RSM) based on the Box–Behnken design (BBD) has been used to study the influence of operation parameters on the ZnO NPs synthesis. The results showed that ZnO NPs had a better effect on photodegradation activity in treating aqueous solutions containing orange G dyes after 120 minutes under sunlight. Under optimal factors for synthesizing ZnO NPs using BBD such as the mass of plant 20 mg, the salt concentration of 0,2, and calcination temperature of 500°C.

Keywords: Zinc oxide nanoparticles, green synthesis, rosa damascena, Plant Extracts, RSM, Dye degradation.

Given the potential of ZnO nanoparticle systems and the environmental advantages of green synthesis, the current study reports the development and characterization of a simple, cost-effective, and sustainable green approach for synthesizing ZnO NPs that employs an aqueous extract of rose waste as a reducing agent without the addition of any acid or base standard component. However, the response surface approach founded on the Box- Behnken

design (BBD) was used to explore the effect of operating factors on the synthesis of zinc oxide nanoparticles (Fig. 1). Various techniques including scanning electron microscopy (SEM), X-ray diffraction (XRD), and UV-visible spectroscopy were used to confirm the composition of ZnO NPs [1,2]. However, ZnO nanoparticles based on Rosa damascena waste extracts were used to study photodegradation in the treatment of

aqueous solutions containing orange-G dyes
after 120 minutes under solair irradiation.

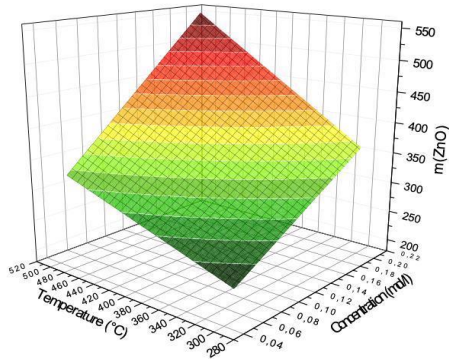


Figure 1. Response surface plot of ZnO NPs
synthesis vs Temperature and concentration.

References

- 1) A. Alshehri, M. Malik, J Mater Sci: Mater Electron 30, 16156–16173 (2019).
- 2) I. Ngom, B.D. Ngom, J. Sackey, S. Khamlich, Materials Today: Proceedings 36:526–533(2021).

Femtosecond Laser-FIB-SEM Triple Beam for Sample Preparation and Large Volume Analysis

Daniel Phifer

*Thermo Fisher Scientific- Materials and Structural Analysis, 5655GG, Eindhoven, The Netherlands,
daniel.phifer@thermofisher.com
ORCID: 0000-0001-9069-6272*

*Cite this paper as: Phifer, D., Femtosecond Laser-FIB-SEM Triple Beam for Sample Preparation
and Large Volume Analysis. Int. Conf. Advanced. Mater. Sci. & Eng. HiTech. and Device Appl. Oct. 24-26 2024,
Ankara, Turkiye*

The challenges of DualBeam (FIB-SEM) sample processing presented by beam-sensitive materials range from simple charging artifacts in imaging to actual beam-induced damage. One of the most common uses of (multiple-species Helios Hydra) focused ion beam (FIB) is to provide a high-resolution means of removing material deterministically so that the sample cross-section may be viewed in situ with an electron microscope (DualBeam™ FIB/SEM process). A few classes of materials/samples present unique challenges to FIB/SEM workflows such as highly non-conductive materials, damage/amorphization-prone samples, weakly-bound composite layers, and an abundance of sensitive polymeric materials. As such, there is a growing interest in multiple non-Ga ion species and non-FIB techniques of *in situ* material removal that may work in concert with FIB to address these challenging samples. Athermally ablative femtosecond (fs) laser technology has been available commercially for a few years to fill this gap. Helios DualBeams equipped with fs laser can pre-process samples to minimize FIB dose and current density requirements for targeted analysis of ion-sensitive samples. In some cases, the fs-laser enables *in situ* processing of materials that cannot be addressed by FIB and enables larger volume serial slicing through volumes up to 1mm.

Keywords: fs Laser, DualBeam, FIB-SEM-Laser
© 2024 Published by ICMATSE

References

1. SJ Randolph et al., *Microsc. Microanal.* 25 (Suppl 2), 2019, p.352
2. SJ Randolph et al., *Journal of Vacuum Science & Technology B*36 (2018), p. 06JB01.
3. MP Echlin and A Mottura et al., *Review of Scientific Instruments* 83 (2012), p. 023701.
4. A Martin et al., *Scientific Reports* 5 (2015), p. 8958

Interplay between laser induced surface nanostructures and superconductivity on Nb thin films

Luis A. Angurel

*Instituto de Nanociencia y Materiales de Aragón, INMA (CSIC-Universidad de Zaragoza), 50018 Zaragoza, Spain,
angurel@unizar.es
ORCID: 0000-0001-5685-2366*

Javier Frechilla

*Instituto de Nanociencia y Materiales de Aragón, INMA (CSIC-Universidad de Zaragoza), 50018 Zaragoza, Spain,
jfrechilla@unizar.es
ORCID: 0009-0007-9057-3943*

Luis Porta-Velilla

*Instituto de Nanociencia y Materiales de Aragón, INMA (CSIC-Universidad de Zaragoza), 50018 Zaragoza, Spain,
porveli@unizar.es
ORCID: 0000-0002-4876-7636*

Elena Martínez

*Instituto de Nanociencia y Materiales de Aragón, INMA (CSIC-Universidad de Zaragoza), 50018 Zaragoza, Spain,
elenamar@unizar.es
ORCID: 0000-0003-4839-5286*

Germán F. de la Fuente

*Instituto de Nanociencia y Materiales de Aragón, INMA (CSIC-Universidad de Zaragoza), 50018 Zaragoza, Spain,
xerman@unizar.es
ORCID: 0000-0002-0500-1745*

Nicolas Lejeune

*Experimental Physics of Nanostructured Materials, Q-MAT, CESAM, Université de Liège, B-4000 Liège, Belgium,
nlejeune@uliege.be
ORCID: 0000-0001-6003-1472*

Emile Fourneau

*Experimental Physics of Nanostructured Materials, Q-MAT, CESAM, Université de Liège, B-4000 Liège, Belgium,
emile.fourneau@uliege.be
ORCID: 0000-0002-7987-889X*

Alejandro V. Silhanek

*Experimental Physics of Nanostructured Materials, Q-MAT, CESAM, Université de Liège, B-4000 Liège, Belgium,
asilhanek@uliege.be
ORCID: 0000-0001-9551-5717*

Jörn Bonse

*Bundesanstalt für Materialforschung und -prüfung (BAM), 12205 Berlin, Germany, joern.bonse@bam.de
ORCID: 0000-0003-4984-3896*

A. Badía-Majós

*Instituto de Nanociencia y Materiales de Aragón, INMA (CSIC-Universidad de Zaragoza), 50018 Zaragoza, Spain,
anabadia@unizar.es
ORCID: 0000-0002-8753-2397*

Cite this paper as: Angurel, LA, Frechilla, J, Porta-Velilla, L, Martínez, E, de la Fuente, GF, Lejeune, N, Fourneau, E, Silhanek, AV, Bonse, J, Badía-Majós, A. Interplay between laser induced surface nanostructures and superconductivity on Nb thin films. Int. Conf. Advanced. Mater. Sci. & Eng. HiTech.and Device Appl.Oct. 24-26 2024, Ankara, Turkiye

Abstract. This presentation is an overview of the last results we have published showing that surface nanostructures, generated when a surface is irradiated with a fs laser, can modify the superconducting properties in materials like Nb thin films. By controlling the laser processing parameters it is possible to generate surface nanostructures with high levels of anisotropy, that are also transferred to the superconducting properties. Laser patterning was performed using a 343 nm fs laser with pulse duration of 238 fs. The control of the laser beam fluence and scanning parameters facilitates the generation of the surface nanostructure without deteriorating the sample. Sample microstructure has been analysed by electronic and atomic force microscopies. Physical properties have been evaluated using magnetometry and magneto-optical microscopy. Surface nanostructure defines directional flux penetration and with an adequate selection of the nanostructure domains it is possible to define the geometry of magnetic flux penetration on the sample. Several geometries have been characterized showing the relevance of the boundaries between different nanostructure domains. This behaviour has also been analysed using modified critical state models of the flux dynamics, combined with the inversion of the magneto-optical records, showing that in some experimental conditions, critical currents of treated regions are higher than in the original ones.

Keywords: Laser Induced Periodic Surface Structures (LIPSS), Superconductivity, Nb, Anisotropy

Acknowledgements

Work funded by the Spanish MCIN/AEI/10.13039/501100011033 (project PID2020-113034RB-I00) and by Gobierno de Aragón (research group T54_23R). Authors also would like to acknowledge the use of Servicio General de Apoyo a la Investigación-SAI and the Spanish National Facility ELECM ICTS, node Laboratorio de Microscopías Avanzadas (LMA), Universidad de Zaragoza.

© 2024 Published by ICMATSE

The effect of Li doping In₂O₃ thin films on structural and optical properties deposited by ultrasonic spray

Bourhefir Ranida

Department of Matter Science, Mohamed Kheidar Biskra University, Biskra 07000, Algeria,
ranida.bourhefir@univ-biskra.dz

Saidi Hanane

Department of Matter Science, Mohamed Kheidar Biskra University, Biskra 07000, Algeria,
h.saidi@univ-biskra.dz

Hamani Nedjette

Department of Matter Science, Mohamed Kheidar Biskra University, Biskra 07000, Algeria,
h.nedjette@univ-biskra.dz

Attaf Abdellah

Department of Matter Science, Mohamed Kheidar Biskra University, Biskra 07000, Algeria,
ab_attaf@univ-biskra.dz

Okba ben khetta

Department of Matter Science, Mohamed Kheidar Biskra University, Biskra 07000, Algeria,
okba.benkhetta@univ-biskra.dz

Abstract. Indium oxide (In₂O₃) is a material belonging to the group of transparent conductive oxides, which are widely used in many fields of technology including optoelectronics and photovoltaics. However, the properties of In₂O₃ thin films depend on many factors. Therefore, the aim of the study was a thorough investigation of the properties of In₂O₃ thin films of different doping concentrations. Indium oxide thin films were deposited by ultrasonic spray at different deposition times to investigate the influence of different doping concentrations on the structural and optical properties of thin films. The structural and optical properties characteristics of these layers were investigated by X-ray diffraction and UV-Vis-NIR spectrophotometer. It is observed that all the films are polycrystalline and crystallize in a cubic structure with a preferential orientation along the (400) plane. While the optical transmittance spectra with high transmittance of more than 80 % for all samples at the visible and near-infrared ranges

Keywords: indium oxide, thin films, doping, ultrasonic spray, lithium.

© 2024 Published by ICMATSE

Development of a Non-Toxic $\text{CuSbSe}_2/\text{Zn}_x\text{Sn}_{1-x}\text{O}$ Thin-Film Solar Cell with Optimized Multilayer Architecture

Rawshan Tareq M.Nadhaif Mohammednadhaif

Department of Electrical and Electronics Engineering, Atılım University, 06836 Ankara, Türkiye,
mohammednadhaif.rawshan@student.atilim.edu.tr
ORCID: 0009-0007-4396-6947

Aysenur Gencer

Department of Physics, Kamil Ozdag Faculty of Science, Karamanoglu Mehmetbey University, 70200,
Karaman, Türkiye, agencer@kmu.edu.tr
ORCID: 0000-0003-2574-3516

Ozge Surucu

Department of Electrical and Electronics Engineering, Atılım University, 06836 Ankara, Türkiye,
ozge.surucu@atilim.edu.tr
ORCID: 0000-0002-8478-1267

Cite this paper as: Surname, FN, Surname, FN. Article title.Int. Conf. Advanced. Mater. Sci.& Eng. HiTech.and Device Appl.Oct. 24-26 2024, Ankara, Türkiye

Abstract. In this work, we present the design and fabrication of a CuSbSe_2 -based thin-film solar cell with a novel multilayer configuration aimed at improving efficiency and stability. The cell structure, as shown in the figure, consists of a gold (Au) back contact, followed by a CuSbSe_2 absorber layer, a $\text{Zn}_x\text{Sn}_{1-x}\text{O}$ buffer layer, and ZnO/ZnO window layers. The topmost layer is a silver (Ag) contact for electron collection.

Keywords: CuSbSe_2 , Solar Cell, Non-toxic
© 2024 Published by ICMATSE

Photovoltaic technology have advanced quickly due to the need for clean and renewable energy sources [1]. Because of its flexibility, reduced material consumption, and potential for cost-effective manufacturing, thin-film technologies are among the most promising forms of solar cells.[2]. CuSbSe_2 -based solar cells, in particular, have drawn interest lately as a possible substitute for conventional materials like silicon because of their abundant component elements, high absorption coefficient, and appropriate bandgap [3,4]. A CuSbSe_2 -based thin-film solar cell with a new multi-layer architecture that improves light absorption and carrier collection efficiency is depicted in the figure.

In this structure, the bottom layer consists of a gold (Au) back contact, which ensures good electrical conductivity and facilitates hole collection.

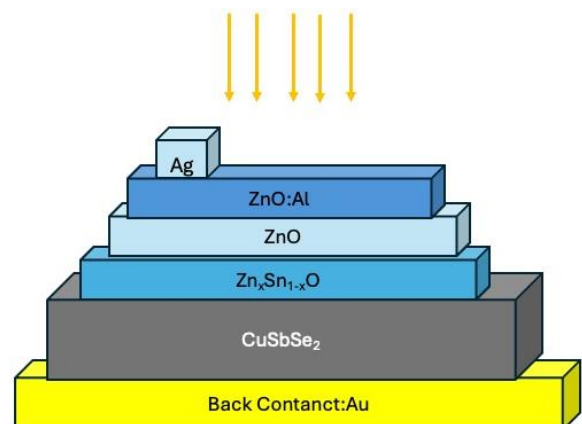


Figure 1. Schematic diagram for CuSbSe_2 thin film solar cell.

The active layer is composed of CuSbSe_2 , which is the primary light-absorbing material. Above this is a $\text{Zn}_x\text{Sn}_{1-x}\text{O}$ buffer layer, providing a suitable interface

for carrier separation and minimizing recombination losses. The window layers consist of ZnO and ZnO (aluminum-doped zinc oxide), which act as transparent conducting oxides (TCOs), allowing

sunlight to pass through while conducting electrons. The silver (Ag) contact at the top completes the architecture, providing an efficient pathway for electron extraction.

References

1. S.A. Khalate, R.S. Kate, R.J. Deokate, A review on energy economics and the recent research and development in energy and the Cu₂ZnSnS₄ (CZTS) solar cells: A focus towards efficiency, *Solar Energy*, 169,2018,2.
2. O. Surucu, M. Isik, M. Terlemezoglu, T. Bektas, N.M. Gasanly, M. Parlak, Temperature effects on optical characteristics of thermally evaporated CuSbSe₂ thin films for solar cell applications, *Optical Materials*, 133, 2022, 113047, doi.org/10.1016/j.optmat.2022.113047.
3. G Surucu, E Bal, A Gencer, M Parlak, O Surucu, Performance analysis of CuSbSe₂ thin-film solar cells with Cd-free window layers, *Materials Letters*, 363, 2024, 136296, doi.org/10.1016/j.matlet.2024.136296.
4. S Rampino, F Pattini, M Bronzoni, M Mazzer, M Sidoli, G Spaggiari, E Gilioli, CuSbSe₂ thin film solar cells with ~4% conversion efficiency grown by low-temperature pulsed electron deposition, *Solar Energy Materials and Solar Cells*, 185, 2018, 86-96, doi.org/10.1016/j.solmat.2018.05.024.

ICMATSE 2024

Integration of Electrospinning and Additive Processing for Harvesting Energy in IoTs

Ashok Vaseashta

*International Clean Water Institute, Applied Research Division, Manassas, VA 20108, USA,
prov.vaseashta@ieee.org
ORCID: 0000-0002-5649-0067*

Cite this paper as: Vaseashta, A. Integration of Electrospinning and Additive Processing for Harvesting Energy in IoTs. Int. Conf. Advanced. Mater. Sci.& Eng. HiTech.and Device Appl.Oct. 24-26 2024, Ankara, Turkiye

Abstract. Advances in polymers and synthesis methods have been used to produce some new and unique devices and are reported in this presentation. One of the strategies is employing digitally controlled fabrication by combinatorial synthesis methods such as electrospinning and 3D printing/additive processing. Using synergistic integration of configurations, elaborate shapes, and patterns are printed with mesostructured stimuli-responsive electrospun membranes, allowing for in-plane modulations, and compensations due to internal interlayer stresses induced by swelling/shrinkage or mismatch, thus guiding shape morphing behaviors of electrospun membranes to adapt to environmental changes. Recent progress in combinatorial processing includes materials and scaffold constructs that are used for tactile and wearable sensors, filtration structures, sensors for structural health monitoring, biomedical scaffolds, tissue engineering, and optical patterning, among many other applications to support the vision of synthetically prepared smart material designs that mimic the structural aspects with digital precision. A novel technology called 3D jet writing was recently reported that propels electrospinning to adaptive technologies for manufacturing scaffolds according to user-defined specifications of the shape and size of both the pores and the overall geometric footprint. This presentation focuses on two specific applications, viz. energy and atmospheric water harvesting. Recent advances in next-generation triboelectric nanogenerators (TENG), the integration of finite-state machines (FSM), and built-in edge computing in onboard IoT devices have reduced the energy requirement, thus shifting the energy storage requirements to built-in power generation and ambient sources. The presentation describes the synergetic integration of exponential technologies in several examples that minimize energy storage and reduce energy consumption. Applications that include IoTs, IoB, and onboard energy harvesting devices include tactile sensing for biomedical applications, smart agriculture, and transportation logistics. A brief discussion of the concerns elaborating on privacy with IoT and IoB will be presented.

Keywords: Harvesting, Energy, Transdisciplinarity, Exponential Technologies, 3D printing, Electrospinning, Sustainability

© 2024 Published by ICMATSE



The article describes a new and innovative methodology of conjoining fabrication technologies to prepare new structures that have desired functionalities as well as mechanical rigidity to withstand surrounding mechanical pressure. In addition, the structures also included piezoelectric materials, which not only provide sensing capabilities but also include the option to store and save power. This leads to the inclusion of artificial intelligence in these devices. The presentation describes some of the strategies to enhance power storage capacity as well as the inclusion of AI.

Figure 1. Sensor system based on electrospinning and 3D printing

References

- 1) doi: 10.1007/978-3-030-99958-2
- 2) doi.org/10.1007/978-3-030-99958-2_22
- 3) doi: 10.1007/978-3-031-37132-5_17

Green Hydrogen Generation Using Innovative MXene/Ni-functionalised Composite Electrodes

Andrei V. Kovalevsky

CICECO – Aveiro Institute of Materials, Department of Materials and Ceramic Engineering, University of Aveiro, 3810-193 Aveiro, Portugal;
akavaleuski@ua.pt
ORCID: 0000-0001-5814-9797

Sergii A. Sergiienko

CICECO – Aveiro Institute of Materials, Department of Materials and Ceramic Engineering, University of Aveiro, 3810-193 Aveiro, Portugal;
Department of Inorganic Chemistry, University of Chemistry and Technology Prague, Technická 5, 166 28 Prague 6, Czech Republic
Sergii1.Sergiienko@vscht.cz
ORCID: 0000-0002-3849-5681

Daniela V. Lopes

CICECO – Aveiro Institute of Materials, Department of Materials and Ceramic Engineering, University of Aveiro, 3810-193 Aveiro, Portugal;
daniela.rosendo.lopes@ua.pt
ORCID: 0000-0003-0652-5070

Cite this paper as: Kovalevsky, AV, Sergiienko, SA, Lopes, DV. Green Hydrogen Generation Using Innovative MXene/Ni-functionalised Composite Electrodes. Int. Conf. Advanced. Mater. Sci. & Eng. HiTech. and Device Appl. Oct. 24-26 2024, Ankara, Turkiye

Abstract. Green hydrogen, produced by alkaline water electrolysis (AWE) using renewable energy sources, holds the potential to revolutionise our energy systems by providing a clean and sustainable alternative to fossil fuels. The emergence of new multifunctional materials continuously increases the expectations for the technologies advancing the hydrogen economy. MXenes, a family of two-dimensional (2D) transition metal carbides, nitrides and carbonitrides based on abundant constituents, has been discovered as an exciting candidate as electrocatalysts for electrochemical water splitting. However, today, these materials are primarily subjects of fundamental research and scientific interest, as challenges with their preparation and environmental stability restrict their use in industrial applications. This work aimed to introduce a simple and inexpensive approach to composite electrodes for hydrogen production, using titanium- and molybdenum-containing MAX phases and MXene/Ni as functional materials. Various MAX phase/ MXene/ Ni electrode concepts were prepared using HF-free etching methodology, followed by detailed structural, microstructural and electrochemical characterisation. The high electrochemical activity of such electrodes towards the hydrogen evolution reaction (HER) was observed, in several cases exceeding that for the Ni electrodes used in industrial electrolyzers.

Keywords: green hydrogen, alkaline electrolysis, MXene, HER, electrocatalyst
© 2024 Published by ICMATSE

Introduction

The increasing demand for energy calls for sustainable methods of energy conversion and storage. Renewable energies are playing an increasingly important role, with their share continuing to grow. This shift is driven by the need to reduce carbon emissions and reliance on fossil fuels. Technologies such as solar, wind, and

hydroelectric power are becoming more efficient and cost-effective, making them attractive alternatives. Governments and industries worldwide are also investing heavily in renewable infrastructure, further accelerating the transition towards cleaner energy sources. As a result, renewables are expected to dominate the energy landscape in the coming decades, contributing to a more sustainable and resilient energy system.

One of the primary challenges in the widescale adoption of renewable energy is its variable or intermittent nature imposing limitations on its further integration in electric grid networks. However, this energy can be exploited for water electrolysis to produce green hydrogen, a fuel of the future, with no carbon footprint, the highest enthalpy of combustion and only water as a by-product of energy release.

The emergence of new multifunctional materials continuously increases the expectations for the performance of energy conversion and storage devices. MXenes, a family of two-dimensional (2D) transition metal carbides, nitrides and carbonitrides based on abundant constituents, has been discovered as an exciting candidate for these applications [1]. In an MXene, $n+1$ layers of transition metals M are interleaved with n layers of X element (C or N), with an overall composition $M_{n+1}X_nT_x$ [2]. The T_x represents the surface -O, -OH, -F and/or -Cl terminations. Such a structure presents a unique combination of high and active surface area, metallic/semiconducting behaviour and hydrophilicity, leading to an outstanding performance in electrochemical applications [3,4]. The exothermic nature of water adsorption on MXenes promotes its dissociation [4]. This property positions MXenes as highly favourable electrocatalysts for electrochemical water splitting, especially for the hydrogen evolution reaction (HER) in alkaline environments, where water dissociation acts as the rate-limiting step [5]. In contrast to acid-based electrolyzers, alkaline systems present distinct benefits for industrial applications, such as the ability to employ non-noble metal catalysts and sidestep the cost and durability challenges posed by highly corrosive acidic conditions [5].

Several critical challenges restrict the widespread use of MXenes, such as the reliance on hazardous HF in their synthesis and their limited stability, which is mainly due to oxidation by water and oxygen exposure and microstructural degradation. This work strives to showcase the approaches which facilitate the design of MXene/Ni-functionalised bulk composite electrodes for green hydrogen production by water electrolysis, while minimising the consequences of the environmental sensitivity of MXenes. The idea originates from the fact that MAX phases (the parent precursor of MXenes) demonstrate high electrical conductivity and excellent corrosion resistance, and can be relatively

easily prepared and further functionalised by an MXene at the surface.

Methods

In this work, various composite electrode concepts, including $Ti_3AlC_2/Ti_3C_2T_x/Ni$ [6] and $Mo_2Ti_2C_3Al/Mo_2Ti_2(OH)_x/Ni$ [7] were prepared using self-propagation high-temperature synthesis (SHS) or conventional sintering followed by alkaline etching in optimised conditions. An excess of aluminium was used to facilitate the formation of MAX phases and posterior etching [6,7]. The composite electrodes of MXene/MAX phase or MXene/MAX phase/nano-Ni were produced by etching the sintered products in an excess of 10M NaOH solution at room temperature, followed by moderate heating. The sample was immersed in 100 ml of the solution for 10 days, after which the solution was replaced, and the etching process continued with constant stirring. Upon completion of the etching, the samples were thoroughly washed with distilled water.

The prepared materials were characterised by X-Ray diffraction (XRD) analysis, and combined structural and microstructural studies involving high-resolution TEM, SEM/EDS and XPS. Electrochemical measurements were performed in a three-electrode electrochemical cell. A platinum wire was used as the counter electrode (CE), while a $Hg|HgO|NaOH$ (1M) electrode (+0.098 V versus the saturated hydrogen electrode) was selected as the reference electrode, which was connected to the electrolyte via a Luggin capillary. All experiments were conducted at room temperature using 1 M NaOH as the electrolyte. The working electrodes tested had a diameter of 25 mm, a thickness of approximately 3 mm, and consisted of around 4 g of material prior to etching. Hydrogen evolution measurements were carried out in the potential range of -0.7 to -1.5 V, with a scan rate of 10 mV/s. Current density values were calculated based on the geometric surface area of each electrode, which was approximately 10 cm^2 . The possibility for in-situ alkaline etching of the electrodes during alkaline water electrolysis (AWE) was also explored.

Results and discussion

The XRD results confirmed the formation of complex multiphase materials after SHS and conventional sintering. While the MAX phases Ti_3AlC_2 are Mo_2TiAlC were detected as predominant in the SHS and conventional sintering products, the mixtures,

depending on initial precursors, also contain TiC, TiAl₃, Ni₂Al₃, TiNi₂Al, Al₅Mo₂Ni, Mo₃Al₈, Mo₂C and Al₄C₃ phases. More details on the phase composition and corresponding mechanisms can be found elsewhere [6,7]. These materials were prepared in a shape suitable for testing as electrodes towards HER. To form an MXene-functionalised porous electrode structure, etching conditions were optimised by tuning temperature and time. Typically, this process was performed in 10M NaOH at temperatures below 70 °C, optimising the etching time. The formation of a functional MXene layer and electrocatalytically-active Ni nanoparticles was confirmed by XRD/TEM/XPS and SEM/EDS. Fig. 1 summarises some relevant microstructural features of the prepared electrodes.

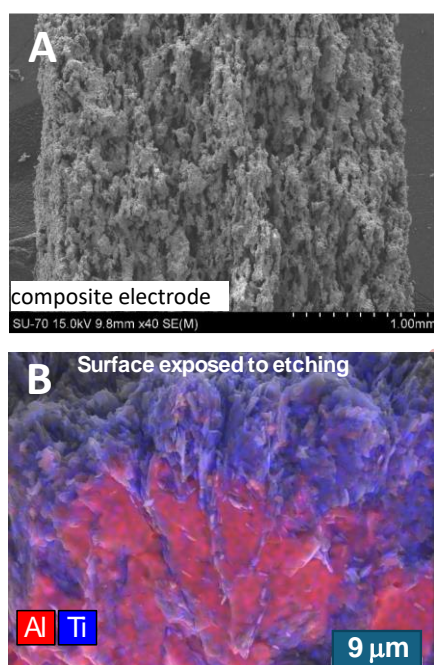


Figure 1. Typical microstructures of the composite electrodes: general view (A) and chemical contrast map of the sample after etching (B) [6,7].

The electrodes are generally characterised by a highly-porous structure (Fig. 1A), which is expected to facilitate the penetration of the electrolyte and, correspondingly, HER reaction. The outer part of the electrode exposed to etching is rich in titanium, while Al is mostly dissolved (Fig. 1B). The etched surface part also exhibits nanostructuring and likely includes MXene particles.

The electrochemical performance of Ti₃AlC₂/Ti₃C₂T_x/Ni electrodes is shown in Fig. 2. Nickel is a known electrode material in industrial alkaline electrolyzers due to its high electrocatalytic

activity. However, both composite electrodes show notably higher hydrogen evolution currents, especially at high current densities. The latter can be attributed to the presence of MXene and metallic Ni nanoparticles in the composition of the electrode after etching. The estimation of price for such electrodes considering only initial precursor materials shows that they can be significantly cheaper than metallic Ni. Even more impressive results were obtained for Mo-containing electrode composite formulations (Fig. 3).

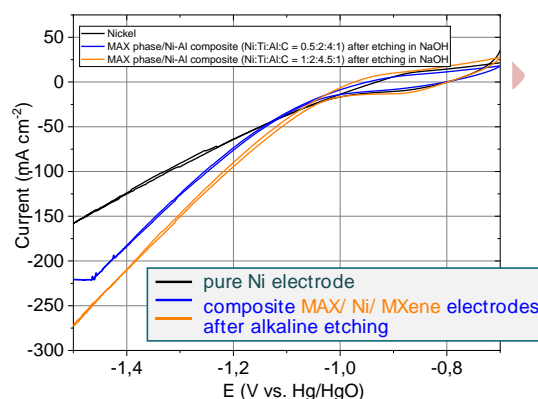


Figure 2. Cyclic voltammetry curves obtained for Ti₃AlC₂/Ti₃C₂T_x/Ni electrodes and pure Ni electrode, used as a reference.

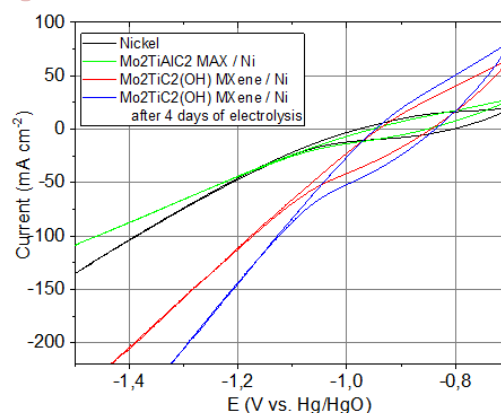


Figure 3. Cyclic voltammetry results obtained for Mo₂Ti₂C₃Al/ Mo₂TiC₂(OH)_x/Ni electrodes [7].

The sample labelled as Mo₂TiAlC₂ MAX/Ni refers to the non-etched electrode, primarily composed of the corresponding MAX phase. Despite this, its performance is comparable to that of a metallic Ni electrode. Significantly higher currents were observed for the etched electrodes. An interesting finding is that the electrode continues to etch and its surface further evolves during the electrolysis process, even though the NaOH concentration in the electrolyte is 10 times lower than that used in the etching solution. This effect is illustrated in Fig. 4, showing a gradual decrease of the applied voltage

during the electrolysis at a constant current. This process can be at least partially attributed to the mechanical action of evolving hydrogen bubbles, which facilitates the mixing of the alkaline electrolyte and its interaction with the electrode. The post-mortem microstructural analysis showed no evidence of electrode degradation or loss of mechanical integrity. Further studies to investigate the mechanisms responsible for this effect are currently underway.

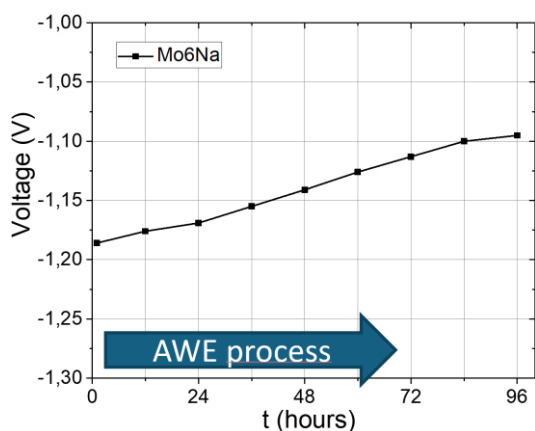


Figure 4. Temporal evolution of the voltage applied during electrolysis at a constant current (1 A) applied [7].

References

1. M. Naguib, M. Kurtoglu, V. Presser, J. Lu, J. Niu, M. Heon, L. Hultman, Y. Gogotsi, M.W. Barsoum, *Advanced Materials*, 23(37) (2011), pp. 4248–4253, 10.1002/adma.201102306
2. Y. Gogotsi, B. Anasori, *ACS Nano*, 13(8) (2019), pp. 8491–8494, 10.1021/acsnano.9b06394
3. H. Kim, Z. Wang, H.N. Alshareef, *Nano Energy*, 60 (2019), pp. 179–197, 10.1016/j.nanoen.2019.03.020
4. J. D. Gouveia, Á. Morales-García, F. Viñes, F. Illas, J.R.B. Gomes, *Applied Catalysis B: Environmental*, 260 (2020) p.118191, 10.1016/j.apcatb.2019.118191
5. N. Mahmood, Y. Yao, J.W. Zhang, L. Pan, X. Zhang, J.J. Zou, *Advanced Science*, 5(2) (2018) p. 1700464, 10.1002/advs.201700464
6. S.A. Sergiienko, D.V. Lopes, G. Constantinescu, M.C. Ferro, N.D. Shcherban, O.B. Tursunov, V.I. Shkepu, H. Pazniak, N.Y. Tabachkova, E.R. Castellón, A.V. Kovalevsky, *Int. J. Hydrogen Energy*, 46 (2021), pp. 11636–11651, 10.1016/j.ijhydene.2021.01.041
7. S.A. Sergiienko, L. Lajaunie, E. Rodriguez-Castellon, G. Constantinescu, D.V. Lopes, N.D. Shcherban, J.J. Calvino, J.A. Labrincha, Z. Sofer, A.V. Kovalevsky, *RSC Advances*, 14 (2024), pp. 3052–3069, 10.1039/D3RA07335A

Acknowledgements

The research leading to these results was supported by the Johannes Amos Comenius Programme, European Structural and Investment Funds, project 'CHEMFELLS V' (No.CZ.02.01.01/00/22_010/0003004). Additionally, this work was funded by Portugal 2020 through European Regional Development Fund (ERDF) in the frame of CENTRO2020 in the scope of the project CENTRO -01-0247-FEDER-181254 and the project CICECO – Aveiro Institute of Materials, UIDB/50011/2020 & UIDP/50011/2020 & LA/P/0006/2020, financed by national funds through the FCT/MEC (PIDDAC).

Conclusions

The innovative MAX phase/MXene/Ni-functionalised composite electrodes, prepared by relatively simple and environmentally-friendly route, demonstrated exceptional performance for hydrogen evolution reaction during alkaline water electrolysis. The etching procedures employed for processing these composite electrodes, based on MAX phases, significantly enhanced their electrochemical activity compared to non-etched electrodes, in several cases exceeding the performance of pure nickel electrodes typically employed in industrial applications. The ability of these electrodes to maintain mechanical integrity and avoid degradation even under prolonged electrolysis conditions further underlines their potential for sustainable hydrogen production. The results also suggest that the etching of the prepared electrodes can proceed even during the electrolysis process, followed by a further increase in their electrochemical activity.

AI-Driven Optimization of Hydrogen Storage in TiO₂/CNTs Nanocomposites-Under Simple Conditions

Behrouz Nemati

*University of Aveiro - Department of Environment and Planning, Center for Environmental and Marine Studies, CESAM, and Department of Materials and Ceramics Engineering, Aveiro Institute of Materials, CICECO, 3810-193 Aveiro, Portugal,
behrouz.nemati@ua.pt.
ORCID: 0000-0003-1581-4368*

Mohammadreza Kamali

*University of KU Leuven - Department of Chemical Engineering, Process and Environmental Technology Lab, J. De Nayerlaan 5, 2860, Sint-Katelijne-Waver, Belgium.
ORCID: 0000-0002-1591-9605*

Shahed Rasekh

*University of Aveiro - Department of Materials and Ceramics Engineering, Aveiro Institute of Materials, CICECO, 3810-193 Aveiro, Portugal.
ORCID: 0000-0003-3466-9952*

M. Elisabete V. Costa

*University of Aveiro - Department of Materials and Ceramics Engineering, Aveiro Institute of Materials, CICECO, 3810-193 Aveiro, Portugal.
ORCID: 0000-0001-7803-6212*

Isabel Capela

*University of Aveiro - Department of Environment and Planning, Center for Environmental and Marine Studies, CESAM, 3810-193 Aveiro, Portugal.
ORCID: 0000-0002-6757-1751*

Cite this paper as: Nemati, B. Kamali, M., Rasekh, Sh., Costa, M., Capela, I., AI-Driven Optimization of Hydrogen Storage in TiO₂/CNTs Nanocomposites-Under Simple Laboratory Conditions. Int. Conf. Advanced. Mater. Sci.& Eng. HiTech.and Device Appl.Oct. 24-26 2024, Ankara, Turkiye

Abstract. Hydrogen (H₂) storage faces significant challenges, including high costs, safety concerns, and the need for specialized equipment. For H₂ to be a viable energy source, efficient storage techniques are essential since current solutions are frequently costly and dangerous. This study explores a novel, low-cost approach using TiO₂/CNTs nanocomposites development, optimized through artificial intelligence (AI), under simple laboratory conditions. The experiment utilized biogas containing 95.48% to 98.31% H₂ in a closed system. Also, two 1-liter sample bags, a pump, and a Nanocomposite Permeation Tube (NPT), with mesh at both ends and nanocomposite in the middle, were employed without the need for specialized materials or additional equipment. Optimization was performed using a Random Forest-Genetic Algorithm (RF-GA), focusing on nanomaterials weight (NW), pump speed (PS), and temperature (T). Data from nine experimental runs showed stored H₂ weight percentages (wt%) ranged from 0 to 2.09 wt%. Following optimization, 2.47 wt% was the greatest H₂ storage capacity; the best outcomes were attained at 0.3 g NW, 25 RPM PS, and -15°C T. It is easy-to-implement design with locally available equipment makes its form a highly adaptable model for low-resource settings.

Keywords: Hydrogen Storage; Nanotechnology; Artificial Intelligence; Random Forest; Genetic Algorithm.

© 2024 Published by ICMATSE

Introduction

Hydrogen (H₂) is widely recognized as a clean and sustainable energy carrier, but its safe and efficient storage remains a major technical challenge. Traditional methods, such as compressed gas storage or liquid H₂, are expensive, pose safety risks, and often require specialized equipment and infrastructure [1]. In this regard, nanomaterials, particularly TiO₂/CNTs nanocomposites, have emerged as a promising solution due to their high surface area and favorable adsorption properties [2]. However, optimizing H₂ storage using these materials for maximum efficiency under simple, cost-effective conditions is essential for wider adoption. This study aims to address these challenges by leveraging AI-driven optimization techniques to enhance the H₂ storage capacity of TiO₂/CNTs nanocomposites, using a straightforward laboratory setup without the need for advanced tools or materials. The goal is to provide a scalable, low-cost alternative that improves storage capacity while maintaining safety and accessibility.

Methodology

The experimental setup utilized biogas containing 95.48% to 98.31% H₂, which was analyzed for its composition using a micro gas chromatograph (Fusion® Gas Analyzer-INFICON) [4]. The analysis employed two analytical columns, with Argon and Helium as carrier gases. H₂ storage experiments were conducted in a closed system comprising two 1-liter sample bags connected to a pump that circulated the biogas through a Nanocomposite Permeation Tube (NPT). The NPT featured a mesh at both ends, with TiO₂/CNTs nanocomposite material in the middle for H₂ adsorption (Figure 1).

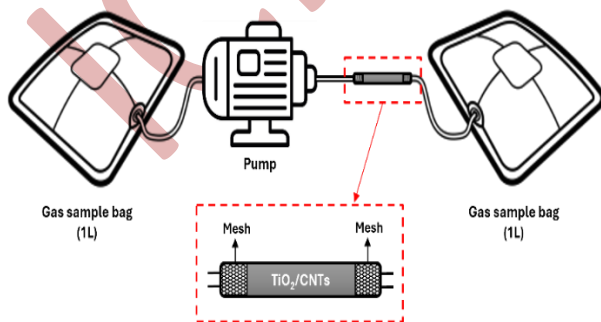


Figure 1. A schematic of the experimental setup for hydrogen storage using TiO₂/CNTs nanocomposites.

In this context, the combination of key experimental parameters (i.e., nanomaterials weight (NW), pump

speed (PS), and temperature (T)) was varied across nine runs. The stored H₂ weight percentage (wt%) was recorded for each run. Also, to optimize the H₂ storage capacity, a Random Forest-Genetic Algorithm (RF-GA) was utilized [3]. This AI-driven method efficiently explored the parameter space and identified optimal conditions for improved H₂ storage (Table 1).

Additionally, Fourier Transform Infrared (FTIR) analysis was conducted to investigate the functional groups present on the surface of the nanocomposite materials [5]. The FTIR analysis was performed using Bruker Tensor 27 equipment, with spectra collected in transmittance mode, covering a range of 4000 – 400 cm⁻¹, at a resolution of 4 cm⁻¹, with 256 scans per sample. The sharper peaks and distinct shifts in the spectra reflected notable chemical interactions during hydrogen storage.

Table 1. Summary of the key parameters and optimization model's characteristics considered in the current investigation.

Optimization Details		Levels / Value		
Key Parameters of Optimization	Nanomaterial weight (g)	0.75	0.150	0.300
	Pump Speed (RPM)	25	50	100
	Temperature (°C)	-15	0	25
Random forest Characteristics	Number of trees in the forest	100		
	The function to measure the quality of a split	Squared error		
	The minimum number of samples to split an internal node.	2		
	The minimum number of samples required to be at a leaf node.	1		
	Max_features	auto		
Genetic Algorithms Characteristics	Number of Generation	100		
	Population Size	50		
	Crossover Probability	0.5		

Mutation probability	0.1
Tournament size	3

Results

Before conducting supplementary tests, the model's performance was assessed using two key metrics: Mean Squared Error (MSE) and R^2 . The MSE was 0.0147, indicating minimal differences between predicted and actual H_2 storage values, reflecting high accuracy. The R^2 value of 0.97 showed that 97% of the variability in H_2 storage was explained by the model, confirming its reliability. A Predicted vs. Actual plot visually demonstrated the model's strong performance, especially for higher storage values, with data points closely aligning along the 45-degree line, indicating accurate predictions and minimal deviation between the model's forecasted and experimentally observed results (Figure 2).

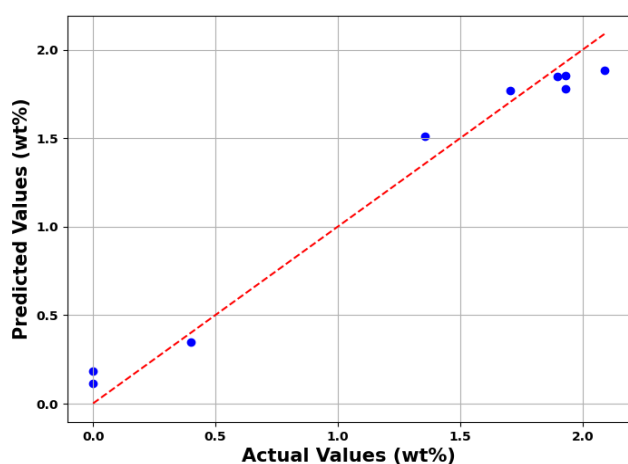


Figure 2. Predicted vs Actual Values of model.

The stored H_2 for the nine experimental runs ranged from 0 to 2.09 wt%. Through RF-GA optimization, the H_2 storage capacity was significantly enhanced, with the maximum storage capacity increasing to 2.47 wt%. The optimal conditions for achieving this improvement were identified as 0.3 g NW, 25 RPM PS, and -15°C T. The FTIR analysis provided valuable insights into the functional groups on the surface of the nanocomposite, aiding in understanding the interaction mechanisms between the nanomaterials and H_2 molecules.

Also, the FTIR analysis of the $TiO_2/CNTs$ nanocomposites reveals how hydrogen storage actively modifies the material's surface chemistry. The sharper O-H peak around 3300 cm^{-1} suggests that hydrogen bonding with hydroxyl groups

becomes more prominent, while the intensified C=O peak at 1520 cm^{-1} and the clearer Ti-O peak at 650 cm^{-1} indicate increased interaction with carbonyl groups and the formation of Ti-H bonds. These shifts suggest that the nanocomposite responds dynamically to hydrogen storage, adapting its surface to enhance bonding, which could play a key role in improving overall storage efficiency (Figure 3).

In addition, GC analysis showed that under optimized conditions, the first sample bag contained 96.55% hydrogen, while the second bag had 88.87%. Based on the closed setup, this slight decrease in hydrogen between the two bags indicates the adsorption of hydrogen by the $TiO_2/CNTs$ nanocomposite. The reduction in hydrogen mass, recorded at 0.0068 grams, highlights the nanocomposite's efficiency in hydrogen capture. These results align with the findings from the optimized run's weight measurements and FTIR analysis, further validating the enhanced interaction between hydrogen and the nanocomposite's surface functional groups.

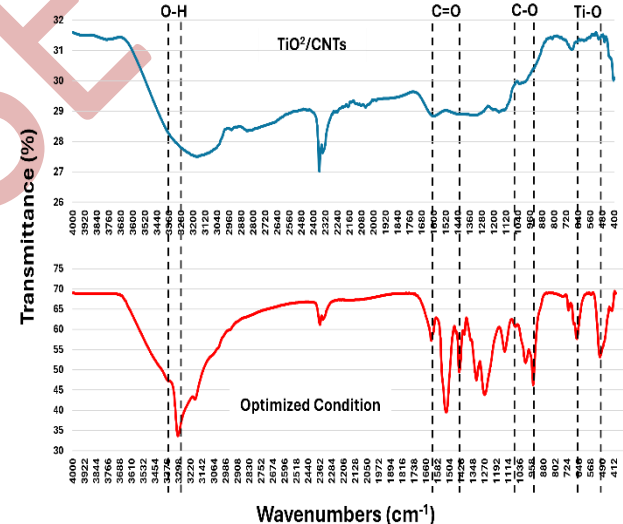


Figure 3. The FTIR spectra of the $TiO_2/CNTs$ nanocomposites, taken before and after H_2 storage, reveal significant alterations in the surface functional groups.

Discussion

This study highlights the potential of hydrogen storage using $TiO_2/CNTs$ nanocomposites with a surface area of $323\text{ m}^2/\text{g}$, achieving a maximum storage capacity of 2.47 wt%. TiO_2 was incorporated into the CNTs to enhance their structural stability and hydrogen adsorption capacity, providing better performance compared to CNTs alone.

While the storage capacity is lower compared to methods using extreme conditions like cryogenic temperatures (-196.15 °C) and high surface area nanomaterials (e.g., 2000 -6000 m²/g, results: 7-9 wt%), the simplicity of the setup using basic equipment and materials at -15°C makes it cost-effective and scalable. The modest surface area likely limited the wt%, but the results are promising given the accessibility of the approach. This method offers a practical solution for hydrogen storage in resource-limited environments without relying on expensive equipment.

The reason this system performs well at -15°C is due to the synergistic design of the nanocomposite and the control overflow dynamics created by the NPT. Additionally, no extra pressure was applied to the system. The internal pressure inside the NPT, generated naturally by positioning it in the direction of the biogas flow and adjusting the PS, increased the interaction between H₂ molecules and the nanomaterial. The increased volume of nanomaterials reduced the permeability, slowing the H₂ flow, which extended the contact time between the H₂ molecules and the nanocomposite, leading to better adsorption. Moreover, the mesh at both ends of the NPT acted as a trap for the gas, slowing down the movement further and forcing the H₂ molecules to stay within the system longer. This mesh design, combined with the reduced permeability, ensured more efficient H₂ capture. In this regard, several equations help explain the dynamics within the system. For instance, the permeability of H₂ through the NPT can be understood by a simplified version of Darcy's Law (Eq. (1)) [6]:

$$Q = \frac{K \cdot A \cdot \Delta P}{\mu \cdot L} \quad (1)$$

References

1. M. R. Usman, "Hydrogen storage methods: Review and current status," *Renew. Sustain. Energy Rev.*, vol. 167, no. July, p. 112743, 2022, doi: 10.1016/j.rser.2022.112743.
2. L. X. Yang, S. L. Luo, Q. Y. Cai, and S. Z. Yao, "A review on TiO₂ nanotube arrays: Fabrication, properties, and sensing applications," *Chinese Sci. Bull.*, vol. 55, no. 4, pp. 331–338, 2010, doi: 10.1007/s11434-009-0712-3.
3. J. Wang, W. Yan, Z. Wan, Y. Wang, J. Lv, and A. Zhou, "Prediction of permeability using random forest and genetic algorithm model," *C. - Comput. Model. Eng. Sci.*, vol. 125, no. 3, pp. 1135–1157, 2020, doi: 10.32604/cmescs.2020.014313.
4. S. W. Kim, B. A. Trisna, M. Yin, J. Lim, T. K. Ahn, and J. Lee, "Development of a hydrogen impurity analyzer based on mobile-gas chromatography for online hydrogen fuel monitoring," *Int. J. Hydrogen Energy*, vol. 48, no. 35, pp. 13012–13023, 2023, doi: 10.1016/j.ijhydene.2022.12.233.
5. J. Zhang et al., "Preparation and temperature regulation properties of TiO₂/CNTs-based form-stable phase change materials," *Colloids Surfaces A Physicochem. Eng. Asp.*, vol. 685, no. December 2023, p. 133278, 2024, doi: 10.1016/j.colsurfa.2024.133278.
6. J. Xiao, Y. Liu, J. Wanga, P. Bénard, and R. Chahine, "Finite element simulation of heat and mass transfer in activated carbon hydrogen storage tank," *Int. J. Heat Mass Transf.*, vol. 55, no. 23–24, pp. 6864–6872, 2012, doi: 10.1016/j.ijheatmasstransfer.2012.06.093.

Where Q is the flow rate of H₂, K is the permeability of the NPT, A is the cross-sectional area of the NPT, ΔP is the pressure difference across the NPT, μ is the viscosity of H₂, and L is the length of the NPT. This equation shows how pressure and material properties (such as permeability K) affect the flow rate of H₂ through the system. Lowering the temperature to -15°C impacts the permeability of nanomaterials by subtly altering their structural properties and the behavior of H₂ molecules. At lower temperatures, the nanomaterial's atomic vibrations decrease, which can lead to a slight contraction in pore size. This reduction in pore size restricts the flow of H₂, effectively lowering the permeability of the material. Additionally, H₂ molecules, with reduced kinetic energy at lower temperatures, move more slowly through the nanomaterial.

Conclusions

This study highlights the effectiveness of a Nanocomposite Permeation Tube (NPT) filled with TiO₂/CNTs nanocomposite for efficient hydrogen storage at -15°C and 25 RPM pump speed. The synergy between TiO₂ and CNTs enhances hydrogen adsorption, without the need for extreme conditions like very low temperatures (e.g., -196 °C) or high pressure. Moreover, AI-driven optimization effectively improved system performance, achieving 2.47 wt% H₂ storage while reducing experimental runs (i.e., to 9 runs). Though this method is in early stages, this approach offers a practical and energy-efficient solution for hydrogen storage, providing valuable insights for making clean energy storage more accessible and feasible in real-world applications.

Acknowledgments

Behrouz Nemati acknowledges FCT for financial support, under the scholarship 2020.05304.BD. This work also received financial support through CESAM by FCT / MCTES (UIDP/50017/2020 + UIDB/50017/2020 + LA/P/0094/2020), through national funds. Thanks are also due to the financial support of the project CICECO-Aveiro Institute of Materials, UIDB/50011/2020 (DOI 10.54499/UIDB/50011/2020), UIDP/50011/2020 (DOI 10.54499/UIDP/50011/2020) & LA/P/0006/2020 (DOI 10.54499/LA/ P/ 0006/2020), and Research Employment Contract FCT–CEECIND/02608/2017, financed by national funds through the FCT/MCTES (PIDDAC). Thanks, are also due to the financial support from the PDM program, KU Leuven.

ICMATSE 2024

Structural, magnetic, and blood compatibility studies of Nickel-Copper nanoferrites produced by laser ablation technique

Can Özçelik

Instituto de Nanociencia y Materiales de Aragón, INMA (CSIC-Universidad de Zaragoza), 50018 Zaragoza, Spain, ozcelik@unizar.es
ORCID: 0000-0002-8100-6417

Sezen Özçelik

Hakkari University, Faculty of Engineering, Department of Food Engineering, Hakkari, Turkey, sezenozcelik@hakkari.edu.tr
ORCID: 0000-0003-2846-2226

Bestenur Yalçın

Department of Medical Laboratory Techniques, Vocational School of Health Services, Bahcesehir University, 34353 Istanbul, Besiktas, Turkey bestenur.yalcin@eng.bau.edu.tr
ORCID: 0000-0002-7233-6561

Lütfi Arda

Bahcesehir University, Faculty of Engineering and Natural Sciences, Department Mechatronics Engineering, 34353, Besiktas, Istanbul, Turkey lutfi.arda@eng.bau.edu.tr
ORCID: 0000-0003-70722-3891

Luis A. Angurel

Instituto de Nanociencia y Materiales de Aragón, INMA (CSIC-Universidad de Zaragoza), 50018 Zaragoza, Spain, angurel@unizar.es
ORCID: 0000-0001-5685-2366

Bekir Özçelik

Department of Physics, Faculty of Sciences and Letters, Çukurova University, 01330 Adana, Türkiye ozcelik@cu.edu.tr
ORCID: 0000-0002-8767-1426

Cite this paper as: C.Özçelik, S.Özçelik, B.Yalçın, L.Arda, L.A. Angurel, B.Özçelik Structural, magnetic, and blood compatibility studies of Nickel-Copper nanoferrites produced by laser ablation technique, Int. Conf. Advanced. Mater. Sci.& Eng. HiTech.and Device Appl.Oct. 24-26 2024, Ankara, Turkiye

Abstract. This study explores the effects of Cu substitution on the structural, morphological, and magnetic properties of nickel ferrite. Cu was substituted into Ni-spinel ferrites ($\text{Ni}_{1-x}\text{Cu}_x\text{Fe}_2\text{O}_4$, where $x = 0.25, 0.50,$ and 0.75) using the laser ablation technique. SEM analysis revealed that the grains are spherical with an average size of 7 nm. The Nickel-Copper ferrite nanoparticles presented a characteristic spinel peak related to the cubic spinel structure of the $Fd3m$ space group, with no secondary phases forming due to Cu substitution. The crystal sizes of Ni-Cu spinel ferrites were calculated to be between 44.9 and 52 nm. FT-IR results indicated increased force constants of octahedral and tetrahedral bonds with higher Cu content, as evidenced by the main vibration bands. M-H curves displayed S-shaped behavior, suggesting that Cu substitution does not cause drastic changes in magnetic properties. The coercivity field (H_c), saturation magnetization (M_s), and remanent magnetization (M_r)

values ranged between 13.54-6.14 Oe, 48.8-52.7 emu/g, and 0.57-1.14 emu/g, respectively. Blood compatibility experiments showed that the $\text{Ni}_{0.25}\text{Cu}_{0.75}\text{Fe}_2\text{O}_4$ composition exhibited the highest blood compatibility at low concentrations among the samples studied.

Keywords: Spinel ferrite, Ni-Cu ferrite, Nanoparticles, FT-IR, Blood compatibility
© 2024 Published by ICMATSE

Introduction

The term 'spinel' refers to a cubic structure with the general formula AB_2O_4 , where A and B symbolizes a divalent cation and a trivalent cation, respectively. Thus, spinel ferrites are expressed as closely packed cubic structures with iron (Fe^{3+}) as the trivalent cation, resulting in the complete formula AFe_2O_4 . The divalent cation (A) can be iron (Fe), nickel (Ni), zinc (Zn), cobalt (Co), manganese (Mn), magnesium (Mg), copper (Cu), cadmium (Cd), or a combination of these elements. These ferrites are named after the naturally occurring mineral MgAl_2O_4 , known as 'spinel,' due to the similarity in their structure. They are also referred to as ferrospinels or cubic ferrites. These materials have attracted the interest of material scientists since their discovery. Spinel ferrites are highly regarded for their intriguing magnetic and electrical properties, including high saturation magnetization, high squareness ratio, significant magnetocrystalline anisotropy, low coercivity [1], high electric resistivity [2], high permeability [3], low eddy current losses [4], high Curie temperature, and mechanical hardness [5], among others. They are traditionally used as microwave absorbers because of their large magnetic losses and high resistivities and are also applicable in the 3–30 GHz frequency range [1]. Properties like high thermodynamic stability, high electrical conductivity, and high corrosion resistance make them suitable for use in metallurgical and other high-temperature fields [6, 7]. Spinel ferrites are often favored over hexaferrites by application designers due to time-consuming, expensive, and not always successful and the challenges caused by chemical instability arising from thermal excitation [8].

In the framework of this study, taking into account the replacement of copper in nickel ferrite, there is significant potential for enhancing the properties of pristine nickel ferrite through laser ablation routes. The physical and the biological properties of the Cu-substituted Ni-ferrite nanoparticles were investigated via XRD, SEM, FT-IR, magnetic and blood compatibility measurements.

Results and discussion

The XRD diffraction patterns of $\text{Ni}_{1-x}\text{Cu}_x\text{Fe}_2\text{O}_4$ nanoparticles with $x=0.25, 0.50,$ and 0.75 , recorded between 10° and 70° diffraction angles, are shown in Fig. 1. The Nickel-Copper ferrite nanoparticles exhibit characteristic spinel peaks associated with the cubic spinel structure of the $Fd\bar{3}m$ space group, labeled as (111), (220), (311), (222), (400), (422), (511), and (440), corresponding to PDF card No.: 98-015-8834. In addition, only one secondary peak concerning CuO is observed in the XRD patterns.

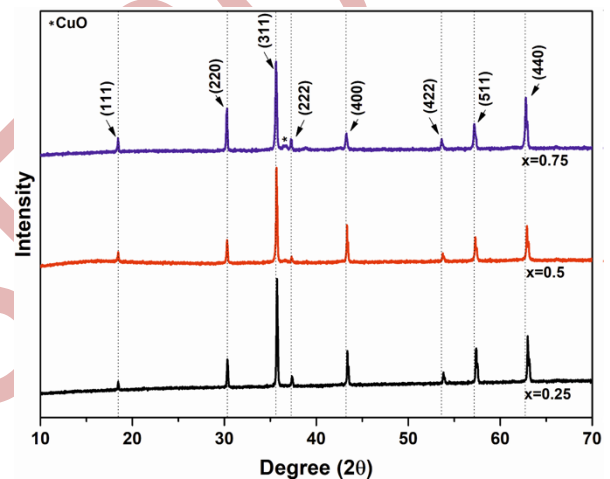


Figure 1. X-ray diffraction patterns of $\text{Ni}_{1-x}\text{Cu}_x\text{Fe}_2\text{O}_4$ ferrites.

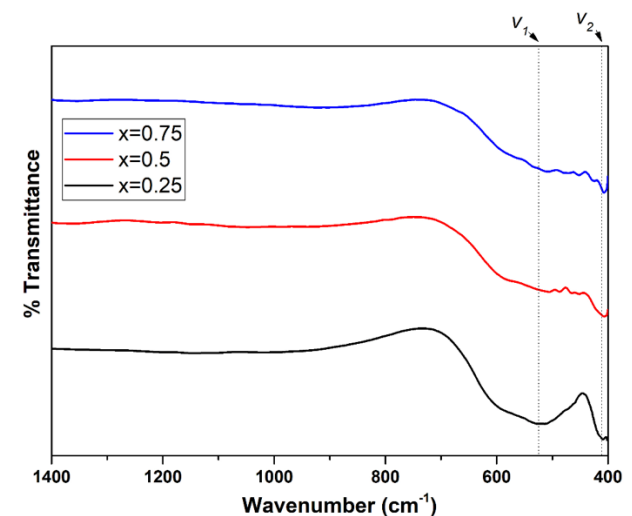


Figure 2. FT-IR spectra of $\text{Ni}_{1-x}\text{Cu}_x\text{Fe}_2\text{O}_4$ nanoparticles

To investigate the cubic spinel structure and absorption bands of $\text{Ni}_{1-x}\text{Cu}_x\text{Fe}_2\text{O}_4$ nanoparticles, FT-

IR analysis was performed, as shown in Fig. 2. The FT-IR spectrum typically shows two peaks between wavelengths of 400-600 cm^{-1} , indicative of the spinel structure. Figure-2 displays the infrared transmittance spectra of Cu-substituted Ni-ferrite materials, where the vibrational frequencies of Cu-O or Ni-O bonds (ν_1) and Fe-O bonds (ν_2) appear as 518.8, 506.2, and 510.6 cm^{-1} and 407.9, 403.0, and 405.5 cm^{-1} for the $x=0.25$, 0.50, and 0.75 Cu-substitutions, respectively.

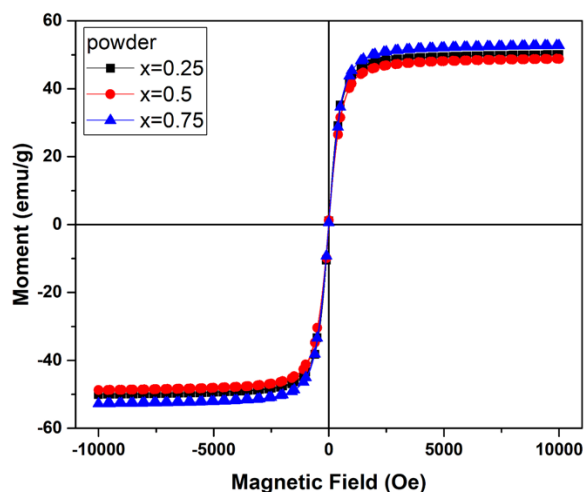


Figure 3. $M-H$ curves measured at room temperature for $\text{Ni}_{1-x}\text{Cu}_x\text{Fe}_2\text{O}_4$ nanoparticles.

The magnetic hysteresis loop results for $\text{Ni}_{1-x}\text{Cu}_x\text{Fe}_2\text{O}_4$ nanoparticles with $x = 0.25, 0.5$, and 0.75 , measured at room temperature under an external magnetic field range of ± 1 T, are shown in Fig. 3. The figure reveals that all samples display an S-shaped hysteresis curve. Magnetic properties such as saturation magnetization (M_S), remanent magnetization (M_R), and coercivity (H_C) are listed in Table 1. According to the table, the M_S and M_R values

initially decrease with increasing Cu content, followed by an increase.

Sample	M_S (emu/g)	M_R (emu/g)	H_C (Oe)	β constant ($\times 10^8$)	K_a anisotropy constant ($\times 10^5$) (erg/g)
$x=0.25$	50.1	1.07	11.76	-0.144	3.67
$x=0.50$	48.8	1.14	13.54	-0.161	3.79
$x=0.75$	52.7	0.57	6.13	-0.155	4.01

Conclusions

This study extensively explores the impact of Cu inclusions on the structural, physical, magnetic, morphological, Fourier Transform Infrared Radiation (FT-IR), and blood compatibility properties of $\text{Ni}_x\text{Cu}_{1-x}\text{Fe}_2\text{O}_4$ nanoparticles. The XRD patterns confirm the presence of characteristic spinel peaks associated with the $Fd3m$ space group cubic spinel structure. The magnetic results indicate that saturation and remanent magnetization, coercivity, and the anisotropy constant are not significantly impacted by Cu substitution. It was concluded that, 1.0 mg/ml was the optimum nanoparticle concentration for all three compositions. Although their intensities varied depending on the composition, the preservation of the Q-bands and Soret band at this concentration was considered as a significant indicator that NPs were not showing adverse effects on blood biochemistry. Additionally, significant findings indicating MetHb formation were found at concentrations of 3.0 and 5.0 mg/ml.

References

- [1] Z.K. Heiba, M.B. Mohamed, H.H. Hamdeh, M.A. Ahmed, "Structural analysis and cations distribution of nanocrystalline $\text{Ni}_{1-x}\text{Zn}_x\text{Fe}_{1.7}\text{Ga}_{0.3}\text{O}_4$ " J. Alloy. Compd. 618 (2015) 755–760.
- [2] Q. Liu, L. Lv, J.P. Zhou, X.M. Chen, X.B. Bian, P. Lu, "Influence of nickel-zinc ratio on microstructure, magnetic and dielectric properties of $\text{Ni}_{1-x}\text{Zn}_x\text{Fe}_2\text{O}_4$ ferrites" J. Ceram. Proc. Res. 13 (2012) 110–116.
- [3] S. Mukharjee, S. Pradip, A.K. Mishra, D. Das, "Zn substituted NiFe_2O_4 with very high saturation magnetization and negligible dielectric loss synthesized via a soft chemical route" Appl. Phys. A 114 (2013) 389–393.
- [4] A. Ghasemi, M. Mousavinia, "Structural and magnetic evaluation of substituted $\text{NiZnFe}_2\text{O}_4$ particles synthesized by conventional sol-gel method" Ceram. Int. 40 (2014) 2825–2834.
- [5] X. Wu, W. Chen, W. Wu, H. Li, C. Lin, "Structural and Magnetic Properties Evolution of Li-Substituted $\text{Co}_{0.5}\text{Ni}_{0.5}\text{Fe}_2\text{O}_4$ Ferrite" J. Electron. Mater. 46, 199-207. <https://doi.org/10.1007/s11664-016-4877-7>
- [6] E. Olsen, J. Thonstad, "Nickel ferrite as inert anodes in aluminium electrolysis: Part I. Material fabrication and preliminary testing" J. Appl. Electrochem. 29 (1999) 293.
- [7] L.J. Berchmans, R.K. Selvan, C.O. Augustin, "Evaluation of Mg^{2+} -substituted NiFe_2O_4 as a green anode material" Mater. Lett. 58 (2004) 1928.
- [8] C. Stergiou, "Magnetic, dielectric and microwave absorption properties of rare earth doped Ni-Co and Ni-Co-Zn spinel ferrites" J. Magn. Mater. 426 (2017) 629–635.

Third Generation Single Crystal Superalloys-A Short Review

Cemre ATALAY

*Department of Metallurgical and Materials Engineering, Graduate School of Natural and Applied Sciences, Gazi University, 06560 Ankara, Turkey,
24833701007@gazi.edu.tr
ORCID: 0009-0001-2562-6742*

Volkan KILICLI

*Department of Metallurgical and Materials Engineering, Faculty of Technology, Gazi University, 06560 Ankara, Turkey,
vkilicli@gazi.edu.tr
ORCID: 0000-0002-0456-5987*

Atalay C., Kilicli V., Third Generation Single Crystal Superalloys-A Short Review. Int. Conf. Advanced. Mater. Sci. & Eng. HiTech. and Device Appl. Oct. 24-26 2024, Ankara, Turkiye

Abstract. A new third generation of single crystal superalloys has been developed for aircraft engine turbine blade applications. This study provides a brief overview of third generation single crystal superalloys. CMSX-10 and Rene N6 alloys are third generation single crystal alloys developed for aerospace applications. Rene N6 is microstructurally stable and approximately 30°C stronger than the second-generation single crystal, Rene N5. The CMSX-10 alloy is a third-generation single crystal (SX) nickel base casting alloy characterised by its 6 wt% rhenium content, relatively high refractory element content (W + Ta + Re + Mo) and low chromium content.

Keywords: Single Crystal, Superalloy, Refractory Element
© 2024 Published by ICMATSE

Introduction

Superalloy and casting process developments occurring over the past 30 years have helped gas-turbine-engine manufacturers achieve dramatic engine performance/efficiency gains [1]. Dramatic improvements in the performance of gas turbines have resulted from the development of directional solidification and the production of single crystal turbine blades and vanes [2]. Several SX superalloys developed since the 1970s are summarized in

Figure 5. Since their development in the late 1980's. second generation, single crystal superalloys have attained success in both commercial and military aircraft engines. These alloys typically contain 3 wt.% Rhenium, which distinguishes them from first generation single crystal superalloys [3]. The introduction of 3 wt. % rhenium to nickel-based alloys resulted in additional strength/temperature capability improvements [1]. Development of third generation single crystal alloys proceeded with increases in refractory element content [3]. Based on published data, the alloy's high-temperature creep-rupture resistance is greater than all other nickel-

based alloys (approximately 30°C better than CMSX-4 and PWA 1484). The usage of 6 wt. % rhenium in the new CMSX-10 alloy results in another 30°C improvement relative to second-generation SX alloys such as CMSX-4, PWA 1484 and Rene N5 [1].

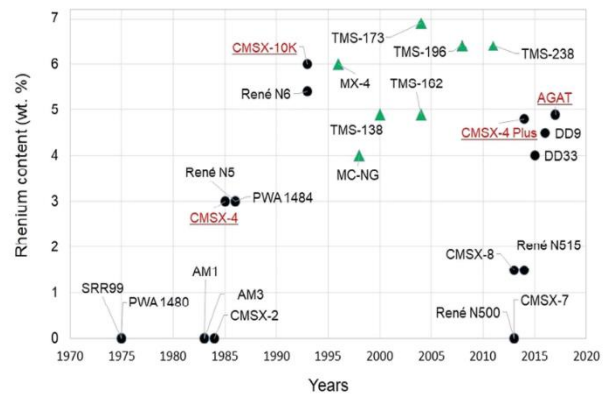


Figure 5. Evolution of rhenium content in nickel-base SX superalloys [13].

Third Generations Single Crystal Superalloys

1. Rene N6

Composition

The compositions of several second and third generation single crystal alloys are shown in Table 1. The second-generation alloys contain 3 wt.% Re, while the third-generation alloys have significantly higher levels of Re. The Re content of Rene N6 was most important in determining the balance between creep rupture strength and microstructural stability with respect to both TCP phase formation and SRZ

occurrence. Relatively high levels of Co and low levels of Cr were also selected to benefit stability. High levels of Ta were found to be beneficial to high temperature strength and castability [4]. While the elements Hf, C and B were initially not utilized in single crystal superalloys, it has been found by GE Aircraft Engines that they are beneficial to improving the tolerance for casting defects, such as low angle grain boundaries [5], and for other properties, such as castability and environmental resistance. Yttrium was intentionally added to improve the adherence of the protective aluminum oxide layer formed in service [6,7].

Table 2. Nominal chemical compositions of single crystal Ni-based superalloys (in wt.%)^a [8]

Alloy	Ni	Cr	Co	Mo	W	Ta	Re	Nb	Al	Ti	Hf	Other	Ref
CMSX-3	Bal	8	5	0.6	8	6			5.6	1.0	0.1		[5]
PWA 1480	Bal	10	5		4	12			5.0	1.5			[5]
Rene' N4	Bal	9.75	7.5	1.5	6	4.8		0.5	4.2	3.5	0.15	0.004B, 0.05C	[15]
CMSX-4	Bal	6.5	9	0.6	6	6.5	3		5.6	1.0	0.1		[5]
PWA 1484	Bal	5	10	2	6	9	3		5.6		0.1		[5]
Rene' N5	Bal	7	8	2	5	7	3		6.2		0.2		[5]
CMSX-10	Bal	2	3	0.4	5	8	6	0.1	5.7	0.2	0.03		[5]
Rene' N6	Bal	4.2	12.5	1.4	6	7.2	5.4		5.75		0.15	0.004B, 0.05C, 0.01Y	[13]

^a Note that, based on Re content, the alloys are grouped as first (0 wt.%), second (3 wt.%) and third (5-6 wt.%) generation alloys.

Heat Treatment

The solution heat treatment cycle for Rene N6 was carefully developed to provide acceptable levels of γ/γ' eutectic and incipient melting. Heat treatment trials to determine the levels of solutioning and incipient melting were conducted, resulting in over a 20°C window for acceptable solution heat treatment, as shown in Figure 6 [3].

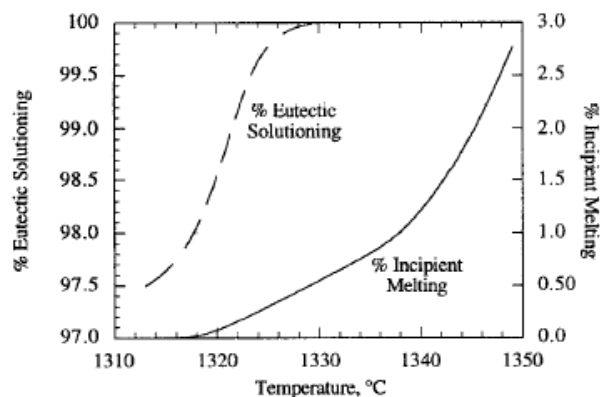


Figure 6. Effect of solution heat treat temperature on the amount of solutioning and incipient melting [3]

Properties

The stress dependence of the minimum creep rates at several temperatures for Rene N6 are shown in Figure 7. Creep stress exponents (n) are in the range of 6.1 to 10.8, similar to other single crystal alloys [9-11]. Rene N6 retains good creep strength even at temperatures as high as 1200°C.

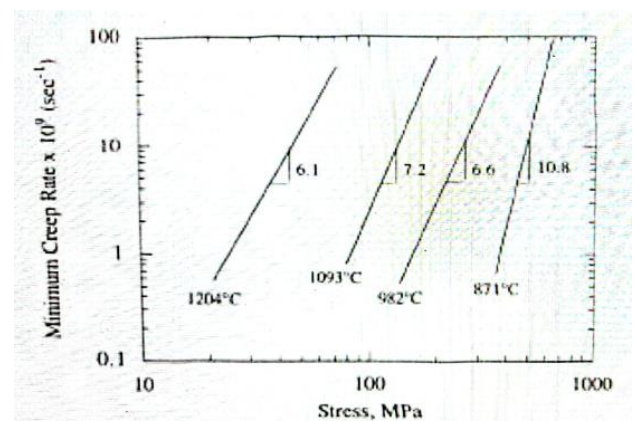


Figure 7. Stress dependence of the minimum creep rate for Rene N6 at several temperatures [3]

Selected creep rupture properties at 982°C are shown in Figure 8. Rene N6 displays about a 30°C benefit compared to Rene N5. The 30°C advantage over Rene

N5 is maintained even at the higher temperatures and longer times due to the good microstructural stability of Rene N6 [3].

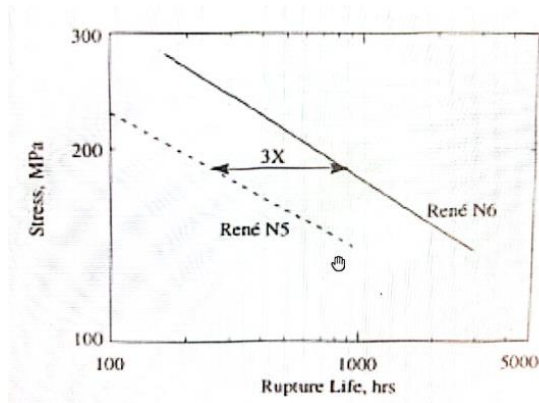


Figure 8. Creep rupture properties of thin wall, PtAl coated specimens tested at 982°C for Rene N5 and Rene N6 [3]

2. CMSX-10

Composition

Along with the relatively high Re level employed in CMSX-10 alloy, experience suggests that creep-strength optimization also requires increased levels of other refractory element hardeners such as W, Ta and Mo [12].

All told, the CMSX-10 alloy system employs the relatively high additive refractory element content of about 20.1 Wt.%; this in comparison to CMSX-4 which is about 16.4% and CMSX-2 at 14.6%. Gamma prime formers such as Al and Ti are similar to second generation SX alloys and the CMSX-10 gamma prime chemistry is actually quite similar to that predominating for CMSX-4 [12].

This, in tandem with the high level of W + Re + MO prevailing throughout the alloy matrix assists in the attainment of the extremely high creep-strength exhibited by the CMSX-10 alloy, particularly at elevated temperatures [12]. Table 1 provides the CMSX-10 alloy chemistry in comparison to other first, second and third generation SX alloys.

Heat Treatment

CMSX-10 alloy also provides attractive solution heat treatment capability. The alloy provides a 21°C heat treatment window and is thereby able to be fully solutioned. Solution heat treatment, undertaken with a final soak temperature of 1366°C results in full coarse γ' solutioning plus complete eutectic γ/γ' dissolution. Precipitation of the dissolved γ' into a

more useful fine γ' results, and primary aging of the fine γ' then occurs at 1152°C [12].

The CMSX-10 alloy primary γ' aging treatment helps develop an array of line cubic γ' with relatively regular alignment, exhibiting average edge dimensions of about 0.5 μm . The primary aging treatment is followed by two secondary aging treatments which promote the formation of finer γ' within the alloy's matrix channels. These secondary aging treatments are preformed at 871°C for 24 hours and at 760°C for 30 hours [12]. The microstructure image after solution heat treatment is given in Figure 5.

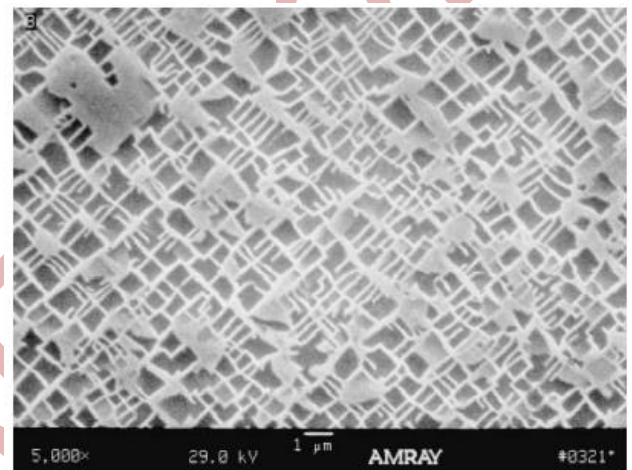


Figure 9. The SEM photomicrograph of the homogeneous γ' distribution after complete standard solution anneal heat treatment [14]

Properties

Third generation SX casting alloys generally exhibit enhanced creep strength relative to their second-generation predecessors. The relative improvement depends upon the alloy systems compared, but for CMSX-10, the advantage is about 30°C relative to CMSX-4 [12].

For specimens which have ruptured, log-log plots of the "long-term" creep results are presented. While Figure 10 presents the 982°C rupture strength of CMSX-10 in comparison to the CMSX-4, DS CM 247 LC and IN 738 LC alloys and Figure 11 illustrates the CMSX-10 alloy strength for exposure temperatures ranging from 913 to 1010°C, and lives approaching 4500 hours. Generally, the CMSX-10 alloy develops significantly greater strength than CMSX-4 in these test conditions. However, at 982°C the CMSX-10 benefit appears to narrow slightly with longer term exposures [12].

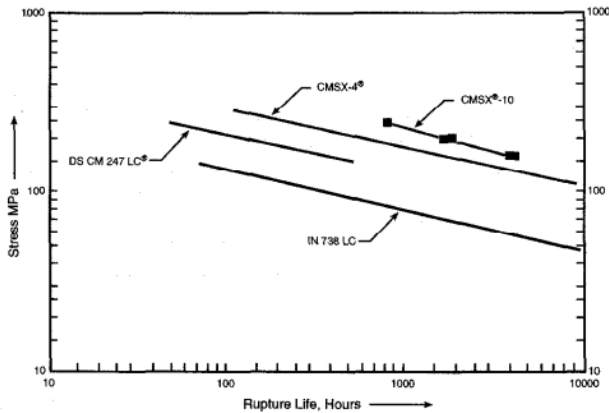


Figure 10. Stress-rupture strength of several alloys at 982°C [12]

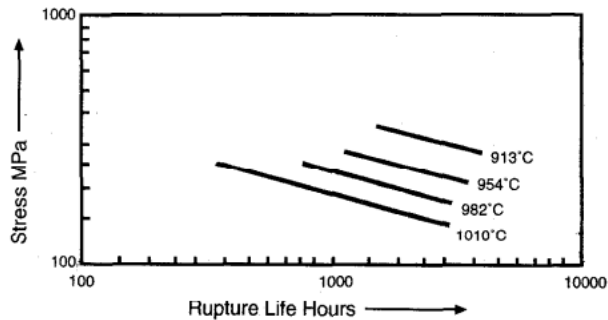


Figure 11. 913-1010°C stress-rupture strength of CMSX-10 [12]

Summary

- The third-generation single crystal superalloys are flight engine qualified and is a production status material exhibiting extremely good foundry functionality, heat treatment characteristics, high strength, environmental properties and coatability.
- This group of alloys is characterized by high rhenium content.
- This new generation alloy group exhibits better mechanical properties compared to the second-generation single crystal superalloys.

References

1. Erickson, G. L. (1995). A new, third-generation, single-crystal, casting superalloy. *JOM*, 47(4), 36-39.
2. J.R. Davis (Ed.), Directionally solidified and single crystal superalloys, *Heat Resistant Materials - ASM Specialty Handbook*, ASM International, Materials Park, OH, 1997, p. 255.
3. Walston, W. S., O'hara, K. S., Ross, E. W., Pollock, T. M., & Murphy, W. H. (1996). Rene n6: Third generation single crystal superalloy. *Superalloy*.
4. T. M. Pollock, W. H. Murphy, E. H. Goldman, D. L. Uram and J. S. Tu, "Grain Defect Formation During Directional Solidification of Nickel Base Single Crystals", *Superalloys 1992*, ed. S. D. Antolovich, et al., TMS, 1992,125-134.
5. E. W. Ross, C. S. Wukusick and W. T. King, U.S. Patent 5.399.313, "Nickel-Based Superalloys for Producing Single Crystal Articles Having Improved Tolerance to Low Angle Grain Boundaries", 1995.
6. E. W. Ross and K. S. CYHara, "U.S. Patent 5,173,255, "Cast columnar grain hollow nickel base alloy articles and alloy and heat treatment for making" - Rente 142, 1992).
7. E. W. Ross and K. S. CYHara, "Rene 142: A High Strength, Oxidation Resistant DS Turbine Airfoil Alloy", *Superalloys 1992*, ed. S. D. Antolovich, et al., TMS, 1992,257-265.
8. Fuchs, G. E. (2001). Solution heat treatment response of a third generation single crystal Ni-base superalloy. *Materials Science and Engineering: A*, 300(1-2), 52-60.
9. W. Murphy, T. Pollock and R. Field, "Creep Mechanism Studies in Rene N5 and Related Single Crystal Superalloys", (GE Aircraft Engines internal report, 1991).
10. M. V. Nathal and L. J. Ebert, "The Influence of Cobalt, Tantalum and Tungsten on the Elevated Temperature Mechanical Properties of Single Crystal Nickel-Base Superalloys", *Metall. u*, 16A(1985), 1863-1870.
11. M. V. Nathal and L. J. Ebert, "Elevated Temperature Creep-Rupture Behavior of the Single Crystal Nickel-Base Superalloy NASAIR 100", *Metall. m*, 16A(1985), 427-439.
12. Erickson, G. L. (1996). The development and application of CMSX-10. *Superalloys*, 1996, 35-44.
13. Rame, J r my, et al. "Computational Design and Experimental Characterization of a Novel Third-Generation Single Crystal Superalloy with Balanced High-Temperature Creep Strength and Oxidation Resistance." *International Symposium on Superalloys*. Cham: Springer Nature Switzerland, 2024.

Preparation and characterization of ZnO- based Schottky diode prepared with sol-gel method

Arab Louiza

Mohamed kheider university- material sciences Department, 7020, Biskra, Algeria,
louiza.arab@univ-biskra.dz
ORCID: 0009-0003-9695-3374

Sengouga Nouredine

Mohamed kheider university- material sciences Department, 7020, Biskra, Algeria,
n.sengouga@univ-biskra.dz
ORCID: 0000-0002-4437-0869

Abdeslam Nora Amel

Mohamed kheider university- material sciences Department, 7020, Biskra, Algeria,
noura.abdeslam@univ-biskra.dz

Chenni Chaima

Mohamed kheider university- material sciences Department, 7020, Biskra, Algeria,
chennimabroka@gmail.com

Latif Aya

aya.latif@univ-biskra.dz

Cite this paper as: Arab, L, sengouga, N, Chenni, C, Abdeslam N.A, Preparation and characterization of ZnO- based Schottky diode prepared with sol-gel method. Int. Conf. Advanced. Mater. Sci.& Eng. HiTech.and Device Appl.Oct. 24-26 2024, Ankara, Turkiye

Abstract. ZnO-based Schottky diode have been fabricate via the deposition of a ZnO film codoped with Al + In on a Gallium-doped ZnO film with sol-gel method. The XRD of the films shows a polycrystalline structure and grains size in nanoscale. The films present a high transmittance in the visible, and the I-V characteristics show a Schottky-type behavior in the dark and under light, which is controlled by the thickness of the resistive layer. and the optical properties will be analyzed with the UV-Vis spectrophotometer.

Keywords: ZnO thin films, sol-gel, junction diodes.

© 2024 Published by ICMATSE

Introduction

ZnO has been widely studied for its application in the development of transparent electronics. Because of their wide bandgap, zinc oxide-based transparent and conductive films have potential application in multiple areas, including solar cells, photonic crystals, lightemitting diodes, photodetectors, modulator waveguides, varistors, gas sensors, and thin film transistors [1]. Zinc oxide, which belongs to the II-VI semiconductors, has distinctive and adaptable physico-chemical characteristics, such as high exciton binding energy (60 meV), non-toxicity, UV light-blocking ability, a wide band gap (3.37 eV),

and thermal stability. Schottky diodes are a type of diode based on a metal half-carrier junction and are known for their unique characteristics such as fast switching and high efficiency. The use of transparent conductive materials (TCO) such as indium tin oxide (ITO) and doped ZnO improves transparency and conductivity of schottky diode [2]. The study and development of transparent Schottky diodes using ITO/ZnO configurations prepared by Sol-Gel techniques is a promising field that aims to improve the electrical and optical performance of these devices [3]. By optimizing material properties and preparation techniques. The main object of this study is to elaborate thin films of ZnO pure, doped

with Ga and co-doped with In-Al. the results obtained have been used in manufacturing a ZnO based Schottky diode. The method adopted in this study is gel sol (spin coating).

Methodology

ZnO- based Schottky diode prepared with sol-gel method, the master solution containing zinc acetate dihydrate solution ($Zn(CH_3COO)_2 \cdot 2H_2O$), it was used as a precursor. Absolute ethanol (C_2H_5-OH) and diethanolamine ($HN(CH_2CH_2OH)_2$, DEA) were used as solvent and stabilizing agents respectively. with a molar concentration of the solution is 0.5 M, and the molar ratio of DEA with the acetate was maintained at unity. Aluminum, indium and Gallium were added in the form of nitrates: $Al(NO_3)_3 \cdot 9H_2O$ and $In(NO_3)_3 \cdot H_2O$, and $Ga(NO_3)_3$. The dopants were dissolved in ethanol to obtain solutions with molar ratios equivalent to 8 at. % for gallium and 4 at. % for (aluminum + indium). The co-doped films were prepared as ZnO:(In 2% + Al 2%). This solution was stirred for 30 min at 60°C temperature to become homogenous. Then it was left to rest for 24h before thin film deposition in a spin-coating system. The layers were deposited by spin coating at a rotation speed of 1000 rpm for 30sc. After spin coating, each layer was immediately treated thermally at 500°C in oven air for 30 min before spinning the next layer. Each film was obtained through repeated layer deposition times. At the end the diode was treated thermally at 500°C for 30 min in air.

Results and Discussion

X-ray diffraction results were obtained using the device "Rigaku MiniFlex 600"(Thin films and their applications Laboratory-Biskra), using $CuK\alpha$ radiation with a 1,541874Å-wavelength. Figure (1), represents X-ray diffractograms of ZnO films with different doping solutions deposited on ITO substrates. The comparison with JCPDS Card No. 01-075-0576 indicates that ZnO films crystallized into the hexagonal wurtzite crystal structure. While the five additional peaks noticed correspond to the ITO substrate, they are marked by (*). And identify by comparison with JCPDS Card No. 01-089-4598).

The figure (2) shows the variation of the grain size for ZnO pure, doped with Ga8% and ZnO co-doped with (Al4%, In4%). The size of the crystals ranges from about 19.973 nm to 37.875 nm. This indicates

that the films elaborated are in nonoscale. The larger crystals that registered for ZnO pure (37.875 nm) indicate films are typically more stable and have better electronic properties compared to smaller crystals. The minimum grain size has been registered for Al-In co-doped ZnO thin film (19,973 nm), it can be explain by the difference in the ratio of the doping which is 8% for Ga, and (2% Al, 2% In) and the difference between the atom radius of Ga, In and Al

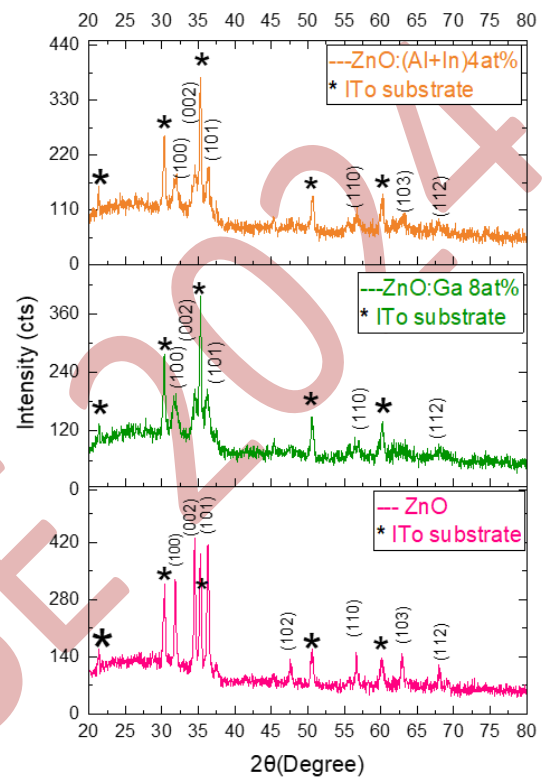


Figure 1. Spectra XRD of ZnO thin films with different solution

On the other hand, analysis of the relationship between strain (ϵ) and dislocation (δ), reveals that all doped samples have higher ϵ and δ values than the undoped ZnO sample, this result confirms the presence of defects in the ZnO crystal as it has been explain

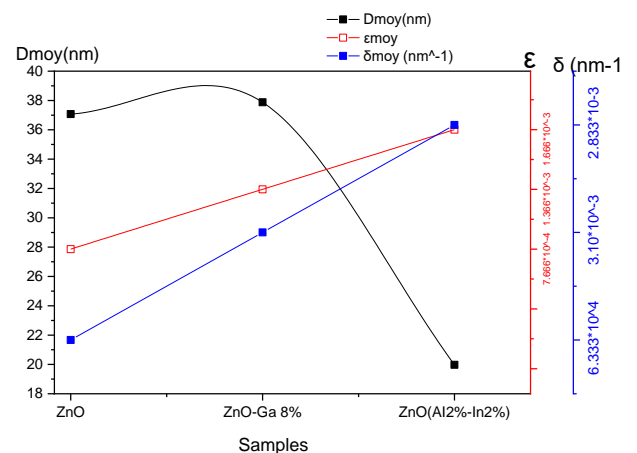


Figure 2. Crystallite size, strain, and dislocation density as a function of the samples.

thin films deposited with different doping elements have been recorded in Figure 3.

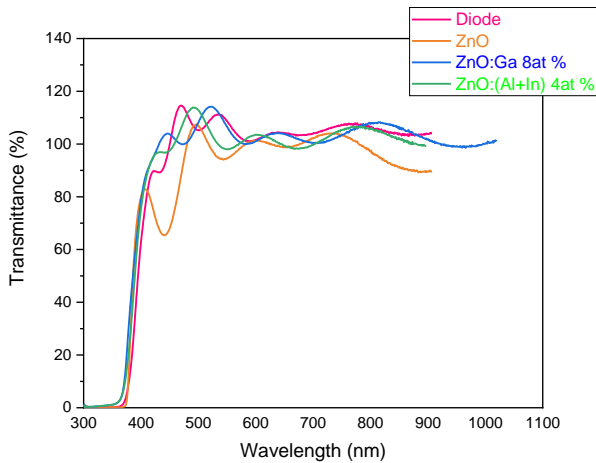


Figure 3. Optical Transmission Spectra of ZnO Thin Films Deposited with Different samples.

The increases of E_g gap for doped films is because the Al, In, and Ga dopants results in a higher carrier

The spectra show that all the films and the diode have a high transparency (>90%) in the visible region, and high absorption (almost 100%) in the UV region. The transmittance decreases slightly with different doping elements. The same observation has been reported in previous works [4]. It is noted the presence of the interference fringes in all spectra, which confirms the smoothing of all films and the high crystalline quality of the prepared films.

The tables 1. summarize the variation of E_g and E_u respectively.

Table 1. Variation of E_g and E_u respectively

	3.25	0.059
	3.27	0.010
	3.01	0.095

Ga-doped ZnO and Al-In co-doped ZnO thin films deposited on ITO substrate significantly affect their optical properties. The Ga doping increases slightly the optical band gap (3,27eV) in comparison with

The optical properties of the films have been obtained by using EVOLUTION 220 UV-VIS spectrophotometer for ultraviolet and visible light. The transmittance spectra of the diode and the ZnO concentration. It is a well-known fact that replacing Al^{+3} , Ga^{+3} , and In^{+3} with Zn^{+2} ions results in an extra free electron [5] as seen from the equation:



The increase in free carrier concentration results in the liberation of electrons that fill the low energy levels beneath the conduction band. These occupying electrons push the Fermi level towards the conduction band, thereby enlarging the forbidden energy range in ZnO thin films [6, 7] The widening of the band gap is also attributed to the shrinkage of the average particle size [8].

The figure (4) shows the variation of the Urbach energy for pure and doped ZnO films deposited on ITO substrate. The Ga-doped ZnO presents an improved crystalline quality and reduced disorder. Conversely, Al+In doping decreases the optical band gap and increases the Urbach energy, which indicating increased disorder.

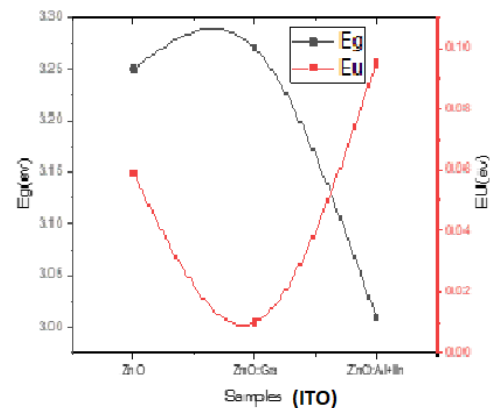


Figure 4. variation of E_g and E_u respectively in ITO substrate

pure ZnO gap (3,25 eV). The optical band gap is decreases remarkably for co-doped ZnO thin films (3,01 eV).

The I-V characteristics of the samples were measured with a B 1500 A semiconductor device analyzes system. The current-voltage data were obtained by applying voltages between 5 V and -5 V to the silver electrode (superior), whereas the inferior electrode (ITO) was grounded. The results are shown in Figures (5) and (6).

At low voltage in (a), the current of the diode increases exponentially with the increase in the forward voltage. In (b), the semi-logarithmic graph of the current with forward bias voltage quickly

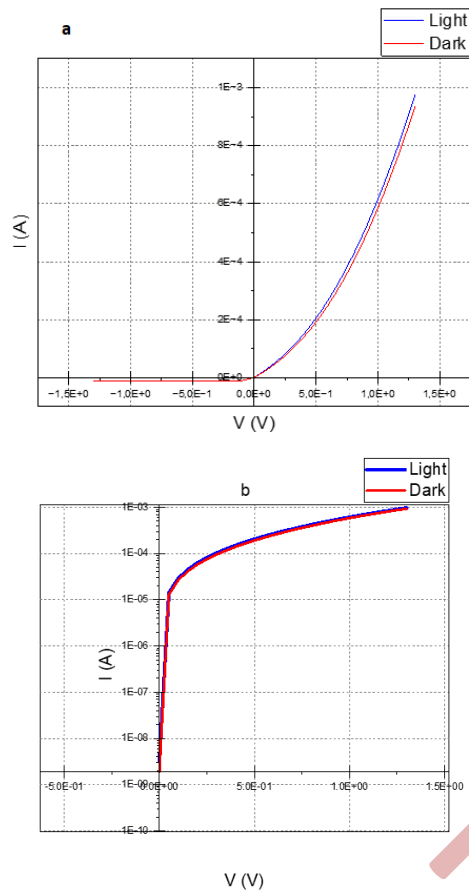


Figure 5. Current–voltage characteristics of the diode sample in (a) forward and reverse polarization in linear scale and (b) semi-logarithmic scale.

The slight difference between the I-V diode characteristic in light and darkness is due to low luminous intensity.

References

1. O. ADEDOKUN, Review on Transparent Conductive Oxides Thin Films deposited by Sol-gel spin coating technique. *International Journal of Engineering Science and Application*, 2 (2018), pp. 88-97, <https://dergipark.org.tr/en/pub/ijesa>.
2. C. Habis, J. Zaraket, & M. Aillerie, Transparent Conductive Oxides. Part II. Specific Focus on ITO, ZnO-AZO, SnO₂-FTO Families for Photovoltaics Applications, *In Defect and Diffusion Forum*, 417 (2022), pp. 257-272, 4028/p-6fqmfi.
3. M. A. Hernández-Ochoa, H. Arizpe-Chávez, R. Ramírez-Bon, A. Pérez-Rodríguez, M. Cortez-Valadez, & M. Flores-Acosta, Current–voltage characterization of transparent ITO/ZnO/ZnO:(Al + In)/Ag Schottky diodes prepared with multilayer films by sol–gel deposition. *J Electronic Materials*. Advance online publication, 3(2019)49, pp. 1993-2002, <https://doi.org/10.1007/s11664-019-07880-6>.
4. K. E. Spear, Principles and applications of chemical vapor deposition (CVD), *J Pure and Applied Chemistry*, 54(1982)7, pp. 1297-1311, <https://doi.org/10.1351/pac198254071297>.
5. S. Mann, S. L. Burkett, S. A. Davis, C. E. Fowler, N. H. Mendelson, S. D. Sims, & N. T. Whilton, Sol–gel synthesis of organized matter. *Chemistry of materials*, 9(1997)11, pp. 2300-2310, <https://doi.org/10.1021/cm970274u>.

becomes dominated by the series resistance of the semiconductor, provoking the curvature of the graph for high currents. The diode shows a Schottky-type behavior, and the current originates mainly from the thermionic emission of carriers.

This means that the charge density generated under light is not significantly higher than the total amount of free electrons moving in dark conditions under the effect of the electric field applied between the semiconductors [9].

Conclusion

Pure and doped ZnO with Ga 8% and co-doped with (Al 4%, In 4%) have been prepared using sol gel method. The doped ZnO films have been used in the elaboration of ZnO-based Schottky diode via the deposition of a ZnO film co-doped with Al + In (4 at. %) on a gallium-doped ZnO film (8 at. %). The energy bandgap values of the un-doped films, mono-doped films, and co-doped films deposited on ITO substrate were 3.25 eV, 3.27 eV, and 3.01 eV, respectively. The spectra show that all the films and the diode have a high transparency (>90%) in the visible region, and high absorption (almost 100%) in the UV region. The transmittance decreases slightly with different doping elements. The diode results show a Schottky-type behavior in the dark and under light, which is controlled by the thickness of the resistive layer. From the I–V curves, the characteristic parameters including barrier height, ideality factor, and series resistance were calculated.

The results presented here indicate that an optimized thickness of the resistive layer must be obtained in order to achieve the maximum performance of the diode.

6. A. E. Danks, S. R. Hall, & Z. Schnepf, The evolution of 'sol-gel' chemistry as a technique for materials synthesis. *Materials Horizons*, 3(2016)2, pp. 91-112, DOI: 10.1039/c5mh00260e.
7. H. Bahadur, A. K. Srivastava, R. K. Sharma, & S. Chandra, Morphologies of sol-gel derived thin films of ZnO using different precursor materials and their nanostructures. *Nanoscale Research Letters*, 2(2007), pp.469-475, <https://doi.org/10.1007/s11671-007-9089-x>.
8. J. Sottmann, V. Pralong, N. Barrier, & C. Martin, An electrochemical cell for operando bench-top X-ray diffraction. *Journal of Applied Crystallography*, 52(2019)2, pp. 485-490, <https://doi.org/10.1107/S1600576719000773>.
9. A. H. Adl, Synthesis and Characterization of Solution Processed ZnO Thin Films, doctoral dissertation, University of Alberta, Department of Electrical and Computer Engineering, <https://doi.org/10.7939/R3MK65D6X>.

ICMATSE 2024

Design Application Against Temperature and Magnetic Noise in Adjustable Constant Current DC LED Drivers Under 50 Volts

Barış GÖKÇE

*Necmettin Erbakan University, Faculty of Engineering, Konya, Türkiye,
barisgokce@hotmail.com
ORCID: 0000-0001-6141-7625*

Mehmet BİNGÜL

*Zenopix Technology Industry and Trade Limited Company, Ankara, Türkiye,
mbingul@zenopix.com
ORCID: 009-0006-8990-3370*

Salih Metin YURTER

*Zenopix Technology Industry and Trade Limited Company, Ankara, Türkiye,
smyurter@gmail.com
ORCID: 0000-0002-4826-1213*

Zuhal ER

*Istanbul Technical University, Maritime Faculty, 34940 Istanbul, Türkiye ,
erzuh@itu.edu.tr
ORCID: 0000-0002-9737-1435*

Cite this paper as: Gökçe, B., Bingül, M., Yurter, S.M., Er, Z. Design Application Against Temperature and Magnetic Noise in Adjustable Constant Current DC LED Drivers Under 50 Volts. Int. Conf. Advanced. Mater. Sci. & Eng. HiTech. and Device Appl. Oct. 24-26 2024, Ankara, Türkiye

Abstract. This study aims to improve the design of LED drivers based on DMX512 protocol, which is frequently used in professional lighting systems. In the design, Mysemi's DMX512 receiver and PWM generator are integrated and 4 channels used for decoding DMX signals. This integrated RGBW (Red, Green, Blue and White) wall painting fixture is defined as a 4-channel fixture and a constant current driver from Microchip is used to drive each channel. Thanks to these integrated circuits, an adjustable constant current between 350mA and 1100mA is provided to the LEDs. The power MOSFET is a Texas Instruments 5.7 m Ω , 60 V SON 5 mm \times 6 mm NexFET™. It was intended to function as the sync FET in a full industrial buck converter chipset solution when paired with the control FET. Additionally, an electronic load device and the KiCAD design program were used for PCB and electronic schematic design. A Tekbox TBLC08 LISN device was used for the emission measurements, and a Rigol brand spectrum analyzer was used for the measurements. Additionally, near-field probes were used to measure magnetic noise, and an infrared thermometer was used to measure the temperature of PCBs and integrated circuits. However, due to the heating and harmonics that occur at high currents, magnetic noise problems were experienced. In this study, improvements were made on the circuit topology, component selection and PCB design in order to solve these problems. As a result of the modifications, lower heating and magnetic noise levels were achieved, thus increasing the life of the LED driver and the overall performance of the system.

Keywords: Constant Current DC Led Drivers, DMX512 Protocol, PCB Overheating

© 2024 Published by ICMATSE

LED drivers are crucial for energy efficiency and long life in professional lighting systems. The DMX512 protocol, introduced by the Stage Lighting and Equipment Council in 1986, offers precise control

over digital signals. PWM-based LED drivers, which use Pulse Width Modulation (PWM), provide efficient and precise control of LED brightness, colors, and light intensity, making them widely used

in stage, architectural, and entertainment lighting. PWM-based LED drivers adjust LED brightness by rapidly switching supply voltages, which is too fast for the human eye to perceive, resulting in an average brightness value for the LEDs. The aim of this study is to design a stable LED driver compatible with the DMX512 protocol and to increase performance by reducing problems such as heating and magnetic noise in the driver circuit. [1-3].

In this study, firstly, a literature research was conducted in the form of examining academic articles, technical reports and patents covering the problems encountered in DMX512 protocol, PWM based LED drivers and similar applications. DMX512 protocol and PWM based LED drivers are widely used in the lighting industry. However, academic research and technical reports show that these technologies need development in areas such as energy efficiency, electromagnetic compatibility, thermal management and intelligent control features. Patents offer innovative approaches such as integrated driver solutions, adaptive color control and wireless DMX applications. In the future, LED drivers and DMX protocol are expected to be supported by more efficient, flexible and intelligent solutions [4-6].

Furthermore, PWM (Pulse Width Modulation) is a modulation method commonly used in LED drivers. PWM varies the pulse width of the voltage or current applied to the LEDs to adjust the brightness of the LEDs. In this method, the power applied to the LEDs is controlled depending on the pulse width. As known that different PWM methods provide various advantages in features such as brightness control of the LEDs, energy efficiency, and EMI (Electromagnetic Interference) reduction [7-11].

Materials and Methods

1. Materials

In this study, a constant current LED driver manufactured by Microchip, DMX512 receivers and decoders produced by MySemi, MOSFETs developed by Texas Instruments, and other active and passive components were used.

The Microchip Constant Current LED driver is an Average-Current mode constant-current control IC that enhances LED current accuracy and line and load regulations without loop compensation or high-side current sensing. Its output LED current accuracy

is $\pm 3\%$, and it can be powered from an 8V–450V supply. It features a PWM dimming input and accepts an external control TTL-compatible signal.

The MySemi DMX512 Decoder is a 4 channels constant current LED driver with 14bits grayscale APDM control, supporting standard/4x DMX512 protocol and a differential interface for long distance cascade applications. It operates over 7V to 40V input voltage range and provides 4 open-drain sinking outputs with up to 350mA high accuracy current to each string of LEDs, programmable via four external current setting resistors.

Texas Instruments mosfet 5.7 m Ω , 60 V SON 5 mm \times 6 mm NexFET™ is power MOSFET. It was designed to pair with the control FET and act as the sync FET for a complete industrial buck converter chipset solution. Additionally, the KiCAD design program and an electronic load device were employed for electronic schematic and PCB design. For measurements, conducted emission measurements were performed using a Tekbox TBLC08 LISN device, and measurements were taken with a Rigol brand spectrum analyzer. Furthermore, magnetic noise measurements were conducted using near-field probes, and PCB and integrated circuit temperature measurements were taken with an IR thermometer.

2. Hardware Design

Designing a highly efficient constant current driver is a crucial aspect of LED driver design. Additionally, an interface that supports the DMX512 protocol is a fundamental component of LED driver design, enabling the driver to communicate with the DMX control device. In this context, Mysemi's DMX512 decoder and PWM (Pulse Width Modulation) generator are integrated into the design. Figure 1 presents the schematic design of the MySemi DMX512 integrated circuit.

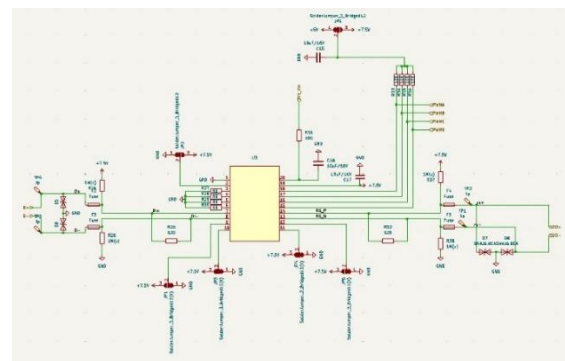


Figure 1. MySemi's DMX512 receiver and decoder schematic

Four channels are used to decode DMX signals, and this configuration is defined as an RGBW (Red, Green, Blue, White) wall-washing fixture. Each channel is controlled by Microchip's constant current driver. The constant current provided by the driver in each channel can be adjusted between 150 mA and 1100 mA. Figure 2 presents the schematic design of the Microchip constant current driver.

Figure 3 presents the overall PCB design of the DMX512 constant current driver. According to this design, the dimensions are 230mm in length and 30mm in width. These dimensions represent the maximum possible size for a standard wallwasher. Therefore, these are the optimal dimensions for maximizing power and efficiency.

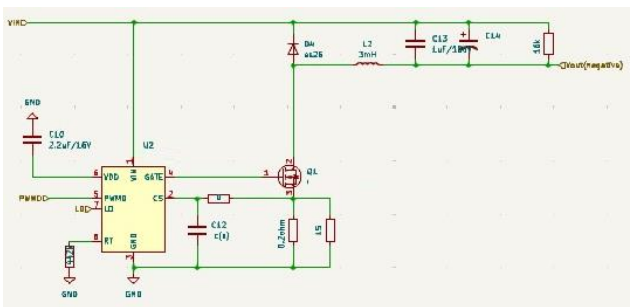


Figure 2. Microchip's constant current driver schematic



Figure 3. DMX512 Constant current driver

3. Design Criteria in Electronic Circuit

Heating and magnetic noise problems produced by harmonic components were observed on the circuit at high currents. These problems are especially associated with factors such as:

- Electromagnetic interference caused by high-frequency PWM signals and high current,
- Cooling problems caused by inadequate component placement and high current,
- Insufficient grounding in PCB design.

Choosing an efficient and temperature-sensitive power converter helps reduce the heating problems of the LED driver. Effective EMI filtering is critical to

reducing magnetic noise levels, and proper component selection and circuit design help solve this problem. Things to do to reduce heating levels are Thermal Management, Circuit Optimization, Active Cooling. Thermal management is a critical issue in LED driver design, and component placement, heat dissipation, and cooling techniques help reduce heating levels. Optimization of LED driver circuits increases energy efficiency and reduces heating problems, and this was achieved in this study with component selection and circuit design. Reducing the temperature levels of heated components using active cooling techniques (fans, heat sinks, etc.) was considered an important solution for LED driver design [12-18].

Conducted Emission Test Setup

Conducted emission tests were performed according to CISPR 16-2-1 standards. This test aims to measure the electromagnetic interference emitted by the device through the power line. Typical conducted emissions compliance configuration about the test setup are given in Figure 4.

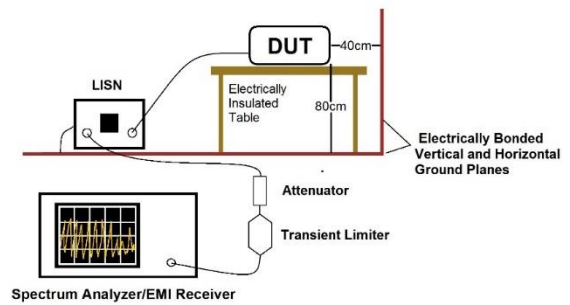


Figure 4: Typical conducted emissions compliance configuration [Int. 1]

Additionally, Figure 5 shows the visual representation of the conducted test. As seen in this figure, the measurements were taken in accordance with the standards.



Figure 5: Conducted emission test setup

The test setup comprises the following components:

- DUT (Device Under Test): Tested under normal operating conditions.
- LISN (Line Impedance Stabilization Network): Enables the measurement of noise emitted from the device's transmission line. A Tekbox TBLC08 model LISN device was employed in the test setup.
- Spectrum Analyzer/EMI Receiver: Analyzes the signals emitted by the device. Measurements were conducted using a Rigol RSA3000 series spectrum analyzer.
- Attenuator and Transient Limiter: Used for signal conditioning and device protection.
- Isolated Table and Grounding Plates: Enhance measurement accuracy and prevent interference.

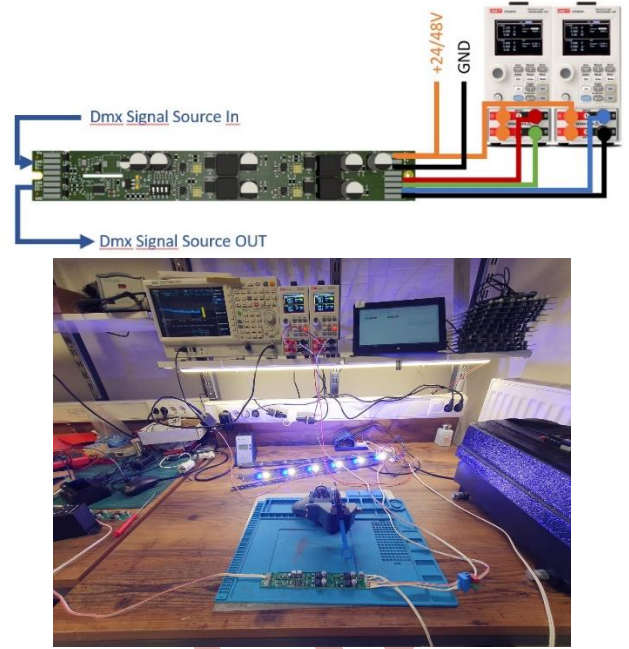


Figure 6: Thermal and pre-radiated test setup

Radiated emission

Radiated emissions are unwanted radio waves given off by electronic devices. These waves can interfere with other devices and so are limited by regulations. To measure radiated emissions, we can use special rooms like anechoic chambers or special equipment like GTEM cells. For quick checks, we can use near-field probes. In this study, we used TBPS01 probes and a TBWA2 amplifier with a Rigol RSA3000 spectrum analyzer.

Thermal Test Setup

A thermal test setup was established to determine the maximum temperature values of the device under full load. Four UNI-T UTL8212+ load banks were used as load and current measurement devices for each channel. During the test, a DMX signal with a maximum PWM value of 8 bits (255,255,255,255) was sent to each channel. The temperature values of the MOSFETs and Coils as the switching elements, were examined. Figure 6 shows the thermal test station.

3. Results and Discussion

In this study, the main components of the constant current LED driver structure are DMX512 Decoder, 4-channel (RGBW) MySemi DMX decoder, which digitally decodes the signals and generates PWM signals for each channel. With this decoder, Microchip's constant current driver was tested at full load on 4 channels at the same time at different current values of 24VDC 350mA, 500mA, 750mA and 1100mA. The driving frequency of the LEDs is 20kHz. In the measurements made, the coil and PCB temperatures according to the current values and the measurements made with the near field (pre-amp 20db) probe are given in Table 1. As can be seen in the table, the temperature increases non-linearly as the current value increases. In addition, while the magnetic noise peaks and the frequencies of these peaks do not change much in the first three current ranges, it is seen that the peak value and frequency increase when the current increases to 1100mA.

Table 1. PCB, Coil temperature and electro magnetic emission peak

Current Rate (mA)	PCB and Coil Temperature (°C)	Peak (dBuV)	Peak Freq. MHz
350	30.2	55.29	58.69
500	32.1	54.27	58.69
750	38.8	55.83	58.69
1100	56.1.2	60.14	60.14

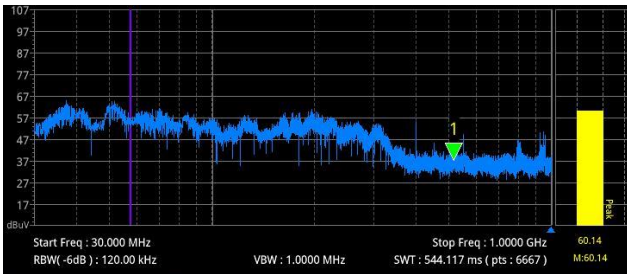
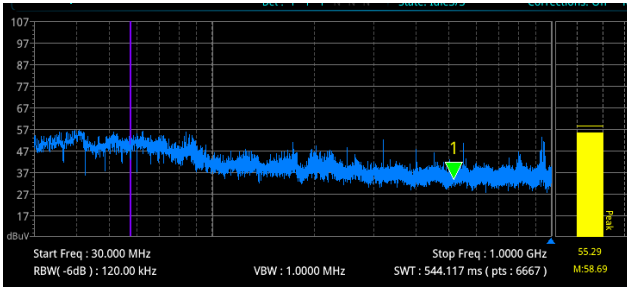


Figure 7. Electro magnetic emission peaks (logarithmic scale between 30MHz-1GHz)

Figure 7 presents the electromagnetic emission peaks (on a logarithmic scale between 30MHz-1GHz) and their corresponding frequencies. The upper image displays the noise characteristics at a current of 350mA, while the lower image shows the noise characteristics at a current of 1100mA. A significant change in noise levels can be observed. Additionally, there is an increase in both the number and frequency of peaks.

Figure 8 presents the conducted emission noise measurement graph of the driver. The measurement range is between 9kHz and 30MHz with a resolution bandwidth (CSPR 16) of 9kHz. The topmost figure shows the emission graph of the driver without a specified current load. The middle figure represents the measured emission values at a current of 350mA, and the bottom figure shows the measured emission values at a current of 1100mA. It is evident from these graphs that the noise increases non-linearly, especially at higher currents.

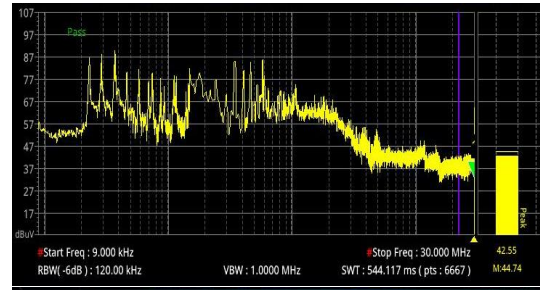
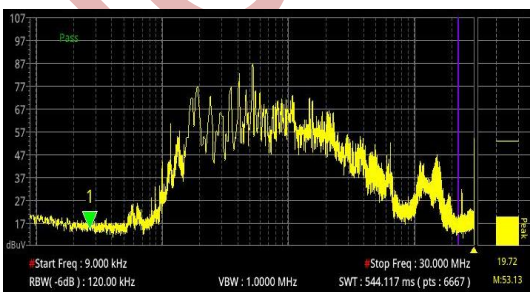


Figure 8. Conducted emission peaks

The Microchip constant current driver provides a specific range of current (350 mA - 1100 mA) to the LEDs based on the duty cycle of the PWM signal. As the PWM signal width increases, more current flows to the LED, resulting in increased brightness. When high currents and intense PWM frequencies are used in the circuit, heat is generated. Therefore, thermal protection mechanisms are incorporated into the constant current driver. Furthermore, thermal vias and copper pads are utilized in the PCB design to facilitate circuit cooling. Additionally, parallel capacitors are added to the power line to mitigate electromagnetic interference (EMI), and the PWM driver circuit and DMX512 signal lines are isolated.

This study reveals that optimizing component selection and circuit design can significantly reduce thermal and magnetic issues in LED drivers using the DMX512 protocol. In this study, digital signals are decoded using a DMX512 decoder and a PWM generator, and the LEDs are driven in a controlled manner with a constant current driver. The circuit provides adjustable current between 350 mA and 1100 mA on each channel, ensuring that the LEDs operate at high performance and have a long life. Thanks to the elimination of cooling and EMI problems with suitable components, this system offers a reliable and efficient solution suitable for use in professional lighting projects.

Conclusion

This study provides an important step towards solving thermal and magnetic problems encountered in the design of LED driver circuits

operating with the DMX512 protocol. Thanks to the improved circuit topology and component selection, LED drivers have been made longer lasting and more efficient. The results of the study can also guide the design of future lighting systems. Constant Current Protection: Thanks to the microchip driver, the current of the LEDs is fixed within the desired range,

which increases the LED life and prevents overheating. Thanks to the DMX512 protocol, the brightness and color of each channel are precisely controlled. Noise and EMI Control: Electromagnetic compatibility is ensured with proper filtering and PCB design.

References

1. M. Esteki, S. A. Khajehoddin, A. Safaee and Y. Li, "LED Systems Applications and LED Driver Topologies: A Review," in *IEEE Access*, vol. 11, pp. 38324-38358, 2023, doi: 10.1109/ACCESS.2023.3267673
2. Neri P, Ciampi G, Neri B. High Power Pulsed LED Driver for Vibration Measurements. *Sensors*. 2024; 24(13):4103. <https://doi.org/10.3390/s24134103>
3. M. S. Perdigão, M. F. Menke, Á. R. Seidel, R. A. Pinto and J. M. Alonso, "A Review on Variable Inductors and Variable Transformers: Applications to Lighting Drivers," in *IEEE Transactions on Industry Applications*, vol. 52, no. 1, pp. 531-547, Jan.-Feb. 2016, doi: 10.1109/TIA.2015.2483580
4. R. M. Ferraz, L. H. G. Resende, H. A. C. Braga, P. S. Almeida and G. M. Soares, "Design of an Off-Line LED Driver Based on the Interleaved BCM Boost PFC and the LLC Converter with Active Ripple Compensation," *2023 IEEE 8th Southern Power Electronics Conference and 17th Brazilian Power Electronics Conference (SPEC/COBEP)*, Florianopolis, Brazil, 2023, pp. 1-5, doi: 10.1109/SPEC56436.2023.10408172.
5. Ferdous, F., Hassan, M., Rahman, N., Hassan, T. and Islam, R. 2024. Design of an Energy Efficient Buck Based LED Driver in DCM and CCM. *European Journal of Engineering and Technology Research*. 9, 3 (Jun. 2024), 40–46. DOI:<https://doi.org/10.24018/ejeng.2024.9.3.3169>.
6. C. Suthar, V. I. Kumar, V. Yousefzadeh, M. Doshi and D. Maksimović, "A Composite Converter based Automotive LED Driver," *2023 IEEE 24th Workshop on Control and Modeling for Power Electronics (COMPEL)*, Ann Arbor, MI, USA, 2023, pp. 1-6, doi: 10.1109/COMPEL52896.2023.10221178.
7. Y. Chi, Z. Sun and Y. Wang, "Analysis and Design of High Efficiency LED Driver with Variable Load," *2023 26th International Conference on Electrical Machines and Systems (ICEMS)*, Zhuhai, China, 2023, pp. 1167-1171, doi: 10.1109/ICEMS59686.2023.10344447.
8. M. S. Mazandarani, G. Gagnon-Turcotte, M. Sawan and B. Gosselin, "A sub-mW Ultra-Low Power Low-Voltage LED Driver for a Patch Pulse Oximetry," *2023 21st IEEE Interregional NEWCAS Conference (NEWCAS)*, Edinburgh, United Kingdom, 2023, pp. 1-4, doi: 10.1109/NEWCAS57931.2023.10198174.
9. J. S. Brand, N. d. S. Spode, G. Z. Abdelmessih, J. M. Alonso, Y. Guan and M. A. Dalla Costa, "Capacitance Analysis for Volume Reduction Based on Integrated Buck and Buck-Boost LED Driver," in *IEEE Transactions on Industry Applications*, vol. 60, no. 2, pp. 2970-2979, March-April 2024, doi: 10.1109/TIA.2023.3280469.
10. M. Lao, X. Xie and H. Dong, "A Novel Isolated LED Driver with Passive Power Factor Correction," *2023 IEEE 2nd International Power Electronics and Application Symposium (PEAS)*, Guangzhou, China, 2023, pp. 2484-2489, doi: 10.1109/PEAS58692.2023.10395082.
11. Liang, G., et al.: Constant frequency, non-isolated multichannel LED driver based on variable inductor. *IET Circuits Devices Syst.* 15(8), 803–813 (2021). <https://doi.org/10.1049/cds2.12072>
12. Fanghui Zhang and Huimin Qiu, 2021. Design of High-efficiency LED Driver Power Supply Based on Improved Particle Swarm Optimization, *Journal of Physics: Conference Series*, IOP Publishing, vol. 2136, no.1, doi:10.1088/1742-6596/2136/1/012021
13. H. Adamas-Pérez, M. Ponce-Silva, R. Osorio-Sánchez and J. M. Alonso, "Electrothermal Model for Power LEDs Based on the Equivalent Resistance Concept for LED Driver Design," in *IEEE Transactions on Electron Devices*, vol. 68, no. 12, pp. 6249-6254, Dec. 2021, doi: 10.1109/TED.2021.3118992.
14. R. B. Pallapati, R. Chinthamalla, R. M. Panuganti and A. Gavvala, "High Efficient High Power Factor Single phase LED Driver with Constant Output Current without Electrolytic Capacitor*," *2023 International Conference on Computer, Electronics & Electrical Engineering & their Applications (IC2E3)*, Srinagar Garhwal, India, 2023, pp. 1-6, doi: 10.1109/IC2E357697.2023.10262568.
15. Y. Wang, J. Tan, S. Han and D. Xu, "High Power Density Matrix Resonant Switched-Capacitor LED Driver," *2023 IEEE Industry Applications Society Annual Meeting (IAS)*, Nashville, TN, USA, 2023, pp. 1-5, doi: 10.1109/IAS54024.2023.10406817.
16. Y. V. Bhavya, V. Prashobh Suresh, S. Mohan, K. Neeraja and V. Chandrasekar, "Design and Implementation of EMI Mitigation in GaN Based LED Driver," *2020 IEEE International Conference on Power Electronics, Smart Grid and Renewable Energy (PESGRE2020)*, Cochin, India, 2020, pp. 1-5, doi: 10.1109/PESGRE45664.2020.9070650.
17. S. V. Patil and M. S. Aspilli, "Fuzzy Logic Control Based Single-Stage LED Driver with Power-Factor Corrections," *2022 IEEE 2nd Mysore Sub Section International Conference (MysuruCon)*, Mysuru, India, 2022, pp. 1-7, doi: 10.1109/MysuruCon55714.2022.9972641.

18. N. H. Reddy, Y. Mani Kiran, B. A. Kumar and M. Alam, "EMI Filter Design and Comparative Analysis of Control Approaches for DC- DC Boost Converter Based LED Drivers," 2024 IEEE International Conference on Electronics, Computing and Communication Technologies (CONECCT), Bangalore, India, 2024, pp. 1-6, doi: 10.1109/CONECCT62155.2024.10677189.
19. Prashant Kumar Soori, Moheet Vishwas, Lighting control strategy for energy efficient office lighting system design, Energy and Buildings, Volume 66, 2013, Pages 329-337, ISSN 0378-7788, <https://doi.org/10.1016/j.enbuild.2013.07.039>.
20. Byung-Lip Ahn, Cheol-Yong Jang, Seung-Bok Leigh, Seunghwan Yoo, Hakgeun Jeong, Effect of LED lighting on the cooling and heating loads in office buildings, Applied Energy, Volume 113, 2014, Pages 1484-1489, ISSN 0306-2619, <https://doi.org/10.1016/j.apenergy.2013.08.050>.

Internet References

- [1] <https://siglentna.com/application-note/electromagnetic-compliance-pre-compliance-conducted-emissions-testing/>
Reached time at 20.10.2024

Effects of Shot Peening Parameters on Low Cycle Fatigue Life of 17-4 PH H1150 Steel

Ramazan Meral

National Defence University, Alparslan Defence Sciences and National Security Institute,
06654, Ankara, Türkiye
Tusas Engine Industries, 26210, Eskisehir, Türkiye, ramazan.meral@outlook.com
ORCID: 0000-0003-2592-1319

Ahmet Özdemir

Gazi University, Faculty of Technology, Manufacturing Engineering, 06560, Ankara, Türkiye,
ahmetoz@gazi.edu.tr
ORCID: 0000-0001-9919-8149

Cite this paper as: Meral, R, Özdemir, A. Effects of shot peening parameters on low cycle fatigue life of 17-4 PH H1150 steel. Int. Conf. Advanced. Mater. Sci.& Eng. HiTech.and Device Appl.Oct. 24-26 2024, Ankara, Türkiye

Abstract. In this study, effects of shot peening process applied to samples were produced from 17-4 PH H1150 stainless steel material on LCF life were experimentally investigated. Shot peening was applied at densities of 3A, 4.5A, and 6A, and coverage rates of 100%, 200%, and 300%. Strain-controlled LCF tests were performed. Microstructures of samples were examined and microhardness values were obtained and commented. Surface roughness of samples was measured and compared. According to the study, it was determined that shot peening increased the LCF life, compared to the unpeened sample, by 13.7%, 44.6%, and 93.1% under 100%, 200%, and 300% coverage, respectively at 3A intensity; by 18.4%, 75.2%, and 89.2% under 100%, 200%, and 300% coverage, respectively at 4.5A intensity; and by 36.3%, 62.3%, and 62.8% under 100%, 200%, and 300% coverage, respectively at 6A intensity. Furthermore, the analysis conducted according to the applied Taguchi experimental design revealed that the effect of shot peening coverage on fatigue life is greater than the effect of shot peening intensity. It has been demonstrated, supported by experimental findings, that shot peening provides improvement in the microstructure.

Keywords: Shot peening, low-cycle fatigue, LCF, 17-4 PH, Taguchi
© 2024 Published by ICMATSE

Introduction. Shot peening, a preferred method for non-cutting surface processing, involves impacting balls made from materials like steel, cast iron, glass, and ceramics onto a workpiece with sufficient kinetic energy, creating indentations that induce plastic deformation and surface hardening [1, 2]. It has been stated in numerous studies that shot peening increases fatigue life [3, 4, 5, 6]. In this study, the effects of shot peening intensity and coverage parameters on low-cycle fatigue (LCF) life were investigated. Samples were subjected to shot peening using the same type of shot, with intensities of 3A, 4.5A, and 6A, and coverage levels of 100%, 200%, and 300%, followed by low-cycle fatigue testing. Additionally, microstructural analysis and microhardness measurements were conducted. The surface roughness values of the samples were measured and compared.

In previous studies it was stated that surface roughness is more effective than residual stress for LCF region of the life after shot peening [7, 8]. Additionally with other studies reviewed it is understood that effect of residual stress and surface roughness on LCF life may vary depending on material, surface roughness and residual stress levels [9, 10, 11].

The residual stresses and microhardness generated by shot peening have been investigated and it has been reported that shot peening creates residual stress in the compression direction in the region close to the surface, and thus increases microhardness in previous works [4, 7, 12, 13].

Surface roughness changes according to peening intensity and coverage. It mostly increases compared to unpeened samples, but it does not always increase with higher coverage and intensity.

After these two parameters reach a certain level, surface roughness may start to decrease. [12, 14, 15].

Table 3. 17-4 PH (AISI 630) Chemical Composition

C	Mn	P	S	Si	Cr	Ni	Cu	Nb
<0.07	<1	<0.04	<0.03	<0.7	15-17	3-5	3-5	0.15-0.45

Table 4. Mechanical Properties of 17-4 PH H1150 [16]

UTS (MPa)	0.2 % YS (MPa)	Elongation %	Hardness (HRC)	Impact, Charpy V-Notch, (J)
1000	862	19	33	68

Shot peening creates finer grains at surface region of material. And depth of grain refinement depends on the intensity and coverage as well [12, 14, 17, 18].

17-4 PH (AISI 630) H1150 material is used for the study. Chemical composition is shown in Table 1. The material was initially acquired in Condition A and subjected to heat treatment in accordance with standard AMS2759/3 and the manufacturer's specifications to achieve condition H1150 [16, 19]. Mechanical properties are given in Table 2.

Samples were produced according to geometry specified in ASTM E606 [20]. To compare samples that were left as-machined and those subjected to shot peening, the test samples without shot peening were manufactured to achieve a surface roughness of $R_a=1.6 \mu\text{m}$. Shot peening was done to nine different samples with ASH 110 media according to AMS2431/2 standard with three different intensities and coverage levels.

Table 5. Shot peening parameters and sample numbers

Sample Number	Intensity	Coverage (%)
1	3A	100
2	3A	200
3	3A	300
4	4.5A	100
5	4.5A	200
6	4.5A	300
7	6A	100
8	6A	200
9	6A	300
10	Unpeened	

Results and Discussion. LCF tests were performed for all samples. Highest load applied to the sample is shared in Figure 12. A 50% reduction in the applied force during testing can be considered a damage criterion, indicating the presence of a crack or cracks

in the specimen [20]. The number of cycles at fracture was accepted as the damage criterion, as

the maximum difference between this and the

cycles where the applied force was halved was only 4%, which does not affect the comparison.

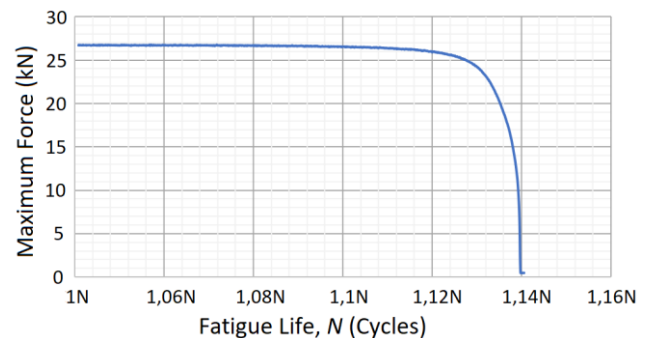


Figure 12. Force and fatigue life graphic of the sample which shot peened with 3A intensity and 100% coverage.

LCF test results are shown in Table 6. The table shows that coverage is more effective than intensity in improving LCF life. As the coverage increases across the columns, the improvement in LCF life is more significant than the improvement observed with increasing intensity down the rows.

Table 6. LCF results of shot peened samples shown in intensity (rows) and coverage (columns)

	100%	200%	300%
3A	1,14N	1,45N	1,93N
4.5A	1,18N	1,75N	1,89N
6A	1,36N	1,62N	1,63N

It was determined that shot peening increased the LCF life, compared to the unpeened sample, by 13.7%, 44.6%, and 93.1% under 100%, 200%, and 300% coverage, respectively at 3A intensity; by 18.4%, 75.2%, and 89.2% under 100%, 200%, and 300% coverage, respectively at 4.5A intensity; and by 36.3%, 62.3%, and 62.8% under 100%, 200%, and 300% coverage, respectively at 6A intensity (Figure 13).

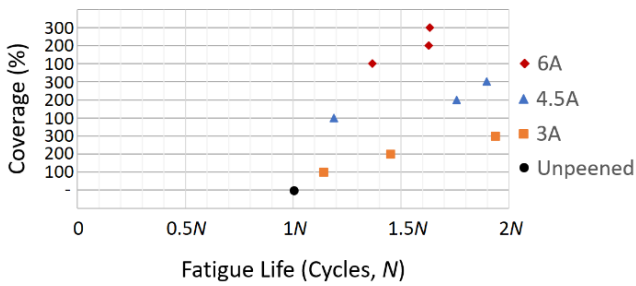


Figure 13. A comparative graph showing the fatigue life of all samples.

The experimental design was structured using a Taguchi L9 array, and the effects of the parameters were also mathematically determined. The previous evaluation that shot peening intensity is more effective than coverage is also confirmed through Taguchi analysis.

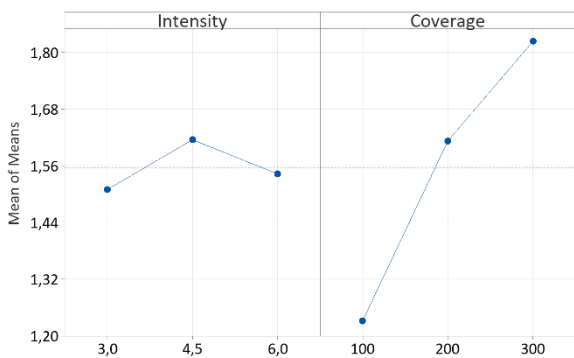


Figure 14. Graph of the effects of parameters for maximum fatigue life

A mathematical expression which is Eq. [1] of fatigue life (FL) as a function of shot peening intensity (I) and coverage (C) has been derived through regression analysis.

$$FL = 0,915 + 0,011.(I) + 0,002954.(C) \quad \text{Eq. [1]}$$

Based on microhardness measurements, surface hardness was highest in shot-peened samples, decreasing with depth, with the highest values observed in sample peened with 6A intensity and 300% coverage (Figure 15). It can be observed in other studies in the literature that microhardness values are proportional to residual stress values [7, 13].

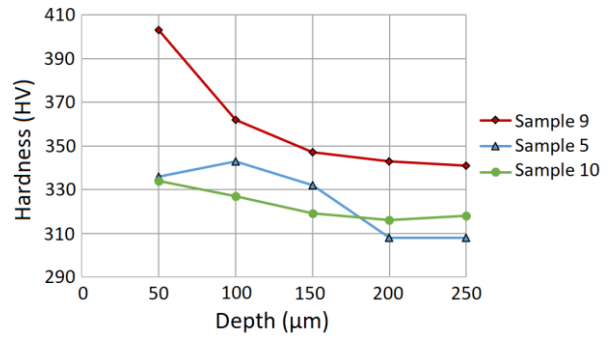


Figure 15. Force and fatigue life graphic of the sample which shot peened with 3A intensity and 100% coverage.

As shot peening intensity and coverage increased, surface roughness also increased. The surface roughness of samples peened at 3A intensity was lower compared to the baseline samples (Table 7).

Table 7. Surface roughness values of samples

Sample Number	R _a	R _z
2	1.400	1.746
3	1.600	9.663
4	1.987	11.665
5	1.523	8.577
6	2.435	14.519
7	1.564	13.395
8	3.035	17.457
9	3.416	19.871
10	1.836	6.908

When examining the surface roughness values in R_a and fatigue life in N presented in Figure 16, it is observed that the surface roughness and fatigue life of samples peened at 3A intensity with 200% coverage, 4.5A intensity with 100% coverage, and 6A intensity with 100% coverage are lower compared to the samples peened at 6A intensity with 200% and 300% coverage. Based on the results of this study, the effect of surface roughness in the LCF region,

where the number of cycles is 1N, was not clearly observed (Figure 16).

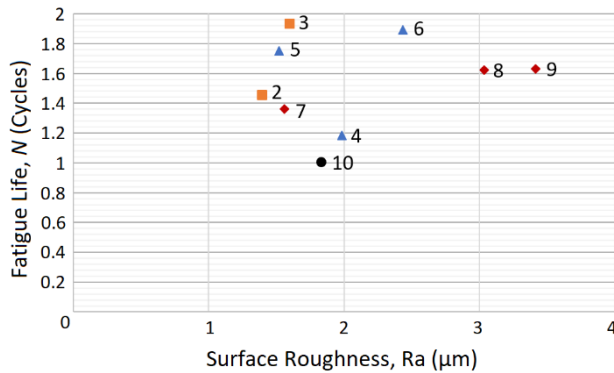


Figure 16. Graph of fatigue life versus surface roughness (R_a) for the samples

Shown in Figure 17, the grain sizes near the surface in samples 5 and 9 were observed to be finer than those in sample 10, with sample 9 exhibiting finer grain sizes and a greater depth of grain refinement compared to sample 5.

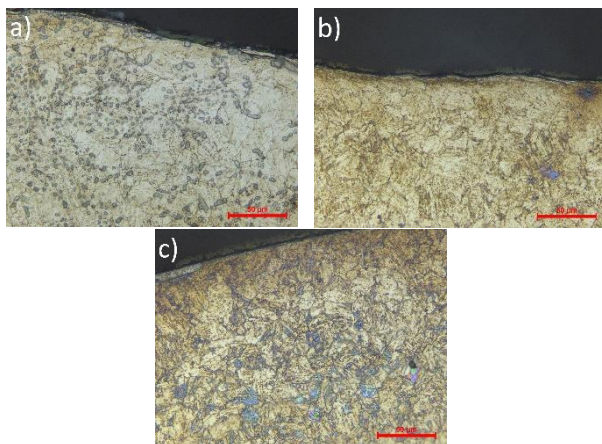


Figure 17. Microstructural images of the near-surface region of unpeened (a), sample 5 which is peened with

4.5A intensity and 200% coverage (b) and sample 9 which is peened with 6A intensity and 300% coverage (c) samples.

Conclusion. This study investigates the effects of shot peening parameters on the LCF life of 17-4 PH H1150 material. It has been determined that shot peening enhances LCF life. Additionally, it has been reported that the effect of shot peening coverage on fatigue life is greater than that of shot peening intensity. An increase in shot peening intensity and coverage was shown to refine grains in the near-surface regions and increase surface roughness. Despite the higher surface roughness at the 1N fatigue life level, the fatigue life of the shot-peened samples was observed to be greater compared to the unpeened samples. Samples with higher shot peening intensity and coverage exhibited higher microhardness values in the near-surface regions, which was associated with the proportional increase in residual stress in these regions.

References

1. B. Scholtes ve O. Voehringer, Mechanical Surface Treatment, Encyclopedia of Materials: Science and Technology, (2001), pp. 5253-5261.
2. G. Leghorn, The Story Of Shot Peening, A.S.N.E. Journal, (1957).
3. J. O. Almen, Shot Blasting To Increase Fatigue Resistance, SAE Transactions, (1943), 51(7).
4. E. Dülek, Ş. Orman, Ç. Karataş ve S. Sarıtaş, Effects Of Shot Peening On Fatigue Strength Of AISI 1020 Steel And Investigation Of Created Residual Stresses By Layer Removal Technique, Journal of the Faculty of Engineering and Architecture of Gazi University, (2013) 20(3).
5. W. Qian, Y. Wang, K. Liu, X. Yin, X. He ve L. Xie, Experimental Study on the Effect of Shot Peening and Re-Shot Peening on the Residual Stress Distribution and Fatigue Life of 20CrMnTi, Coatings, (2023), 13(7), pp. 1210.
6. Z. Qin, B. Li, R. Chen, H. Zhang, H. Xue, C. Yao ve L. Tan, Effect of Shot Peening on High Cycle and Very High Cycle Fatigue Properties of Ni-based Superalloys, Fatigue, (2023), 168.
7. T. Klotz, D. Delbergue, P. Bocher, M. Lèveque ve M. Brochu, Surface characteristics and fatigue behavior of shot peened Inconel 718, Fatigue, (2018) 110, pp. 10-21.

8. P. Q. Trung, N. W. Khun ve D. L. Butler, Effect of Shot Peening Process on the Fatigue Life of Shot Peened Low Alloy Steel, *J. Eng. Mater. Technol.*, (2017), 140(1).
9. A. Bag, D. Delbergue, J. Ajaja, P. Bocher, M. Lévesque ve M. Brochu, Effect of Different Shot Peening Conditions on the Fatigue Life of 300 M Steel Submitted to High Stress Amplitudes, *Fatigue*, (2020), 130, pp. 105274.
10. B. Sahoo, R. K. Satpathy, K. Prasad, S. Ahmed ve V. Kumar, Effect of Shot Peening on Low Cycle Fatigue Life of Compressor Disc of a Typical Fighter Class Aero-Engine, *Procedia Engineering*, (2013), 55, pp. 144-148.
11. Y. H. Chung, T. C. Chen, H. B. Lee ve L. W. Tsay, Effect of Micro-Shot Peening on the Fatigue Performance of AISI 304 Stainless Steel, *Metals*, (2021), 11(9), pp. 1408.
12. J. González, I. -B. Peral, C. Colombo ve I. F. Pariente, A Study on the Microstructural Evolution of a Low Alloy Steel by Different Shot Peening Treatments, *Metals*, (2018), 8(3), pp. 187.
13. H. Wang, X. Yuan, K. Wu, C. Xu, Y. Jiao, G. Wang ve J. Luo, Effect of High Energy Shot-Peening On The Microstructure And mechanical Properties of Al5052/TiAl4V Lap Joints, *Journal of Materials Processing Tech.*, (2018), pp. 76-85.
14. H. Yan, P. Zhu, Z. Chen, H. Zhang, Y. Zhang ve Y. Zhang, Effect of Shot Peening on the Surface Properties and Wear Behavior of Heavy-Duty-Axle Gear Steels, *Journal of Materials Research and Technology*, (2022), 17, pp. 22-32.
15. J. Wu, H. Liu, P. Wei, C. Zhu ve Q. Lin, Effect of Shot Peening Coverage on Hardness, Residual Stress and Surface Morphology of Carburized Rollers, *Surface & Coatings Technology*, (2020), 384, p. 125273.
16. AK Steel International, Armco 17-4 PH Stainless Steel Product Data Bulletin, (2018).
17. H. Liu, Y. Wei, C. K. I. Tan, D. T. Ardi ve D. C. C. Tan, XRD and EBSD Studies of Severe Shot Peening Induced Martensite Transformation and Grain Refinements in Austenitic Stainless Steel, *Materials Characterization*, (2020), 168, p. 110574.
18. S. Bagherifard, S. Slawik, I. Fernández-Pariente, C. Pauly, F. Mücklich ve M. Guagliano, Nanoscale Surface Modification of AISI 316L Stainless Steel By Severe Shot Peening, *Materials and Design*, (2016), 102, pp. 68-77.
19. SAE International, Heat Treatment Precipitation-Hardening Corrosion-Resistant, Maraging, and Secondary Hardening Steel Parts, SAE International, (2020).
20. ASTM International, Standard Test Method for Strain-Controlled Fatigue Testing, ASTM International, (2021).

Considerations on surface roughness for additively manufactured structures using non-explosible AlSi10Mg feedstock on a medium-wattage L-PBF machine

Fatma Nur Depboylu

*Institute of Mechanical and Electrical Engineering - Centre for Industrial Mechanics, University of Southern Denmark, DK-6400, Sønderborg, Denmark,
fatmanurdepboylu@sdu.dk
ORCID: 0000-0003-0401-5923*

Andrei-Alexandru Popa

*Institute of Mechanical and Electrical Engineering - Centre for Industrial Mechanics, University of Southern Denmark, DK-6400, Sønderborg, Denmark,
andrei@sdu.dk
ORCID: 0000-0002-5729-464X*

Depboylu, FN, Popa, AA. Considerations on surface roughness for additively manufactured structures using non-explosible AlSi10Mg feedstock on a medium-wattage SLM machine. Int. Conf. Advanced. Mater. Sci. & Eng. HiTech. and Device Appl. Oct. 24-26 2024, Ankara, Turkiye

Abstract. This study investigates optimizing process parameters to control surface roughness in AlSi10Mg components produced via Laser Powder Bed Fusion (L-PBF) on a medium-wattage machine. The use of non-explosive AlSi10Mg feedstock, while safer, is typically linked to higher surface roughness compared to its standard counterpart, due to its distinct powder size distribution and characteristics. Surface roughness is a key factor affecting the performance and quality of printed parts, particularly along borders and complex geometries. Focusing on the Downskin, Infill, and Upskin printing sequence, this research identifies parameters that significantly impact roughness. Test samples were produced using AlSi10Mg, and roughness was measured via profilometry. Results show that the sequence of Downskin, Infill, and Upskin printing stages plays a crucial role in surface quality. The Upskin region exhibited higher roughness when the sequence was not optimized, while specific settings for Downskin improved the surface finish. Key factors influencing roughness include laser power, scanning speed, and layer thickness, but their effects vary based on the printing sequence. By optimizing this sequence, more uniform surface finishes can be achieved across different regions. These findings are valuable for industries seeking enhanced surface quality in SLM-manufactured aluminium components.

Keywords: Surface Roughness, AlSi10Mg, Laser Powder Bed Fusion, Parameter Optimization

© 2024 Published by ICMATSE

Introduction

Surface roughness causes lower fatigue resistance and crack initiation for additively manufactured aluminum with laser powder bed fusion (L-PBF) technology [1]. To control roughness values, the powder size, shape and various L-PBF fine-tuning parameters are utilized along with infill process parameters such as laser power, laser scanning speed, hatch distance and layer thickness [2]. In literature, commercially available AlSi10Mg powder typically ranges between 20-70 μm and is uniformly

spherically shaped for medium-wattage industrial L-PBF machines [3]. This powder size's surface roughness value range varies between 3.5-4.5 μm [4] for the horizontal surface parallel to the building direction. However, the NeXP-1 AlSi10Mg from Equispheres, which is used for this study, comes in above 100 μm powder size distribution and uniform spherical powder shape [5]. This effort therefore aims to perform an unused optimization study with fine-tuning parameters (Fig.1) for reducing the surface roughness of NeXP-1 powder, with its atypically large particle size. For this purpose, the

effects of the distance between border-following border, hatch offset, and their combination, printing sequence and upskin-downskin parameters were investigated.

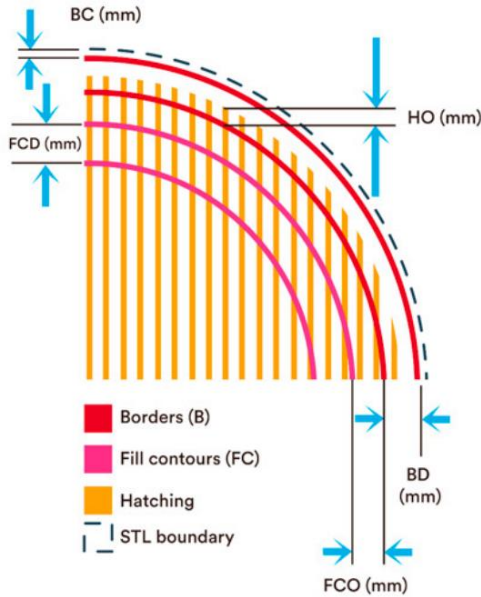


Figure 1. Fine-tuning parameters: border, hatching, fill contour (FC) and hatch offset (HO), fill contour offset (FCO) beam compensation (BC), border distance (BD) under licensed by Ramirez-Cedillo et al. [6].

The effects of distance between the border and following border parameter were examined in 1st and 2nd parameter sets as shown in Table 1. The 3rd and 4th parameter sets displayed hatch offset (the distance between hatch and borderline) effects on surface roughness while the 5th to 8th parameters were created with the combined effects of border and hatch offsets. The L-PBF printing sequence (parameters 9 and 10) and upskin-downskin parameter effects (parameters 11 and 12) on surface roughness were investigated. 12 mm cubes were manufactured with one cube per set on a medium-wattage L-PBF machine (XM200G, Xact Metal, USA) while adopting a stripe scanning strategy. 390 W laser power, 1100 mm/s laser scanning speed, 0.13 mm hatch distance, and 0.06 mm layer thickness parameters were used as infill process parameters. The same laser power and scanning speed values were repeated in the border and following-border parameters. A surface profilometer (Veeco Dektak 150) was used to measure surface roughness on the as-built parts. All measurements were taken from the top surface as a horizontal side to the building direction.

Table 1. Fine-tuning parameter optimization for surface roughness measurements

Param. Number	Parameter Optimization	Effects
1	0.05 mm border-following border (BD)	Border-Following Border Parameter
2	0 mm border-following border (BD)	
3	0.1 mm for hatch offset	Hatch Offset
4	0 mm for hatch offset	
5	Combination of 1-3	Border and Hatch Offset
6	Combination of 1-4	
7	Combination of 2-3	
8	Combination of 2-4	
9	Downskin-Infill-Upskin	Printing Sequence
10	Infill-Downskin-Upskin	
11	Upskin and downskin are open	Upskin-Downskin
12	Upskin and downskin are closed	

Results and Discussion

Surface roughness results showed that overlap between the border and the following border generated a remelting effect and caused slightly lower surface roughness (4.6 μm) than 0.05 mm distance (5.3 μm) (Fig.2). There was no significant roughness difference observed (3.5 μm) among hatch offset values. On the other hand, the 5th and 7th parameter set values are approximately 3.3 μm while the 6th and 8th parameter set values were 4.7 and 5.2 μm , respectively. The 0.1 mm hatch offset revealed a smoother surface performance than the 0 mm hatch offset in the border and hatch offset combination. L-PBF printing sequence effect exhibited that downskin-infill-upskin sequence has the lowest surface roughness value as 2.1 μm while infill-downskin-upskin sequence produced a roughness of 3.85 μm . The highest surface roughness (9.18 μm) was measured when upskin and downskin parameters were opened (Fig.3).

Afroz et al., 2023 [7] mentioned that the surface roughness for their alloy was 2.1 μm while Zimmermann et al., 2020 [8] presented values of 3.8 μm . It is revealed that NExP-1 powder over 100 μm size having 2.1 μm surface roughness is in line with powders of smaller sizes.

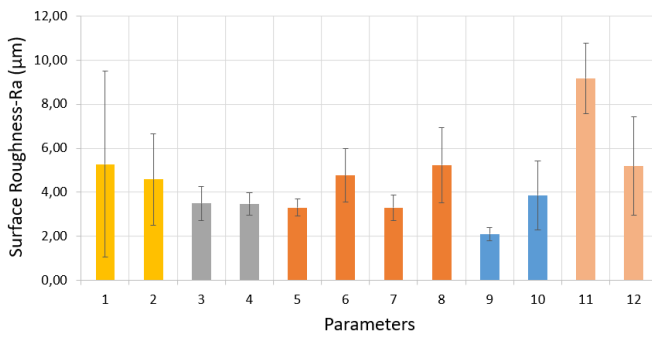


Figure 2. Surface roughness-parameter number graph.

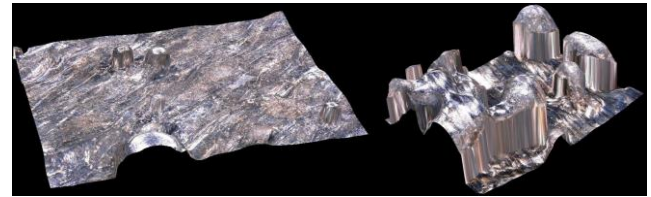
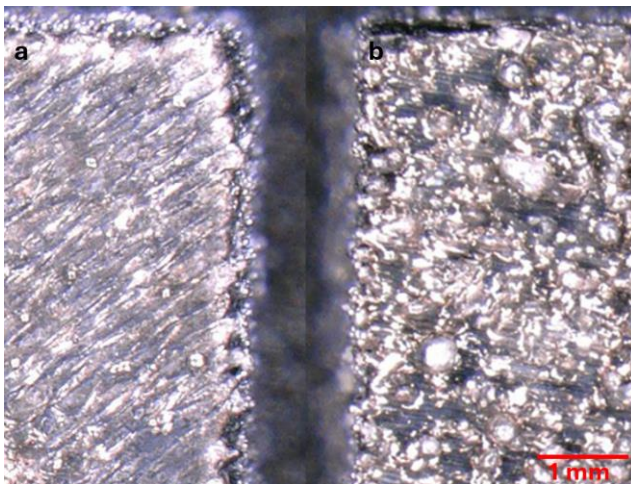


Figure 3. The top surfaces of Parameter 9 (a) and 11 (b), respectively.

Conclusion

The surface roughness of NExp-1 printed parts increased when upskin and downskin parameters were opened with default border (0.05 mm) and hatch offset (0.1 mm). Hatch offset can be used at 0.1 mm to get a smoother surface. The distance between the border and the following border parameter did not expose a significant effect. The L-PBF manufactured NExp-1 AlSi10Mg parts were investigated to get lower surface roughness. Downskin-infill-upskin printing sequence gave the lowest surface roughness, therefore it might be followed as a promising optimization strategy instead of the default infill-downskin-upskin sequence. In the future, defect-free bulk AlSi10Mg structures will be examined by a mechanical and microstructural analysis.

References

1. Aboulkhair, Nesma T., et al. "Improving the fatigue behaviour of a selectively laser melted aluminium alloy: Influence of heat treatment and surface quality." *Materials & Design* 104 (2016): 174-182.
2. Cao, L., Li, J., Hu, J., Liu, H., Wu, Y., & Zhou, Q. (2021). Optimization of surface roughness and dimensional accuracy in LPBF additive manufacturing. *Optics & Laser Technology*, 142, 107246.
3. Yang, Pin, et al. "Effect of thermal annealing on microstructure evolution and mechanical behavior of an additive manufactured AlSi10Mg part." *Journal of Materials Research* 33.12 (2018): 1701-1712.
4. Limbasiya, N., Jain, A., Soni, H., Wankhede, V., Krolczyk, G., & Sahlot, P. (2022). A comprehensive review on the effect of process parameters and post-process treatments on microstructure and mechanical properties of selective laser melting of AlSi10Mg. *Journal of materials research and technology*, 21, 1141-1176.
5. Equispheres Inc., "Chemical Composition * Per ASTM B213-20 ** Per ASTM B964-16," 2022. Accessed: Jun. 24, 2024. [Online]. Available: <https://equispheres.com/material-data-sheet-nexp-1-alsi10mg/>
6. Ramirez-Cedillo, Erick, et al. "Process planning guidelines in selective laser melting for the manufacturing of stainless steel parts." *Procedia Manufacturing* 26 (2018): 973-982.
7. Afroz, Laboni, et al. "Fatigue life of laser powder bed fusion (L-PBF) AlSi10Mg alloy: effects of surface roughness and porosity." *Progress in Additive Manufacturing* (2024): 1-19.
8. Zimmermann, Marco, et al. "Analysis of the machinability when milling AlSi10Mg additively manufactured via laser-based powder bed fusion." *The International Journal of Advanced Manufacturing Technology* 112 (2021): 989-1005.

Quantum Computational Discovery of Novel High-Entropy Alloys

Houlong Zhuang

Arizona State University
zhuanghl@asu.edu

Payden Brown

Arizona State University
plbrown5@asu.edu

Cite this paper as: Zhuang H., Brown P. Lemon peel incorporated PVA/chitosan composites for advanced bioactive food packaging : Physico-chemical properties and interfacial dynamics.Int. Conf. Advanced. Mater. Sci.& Eng. HiTech.and Device Appl.Oct. 24-26 2024, Ankara, Turkiye

Abstract. High-entropy alloys (HEAs), which consist of multi-principal elements and a wide range of molar ratios of constituent elements, have emerged as a promising group of materials to tackle pressing energy and environmental challenges. These challenges encompass issues such as climate change and semiconductor chip shortages. This family of materials includes various variants, such as high-entropy catalysts, high-entropy oxides, high-entropy semiconductors, high-entropy superconductors, high-entropy ceramics, and more. A common challenge shared by these frontiers is the selection of elements and their molar ratios from the vast compositional space. In this presentation, I will provide examples of how emerging quantum computers, including quantum simulators and quantum hardware, can address this elemental design problem and contribute to the discovery of novel HEAs. I will also demonstrate how quantum machine learning algorithms exhibit the potential to accelerate the training process. Finally, I will outline several potential directions for HEA research that can benefit from the power of quantum computing.

Keywords: quantum computing, High-entropy alloys, machine learning.

© 2024 Published by ICMATSE

Lemon peel incorporated PVA/chitosan composites for advanced bioactive food packaging : Physico-chemical properties and interfacial dynamics

Oumaima Fakraoui

LaMaCoP, Faculté des Sciences de Sfax, Université de Sfax, 3018 Sfax, Tunisie.

IJL, CNRS, Université de Lorraine, Campus Artem, 54000 Nancy, France.

ORCID: 0000-0001-5401-1766

Isabelle Royaud

IJL, CNRS, Université de Lorraine, Campus Artem, 54000 Nancy, France.

ORCID: 0000-0001-5469-2995

Mourad Arous

LaMaCoP, Faculté des Sciences de Sfax, Université de Sfax, 3018 Sfax, Tunisie.

ORCID: 0000-0001-6505-1480

Zoubir Ayadi

IJL, CNRS, Université de Lorraine, Campus Artem, 54000 Nancy, France.

ORCID: 0000-0002-3256-1334

Cite this paper as: Fakraoui O, Royaud I, Arous M, Ayadi Z. Lemon peel incorporated PVA/chitosan composites for advanced bioactive food packaging : Physico-chemical properties and interfacial dynamics. Int. Conf. Advanced. Mater. Sci. & Eng. HiTech. and Device Appl. Oct. 24-26 2024, Ankara, Turkiye

Abstract. Lemon peel (LP) was incorporated on PVA/chitosan (CS) to develop novel active food packaging films. The effect of various lemon peel contents (1, 3 and 5 wt.%) on the thermal, biodegradability, mechanical and bioactivity properties of the chitosan/PVA films were investigated. Additionally, dielectric studies were conducted to probe the interfacial properties between the matrix and biofillers, shedding light on the compatibility and interactions within the composite structure. The inclusion of LP has demonstrated enhancements in the properties and biodegradability of the PVA/CS films. The dielectric study reveals the good interfacial compatibility between the PVA/CS matrix and LP bioreinforcements. Furthermore, taking advantages of good mechanical properties and biodegradability, cherry tomatoes were wrapped in the PVA/CS/LP films for preservation experiment. Considering the evaluated properties, PVA/CS/lemon peel composites may be potential ecofriendly bioactive packaging candidates for food preservation.

Keywords: biocomposites, physico-chemical properties, interfacial properties, bioactive food packaging.

© 2024 Published by ICMATSE

I. Introduction

The growing demand for petroleum-based plastics has intensified concerns over the depletion of nonrenewable resources and environmental pollution due to improper disposal [1]. As a sustainable alternative, biobased and biodegradable polymers have gained attention, with polyvinyl alcohol (PVA) emerging as a leading candidate in food packaging due to its biocompatibility, chemical stability, and excellent film-forming properties [2]. Despite its advantages, the relatively high cost of PVA necessitates enhancement through blending with other polymers, such as chitosan (CS). CS, derived from chitin, is valued for its biodegradability, biocompatibility, antimicrobial activity, and barrier properties [3]. PVA/CS blends exhibit strong

intermolecular interactions, resulting in improved mechanical and barrier characteristics, highlighting the potential of the blend for advanced bio-based packaging solutions [4].

Additionally, natural active substances from citrus wastes, like lemon peel, are increasingly used to enhance the antioxidant and antimicrobial properties of food packaging films. Lemon peel (LP), is rich in pectin, cellulose, and bioactive compounds, which improve mechanical strength and barrier properties [5,6]. Direct incorporation of lemon peel powder, rather than complex extraction processes, offers a practical approach for developing active packaging films, effectively extending the shelf life of food products [7].

This work aims to develop a novel biodegradable food packaging film by reinforcing PVA/CS with LP as a natural additive. The effect of LP contents on the physico-chemical properties of the PVA/CS films were investigated. Furthermore, a dielectric study was carried out to probe the interfacial compatibility between the PVA/CS matrix and LP, essential for achieving the optimal performance of biocomposite materials.

II. Methods

1. Preparation of biocomposite films

Biocomposite films were prepared by solution casting. PVA was dissolved in water (20% w/v) at 80°C, and CS in citric acid (1% w/v) at 30°C. The solutions were blended at a 4:1 PVA/CS ratio for 2 hours. Lemon peels were cleaned, dried at 100°C, ground into powder, and filtered. The powder (1, 3, and 5 wt.%) was added to the PVA/CS mixture, stirred for 2 hours at 30°C, and sonicated for 2 minutes. The solutions were cast into petri dishes and dried at 50°C, resulting in films labeled PVA, PVA/CS, PVA/CS/LP1, PVA/CS/LP3, and PVA/CS/LP5.

2. Thermogravimetric analysis

Thermal stability and decomposition of composite films were assessed using a Setsys Ev 1750 TGA-SETARAM analyzer. Approximately 7 mg samples in alumina crucibles were pyrolyzed in air (20 mL/min) from 20–600°C at a heating rate of 10°C/min.

3. Biodegradation in soil

Biodegradability was assessed by burying 2×2 cm film samples in soil for 30 days. After extraction, samples were rinsed with deionized water, dried under vacuum at 60°C, and weighed to determine degradability using the subsequent equation:

$$D (\%) = \frac{W_I - W_D}{W_I} \times 100$$

where W_I and W_D are the initial weight and the weight after 30 days, respectively.

4. Tensile test

Mechanical behavior of specimens, cut to 25 × 10 mm, was studied using an MTS electromechanical test machine with a 10 kN load cell and a strain rate of 1 mm/min until failure.

5. Application for food packaging

Cherry tomatoes were washed, packed with film samples, and stored at 26°C for 30 days. The fresh-keeping effect of the films was measured by the weight loss rate of the tomatoes using the formula:

$$W_{\text{loss}} (\%) = \frac{W_0 - W_L}{W_0} \times 100$$

where W_0 and W_L are the weight of cherry tomatoes before and after packaging, respectively.

6. Interfacial properties

Dielectric experiments were conducted using a Novocontrol Broadband Dielectric Spectrometer. Measurements were performed from 10^{-1} to 10^6 Hz and -40 to 150°C in 3°C steps. Interfacial properties were analyzed through theoretical fitting using the WinFit software.

III. Results and discussions

1. Thermal properties

Thermogravimetric analysis (TGA) is crucial for assessing the thermal stability of biocomposites used in packaging. Figure 1 shows TGA curves for biocomposite films, revealing similar decomposition trends, indicating good PVA/CS matrix-LP compatibility. The TGA thermograms show three decomposition stages: 1) evaporation and polymer degradation (80-240°C), 2) complete decomposition (210-380°C), and 3) oxidative degradation of residues (400-500°C) [8]. The addition of CS and LP enhanced thermal resistance, with higher degradation temperatures in PVA/CS and PVA/CS/LP films compared to pure PVA, attributed to stronger hydrogen bonding with CS. The small amount of LP did not significantly alter thermal behavior.

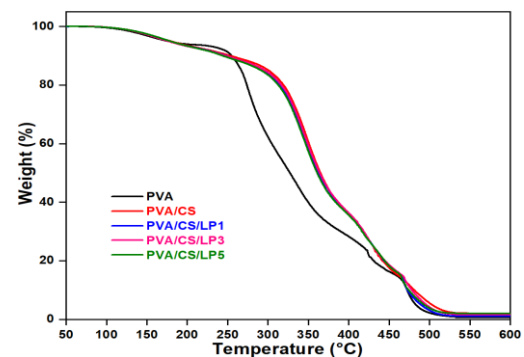


Figure 18. TGA thermograms of PVA, PVA/CS and LP biocomposite films.

2. Soil biodegradability

Soil burial tests were conducted to evaluate the biodegradability of biocomposite films in natural conditions. As presented in Figure 2, after 30 days, all films showed weight losses exceeding 60%.

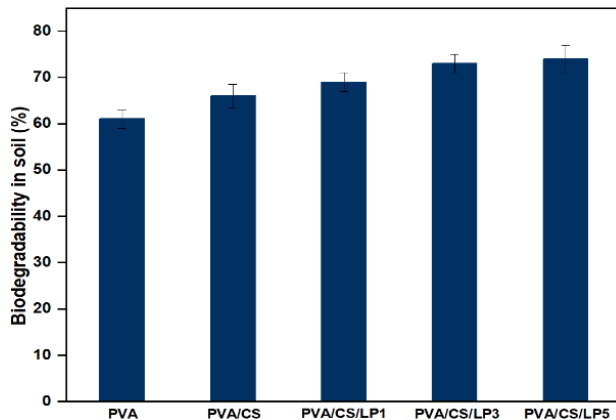


Figure 19. Degradation of the optimized films in soil 30 days.

The PVA film achieved a biodegradation rate of 61%, indicating its biodegradability [9]. The PVA/CS blend exhibited higher degradation than PVA, due to the superior biodegradability of natural polysaccharides. Incorporating LP further improved biodegradation, as the organic content in lemon peels supports microbial growth and accelerates the degradation process [10–12].

3. Mechanical properties

The tensile properties of PVA, PVA/CS, and PVA/CS/LP biocomposites were evaluated through uniaxial tensile tests. Young's modulus and tensile strength are detailed in Table 1 as functions of LP content. The neat PVA film has a Young's modulus of 679 MPa and tensile strength of 108 MPa. Blending PVA with CS increases the Young's modulus to 797 MPa and tensile strength to 109 MPa. The enhanced properties are attributed to the reinforced network formed by interactions between PVA and CS [13,14]. Adding 5 wt.% LP to the PVA/CS blend boosts the Young's modulus to 1322 MPa and improves tensile strength to 146 MPa, 164 MPa, and 193 MPa for 1, 3, and 5 wt.% LP, respectively. Yield strength also increases by 26% to 33 MPa with 5 wt.% LP. These improvements are due to hydrogen bonding between LP and the PVA/CS blend and the crosslinking effect of lignin on LP [15].

Table 1: Young's modulus and Tensile strength of PVA, PVA/CS and PVA/CS/LP biocomposites.

Sample	Young's modulus (MPa)	Tensile strength (MPa)
PVA	679 ± 53	108 ± 10
PVA/CS	797 ± 61	109 ± 7
PVA/CS/LP1	1236 ± 97	146 ± 12
PVA/CS/LP3	1249 ± 115	164 ± 19
PVA/CS/LP5	1322 ± 122	193 ± 15

4. Application for food packaging

Weight loss in cherry tomatoes is a key measure of how effectively the studied biocomposite films maintain freshness and minimize moisture loss. Figure 3 illustrates the weight loss and condition of cherry tomatoes packaged in biocomposite films.

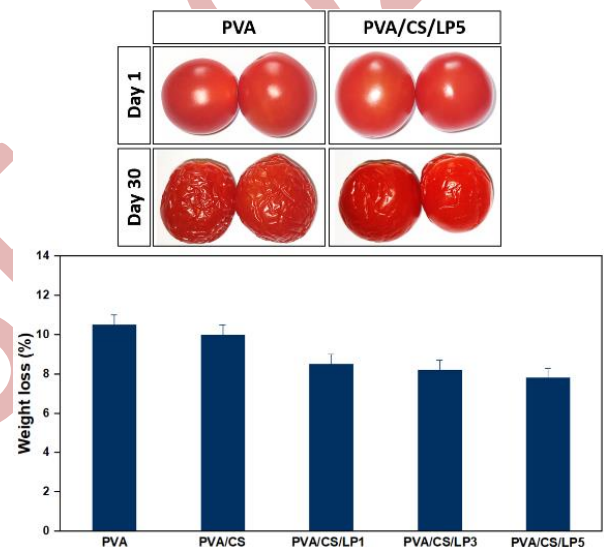


Figure 20. Cherry tomatoes appearance; not covered at day 1 and after 30 days packed using PVA/CS/LP5 film, and weight loss rate of cherry tomatoes after 30 days of preservation.

PVA film led to the highest weight loss due to increased respiration and evaporation. Incorporating CS improved film performance, as its antimicrobial and antioxidant properties help reduce microbial degradation and oxidation, thus lowering weight loss [16]. Among the films tested, PVA/CS/LP biocomposites resulted in the least weight loss. LP, with its natural antimicrobial compounds, aids in preserving tomato freshness and reducing weight loss from microbial activity [17,18]. These findings are consistent with biodegradability test results.

5. Interfacial properties

Composite properties are significantly influenced by the characteristics and proportions of their individual phases, as well as their interactions. The dispersion of reinforcements and their interactions with the polymer matrix are critical for performance [19]. Dielectric spectroscopy (DS) is effective for exploring structure-property relationships and interfacial properties in composites, including interfacial relaxation [20]. The dielectric permittivity data were analyzed using WinFit software with the Havriliak-Negami function [21], as outlined in the following equation:

$$\epsilon_{HN}^*(\omega) = \sum_{k=1}^N \left(\epsilon_{\infty} + \frac{\Delta\epsilon_k}{[1 + (i\omega\tau_{HNk})^{\alpha_{HNk}}]^{\beta_{HNk}}} \right) - j \left(\frac{\sigma_{dc}}{\epsilon_0\omega} \right)^N$$

where k is the number of different relaxation processes that can occur, $\Delta\epsilon = \epsilon_s - \epsilon_{\infty}$ is the dielectric relaxation strength (ϵ_s is the real part of permittivity at $\omega = 0$ and ϵ_{∞} is the unrelaxed value of the dielectric constant), α_{HN} and β_{HN} are the Havriliak-Negami parameters, which correspond to the width and asymmetry of the relaxation times, respectively. The expression $j \left(\frac{\sigma_{dc}}{\epsilon_0\omega} \right)^N$ represents the conductivity where σ_{dc} is the direct current conductivity, ϵ_0 is the vacuum permittivity and N is a fitting parameter that ranges from 0 to 1.

To evaluate the quality of the fiber/matrix interfacial adhesion between PVA/CS and LP, it is essential to examine the dielectric strength $\Delta\epsilon$. This parameter measures the density, dipolar moment, and interconnection of dipoles that accumulate and interact at the fiber/matrix interfaces, which contributes to interfacial polarization. The $\Delta\epsilon$ values for LP biocomposites are provided in Table 2.

References

1. Fakraoui O, Hammami H, Naveen J, Jawaid M, Kallel A. Evolution of dielectric properties of Kevlar/epoxy laminated composites after hybridization by naturally woven *Coco Nucifera* sheaths. *J Compos Mater* 2023. <https://doi.org/10.1177/00219983231181943>
2. Zhang P, Feng Z, Yuan W, Hu S, Yuan P. Effect of PVA fiber on properties of geopolymer composites: A comprehensive review. *J Mater Res Technol* 2024. <https://doi.org/10.1016/j.jmrt.2024.02.151>
3. Rata DM, Cadinoiu AN, Popa M, Atanase LI, Daraba OM, et al. Biocomposite hydrogels for the treatment of bacterial infections: physicochemical characterization and in vitro assessment. *Pharmaceutics* 2021. <https://doi.org/10.3390/pharmaceutics13122079>
4. Flórez M, Guerra-Rodríguez E, Cazón P, Vázquez M. Chitosan for food packaging: Recent advances in active and intelligent films. *Food Hydrocoll* 2022. <https://doi.org/10.1016/j.foodhyd.2021.107328>
5. Suri S, Singh A, Nema PK. Current applications of citrus fruit processing waste: A scientific outlook. *Appl Food Res* 2022. <https://doi.org/10.1016/j.afres.2022.100050>

Table 2. Dielectric strength $\Delta\epsilon$ of LP biocomposites as a function of temperature.

Temperature (°C)	PVA/CS/LP1	PVA/CS/LP3	PVA/CS/LP5
49.6	3.856	3.750	3.230
52.6	4.126	4.025	3.300
55.6	4.186	4.458	3.620
58.6	4.236	4.685	3.730

It is notable that $\Delta\epsilon$ decreases progressively with higher concentrations of LP. Among the biocomposites, PVA/CS/LP1 exhibits the highest dielectric intensity. This higher dielectric strength indicates that more dipoles are being obstructed at the interfaces, suggesting weaker interfacial adhesion [22]. In contrast, the PVA/CS/LP5 composite shows the lowest $\Delta\epsilon$ values, indicating better interfacial adhesion. This improvement is attributed to the formation of a network through hydrogen bonding between the LPP and the PVA/CS blend, as well as the crosslinking effect of lignin present on the LP surface [23].

IV. Conclusion

In this paper, biodegradable food packaging films (PVA/CS/LP) were successfully prepared using a casting method. The addition of LP improved the thermal stability and biodegradability of the PVA/CS films, achieving a 74% degradation rate after 30 days in soil. Tensile tests showed that blending PVA with CS increased the Young's modulus, and the inclusion of LP further enhanced it to 1322 MPa, with a tensile strength of 193 MPa, due to strong hydrogen bonding. Additionally, PVA/CS/LP biocomposites effectively minimized weight loss in cherry tomatoes, indicating their potential as eco-friendly, bioactive packaging materials. Dielectric studies confirmed good interfacial compatibility between the PVA/CS matrix and LP reinforcements.

6. Singh B, Singh JP, Kaur A, Singh N. Phenolic composition, antioxidant potential and health benefits of citrus peel. *Food Res Int* 2020. <https://doi.org/10.1016/j.foodres.2020.109114>
7. Yun D, Liu J. Recent advances on the development of food packaging films based on citrus processing wastes: A review. *J Agric Food Res* 2022. <https://doi.org/10.1016/j.jafr.2022.100316>
8. Wen L, Liang Y, Lin Z, Xie D, Zheng Z, et al. Design of multifunctional food packaging films based on carboxymethyl chitosan/polyvinyl alcohol crosslinked network by using citric acid as crosslinker. *Polymer* 2021. <https://doi.org/10.1016/j.polymer.2021.124048>
9. Dey D, Dharini V, Selvam SP, Sadiku ER, et al. Physical, antifungal, and biodegradable properties of cellulose nanocrystals and chitosan nanoparticles for food packaging application. *Mater Today Proc* 2021. <https://doi.org/10.1016/j.matpr.2020.04.88>
10. Merino D, Athanassiou A. Biodegradable and Active Mulch Films: Hydrolyzed Lemon Peel Waste and Low Methoxyl Pectin Blends with Incorporated Biochar and Neem Essential Oil. *ACS Sustain Chem Eng* 2022;10:10789–802. <https://doi.org/10.1021/acssuschemeng.2c01539>.
11. Sivalingam A, Perumal Venkatesan E, Roberts KL, Asif M. Potential Effect of Lemon Peel Oil with Novel Eco-Friendly and Biodegradable Emulsion in Un-Modified Diesel Engine. *ACS Omega* 2023;8:18566–81. <https://doi.org/10.1021/acsomega.3c00325>.
12. Karim R, Nahar K, Zohora FT, Islam MM, Bhuiyan RH, Jahan MS, et al. Pectin from lemon and mango peel: Extraction, characterisation and application in biodegradable film. *Carbohydr Polym Technol Appl* 2022. <https://doi.org/10.1016/j.carpta.2022.100258>
13. Bazzi M, Shabani I, Mohandesi JA. Enhanced mechanical properties and electrical conductivity of Chitosan/Polyvinyl Alcohol electrospun nanofibers by incorporation of graphene nanoplatelets. *J Mech Behav Biomed Mater* 2022. <https://doi.org/10.1016/j.jmbbm.2021.104975>
14. Fakraoui O, Ghorbel N, Noirel C, Royaud I, Arous M, Ayadi Z, et al. Comparative analysis of cellulose nanocrystals and cellulose nanofibrils on the physico-chemical properties of polyvinyl alcohol/chitosan blend for sustainable food packaging. *J Appl Polym Sci* 2022. <https://doi.org/10.1002/app.54024>.
15. Rathinavel S, Saravanakumar SS. Development and Analysis of Poly Vinyl Alcohol/Orange peel powder biocomposite films. *J Nat Fibers* 2021. <https://doi.org/10.1080/15440478.2019.1711285>
16. Yu D, Yu Z, Zhao W, Regenstein JM, Xia W. Advances in the application of chitosan as a sustainable bioactive material in food preservation. *Crit Rev Food Sci Nutr* 2022;62:3782–97. <https://doi.org/10.1080/10408398.2020.1869920>.
17. Shehata SA, Abdeldaym EA, Ali MR, Mohamed RM, Bob RI, Abdelgawad KF. Effect of some citrus essential oils on post-harvest shelf life and physicochemical quality of strawberries during cold storage. *Agronomy* 2020. <https://doi.org/10.3390/agronomy10101466>
18. Fakraoui O, Atanase LI, Salhi S, Royaud I, Arous M, Ayadi Z. Investigation of lemon peel extract as a natural additive in polyvinyl alcohol/chitosan blend for advanced bioactive food packaging. *J Polym Sci* 2024. <https://doi.org/10.1002/pol.20240268>.
19. Ouled Ltaief A, Ghorbel N, Benhamou K, Arous M, Kaddami H, Kallel A. Impact of cellulose nanocrystals reinforcement on molecular dynamics and dielectric properties of PCL -based polyurethane. *Polym Compos* 2021. <https://doi.org/10.1002/pc.26009>.
20. Fakraoui O, Arous M, Royaud I, Ayadi Z. Correlation between Mechanical and Dielectric Dynamic Behavior Using Fractional Models: Application to Polylactic Acid. *ACS Appl Polym Mater* 2024;6:1483–94. <https://doi.org/10.1021/acsapm.3c02691>.
21. Havriliak S, Negami S. A complex plane representation of dielectric and mechanical relaxation processes in some polymers. *Polymer* 1967. [https://doi.org/10.1016/0032-3861\(67\)90021-3](https://doi.org/10.1016/0032-3861(67)90021-3)
22. Naveen J, Jawaid M, Zainudin ES, Sultan MT, Yahaya R. Evaluation of ballistic performance of hybrid Kevlar®/Cocos nucifera sheath reinforced epoxy composites. *J Text Inst* 2018. <https://doi.org/10.1080/00405000.2018.1548801>
23. Taghavi Kevij H, Salami M, Mohammadian M, Khodadadi M, Emam-Djomeh Z. Mechanical, physical, and bio-functional properties of biopolymer films based on gelatin as affected by enriching with orange peel powder. *Polym Bull* 2021. <https://doi.org/10.1007/s00289-020-03319-9>

Machine Learning-Based Optimization of the Synthesis of TiO₂/CNTs Composites via Genetic Algorithms (GA)

Sara Zandi

University of Aveiro - Department of Environment and Planning, Centre for Environmental and Marine Studies, CESAM, and Department of Materials and Ceramics Engineering, Aveiro Institute of Materials, CICECO, 3810-193 Aveiro, Portugal,
sara.zandi@ua.pt.
ORCID: 0000-0003-4201-2053

Behrouz Nemati

University of Aveiro - Department of Environment and Planning, Centre for Environmental and Marine Studies, CESAM, and Department of Materials and Ceramics Engineering, Aveiro Institute of Materials, CICECO, 3810-193 Aveiro, Portugal.
ORCID: 0000-0003-1581-4368

Mohammadreza Kamali

University of KU Leuven - Department of Chemical Engineering, Process and Environmental Technology Lab, J. De Nayerlaan 5, 2860, Sint-Katelijne-Waver, Belgium.
ORCID: 0000-0002-1591-9605

Shahed Rasekh

University of Aveiro - Department of Materials and Ceramics Engineering, Aveiro Institute of Materials, CICECO, 3810-193 Aveiro, Portugal.
ORCID: 0000-0003-3466-9952

M. Elisabete V. Costa

University of Aveiro - Department of Materials and Ceramics Engineering, Aveiro Institute of Materials, CICECO, 3810-193 Aveiro, Portugal.
ORCID: 0000-0001-7803-6212

Isabel Capela

University of Aveiro - Department of Environment and Planning, Centre for Environmental and Marine Studies, CESAM, 3810-193 Aveiro, Portugal.
ORCID: 0000-0002-6757-1751

Cite this paper as: Zandi, S., Nemati, B., Kamali, M., Rasekh, Sh., Costa, M., Capela, I., Machine Learning-Based Optimization of the Synthesis of TiO₂/CNTs Composites via Genetic Algorithms (GA). Int. Conf. Advanced. Mater. Sci. & Eng. HiTech. and Device Appl. Oct. 24-26 2024, Ankara, Turkiye

Abstract. Titanium dioxide (TiO₂) and carbon nanotubes (CNTs) composites have emerged as advanced materials with exceptional properties, rendering them highly suitable for applications in wastewater treatment, energy conversion, and storage. These composites exhibit remarkable specific surface area (SSA), excellent electrical conductivity, and potent photocatalytic activity. This study presents a novel approach for optimizing the synthesis of TiO₂/CNTs composites via the sol-gel method, employing a Genetic Algorithm (GA). Key parameters, including Titanium isopropoxide (TTIP) concentration (ml), CNTs concentration (%), ultrasonic time (%), and microwave exposure time (min), were strategically optimized using GA. Comprehensive material characterization was performed through X-ray diffraction (XRD), scanning electron microscopy (SEM), Brunauer-Emmett-Teller (BET) analysis, and Zeta potential measurements. Initial experiments revealed SSA values ranging from 15 to 264 m²/g. However, the optimized conditions, comprising 20 ml TTIP concentration, 0.5% CNTs concentration, 100% ultrasonic time, and 8 minutes of microwave exposure, led to a significant enhancement in SSA,

reaching 342 m²/g. It should be highlighted the use of microwave calcination also reduced energy consumption and environmental impact, underscoring the method's sustainability. Obtained results establishes the use of GA as a promising approach for further enhancing the desirable properties of TiO₂/CNTs composites.

Keywords: Nanocomposite Synthesis; Genetic Algorithm; Microwave Irradiation; Titanium Dioxide; Carbon Nanotubes.

© 2024 Published by ICMATSE

Introduction

Titanium dioxide (TiO₂) and carbon nanotubes (CNTs) composites have garnered attention for their exceptional structural, electrical, and photocatalytic properties, making them ideal for wastewater treatment, energy conversion, and storage. TiO₂ provides excellent photocatalytic activity and stability, while CNTs offer superior electrical conductivity and mechanical strength [1]. Their synergy enhances performance in catalytic and energy applications. Traditional synthesis methods, like furnace calcination, consume significant energy while releasing CO₂. This study replaces the furnace with microwave-assisted synthesis, offering a more energy-efficient and environmentally friendly alternative, reducing energy consumption and emissions. This work tend to optimize the synthesis parameters, Titanium isopropoxide (TTIP) concentration, CNT concentration, ultrasonic time, and microwave exposure time, using a Genetic Algorithm (GA) to maximize the specific surface area (SSA), a critical factor for their performance [2]. The optimization process led to a composite with the highest possible SSA, significantly improving material properties and ensuring sustainability in the synthesis process.

Methodology

Based on the sol-gel method, the CNTs were dispersed in a suspension of TTIP and ethanol using ultrasonic agitation [3]. Ultrasonication and stirring ensured proper interaction and uniformity. The mixture was then subjected to microwave irradiation for calcination.

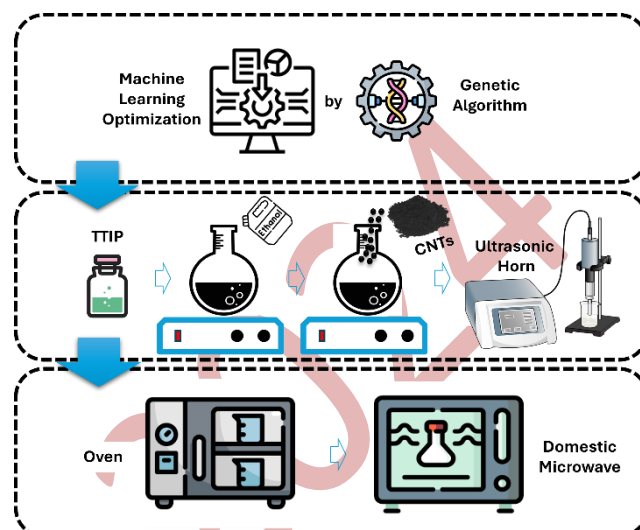


Figure 1. A schematic of TiO₂/CNTs nanocomposite synthesis procedure.

Four key synthesis parameters (i.e., TTIP concentration (ml), CNT concentration (%), ultrasonic time (%), and microwave exposure time (min)) were optimized employing GA in 16 runs. GA systematically explored the parameter space to identify the optimal conditions that maximize the SSA of the composite.

Results

The optimization of TiO₂/CNT composites using a GA yielded significant improvements in the material's properties. Initial experiments produced SSA values ranging from 15 to 264 m²/g, depending on the synthesis parameters. Through GA optimization, the best conditions were identified as 20 ml of TTIP concentration, 0.5% CNT concentration, 100% ultrasonic time, and 8 minutes of microwave exposure. Under these optimized conditions, the SSA increased to 342 m²/g, indicating a substantial improvement in the material's performance. In addition, microwave calcination, played a crucial role by reducing energy consumption compared to conventional furnace methods while forming the desired composite structure.

The X-ray diffraction (XRD) pattern displays the crystalline structure of the TiO₂/CNT

nanocomposite, highlighting distinct peaks that correspond to different phases within the material [4]. Carbon nanotubes (ICDD No. 00-068-1638) are denoted by red triangles, with a prominent peak around 26° corresponding to the (002) crystallographic plane of the graphitic structure. Titanium oxide is observed in both its anatase (ICDD No. 04-002-8296) and rutile (ICDD No. 01-079-5860) forms, marked by green and orange triangles, respectively. Peaks for anatase are identified at 26° (101), 37.8° (004), 48.1° (200), and 55.1° (211), while the rutile phase is confirmed with peaks at 27.5° (110), 36.1° (101), and 54.4° (211) (Figure 2). These well-defined peaks confirm the successful synthesis of the nanocomposite and indicate a crystalline structure that combines both carbon nanotubes and titanium dioxide in its anatase and rutile forms. The sharpness and intensity of the peaks further suggest the composite's potential for advanced applications, such as catalysis or adsorption, where crystallinity plays a crucial role in performance.

The scanning electron microscopy (SEM) images show the morphology of the TiO_2/CNT nanocomposite at a scale of $1\ \mu\text{m}$, revealing the interconnected network of CNTs embedded with TiO_2 nanoparticles [5]. The lower section presents EDS elemental mapping of the same area, highlighting the distribution of key elements. Carbon (C), represented in red, is uniformly distributed, indicating the presence of CNTs throughout the sample. Titanium (Ti), shown in blue, marks the locations of TiO_2 particles, while oxygen (O), depicted in green, aligns with the distribution of Ti, further confirming the presence of TiO_2 (Figure 3). The overlapping image at the bottom right combines these elemental maps, illustrating the successful integration of CNTs and TiO_2 within the nanocomposite. This combination of SEM and EDS provides a detailed look at both the structure and elemental composition, verifying the uniform distribution and interaction between CNTs and TiO_2 .

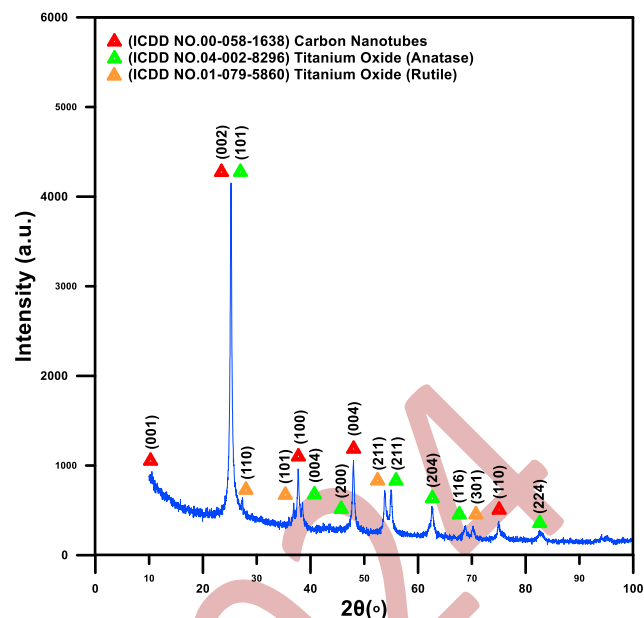


Figure 2. XRD pattern of synthesized TiO_2/CNTs nanocomposite.

In addition, Figure 4 presents the nitrogen adsorption-desorption isotherm for the TiO_2/CNT nanocomposite, showcasing its surface area and porosity characteristics. The isotherm follows a Type IV pattern, typical of mesoporous materials, with a clear hysteresis loop observed between the adsorption (red) and desorption (blue) curves, indicating the presence of mesopores [6]. SSA of the nanocomposite is measured at $342\ \text{m}^2/\text{g}$, demonstrating a high surface area that is beneficial for applications such as gas adsorption or catalysis. The upward trend in the isotherm at higher relative pressures (P/P_0) suggests increased adsorption in larger pores. This result confirms the successful synthesis of a material with a well-developed porous structure.

Furthermore, the Zeta Potential (ZP) versus pH graph [7] for TiO_2/CNTs nanocomposites illustrates the variation in surface charge as a function of pH (Figure 5). The point of zero charge (ZCP) occurs at pH 6.4, where the surface charge is neutral. Below this pH, the nanocomposite surface carries a positive charge, attracting negatively charged species, while above this pH, the surface becomes negatively charged, repelling anions. This behaviour is essential for understanding the nanocomposite's stability, dispersibility, and interaction with different substances in various environmental and industrial

applications.

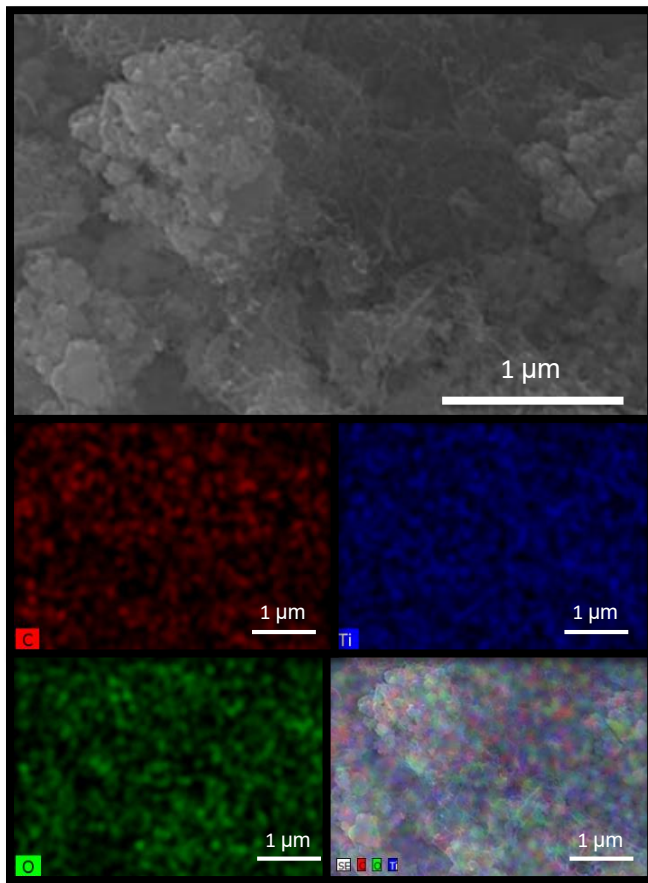


Figure 3. SEM images and EDS analysis of synthesized $TiO_2/CNTs$ nanocomposite.

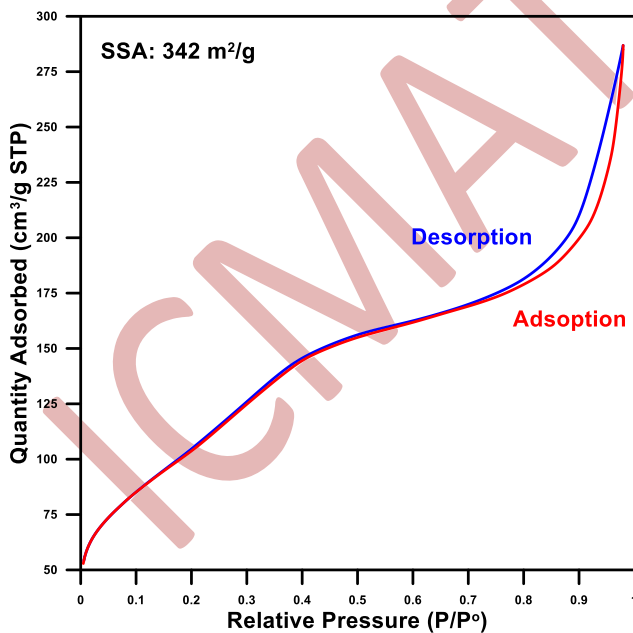


Figure 4. Adsorption/desorption isotherms of synthesized $TiO_2/CNTs$ nanocomposite.

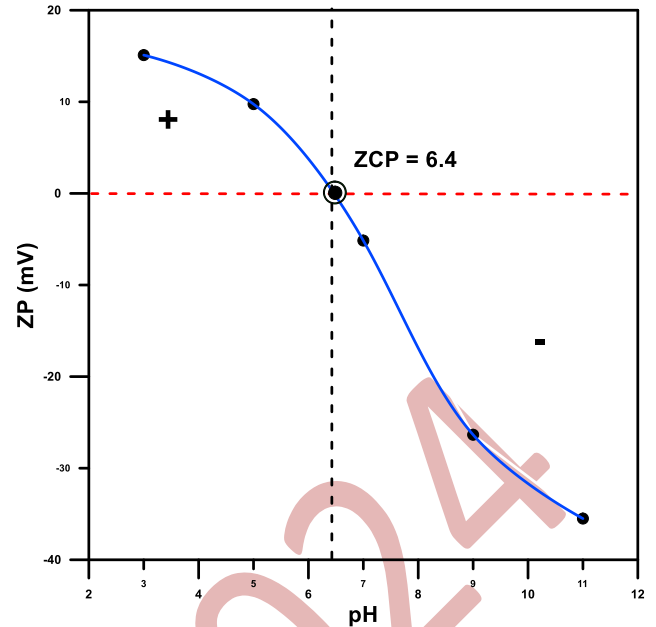


Figure 5. ZP of the synthesized $TiO_2/CNTs$ (ZCP being detected at approximately pH 6.4).

Discussion and Conclusions

Characterization techniques further confirmed the successful synthesis of the TiO_2/CNT nanocomposite. XRD revealed distinct crystalline phases of both CNTs and TiO_2 , with notable peaks at 26° corresponding to the (002) crystallographic plane of CNTs and 27.5° corresponding to anatase and rutile forms of TiO_2 , respectively. SEM images provided a closer look at the nanocomposite's morphology, showing a uniform distribution of TiO_2 nanoparticles embedded within the CNTs network. This was further confirmed by EDS, which mapped the even presence of carbon, titanium, and oxygen throughout the material. In addition, the nitrogen adsorption-desorption isotherms demonstrated a high SSA of $342\text{ m}^2/\text{g}$, along with a Type IV isotherm and a clear hysteresis loop, confirming the mesoporous nature of the material. Furthermore, the study emphasizes the efficiency of GA optimization, which improved the SSA from initial values of $15\text{-}264\text{ m}^2/\text{g}$ to $342\text{ m}^2/\text{g}$, significantly enhancing the nanocomposite's performance. Moreover, the optimization process, coupled with microwave-assisted calcination, reduced energy consumption and minimized CO_2 emissions, showcasing the sustainability of this synthesis approach. These results position the optimized TiO_2/CNT nanocomposite as a strong candidate for advanced technological applications that demand high surface areas and efficient material performance with a reduced environmental footprint.

References

1. R. Mutsak Ahmed and I. Hasan, "A review on properties and applications of TiO₂ and associated nanocomposite materials," *Mater. Today Proc.*, vol. 81, no. 2, pp. 1073–1078, 2021, doi: 10.1016/j.matpr.2021.04.381.
2. H. Liang, J. Zou, K. Zuo, and M. J. Khan, "An improved genetic algorithm optimization fuzzy controller applied to the wellhead back pressure control system," *Mech. Syst. Signal Process.*, vol. 142, p. 106708, 2020, doi: 10.1016/j.ymssp.2020.106708.
3. T. T. Le Nguyen et al., "Fabrication of TiO₂/CNTs composite electrode with improved performance in capacitive deionization," *Clean - Soil, Air, Water*, vol. 52, no. 5, pp. 1–10, 2024, doi: 10.1002/clen.202300037.
4. Y. Xue, M. Kamali, X. Yu, L. Appels, and R. Dewil, "Novel CuO/Cu₂(V₂O₇)/V₂O₅ composite membrane as an efficient catalyst for the activation of persulfate toward ciprofloxacin degradation," *Chem. Eng. J.*, vol. 455, no. October 2022, p. 140201, 2023, doi: 10.1016/j.cej.2022.140201.
5. M. Kamali, M. Khalaj, M. E. V. Costa, I. Capela, and T. M. Aminabhavi, "Optimization of kraft black liquor treatment using ultrasonically synthesized mesoporous tenorite nanomaterials assisted by Taguchi design," *Chem. Eng. J.*, vol. 401, no. June, p. 126040, 2020, doi: 10.1016/j.cej.2020.126040.
6. V. G. Baldovino-Medrano, V. Niño-Celis, and R. Isaacs Giraldo, "Systematic Analysis of the Nitrogen Adsorption-Desorption Isotherms Recorded for a Series of Materials Based on Microporous-Mesoporous Amorphous Aluminosilicates Using Classical Methods," *J. Chem. Eng. Data*, vol. 68, no. 9, pp. 2512–2528, 2023, doi: 10.1021/acs.jced.3c00257.
7. K. Cagua, F. Ordoñez, C. Zapata, B. Herrera, E. Pabón, and R. Buitrago-Sierra, "Surfactant concentration and pH effects on the zeta potential values of alumina nanofluids to inspect stability," *Colloids Surfaces A Physicochem. Eng. Asp.*, vol. 583, no. July, 2019, doi: 10.1016/j.colsurfa.2019.123960.

Acknowledgments

Sara Zandi acknowledges FCT for financial support, under the scholarship 2021.07172.BD. Also, Behrouz Nemati acknowledges FCT for financial support, under the scholarship 2020.05304.BD. This work also received financial support through CESAM by FCT / MCTES (UIDP/50017/2020 + UIDB/50017/2020 + LA/P/0094/2020), through national funds. Thanks are also due to the financial support of the project CICECO-Aveiro Institute of Materials, UIDB/50011/2020 (DOI 10.54499/UIDB/50011/2020), UIDP/50011/2020 (DOI 10.54499/UIDP/50011/2020) & LA/P/0006 /2020 (DOI 10.54499/LA/P/ 0006/2020), and Research Employment Contract FCT–CEECIND/02608/2017, financed by national funds through the FCT/MCTES (PIDDAC). Thanks, are also due to the financial support from the PDM program, KU Leuven.

Fabrication of Thermoelectric Legs and Their Integration Into A Prototype Thermoelectric Generator

Sotelo, Andres

*INMA (CSIC-Universidad de Zaragoza) Department of Materials Science, 50059, Zaragoza, Spain,
asotelo@unizar.es*

ORCID: 0000-0001-7056-0546

Amirkhizi, Parisa

*Department of Materials and Ceramic Engineering, CICECO-Aveiro Institute of Materials, University of Aveiro,
3810-193 Aveiro, Portugal,
parisa.amirkhizi@ua.pt*

ORCID: 0000-0003-2764-4108

Hedayati, Mehdi

*University of Aveiro- Department of Materials and Ceramic Engineering, CICECO-Aveiro Institute of Materials, 3810-193,
Aveiro, Portugal, mehdi.hedayati@ua.pt*

ORCID: 0009-0003-0289-3439

Madre, Maria A.

*INMA (CSIC-Universidad de Zaragoza) Department of Materials Science, 50059, Zaragoza, Spain,
amadre@unizar.es*

ORCID: 0000-0002-0794-3998

Torres, Miguel A.

*INMA (CSIC-Universidad de Zaragoza) Department of Materials Science, 50059, Zaragoza, Spain,
matorres@unizar.es*

ORCID: 0000-0003-3995-5763

Kovalevsky, Andrei

*Department of Materials and Ceramic Engineering, CICECO-Aveiro Institute of Materials, University of Aveiro,
3810-193 Aveiro, Portugal,
akavaleuski@ua.pt*

ORCID: 0000-0001-5814-9797

Rasekh, Shahed

*Department of Materials and Ceramic Engineering, CICECO-Aveiro Institute of Materials, University of
Aveiro, 3810-193 Aveiro, Portugal,
shahedvrm@ua.pt*

ORCID: 0000-0003-3466-9952

*Cite this paper as: Sotelo, A., Amirkhizi, P., Hedayati, M., Madre, MA, Torres, MA, Kovalevsky, A, Rasekh, Sh.
Fabrication of thermoelectric legs and their integration into a prototype thermoelectric generator.
Int. Conf. Advanced. Mater. Sci.& Eng. HiTech.and Device Appl.Oct. 24-26 2024, Ankara, Turkiye*

Abstract. Sr-doped $\text{Ca}_3\text{Co}_4\text{O}_9$ p-type, and Ce-doped CaMnO_3 n-type compounds were prepared through the solid-state method. XRD patterns showed that both samples are nearly single phase, with very small amounts of secondary phases. SEM observation indicated that p-type compound is composed by plate-like grains, with some degree of porosity, while n-type compound presents very low porosity. Electrical resistivity evolution with temperature is metallic-like for the n-type compound while for the p-type it is semiconducting-like below 400 °C and metallic-like at higher temperatures. Seebeck coefficient is negative for the n-type compound and positive for the p-type. Absolute Seebeck coefficient increases with temperature in both cases. The highest PF values are very close for both compounds at 800 °C, 0.30 mW/K²m for the p-type compound, and around 0.32 mW/K²m for the n-type. These materials were used to build a thermoelectric generator using

17 thermoelectric pairs in the classical configuration and evaluated at different temperatures, maintaining constant the cold side at 18 °C, reaching its maximum power, 80 mW, when the hot side reached 900 °C.

Keywords: Ceramics, Oxides, Thermoelectric module, Power generation

© 2024 Published by ICMATSE

Introduction

Thermoelectric (TE) materials can transform a temperature gradient to electrical power directly due to the well-known Seebeck effect. The conversion efficiency of such materials is usually quantified by the dimensionless figure of merit ZT , $TS^2/\rho\kappa$ (in which the electrical part S^2/ρ is also called power factor, PF), where S is the Seebeck coefficient, ρ the electrical resistivity, κ the thermal conductivity, and T is the absolute temperature [1]. This important characteristic has focused attention on this type of materials in order to be applied as waste heat recovery devices [2] or solar thermoelectric generators [3]. Furthermore, they can also be used as heating/refrigeration devices [4]. Taking into account the above expression, high performance thermoelectric materials should possess large Seebeck coefficient and low electrical resistivity and thermal conductivity. Low electrical resistivity is necessary to minimize Joule heating, while a low thermal conductivity helps to maintain a large temperature gradient between the hot and cold sides in the thermoelectric device.

As it is well known, two different thermoelectric families are known, p-type which possesses holes as charge carriers, and n-type, with electrons as charge carriers. These two families are characterized by positive, and negative S values, respectively. Among these families, the most studied members are $\text{Ca}_3\text{Co}_4\text{O}_9$ and CaMnO_3 compounds as p-, and n-type, respectively [5,6].

When building a thermoelectric module, it is necessary to use p-n thermoelectric pairs which should be connected electrically in series and thermally in parallel. Consequently, the thermoelectric module is composed of two electrically isolating ceramic layers, where the electric circuit is printed with metallic Ag. Finally, the central part is formed by the connection of thermoelectric elements to the circuit.

In this work, $\text{Ca}_{2.93}\text{Sr}_{0.07}\text{Co}_4\text{O}_9$ (p-type compound) and $\text{Ca}_{0.95}\text{Ce}_{0.05}\text{MnO}_3$ (n-type compound) were prepared by the classical solid-state route, previously described for both compounds [7,8].

Precursors were ball milled at 300 rpm for 30 min, and calcined twice, at 750 and 800 °C for 12 hours for the p-type, and at 950 and 1050 °C for 12 hours for the n-type. These materials were then uniaxially pressed in form of pellets ($\sim 3 \times 3 \times 15 \text{ mm}^3$) under 400 Mpa, and sintered at 900, and 1310 °C, for the p- and n-type compounds, respectively.

Powder X-ray diffraction (XRD) has been performed in a Rigaku Ru300 between 5 and 60 ° to identify the phases in the samples. Microstructural observations were performed on samples surfaces after sintering in a FESEM (Zeiss Merlin) fitted with an energy dispersive spectrometer (EDS) used to determine the elemental composition of each phase. Electrical resistivity and Seebeck coefficient were simultaneously determined in the steady state mode, using the standard dc four-probe technique, in a LSR-3 apparatus (Linseis GmbH) between 50 and 800 °C under the atmosphere. With these data, PF was calculated to determine the samples performances.

Module characterization has been performed in a home-made system, which cools down the lower part of the module with water flow at 18 °C, while a heating device heats the upper part of the modules at temperatures up to 900 °C.

Results and discussion

XRD patterns presented in Figure 1 show that all samples are nearly single phase, and only small amounts of $\text{Ca}_3\text{Co}_2\text{O}_6$ secondary phase (indicated by *) have been identified.

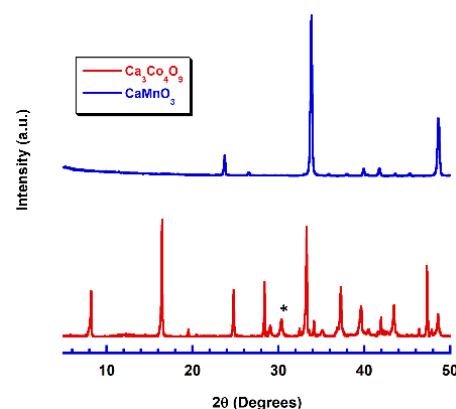


Figure 1. XRD patterns of both compounds. The peak identified by * indicates the $Ca_3Co_2O_6$ secondary phase

Representative SEM images shown in Figure 2, indicate that the p-type compound is formed by plate-like grains, with relatively high porosity, while the n-type is composed of larger polygonal grains and very low amount of porosity. The difference between these samples is due to the fact that n-type compounds are sintered at temperatures close to their melting point, while n-type ones should be sintered at temperatures far from their melting point (1350 °C) due to the maximum stability temperature of the thermoelectric phase (926 °C) [9].

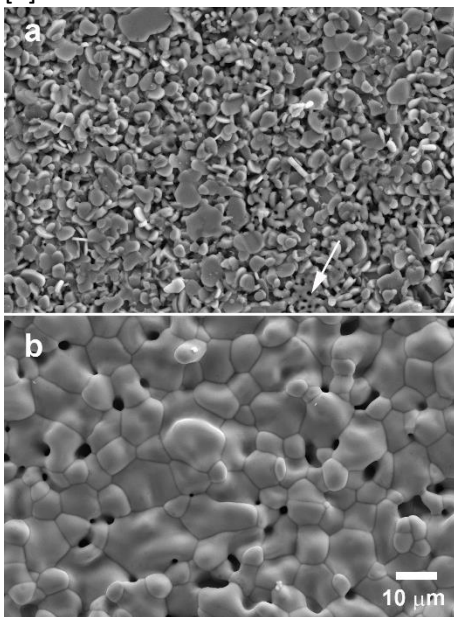


Figure 2. SEM images of a) p-type compound; and b) n-type compound. The arrow indicates the $Ca_3Co_2O_6$ secondary phase

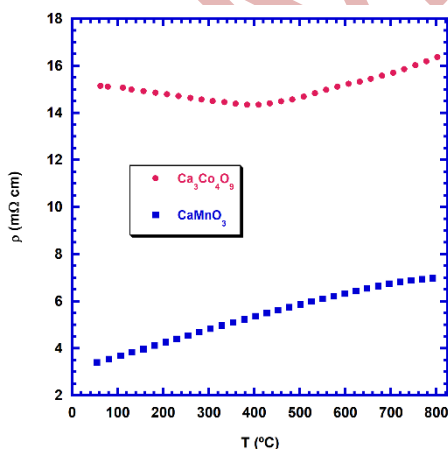


Figure 3. Electrical resistivity variation with temperature for both compounds

Electrical resistivity variation with temperature displayed in Figure 3 illustrates metallic-like

behaviour for the n-type compound, while the p-type was semiconducting-like up to 400 °C, and metallic-like for higher temperatures. The values at 800 °C were about 16, and 7 mΩ cm, for the p-, and n-type compounds, respectively. This large value measured in the p-type compound can be explained by the large amount of porosity and the much lower grain sizes found in these samples. In any case, both values are around the best reported in literature.

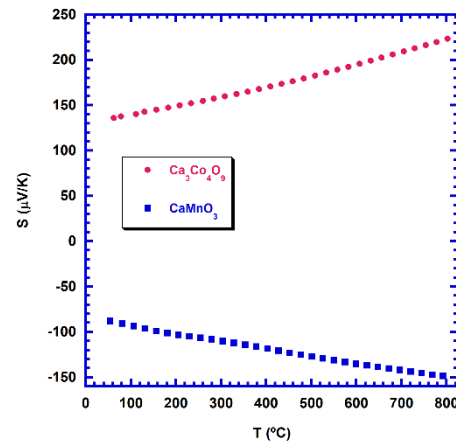


Figure 4. Seebeck coefficient variation with temperature for both compounds

S variation with temperature, shown in Figure 4 displays positive values in p-type, while it is negative in n-type compounds. However, |S| increases with temperature for both compounds, reaching 220, and 150 μV/K for the p-, and n-type compounds, respectively. These relatively close values, reflect the low sensitivity of S to microstructural modifications. However, the values are among the best found in the available literature.

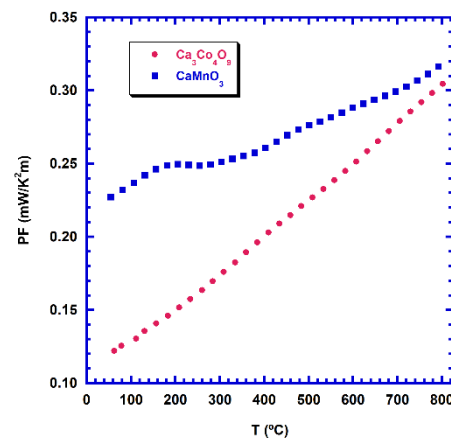


Figure 5. PF variation with temperature for both compounds

The thermoelectric performances of these samples were determined through their PF, and its variation with temperature is illustrated in Figure 5. The highest values at 800 °C for p-, and n-type compounds reached 0.30, and 0.32 mW/K²m,

respectively, which are among the best reported in literature.

These compounds were then integrated into a thermoelectric module, as shown in Figure 6.



Figure 6. Thermoelectric module where the thermoelectric compounds, silver electric circuit, and output wires can be observed

This assemblage was sintered to form the electric circuit at 900 °C for 2 hours, and characterized at different temperatures on the hot side, while the cold side was maintained at 18 °C. The obtained I-V curves are shown in Figure 7.

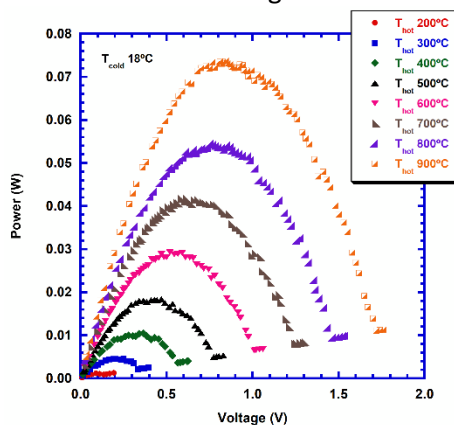


Figure 7. Power vs. Voltage at different hot-side temperatures

References

1. D.M. Rowe, in: D.M. Rowe (Ed.), *Thermoelectrics Handbook: Macro to Nano*, 1st edn, CRC Press, Boca Raton, FL, 2006, pp. 1-3–1-7.
2. G. Mahan, B. Sales, J. Sharp, *Thermoelectric materials: New approaches to an old problem*, *Phys. Today* 50 (1997), pp. 42-47, 10.1063/1.881752
3. H. Naito, Y. Kohsaka, D. Cooke, H. Arashi, *Development of a solar receiver for a high-efficiency thermionic/thermoelectric conversion system*, *Solar Energy* 58 (1996), pp. 191-195, 10.1016/S0038-092X(96)00084-9
4. C. M. Kim, Y. J. Hwang, Y. H. Ryu, *Air conditioner for individual cooling/heating*, US Patent US6393842. May, 2002
5. R. Funahashi, I. Matsubara, H. Ikuta, T. Takeuchi, U. Mizutani, S. Sodeoka, *An oxide single crystal with high thermoelectric performance in air*, *Jpn. J. Appl. Phys.* 39 (2000), pp. L1127-1129, 10.1143/JJAP.39.L1127
6. M. Ohtaki, H. Koga, T. Tokunaga, K. Eguchi, H. Arai, *Electrical transport properties and high-temperature thermoelectric performance of (Ca_{0.9}M_{0.1})MnO₃ (M= Y, La, Ce, Sm, In, Sn, Sb, Pb, Bi)*, *J. Solid State Chem.* 120 (1995), pp. 105-111, 10.1006/jssc.1995.1384
7. G. Constantinescu, Sh. Rasekh, M.A. Torres, J.C. Diez, M.A. Madre, A. Sotelo, *Effect of Sr substitution for Ca on the Ca₃Co₄O₉ thermoelectric properties*, *J. Alloy. Compd.* 577 (2013), pp. 511-515, 10.1016/j.jallcom.2013.07.005
8. A. Sotelo, P. Amirkhizi, O.J. Dura, G. García, A.C. Asensio, M.A. Torres, M.A. Madre, A. Kovalevsky, Sh Rasekh, *Significant reduction in processing time for Ca_{0.95}Ce_{0.05}MnO₃ thermoelectric ceramics*, *Ceram. Int.* 49 (2023), pp. 37793-37799, 10.1016/j.ceramint.2023.09.107

As it can be observed, the power increases when the hot-side temperature is increased, reaching nearly 80 mW when at 900 °C. Even if it seems to be low, it should be mentioned that the size of the module is 5 x 5 cm² (0.0025 m²), which corresponds to around 32 W/m². This value is still far from the typical values in solar generators, but it is mainly due to the large space between thermoelectric elements in this module.

Conclusions

In this work, Ca_{2.93}Sr_{0.07}Co₄O₉ and Ca_{0.95}Ce_{0.05}MnO₃ compounds have been successfully prepared through the solid-state method. XRD patterns showed that the samples were nearly single phase. SEM observation agreed with these data, showing that p-type compounds possessed lower particle sizes and higher porosity. Electrical resistivity values at 800 °C were among the best reported in literature for both compounds, even if p-type compounds displayed much higher values than the n-type ones. |S| values were much closer due to the lower effect of microstructure on this parameter. Power factor was nearly the same at 800 °C for both compounds, and among the best in literature. The thermoelectric module prepared with these compounds has reached a maximum power of about 80 mW when the hot-side was at 900 °C, which corresponds to around 32 W/m², still far from the typical values in solar generators due to the small number of thermoelectric elements used in this module.

9. E. Woermann, A. Muan, Phase equilibria in the system CaO-cobalt oxide in air, J. Inorg. Nucl. Chem. 32 (1970), pp. 1455-1459, 10.1016/0022-1902(70)80631-5

ICMATSE 2024

Surface Treatment Application of Bulk Amorphous Steel

Amdulla O. MEKHRABOV

¹UNEC Research Center of Composite Materials, Azerbaijan State University of Economics (UNEC), Az1001, Baku, Azerbaijan Republic, amekhrabov@unec.edu.az
ORCID: 0000-0003-3301-8971

Hafize ÇAKMAK ALPASLAN

²Structural Integrity Program and System Manager, Ion Industrial Metallurgy Research and Development Inc., Middle East Technical University, 06800-Ankara, Türkiye, hafizecakmakalpaslan@gmail.com
ORCID: 0000-0001-7231-9780

M. Vedat AKDENİZ

³Novel Alloy Design and Development Laboratory (NOVALAB), Department of Metallurgical and Materials Engineering, Middle East Technical University, 06800-Ankara, Turkey, akdeniz@metu.edu.tr
ORCID: 0000-0001-5127-7796

Cite this paper as: Mekhrabov, AO, Cakmak Alpaslan, H, Akdeniz, MV. Surface Treatment Application of Bulk Amorphous Steel. Int. Conf. Advanced. Mater. Sci. & Eng. HiTech. and Device Appl. Oct. 24-26 2024, Ankara, Türkiye

Abstract. Bulk amorphous steels (BASs) have promising future due to their superior mechanical and physical properties compared with their crystalline states. BASs display very high hardness, Young's modulus, wear and corrosion resistance due to their amorphous nature. These unique characteristics make BAS a potential candidate for coating studies. In this respect, the purpose of this study is to enhance a new alternative coating material based on BAS in place of traditional coating materials used in industrial coating and surface treatment implementations. For this application, the BASs of $M_{60}Cr_{13}Mo_{10}B_8Y_2Mn_7$ were synthesized by alloying cast iron scraps (3.5-4.5 % C) with potential candidate alloying elements derived from our theoretical predictions in order to enhance the glass forming ability of Fe-based metallic glasses, by arc melting under controlled atmosphere. Suction casting technique has been employed for the direct production of 3 mm in diameter of $M_{60}Cr_{13}Mo_{10}B_8Y_2Mn_7$ BASs rod subsequently utilized as a filler material in Tungsten Inert Gas (TIG) welding process for hardfacing of a relatively cheap low/medium carbon steel base material.

Keywords: Bulk metallic glasses, Amorphous steel, Metallic glass coating, Hardfacing
© 2024 Published by ICMATSE

Introduction

The amorphous/glassy alloys possess excellent properties, such as high corrosion and wear resistance, due to the disordered atomic arrangement and the absence of crystal defects, such as grain boundaries and dislocations [1, 2]. Bulk metallic glasses (BMGs) with millimetre scales dimensions were enhanced in 1982 [3, 4]. However, among the BMG alloys, Fe-based BMGs have shown an attractive potential with their relatively low cost, good mechanical and physical properties including

soft magnetic, relatively strong and satisfied corrosion resistance characteristics [5-7]. However, usage of high purity constituent elements and advanced production methods, made commercial spread of BMGs difficult due to production cost. The material expenses in the BMGs fabrication could be reduced by using commercially available materials such as ferrous-alloys [8-10]. Recently, at METU-NOVALAB Bulk Amorphous Steels (BASs) were produced with economical way by alloying commercially available cast irons scrap (denoted as M, which consist of 92 % Fe, 2 % Si, 4.5 % C by

weight) with pure elements of Cr, Mo, B, Mn and Y [11]. The base of the BASs system contains 60 at. % cast iron scraps and pure elements such as Cr, Mo, B, Mn and Y which were selected according to theoretical and experimental studies in our NOVALAB and denoted as $M_{60}Cr_{13}Mo_{10}B_8Y_2Mn_7$ [12-14].

In the industrial applications, surface modification/treatment techniques give preference to reach the better service life for components which encounter the problem of wear. In practice, worn components either have to be rejected or rebuilt by employing various surface treatment applications which actually do not only improve the wear resistant of the surface, but also it helps preserve against corrosion and oxidation problems at higher temperature. Among industrial coating & surface treatment applications, hardfacing is a more conventional surface treatment technique, which is implemented by welding, to grade up the surface specialty of the base/substrate materials [15-17]. By using hardfacing application, the production of a new surface layer which is hard and implicitly good at wear resistant will be possible. The hardfacing application steps include homogeneous deposition of an alloy onto the surface of a soft material (usually low or medium carbon included steels) by welding and this implementation leads to increase in hardness, corrosion and wear resistance. In this respect, the purpose of this study is to investigate the usage possibilities of a new alternative coating material based on BAS of $M_{60}Cr_{13}Mo_{10}B_8Y_2Mn_7$, in order to replace traditional coating materials which would be utilized in industrial coating and surface treatment implementations by hardfacing.

Experimental

In the surface treatment study, an amorphous coating application is carried out with BAS of $M_{60}Cr_{13}Mo_{10}B_8Y_2Mn_7$ onto S275 carbon steel substrate (70x50x15 mm) via Tungsten Inert Gas (TIG) welding processing. TIG welding was favored because it can be used with different types of materials, like, steels, titanium and aluminum alloys etc. BAS of $M_{60}Cr_{13}Mo_{10}B_8Y_2Mn_7$ was used as a filler material in TIG welding process. To analyse the structure of BAS and hardfaced surface, samples were examined by Bruker S8 Tiger Diffractometer with $Cu-K\alpha$ radiation at the scanning rate of $1^\circ/\text{min}$ in the diffraction angle range of $2\theta=5-110^\circ$. Microstructural

characterizations of the samples were investigated with FESEM/FEI NOVA NANO430 scanning electron microscope (SEM) which was supported with energy dispersive spectroscopy (EDS). For microstructural examination, polished samples were etched with Marble solution, containing 10 gr $CuSO_4$, 50 ml HCl and 50 ml water in the solution. Vickers micro-hardness measurements of all produced samples was performed by an automated micro-hardness tester Shimadzu-2 Micro-hardness Tester by applying 1 kgf load. The reported averages of micro-hardness values were the sum up of minimum six measurements from the surface of the specimens.

Corrosion resistances of BASs samples were measured by applying extreme corrosive environment: 0.5M H_2SO_4 acidic solution with 1.12 pH solution, 1M NaOH basic solution with 14 pH solution and 0.6M NaCl salt solution with 7 pH solutions. Five different sample which were BAS, pig iron, carbon steel (S275), titanium (pure) and stainless steel (304) were subordinated to these solutions throughout 80 and 120 days. The calculation carried out according to measurement of the weight loss per area of samples. Before the experiment, the primary weight and primary surface areas of the samples were measured and weight and surface area changes were persuaded in interval of five days.

Table 1 Pin-on disk tribometer test parameters

Testing Parameters	Test Condition
Ball Material	High purity zirconia
Ball Radius	3 mm
Tested Material	BAS after Hardfacing application
Applied Load	7 N
Sliding Speed	5 cm/s
Application Rate	100 Hz
Sliding Distance	158 m
Testing Environment	Ambient atmosphere

To gain insight about wear/abrasion properties of hardfaced layer tribological test was carried out under computer controlled pin-on-disk tribometer (TRB, CSM+ Instruments, Switzerland). A normal load of 7 N with 100 Hz rate was applied at room temperature using parameters stated in Table 1 and during the

tribological tests ASTM G99-17 standard flowed as a reference document. During the experiments, to create the wear, a sample is fixed on a turning stage. The perpendicular force is applied on a zirconia ball, that is contacted with the sample surface. The pin-on-disk test is usually used during determination of the tribological properties of the materials with the friction coefficient (COF), μ , output. At the end of the experiment, volume loss of the sample enables wear rate calculation.

Results & Discussion

The examination of the amorphous phase was carried out with XRD and SEM analysis. The existence of amorphous phase in BAS samples was confirmed by the presence of halo in XRD patterns, Fig. 1, in which the peaks detected were completely vanished and characteristic amorphous humps were obtained in the XRD diffractogram. It is clearly seen that, hardfaced surface also have characteristic amorphous halo shaped XRD patterns. The intensity difference in the diffractograms would be associated with the form of the samples prepared for experiments, as cast BAS was measured in bulk form, whereas hardfaced was in powder form.

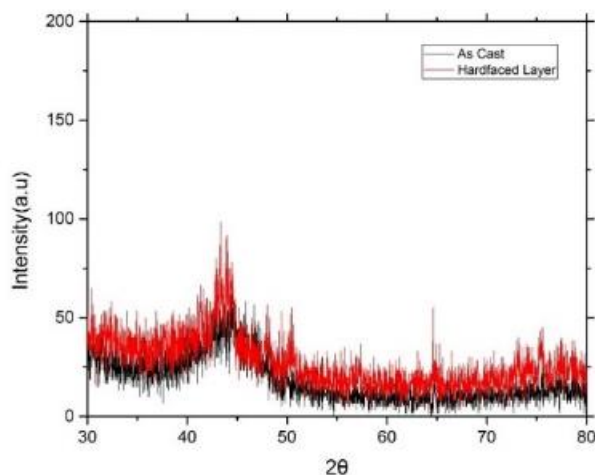


Fig. 1. XRD pattern of as cast $M_{60}Cr_{13}Mo_{10}B_8Y_2Mn_7$ (BAS) alloy and hardfaced coating surface

SEM results of the both as cast alloy and the surface treated (hardfaced) surfaces were given in Fig. 2.

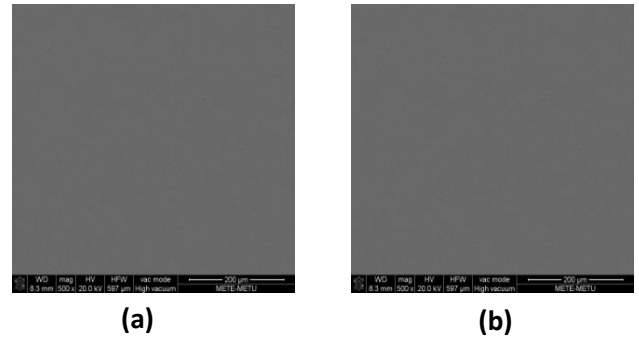


Fig. 2. SEM image of as cast of $M_{60}Cr_{13}Mo_{10}B_8Y_2Mn_7$ alloy (a) and carbon steel substrate with water quenched hardfaced coating surface (b)

It is evident from Figure 2, that none of the as-cast and hardfaced sample's matrix does show any contrast in SEM images and has the featureless structure, which is the natural result of the fully amorphous structures.

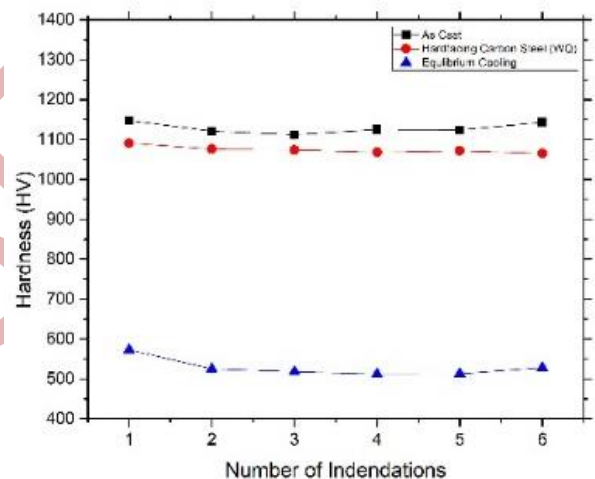


Fig. 3. Micro hardness result of the as cast BAS and hardfaced surface

To examine the mechanical properties of these samples, micro hardness measurements were performed and samples having glassy phase in their structure showed high hardness values around $\sim 1100 \pm 50$ HV, Fig. 3. As can be seen from the Fig. 3, the coated surface also has almost same hardness value with as cast sample, hence, carbon steel substrate (S275) and water quenching condition gives similar unique mechanical property with the as cast BAS sample.

While comprehending the corrosion resistance of surface coated sample with BAS, immersion corrosion tests were applied after hardfacing application. Results of corrosion experiments in terms of weight

loss/gain per area for all samples are given in Fig.-s 4-6.

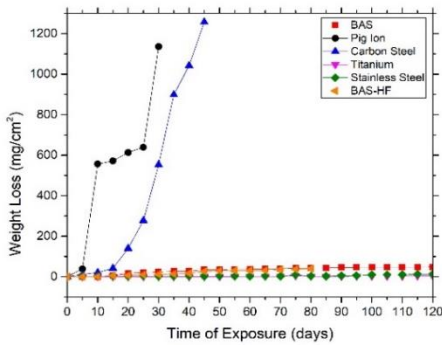


Fig. 4. Weight loss measurements of the samples in 0.5M H₂SO₄ solution

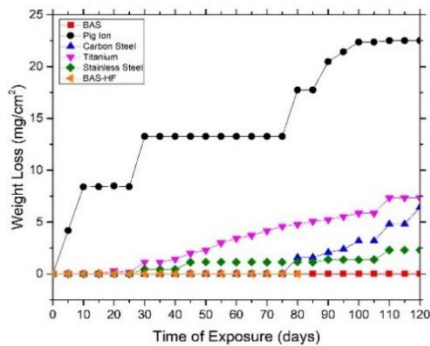


Fig. 5. Weight loss measurements of the samples in 1M NaOH solution

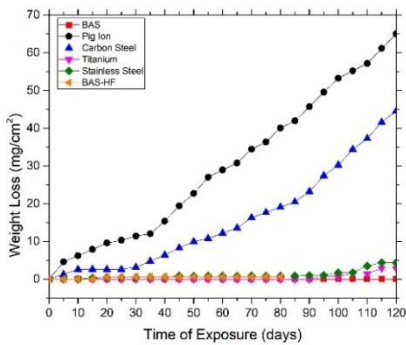


Fig. 6. Weight loss measurements of the samples in 0.6M NaCl solution

As can be seen from Fig.-s 4-6, that in between all the samples, BAS with hardfacing application shows similar behaviour with as cast BAS in the 0.5M H₂SO₄, 1M NaOH and 0.6M NaCl solutions. Moreover, corrosion resistance of hardfaced sample in H₂SO₄ solution even is a little better than in BAS sample. This result is a strong sign that after coating application, the surface of the substrate acts as cast BAS and hence, this study showed that BAS's does not lose their good corrosion behavior after hardfacing

application. The all corrosive environment outcomes are tabulated in Table 2.

Table 2 Corrosion study results for 80 days

Material	Corrosive Environment	Total Weight Loss (mg/cm ²)	Weight Loss Percentage
BAS (As Cast)	0.5M H ₂ SO ₄	43.295	9.34%
	1M NaOH	0	0%
	0.6M NaCl	0	0%
Hardfaced BAS	0.5M H ₂ SO ₄	39.569	5.12%
	1M NaOH	0	0%
	0.6M NaCl	0.599	0.12%
Pig Iron	0.5M H ₂ SO ₄	1135.458	100%
	1M NaOH	17.749	2.47%
	0.6M NaCl	40.062	2.38%
Carbon Steel (S275)	0.5M H ₂ SO ₄	1257.784	100%
	1M NaOH	1.579	0.13%
	0.6M NaCl	19.070	1.30%
Stainless Steel (304)	0.5M H ₂ SO ₄	2.453	0.34%
	1M NaOH	1.136	0.12%
	0.6M NaCl	0.870	0.08%
Titanium (Pure)	0.5M H ₂ SO ₄	1.509	0.22%
	1M NaOH	4.765	0.69%
	0.6M NaCl	0	0%

Tribology properties become the main topic of conversation when a problem is concerned with carrying some load across interfaces in relative motion [18]. While providing tribological testing of samples there are some critical preparation and testing requirements to be followed, which are: surface finish is critical-while determining the friction coefficient (COF), μ , the surface roughness has an important effect associated with machine marks,

inhomogeneous difficulties, etc.; properly clean and dry the specimens; horizontal test surface; selection of proper sliding velocity and normal force [19]. Generally, there are two kinds of friction coefficients which are static and dynamic (kinetic). The static friction coefficient can be achieved by dividing the maximum friction force to relative motion to the normal load. The dynamic (or kinetic) friction coefficient can be obtained by dividing the friction force during sliding to the applied normal load. The obtained results from pin-on-disc tribological analysis are given in the Fig. 7 and tabulated in Table 3 for different materials.

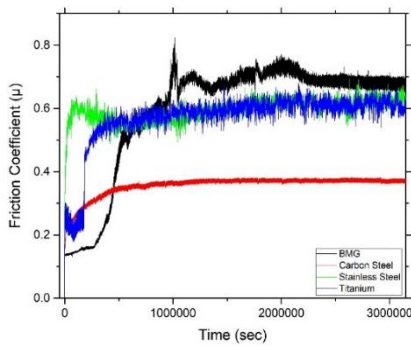


Fig. 7. Friction profile for hardfaced-BAS, carbon steel (S275), stainless steel (304) and titanium

Table 3 Static and dynamic COFs of Different Materials

Sample	Static COFs	Dynamic COFs	Weight Loss (mg)
BAS	0.81	0.65	1.7
Carbon Steel (S275)	0.37	0.37	1
Stainless Steel (304)	0.63	0.59	7
Titanium (Pure)	0.60	0.60	3

It is seen from Table 3 that hardfaced-BAS has higher friction coefficient (COF) and there are some critical reasons for that. One of them is related with the hardness of the contact surfaces: the friction, as widely accepted, depend on hardness and when the slider is harder than the plate, minimum friction occurs at the maximum hardness point. However, if

the slider is softer or has nearly equal hardness, there is some gather of slider (zirconia) on the plate. Hence, if the slider is softer or has equal hardness the friction is very unstable and there is no exact relationship between hardness and friction coefficient [20]. Moreover, Fe-based metallic glass coating with high hardness indents into the surface of ball and the hard particles dug into the ball surface and scratch out the material (zirconia) as illustrated in Fig. 8. As a result, way of contact changes from ball-to-disk to disk-to-disk, which leads to increasing the roughens and the friction coefficient of the surface [21].

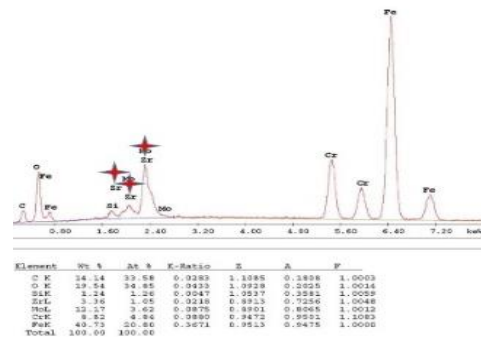
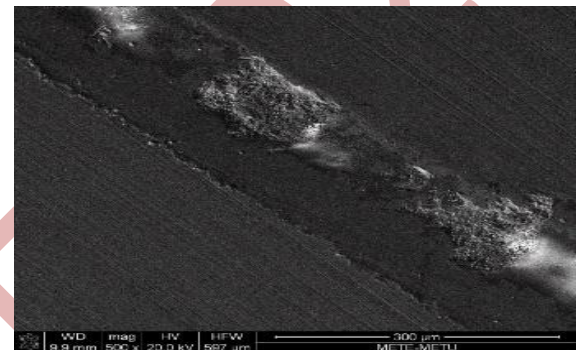


Fig. 8. SEM and EDS analysis of sample surface after wearing application

The second reason is related with microstructural mismatches, which are overlapping areas, that create taps between the pre-remelted layer and the new ones. Therefore, amorphous/crystalline ratio of the sample decreases throughout the wear test, and the higher friction results comes from the crystalline/crystalline interaction [22].

Conclusions

Suction casting technique has been employed for the direct production of 3 mm in diameter bulk amorphous steels (BASs) from cast iron scraps of $M_{60}Cr_{13}Mo_{10}B_8Y_2Mn_7$ by arc melting under controlled

atmosphere. After the BAS sample were successfully synthesized, it was utilized as a filler material in Tungsten Inert Gas (TIG) welding process for a surface treatment of S275 carbon steel substrate (70x50x15 mm). XRD and SEM analysis reveals that, BAS and hardfaced samples has fully amorphous structure. It was observed that owing to high bulk glass forming ability (BGFA), BAS coating material preserved its amorphous structure with extreme levels of high hardness values around $\sim 1100 \pm 50$ HV, which in fact is 3-4 times higher than the substrate metal.

BAS with hardfacing application shows similar behaviour with as cast BAS in the extreme corrosive solutions of 0.5M H_2SO_4 , 1M NaOH and 0.6M NaCl and corrosion resistance of hardfaced sample in

H_2SO_4 solution even is better than in BAS sample. This result is a strong sign that after coating application, the surface of the substrate acts as cast BAS and hence, this study showed that BAS's does not lose their good corrosion behavior after hardfacing application. It was find out that, hardfaced-BAS samples has higher friction coefficient (COF) in comparisons to carbon steel (S275), stainless steel (304) and titanium (pure) and possible reasons for that were explained in terms of magnitude of hardness value differences of contact surfaces and microstructural mismatches of overlapping areas, that create taps between the pre-remelted and new layers.

References

1. Y.Q. Cheng et al., Atomic-level structure and structure–property relationship in metallic glasses, *Prog. Mater. Sci.*, 56(4), (2011), pp. 379–473, 10.1016/j.pmatsci.2010.12.002
2. J.F. Löffler, Bulk metallic glasses, *Intermetallics*, 11, (2003), pp. 529-540, 10.1016/S0966-9795(03)00046-3
- [3] A.J. Drehman, A.L. Greer, D. Turnbull, Bulk formation of a metallic glass: $Pd_{40}Ni_{40}P_{20}$, *Appl. Phys. Lett.*, 41(8), (1982), pp. 716-717
- [4] H.W. Kui, A.L. Greer, D. Turnbull, Formation of bulk metallic glass by fluxing, *Appl. Phys. Lett.*, 45(6), (1984), pp. 615-616, 10.1063/1.95330
- [5] S.F. Guo et al., Fe-based bulk metallic glasses: Brittle or ductile? *Appl. Phys. Lett.*, 105(16), (2014), 161901, 10.1063/1.4899124
- [6] K. Amiya, A. Inoue, Fe-(Cr, Mo)-(C, B)-Ti Bulk Metallic Glasses with High Strength and High Glass-Forming Ability, *Mater. Trans.*, 47(6), (2006), pp. 1615-1618, 10.2320/matertrans.47.1615
- [7] X.J. Gu, S.J. Poon, G.J. Shiflet, Mechanical properties of iron-based bulk metallic glasses, *J. Mater. Res.*, 22(02), (2011), pp. 344- 351, 10.1557/jmr.2007.0036
- [8] H. Li, S. Yi, H.S. Sohn, Fe-based bulk metallic glasses $Fe_{73.8-x}C_{7.0}Si_{3.5}B_xP_{9.6}Cr_{2.1}Mo_{2.0}Al_{2.0}$ ($x=3\sim 9$) prepared using hot metal and industrial raw materials, *J. Mater. Res.*, 22, (2007), pp. 164-168, 10.1557/jmr.2007.0008
- [9] M. Iqbal, J. Akhter, H. Zhang, Z. Hu, Synthesis and characterization of bulk amorphous steels, *J. Non-Cryst. Sol.*, 354, (2008), pp. 3284-3290, 10.1016/j.jnoncrysol.2008.02.009
- [10] P. Tsai, A. Xiao, J. Li, J. Jang, J. Chu, J. Huang, Prominent Fe-based bulk amorphous steel alloy with large supercooled liquid region and superior corrosion resistance, *J. All. Comp.*, 586, (2013), pp. 94-98, 10.1016/j.jallcom.2013.09.186
- [11] B. Yagmurcu, M.V. Akdeniz, A.O. Mekhrabov, Synthesis of Bulk Amorphous Steels Having Extreme High Hardness, 17th International Metallurgy & Materials Congress – IMMC 2014, Congress Papers e-Book, 11-13 September, 2014, pp. 637-644, UCTEA Chamber of Metallurgical Engineers, Istanbul, Turkey
- [12] E. Erdiller, A.O. Mekhrabov, M.V. Akdeniz, Prediction of Bulk Glass Forming Ability of Fe-Mo-based Alloy Systems, 12th International Metallurgy & Materials Congress, UCTEA Chamber of Metallurgical Engineers, Proceedings e-book, September 28-October 02, 2005, pp. 1197-1204, Istanbul, Turkey
- [13] S. Suer, A.O. Mekhrabov, M.V. Akdeniz, Theoretical Prediction of Bulk Glass Forming Ability (BGFA) of Ti-Cu based Multicomponent Alloys, *J. of Non-Crystal. Sol.*, 355, (2009), pp. 373-378, 10.1016/j.jnoncrysol.2008.12.002
- [14] M. Aykol, M.V. Akdeniz, A.O. Mekhrabov, Solidification behavior, glass forming ability and thermal characteristics of soft magnetic Fe-Co-B-Si-Nb-Cu bulk amorphous alloys, *Intermetallics*, 19, (2011), pp. 1330-1337, 10.1016/j.intermet.2011.05.004
- [15] R.R. Garbade, N.B. Dhokey, Overview on Hardfacing Processes, Materials and Applications, *IOP Conf. Series: Mater. Sci. Eng.*, 1017, (2021), 012033, 10.1088/1757-899X/1017/1/012033
- [16] S.S. Joshi, Sh. Katakam, H.S. Arora, S. Mukherjee, N. B. Dahotre, Amorphous Coatings and Surfaces on Structural Materials, *Crit. Rev. Solid State Mater. Sci.*, 41, (2015), pp. 1–46, 10.1080/10408436.2015.1053602
- [17] S. Balaguru, M. Gupta, Hardfacing studies of Ni alloys: a critical review, *J. Mater. Res. Tech.*, 10, (2021), pp. 210 -1242, 10.1016/j.jmrt.2020.12.026
- [18] S. Atamert, Stability, Wear Resistance, and Microstructure of Iron, Cobalt and Nickel-Based Hardfacing Alloys, PhD Thesis, University of Cambridge, 1989, 10.17863/CAM.14238
- [19] D. Li, Static Coefficient of Friction Measurement using Tribometer, NANOVEA, Irvine CA, USA, 2014

- [20] P. Tian et al., Tribological behavior of Zr-based bulk metallic glass sliding against polymer, ceramic, and metal materials, *Intermetallics*, 61, (2015), pp. 1-8, 10.1016/j.intermet.2015.02.008
- [21] H. Wu et al., Fabrication, tribological and corrosion behaviors of detonation gun sprayed Fe-based metallic glass coating. *Trans. Nonfer. Metal. Soc. China*, 26(6), (2016), pp. 1629-1637, 10.1016/S1003-6326(16)64271-1
- [22] D.T.A. Matthews, V. Ocelik, J.T.M. de Hosson, Tribological and mechanical properties of high power laser surface-treated metallic glasses, *Mater. Sci. Eng.: A*, 471(1-2), (2007), pp. 155-164, 10.1016/j.msea.2007.02.119

ICMATSE 2024

A5356 Material Production and Characterization by Waam Technique

Berfin GURSU

Gazi University, Department of Metallurgical and Materials Science Engineering, 06560, Ankara, Turkiye
berfingrs20@gmail.com,
ORCID: 0009-0005-7894-8672

Murat KAYAALP

Gazi University, Division of Metallurgical and Materials Science Engineering, 06560, Ankara, Turkiye
kayaalpmurat@gmail.com,
ORCID: 0009-0001-3655-1619

Hakan ATES

Gazi University, Department of Metallurgical and Materials Science Engineering, 06560, Ankara, Turkiye
hates@gazi.edu.tr,
ORCID: 0000-0002-5132-4107

Cite this paper as Gursu B., Kayaalp M., Ates H. A5356 Material Production and Characterization by Waam Technique, Int. Conf. Advanced. Mater. Sci. & Eng. HiTech. and Device Appl. Oct. 24-26 2024, Ankara, Turkey

Abstract. Wire-arc additive manufacturing (WAAM) is a sub-branch of metal additive manufacturing that has been developed in recent years. It has proven to be a highly competitive production method for structural parts, especially due to its much lower consumption of consumables and high deposition rates compared to full discharge welding. In this study, a 1.2 mm welding wire was produced using the WAAM CMT-MIG (Cold Metal Transfer - Metal Inert Gas) method with three different wire feed rates (WFS) and three different heat input values at high layer thicknesses. Various tests, including tensile test, bending test, notch impact test, microhardness, XRD, microstructure analysis, and non-destructive testing methods such as visual inspection (VT), penetrant test (PT), and ultrasonic inspection (UT), were performed on samples obtained from the produced walls. The results were then analyzed, revealing that flexural strength and microhardness increased at low heat input.

Keywords: WAAM, MIG-CMT, heat input, A5356

© 2024 Published by ICMATSE

1. Introduction

Additive manufacturing (AM) technology, now known as rapid prototyping, emerged in the 1970s and has made it possible to produce custom, complex-shaped parts that are difficult to manufacture using traditional methods [1-3]. WAAM, a type of Direct Energy Deposition (DED) under AM, is a production method based on layered material deposition. This method is particularly effective in producing parts with complex geometries and reducing material waste [4-6]. The heat input in WAAM processes can influence the mechanical properties of the final product by affecting the material properties [6]. The goal is to better understand the potential of WAAM

technology in producing Al-5356 alloy, develop a fundamental understanding for optimizing process parameters, and enable more reliable and effective material production in industrial applications [1-11].

Controlled arc power source is necessary for successful production of aluminum alloy in the WAAM process, and heat input is an important factor. Research suggests that better mechanical properties are achieved for WAAM Al-Mg alloy compared to wrought alloy using low heat input by CMT process, leading to increased hardness and tensile strength due to reduced porosity and fines [11]. It's been found that welding parameters such as wire feed and welding speed greatly influence the

geometrical properties of components processed by WAAM [12]. Therefore, different heat inputs were obtained by changing the welding parameters, and the effects of these different heat inputs on the internal structure of the material were investigated [1-12].

Al-5356 is the aluminum alloy used in the welding applications in this study.

In this study, the mechanical properties of A5356 (ER5356) welding wire with a diameter of 1.2 mm, which is used as an additional wire, are provided in Table 1, and its chemical composition is listed in Table 2.

Table 1. Mechanical properties of Al-5356 Alloy [8]

AWS Code	Chemical Composition (%)							
	Si	Fe	Cu	Mn	Mg	Cr	Zn	Ti
ER5356	0.25	0.40	0.10	0.05-0.20	4.5-5.5	0.05-0.20	0.10	0.06-0.20

2. Materials and Methods

Table 2. Chemical composition of ER5356 wire [8]

Mechanical Properties	Tensile Strength (MPa)	Yield Strength (MPa)	Elongation (%)
Al-5356	~240	~195	~10 (with 50 mm elongation)

The arm of the device from MetalWorm shown in Fig. 1 is from ABB, the welding machine and the CMT unit are from Fronius. This robot has 6 axes, and the device has 2 axes. The wire feed rate (WFS) used for welding wire with a diameter of 1.2 mm was set at 4.5 m/min for the 1st wall, 6 m/min for the 2nd wall, and 8 m/min for the 3rd wall as indicated in Table 3, using the MIG-CMT method under 100% Ar gas.

Wall 1 has low heat input and wall 3 has high heat input. The first three layers of the 1st wall were set at 8 m/min, the next three layers at 6 m/min, and the first three layers of the 2nd wall were set at 8 m/min WFS to facilitate bonding between the substrate and the wall. Each wall was produced with a height of 200 mm, a length of 200 mm, and 100 layers, with a distance of 2.05 mm between the layers.



Figure 1. WAAM welding machine

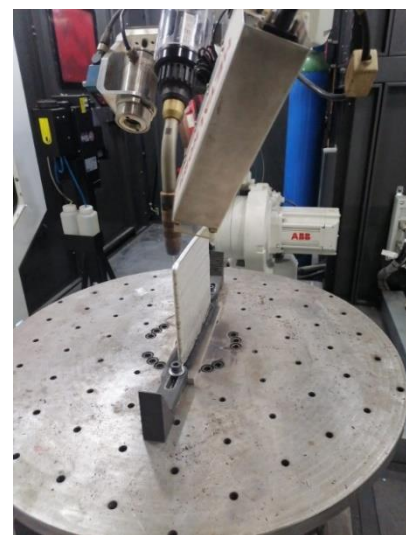


Figure 2. Production of A5356 first wall by WAAM welding machine

Table 3. Welding parameters for the manufacture of walls

Walls	WFS (m/min)	Voltage (V)	Current (A)	Heat Input (J/mm)
1 st Wall	4.5	11.8	61	97.17
2 nd Wall			6	12.8
3 rd Wall			8	13.8

The production process based on the welding parameters given in Table 3 is explained above. Three specimens were taken perpendicular to the production direction for the tensile test, three for the bending test, three for microhardness measurement, three for microstructure analysis, three for XRD analysis, and finally the three largest pieces of the walls were used for non-destructive testing. Visual test (VT), penetrant test (PT), and ultrasonic test (UT) methods were performed as part of the non-destructive testing process.

2.1. Tensile Test

Following the tensile test, the average tensile strength of the A5356 material produced by the WAAM method was measured as 214 MPa. Additionally, the test revealed that the tensile strength of the specimens varied based on the direction of the weld seam. The vertical specimens exhibited lower tensile strength compared to the horizontal ones. The results from Tab. 4 and 5 indicated that the average tensile strengths were 184.53 MPa (perpendicular to the production direction) and 270.97 MPa (parallel to the production direction). These findings demonstrate that the A5356 material produced by the WAAM method exhibits high strength under specific conditions. However, since the tensile strength varies depending on the direction of the weld seam, it is essential to evaluate the specimens accordingly.

Tablo 4. Tensile strength values in the direction of production

Walls	Average Tensile Strength (To the direction of production) (MPa)
1 st Wall	270.97037
2 nd Wall	263.00076
3 rd Wall	272.87086

Tablo 5. Perpendicular tensile strength values of the production direction

	Average Tensile Strength (Perpendicular to the direction of production) (MPa)
1 st Wall	184.53488
2 nd Wall	191.84362
3 rd Wall	219.19902

2.2. Flexure Test

Based on the results of the bending test, the distance between the supports was adjusted to 80 mm. The upper bearings were lowered at a speed of 3 mm/min with a 5-ton load, and the bending test was conducted. Figure 3 depicts the slope plot. The bending stress varies based on the condition of the specimen. The graph indicates that the bending resistance of wall 1 and wall 2 is high.

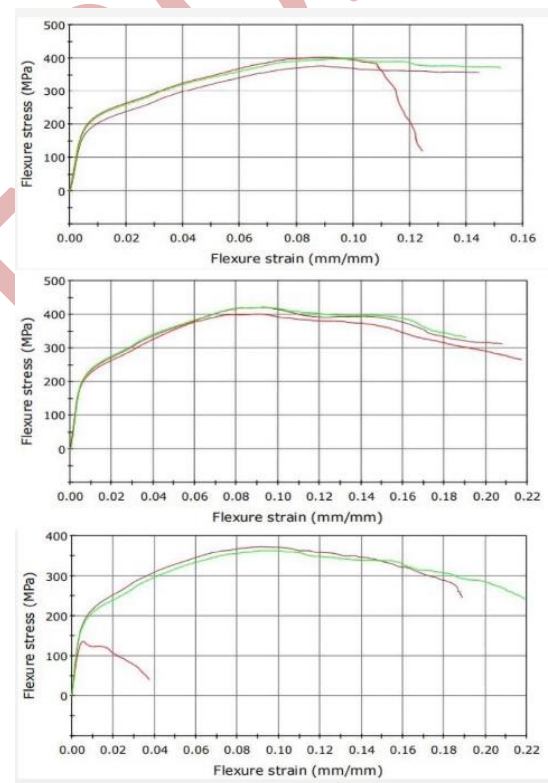


Figure 3. Graphs of the bending test of the 1st-2nd-3rd wall from top to bottom

2.3. Hardness Test

The microhardness test results were obtained by pressing the pre-sanded and polished surfaces of the bakelite samples according to HV 0.5 standards, using a pyramid tip weighing 500 grams for 10 seconds. Hardness values were obtained by taking 3 measurements from different parts of the sample. All values are shown in Table 6. The results indicate variations in hardness values across different regions of the samples, suggesting non-uniform

surface hardness. This could be attributed to differences in the material production process. Microhardness test results are vital for assessing the material's surface hardness and understanding its usage properties. Based on the results in the table, the microhardness of the 1st wall is higher.

Table 6. Microhardness measurement results.

Measurement	1 st Wall	2 nd Wall	3 rd Wall
1.	73 HV	70 HV	66 HV
2.	68 HV	72 HV	71 HV
3.	73 HV	71 HV	68 HV
Average	71.33 HV	71 HV	68.33 HV

2.4. XRD Analysis

The X-ray Diffraction (XRD) analysis involved sending X-rays to a pre-sanded and polished sample and measuring the peak angles of the reflected rays from the atoms. The angle range for the device's movement was set to 10-90, and X-rays were directed at the sample for 15 minutes. The analysis results indicated that three samples, produced with the same welding wire, had similar characteristics. Figure 4 shows the results of the common analysis, displaying the crystal lattice structure directions and intensity values. The material peaks occurred at the following angles: 38.3239 for the first peak, 44.6357 for the second peak, 64.7937 for the third peak, 77.7328 for the fourth peak, and 81.8551 for the final peaks.

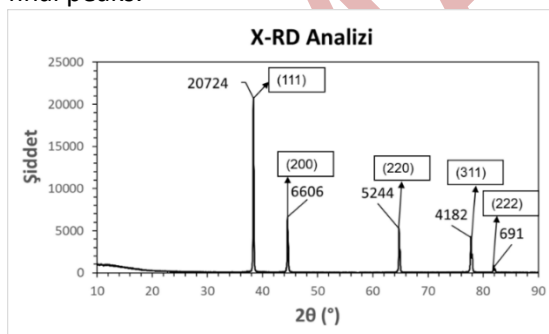


Figure 4. XRD analysis chart

2.5. Non-Destructive Testing

Visual, penetrant, and ultrasonic tests were performed according to standards to detect possible defects in walls produced with the A5356 additional wire MIG-CMT technique.

a. Visual Test (VT)

In the Fig. 5 visual test, we thoroughly examined the transitions between the layers and all surfaces. No cracks, notches, or discontinuities exceeding the acceptance criteria were found on the material surface.



Figure 4. Specimens with visual testing

b. Penetrant Test (PT)

The materials were non-magnetic, so liquid penetrant testing was conducted on the samples. Red dye was applied to both surfaces of the specimens, and then we waited for 10 minutes before cleaning the red dye. After that, developer was applied for 5 minutes. The test results showed that no defects exceeding the acceptance criteria were found on the tested sample surfaces or in the transitions between layers. [13]



Figure 5. Samples treated with red penetrant

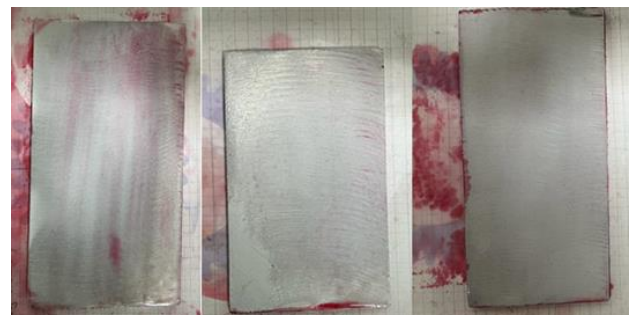


Figure 6. Developed and cleaned samples

c. Ultrasonic Test (UT)

Ultrasonic examinations of the samples in Fig. 7 did not reveal any volumetric defects exceeding the acceptance criteria, separation between layers, or discontinuity exceeding the acceptance criteria. [14]



Figure 7. Ultrasonically inspected specimens

2.6. Archimedes' Principle

Archimedes' principle explains that when an object is placed in a fluid, it is pushed upward by a force equal to the weight of the fluid that the object displaces.

Table 7. Density results from Archimedes' principle. (R.D: Rolling Direction, P.R: Perpendicular Rolling)

Specimen	Air (g)	Aqua (g)	Density (g/cm ³)
1 st Wall R.D.	6.26	2.39	2.6152
1 st Wall P.R.	7.15	2.74	2.6016
2 nd Wall R.D.	6.52	2.51	2.5993
2 nd Wall P.R.	6.07	2.33	2.5954
3 rd Wall R.D.	6.42	2.44	2.6268
3 rd Wall P.R.	6.57	2.50	2.6200

Köhler, Fiebig, Hensel, & Dilger (2019) studied the heat accumulation and the effect of different temperature-time conditions on the properties of components made through Wire Arc Additive Manufacturing (WAAM) using the 5356 aluminum alloy. The researchers found that heat accumulation varied with travel speed and cooling time. Reducing the heat input can enhance the microstructure and decrease the porosity of aluminum alloy components. To achieve this, higher travel speeds and longer cooling times should be included in the optimal setup to reduce pore diameter. Consequently, smaller heat input and lower heat accumulation result in smaller pore sizes. The pore diameter slightly decreases with an increase in travel speed and cooling time. Lower heat accumulation yields positive results in terms of porosity.

However, it was observed that the second wall perpendicular to the rolling direction has the optimal heat input and porosity. When the density

of all the walls is considered, specimens taken perpendicular to the rolling direction have lower densities compared to the ones taken in the rolling direction.

3. Conclusion

Based on the research results, the characteristics of the material designated as A5356, produced using the WAAM (Wire Arc Additive Manufacturing) method, were assessed using various tests and analyses. The findings revealed an increase in flexural strength and microhardness at low heat input. Furthermore, the mechanical properties, microstructure, and defects of the WAAM-produced A5356 material were examined through tensile testing, bending testing, notch impact testing, microhardness testing, XRD (X-ray diffraction), microstructure analysis, and non-destructive testing methods. The data obtained from these analyses demonstrated higher mechanical strength and microhardness values under specific conditions for the WAAM-produced A5356 material. These outcomes suggest that the WAAM method holds promise as a manufacturing method for the A5356 material.

1. When using low heat input in the welding process, the 1st wall, which has a low Wire Feed Speed (WFS) welding parameter, exhibits better bending resistance and microhardness compared to the 2nd and 3rd walls.
2. Tensile test results in the production direction and perpendicular to the production direction yielded values of 270.97037 and 184.53488 MPa, respectively (see Table 4 and 5). The results indicate that the tensile strength of samples taken from the production direction was higher.
3. The low heat input resulted in high flexural strength and microhardness, while low tensile strength was observed in longitudinal tensile testing. Comparable tensile values were obtained between the walls in transverse tensile testing.
4. Non-destructive testing results revealed no discontinuities exceeding the acceptance criteria on the material surface or in transitions

between layers during Visual Testing (VT) and Penetrant Testing (PT).

5. Ultrasonic Testing (UT) did not detect any volumetric errors, separation between layers, or discontinuities exceeding the acceptance criteria.

6. More comprehensive results should be obtained and discussed through mechanical tests, microstructure examinations, structural

characterizations, and non-destructive tests involving various heat inputs.

7. The goal is to achieve better results by utilizing optimized heat input.

8. The optimum porosity in density calculation by Archimedes' principle was found in the sample perpendicular to the rolling direction of the second wall, with a heat input of 125.95 J/mm.

Acknowledgment: The authors would like to thank the TUBITAK 2209-B project support code 1139B412302655.

References

1. Tekeli A. F., & Seçkin B. Tel Beslemeli Ark Eklemeli İmalat Yönteminde Soğuk Metal Transferi Teknolojisinin Kullanımı. *Mühendis ve Makine Dergisi*, 44 (2020), pp. 26-30. In Turkish
2. Ayan, Y. (2022), Farklı Malzeme Katmanlı Ürünlerin Tel Ark Eklemeli İmalatı [Ph.D. Thesis]. Karabük University Institute of Graduate Studies, Karabuk, pp. 1-25. In Turkish
3. Çakır E., & Ulutan M., Tel Ark Katmanlı İmalat (TAKİ) Yöntemi ve Farklı Malzemelerde Mekanik Özelliklerinin İncelenmesi. *Bilecik Seyh Edebali University Fen Bilimleri Dergisi*, 10 (2023), pp. 217-235. In Turkish
4. Özsoy K., Duman B., Eklemeli İmalat (3 Boyutlu Baskı) Teknolojilerinin Eğitimde Kullanılabilirliği. *International Journal of 3D Printing Technologies and Digital Industry*, 1 (2017), pp. 36-48. In Turkish
5. Karayel E., Bozkurt Y., Özdemir C., Kalender M. (2022), Investigation of Mechanical Properties of Aluminum Alloys Produced by Wire Arc Additive Manufacturing Method. Master's Thesis, Marmara University Institute of Natural and Applied Sciences, Istanbul, pp. 3-67.
6. Mercan E., Ayan Y., Kahraman N., Gazaltı metal ark kaynak (GMAK) yöntemiyle birleştirilen AA5754 ve AA6013 alüminyum alaşımlarının mikro yapı ve mekanik özellikleri. *Pamukkale University Mühendislik Bilimleri Dergisi*, 26 (2020), pp. 82-87. In Turkish
7. Ayan D., Nizamettin K., Metal Eklemeli İmalat: Tel Ark Yöntemi ve Uygulamaları, *International Journal Of 3d Printing Technologies And Digital Industry*, 2 (2018), pp. 74-84. In Turkish
8. Özsolak O., Eklemeli İmalat Yöntemleri ve Kullanılan Malzemeler. *International Journal of Innovative Engineering Applications* 3, 1 (2019), pp. 9-14. In Turkish
9. Evrensel R., Ertek C., Eklemeli İmalatta Alüminyum ve Alüminyum Alaşımlarının Uygulamaları ve Topoloji Optimizasyonu. *Journal of the Institute of Science and Technology*, 13 (2023), pp. 2008-2025. In Turkish
10. Gierth M., Henckell P., Ali Y., Scholl J., Bergmann J. P., Wire Arc Additive Manufacturing (WAAM) of Aluminum Alloy AlMg5Mn with Energy-Reduced Gas Metal Arc Welding (GMAW). *Materials*, 13 (2020), pp. 2671-2693.
11. Nagasai B. P., Malarvizhi S., Balasubramanian V., Wire Arc Additive Manufacturing of 5356 Aluminum Alloy Cylindrical Component: Mechanical Properties and Microstructural Characteristics, *Kaynak Fab Tech Times, Wire Arc Additive Manufacturing of 5356 Aluminum Alloy Cylindrical Component: Mechanical Properties and Microstructural Characteristics | Weld Fab Tech Times* (2023).
12. Köhler M., Hensel J., Dilger K., Effects of Thermal Cycling on Wire and Arc Additive Manufacturing of Al-5356 Components. *Metals*, 10 (2020), pp. 952-963.
13. EN ISO 23277 Non-destructive testing of welds - Penetrant testing of welds - Acceptance Levels
14. EN ISO 11666-1 Non-destructive testing of welds - Ultrasonic testing - Acceptance levels

Thermo-Calc Investigation of the Ga-As Binary System

Shadia J. Ikhmayies

The University of Jordan - Department of Physics, 11942, Amman, Jordan,
shadia_ikhmayies@yahoo.com,
s.ikhmayies@ju.edu.jo
ORCID: 0000-0002-2684-3300

Cite this paper as: Ikhmayies, S. J. Thermo-Calc Investigation of the Ga-As Binary System. *Int. Conf. Advanced Mater. Sci. & Eng. HiTech. and Device Appl.* Oct. 24-26 2024, Ankara, Turkiye

Abstract. To produce a material with the required stoichiometry for a certain application, the Phase diagram diagram is the main base for such goal. Moreover, for the use of a material in extreme conditions such as high temperature and pressure, one has to be familiar with the thermodynamic properties of the material. GaAs is the most important material in the Ga-As system, and it has high technological importance in optoelectronics, spintronics, photovoltaics and others. Each of these applications requires certain properties. Hence the importance of deducing its phase diagram and thermodynamic properties depending on the most recent databases. In this work Thermo-Calc software was used to deduce the phase diagram, and some thermodynamic properties such as Gibbs energy (G), entalpy (H), and entropy (S). at different compositions and temperatures. The results are discussed in the light of experimental findings found in the literature.

Keywords: Thermo-Calc software, Ga-As binary system, Phase diagram, thermodynamic properties, Solar cells.
© 2024 Published by ICMATSE

1. Introduction

The III-V binary alloys are of extensive technological importance, and the Ga-As system gains its importance from gallium arsenide (GaAs), a prototypical III-V compound semiconductor [1]. GaAs has a zincblende structure as shown in Fig.1 [2], and a direct band gap of about 1.42 eV, which allows it to operate at high voltages, high frequencies, and elevated temperatures [1]. It has a high technological importance, where it was described as the "semiconductor of the future, and always will be." [3].

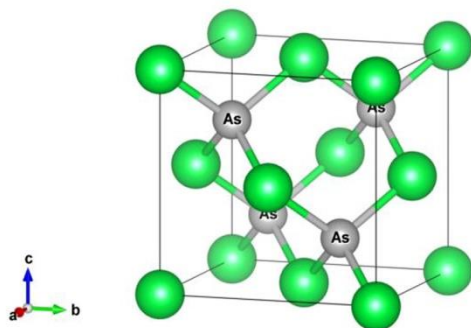


Figure 1. Zinc blende crystal structure of GaAs. Reprinted from Azza et al. [2], under the terms and conditions of the Creative Commons Attribution (CC BY) license (<https://creativecommons.org/licenses/by/4.0/>).

GaAs has a wide usage area including photovoltaics, semiconductor lasers, light-emitting diodes, optoelectronic industry, optical windows, compact-disc (CD) technology, fibreoptic communications, mobile phone, as well as spintronic and photonic devices [3]. Knowledge of the phase diagram, and the thermodynamic properties of this system is required for the fabrication of a high quality material with properties suitable for these applications. In this work Thermo-Calc software was used to deduce the phase diagram, and some thermodynamic properties such as Gibbs energy (G), entalpy (H), and entropy (S) at different temperatures and compositions.

2. Methodology

The phase diagram and thermodynamic properties presented in this work are all obtained using the Thermo-Calc software 2024b. This software utilizes Gibbs free energy (G) minimization procedure to calculate phase equilibrium and thermodynamic properties of a chosen system, where it uses Calphad (CALculation of PHase Diagrams) method, which is based on the fact that; a phase diagram is a representation of the thermodynamic properties of a system. The Calphad method derives the thermodynamic functions of a system from all available experimental data, and the thermodynamic functions are represented as polynomials of chemical composition and temperature. The values of the

polynomial coefficients are obtained using numerical optimization techniques [4]. The software has two main components: the application, and the internally-consistent thermodynamic dataset it uses.

To deduce the phase diagram of GaAs the database used is "G35 Binary Semiconductor TDB v1.2". The total pressure is 1 bar, temperature ranges were automatically selected, and just stable phases were credited. The same settings were used to deduce the Gibbs energy versus temperature curves. Moreover, the Gibbs energy, enthalpy, and entropy were investigated as functions of composition at selected temperatures, where all curves were deduced relative to the standard element reference (SER). The results are discussed in the light of experimental findings found in the literature.

3. Results and Discussion

Fig.2 shows the phase diagram of Ga-As binary system obtained in this work as a function of temperature, where Fig.2a is the phase diagram calculated with considering the gaseous phase, and Fig.2b is calculated without the presence of the gaseous phase, and it is similar to the one found in the literature. In both figures the vertical line at As mole fraction 0.5 represents GaAs compound semiconductor. All other phases are displayed in both Fig.1a and Fig.1b. From Fig.2a the melting points (T_m) of Ga, and GaAs are obtained as $T_m(\text{Ga}) = 302.915 \text{ K}$ ($29.765 \text{ }^\circ\text{C}$), and $T_m(\text{GaAs}) = 1509.35 \text{ K}$ ($1236.2 \text{ }^\circ\text{C}$) respectively. But As doesn't melt but sublimates, and its sublimation temperature from Fig.2a is $T_s = 887.786 \text{ K}$ ($614.636 \text{ }^\circ\text{C}$). The experimental values are, $T_m(\text{Ga}) = 303 \text{ K}$ ($29.85 \text{ }^\circ\text{C}$), and $T_m(\text{GaAs}) = 1511 \text{ K}$ ($1237.85 \text{ }^\circ\text{C}$) [5]. For As the given experimental value is $T_m(\text{As}) = 1090 \text{ K}$ ($816.85 \text{ }^\circ\text{C}$) [5], which is in good agreement with the value obtained from Fig.2b $T_m(\text{As}) = 1091.53 \text{ K}$ ($818.38 \text{ }^\circ\text{C}$). It is evident from the phase diagram (Fig.2a) that GaAs is a dissociable compound at the melting point. In fact at that point As element sublimates or evaporates with a vapor pressure of about 1 atm. Hence, this is the major problem to be overcome in the GaAs growth [6].

The phase diagram includes an eutectic point at $T = 1066.63 \text{ K}$ ($793.48 \text{ }^\circ\text{C}$) and As mole fraction 0.953. This value is the same as that deduced by Elayech et al. [7]. The experimental value of temperature at eutectic point is $T = 1083 \text{ K}$ ($809.85 \text{ }^\circ\text{C}$) that is lower than the value obtained in this work, but the experimental value of AS mole fraction is $x = 0.95$, which is close to the value obtained in this work [5]. From the phase

diagram it is noticed that the mutual solubility of Ga in As or vice versa is negligible.

Fig.3a displays the Gibbs energy (G) against temperature for zinc blende GaAs, which deduced in this work. As expected, the Gibbs energy decreases with increasing temperature. Fig. 3b shows the same plot for the system (including all phases), where it is noticed that the behaviour of G with temperature is the same (decreasing with temperature for all other phases).

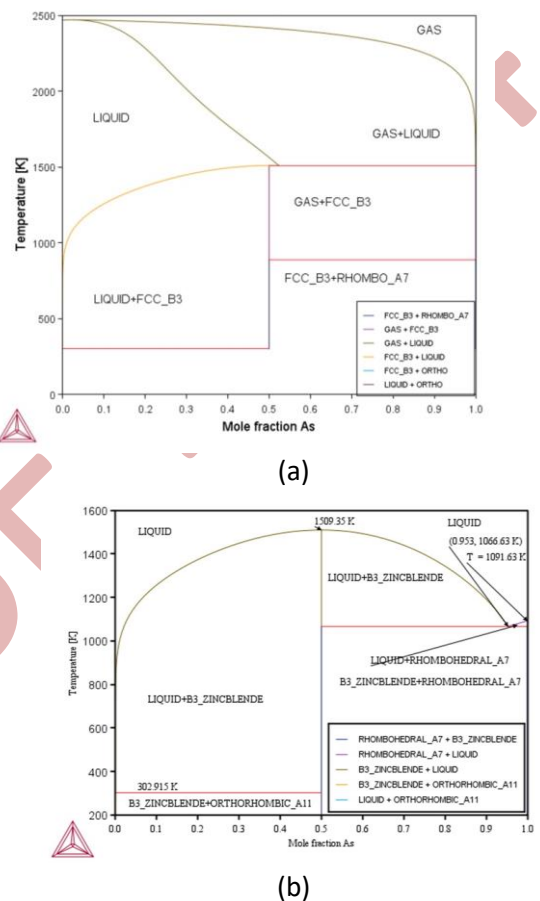
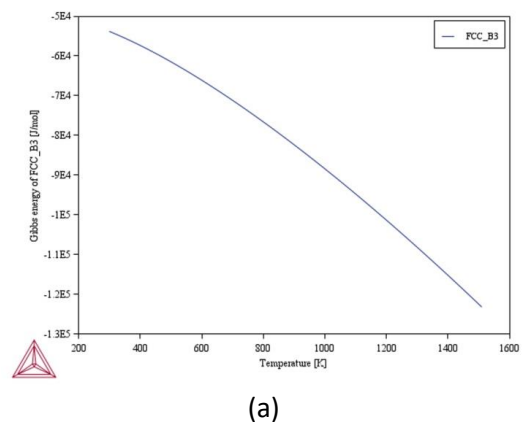
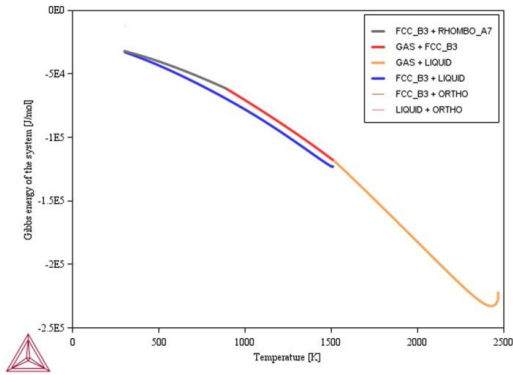


Figure 2. Phase diagram of Ga-As binary system deduced by Thermo-Calc software. a) Gas phase is considered. b) Gas phase is not considered.

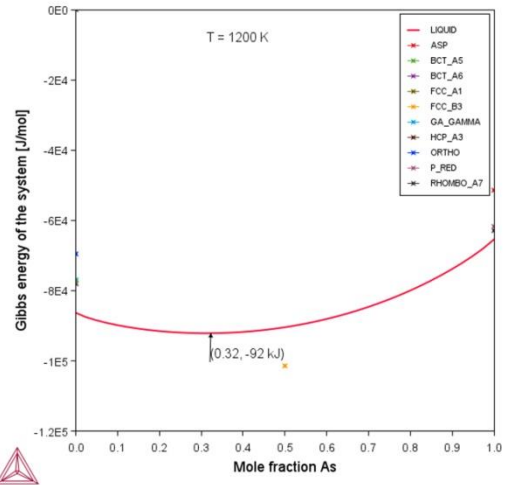




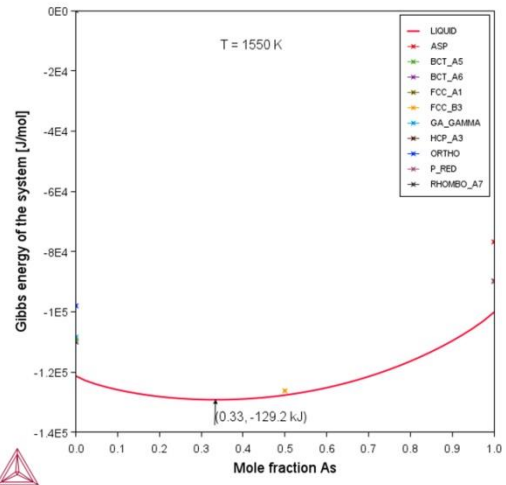
(b)

Figure 3. Gibbs energy vs. temperature of a) FCC-B3 GaAs phase, and b) the system with all phases

Fig.4 shows the The Gibbs energy (G) of the system as a function of composition at constant temperature, where three temperatures were chosen; 400, 1200, and 1550 K, that is after melting of Ga, after melting of As, and after melting of GaAs. The Gibbs energy shows a minimum, at which the system is at equilibrium. The position of this minimum as shown in the three figures is 0.22, 0.32, and 0.33 As mole fraction for the 400, 1200, and 1550 K respectively. The position of the minimum shifts towards higher concentration with increasing temperature. So, the stoichiometric GaAs (at 0.5 As mole percent) is not at equilibrium at these temperature, but it is the Ga-rich GaAs. This is due to the evaporation of As after melting of GaAs. It is also obvious in the parts of Fig.4 that G decreases with temperature.

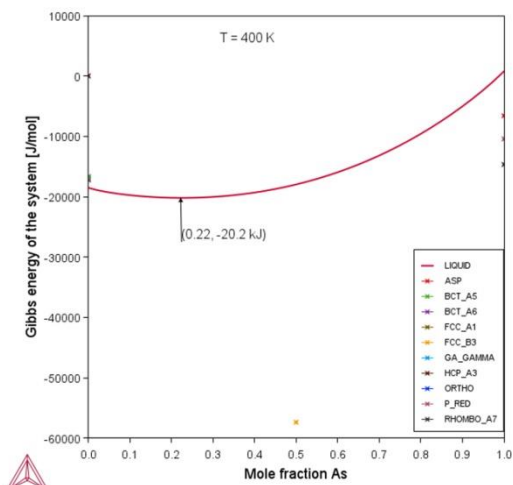


(b)



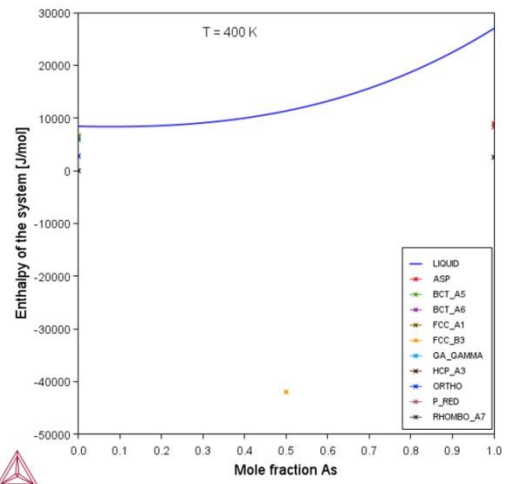
(c)

Figure 4. Gibbs energy of the system vs. composition (As mole fraction) for a) T = 400 K. b) T = 1200 K. c) T = 1550 K.



(a)

Fig.5 displays the enthalpy of the at the same aforementioned temperatures. It is noticed that the position of the minimum shifts towards lower composition (As mole percent) with increasing temperature. Also it is noticed that the enthalpy increases with increasing temperature.



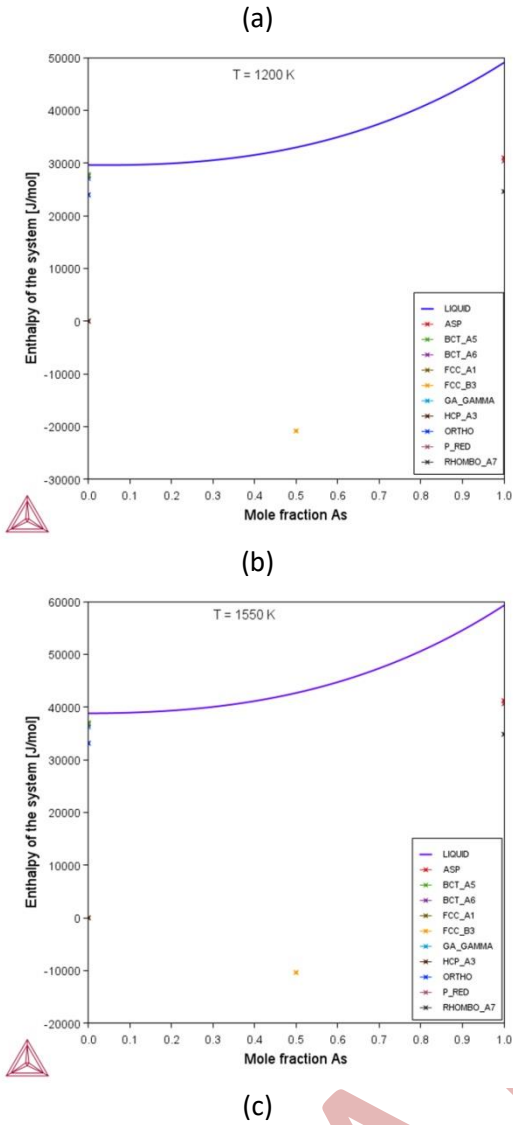


Figure 5. Enthalpy of the system against composition (As mole fraction) at a) T = 400 K (at 0.07). b) T = 1200 K (at 0.047). c) T = 1550 K (at 0.0).

Fig.6 displays the entropy of the system at the same aforementioned temperatures. The figure shows that the entropy increases with increasing temperature, and the position of the maximum shifts towards higher composition. This means that the dissociation of GaAs increases with increasing As concentration, and it is maximum when GaAs is close to stoichiometry due to evaporation of As. The dissociation is stronger after melting of stoichiometric GaAs as the case of Fig.6c.

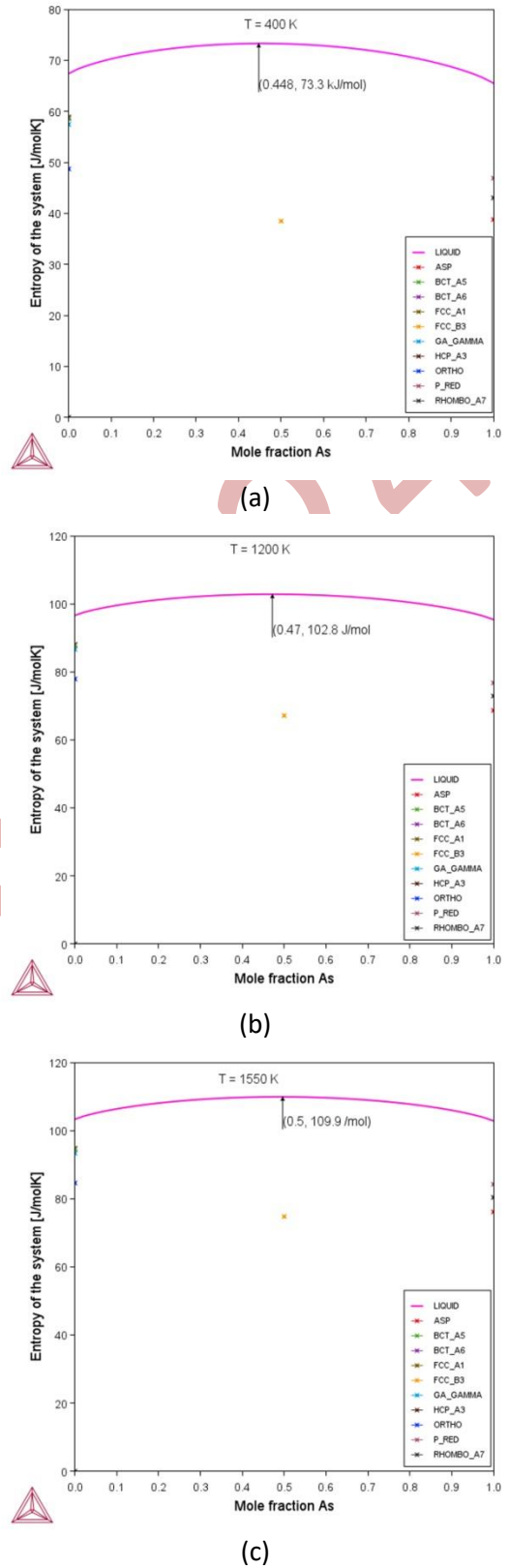


Figure 6. Entropy of the system against composition (As mole fraction) for different temperatures. a) T = 400 K. b) T = 1200 K. c) T = 1550 K.

4. Conclusion

In this work -the phase diagram and thermodynamic properties of GaAs compound semiconductor were investigated using thermo-Calc software 2034b. The

phase diagram was obtained with and without the gaseous phase, and melting temperatures of Ga, GaAs, and Ga were determined in addition to the sublimation temperature of As. Besides, the eutectic point in the As side of the phase diagram was determined. All these results were compared with

the experimental results. The Gibbs energy was investigated as a function of temperature and composition. Furthermore, the enthalpy and entropy were investigated as functions of composition at different temperatures, and the results are discussed.

References

1. G. Imbalzano, M. Ceriotti, Modeling the Ga/As binary system across temperatures and compositions from first principles, *Physical Review Materials* 5, (2021), Article No. 063804
2. M. Azza, E. Chahid, A. Hmairrou, R. Abdia, M. Tridane, A. Malaoui, S. Belaouad, Numerical Simulation of p-i-n GaAs Photovoltaic Cell Using SCAPS-1D, *Biointerface Research in Applied Chemistry* 13(4) (2023), Article No. 253. <https://doi.org/10.33263/BRIAC133.253>
3. M. Brozel, Gallium Arsenide. In: Kasap, S., Capper, P. (eds), *Springer Handbook of Electronic and Photonic Materials*. Springer Handbooks. (Springer, Boston, MA, 2006), pp. 499-536. https://doi.org/10.1007/978-0-387-29185-7_23
4. B. A. Boutwell, R. G. Thompson, N. Saunders, S. K. Mannan, J. J. deBarbadillo, Phase formation modeling of an alloy casting using computational thermodynamics. Paper is presented at the 4th International Symposium on Superalloys and Derivatives", June 15-18, 1997. Pittsburgh, Pennsylvania.
5. G. Imbalzano, M. Ceriotti, Modeling the Ga/As binary system across temperatures and compositions from first principles, *Physical Review Materials* 5, 063804 (2021). DOI: 10.1103/PhysRevMaterials.5.063804
6. R. Fornari, *Solar Energy Materials* 11 (1985) 361-379.
7. N. Elayech, H. Fitouri, Y. Essouda, A. Rebey, and B. El Jani, Thermodynamic study of the ternary system gallium-arsenic-bismuth, *P hys. Status Solidi C*, 1–4 (2014) / DOI 10.1002/pssc.201400147

Phase Diagram and Thermodynamic Properties of the Fe-Cu Binary System

Shadia J. Ikhmayies

*The University of Jordan - Department of Physics, 11942, Amman, Jordan,
shadia_ikhmayies@yahoo.com, s.ikhmayies@ju.edu.jo
ORCID: 0000-0002-2684-3300*

Cite this paper as: Ikhmayies, S.J. Phase Diagram and Thermodynamic Properties of the Fe-Cu Binary System.Int. Conf. Advanced. Mater. Sci.& Eng. HiTech.and Device Appl.Oct. 24-26 2024, Ankara, Turkiye

Abstract. The iron-copper (Fe-Cu) binary system has high strength and attractive electrical and thermal properties which make it important for many applications. But this system is a metastable alloy system, which makes difficulties in its synthesis. So, it is necessary to understand its phase diagram and to investigate its thermodynamic properties. In this work the phase diagram of this system was retrieved using thermo-Calc software 2024b, where it includes three fields of solid solutions, (one in the Cu rich side and two in the Fe-rich side), four fields of mixed solid phases, three fields of mixed (liquid +solid) phases, and a field of liquid phase that extends on the whole composition range at high temperatures. The melting points, invariant reactions, and solubilities were determined and discussed. There are three invariant reactions two of them are peritectic reactions. while the other is eutectoid. The maximum solubility of Fe- γ in Cu- ϵ is found to be 4.68 at.% at $T = 1371.17$ K, maximum solubility of Cu- ϵ in Fe- α is 1.6 at.% at $T = 1115.92$ K, and in Fe- γ is 10.4 at.% at $T = 1706.21$ K. The Gibbs energy was plotted against composition for different temperatures and revealed a wide miscibility gap. The width of this gap decreases with temperature and it becomes zero at a critical temperature.

Keywords: Phase diagram, Thermodynamic properties, Fe-Cu alloys, Miscibility gap.

© 2024 Published by ICMATSE

1. Introduction

The thermodynamics of liquid and solid iron-copper (Fe-Cu) alloy has received continuous attention from different groups of researchers over the past few decades. Cu-Fe alloy has high strength, good plasticity, giant magnetoresistance (GMR), and excellent electrical and thermal conductivity [1]. Therefore, this alloy is widely applied in the fields of automobile, communication, aviation, and electronic manufacturing [2]. In addition, Fe has the advantages of low price and abundant resources including recycling of Cu-containing ferrous scrap, where the removal of copper from the steel scrap in the recycling process is necessary, because it has serious negative effects such as thermal shrinkage (surface cracking) during rolling at high temperatures [3]. Therefore, understanding the phase diagram and thermodynamic properties of Fe-Cu binary system is essential for all these applications and issues. It should be noted that iron and copper have different structure, where iron is BCC at temperatures lower than 1200 K, and copper is FCC as seen in the phase diagram shown in Fig.1. But both iron and copper can exist as an FCC phase as seen in Fig.1 too. Although their structure is the same, Fe and Cu are only partially miscible in each other [4], and the existence of a wide liquid

metastable miscibility gap has been proved [5] experimentally and by computation.

The objective of this work is to retrieve the phase diagram of Fe-Cu binary system, determine the invariant reactions and solubilities of Cu in Fe and of Fe in Cu, as well as to investigate some thermodynamic properties such as Gibb's energy, then comparing the results with previous works.

2. Methodology

The phase diagram and Gibbs energy curves presented in this work are obtained using the Thermo-Calc software 2024b. To calculate the phase diagram and thermodynamic properties of a chosen system, this software utilizes the minimization procedure of Gibbs free energy, where it uses Calphad (CALculation of PHase Diagrams) method. This method is based on the fact that; a phase diagram is a representation of the thermodynamic properties of a system, and it derives the thermodynamic functions of a system from all available experimental data. The thermodynamic functions are represented as polynomials of chemical composition and temperature. The values of the polynomial coefficients are obtained by utilizing a

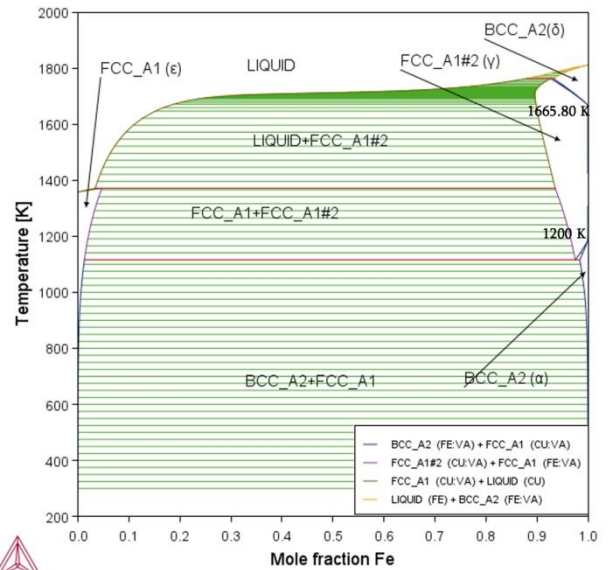
numerical optimization techniques [6]. The software possesses two main components: The application, and the internally-consistent thermodynamic dataset it uses.

To deduce the phase diagram of Fe-Cu system the database used is "TCBIN: TC Binary Solutions v1.1". The total pressure is 1 bar, temperature ranges were automatically selected. The same settings were used to deduce the Gibbs energy curves, where all curves were deduced relative to the standard element reference (SER).

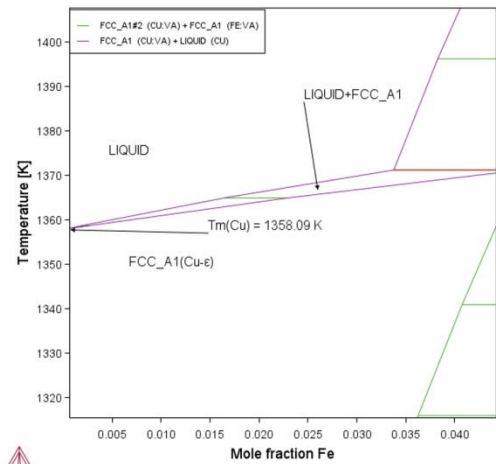
3. Results and Discussion

Fig. 1a shows the phase diagram of Fe-Cu binary system deduced using Thermo-Calc software 2024b, where all phases are displayed on the figure. The figure shows three fields of solid solution all in white color (one is on the copper-rich side and two on the iron-rich side), four mixed solid phase fields all in green color (BCC-A2(Fe- α)+FCC-A1(Cu- ϵ), FCC-A1(Cu- ϵ)+FCC-A1#2(Fe- γ), BCC-A2(Fe- α)+FCC-A1#2(Fe- γ), FCC-A1#2(Fe- γ + BCC-A2(Fe- δ), and three mixed (liquid + solid) fields (LIQUID+ FCC-A1#2(Fe- γ)), (LIQUID+ BCC-A2(Fe- δ), LIQUID+ FCC-A1(Cu- ϵ)), and a liquid phase field that spans the entire compositional range at high temperatures.

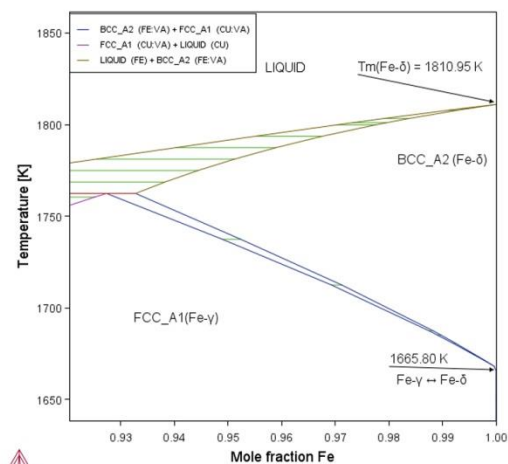
Also from Fig.1a it can be found that the phase transformation Fe- α \leftrightarrow Fe- γ takes place at $T = 1200$ K, and phase transformation Fe- γ \leftrightarrow Fe- δ takes place at $T = 1665.80$ K. In addition, the melting point of Cu is found from Fig.1b (which is a magnified portion of the left side of Fig.1a) as $T_m(\text{Cu}) = 1358.09$ K, while the melting point of Fe- δ is found from Fig.1c (which is a magnified portion of the right side of Fig.1a) as $T_m(\text{Fe-}\delta) = 1810.95$ K.



(a)

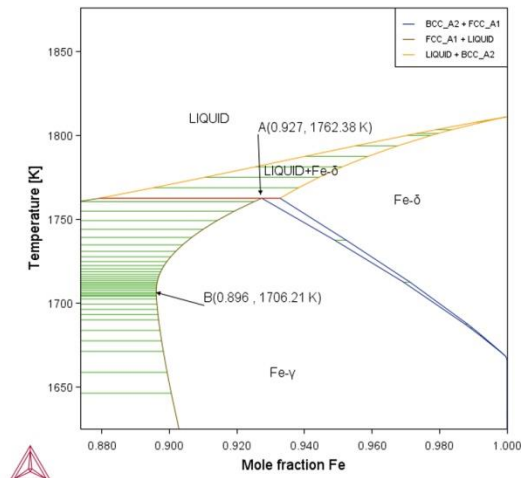


(b)

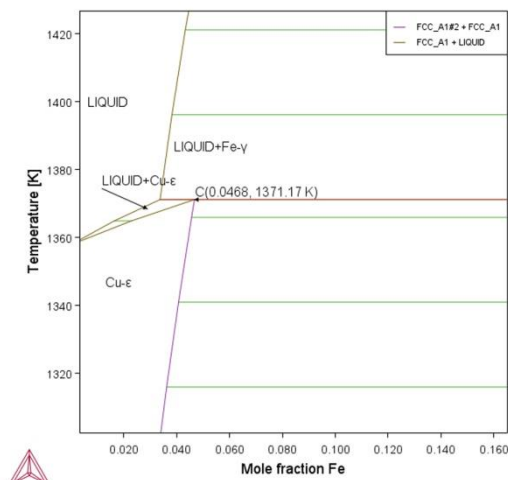


(c)

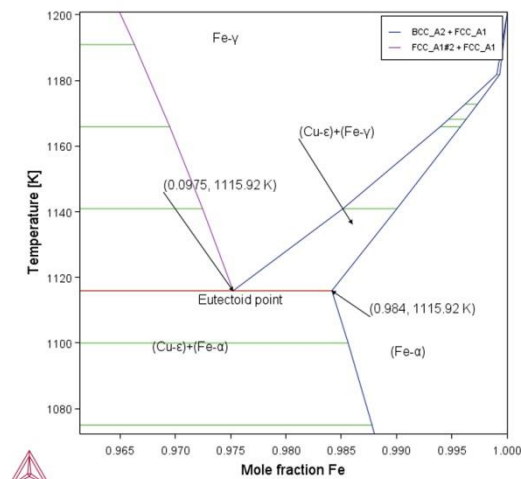
Figure 1. a) Phase diagram of the Fe-Cu binary system obtained in this work. b) The upper part of the Cu-rich side magnified. c) The upper part of the Fe-rich side magnified.



(a)



(b)



(c)

Figure 2. Magnified parts of the Phase diagram in Fig.1 a) The upper part of the Fe-rich side. b) The upper part of the Cu-rich side. c) The lower part of the Fe-rich side.

Fig.2 shows the invariant reactions in this system, which are three reactions of which are two peritectic. The first one is:



that takes place at point A in Fig.2a (at 0.927 mole fraction Fe and $T = 1762.38\text{K}$). This result is consistent with the experimental and computed results listed in table 2 of ref. [1] which are all restricted in the range 1752-1764 K. The second peritectic reaction is:



as shown in Fig.2b at point C in the figure corresponding to 0.0468 mole fraction Fe and $T = 1371.17\text{K}$, which is consistent with the experimental and computed results listed in table 2 of ref. [1] that are all restricted in the range 1363-1371 K. The third invariant reaction is eutectoid given as



which takes place at $T = 1115.92\text{K}$ as shown in Fig. 2c. This value is also in good agreement with experimental and computed values listed in Table 2 of ref. [1] that are restricted in the range 1115-1139 K.

The maximum solubility of liquid Cu in Fe- γ can be determined from Fig.2b at point B as 0.104 mole fraction Fe (or 10.4 at.%) at $T = 1706.21\text{K}$. From Fig.2c the maximum solubility of Cu- ϵ in Fe- α is found to be 0.016 mole fraction Fe (or 1.6 at.%) at $T = 1115.92\text{K}$. Then the maximum solubility of Fe- γ in the Cu- ϵ phase can be determined from Fig.2b at point C as 0.0468 mole fraction Fe (4.68 at.%) at $T = 1371.17\text{K}$.

Fig.3 shows the plot of Gibbs energy of the system against temperature. It is noticed that Gibbs energy decreases with temperature as usual for all phases.

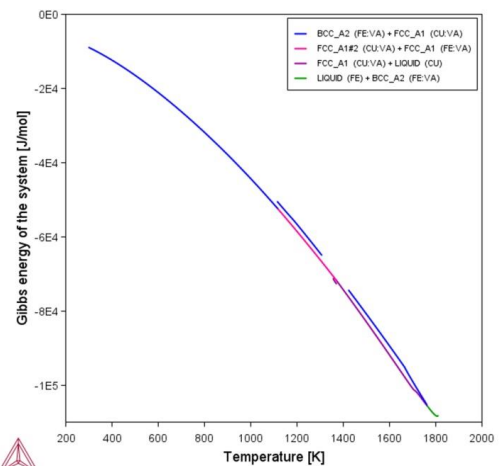
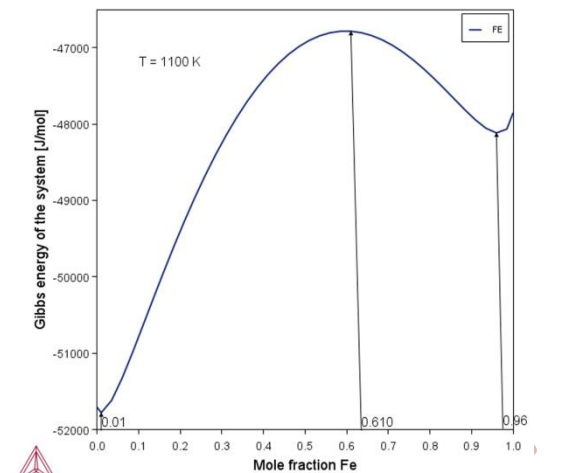


Figure 3. Gibbs energy of the system against temperature.

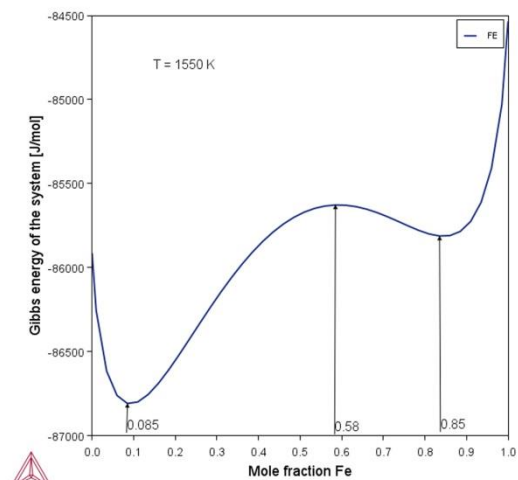
As mentioned in the introduction section, there is a large miscibility gap between iron and copper [7], which results in suffering through the synthesis of the alloy. Fig.4 presents the plot of Gibbs energy of the system against composition (Fe mole fraction) at temperatures 1100, 1550, 1820 K. The curves show the miscibility gap through the presence of two minima of the curves which concave down. In Fig.4a the minima are at 0.01 and 0.95 mole fraction Fe, while the maximum of the curve is centered at 0.61, and in Fig.4b the two minima are found at 0.085 and 0.85 mole fraction Fe, but the maximum of the curve is centered at 0.58. The two phases (copper and iron) become miscible at the critical temperature when both minima coincide (or the difference between them becomes zero) at the peak of the curve. Fig.4c shows the same plot at $T = 1820$ K, where the two minima became closer to each other and the peak at the center approximately disappeared, and the Gibbs energy curve is concaving up, but with a wide minimum, which means that this temperature is close to the critical temperature. Nakagawa [8] found the critical temperature by the measurement of the magnetic susceptibility of supercooled melts and by the microscopic analysis of quenched samples at $T = 1696$ K and composition of 0.56 Fe.

4. Conclusions

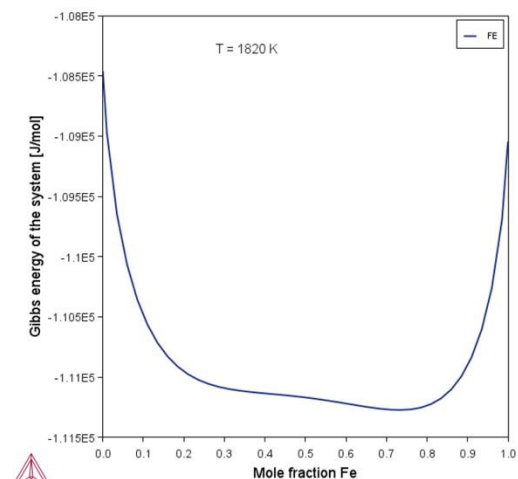
In this work the phase diagram of the Fe-Cu binary system was retrieved and found to be consistent with those obtained by the other authors. The invariant reactions and solubilities are also determined and the results are consistent with those found in the literature. The Gibbs energy curves plotted with composition at different temperatures confirmed that the system is metastable with a wide miscibility gap, and that this gap decreases with temperature and becomes zero at the critical temperature.



(a)



(b)



(c)

Figure 4. Gibbs energy against composition (mole fraction Fe) at different temperatures. a) $T = 1100$ K. b) $T = 1550$ K. c) $T = 1820$ K.

References

1. M.A. Turchanin, P.G. Agraval, I.V. Nikolaenko, Thermodynamics of alloys and phase equilibria in the copper-iron system, *Journal of Phase Equilibria* 24(4) (2003), pp. 307-319.
2. X. Sun, W. Hao, G. Geng, T. Ma, Y. Li, Solidification microstructure evolution of undercooled Cu-15 wt.% Fe Alloy Melt, *Advances in Materials Science and Engineering* (2018), Article ID 6304518. <https://doi.org/10.1155/2018/6304518>

3. K. Shubhank, Y.-B. Kang, Critical evaluation and thermodynamic optimization of Fe–Cu, Cu–C, Fe–C binary systems and Fe–Cu–C ternary system, *Calphad* Volume 45, (2014), pp. 127-137. <https://doi.org/10.1016/j.calphad.2013.12.002>.
4. D. Shishin, T. Hidayat, E. Jak, S. A. Decterov, Critical assessment and thermodynamic modeling of the Cu–Fe–O system, *Calphad* 41, (2013), pp. 160-179. <https://doi.org/10.1016/j.calphad.2013.04.001>.
5. Y.Z. Chen, F. Liu, G.C. Yang, X.Q. Xu, Y.H. Zhou, Rapid solidification of bulk undercooled hypoperitectic Fe–Cu alloy, *Journal of Alloys and Compounds* 427(1–2), (2007), pp. L1-L5. <https://doi.org/10.1016/j.jallcom.2006.03.012>.
6. B. A. Boutwell, R. G. Thompson, N. Saunders, S. K. Mannan, J. J. deBarbadillo, Phase formation modeling of an alloy casting using computational thermodynamics. Paper is presented at the 4th International Symposium on Superalloys and Derivatives”, June 15-18, 1997. Pittsburgh, Pennsylvania.
7. A. H. Alami, A. Abu Hawili, Synthesis, characterization and applications of FeCu alloys, *Applied Surface Science Advances* 1, (2020), 100027. <https://doi.org/10.1016/j.apsadv.2020.100027>.
8. Y. Nakagawa, Liquid Immiscibility in the Copper-Iron and Copper-Cobalt Systems in the Supercooled State, *Acta Metall.* 6(11) (1958), pp. 704-711. [https://doi.org/10.1016/0001-6160\(58\)90061-0](https://doi.org/10.1016/0001-6160(58)90061-0)

ICMATSE 2024

The Importance of Surface Topography

Marek Jemelka

*EVIDENT Europe GmbH – branch office CZ Evropska 16/176 160 00 Prague 6 - Vokovice
Czechia, marek.jemelka@evidentscientific.com*

ORCID: xxxx-xxxx-xxxx-xxxx

*Cite this paper as: Jemelka, M.,. The Importance of Surface Topography.Int. Conf. Advanced. Mater. Sci.& Eng.
HiTech.and Device Appl.Oct. 24-26 2024, Ankara, Turkiye*

Abstract. Short description: Introduction to Surface Roughness Measurement with Emphasis on Analysis with Laser Scanning Confocal Microscope (LSCM). Long description: In the presentation, I will be focusing on the introduction of the surface topography and surface roughness analysis itself. Usual vocabulary and important roughness parameters will be discussed, along with new trends in the surface roughness measurement field. As the last part, I will deep dive into the world of laser scanning confocal microscopy showing its importance and benefits in terms of roughness analysis and will compare it to the other available measurement methods on the market.

Keywords: Surface Topography
© 2024 Published by ICMATSE

ICMATSE 2024

Investigating the Solidification Temperature Range of High Strength Low Alloy Steels Using the Scheil Solidification Model with CALPHAD Methodology

Adem KAYADELEN

Gazi University, Advanced Technologies Department, 06560, Ankara, Turkiye,
adem.kayadelen@gazi.edu.tr,
ORCID: 0000-0002-4982-7215

Oguzhan YILMAZ

Advanced Manufacturing Technologies Research Group (AMTRG), Faculty of Engineering Gazi University, Gazi University Welding and Joining Technologies Research and Application Center (KABTEM), Celal Bayar Boulevard, 06570, Maltepe, Ankara, Turkiye,
oguzhanyilmaz@gazi.edu.tr
ORCID: 0000-0002-2641-2324

Hakan ATES

Gazi University, Department of Metallurgical and Materials Science Engineering, 06560, Ankara, Turkiye Gazi University Welding and Joining Technologies Research and Application Center (KABTEM)
hates@gazi.edu.tr,
ORCID: 0000-0002-5132-4107

Cite this paper as: Kayadelen A., Yilmaz, O. Ates H., Investigating the Solidification Temperature Range of High Strength Low Alloy Steels Using the Scheil Solidification Model with CALPHAD Methodology. Int. Conf. Advanced. Mater. Sci.& Eng. HiTech. and Device Appl. Oct. 24-26 2024, Ankara, Turkiye

Abstract. Solidification is a fundamental aspect of various manufacturing processes like casting, welding, and additive manufacturing. The "Scheil-Gulliver" model, initially formulated in 1913, provides a framework for understanding solute redistribution during solidification, assuming no diffusion in the solid phase and instantaneous solute movement in the liquid. While the classic Scheil model is widely applicable, modified versions have been developed to better capture solidification behavior under specific conditions, such as high solidification rates encountered in additive manufacturing. The Scheil solidification model was applied to three different steel types using Thermo-Calc. Three scenarios were analyzed: (1) where only carbon is a fast diffuser, (2) where all alloying elements are fast diffusers, and (3) where only carbon is a fast diffuser with back diffusion occurring from the first formed phase. The results demonstrate that the solidification range in Scenario 1 is larger than in Scenario 2, due to carbon's rapid diffusion. Scenario 3, using the Scheil with Back Diffusion model, yielded a similar solidification range to Scenario 1 when the cooling rate was set to 15 K/sec. It was also predicted that an increase in the cooling rate would result in a decreased solidification range.

Keywords: Scheil, Calphad, HSLA
© 2024 Published by ICMATSE

Introduction

Solidification plays a crucial role in various manufacturing techniques, including casting, welding, and additive manufacturing. Originally conceptualized by Gulliver in 1913, the "Scheil-Gulliver" model provides a theoretical framework for understanding the redistribution of solutes during the solidification process [1 - 4]. This model posits that there is no diffusion within the solid

phase and that solute movement within the liquid occurs instantaneously. Scheil solidification models based on CALPHAD are commonly employed to estimate the solidification temperature range, segregation patterns, and phase transformations during cellular or dendritic solidification of multicomponent alloys. Although these models are applicable to many material systems and solidification conditions, certain scenarios arise where the initial assumptions of the Scheil model

do not fully represent the actual solidification behavior. Consequently, modified versions of the model have been developed to address these specific cases. [5] There are 4 Scheil solidification models in ThermoCalc which based on CALPHAD methodology. The first model is based on the classic Scheil-Gulliver model, which assumes no diffusion occurs in the solidifying phase. The second model allows for the assumption that one or more alloying elements rapidly diffuse, depending on the situation. The third model is known as the Back Diffusion in the Primary Phase model, with Thermo-Calc providing satisfactory results for all three of these models. A fourth model incorporates Solute Trapping in the primary phase for calculations involving high solidification rates, such as those encountered in Additive Manufacturing applications. [6]

Results and Discussions

In this study, Thermo-Calc 2024b version was used. The TCFE13 database, defined for steel materials, was utilized alongside the MOBFE8 database, which is used for mobility calculations. The chemical composition of the three different steel materials used in this study is provided in Table 1. Three different calculation methods were employed: the first model assumes carbon as the only fast diffuser, the second model assumes all alloying elements as fast diffusers, and the third is the Scheil with Back Diffusion model where carbon is set as the fast diffuser. The Scheil with Back Diffusion model is the most advanced Scheil model available in Thermo-Calc, and it provides the most accurate results for steel materials.[5]

Table 1. Chemical Composition of the Steels

AWS Code	% Content	% C	% Si	% Mn	% Cr	% Ni	% Mo	% Ti
ER70S-A1		0,1	0,6	1,2	-	-	0,5	-
ER90S-G		0,08	0,65	1,0	2,5	-	1,0	-
ER110S-G		0,09	0,55	1,55	0,25	1,35	0,25	0,07

A summary of the computational models used for ER70SA-1, ER90S-G and ER110S-G can be seen in Table 2. When performing a calculation in

Thermocalc some inputs must be arrange. Also, these inputs can be seen in Table 2. As seen in Table 2 all of the inputs are same for each steels.

Table 2. Parameters for calculation

ER70S-A1	1	Only C is fast diffuser
	2	All alloy elements fast diffuser
	3	Back Diffusion Calculation with back diffusion in primary phase ; Cooling Rate: 15 K/s; Primary Phase: Automatic Only C fast diffuser
ER90S-G	1	Only C fast diffuser
	2	All alloy elements fast diffuser
	3	Back Diffusion Calculation with back diffusion in primary phase ; Cooling Rate: 15 K/s; Primary Phase: Automatic Only C fast diffuser
ER110S-G	1	Only C fast diffuser
	2	All alloy elements are fast diffuser
	3	Back Diffusion Calculation with back diffusion in primary phase ; Cooling Rate: 15 K/s; Primary Phase: Automatic Only C fast diffuser

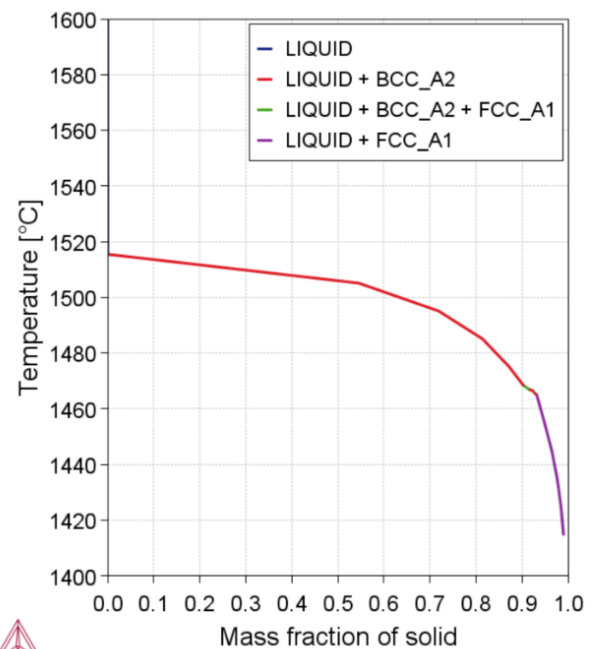


Fig 1. Scheil model with only carbon is fast diffuser for ER70S-A1

Table 3. Scheil model with. only carbon is fast diffusor
for ER70S-A1

Temperature (°C)	Mass Fraction (%)	Phase
>1515,39	100	LIQUID
1515,07	1,97	LIQUID + BCC_A2
1505,07	54,56	LIQUID + BCC_A2
1495,07	71,89	LIQUID + BCC_A2
1485,07	81,42	LIQUID + BCC_A2
1475,07	87,21	LIQUID + BCC_A2
1468,38	90,30	LIQUID + BCC_A2
1466,79	91,73	LIQUID + BCC_A2
1466,47	92,32	LIQUID + BCC_A2
1465,51	92,79	LIQUID + BCC_A2
1465,19	93,04	LIQUID + BCC_A2
1468,38	90,30	LIQUID + BCC_A2 + FCC_A1
1466,79	91,73	LIQUID + BCC_A2 + FCC_A1
1466,47	92,32	LIQUID + BCC_A2 + FCC_A1
1465,51	92,79	LIQUID + BCC_A2 + FCC_A1
1465,19	93,04	LIQUID + FCC_A1
1464,87	93,23	LIQUID + FCC_A1
1454,87	94,91	LIQUID + FCC_A1
1444,87	96,49	LIQUID + FCC_A1
1434,87	97,66	LIQUID + FCC_A1
1424,87	98,48	LIQUID + FCC_A1
1414,87	99,02	LIQUID + FCC_A1

Fig. 1 and Table 3 show the case of ER70SA-1 steel where only carbon is a fast diffusor. According to this graph and table, solidification starts at 1515 °C and ends at 1414 °C. The solidification interval is calculated as 101 °C.

I

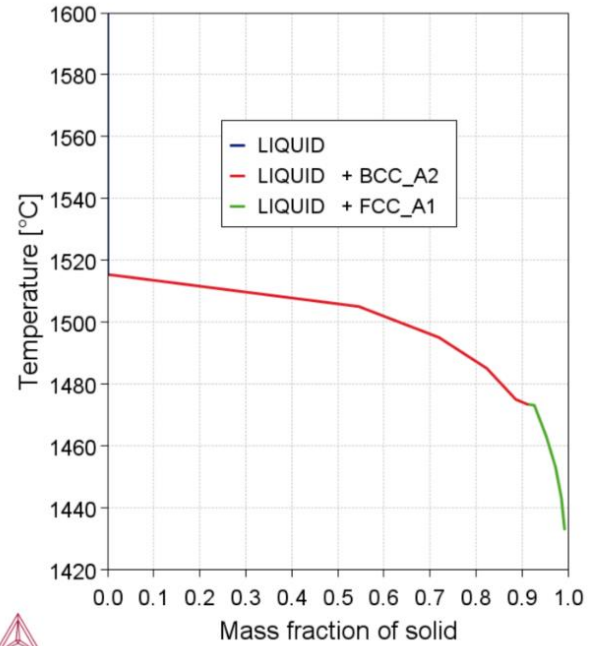


Fig 2. Scheil model with full alloy elements are fast diffusor for ER70S-A1

Table 4. Scheil model with full alloy elements are fast diffusor for ER70S-A1

Temperature °C	Mass Fraction (%)	Phase
>1515,39	100,00	LIQUID
1515,07	1,97	LIQUID + BCC_A2
1505,07	54,56	LIQUID + BCC_A2
1495,07	71,97	LIQUID + BCC_A2
1485,07	82,36	LIQUID + BCC_A2
1475,07	88,64	LIQUID + BCC_A2
1473,48	91,15	LIQUID + BCC_A2
1473,48	91,15	LIQUID + FCC_A1
1473,16	92,69	LIQUID + FCC_A1
1463,16	95,27	LIQUID + FCC_A1
1453,16	97,30	LIQUID + FCC_A1
1443,16	98,57	LIQUID + FCC_A1
1433,16	99,26	LIQUID + FCC_A1

Fig. 2 and Table 4 show the fast diffusor state of all alloying elements of ER70SA-1 steel. According to this graph and table, solidification starts at 1515 °C and ends at 1433 °C. The solidification interval is calculated as 82 °C.

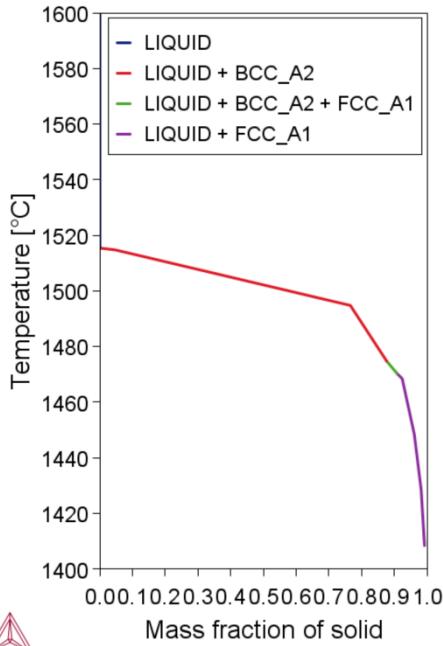


Fig 3. Scheil model with back diffusion in primary phase for ER70S-A1

As can be seen in Fig 3 and Table 5, solidification starts at 1515 °C and ends at 1414 °C in the Scheil with back diffusion model where only carbon is a fast diffuser. The solidification interval is calculated as 82 °C. In summary, the solidification intervals for ER70S-A1 material were calculated as 101 °C, 82 °C and 101 °C, respectively.

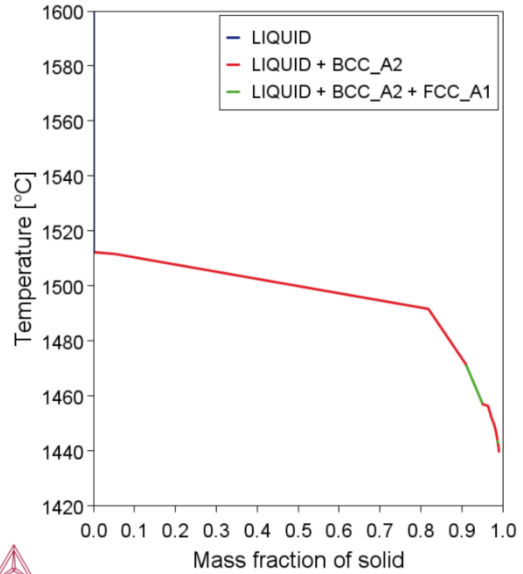


Fig 4. Scheil model with only carbon is fast diffusor for ER90S-G

Table.5 Scheil model with back diffusion in primary phase for ER70S-A1

Temperature °C	Mass Fraction (%)	Phase
1515,39		LIQUID
1515,07	1,97	LIQUID + BCC_A2
1505,07	54,56	LIQUID + BCC_A2
1495,07	71,89	LIQUID + BCC_A2
1485,07	81,42	LIQUID + BCC_A2
1475,07	87,21	LIQUID + BCC_A2
1468,38	90,30	LIQUID + BCC_A2
1466,79	91,73	LIQUID + BCC_A2
1466,47	92,32	LIQUID + BCC_A2
1465,51	92,79	LIQUID + BCC_A2
1465,19	93,04	LIQUID + BCC_A2
1468,38	90,30	LIQUID + BCC_A2 + FCC_A1
1466,79	91,73	LIQUID + BCC_A2 + FCC_A1
1466,47	92,32	LIQUID + BCC_A2 + FCC_A1
1465,51	92,79	LIQUID + BCC_A2 + FCC_A1
1465,19	93,04	LIQUID + FCC_A1
1464,87	93,23	LIQUID + FCC_A1
1454,87	94,91	LIQUID + FCC_A1
1444,87	96,49	LIQUID + FCC_A1
1434,87	97,66	LIQUID + FCC_A1
1424,87	98,48	LIQUID + FCC_A1
1414,87	99,02	LIQUID + FCC_A1

Table 6. Scheil model with only carbon is fast diffusor for ER90S-G

Temperature °C	Mass Fraction (%)	Phase
>1511,62	100,00	LIQUID
1511,62	5,19	LIQUID + BCC_A2
1491,62	81,84	LIQUID + BCC_A2
1471,62	90,96	LIQUID + BCC_A2
1456,96	95,14	LIQUID + BCC_A2
1456,32	96,43	LIQUID + BCC_A2
1451,86	97,32	LIQUID + BCC_A2
1449,95	97,85	LIQUID + BCC_A2
1448,03	98,21	LIQUID + BCC_A2
1446,12	98,48	LIQUID + BCC_A2
1444,21	98,69	LIQUID + BCC_A2
1442,30	98,87	LIQUID + BCC_A2
1441,66	98,98	LIQUID + BCC_A2
1439,75	99,09	LIQUID + BCC_A2
1471,62	90,96	LIQUID + BCC_A2 + FCC_A1
1456,96	95,14	LIQUID + BCC_A2 + FCC_A1
1444,21	98,69	LIQUID + BCC_A2 + FCC_A1
1442,30	98,87	LIQUID + BCC_A2 + FCC_A1

Fig 4 and Table 6 show the case of ER90S-G steel where only carbon is a fast diffusor. According to this graph and table, solidification starts at 1511 °C and ends at 1442 °C. The solidification interval is calculated as 69 °C. For ER90S-G, in the calculation where only carbon is a fast diffusor, the calculation ends at 98.8% solidification. This is assumed to be a calculation error and it is thought that the temperature will drop below 1439°C when the calculation approaches the 100% solidification limit.

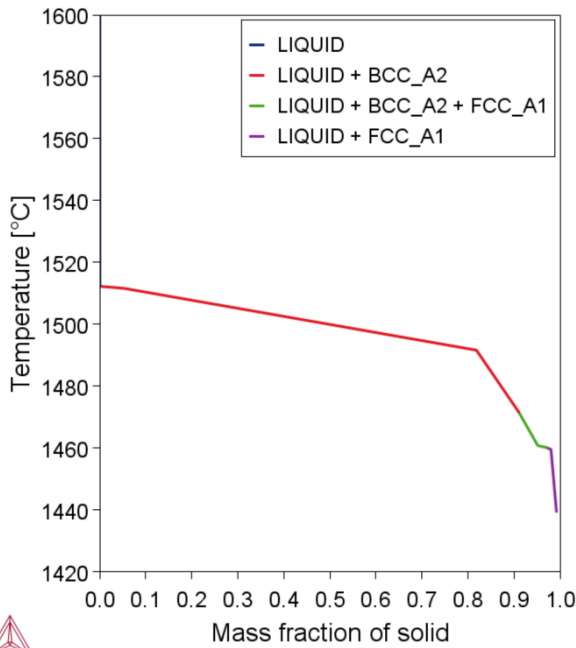


Fig.5 Scheil model with full alloy elements are fast diffusor for ER90S-G

Table 7. Scheil model with full alloy elements are fast diffusor for ER90S-G

Temperature °C	Mass Fraction (%)	Phase
>1511,62	100	LIQUID
1511,62	5,19	LIQUID + BCC_A2
1491,62	81,84	LIQUID + BCC_A2
1471,62	91,04	LIQUID + BCC_A2
1471,62	91,04	LIQUID + BCC_A2 + FCC_A1
1460,78	95,18	LIQUID + BCC_A2 + FCC_A1
1460,15	97,06	LIQUID + BCC_A2 + FCC_A1
1460,15	97,06	LIQUID + FCC_A1
1459,51	98,05	LIQUID + FCC_A1
1439,51	99,24	LIQUID + FCC_A1

Fig. 5 and Table 7 show the fast diffusor state of all alloying elements of ER90S-G steel. According to this graph and table, solidification starts at 1515 °C and ends at 1439 °C. The solidification interval is calculated as 72 °C.

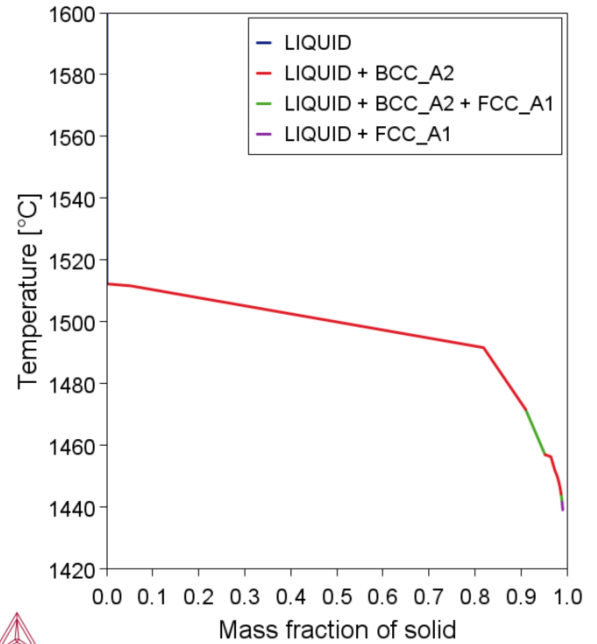


Fig 6 Scheil model with back diffusion in primary phase for ER90S-G

Table 8. Scheil model with back diffusion in primary phase for ER90S-G

Temperature °C	Mass Fraction (%)	Phase
>1511,62	100	LIQUID
1511,62	5,19	LIQUID + BCC_A2
1491,62	81,88	LIQUID + BCC_A2
1471,62	91,01	LIQUID + BCC_A2
1456,96	95,24	LIQUID + BCC_A2
1456,32	96,50	LIQUID + BCC_A2
1451,86	97,37	LIQUID + BCC_A2
1449,95	97,90	LIQUID + BCC_A2
1448,03	98,26	LIQUID + BCC_A2
1446,12	98,52	LIQUID + BCC_A2
1444,21	98,73	LIQUID + BCC_A2
1471,62	91,01	LIQUID + BCC_A2 + FCC_A1
1456,96	95,24	LIQUID + BCC_A2 + FCC_A1
1444,21	98,73	LIQUID + BCC_A2 + FCC_A1
1442,30	98,90	LIQUID + BCC_A2 + FCC_A1
1442,30	98,90	LIQUID + FCC_A1
1439,11	99,09	LIQUID + FCC_A1

As can be seen in Fig 6 and Table 8, solidification starts at 1515 °C and ends at 1439 °C in the Scheil with back diffusion model where only carbon is a fast diffuser for ER90S-G. The solidification interval is calculated as 76 °C. For the ER90S-G material, the solidification intervals were determined to be 69, 72, and 76 °C, respectively.

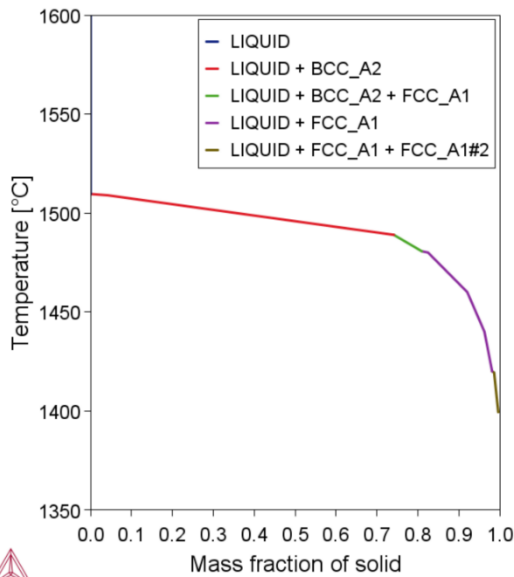


Fig 7. Scheil model with only carbon is fast diffusor ER110S-G

Table 9. Scheil model with only carbon is fast diffusor ER110S-G

Temperature °C	Mass Fraction (%)	Phase
>1508,91	100,00	LIQUID
1508,91	4,13	LIQUID + BCC_A2
1488,91	74,13	LIQUID + BCC_A2
1488,91	74,13	LIQUID + BCC_A2 + FCC_A1
1480,63	80,96	LIQUID + BCC_A2 + FCC_A1
1480,63	80,96	LIQUID + FCC_A1
1479,99	82,48	LIQUID + FCC_A1
1459,99	92,08	LIQUID + FCC_A1
1439,99	96,28	LIQUID + FCC_A1
1419,99	98,16	LIQUID + FCC_A1
1419,99	98,16	LIQUID + FCC_A1 + FCC_A1#2
1419,35	98,65	LIQUID + FCC_A1 + FCC_A1#2
1399,35	99,67	LIQUID + FCC_A1 + FCC_A1#2

Fig 4 and Table 6 show the case of ER110S-G steel where only carbon is a fast diffusor. According to this graph and table, solidification starts at 1509 °C

and ends at 1399 °C. The solidification interval is calculated as 110 °C.

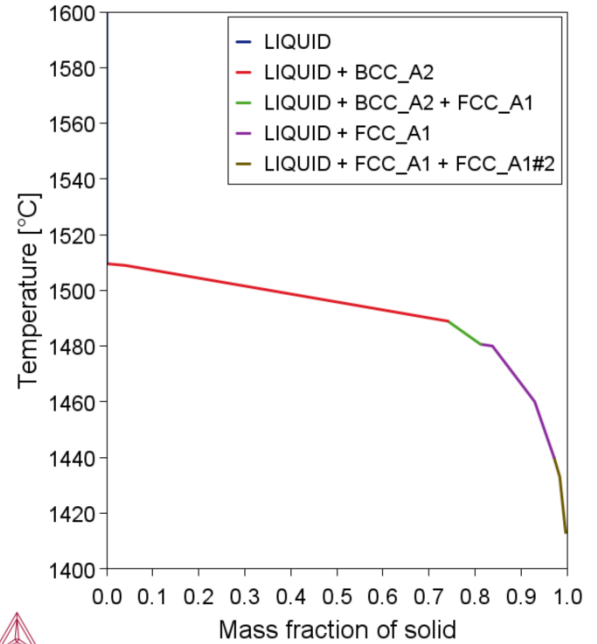


Fig.8. Scheil model with full alloy elements are fast diffusor for ER110S-G

Table 10. Scheil model with full alloy elements are fast diffusor for ER110S-G

Temperature °C	Mass Fraction (%)	Phase
>1509,55	100	LIQUID
1508,91	4,13	LIQUID + BCC_A2
1488,91	74,13	LIQUID + BCC_A2
1488,91	74,13	LIQUID + BCC_A2 + FCC_A1
1480,63	81,20	LIQUID + BCC_A2 + FCC_A1
1480,63	81,20	LIQUID + FCC_A1
1479,99	83,81	LIQUID + FCC_A1
1459,99	92,99	LIQUID + FCC_A1
1439,99	97,19	LIQUID + FCC_A1
1439,99	97,19	LIQUID + FCC_A1 + FCC_A1#2
1432,98	98,44	LIQUID + FCC_A1 + FCC_A1#2
1412,98	99,71	LIQUID + FCC_A1 + FCC_A1#2

Fig. 8 and Table 10 show the fast diffusor state of all alloying elements of ER110S-G steel. According to this graph and table, solidification starts at 1509 °C and ends at 1412 °C. The solidification interval is calculated as 97 °C

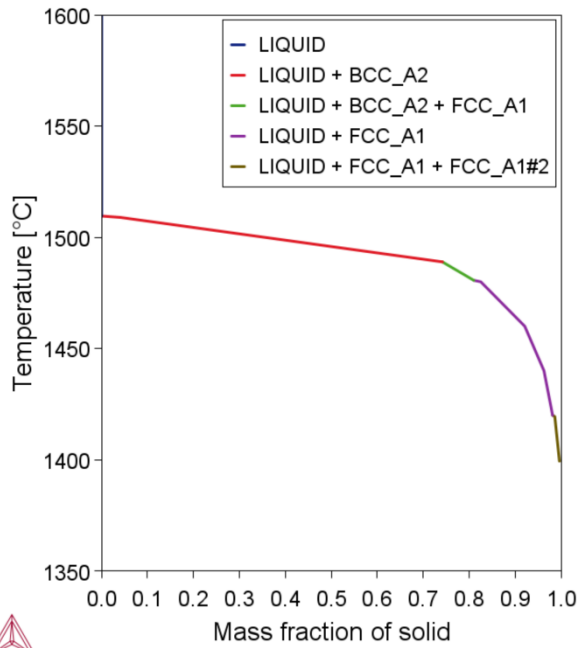


Fig.9. Scheil model with back diffusion in primary phase for ER110S-G

Table. 11 Scheil model with back diffusion in primary phase for ER110S-G

Temperature °C	Mass Fraction (%)	Phase
>1509,55	100	LIQUID
1508,91	4,13	LIQUID + BCC_A2
1488,91	74,13	LIQUID + BCC_A2
1488,91	74,13	LIQUID + BCC_A2 + FCC_A1
1480,63	81,2	LIQUID + BCC_A2 + FCC_A1
1480,63	81,01	LIQUID + FCC_A1
1479,99	82,53	LIQUID + FCC_A1
1459,99	92,11	LIQUID + FCC_A1
1439,99	96,29	LIQUID + FCC_A1
1419,99	98,17	LIQUID + FCC_A1 + FCC_A1#2
1419,35	98,65	LIQUID + FCC_A1 + FCC_A1#2
1399,35	99,67	LIQUID + FCC_A1 + FCC_A1#2

As can be seen in Fig 9 and Table 11, solidification starts at 1509 °C and ends at 1399 °C in the Scheil with back diffusion model where only carbon is a fast diffuser for ER110S-G. The solidification interval is calculated as 110 °C. In summary, the solidification intervals for ER110S-G material were calculated as 110 °C, 97 °C and 110 °C, respectively.

Conclusion

Scheil solidification model for all 3 steel types was calculated in Thermocalc. According to this;

1. Only carbon is a fast diffuser,
2. All alloying elements are fast diffusers,
3. Only carbon is a fast diffuser and back diffusion occurs from the first formed phase, results were obtained in the scenarios.

These results are detailed in Table 12. Since the carbon atom can diffuse rapidly due to its size, the solidification range in Case 1 is expected to be higher than the solidification range in Case 2. As a matter of fact, Thermocalc calculation results confirm this. This was not the case only for ER90S-G steel. The ER90S-G computation stops at 98.8% solidification in the scenario where carbon is the only fast diffuser. It is considered that this is a computation mistake and that when the calculation gets closer to the 100% solidification limit, the temperature will decrease below 1439 °C.

Table 12. Comparison of the results

Material	#	Scheil Model	Solidification Range °C
ER70S-A1	1	Only C is fast diffuser	101
	2	All alloy elements fast diffuser	82
	3	Back Diffusion Calculation with back diffusion in primary phase ; Cooling Rate: 15 K/s; Primary Phase: Automatic Fast diffuser: only C	101
ER90S-G	1	Only C fast diffuser	69
	2	All alloy elements fast diffuser	72
	3	Back Diffusion Calculation with back diffusion in primary phase ; Cooling Rate: 15 K/s; Primary Phase: Automatic Fast diffuser: only C	76
ER110S-G	1	Only C fast diffuser	110
	2	All alloy elements are fast diffuser	97
	3	Back Diffusion Calculation with back diffusion in primary phase ; Cooling Rate: 15 K/s; Primary Phase: Automatic	110

	Fast diffusor: only C	
--	-----------------------	--

On the other hand, according to the Scheil with Back Diffusion model, which is Case 3, all alloying elements are at infinite velocity in the liquid phase. In addition, alloying elements can move in the first formed solid phase according to their mobility values and at a determined cooling rate and thermodynamically the solid and liquid interface is

in equilibrium [6]. Thus, as in scenario 1, when only carbon is set as a fast diffusor and the cooling rate is 15 K/sec, a solidification ranges similar to scenario 1 is obtained in scenario 3. When it is assumed that the mobility of the atoms will decrease with the increase in the cooling rate, it is estimated that the solidification range will decrease [7]. In addition, in another scenario where all alloying elements are selected as fast diffusors, it can be predicted that a scenario close to Case 2 will emerge.

Acknowledgements

The authors thank to Scientific and Technological Research Council of Turkiye for their supports under the Grant Number 124M167.

The authors thank to Gazi University Scientific Research Coordinate (GAZİ-BAP) for their supports under the Grant Number FDK-2023-8477.

References

1. Schaffnit, P., Stallybrass, C., Konrad, J., Stein, F., & Weinberg, M. (2015). A Scheil–Gulliver model dedicated to the solidification of steel. *Calphad*, 48, 184–188. <https://doi.org/10.1016/j.calphad.2015.01.002>
3. G.M. Gulliver. *J. Inst. Metals*, 9 (1913), pp. 120-157
4. Scheil, E. (1942). Bemerkungen zur schichtkristallbildung. *International Journal of Materials Research*, 34(3), 70-72
5. Selecting Scheil Solidification Calculation. (2023, January 12). Thermo-Calc Software. <https://thermocalc.com/blog/tips-and-tricks-selecting-the-right-model-for-your-scheil-solidification-calculation/>
6. Scheil Equations Simulations. (n.d.). Thermo-Calc Software. Retrieved September 8, 2024, from <https://thermocalc.com/products/thermo-calc/scheil-solidification-simulations/>
7. Kurz, W., Fisher, D., & Rappaz, M. (2023). *Fundamentals of solidification*.

Thermoluminescence of hydrothermally grown ZnO nanorods

Mohammed Khenfouch

*Ibn Zohr University/Faculty of Applied Sciences, Department of Applied Physics, Ait Melloul, , 86150
Agadir, Morocco, m.khenfouch@uiz.ac.ma
ORCID: 0000-0001-9259-769X*

Issam Derkaoui

*Sidi Mohamed Ben Abdellah University/Faculty of Sciences, Department of Physics, 30000 Fez,
Morocco, derkaouiissam@gmail.com
ORCID: 0000-0002-2009-082X*

Mohammed Hamzah

*Sidi Mohamed Ben Abdellah University/Faculty of Sciences, Department of Physics, 30000 Fez,
Morocco, hamzah.13.mohammed@gmail.com
ORCID: 0000-0002-8586-446X*

Issam Boukhoubza

*Sidi Mohamed Ben Abdellah University/Faculty of Sciences, Department of Physics, 30000 Fez,
Morocco, boukhoubza.issam00@gmail.com
ORCID: 0000-0003-0088-9535*

Mohamed Achehboune

*Sidi Mohamed Ben Abdellah University/Faculty of Sciences, Department of Physics, 30000 Fez,
Morocco, achehboune.mohamed01@gmail.com
ORCID: 0000-0002-7716-8085*

Rhizlane Hatel

*Sidi Mohamed Ben Abdellah University/Faculty of Sciences, Department of Physics, 30000 Fez,
Morocco, hatel.rhizlane@gmail.com
ORCID: 0000-0002-8627-1682*

Dumisani Mlotswa

*University of south Africa/Engineering and Technology, Science Campus, Department of Physics, 1709,
Johannesburg, South Africa,
dumisanimlotswa@gmail.com
ORCID: 0000-0002-3896-0395*

Bakang Moses Mothudi

*University of south Africa/Engineering and Technology, Science Campus, Department of Physics, 1709,
Johannesburg, South Africa,
mothubm@unisa.ac.za
ORCID: 0000-0002-1331-6085*

*Cite this paper as: Khenfouch, M, Derkaoui, I, Hamzah, M, Boukhoubza, I, Achehboune, M, Hatel, R, Mlotswa, D,
Mothud,i MB. Surname, FN. Article title.Int. Conf. Advanced. Mater. Sci.& Eng. HiTech.and Device Appl.Oct. 24-
26 2024, Ankara, Turkiye*

Abstract. In order to study their thermoluminescence properties, ZnO nanorods have been exposed to gamma radiation. For this purpose, nanorods of an average diameter of 240 nm and an average length of 1108 nm were prepared through a

hydrothermal synthesis method. They produced a low fading and a single thermoluminescence glow peak structure which is making from them adequate nanostructures for thermoluminescence related applications. In this sense we can say that these nanostructures have a great potential for applications such as monitoring dosimeters in ionizing radiation fields.

Keywords: ZnO nanorods; Thermoluminescence
© 2024 Published by ICMATSE

Introduction

Zinc oxide materials show interesting optoelectronic properties and efficiency in many vital sectors.

Among ZnO interesting characteristics, its wide band gap semiconductor with an energy gap of 3.37 eV and its binding energy of the free exciton with a value of 60 meV leading to excitonic emission at room temperature [1]. This particular material has been a good candidate for many areas such as catalytics, optoelectronics and photochemicals [2-4].

One-dimensional ZnO nanowires have a lower threshold lasing-energy due to quantum effects. This results in a substantial density of states near band-edges and enhances radiative recombination due to carrier confinement [5], which leads to many optical and opto-electronic applications [6,7]. In this sense, and as the properties become more and more important in nano systems, hydrothermal growth method was promising with preparing ZnO nanomaterials with appropriate morphology at a low-temperature.

The Thermoluminescence (TL) properties of undoped zinc oxide (Cruz-Vazquez et al., 2005; Pal et al., 2006) and doped with Ce, Yb, Tb, Eu, Dy, and La ions, have been studied by many authors (Kucuk et al., 2016; Goswami et al., 2015; Sunta et al., 2002) making serious efforts to improve TL responses such as fading and dose-response at low doses from 143 mGy up to 60 Gy from gamma radiation.

Such responses are dependents of many factors. For example, in addition to doping, the optical and luminescent properties strongly depend on the preparation route.

Hence, this study aims to discuss the thermoluminescence response of hydrothermally grown ZnO nanorods as well as its possible origins then propose these nanostructures for specific applications.

Experimental details

The synthesis method was adopted from our previous work [14]. The obtained nanorods were analyzed by various techniques. XRD measurements were recorded using Rigaku smartLab X-ray diffractometer (using Cu α emission as the X-ray source ($\lambda = 1.54178 \text{ \AA}$), 45 kV and 200 mA). Morphology was obtained using an electron microscope unit with a FEICO system. RISO TL/OSL reader supplied by DTU Nutech was used to collect thermoluminescence glow curves at room temperature.

Material synthesis

To synthesize ZnO nanorods, an equi-molar aqueous solution of 0.1 M Zinc nitrate ($\text{Zn}(\text{NO}_3)_2$) and hexamethylenetetramine ($\text{C}_6\text{H}_{12}\text{N}_4$, HMT) with 0.001 M NaOH was prepared using deionized water. Si(100) substrates introduced so as to sit in the middle of the reactive solution, on the underside of its glass slide, at a tilt angle of $\sim 80^\circ$ to the horizontal. This mixture was heated at a constant temperature of 90°C in an oven for 24 h.

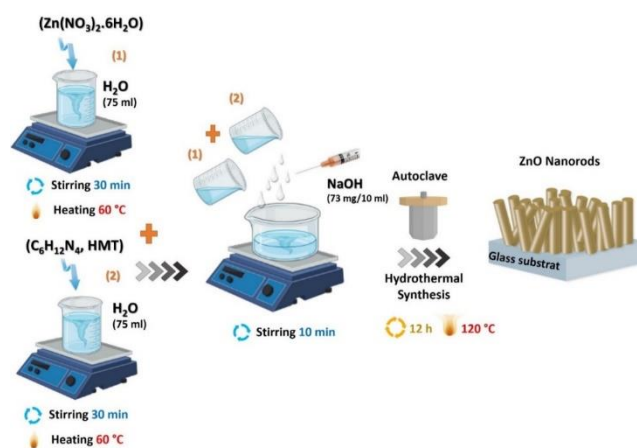


Figure 1. Schematic process of the synthesis of ZnO nanorods.

Results and discussion

X-Ray diffraction

The microstructure properties were studied by using the powder X-ray diffraction technique. Figure 2 illustrates the XRD pattern of ZnO nanorods prepared by the hydrothermal method. High intensity XRD peaks characteristic of zinc oxide were recorded indicating a high degree of crystallinity of the prepared ZnO. Moreover, these results show a preferred growth direction which was following C-axis supported by the highest intensity diffraction peak that was observed at 36.519 for the crystallographic plane (101).

The registered XRD pattern confirmed the formation of the wurtzite hexagonal structure of ZnO which is in accordance with the standard JCPDS data card (JCPDS Card no. 01-075-1526) and has the space group P63mc with lattice parameters $a = b = 3.245 \text{ \AA}$ and $c = 5.207 \text{ \AA}$. The diffraction peaks situated at 31.91° , 34.59° , 36.42° , 47.77° , 56.86° , 63.19° , 66.70° , 68.29° and 69.43° are assigned to the (100), (002), (101), (102), (110), (103), (200), (112), and (201) lattice planes of ZnO, respectively. No diffraction peaks from impurities were detected.

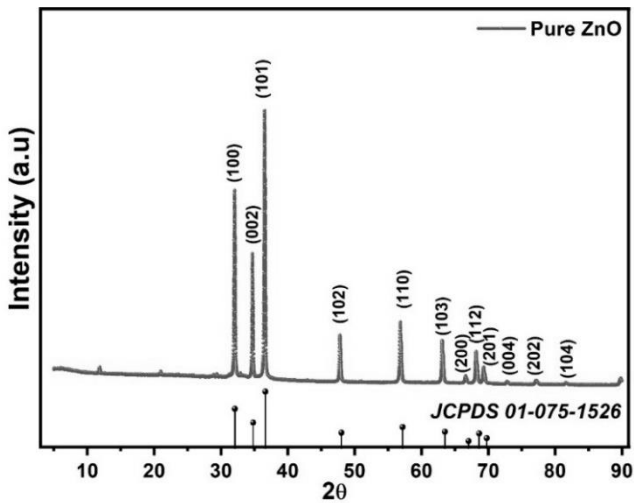


Figure 2. XRD pattern of ZnO nanorods

Scanning Electronic Microscope (SEM)

The SEM observation (Figure 3) clearly shows the formation of a ZnO nanorods with a hexagonal shape using the hydrothermal process. These structures were grown relatively vertically with a high degree of crystallinity.

The average diameters and lengths were determined by measuring 50 nanorods from SEM image using ImageJ software. The characterized ZnO nanorods have an average diameter of 240 nm and an average length of 1108 nm.

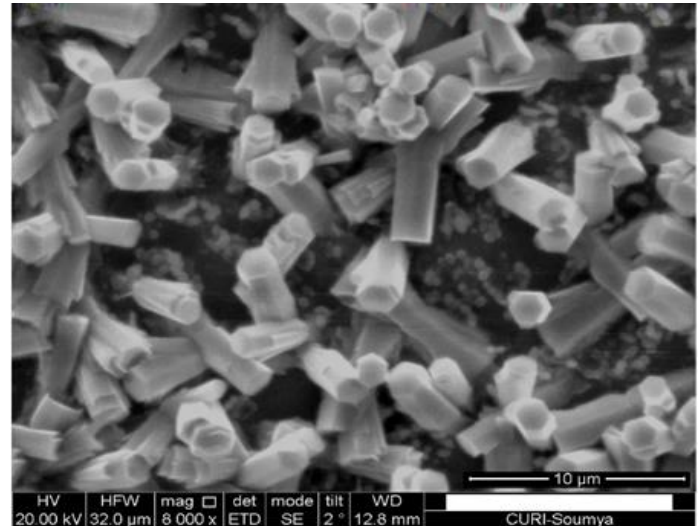


Figure 3. SEM image of ZnO Nanorods

Thermoluminescence measurements:

In order to study the electron traps of the hydrothermally synthesized ZnO nanophosphor via thermoluminescence, the powder form of these nanostructured material was irradiated by a gamma source.

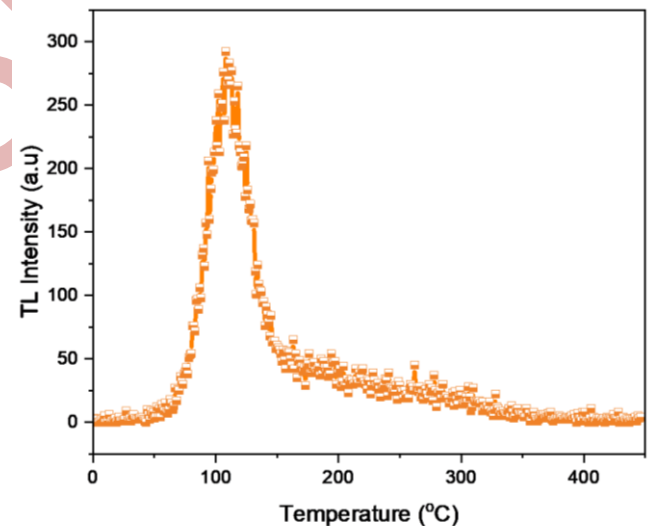


Figure 4. Typical TL glow curve of ZnO nanorods

In general, ZnO can show two main peaks, one at low temperatures and the second towards high temperature region.

The analyzed TL curve obtained from the powder form of ZnO nanorods shows the appearance of a band with a maximum around 108°C . Such response is generally attributed to charge carriers trapped at shallow defect levels. The existence of such TL glow peak is related to the electrons or holes trapped at deep localized trap states, which are adequate for

dosimetry applications due to characteristic low TL fading losses.

When talking about glowing responses towards high temperatures the appearance, the characterized material shows no glow peaks towards this region. This glowing informs the existence of different trapping levels, that may be classified as shallow trapping, intermediate trapping or deep trapping.

Conclusion

While ZnO materials are known by displaying two TL main peaks, the results of this work demonstrated

that hydrothermally grown ZnO nanorods exhibits a single TL glow peak with a maximum intensity at around 108°C.

It is worthy to note that the utilized processing method can play an important role in controlling materials properties as shown in this case.

Hence, these hydrothermally grown ZnO nanostructures can be promising nanophosphors for thermoluminescence related applications.

References

1. D. Look, , Recent Advances in ZnO Materials and Devices. *Materials Science and Engineering: B*, 80 (2001), pp 383-387, Doi.org/10.1016/S0921-5107(00)00604-8
2. Z. Sofiani, B. Sahraoui, M. Addou, R. Adhiri, M. Alaoui, L. Dghoughi, N. Fellahi, B. Derkowska, and W. Bala, Third harmonic generation in undoped and X doped ZnO films (X: Ce, F, Er, Al, Sn) deposited by spray pyrolysis, *J. Appl. Phys.* 101 (2007), 063104, Doi.org/10.1063/1.2711143
3. D.S. King and R.M. Nix, Thermal Stability and Reducibility of ZnO and Cu/ZnO Catalysts, *J. Catal.* 160 (1996) pp. 76-83, Doi.org/10.1006/jcat.1996.0125
4. J. Zhong, A.H. Kitai , P. Mascher, Influence of processing conditions on point defects and luminescence centers in ZnO. *Journal of the Electrochemical Society*, 140 (1993) pp. 3644-3649, DOI 10.1149/1.2221143.
5. M.H. Huang, S. Mao, H. Feick, H. Yan, Y. Wu, H. Kind, E. Weber, R. Russo and .P Yang, Room-Temperature Ultraviolet Nanowire Nanolasers, *Science* 292 (2001) 1897-1899, DOI:10.1126/science.1060367
6. H. Kind, H. Yan, B. Messer, M. Law and P. Yang, Nanowire Ultraviolet Photodetectors and Optical Switches, *Advanced Materials*, 14 (2002), 158-160, Doi.org/10.1002/1521-4095
7. M.S. Arnold, Phaedon Avouris, Zheng Wei Pan, and Zhong L. Wang, Field-Effect Transistors Based on Single Semiconducting Oxide Nanobelts, *The Journal of Physical Chemistry B*, 107 (2003), pp. 659-63, Doi:10.1021/jp0271054
8. C. Cruz-Vázquez, V.R. Orante-Barrón, H. Grijalva-Monteverde, V.M. Castaño and R. Bernal, Thermally Stimulated Luminescence of New ZnO-CdSO₄ Exposed to Beta Radiation, *Materials Letters*, 61.4 (2007), pp. 1097-1100, Doi:10.1016/j.matlet.2006.06.055
9. P.P. Pal and J. Manam, Photoluminescence and Thermoluminescence Studies of Tb³⁺ Doped ZnO Nanorods, *Materials Science and Engineering: B*, 178.7 (2013), pp. 400-408, Doi:10.1016/j.mseb.2013.01.006
10. N. Kucuk, I. Kucuk, M. Yüksel and M. Topaksu, Thermoluminescence Characteristics of Zn(BO₂)₂:Ce³⁺ under Beta Irradiation, *Radiation Protection Dosimetry*, 168.4 (2016), pp. 450-58, doi:10.1093/rpd/ncv360
11. L. Goswami, N. Aggarwal, R. Verma, S. Bishnoi, S. Husale, R. Pandey, G. Gupta, *ACS Appl. Mater. Interfaces*, 12 (2020), pp. 47038-47047, Doi: 10.1021/acsami.0c14246
12. C.M. Sunta, W.E.F. Ayta, J.F.D. Chubaci and S. Watanabe, General Order and Mixed Order Fits of Thermoluminescence Glow Curves-Comparison, *Radiation Measurements*, 35 (2002), pp. 47-57, Doi:10.1016/S1350-4487(01)00257-8
13. C. Klingshirn, ZnO: Material, Physics and Applications, *ChemPhysChem*, 8.6 (2007), pp. 782-803, Doi:10.1002/cphc.200700002
14. M. Khenfouch, M. Baïtoul and M. Maaza, White Photoluminescence from a Grown ZnO Nanorods/Graphene Hybrid Nanostructure, *Optical Materials*, 34.8 (2012), pp. 1320-1326, Doi:10.1016/j.optmat.2012.02.005

Extending Synchrotron X-ray Microscopy to the Laboratory – X-Ray Microscopy as a correlative imaging technique

Mohsen Samadi Khoshkhoo

Carl Zeiss Microscopy GmbH,
mohsen.samadi@zeiss.com

ORCID: xxxx-xxxx-xxxx-xxxx

Cite this paper as Khoshkhoo Mohsen S., Extending Synchrotron X-ray Microscopy to the Laboratory – X-Ray Microscopy as a correlative imaging technique. Int. Conf. Advanced. Mater. Sci. & Eng. HiTech. and Device Appl. Oct. 24-26 2024, Ankara, Turkiye

Abstract. The progress of scientific research and technology development depends heavily on effective imaging solutions to characterize the properties and behaviors of materials. Revealing details of microstructure, ideally in 3D, are a critical part of this understanding, whether developing and confirming models that describe material properties and behavior, or simply visualizing structural details. ZEISS offers 3D X-ray microscopes (XRM): advanced imaging solutions that have overcome major hurdles to three-dimensional imaging by providing high-contrast, sub-micron imaging, even for relatively large samples. These breakthrough advances in nondestructive, three-dimensional (3D) imaging enable a wide range of engineering disciplines.

The nondestructive nature of X-ray microscopy (XRM) enables multiscale or multimodal imaging of the same sample for analysis the hierarchical structures. Two families of X-ray microscopes are available for this purpose and will be presented in this talk. These include the Zeiss Xradia Versa and Zeiss Xradia Ultra laboratory-based X-ray microscopes. They provide the highest resolution for the study of internal structures at true spatial resolutions from submicron (< 450 nm for Versa) to nanometer (< 50 nm for Ultra). 3D-XRM architectures feature several key advantages, including characterization of large samples without loss of resolution, high contrast for improved clarity, minimal sample preparation, the ability to perform in situ experiments, and synchrotron-quality imaging in a laboratory system. In addition, it provides excellent contrast capabilities through different imaging modes, i.e., (i) absorption, (ii) absorption and propagation phase contrast, (iii) dual-energy scanning modes, and (iv) diffraction contrast tomography. These unique features make all families of X-ray microscopes powerful tools for applications in a very wide range of scientific and industrial fields. Correlative workflow from XRM to FIB-SEM is also presented as a unique technique for comprehensive multiscale characterization of a large number of samples.

Keywords: Synchrotron X-ray Microscopy
© 2024 Published by ICMATSE

Self-Healing Metals versus Microcrack Healing of Metals

Volkan Kilicli

*Gazi University Faculty of Technology Department of Metallurgical and Materials Engineering, 06560,
Ankara, Turkiye Country, vkilicli@gazi.edu.tr
ORCID: 0000-0002-0456-5987*

*Cite this paper as: Kilicli V. Self-Healing Metals versus Microcrack Healing of Metals. Int. Conf. Advanced.
Mater. Sci.& Eng. HiTech.and Device Appl.Oct. 24-26 2024, Ankara, Turkiye*

Abstract. The development of advanced materials has led to considerable interest in self-healing metals, which have the ability to heal micro-damage autonomously. Two primary concepts within this field are self-healing metals and microcrack healing in metals. While both aim to extend the lifetime and reliability of materials, they work on different scales and mechanisms. This study provides a comparative analysis of self-healing metals and microcrack healing, examining their advantages, disadvantages, and potential applications in various industries.

Keywords: Self-healing materials, self-healing metals, crack healing, crack repairing, micro-damage healing.

© 2024 Published by ICMATSE

Introduction

Self-healing materials are inspired by natural biological materials and have the ability to repair micro-cracks when they are micro-damaged [1]. Most of the recent studies on self-healing materials have focused on polymers and ceramics, which are easier to manufacture than metallic materials [2-11]. In critical applications such as aerospace, defense, and automotive, material failure due to cracking or fatigue can lead to catastrophic failure. The development of self-healing metals offers a promising way to increase durability, reduce maintenance costs, and improve safety. Within this field, two fundamental mechanisms have emerged: self-healing metals, which encompass a broad range of damage repair, and microcrack healing, which specifically targets the repair of microcracks only. This study examines the differences between these concepts, their respective mechanisms, and their implications for material design and application.

Mechanisms of self-healing metals

Self-healing metals can repair a wide range of damage through both intrinsic (autonomous) and extrinsic (non-autonomous) mechanisms (Table 1) [11]. Intrinsic self-healing involves the natural properties of the metal, such as grain boundary migration and dislocation movement, which allow the material to close small cracks or defects under certain conditions, typically through thermal activation [10]. Extrinsic self-healing involves

incorporating external agents such as microcapsules or fibers containing healing agents. When a crack forms, these capsules rupture, releasing the healing agent reacting with the surrounding material to fill the crack and restore structural integrity [11]. Shape memory alloys (SMAs) also exhibit self-healing by returning to their original shape when heated, thus closing cracks or other deformations [12-14].

Mechanisms of microcrack healing

Microcrack healing is specifically concerned with repairing micro-cracks, typically on the order of microns in size [15]. This process is often driven by localized plasticity, which can effectively seal microcracks before they propagate into larger, more dangerous fractures. The primary goal of microcrack healing is to stop the initiation and growth of cracks that can lead to fatigue failure, making this approach particularly valuable in cyclic loading environments [16]. Unlike self-healing metals, which can target larger damage, microcrack healing focuses on early-stage repair, preventing the accumulation of damage over time.

Comparative analysis

Advantages:

Self-healing metals offer broader applications by addressing different levels of damage, from micro-cracks to larger structural defects. This versatility makes them suitable for use in high-risk industries

such as aerospace and automotive, where material integrity is critical. However, the complexity of integrating extrinsic mechanisms and the potentially high cost are notable challenges.

In contrast, microcrack healing is a more targeted approach that effectively improves fatigue resistance by preventing crack propagation [16]. It is generally less expensive and can be implemented without significantly altering the overall properties of the metal. However, it is limited in scope as it primarily addresses small-scale damage and may not fully restore the original properties of the material.

Disadvantages:

Self-healing metals may not always fully restore the original mechanical properties of the material, especially if the healing involves different phases or materials. In addition, the environmental conditions required for healing (e.g., temperature, stress) may not be present in all applications. Scalability and production costs are also significant concerns. While effective in certain scenarios, microcrack healing is limited to minor defects and may leave residual stresses or small defects that could serve as sites for future damage. Detecting and initiating the healing process on time is another challenge, particularly in applications where early-stage damage is difficult to monitor.

References

1. M. Nosonovsky, P.K. Rohatgi, *Biomimetics in Materials Science: Selfhealing, Self-lubricating, and Self-cleaning materials*, Springer, 2011, p 1-122.
2. B. Aïssa, D. Therriault, E. Haddad, W. Jamroz, Self-healing materials systems: Overview of major approaches and recent developed technologies, *Adv. Mater. Sci. Eng.*, 2012, (2012).
3. D. Bekas, K. Tsirka, D. Baltzis, A. Paipetis, Self-healing materials: a review of advances in materials, evaluation, characterization and monitoring techniques, *Compos. Pt. B-Eng.*, 87, 92-119 (2016).
4. M. Kessler, Self-healing: a new paradigm in materials design, *Proc. Inst. Mech. Eng. Part G-J. Aerosp. Eng.*, 221(4), 479-495 (2007).
5. M. Samadzadeh, S.H. Boura, M. Peikari, S. Kasiriha, A. Ashrafi, A review on self-healing coatings based on micro/nanocapsules, *Prog. Org. Coat.*, 68(3), 159-164 (2010).
6. R.P. Wool, Self-healing materials: a review, *Soft Matter*, 4(3), 400-418 (2008).
7. D.Y. Wu, S. Meure, D. Solomon, Self-healing polymeric materials: a review of recent developments, *Prog. Polym. Sci.*, 33(5), 479-522 (2008).
8. Y. Yuan, T. Yin, M. Rong, M. Zhang, Self-healing in polymers and polymer composites. Concepts, realization and outlook: a review, *Express Polym. Lett.*, 2(4), 238-250 (2008).
9. P. Zhang, G. Li, Advances in healing-on-demand polymers and polymer composites, *Prog. Polym. Sc.*, 57, 32-63 (2016).
10. B. Grabowski, C.C. Tasan, *Self-Healing Metals, Self-Healing Materials*, ed., M.D. Hager, S. van der Zwaag, U.S. Schubert, Eds., Springer, 2016, p 387-407.
11. Kilicli V., Yan X., Salowitz N. and Rohatgi P., Recent Advancements in Self-Healing Metallic Materials and Self-Healing Metal Matrix Composites, *JOM*, 70(6), 846-854, 2018. <https://doi.org/10.1007/s11837-018-2835-y>.
12. J. Ferguson, B. Schultz, P. Rohatgi, Zinc alloy ZA-8/shape memory alloy self-healing metal matrix composite, *Mater. Sci. Eng. A*, 620, 85-88 (2015).

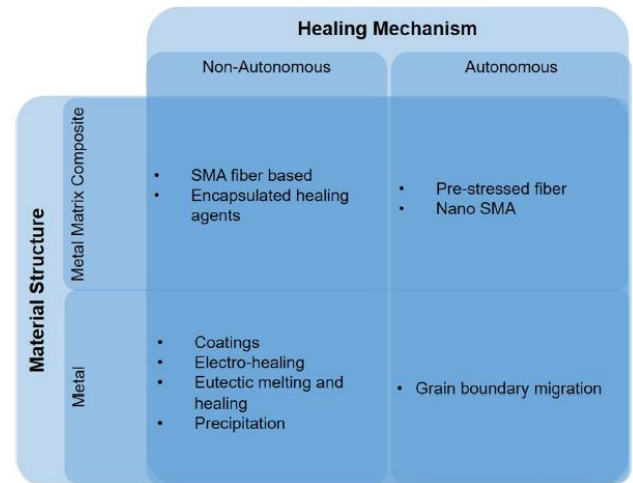


Figure 1. Classification of current self-healing mechanisms for metals and metal matrix composites [11].

Conclusion

Self-healing metals and microcrack healing are two promising ways to improve the durability and reliability of metallic materials. While self-healing metals offer broader applicability and the potential to repair larger damage, they present challenges in terms of complexity and cost. Although more limited in scope, microcrack healing provides an effective solution for preventing the propagation of small cracks, particularly in fatigue-prone environments. The choice between these two approaches depends on the application's specific requirements, including the extent of damage, environmental conditions, and cost considerations.

13. M.V. Manuel, G.B. Olson, Biomimetic Self-healing Metals, 1st International Conference on Self-Healing Materials, 2007, p 1-8.
14. P. Rohatgi, Al-shape memory alloy self-healing metal matrix composite, *Mater. Sci. Eng. A*, 619, 73-76 (2014).
15. Awaja, F., Zhang, S., Tripathi, M., Nikiforov, A., & Pugno, N. Cracks, microcracks and fracture in polymer structures: Formation, detection, autonomic repair. *Progress in Materials Science*, 83, 536-573 (2016).
16. Zhang, H. L., & Sun, J. Diffusive healing of intergranular fatigue microcracks in iron during annealing. *Materials Science and Engineering: A*, 382(1-2), 171-180 (2004), <https://doi.org/10.1016/j.msea.2004.04.069>.

ICMATSE 2024

Amorphous Matrix Nanocomposites in Three-component Manganese-containing Borate Systems

Marina Kapanadze

Georgian Technical University - Department of Chemical and Biological Engineering, 0175,
Tbilisi, Georgia,
m.kapanadze@gtu.ge
ORCID: 0009-0009-7876-4485

Maia Mshvildadze

Georgian Technical University - Department of Chemical and Biological Engineering, 0175,
Tbilisi, Georgia,
maia_mshvildadze@gtu.ge
ORCID: 0009-0003-8362-3819

Tamar Loladze

Georgian Technical University - Department of Metallurgy, Materials Science and Metal Treatment, 0175,
Tbilisi, Georgia,
t.loladze@gtu.ge
ORCID: 0000-0002-3104-8459

Nino Kebabze

Georgian Technical University - Department of Chemical and Biological Engineering, 0175,
Tbilisi, Georgia,
n_kebadze@gtu.ge
ORCID: 0000-0002-8248-7689

Zurab Sabashvili

Georgian Technical University - Department of Metallurgy, Materials Science and Metal Treatment, 0175,
Tbilisi, Georgia,
z_sabashvili@gtu.ge
ORCID: 0000-0003-4766-2661

Cite this paper as: Kapanadze M., Mshvildadze M., Loladze T., Kebabze N., Sabashvili Z. Amorphous Matrix Nanocomposites in Three-component Manganese-containing Borate Systems Int. Conf. Advanced. Mater. Sci&Eng. HiTech.and Device Appl. Oct. 24-26 2024, Ankara, Turkiye

Abstract. In this work, glasses based on the $\text{PbO-MnO-B}_2\text{O}_3$ system are considered nanocomposites because they exhibit features inherent to amorphous-matrix nanocomposite materials. It is assumed that the amorphous materials obtained in this system consist of several types of structural units, which can be considered nano-sized inclusions. This study demonstrates how the ratio and size of these inclusions affect the nature of dilatometric curves and the volumetric electrical resistivity of the resulting materials.

Keywords: manganese containing borate glasses, lead borate glasses, amorphous matrix nanocomposites.
© 2024 Published by ICMATSE

Introduction

Recent studies of simple and complex glass systems have established that they belong to the category of nanocomposites. Amorphous and sub-microcrystalline phases are distinguishable within an amorphous (glassy) matrix. These glasses often

serve as the basis for creating materials with new sets of properties, such as glass-crystalline or porous materials [1,2].

However, it should be noted that the original microheterogeneous glasses are also

nanocomposites, with properties that depend on the degree and size (fraction) of the second phases.

This paper presents the research results of the PbO-MnO-B₂O₃ glass system. Studying this system is part of systematic research on multi-manganese glasses conducted at Georgian Technical University. It represents the culmination of a critical review of earlier works [3-5] and subsequent studies carried out in the same direction.

Results and discussion

The study of the glass-forming limits and various glass properties in this system were carried out, which led to the conclusion that, similar to other three-component manganese-containing borate systems, the glass formation region includes the glasses that, according to available references, should not form - even considering the possibility of Pb²⁺ ions acting as glass-formers. The boundaries of the glass-forming region were found to depend on the type of material introducing manganese into the glass -MnCO₃ resulted in a smaller region, while MnO₂ resulted in a larger region.

The hypothesis was proposed that this is due to the presence of manganese in lead borate glasses in the form of divalent Mn²⁺ ions and Mn. The latter, because of its crystal chemical parameters, can exist in a tetrahedral state.

Based on the analysis of the dependence of various properties on composition, the presence of the following structural units is assumed in the investigated glasses: Pb(BO_{4/2})₂, Pb²⁺Pb²⁻O_{4/2}, MnO_{4/2}, Mn(BO_{4/2}), BO_{3/2}. The ratio of these units determines specific properties, primarily the peculiar behavior of the dilatometric curve of the series of glasses and the dependence of electrical resistance on composition.

The results of the calculations of ion concentrations and the structural-chemical composition of the glasses, based on Müller's ion-atom valence hypothesis [6], are presented in Table 1.

Table 1. Ion concentration and structural-chemical compositions of glass

Glass compositions, Mol %	Ion concentration, mol/sm ³				Structural - chemical composition, mol %					
	[Pb ²⁺]	[Mn ²⁺]	[Mn ⁴⁺]	[B ³⁺]	Pb(BO _{4/2}) ₂	MnO _{4/2}	Pb ²⁺ Pb ²⁻ O _{4/2}	BO _{3/2}	Mn(BO _{4/2}) ₂	
Glass series xPbO*(60-x)MnO*40B ₂ O ₃										
50 PbO*50MnO*40B ₂ O ₃	19.06	2.54	1.25	30.48	66.7	3.3	16.7	-	13.3	
40 PbO*20MnO*40B ₂ O ₃	15.86	5.28	2.64	31.74	53.0	6.7	13.3	-	26.6	
30 PbO*30MnO*40B ₂ O ₃	12.53	8.34	4.17	33.44	40.0	10.0	10.0	-	40.0	
20 PbO*40MnO*40B ₂ O ₃	8.34	11.13	5.56	33.48	27.7	13.4	6.6	-	55.3	
10 PbO*50MnO*40B ₂ O ₃	4.25	14.19	7.09	34.07	13.3	16.7	3.3	-	66.7	
Glass series xPbO*(50-x)MnO*50B ₂ O ₃										
40 PbO*10MnO*50B ₂ O ₃	15.06	2.50	1.24	37.64	77.5	3.2	-	6.5	12.8	
30 PbO*20MnO*50B ₂ O ₃	12.06	5.33	2.68	40.19	56.2	6.6	-	12.7	24.9	
20 PbO*30MnO*50B ₂ O ₃	8.28	8.28	4.14	41.44	36.4	9.0	-	18.2	36.4	
10 PbO*40MnO*50B ₂ O ₃	3.25	11.07	5.53	41.53	15.0	11.5	-	26.2	47.0	
Glass series xPbO*(40-x)MnO*60B ₂ O ₃										
30 PbO*10MnO*60B ₂ O ₃	11.12	2.47	1.12	44.55	48.7	2.4	-	38.1	10.8	
20 PbO*20MnO*60B ₂ O ₃	7.64	5.09	2.54	45.86	36.5	5.2	-	42.3	20.3	
10 PbO*30MnO*60B ₂ O ₃	4.01	8.01	4.01	48.09	15.4	7.7	-	46.2	30.7	

The dependence of electrical resistance values (I_{gp}) on composition varies significantly (Figs. 1, 2, 3).

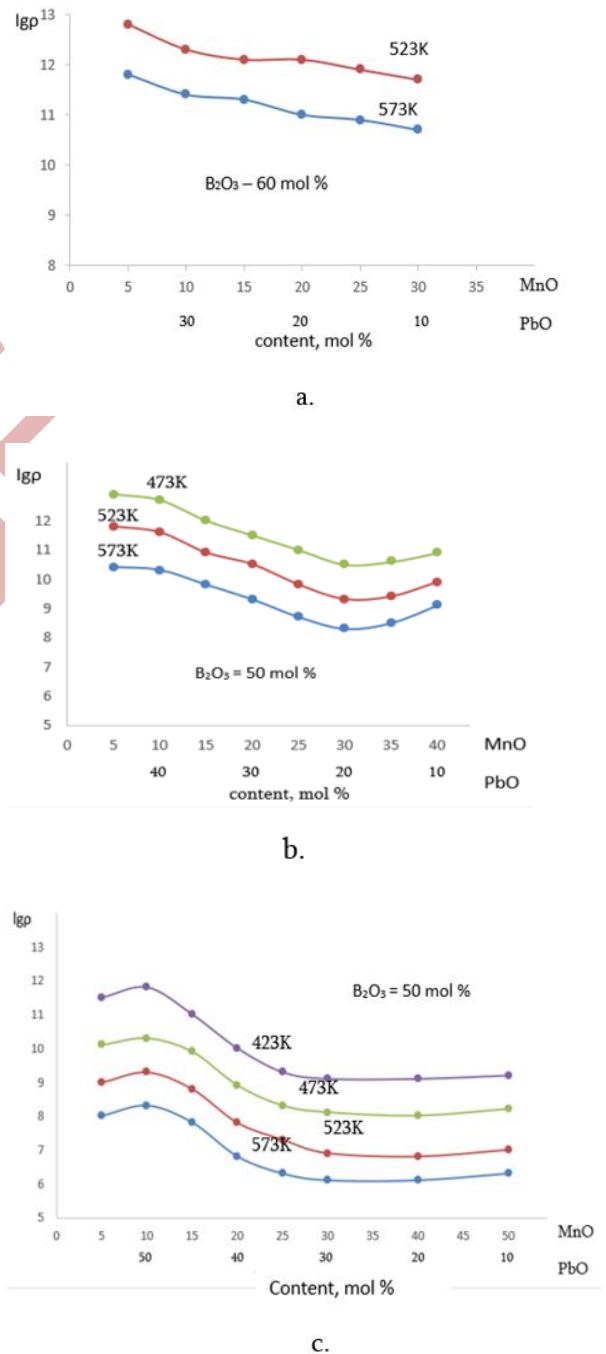


Fig. 1. a,b,c. Dependence of electrical resistance values (I_{gp}) on composition

The highest I_{g_p} values are found in glasses with $B_2O_3=60$ mol% (Fig. 1a), while the lowest values are found in glasses with $B_2O_3=40$ mol%. The glasses in the series $xPbO \cdot (50-x) \cdot 50B_2O_3$ exhibit intermediate I_{g_p} values. Increasing the MnO content at the expense of PbO in the series of glasses $xPbO \cdot (40-x) \cdot 60B_2O_3$ results in a gradual but negligible decrease in I_{g_p} values, often within the experimental error margins. The glasses in the series $xPbO \cdot (50-x)MnO \cdot 50B_2O_3$ exhibit a more significant decrease in electrical resistance up to the composition $20PbO \cdot 30MnO \cdot 50B_2O_3$. After reaching a minimum, I_{g_p} increases again.

The decrease in I_{g_p} due to the aforementioned substitution is similarly significant in the series of glasses with a B_2O_3 content of 40 mol%. However, the dependence curve shows an extremum corresponding to the composition $50PbO \cdot 10MnO$.

An attempt was made to correlate the obtained results with the data presented in the table.

First of all, it is necessary to consider the possible reason for the difference in I_{g_p} values depending on the B_2O_3 content. Calculations show that at 40 mol%, structural units of the $BO_{3/2}$ type are absent. This contradicts the information about the structures of borate glasses. According to this information, a complete transition from $BO_{3/2}$ to $BO_{4/2}$ is practically impossible. According to data [7], the maximum transition of three-coordinated boron to four-coordinated boron is possible only in the presence of oxygen suppliers such as R_2O and RO in amounts of 20 and 40 mol%, respectively. It can be extended by the formation of neutral structural units $MnO_{4/2}$ in the glass, which apparently manifests itself in glasses with $B_2O_3 = 40$ mol%.

In the absence of $BO_{3/2}$ and the possibility of the formation of lead structural units, one should expect the formation of structural units (s.u.) of the type $Pb^{2+}Pb^{2-}O_{4/2}$, which are not integrated into a single boron-manganese mesh, which, incidentally, can also be heterogeneous. This phenomenon can explain the presence of a maximum on the curve of the dependence of I_{g_p} on the glass composition with $B_2O_3=60$ mol% - the isolated lead structural units block the transfer of electricity by divalent ions.

Increasing the MnO content should lead to a decrease in the tendency of some Pb^{2+} to form lead

References

1. Miller M.K. Bulk Metallic Glasses: An Overview. Springer Science+Business Media, LLC, New York, NY, USA, 2008. – 242 p. – ISBN: 0387489207.

structural units, i.e., to a reduction in the degree of blocking. The ratio of lead and manganese-borate polar groupings with lead increases from 4.7 to 24.2, which leads to an increase in conductivity. The conductivity should be higher than indicated by the I_{g_p} values, but the matrix apparently does not exhibit homogeneity. Lead-borate and manganese-borate groups may differentiate.

Figure 1, corresponding to the glass composition $40PbO \cdot 20MnO \cdot 40B_2O_3$, still indicates the presence of distinct groupings but with smaller sizes, and shows a fairly uniform distribution of nanoscale inhomogeneities.

According to calculations, glasses with $B_2O_3 = 50$ mol% do not form lead compounds. However, they exhibit a polar component, which should result in higher I_{g_p} values compared to the previous series of glasses.

This phenomenon is also facilitated by the lower concentration of polar groups, which differentiate based on the type of cation. The accumulation of manganese-containing complexes, possibly of the type $Mn_2^{2+}MnO_4^{4+}$, can form combinations with $Mn^{2+}(BO_{4/2})$, leading to the formation of "chains."

Glasses with $B_2O_3 = 60$ mol% exhibit only small changes in I_{g_p} compared to the other two series. The presence of significant concentrations of nonpolar complexes leads to an increase in I_{g_p} values. Based on this, the glass should also be nanoinhomogeneous, consisting of lead-borate and manganese-borate complexes.

Conclusions

Electron microscopy shows that most of the examined glasses, in terms of their "texture," closely resemble amorphous (glassy) manganese nanocomposites, in which a direct relationship between structure and properties is observed. By adjusting the composition of these nanocomposites, materials with various properties can be obtained. This must be considered when introducing foreign nanoscale inclusions into such glasses by different means. The inherently inhomogeneous amorphous matrix should be regarded both as a nanocomposite and as a basis for creating amorphous matrix nanomaterials.

2. Movahedi B. (Ed.) *Metallic Glasses: Formation and Properties*. ExLi4EvA, 2016. – 170 p. – ISBN: 9535125125; 9535125117.
3. Cheishvili T. Estimation of the processes going on glass surface with new electrical measuring instrument with controlled parameters of temperature and pressure. - *Trans. of the GTU*, 2005, 4(458), p. 45-49.
4. Gordeladze V., Sarukhanishvili A. Enamel on the basis of manganese-containing carbonate ore. - *Trans. of the GTU*, 2005, 4(458), p. 34-37.
5. Karmakar B., Rademann K., Stepanov A. (ed.) *Glass Nanocomposites: Synthesis, Properties and Applications*. Elsevier Inc., 2016. — 392 p. — ISBN: 978-0-323-39309-6.
6. Müller R. L. *Solid State Chemistry and the Glassy State//Solid State Chemistry*. L.: Leningrad State University Press. 1965. P. 9-63.
7. W.M. Awad, Hanan Al-Ghamdi, Norah Ahmed alsaif, G. O. Rabiea. Physical, Structural, and Optical Characteristics of Manganese Ion-Containing Low-Melting Borate Glasses. August 2023. *Journal of Electronic Materials*, 52(1). DOI:10.1007/s11664-023-10649-7

ICMATSE 2024

Plasma Cutting of High-Strength Non-Metallic Fiber Composite Materials

Zurab Sabashvili

Georgian Technical University - Department of Metallurgy, Materials Science and Metal Treatment, 0175,
Tbilisi, Georgia,
z_sabashvili@gtu.ge
ORCID: 0000-0003-4766-2661

Tamar Loladze

Georgian Technical University - Department of Metallurgy, Materials Science and Metal Treatment, 0175,
Tbilisi, Georgia,
t.loladze@gtu.ge
ORCID: 0000-0002-3104-8459

Gela Otarashvili

Georgian Technical University - Department of Metallurgy, Materials Science and Metal Treatment, 0175
Tbilisi, Georgia,
otarashviligela04@gtu.ge
ORCID: 0009-0000-0096-4270

Nino Kenchiashvili

Georgian Technical University - Department of Metallurgy, Materials Science and Metal Treatment, 0175
Tbilisi, Georgia,
n.kenchiashvili@gtu.ge
ORCID: 0000-0002-3650-0990

Marina Kapanadze

Georgian Technical University - Department of Chemical and Biological Engineering, 0175,
Tbilisi, Georgia,
m.kapanadze@gtu.ge
ORCID: 0009-0009-7876-4485

Cite this paper as: Sabashvili Z., Loladze T., Otarashvili G., Kenchiashvili N., Kapanadze M. Plasma Cutting of High-Strength Non-Metallic Fiber Composite Materials. Int. Conf. Advanced. Mater. Sci&Eng. HiTech.and Device Appl. Oct. 24-26 2024, Ankara, Turkiye

Abstract. High-strength, highly modular polymeric fibers are used to produce materials with high toughness and impact strength at low density. One of such materials is a high-strength composite made of aramid fibers, which is used for making armour. The challenge lies in machining these materials. The low resistance of the cutting tool can lead to the separation of material layers, fiber tearing, and temperature increases in the cutting area, resulting in thermal destruction of the matrix. To address this, plasma arc-cutting technology was developed to avoid splitting and destruction of the material. The material was secured between two water-cooled copper plates, and a water jet was sprayed into the cutting area. This ensured that the cutting surface remained monolithic, easily machined, and free from destruction. Studies were conducted for both air plasma arc cutting and cutting in superheated water vapour.

© 2024 Published by ICMATSE

Introduction

Modern industries widely use high-strength non-metallic fiber composite materials. These materials consist of two or more components combined into a single monolithic structure,

whose physical and mechanical properties differ from those of each constituent component. High-strength, highly modular polymeric fibers are used to produce these materials, ensuring toughness and impact strength at low density. Mechanical processing of such materials is common in production. However, this treatment often results in low performance and, in many cases, destruction of the material.

The research goal was to develop and explore plasma cutting techniques for high-strength aramid fiber composites. Para-aramids, also known as “Kevlar” and developed by DuPont, are used for manufacturing armored products, such as body armour. The material withstands temperatures up to 430°C, but begins to break down above this temperature. Prolonged exposure to ultraviolet rays and moisture can degrade the material properties. Para-aramids are characterized by low density, high mechanical and thermal strength, and tear strength ranging from 2800 N/mm² to 5500 N/mm², depending on the manufacturing brand. The decomposition temperature of the material depends on the heating rate and the duration of exposure to heat. At temperatures above 150°C, the strength of Kevlar decreases; for instance, at 160°C for over 500 hours, the tensile strength decreases by 10-20%, and at 250°C, Kevlar loses 50% of its strength in 70 hours [1,2,3]. Additionally, aramids are easily flammable. The main goal was to solve the aforementioned problems when developing the plasma arc cutting technology.

Results and discussion

In the initial stage of the experiment, the drawbacks of mechanical cutting high-strength fibrous composite materials made of Kevlar were confirmed. During mechanical cutting, the following shortcomings were revealed:

- Poor productivity;
- High cost associated with frequent failure of mechanical cutting tools;
- Destruction of the cutting surface;
- Breakage of the surface film of a workpiece causing damage to the monolith and resulting in a loss of its properties.

To develop plasma arc cutting technology, the problem of burning aramid fibers in oxygen

needed to be solved. References indicate that at low concentrations of oxygen, fiber burning occurs briefly, and the flame dies quickly. On one hand, it might be possible to solve the problem by selecting a plasma-forming environment that does not contain oxygen. However, from an economic point of view, using inert gases, for example, was unprofitable. Therefore, the first cycle of the study was conducted using compressed air, and the second cycle using water vapor. Fiber burning was observed in both cycles.

For plasma arc cutting in compressed air, an indirect plasma torch with a plasma arc of 10 kW was used. The technical parameters of the power supply are provided in Table 1.

Table 1. Power supply electrical parameters

Parameters	Magnitude
No-load voltage, U_{xx}, V	360
Nominal operating voltage, U, V	220
Nominal operating current, I, A	45
Power consumption from the electrical network, kVA	16,2

During the first cycle of experiments, it was found that at the maximum cutting speed, the plasma arc flame was sucked into the cutting cavity, which contributed to the burning of fibers. The burning process lasted for a few seconds, but even in such a short period, it caused an increase in the cutting width, the detachment of material layers, and the tearing of fibers. The sucking of the flame into the cutting cavity at maximum speed can be explained by the small angle (30°) between the flame and the workpiece surface. During the experiments, it was determined that at an angle of 90°, no flame was sucked into the cutting cavity.

Since the material loses its mechanical properties when heated to temperatures above 250°C and its layers tend to separate, it is essential to prevent overheating near the cutting zone. The solution to these problems is as follows: two copper plates, each 6 mm thick and 8 cm wide, were used. Their length matched

the length of the workpiece. Grooves were cut along the entire length on one side of both plates to allow water to be supplied for cooling the workpiece's surface. To prevent delamination, the material was placed between the copper plates with the grooved sides facing the material and secured with mechanical clamps. Additionally, an extra stream of water was directed into the cutting cavity, completely preventing the ignition of the fibers.

In plasma arc cutting using the proposed technical solutions, the process is accompanied by the melting of the material. The cutting surface has a molten, monolithic appearance, which is easily machined, and no separation or destruction of the material occurs.

The second study cycle was conducted using superheated water vapor as a plasma-forming medium. Previous studies have shown the following advantages of using water vapor compared to compressed air [4], including:

- High plasma redox potential;
- Higher values of thermophysical parameters create excellent conditions for converting arc electric energy into thermal energy and maximizing its usage;
- The increased electric field intensity of the plasma arc in the water vapor medium allows for the generation of the required arc power at a reduced current intensity compared to compressed air;
- The possibility of conducting the plasma cutting process at high pressure, which also allows for reducing arc current;
- The reduction in current value increases the service life of the cathode.

It is known that a layer of plasma-forming gas of a certain thickness forms around the arc, providing thermal insulation from the nozzle walls. In the case of water vapor, the dissociation of hydrogen consumes a large amount of heat, providing intensive cooling of the arc's periphery. Additionally, the presence of a radial velocity component in the gas flow, directed into the arc column, enhances thermal compression of the arc column. This intensifies the deionization of its peripheral region,

contributing to the elongation of the arc and increasing the arc voltage. The increased arc voltage allows generating the required power at lower currents than with compressed air. Both the pressure and temperature of the plasma-forming medium influence the increase in voltage [5]. Superheated water vapor was used in the experiments because it contains no moisture. Moisture evaporates at temperatures above 125°C, and there is no condensation in the superheated vapor caused by the heated walls of the superheater tank.

Comparative studies were conducted for both plasma-forming environments. Table 2 shows the values of the main technological parameters.

Table 2. Technological Parameters

Water Vapour				Compressed Air			
I,A	U,V	P,at	t°C	I,A	U,V	P,at	t°C
40	242	3	160	48	210	3	-
40	246	4	170	45	220	4	-
36	248	5	180	-	-	-	-
30	254	6	190	-	-	-	-

The data in Table 2 confirm the aforementioned advantages of water vapour. The plasma-cutting surface, in this case, also exhibited a molten monolithic appearance. The plasma cutting speed was nearly identical in both cases.

Naturally, indirect plasma torches were used for plasma cutting. The optimal design was found to be a nozzle with a channel diameter of 2 mm and a height of 18 mm.

Based on the accepted technological solutions, two designs of plasma cutting units were developed: one for compressed air and the other for superheated water vapor.

For compressed air, the plasma torch is cooled by running water. At the inlet of the plasma torch, part of the water is supplied to the cutting cavity, while the rest is drained from the plasma torch into the copper plates. A valve is installed at the bottom of the bath to drain the water.

In the case of superheated water vapor, the plasma torch is cooled with compressed air to prevent the cooling and condensation of vapor. Water is fed into the cutting cavity and copper plates from the central water supply.

Figure 1 presents the system communication connection diagram, illustrating the developed technological solutions for compressed air.

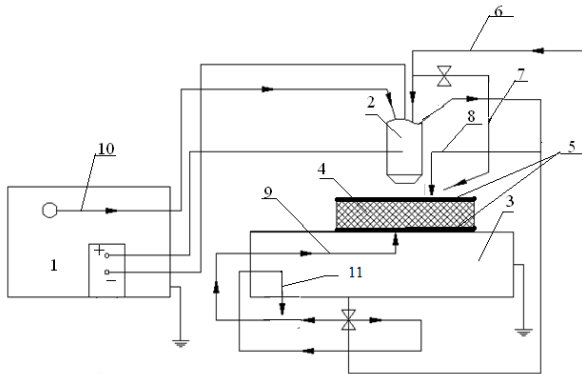


Fig. 1. Plasma cutting machine communication circuit

1. Power supply; 2. Plasma torch; 3. Bath; 4. Material to be cut; 5. Copper plates; 6. Communication for supplying cooling water to the plasma torch; 7. A

References

1. Mustafa Ertekin, Aramid fibers: Fiber Technology for Fiber-Reinforced Composites, 2017, pp.153-167. DOI:10.1016/B978-0-08-101871-2.00007-2 https://www.researchgate.net/publication/317336884_Aramid_fibers
2. ARAMID FIBER CHARACTERISTICS. <http://www.aramid.eu/characteristics.html>
3. Aramid Fiber (Kevlar / Twaron) – Properties and Applications. (2015.10.15). <http://www.azom.com/article.aspx?ArticleID=1384>
4. Sabashvili Z.V., Tavkheldze D.D., Mchedlishvili Z.T.. Water vapor as a plasma-forming medium. Problems of mechanics. International Scientific Journal N4(21)/2005 Pp. 79-83. file:///C:/Users/TATA/Desktop/irodonaia,+1.pdf
5. Z. Sabashvili, T. Loladze, N. Kenchiashvili. Effect of temperature and water vapor pressure on surface quality of the cutting during water vapor plasma cutting. Book of abstracts International conference "Innovative Technologies in Metallurgy and Materials Science". Georgian Technical University. Tbilisi, Georgia. 16-18 July, 2015 .p. 70 – 71. <https://gtu.ge/ctmf/pdf/conferences/file1.pdf>

stream of water fed into the cutting area; 8. & 9. Communication of water supply to copper plates; 10. Communication for supplying compressed air to the plasma torch.

Conclusions

The technology for plasma arc cutting of non-metallic fibrous composite high-strength materials, particularly aramid fibers, in both compressed air and superheated water vapor environments, has been developed. The electrical parameters of the power source are selected to ensure that, in addition to providing the required power for the plasma arc, the maximum working life of the plasma torch is achieved. The application of this technology eliminates the burning of fibers and produces a molten, monolithic cutting surface that is easily machined and not prone to destruction.

Silica Nanoparticles and CVD Graphene for Hydrophobic Modified Surfaces

Majid S. Al-Ruqeishi

*Physics Section Department of Mathematical and Physical Sciences, College of Sciences and Arts,
University of Nizwa, P.O. Box 33, P.C. 616, Nizwa, Oman,
majiduon@unizwa.edu.om
ORCID: 0000-0003-1626-8661*

Balqis Al-Yaqoubi

*Physics Section, Department of Mathematical and Physical Sciences, College of Sciences and Arts,
University of Nizwa, P.O. Box 33, P.C. 616, Nizwa, Oman,
6674836@uofn.edu.om*

Cite this paper as: Al-Ruqeishi, M., Al-Yaqoubi, B.. Silica Nanowires and CVD graphene for Hydrophobic modified surfaces. Int. Conf. Advanced. Mater. Sci. & Eng. HiTech. and Device Appl. Oct. 24-26 2024, Ankara, Turkiye

Abstract. Hydrophobic surfaces are utilized to reduce wetting behavior of surfaces. To repel water, material with such a property can be exploited on surfaces of buildings near humid areas like or even in the inner side of water pipelines or for water/oil. Particularly, hydrophobic surfaces are in great demand for a variety of applications due to their outstanding attributes such as environmental protection and solar energy harvesting applications. Surface free energy, SFE, and texture are two crucial surface parameters that play a significant role in determining hydrophobicity. Low surface energy and surface texture with micro/nano pillars provide advantages for improving surface hydrophobicity. In this presentation, the utilization of silica nanoparticles, part 1, and FL graphene, part 2, as coating layers will be explored to examine the influence of surface texture and low SFE, respectively.

Keywords: hydrophobic surfaces, Contact angle, Self-cleaning, silica nanoparticles

© 2024 Published by ICMATSE

1.1 Silica nanoparticle (Re-engineering the surface)

Surface wetting is the result of physical contact between two phases that creates interactions between a solid and a liquid at the solid-liquid interface. At the most basic level, these interactions are atomic in nature and reflect contributions of gravitational, polar, electrostatic, and intermolecular energy [1]. When a liquid droplet comes into contact with a solid surface, it will take on a geometric shape that reduces the overall energy of the solid-liquid system because of these energy contributions [2]. The surface free energy (SFE), which is the reversible work necessary to produce a unit of fresh surface area [3], is the pertinent energy parameter in this case. Surface tension and SFE are interchangeable for a liquid. The SFE is known as the solid-liquid interfacial energy when the "new surface" that is produced is the interfacial surface area between the solid and liquid. A thermodynamic energy equilibrium can be used to determine the shape of a liquid droplet contacting a solid surface based on these energy considerations. The angle between the liquid surface free energy and

the solid/liquid interfacial free energy is known as the water contact angle, or WCA. Although any liquid can be used in practice, water is a common liquid for contact angle measurements. We must examine the connection between surface energy and surface roughness and surface wettability in order to comprehend surface hydrophobicity. The well-known fundamental equation that characterizes these energy interactions and is applicable to smooth and level surfaces is Young's equation. Surfaces with $\theta > 90^\circ$ are hydrophobic, but those with $\theta < 90^\circ$ are hydrophilic when water droplets are present. In this study we report the effect of Silica nanoparticles (SiO₂ NP) and reduced Graphene oxide (rGO) on the surface wettability nature. The first part will focus on the intrinsic effect of SiO₂ NP on cement blocks hydrophobicity and in the second part rGO/galss substrate will be utilized to test the surface morphology effect on hydrophobicity and its relation to SFE.

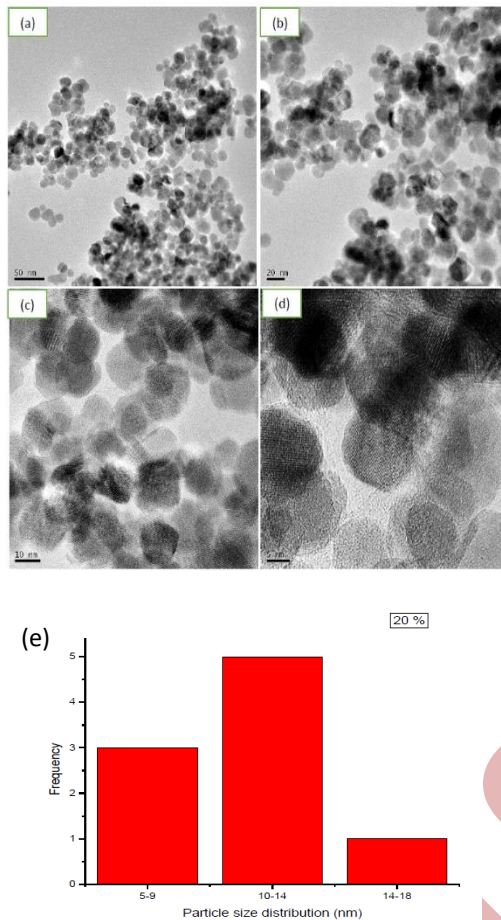


Figure 1. (a-d) TEM images of hydrophobic silica nanoparticles prepared by using 50 ml of SiO₂ NPs solution in 470 ml of distilled water. (e) The average particle size of silica nanoparticles distribution.

1.2 Experimental work Cement block

A 1110 g of washed sand was mixed with 550g of cement from Raysut Cement Company, and then 150 mL of 1000 ppm nano-silica solution is added to 300 ml water and mixed very well for 5 minutes. After that the cement block was kept outdoor for naturally dry and hence, the block was immersed in the same nanosilica solution and soaked for 30 minutes. Finally, the block left to dry naturally outdoor again.

1.3 Results-1

1.3.1 TEM analysis of silica nanoparticles

TEM was used to examine the morphology of the silica nanoparticles that were synthesized. Semi-

spherical nanoparticles were evident in every block sample, as shown in Fig. 1(a-d). These particles are depicted in TEM pictures without the strong aggregation and accumulation effects seen in SEM data. Furthermore, as illustrated in Fig. 1(e), the typical particle size distribution falls between (5 and 18 ± 2 nm).

1.3.2 Cement block surface modification results.

High WCA with a water droplet surface, $\theta > 90^\circ$, is revealed by the optical picture of the treated block surface displayed in Fig. 3 (a and b). When the block surface is shaken, water droplets immediately fall off. Numerous optical pictures of WCA were acquired at various periods in order to verify the stability of the block surface change. Block WCA is always $\theta > 90^\circ$, as shown in Fig. 2 (c-e). WCA was shown to decrease after 65 days, which could be related to the unstable silica nanoparticles at the block surface. Here, we propose that it might become more stable by combining these nanoparticles with a better binding material.

Surface morphology, roughness, and water contact angles (WCAs) were used to describe the consequences of these surface alterations. The resultant WCAs for cement block are $148^\circ > \theta > 90^\circ$, which make water runs off easily without further cleaning as shown in Fig2 (a).

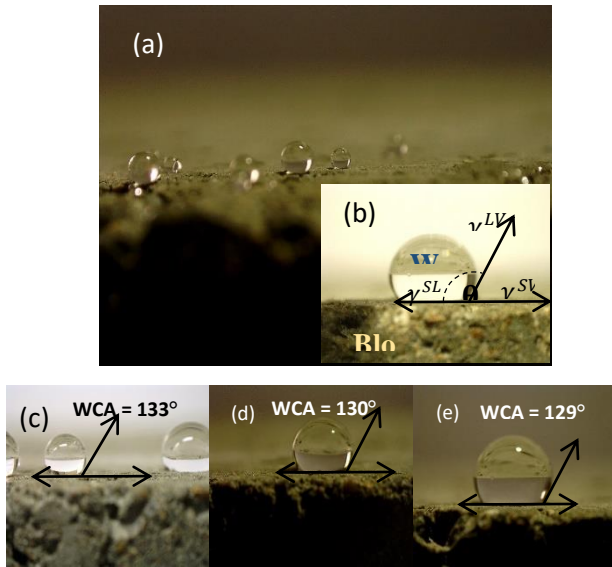


Figure 2 (a) water droplets over treated cement block surface and (b) water droplet surface tension energy diagram and the surface free energy conurbations. (c-e) Optical images showing the initial wetting behavior of cement block after 1h, 1 day and 3 days from preparation respectively.

2.1 Hydrophobicity of rGO

Five rGO-coated glass samples (rGO/SiO₂) were prepared in which the rGO was stuck in the glass surface with a binding material (polymer). The contact angle was measured by placing a water droplet on the surface of rGO/SiO₂ using a dispensing needle. These tests were performed at a room temperature. To find the contact angle at the solid-liquid interface, a tangent line was marked at the droplet's edge and the angle formed with the baseline was measured. Additionally, the free surface

energy was calculated using an empirical equation for surface free energy.

Table 8: Raman Spectroscopy of GO and rGO sheets.

	Graphene oxide	Reduced graphene oxide
Bands	D band	G band
Graphite		
Raman shift (cm ⁻¹)	1350	1530
Intensity	1324	1599
GO-1		
Raman shift (cm ⁻¹)	1350	1600
Intensity	1344.04	1595.04
GO-2		
Raman shift (cm ⁻¹)	1400	1650
Intensity	1366.34	1617.34
rGO-1		
Raman shift (cm ⁻¹)	1340	1592
Intensity	1.46840	1.37583
rGO-2		
Raman shift (cm ⁻¹)	1340	1592
Intensity	0.48457	0.45547

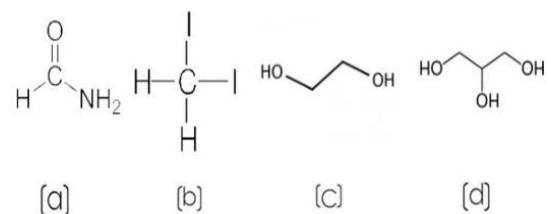


Figure 3: The structure of polar liquids: (a) formamide, (b) diiodomethane, (c) ethylene glycol, and (d) glycerol.

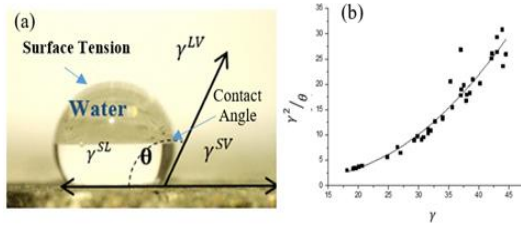


Figure 4. (a) Schematic drawing of a water droplet and the balance of surface tensions at three-phases contact line. (b) The surface free energy, γ , is related to ϑ by plotting γ^2/ϑ with γ .

Raman spectroscopy results we utilized to make sure the reduction of GO to rGO. Table (1) summarizes the Raman spectrum results. The variety of degrees of disorder, defects, and the chemical modification introduced during the oxidation and reduction processes may effect the peak intensity and location

2.2 Graphene SFE and WCA measurements

The contact angle of water was measured to determine whether graphene layers were wettable on silicon or on copper and graphene oxide substrates. It was discovered that the contact angle between the water and the G/Si substrate was around 87° . The G/Cu substrate's temperature is then around 93° . The oxidized and isolated graphite that made up the GO substrate had a WCA of about 66.81° , indicating that GO had hydrophilic properties. Additionally, different organic liquids' wettability was investigated. As seen in Fig. 3, these tested liquids are polar organic.

The graphene substrates show varying wettability strengths due to distinct polarity groups. Because of their functional groups, the liquids are wettable on GO surfaces. To invitigate the relation between WCA and surface free energy lets start with Young's condition where WCA or θ is known as in Equation (1):

$$\gamma_s = \gamma_{sl} + \gamma_l \cos \theta \quad (1)$$

By using Equation (2) the adhesion work of solid-liquids interface has been characterized Invalid source specified.:

$$W_{sl} = \gamma_s + \gamma_l - \gamma_{sl} \quad (2)$$

And by combining Equation 1 and 2 in equation (3), we get:

$$W \text{ of adhesion} = -\gamma_l(1 + \cos \theta) \quad (3)$$

From Table 1 and previous equations, the adhesion work of graphene liquids interface can be measured

and represented in Table 2. The surface free energy of graphene can be calculated by using Neumann's model. The contact angle between the solid and liquid is given as follows:

$$W \text{ of adhesion} = 2e^{-\beta(\gamma_l - \gamma_s)^2} \sqrt{\gamma_s \gamma_l} \quad (4)$$

Where β is the constant coefficient of a specific surface, which equal 0.00017 for graphene. Then by using fowkes method to find the dispersive surface energy of solid:

$$W \text{ of adhesion} = 2 \sqrt{\gamma_s^d \gamma_l^d} \quad (5)$$

The dispersive components of liquids and solids are denoted by γ_l^d and γ_s^d . According to the Fawkes technique, the dispersive and polar components of the total surface energy for liquids and solids are added together, as demonstrated by Equations 6 and 7.

$$\gamma_s = \gamma_s^d + \gamma_s^p \quad (6)$$

$$\gamma_l = \gamma_l^d + \gamma_l^p \quad (7)$$

The relation between $\frac{\gamma_s^2}{\theta}$ versus γ_s is illustrated in Fig 6. The following relation can be deduced from the graph in Fig 5.

$$\gamma_s^2/\theta = A + B\gamma + C\gamma^2$$

$$\gamma^2(1 - \theta C) - B\gamma\theta - A\theta = 0$$

$$\gamma = \frac{B\theta - \sqrt{(B\theta)^2 + 4A(1 - \theta C)\theta}}{2(1 - \theta C)}$$

$$\gamma = \frac{B\theta - \sqrt{(B^2 - 4A)\theta^2 + 4A\theta}}{2(1 - \theta C)}$$

$$\gamma = \frac{-0.57113 - \sqrt{0.14407\theta^2 + 18.81324\theta}}{2(1 - 0.00968\theta)}$$

$$A=4.70331 \quad B= -0.57113 \quad C=0.00968$$

$$\frac{d\theta}{d\gamma} = \frac{(1 - 0.00968\theta)(-1.05618 - \frac{0.188 + 18.8132}{\sqrt{0.14407\theta^2 + 18.81324\theta}} + (-0.00968 - 0.046\sqrt{0.14407\theta^2 + 18.81324\theta}))}{4(1 - 0.00968\theta)^2}$$

$$\gamma_s^2(1 - 0.00968\theta) + 0.571\theta \gamma_s - 4.703=0$$

Finally, the empirical relation can be derived as shown below:

$$\gamma = x = \frac{-0.571\theta \pm \sqrt{(0.571\theta)^2 + 18.81(1 - 0.00968\theta)\theta}}{2(1 - 0.00968\theta)} \quad (8)$$

γ , in the empirical Eq (8) is related to θ , which is the water contact angle with the horizontal line. Next, using Eq. (8), the surface free energy was determined for the different substrates and liquids shown in Table 2.

Table 9 Adhesion work and surface free energy for different Gr/substrates under different liquids tests.

liquids	substrate	Contact angle θ	work of adhesion (Wad) (mJ/m ²)	γ_s (mJ/m ²) \pm error	γ_s^2 / θ	γ_s^d (mJ/m ²)
water	Si	81	83.2	44.06 \pm 1.05	23.96	82.54
	Cu	85	78.24	44.33 \pm 1.02	23.11	72.98
	Gr/Si	87	68.2	44.96 \pm 0.93	23.23	55.45
	Gr/Cu	93	75.7	44.49 \pm 0.99	21.28	68.31
	GrO	66.8	104.4	61.8 \pm 0.004	57.1	44.0
Ethylene glycol	Si	82	54.68	29.13 \pm 0.38	10.35	25.77
	Cu	83	53.84	28.87 \pm 0.15	10.05	24.98
	Gr\Cu	85	52.18	27.58 \pm 1.75	8.95	23.47
	Gr\Si	89	48.83	28.6 \pm 0.39	9.21	20.55
Glycol	Gr\Si	91	62.29	33.86 \pm 1.78	12.59	28.36
	Cu	81	73.3	32.95 \pm 1.99	13.40	39.27
	Gr/Cu	90	63.4	33.75 \pm 1.81	12.65	29.38
	Ni	88	65.61	33.56 \pm 1.85	12.79	31.46
Formamide	plastic	70	85.08	32.13 \pm 2.18	14.74	52.91
	Gr\Si	90	58.2	26.36 \pm 2.89	7.72	36.65
	Cu	80	68.30	25.27 \pm 3.26	7.98	50.48
	Gr/Cu	89	59.21	26.26 \pm 2.92	7.74	37.94
	Ni	80	68.30	25.27 \pm 3.26	7.98	50.48
blastic		79	69.30	25.17 \pm 3.29	8.01	51.97

The hydrophobicity of graphene layers is indicated by the fact that both Cu and Si-coated substrates raise

References

1. Kim, K.-S., Lee, H.-J., Lee, C., Lee, S.-K., Jang, H., Ahn, J.-H., . . . Lee, H.-J. (2011). Chemical Vapor Deposition-Grown Graphene: The Thinnest Solid Lubricant. *ACS Nano*, 5107–5114.
2. Kwok, D. Y., Ng, H., & Neumann, A. W. (2000). Experimental Study on Contact Angle Patterns: Liquid Surface Tensions Less Than Solid Surface Tensions. *J. Colloid Interface Sci*, 323–328.
3. Gao, L., & He, J. (2013). Surface hydrophobic co-modification of hollow silica nanoparticles toward large-area transparent superhydrophobic coatings. *Journal of Colloid and Interface Science*, 396, 152–159. <https://doi.org/10.1016/j.jcis.2013.01.014>
4. Rohman, N., Mohiuddin, T., & Al-Ruqeishi, M. S. (2023). Surface free energy of graphene-based coatings and its component elements. *Inorganic Chemistry Communications*, 153, 110855. <https://doi.org/10.1016/j.inoche.2023.110855>.

the static water contact angle, see Table 2. There are a number of possible causes for this growth, including: First, when graphene reaches a few layers of sheets between 4 and 9, it becomes hydrophobic. Second, the graphene coating is the cause of the increased surface roughness, which raises the solid's surface area and geometrically improves its hydrophobicity. Third, waterproof behavior results from the surface installation of air around the liquid-solid boundary. The surface energies of GrO, Gr/Si and Gr/Cu were determined. Their values found to be about 61.8 mJ/m², 44.96 mJ/m² and 44.49mJ/m² respectively. The results show that SFE of GrO graphene oxide is the highest because of its components and synthetic groups as it can be seen in Fig. 4.

4. Conclusion

Conclusion-1

Silica nanoparticles with diameters (5 to 18 \pm 1 nm) to convert a normal glass and cement block surfaces to hydrophobic or water repellent. A smart hydrophobic cement block was prepared by well mixed silica nanoparticle solution with cement block ingredients. This make cement block intrinsically hydrophobic for a long period of time with WCA $\theta > 90^\circ$. Graphene surface free energies over different substrates when put in contact with liquids were measured and calculated using Neumann's method. The results showed that a graphene oxide sheet is hydrophilic and a graphene on copper or silicon sheets were hydrophobic. The experiment showed the WCA of Gr/Cu and Gr/Si are 93^o and 87^o respectively. In addition, their surface energy are 44.96 mJ/m² 44.49mJ/m² respectively, according to fowkes method, while the surface energy of GrO was found to be 61.8 mJ/m².

Electrochemical synthesis of Oleic Acid coated Magnetite nanoparticles from water/ethanol media

Nino Makhaldiani

Georgian Technical University, Department of Chemical and Biological Technologies, 0160, Tbilisi,
Georgia,
info@gtu.ge
ORCID: 0009-0001-2068-5110

Marine Donadze

Georgian Technical University, Department of Chemical and Biological Technologies, 0160, Tbilisi,
Georgia,
info@gtu.ge
ORCID: 0009-0003-5505-7274

Makhaldiani, N., Donadze, M. Electrochemical synthesis of Oleic acid coated Magnetite nanoparticles from water/ethanol media Int. Conf. Advanced. Mater. Sci. & Eng. HiTech. and Device Appl. Oct. 24-26 2024, Ankara, Turkiye

Abstract. Magnetite nanoparticles, especially magnetite (Fe_3O_4) and maghemite ($\gamma\text{-Fe}_2\text{O}_3$), have versatile applications as ferrimagnets. Magnetic particles of iron oxides are less toxic, biocompatible and more often used in the medical field. Magnetic fluids are used in hyperthermia (an alternative way to treat tumor cells), to transfer therapeutic drugs under the action of a magnetic field, as a contrast liquid in magnetic resonance imaging, as well as in quantum computers, in the ecological direction in the field of cleaning water and soil from organic pollutants, it is a good adsorbent, separator and catalyst. We used the electrochemical synthesis method to obtain magnetic nanoparticles. In earlier studies, we synthesized nanoparticles at 45°C on a rotating cathode in a two-layer bath, where we used hexane as an organic solvent, which practically evaporated after 1 hour of synthesis [1-3].

From the ecological point of view of the toxicity of the process, the organic solvent hexane was replaced by water with an alcohol mixture. Nanomagnetite obtained under different conditions is characterized by various instrumental research methods and Instruments, namely: Zeta Sizer Malvern, SEM, TEM, XRD and FTIR.

Keywords: Magnetite, nanoparticles, Oleic Acid, electrochemical synthesis

© 2024 Published by ICMATSE

Introduction

Interest in magnetic nanoparticles is growing due to their versatile applications. Co-precipitation, hydrothermal, strip-gel, microemulsion, microwave, laser pyrolysis, photochemical, ultrasonic, air-phase and electrochemical methods are used to obtain magnetic nanoparticles. Electrochemical synthesis is the simplest and safest among them. By using electrical energy, electrolyte, surfactant and creating appropriate conditions (current density, voltage, temperature), it is possible to obtain magnetic nanoparticles with controlled size and shape. The process is described in many articles, the electrolyte of different composition is used everywhere, the material of anode and cathode is

different, as well as acidity, current density, synthesis temperature and others.

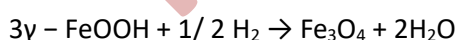
Electrochemical synthesis mainly takes place in a two-electrode or three-electrode electrochemical cell, in galvanostatic (constant current) or potentiostatic (constant potential) mode. Other modes - cyclic voltammetry, impulse potential and impulse current - are often found in research.

The application of a pulsed current, or potential, dramatically reduces particle aggregation and the number of bubbles formed during water electrolysis. The formed particles are dispersed in the electrolyte and become charge carriers due to contact with the ions in the solution. When the

electric field near the surface of the electrode increases, the increased forces of electrophoresis and electroosmosis act on the particle, as a result of which the particles collide with each other as a result of rapid displacement and undergo aggregation. During impulse current and impulse potential, the process stops, and therefore the probability of collision and aggregation decreases. The articles more often describe the electrochemical preparation of magnetite nanoparticles in galvanostatic and potentiostatic mode.

In the galvanostatic mode, the particle size significantly depends on the current density. As Fajarro describes, the particle size (12-25 nm) increases with increasing current density, however, in his study, no surfactant was used in the synthesis, and to prevent aggregation, the current density is generally low and 100-500 $\mu\text{A}/\text{cm}^2$ (0.01- 0.05 A/dm^2) will connect. In Cabrera's article, the electrochemical process takes place at a relatively high current density of 10-200 mA/cm^2 (0.1-2 A/dm^2), and with increasing current density, the particle size (25-27 nm) does not change significantly. At high current density, the influence of diffusion rate and Helmholtz layer can be neglected, while at low current density (low reaction rate) they have a significant influence [4]. Lozano and his colleagues conducted research under oxygen and nitrogen inflation conditions. In a nitrogen atmosphere, the electrolyte acquired a greenish color, which indicates the formation of iron hydroxide ($\text{Fe}(\text{OH})_2$), while the formation of magnetite (black color) was not observed. In an Erlenmeyer flask, the black color characteristic of the formation of magnetite is clearly visible in the oxygen environment [5].

Intensive recovery of hydrogen is actively taking place at the cathode, which, according to some authors, may be a condition for the formation of magnetite [6,7].



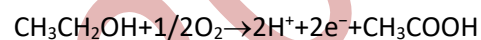
In the experiment conducted by Lozano, as a result of artificially inflating hydrogen in the environment of electrochemically formed hydroxide ($\gamma\text{-FeOOH}$), no magnetite was formed (checked with a diffractometer), which indicates that the hydrogen separated on the cathode comes out of the reaction zone and does not take a substantial part in the formation of magnetite. In the process of

electrolysis, intermediate products are formed, which can be clearly seen by the change in the color of the electrolyte, from transparent, brownish-reddish color to black.

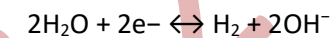
As can be seen from the study of Lozano and his co-workers, the diffractograms taken from 2 to 90 min confirm the formation of lepidocrite ($\gamma\text{-FeOOH}$), the magnetite peak formed after 4 min is quite low, and with time the lepidocrite peak decreases and the magnetite peak becomes more pronounced. After 30 min, only the peak characteristic of magnetite remains.

Based on the obtained results, they developed the mechanism of magnetite production by electrolysis:

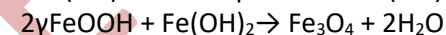
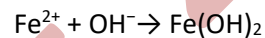
Anode



cathode



In the volume of the solution:



Finally, the topotactic transformation of iron divalent hydroxide and lepidocrite into magnetite [5].

Results and Discussion

Ferric sulfate ($\text{FeSO}_4 \cdot 7\text{H}_2\text{O}$) solutions of different concentrations (0.05, 0.8 and 1M) were prepared for electrochemical synthesis. Steel cathode (arc) and anode plate were prepared. Before electrolysis, the electrodes are subjected to cleaning with sandpaper, degreasing with ethanol, washing with distilled water, drying at 100°C and weighing before and after electrolysis. After 15 minutes of electrolysis, the strip obtained after 10 minutes of centrifugation (8000 rpm) was determined by the particle size. and zeta potential. Based on the theoretically and practically calculated mass of the obtained magnetite, the output (efficiency) of the process is calculated.

A 0.05-1 M iron sulfate ($\text{FeSO}_4 \cdot 7\text{H}_2\text{O}$, chemically clean) solution was prepared in different ethanol/water ratios (50/50, 40/60; 30/70; 20/80; 10/90 %). Different concentrations of oleic acid (0.5%, 1%, 1.5%) were added to each ratio. The dependence of the particle size on the current density and electrolysis temperature was determined. To obtain magnetite nanoparticles, we

used an iron anode (99.19% Fe, 0.75% Mn; 0.053% Cu) and an aluminum cathode-arc.

Based on our research, the water/ethanol ratio of -30/70 gives better results in terms of particle size and band stability when changing various parameters; 20/80; 10/90. The higher the amount of ethanol in the volume, the better the distribution of oleic acid throughout the volume (Figure 1.). To stabilize nanoparticles, we used oleic acid, which forms a bidentate bond with magnetite nanoparticles. The greater the amount of ethanol in the electrolyte, the better the distribution of oleic acid in the entire volume (Figure 2).

As can be seen from the figure, the size of the particle obtained in the strip obtained under the selected optimal conditions with 1% oleic acid content is twice as small as compared to 1.5% oleic acid, which can be explained by the excess of oleic acid (the length of the oleic acid molecule is 2 nm). 0.5% oleic acid fails to prevent aggregation.

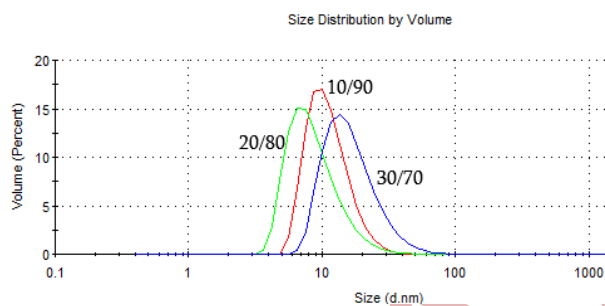


Figure.1 Magnetite particle size at different water/ethanol ratios (10/90; 20/80; 30/70) Electrochemical synthesis conditions: $T=45^{\circ}\text{C}$; $i=40\text{ A/dm}^2$; $C_{\text{FeSO}_4}=0.05\text{M}$; Oleic acid concentration 1%

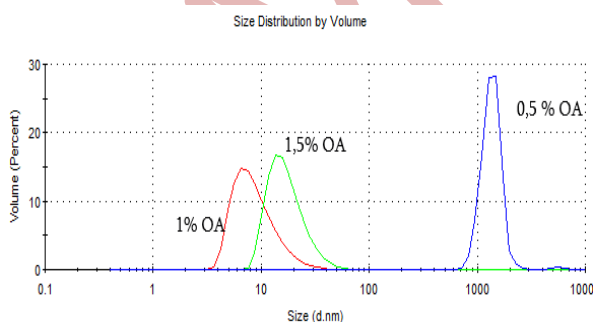


Figure.2 Magnetite particle size in the band obtained at 0.5-1.5% oleic acid concentration ($T=45^{\circ}\text{C}$; $i=40\text{ A/dm}^2$; $C_{\text{FeSO}_4}=0.05\text{M}$; water/ethanol ratio=20/80)

Based on the selected mode, we can conclude that 70 gives better results for dispersion in oleic acid solution; 80; A solution containing 90% ethanol.

45°C temperature is also better for dispersion, particle size inhibition and stabilization of oleic acid in solution. High current density (60 A/dm^2) turned out to be undesirable in terms of particle size, as current density increases, nucleation (predominance of seeds) increases, therefore, stabilization by oleic acid precedes aggregation and particle size increases. At 50/50 - 40/60% water/ethanol ratio, 0.5% oleic acid content, 25°C temperature and $1\text{M FeSO}_4\cdot 7\text{H}_2\text{O}$ concentration, non-stable (precipitates instantly) and polydisperse bands are obtained.

We selected the samples obtained under the best conditions for synthesis ($T=45^{\circ}\text{C}$; $i=40\text{ A/dm}^2$; Oleic acid concentration 1%, cathode rotation speed 600 rpm $C_{\text{FeSO}_4}=0.05\text{M}$) and analyzed them by scanning, transmission microscopy, infrared spectroscopy and by X-ray diffraction methods.

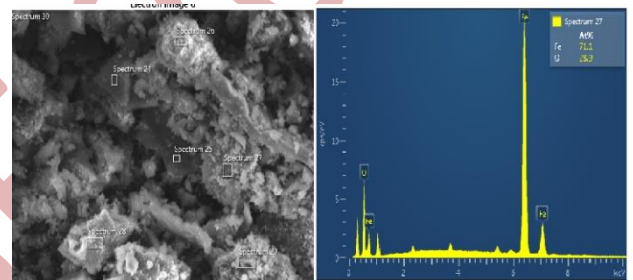


Figure 3. SEM-EDS Spectra of Fe_3O_4 nanoparticles

As can be seen from the elemental analysis, the composition of the obtained substance corresponds to the formula of magnetite.

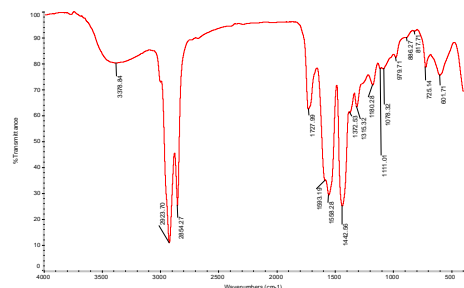


Figure 4. Fourier-infrared spectrum of Fe_3O_4 &1%OA

On the FT-IR spectrum, the spectrum of Fe_3O_4 modified with oleic acid shows a peak at 1727 cm^{-1} , characteristic of the vibration of the C=O bond, and two peaks at 1593 and 1558 cm^{-1} , corresponding to the asymmetric and symmetric vibrations of the carboxyl (COO-) group. Peaks at 2923 cm^{-1} and 2854 cm^{-1} correspond to asymmetric and symmetric vibrations of CH₂ groups, and 601 cm^{-1} and 510 cm^{-1} correspond to the Fe-O bond [8-9].

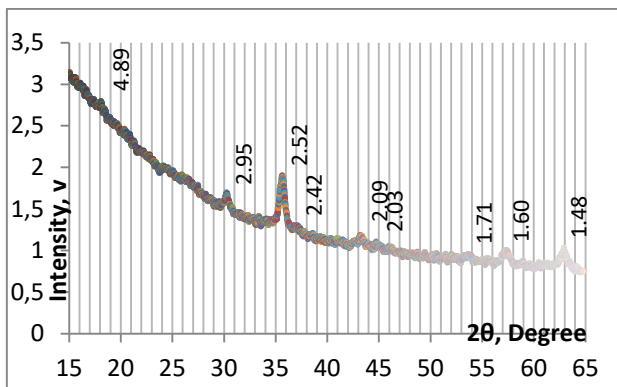


Figure 5. X-ray phase analysis of magnetite

In the X-ray phase diagram, the main phase coincides with the peaks characteristic of magnetite (ASTM 19-629).

The transmission electron microscope image of the sample obtained under specific conditions reveals the particle size ranging from 6 to 25 nm.

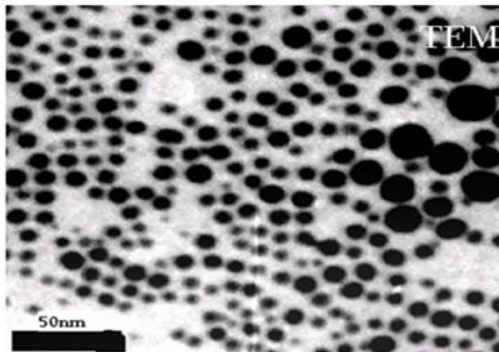


Figure 6. TEM image of Fe_3O_4 nanoparticles

Conclusion

We used a double-layer bath with a rotating cathode to obtain magnetite nanoparticles. We

References

1. S. Khutsishvili, P. Toidze, M. Donadze, M. Gabrichidze, N. Makhaldiani, T. Agladze, Structural Surface Features of Paramagnetic Multifunctional Nanohybrids Based on Silver Oleic Acid, *J of Cluster Sci.* (2021), pp1351-1359, doi.org/10.1007/s10876-020-01904-6
2. S. Khutsishvili, P. Toidze, M. Donadze, M. Gabrichidze, T. Agladze, N. Makhaldiani, Structural and Magnetic Properties of Silver Oleic Acid Multifunctional Nanohybrids, *J Annals of Agr. Sci* (2019), ISSN: 1512-1887
3. M. Donadze, N. Makhaldiani, Electrosynthesis of Nanomagnetite and Application for Purification of Phenol Previously Contaminated Water, *Advanced Polymer Structures Chemistry for Engineering Applications*, Appl. Acad. Press. 25. <https://dokumen.pub/advanced-polymer-structures-chemistry-for-engineering-applications-9781774913017.html>
4. L.Cabrera, S.Gutierrez, N. Menendez, M. P.Morales, P. Herrasti, Magnetite Nanoparticles: Electrochemical Synthesis and Characterization. *J Electrochim. Acta* (2008), pp 3436–3441.
5. I.Lozano, N.Casillas, C. P. de León, F. C. Walsh, P. Herrasti, New Insights into the Electrochemical Formation of Magnetite Nanoparticles, *J Electrochem. Soc.*(2017), pp 184–191.
6. S. Franger, P. Berthet, J. Berthon, Electrochemical synthesis of Fe_3O_4 nanoparticles in alkaline aqueous solutions containing complexing agents, *J Solid State Electrochem*, (2004), pp 218–223, DOI 10.1007/s10008-003-0469-6.

used oleic acid dispersed in hexane as an organic solution, and iron sulfate dissolved in deionized water was the electrolyte. In this case, in order to simplify the process and improve it from an ecological point of view, instead of an organic solvent (hexane), we used a mixture of ethanol and water in which iron sulfate was dissolved.

The process was simplified and both the synthesis and the stabilization process were carried out in a mixture of water and alcohol in which oleic acid was dispersed.

The synthesized nanomagnetite was characterized by instrumental methods (Zeta Sizer Malvern, SEM-EDS, TEM, FT-IR, XRD), from which it can be seen that replacing hexane with ethanol did not worsen the characteristics of nanomagnetite. Both Malvern and TEM analyzes show particle sizes ranging from 6 to 25 nm, while FT-IR and XRD studies show peaks characteristic of magnetite.

This work was supported by Shota Rustaveli national Science Foundation of Georgia (SRNSFG) (Grant number YS-23-511)

7. J. Manrique-Julio, F. MacHuca-Martinez, N. Marriaga-Cabrales, M. Pinzon-Cardenas, Production of magnetite by electrolytic reduction of ferric oxyhydroxide, *J of Magn. and Magn. Mater.*, (2016) pp. 81–85. DOI: 10.1016/j.jmmm.2015.10.018
8. Zhang L., He R., Gu H. C., Oleic acid coating on the monodisperse magnetite nanoparticles, *J. Appl. Surf. Sci.* 2006, 2611-2617.
9. K. Yang, H. Peng, Y. Wen, N. Li, Re-examination of characteristic FTIR spectrum of secondary layer in bilayer oleic acid-coated Fe₃O₄ nanoparticles, *J. App. Surf. Sci.*, (2010) pp 3093–3097.

ICMATSE 2024

Investigation of The Life Time of The Coating Applied on The Steam Turbine Blade In Terms of Corrosion And Erosion

Mehmet Seyrek

*Gazi University, Graduated School Department of Advanced Technologies, 06560, Ankara, Turkiye
mehmet.seyrek81@gmail.com
ORCID: 0009-0006-4765-2243*

Murat Kayaalp

*Gazi University, Division of Metallurgical and Materials Science Engineering, 06560, Ankara,
Turkiye kayaalpmurat@gmail.com,
ORCID: 0009-0001-3655-1619*

Hasan Hasirci

*Gazi University, Department of Metallurgical and Materials Science Engineering, 06560, Ankara,
Turkiye
hasirci@gazi.edu.tr,
ORCID: 0000-0001-5520-4383*

Hakan ATES

*Gazi University, Department of Metallurgical and Materials Science Engineering, 06560, Ankara,
Turkiye
hates@gazi.edu.tr,
ORCID: 0000-0002-5132-4107*

*Cite this paper as: Seyrek M. , Kayaalp M., Hasirci H., Ates H. Investigation Of The Life Time Of The Coating Applied On
The Steam Turbine Blade In Terms Of Corrosion And Erosion Int. Conf. Advanced. Mater. Sci.& Eng. HiTech.and Device
Appl.Oct. 24-26 2024,Ankara, Turkey*

Abstract. In this study, the amount of corrosion and abrasion and the strength/operational life of a turbine blade used in a Thermal Power Plant after 25 years of operation were investigated and case analyzed. For comparison, the original unused turbine blade material and areas with the same coating were compared. It was determined that the turbine blade examined in the study was coated with Co-based material (containing Cr, Mo, Ni, Mn) by thermal metal spray coating method. AgCuZn based bonding coating was applied between the coating and the substrate. After 25 years of service with an average energy production of 69,466,700 MWh, the turbine blade was removed from the turbine and examined for corrosion and erosion properties. In the experimental study, chemical and dimensional measurements, optical microscopy, SEM and EDX measurements were carried out as a result of metallographic preparation of the samples. Structural analysis was performed by XRD, hardness and wear inverses were used to determine the mechanical properties and life of the samples. As a result of the investigations; it was determined that the turbine blade was subjected to both corrosion and erosion and corrosive erosion, the coating on the surface was completely worn locally, and there was a cross-sectional reduction due to wear (corrosive and erosive) at the blade tips. The coated parts were found to be more resistant to erosive and corrosive effects. The transition zone between the base material and the coating starting point was found to be very effective in coating wear. It has been observed that corrosion and erosion effects cause abrasion effect together.

Keywords: Steam turbine blade, Erosion, Corrosion

© 2024 Published by ICMATSE

Intorduction

In materials science, the term erosion is used to describe mechanical damage caused by high-velocity impacts. Erosion usually occurs as a result of solid/solid or liquid/solid interactions. Another

definition defines erosion as the gradual loss of original material due to the mechanical interaction between a solid surface and a fluid, a multicomponent fluid, or impinging liquid or solid particles. [1] There are different types of erosion, such as solid particle erosion, cavitation erosion,

liquid impact erosion, and cyclic erosion. All of these occur as a result of cyclic loading and sharp pressure pulses [1]. Solid particle erosion is an important material degradation mechanism encountered in a number of engineering systems, such as thermal power plants, aircraft gas turbine engines, pneumatic mass transportation systems, coal liquefaction/gasification plants, and ore or coal slurry pipelines. [3]

Although it seems simple, the erosion process is much more complex. After the plastic deformation that occurs in the form of a very shallow/thin layer as a result of solid or liquid impact on the surface of the metal material, metal loss occurs in the form of particles breaking off from the surface. In the early stages of erosion, while the first plastic deformation occurs, a period of symptoms is observed when erosion is not fast or very low. After this initial damage, wear begins at the weakest points [2]. Sudden cross-section changes or material wall edges are the areas where erosion damage is clearly observed. As a result of cross-section changes and high-pressure flow or water penetration at the ends, erosion craters are usually formed. This crater's sharp corners lead to the formation of narrow pits or lower tunnels. This situation is seen in Figure 1. After the formation of these pits, the real destructive wear will occur and wear will continue in the form of larger pieces breaking off. If the first wear crater has a flat surface, the wear rate will be lower [3,4].

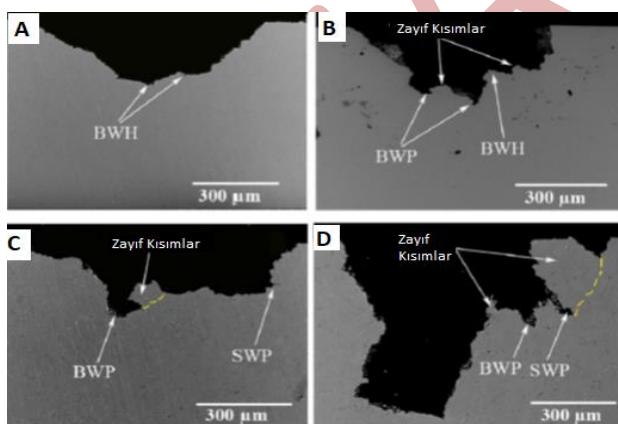


Figure 1. SEM image of the initial flat and ridged surface characteristic of erosion damage [3]

Erosion is caused by the mechanical interaction between the material surface and steam at high temperature and pressure. Erosion, which is visually evident as material loss, especially at the blade tips, is the loss of metal due to the impact of liquids or solids. Attack is promoted by turbulent,

high-velocity fluid flow. Rapid pressure changes promote shock waves and turbulence. Sudden changes in flow direction and entrainment of solid particulate matter in the fluid also contribute to erosion. Turbulence is also caused by a change in flow direction, a sudden change in cross-section, a thick deposit of sediment, or the presence of an obstruction that disrupts the flow. Although several factors affect the formation of deposits on turbine components, the general effect is the same regardless of the cause. Adherent deposits form in the steam passage and distort the original shape of the turbine blades. These deposits, which are usually rough or irregular on the surface, increase resistance to the steam flow. The disruption of the steam passages alters steam velocities and pressure drops, reducing the capacity and efficiency of the turbine. In severe conditions, deposits can cause excessive rotor thrust. Irregular accumulation causes vibration problems by disrupting the balance of the turbine rotor [5]. In the study on material erosion [6], the effect of surface roughness on erosion and long erosion formations using low impact velocities (<100m/s) were investigated. After several thousand impacts, numerous depressions were observed on the surface of the attacked copper. Such localized material flow and surface roughness were suggested as the main reason for the onset of material loss. It was evaluated that the formation of pits on the material surface and the resulting material loss were formed due to the effect of the high-speed fluid flowing on the surface.

Materials and Methods

Chemical analysis, SEM, EDX, XRD, micro and macrostructure studies, dimensional measurements and surface damages on the coating and base material were performed on a low-pressure steam turbine blade of a thermal steam turbine that has been used for 25 operating years and an unused steam turbine blade [Fig. 2].



Figure 2. Used and unused steam turbine blades

Experimental Studies

First of all, chemical analysis of the turbine blade material was performed. As a result of the analysis made with the sample taken from the turbine blade area, it was determined that the material was 420 quality stainless steel [Table 1.].

Table 1. Sample chemical analysis

C	Si	S	P	Mn	Cr
0.16-0.25	≤1.00	≤0.015	≤0.040	≤1.50	12.00-14.00



Figure 3. Microstructure images of sample C

The microstructure, SEM images and EDS analyses of sample S are given in Figure 4. The images and analyses show that there is a turbine blade structure with a 3-layer (base, intermediate coating and coating) structure consisting of 3 different materials (420 stainless steel, hard solder and Co-based).

Figure 5 Sem images show that sample B intermediate coating-coating and intermediate coating-substrate interfaces, we see a diffusion-free coating structure. The coating is applied only to the middle and wing tip of the wing, where the steam directly hits, and to the shoulder area (the part towards the wing edge tip and back in the direction of the steam arrival). The corrosion products formed were determined by XRD analysis of sample surfaces A, B and C. It was determined that oxides of the elements forming the substrate were formed in sample A, and the coating material in samples B and C. The formation of chemically

Fig. 3 shows the microstructure images obtained from sample C. It was observed that there was very severe wear on both the wing shoulder tip coating and the backing material. Defects in the form of irregularities and gaps in the thicknesses were detected in the intermediate coating.

and mechanically stable oxides at high temperatures in the coating and substrate surface will provide surface passivation and protection in a way. However, since very mixed oxides were formed together here and there was a continuous mechanical abrasion effect, the corrosion abrasive wear process continued together.

Figure 6 shows the microstructure images and chemical analysis data obtained from sample C. It was observed that there was very severe wear on both the wing shoulder tip coating and the backing material. Irregularity and gap-shaped defects were detected in the intermediate coating. The coating had a dendritic structure and there was a lot of segregation.

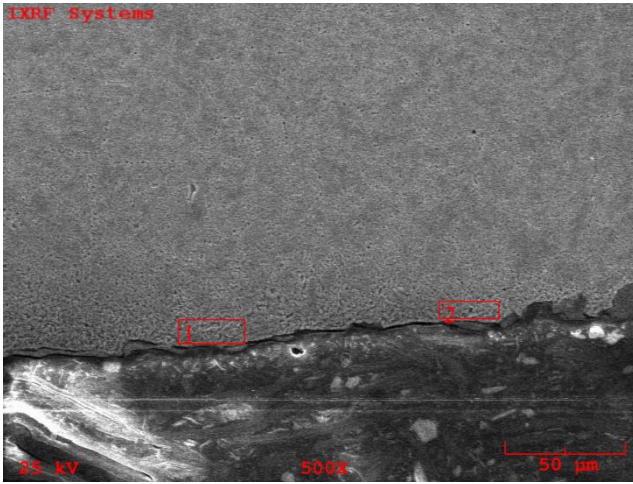


Figure 4. SEM-EDS analysis of sample A

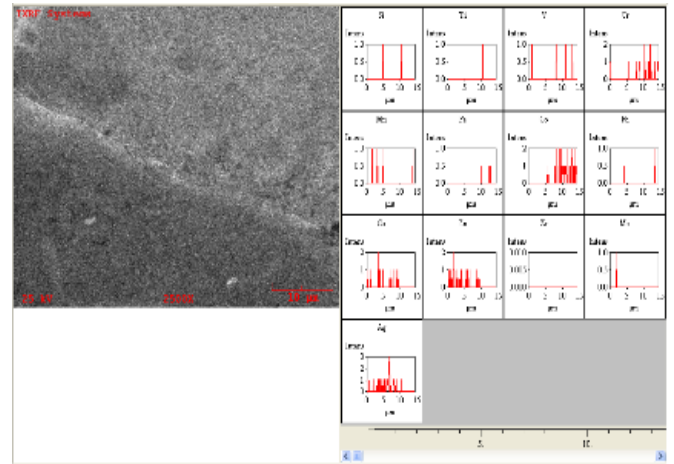


Figure 5. SEM-EDS analysis of sample B,

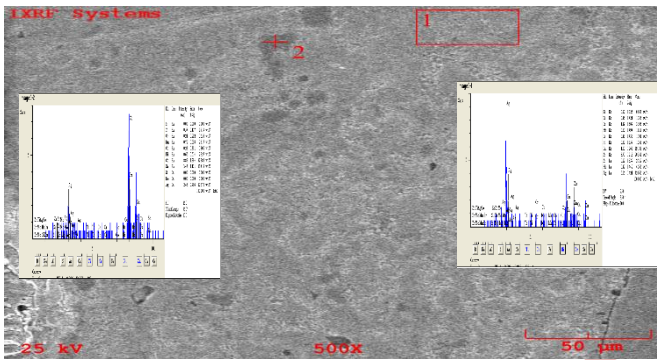


Figure 6. SEM-EDS analysis of sample C,

Corrosion products were determined by XRD analysis of sample surfaces A, B and C. It was determined that oxides of the elements forming the substrate were formed in sample A, and the coating material in samples B and C.

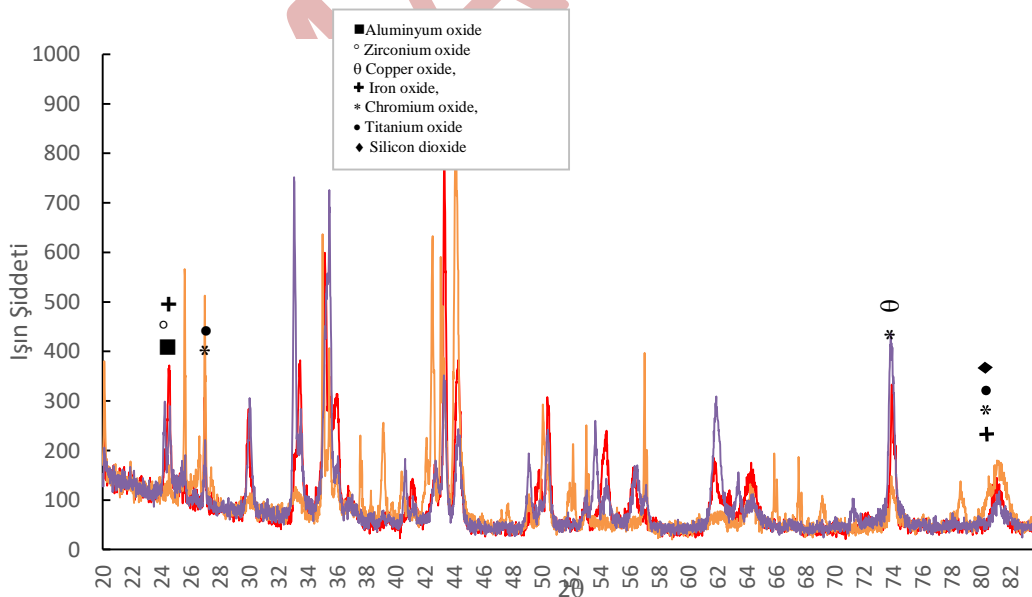


Figure 7. XRD analysis of sample A, B, C

Conclusion

After structural examination and analysis of the steam turbine blade that was scrapped after 25 years of operation;

1. In steam turbines, corrosion and erosion occur separately and/or together, especially due to the effect of high temperature,

2. In steam turbine blades, especially the areas where the effects of high temperature steam are high (shoulder and upper shoulder part) must be coated,

3. Shock-intensive and destructive wear occurs on the uncoated base material and as a result, the blade shoulder part becomes 65% thinner,

4. During the coating process, an intermediate bonding coating is made using a Cu-based hard solder material, and there are defects in the form of voids in this coating,
5. The main coating is a Co-based superalloy material, but despite this, it is subject to corrosion and erosion wear,

6. The structure of the coating contains dendritic and segregations, which accelerates the formation of corrosion,

7. Wear is high because the compounds formed by the elements in the coating structure in the corrosive environment do not allow the formation of a stable surface layer,

8. The coating structure should be produced in a homogeneous composition and without segregation.

References

1. E. Huttunen-Saarivirta, H. Kinnunen, J. Tuiremo, M. Uusitalo, M. Antonov, "Erosive wear of boiler steels by sand and ash," in *Wear* 317 213–224(2014),
2. Mohammad Sadegh Mahdipoor; *Water Droplet Erosion Resistant Materials and Surface Treatments* (2016) 1-2
3. *Water Droplet Erosion Resistant Materials and Surface Treatments* Mohammad Sadegh Mahdipoor Concordia University, 2016 pp.70
4. I.M. Hutchings, A.V. Levy, "Thermal effects in the erosion of ductile metals," in *Wear* 131, 105–121(1989).
5. *Suez Water technology handbook/chapter-18-steam-turbine-deposition-erosion-and-corrosion*
6. N. L. Hancox and J. H. Brunton, The erosion of solids by the repeated impact of liquid drops, *Philosophical Transactions of the Royal Society of London A: Mathematical, Physical and Engineering Sciences*, 260.1110 (1966) 121-139.

Enhancing Desalination Rates of Saltwater using Superhydrophobic Nanomembranes and Machine Learning Approaches

Nikhil Paranjpe

Department of Mechanical Engineering
Wichita State University, 1845 Fairmount, Wichita, KS, 67260, USA
nxparanjpe@shockers.wichita.edu
ORCID: 0009-0006-7342-4930

Shruti R. Kshirsagar

School of Computing, Wichita State University
Wichita State University, 1845 Fairmount, Wichita, KS, 67260, USA
shruti.kshirsagar@wichita.edu
ORCID: 0000-0002-7191-4251

Ramazan Asmatulu

Department of Mechanical Engineering
Wichita State University, 1845 Fairmount, Wichita, KS, 67260, USA
ramazan.asmatulu@wichita.edu
ORCID: 0000-0001-8104-2285

Cite this paper as: Paranjpe, Nikhil, Kshirsagar, Shruti, Asmatulu, Ramazan. Enhancing Desalination Rates of Saltwater using Superhydrophobic Nanomembranes and Machine Learning. Int. Conf. Advanced Mater. Sci. & Eng. HiTech. and Device Appl. Oct. 24-26 2024, Ankara, Turkiye.

Abstract. Desalination of saltwater using superhydrophobic coated materials is a cutting-edge advancement in water purification technology, offering significant improvements in efficiency and cost-effectiveness. This study investigates the application of superhydrophobic coated materials and nanomaterials in membrane distillation processes, where the unique water-repellent properties of these materials enhance vapor transport and minimize membrane fouling. The superhydrophobic membranes demonstrate a remarkable ability to resist salt and contaminant deposition, thereby prolonging membrane life. This research highlights the fabrication techniques, material properties, and performance metrics of superhydrophobic membranes in various desalination scenarios using machine learning methods. Integrating machine learning into the desalination process using superhydrophobic materials can significantly enhance system performance, reliability, and operational efficiency. Machine learning algorithms can be employed to analyze vast amounts of operational data, including feed water characteristics, temperature gradients, and permeate flux rates, to optimize the desalination process in real-time. Predictive models can be developed to forecast membrane performance, identify potential fouling or scaling events, and suggest timely maintenance actions. By continuously monitoring and analyzing data, machine learning can provide insights into the most effective operational parameters, ensuring optimal performance under varying conditions. In conclusion, the integration of machine learning with superhydrophobic coated materials and nanomaterials not only maximizes the efficacy of the desalination process but also contributes to the development of smart, resilient water treatment systems capable of meeting the growing global demand for clean water.

Keywords: Superhydrophobic Nanomembranes, Desalination Rates, Machine Learning, Freshwater.

This research focuses on the membrane distillation process for desalination purposes. To achieve these objective natural materials such as coconut shell, muslin cloth along with carbon felt will be used as a membrane. The idea is to prepare a superhydrophobic coating which will then be applied on various materials mentioned above to separate salt from the water. Additionally polystyrene polymer mixed with DMF (Dimethylformamide) with an inclusion of SiO_2 nanoparticles will be used for electrospinning the superhydrophobic nanofibers which are very effective for desalination process. A prototype will be designed where the salt water will be heated in a container at a regulated temperature. Once the water is heated to a required temperature it will be transferred to a secondary tank with a superhydrophobic membrane. In the secondary tank the vapor will pass through the superhydrophobic membrane thus separating salt from the water. The filtered vapor will then encounter a cooler surface where condensation occurs converting the vapors to freshwater. The accumulated fresh water will then be checked with the salinity meter to determine the salt content in the water.

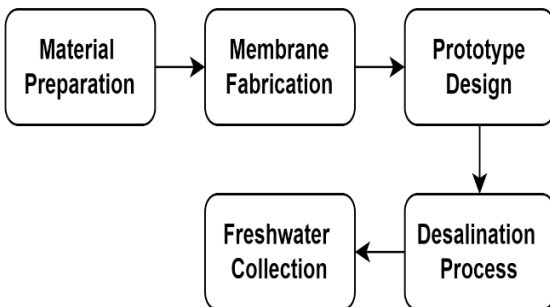


Figure 1. Pipeline for a Desalination process.

For the desalination process some of the important calculations are calculating Permeate flux and salt rejection rate. The permeate flux is calculated using the equation 1.[1]

$$J_v = \frac{\Delta W}{At} \quad (1)$$

Here, J_v is permeate flux, ΔW is permeation weight collection over set time, A is the permeation area and this the predetermined time

The salt rejection rate is calculated using equation 2. [2]

$$R_s = \left(1 - \frac{C_p}{C_f} \right) \quad (2)$$

Here, R_s is the salt rejection rate (%), C_p is the salt concentration in the permeate (mg/L or ppm), C_f is the salt concentration in the feed (mg/L or ppm).

For the surface characterization of the superhydrophobic coated samples the samples will be tested for Water Contact Angle (WCA), surface energy calculations and Fourier-Transform Infrared Spectroscopy (FTIR) analysis. Some of the results for water contact angle calculations from the initial testing are listed in table 1.

Table 1. Water contact angle for different coated and uncoated materials.

WCA (°)	Uncoated	Coated
Carbon Felt	94.35°±0.78	171.70°±2.26
Muslin Cloth	134.47°±0.65	167.46°±1.69
Coconut Shell	124.41°±0.7	159.21°±0.68

These results from WCA tests indicate the $WCA > 150^\circ$ which concludes that all the three

materials are superhydrophobic. The FTIR analysis detected C-H stretching vibrations in alkyl chains, indicating the presence of

hydrophobic functional groups on the coated surfaces.

References

- [1] H. Wang, J. Zhang, Y. Li, and X. Li, "Desalination of Water by Using Superhydrophobic Fabric," *Res. J. Text. Apparel*, vol. 19, no. 3, pp. 19-25, 2015.
- [2] G. Tchobanoglous and F. L. Burton, *Wastewater Engineering: Treatment, Disposal, and Reuse*, 3rd ed. New York, NY, USA: McGraw-Hill, 1991.

ICMATSE 2024

Development of biodegradable Mg-Zn-Ca alloys to be used in bone fracture treatments

Jameel Fadhil Hassan Al – Ogaidi

*Ministry of Higher Education and Scientific Research
Middle Technical University Suwaira Technical Institute, Baghdad, Iraq
jameelfh74@gmail.com*

Ali Güngör

*Metallurgical and Materials Engineering, Karabuk University, 78050 Karabuk, Turkey
agungor@karabuk.edu.tr*

Cite this paper as: Al – Ogaidi, Jameel Fadhil Hassan, Güngör, Ali,. Development of biodegradable Mg-Zn-Ca alloys to be used in bone fracture treatments. Int. Conf. Advanced. Mater. Sci.& Eng. HiTech.and Device Appl.Oct. 24-26 2024, Ankara, Turkiye.

Abstract. Influences of deformation ratio and post heat treatment on the microstructure, mechanical properties, and immersion corrosion resistance of nominally Mg-1.0Zn-0.2Ca (ZX10) alloy were investigated in this study. The alloy was cast using gravity die casting method under protective gas atmosphere. After homogenization heat treatment, hot rolling was applied to the samples at three different deformation ratio (5 %, 10 %, and 20 %). Then, microstructure, mechanical properties, and immersion corrosion resistance of the alloy were determined experimentally. The results showed that both hot rolling and post heat treatment have positive effects on the yield strength, tensile strength, and corrosion resistance of the alloy.

Keywords: Mg alloy, casting, mechanical properties.

© 2024 Published by ICMATSE

Introduction

The development of bio-based magnesium alloys has been an area of intense research in the fields of materials science and biomedical engineering. Magnesium alloys are an attractive choice for various biomedical applications owing to their low density, excellent mechanical properties, and inherent biodegradability [1]. In spite of these advantages, the major hurdles that hampers their wide-scale adoption are their low mechanical properties and corrosion resistance. When used in a biological environment, rapid corrosion can compromise the mechanical integrity of the material, thus undermining its potential benefits [2]. Additionally, mechanical properties are crucial for the alloy's usability, as they dictate the strength, durability, and overall reliability of the material [3]. Magnesium alloys have long been the subject of research due to their promising properties. Not only are they lighter than aluminum and stronger than polymers, but they also offer specific bio-advantages such as biodegradability and biocompatibility, making them particularly useful in temporary

implants, screws, and other bio-resorbable applications [4]. Despite these prospects, especially the poor corrosion resistance of magnesium alloys restricts their use. Corrosion leads to premature material failure, causes the release of hydrogen gas as a by-product, and may elicit an undesirable biological response. Therefore, mitigating corrosion remains a prime concern for researchers and manufacturers alike. Bio-based magnesium alloys, particularly those comprising zinc and calcium, have shown great promise in this regard. Zn and Ca are not only essential trace elements in the human body but also known to enhance the alloy's mechanical properties and corrosion resistance [6]. Mg-Zn-Ca alloys have been investigated in various studies, focusing on their use in orthopedic applications like bone screws and pins, where both mechanical strength and controlled degradation are crucial [7].

In this study, effect of hot rolling and post heat treatment on the mechanical and corrosion properties of the Mg-1.0Zn-0.2Ca alloy was investigated experimentally. Homogenization heat

treatment of the alloy was carried out at 400 °C for 12 hours. Hot rolling (5, 10, and 20 % deformation) was applied at 350 °C. Post heat treatment after hot rolling was done at 300 °C for 30 min. The alloy was characterized using XRF and XRD measurements, optic microscope, tensile tests, and hardness measurements.

Results and Discussions

Chemical composition of the cast alloy after homogenization heat treatment is given in Table 1. XRF results shows that the designed composition of the alloy was obtained closely.

Table 1. Chemical composition of the alloy (wt.%).

Mg	Zn	Ca
98.89	0.94	0.17

The XRD patterns of the homogenized, hot rolled, and post heat treated alloys are given in Figure 1.

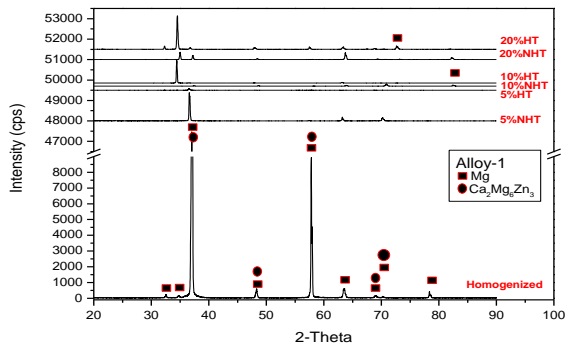


Figure 1. XRD patterns of the ZX10 alloy (HT: Post heat treated and NHT: Not heat treated).

As it is seen from the XRD patterns of the alloys, both of the alloys consist of α -Mg and $Ca_2Mg_6Zn_3$ phases. In addition, scattering of the X-rays from all planes in homogenized samples indicates that homogenized sample has random crystal orientations. After 5% hot rolling, the intensity of some peaks diminishes that indicates preferred orientation occurs upon hot rolling. Increasing deformation ratio further, additional peaks appear again indicating that randomly oriented grains form. This can be understood by dynamic recrystallization process. When hot rolled samples with and without heat treatment were compared, it is seen that heat treatment after hot rolling results in more uniform X-ray intensity distribution indicating that static recrystallization process takes place and randomly oriented fine crystal forms. The strong (002) diffraction intensity compared to the other intensities

observed in all hot rolled alloy indicates that mainly (002) type orientation develops upon hot rolling.

Microstructure analyses of the samples showed that homogenized alloy has relatively large and uniform grain size. Upon hot rolling elongated grains form and grain size decreases. Selected surface images of the ZX10 alloy is given in Figure 2. As it is seen from the figures, some small grains along with the large grains are observed in hot rolled samples. These small grains indicate that dynamic recrystallization process started during hot rolling. In addition, it is observed that grain growth occurs after post heat treatment.

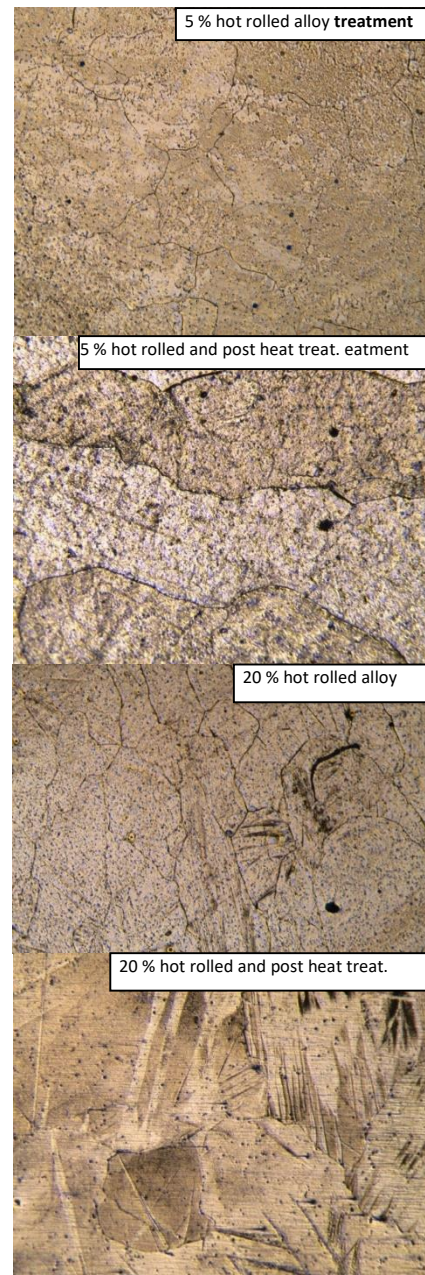


Figure 2. Surface images of the hot rolled alloys. In addition, twin bands are observed in 20 % hot rolled and post heat treated sample.

The Vickers hardness of the samples measured using 500 g load for 15 seconds are given in Table 2. The results showed that hot rolling and post heat treatment don't have significant effect on the hardness of the homogenized alloy.

Table 2. Average Vickers hardness (HV0.5) of the alloys.

Sample	Average Hardness
Homogenous	50.43
5% hot rolled	51.43
5% hot rolled and heat treated	50.43
10% hot rolled	50.73
10% hot rolled and heat treated	50.73
20% hot rolled	50.63
20% hot rolled and heat treated	52.03

Immersion corrosion rate of the alloy after 10 days of immersion in simulated body fluid was calculated using the weight loss method. The corrosion rates in mm/year is given in Table 3.

Table 3. Immersion corrosion rates of the samples (mm/year).

Sample	Corr. Rate
Homogenous	0.8195
5% hot rolled	0.3295
5% hot rolled and heat treated	0.3876
10% hot rolled	0.3727
10% hot rolled and heat treated	0.4948
20% hot rolled	0.7299
20% hot rolled and heat treated	0.5015

It is seen that corrosion rate of the homogenized alloy is the highest. After hot rolling, a significant reduction in corrosion rates of the 5 % and 10 % hot rolled alloy is observed. However, reduction in corrosion rate of 20 % hot rolled alloy is small. Higher corrosion rate of the homogenized alloy can be attributed coarsa secondary phases. During hot rolling, fracture of intermetallic phase occurs. Distribution of small particles don't have accelerating effect as in the case of long continuous phase. In addition, post heat treatment slightly increases the corrosion rates except for the 20% hot rolled alloy.

Tensile tests were done at room temperature using MTS Landmark 100 kN Dynamic Test Devie and 1 mm/s pulling rate. The results are given in Table 3 and stress-strain curves of the samples are given in Figure 3. The results indicate that hot rolling improve the

yield strength and tensile strength of the alloy. In addition, at low deformation ratios (5% and 10%), hot rolled alloys have similar or better ductility. At high deformation (20%), strain decreases substantially. Strength and ductility of the materials depend on the grain size and size, shape, and distribution of the secondary phase. Therefore, higher yield and tensile strength, and lower ductility of the 20% hot rolled alloy can be explained with reduced grain size and finer particles.

Table 4. Mechanical properties of the homogenized and hot rolled alloy with and without heat treatment (HT: post heat treated).

Sample	Elas. Mod. MPa	Yield Str. GPa	Ten. Str. MPa	Strain (%)
Homog.	17.8	7.8	92.4	5.85
5% Hot Rolled	16.5	14.069	77.4	5.21
5% Hot Rol. HT	19.2	24.743	93.1	5.59
10% Hot Rolled	18.4	27.35	107.8	8.19
10% Hot Rol.HT	22.2	30.413	102.4	6.11
20 % Hot Rolled	25.7	76.625	159.2	3.43
20 % Hot Rol.HT	21.8	63.010	131.5	2.70

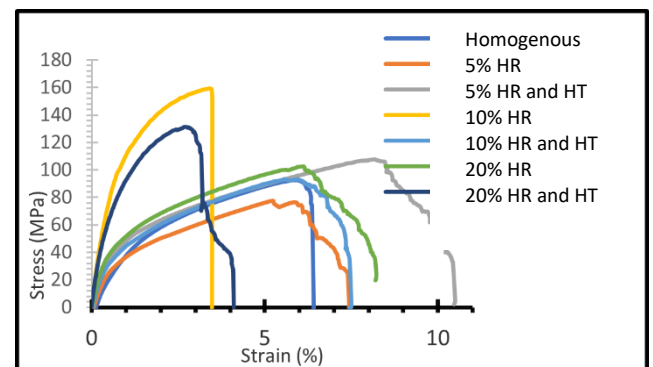


Figure 3. Stress-strain curves of the hot rolled (HR) and post heat treated (HT) alloys.

Conclusions

XRD results showed that the alloy consist of α -Mg and $\text{Ca}_2\text{Mg}_6\text{Zn}_3$ phases Increasing hot rolling ratio results in lower grain size.

Texture development and dynamic recrystallization occur during hot rolling.

Hot rolling does not have significant effect on the hardness but it has important effect on the yield and tensile strength of the alloy.

Hot rolling has also positive effect on the corrosion resistance of the alloy.

Post heat treatment applied after hot rolling does not have significant effect on the hardness but it has important effect on the yield strength, tensile strength, and corrosion resistance of the alloy.

Acknowledgement

We would like to thank to the Scientific Research Projects Coordination Unit of Karabük University with KBÜBAP-22-YL-111 project number for the financial support.

References

1. Aziz T, Ullah A, Ali A, Shabeer M, Shah MN, Haq F, et al. Manufactures of bio-degradable and bio-based polymers for bio-materials in the pharmaceutical field. *Journal of Applied Polymer Science.*;13929.2022.
2. Blitz MJ. Video surveillance and the constitution of public space: Fitting the fourth amendment to a world that tracks image and identity. *Tex L Rev.*;82:1349. 2003.
3. Li W, Xie D, Li D, Zhang Y, Gao Y, Liaw PK. Mechanical behavior of high-entropy alloys. *Progress in Materials Science.*;118:100777. 2021.
4. Pałka K, Pokrowiecki R. Porous titanium implants: a review. *Advanced Engineering Materials.*;20[5]:1700648. 2018.
5. Venezuela J, Dargusch M. The influence of alloying and fabrication techniques on the mechanical properties, biodegradability and biocompatibility of zinc: A comprehensive review. *Acta biomaterialia.*;87:1-40. 2019.
6. Witte F, Hort N, Vogt C, Cohen S, Kainer KU, Willumeit R, et al. Degradable biomaterials based on magnesium corrosion. *Current opinion in solid state and materials science.*;12[5-6]:63-72. 2008.
7. Gu X-N, Zheng Y-F. A review on magnesium alloys as biodegradable materials. *Frontiers of Materials Science in China.*;4:111-5. 2010.

The Effects of Ni-SiC Electrocomposite Coating on the Mechanical Properties of Aviation Piston Engine Cylinders

Mehmetcan OKSUZ

*EST Endüstri Teknik Yüzey Kaplama İml. San. ve Tic. A.Ş.- R&D, 06378, Ankara, Türkiye,
mehmetcanoksuz@estyuzeykaplama.com
ORCID: 0009-0001-1147-8603*

Ugur KARAHAN

*EST Endüstri Teknik Yüzey Kaplama İml. San. ve Tic. A.Ş.- R&D, 06378, Ankara, Türkiye,
ugurkarahan@estyuzeykaplama.com
ORCID: 0000-0003-4156-792X*

Güven CANKAYA

*Ankara Yıldırım Beyazıt University- Faculty of Engineering and Natural Sciences, Metallurgical and
Materials Engineering, 06010, Ankara, Türkiye, erguvan@rocketmail.com
ORCID: 0000-0003-2932-1695*

*Oksuz, Mehmetcan, Karahan, Ugur, Cankaya, Güven. The Effects of Ni-SiC Electrocomposite Coating on the
Mechanical Properties of Aviation Piston Engine Cylinders. International Conference on Advanced Materials
Science & Engineering and High Tech Devices Applications. October 24-26 2024, Ankara, Türkiye*

Abstract. In this study, the electrolytic nickel coating process reinforced with ceramic particles was investigated in order to increase the wear resistance of cast aluminum alloy single-piston cylinders used especially in unmanned aerial vehicles (UAVs) and drones. Coating experiments were carried out in a 2-liter glass beaker using a heating magnetic stirrer; the effects of parameters such as temperature, time, current density, bath composition and pH on the thickness, hardness and ceramic dispersion of the coating were investigated. After metallographic preparation, the samples were analyzed in detail with scanning electron microscope and microhardness measurements were performed. The findings showed that a coating with a thickness of at least 70 microns was obtained with the coating process applied between 60 and 100 minutes at the optimized current density, the silicon carbide (SiC) content of this coating varied between 7-13% and the coating hardness ranged between 450-550 Vickers. These results indicate that the Ni-SiC electrocomposite coating provides significant wear resistance on the surface of cast aluminum alloy and offers a potential solution for improving the mechanical properties of single-piston aviation cylinders. Future studies promise more comprehensive investigations to evaluate the long term performance of these coatings in operational conditions, both tribologically and corrosively.

Keywords: Single-piston aviation cylinders, cast aluminum alloy, Ni-SiC electrocomposite coating, microhardness
© 2024 Published by ICMATSE

Introduction

The aviation industry consistently requires high-performance materials capable of withstanding harsh operational environments, including high temperatures, pressures, and mechanical stress. One of the key components in unmanned aerial vehicles (UAVs) and drones is the single-piston cylinder, which is primarily constructed from cast aluminum alloys due to their favorable combination of strength and low weight [1].

However, despite these advantages, aluminum alloys often suffer from insufficient wear resistance, which can reduce the durability and efficiency of the cylinders during prolonged use [2]. Enhancing the wear resistance and overall mechanical properties of these critical parts has become a primary focus in improving their operational lifespan and performance.

Nickel-based composite coatings, especially those reinforced with hard ceramic particles such as silicon carbide (SiC), have emerged as a promising solution to this issue [3]. The incorporation of SiC into nickel matrices offers superior mechanical strength, hardness, and wear resistance, making it a highly effective approach for protecting aluminum alloy surfaces in high-performance aviation applications. Previous studies have shown the potential of Ni-SiC electrocomposite coatings in providing significant improvements in surface properties, such as increased hardness and enhanced corrosion resistance, which are essential for the long-term functionality of engine components subjected to extreme conditions.

In this study, we specifically investigate the effects of Ni-SiC electrocomposite coating on the mechanical properties, focusing on wear resistance and hardness, of single-piston cylinders used in UAVs and drones. By optimizing the electroplating parameters, including temperature, current density, and bath composition, we aim to achieve a uniform and durable coating that enhances the longevity and performance of these vital components in aerospace applications.

Result and Discussion



Figure 1. Aluminum Alloy Piston

Table 1. Experimental Design

	Exp 1	Exp 2	Exp 3
<i>T</i> (°C)	40:50:60	40:50:60	40:50:60
<i>SiC</i> (g/L)	20:30:40	20:30:40	20:30:40
<i>J</i> (A/dm ²)	2.5:5:10	2.5:5:10	2.5:5:10
<i>pH</i>	3.5	4	4.5
<i>Time</i> (min)	60:70:80	70:80:90	80:90:100

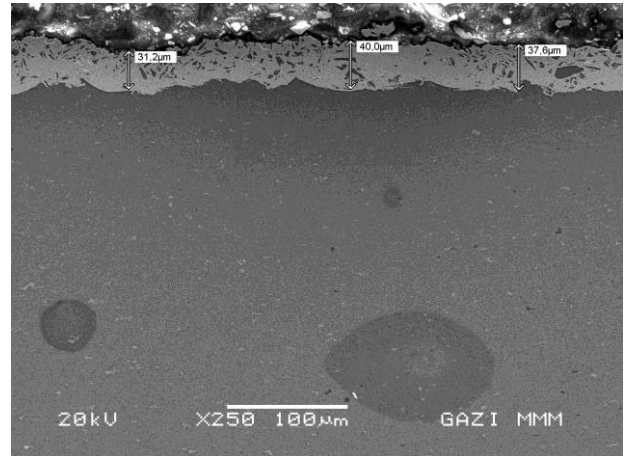


Figure 2 Cross-sectional SEM image (250X) of Ni-SiC coating applied at 2.5 A/dm²

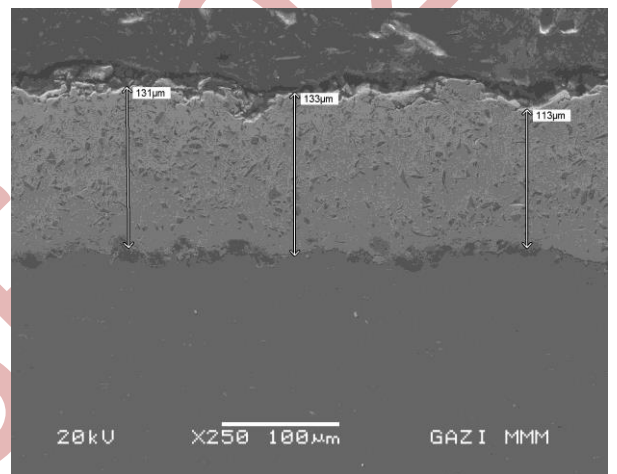


Figure 3. Cross-sectional SEM image (250X) of Ni-SiC coating applied at 10 A/dm²

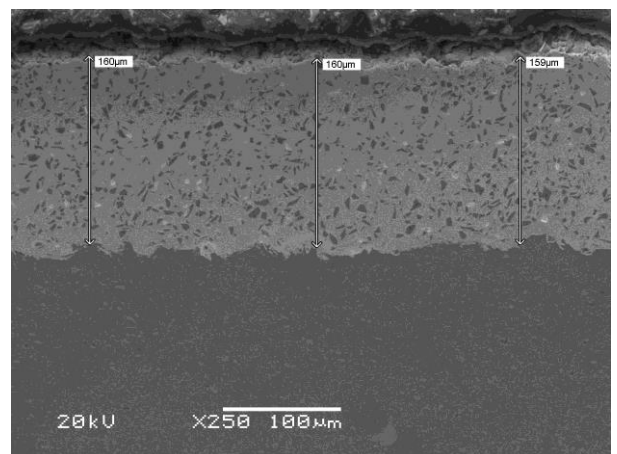


Figure 4. Cross-sectional SEM image (250X) of Ni-SiC coating applied at 5 A/dm²

In this study, a Ni-SiC electrocomposite coating was applied to aluminum alloy piston cylinders, which are critical components in UAV and drone engines. The coating process was optimized to enhance the wear resistance and mechanical properties of the cylinders. Figure 1 shows the piston cylinder used in the study, highlighting its structural features.

Figure 2 presents the SEM image of the coating applied at a current density of 2.5 A/dm² and a temperature of 45°C. This coating resulted in a hardness of 520 HV, demonstrating the effectiveness of the Ni-SiC reinforcement under these conditions.

Figure 3 shows the SEM analysis of the coating obtained at a higher current density of 10 A/dm² and a temperature of 55°C. The increased current density led to a higher coating hardness of 555 HV, indicating that both current density and temperature significantly affect the coating properties.

Figure 4 illustrates the SEM image of the coating formed at 5 A/dm² and 60°C. Under these conditions, the hardness reached 600 HV, the highest among the tested samples, suggesting that the combination of moderate current density and higher temperature is optimal for achieving superior hardness in the Ni-SiC composite coating.

References

1. R. W. Hertzberg, R. P. Vinci, J. L. Hertzberg, Deformation and Fracture Mechanics of Engineering Materials, 5th ed., Wiley, 2012.
2. M. H. Staia, "Wear resistance of aluminum alloy coatings for aerospace applications," Surface and Coatings Technology, vol. 201, pp. 6712-6719, 2007.
3. D. R. Gabe, "The role of nickel in electrocomposite coatings," Transactions of the Institute of Metal Finishing, vol. 79, no. 4, pp. 147-153, 2001.

Conclusion

This research has demonstrated the effectiveness of Ni-SiC electrocomposite coatings in enhancing the mechanical properties of cast aluminum alloy single-piston cylinders, which are widely used in UAV and drone applications. As outlined in Table 1, the optimized coating process produced a uniform coating layer with a minimum thickness of 70 microns, and SiC particle distribution between 7-13%. The coating's hardness values, ranging from 450 to 550 Vickers, emphasize the significant improvement in wear resistance.

The microstructural analysis that shown in Figure 1, provides a clear depiction of the uniform ceramic particle distribution within the nickel matrix, validating the consistency of the coating process. Additionally, as shown in Figure 2 offers a comprehensive overview of the piston engine cylinder's geometry and structure, further illustrating the coating's practical application on complex components.

These results indicate that Ni-SiC electrocomposite coatings offer a promising solution to enhance the durability and mechanical performance of aviation cylinders. Future studies should focus on evaluating the coating's long-term performance tribological and corrosive environments, aiming to further optimize its use in aerospace engineering

Friction Welding of Dissimilar Steels

Zakaria Boumerzoug

*LMSM, Department of Mechanical Engineering, University of Biskra, 07000, Biskra, Algeria,
z.boumerzoug@univ-biskra.dz
ORCID: 0000-0002-1723-9849*

Cite this paper as: Boumerzoug, Z, Friction Welding of Dissimilar Steels. Int. Conf. Advanced. Mater. Sci. & Eng. HiTech. and Device Appl. Oct. 24-26 2024, Ankara, Turkiye

Abstract. Welding is an essential assembly process in the manufacturing industry. Friction welding is a process that is becoming more and more widely used because it is an environmental process and has an economic interest. This process is based on friction between the parts to be welded. Likewise, this process is divided into three types of welding and which are linear friction welding, rotational friction welding and friction stir welding. One of the advantages of this process is that it is used in joining dissimilar metals such as welding steel with an aluminum alloy. Despite the number of dissimilar metals welded by friction, it was noted that this number remains limited because certain challenges remain to be overcome to achieve a weld joint with good mechanical properties. This is why several research projects are being carried out to answer all the questions that require solutions. In this context, a bibliographic review will be presented, with examples of friction welding of some dissimilar steels and especially our research work which has been carried out on this theme.

Keywords: Friction welding, Dissimilar steels, Microstructures, Mechanical properties
© 2024 Published by ICMATSE

Literature Review

Welding of dissimilar metals has become an essential technology in many fields where both strength and corrosion resistance are required [1]. Joining of dissimilar metal combinations is used in various applications requiring specific combinations of welding properties and cost savings [2]. Welding of dissimilar metals offers possibilities in terms of versatility of the article by using each material effectively and efficiently, i.e., by taking advantage of the specific properties of each material [3].

Friction welding is one of the joining processes used to produce high-quality weld joints between two materials that have similar or dissimilar chemical compositions. Friction welding is achieved by friction between the parts to be welded either by rotation (called: rotary friction welding) or translation (linear friction welding), or by using a tool that will cause friction between the two parts to be welded (called friction stir welding). These three friction welding processes have been used to weld dissimilar steels. Firmanto et al. [4] succeeded in welding by rotary friction welding process a carbon-steel to stainless-steel. They found that the combination of different welding parameters resulted in a weld joint of very high tensile strength. Mattie et al. [5] have welded by rotary friction

welding process an austenitic stainless steel to ferritic stainless-steel. They found that the speed and forging pressure have a greater influence on total deformation and the amount of flash extruded from both steels are approximately similar. Magudeeswaran et al. [6] welded duplex stainless steel to mild steel by linear friction welding process. The friction force alone was modified because it proved to be more important for obtaining a welded joint with good mechanical properties. Rahimi et al. [7] welded a duplex stainless steel to a low-carbon steel using a friction stir welding process. The results of microstructural analyses showed that the temperature at the center of the stirred zone reached temperatures between Ac1 and Ac3 during welding, which caused phase transformations such as a minor ferrite-austenite phase transformation on the duplex stainless-steel side. Malekan et al. [8] welded 316 stainless steels to 4140 steels using a friction stir welding process. They studied the microstructure and mechanical properties of the welded joint. The microhardness measurement results showed that the kneading zones have higher hardness than the base metals due to dynamic recrystallization and fine-grained structure. According to the various research works published in the last twenty years on friction welding of

dissimilar steels [2, 4-6, 9-34], the majority of these works have focused on friction stir welding, followed by rotary friction welding and very little research has been devoted to linear friction welding. The number of dissimilar steels being friction welded has increased in the last five years, but has increased relatively slowly compared to the large number of steels used in the industry. The type of different steels that were welded together, it can be found stainless steel with stainless steels or stainless steel with ordinary steel or welding ordinary steel with ordinary steel .

Case study

As example, a rotary friction welding of stainless steel welded to ordinary steel is presented (Fig1.). It is important to notice that a rotary friction welding is a friction welding process where the parts to be weld are turned against each other under the action of an axial force, in order to produce the heat required for assembly [35]. It is noted that when the desired speed of rotation is reached, the fixed part is moved along its axis so as to press the rotating part [36]. The faces in contact heat up and become the source of heat which, by diffusion, raises the temperature of the ends of the parts. These become plastic and creep produced towards the periphery forming a characteristic bead, while the heat continues to spread. When the welding temperature is reached, the rotation is stopped and a forging force is applied to form the weld [37]. Generally, friction welding is divided into two stages, stage I is the friction stage which will cause plastic deformation in the contact area of the two parts to be welded and the second stage (stage II) is the forging stage which will allow the assembly of the two parts by forming a bead at the level of the welded joint. The complete cycle of the friction rotation welding process has been established and adopted by many authors [38-40].

These two dissimilar steels were successfully welded with no apparent defects (Fig.2). The welding mechanism consisted of two main stages, the friction stage followed by the forging stage, where each stage also has its own mechanism.

References

1. Mvola B, Kah P, Martikainen J. Welding of dissimilar ferrous–nonferrous metals. *Advanced Materials and Information Technology Processing*; 01/02/2014: WIT Press; 2014.

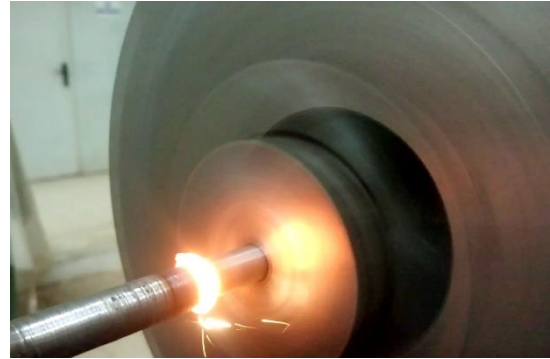


Figure 1. Rotary friction welding of stainless steel to ordinary steel.



Figure 2. Macrographic view of the welded joint with a rotation speed of 2000 rpm.

Conclusion

This paper presented the main friction welding processes and their applications for joining dissimilar steels with a case study. The most important conclusions are the following:

- Different types of friction welding can be used to join dissimilar steels.
- Most of the research work has been devoted to the use of friction stir welding for welding dissimilar steels
- The experimental example of rotary friction welding of stainless steel to ordinary steel was successfully carried out without apparent defects.
- Several challenges remain to be addressed such as the very limited number of dissimilar steels welded by friction compared to the large number of industrial steel grades

2. Pouraliakbar H, Hamed M, Kokabi AH, Nazari A. Design of dissimilar welds in CK45 carbon steel and AISI 304 stainless steel. *Materials Research* (2013) 17(1): 106–14.
3. Maurya AK, Pandey C, Chhibber R. Dissimilar welding of duplex stainless steel with nickel alloys: a review. *International Journal of Pressure Vessels and Piping* (2021), 192: 104439.
4. Firmanto H, Candra S, Hadiyat M.A, Triastomo Y.P, Wirawan I. Tensile Strength and Microstructure of Rotary Friction-Welded Carbon Steel and Stainless Steel Joints. *J. Manuf. Mater. Process* (2023) 7, 7.
5. Mattie AA, Ezdeen SY, Khidhir GI. Optimization of parameters in rotary friction welding process of dissimilar austenitic and ferritic stainless steel using finite element analysis, *Advances in Mechanical Engineering* (2023), Vol. 15(7) 1–16.
6. Magudeeswaran G, Rajapandiyar P, Balasubramanian V, Sivaraj P. Establishing the Process Parameters of Linear Friction Welding Process for Dissimilar Joints, *International Journal of Mechanical Engineering and Technology*, 10(6), 2019, pp. 01–10
7. Rahimi S, Konkova T.N, Violatos I. et al. Evolution of Microstructure and Crystallographic Texture During Dissimilar Friction Stir Welding of Duplex Stainless Steel to Low Carbon–Manganese Structural Steel. *Metall Mater Trans A* (2019), 50, 664–687.
8. Malekan A, Malekan M, Banimostafa Arab N, Bayat Tork H. Microstructure and mechanical properties in dissimilar friction stir welding of 316 stainless steel to 4140 steel, *Journal of Ultrafine Grained and Nanostructured Materials* (2023), Vol. 56, No.2, pp. 147–156.
9. Gupta SK, Patil AP, Rathod RC, et al. Cold Metal Transfer Welding of Ferritic and Austenitic Stainless Steel: Microstructural, Mechanical, and Electrochemical Studies. *J. of Mater Eng and Perform* (2024).
10. Emami S, Sadeghi-Kanani S, Saeid T. et al. Dissimilar friction stir welding of AISI 430 ferritic and AISI 304L austenitic stainless steels. *Archiv.Civ.Mech.Eng* (2020); 20, 131.
11. Jafarzadegan M, Abdollah-zadeh A, Feng AH, Saeid T, Shen J, Assad H. Microstructure and Mechanical Properties of a Dissimilar Friction Stir Weld between Austenitic Stainless Steel and Low Carbon Steel, *J. Mater. Sci. Technol.* (2013), 29(4), 367–372
12. Wang H, Wang K, Wang W, Huang L, Peng P, Yu H. Microstructure and mechanical properties of dissimilar friction stir welded type 304 austenitic stainless steel to Q235 low carbon steel. *Materials Characterization* (2019), 155, 109803.
13. Jafarzadegan M, Feng AH, Abdollah-zadeh A, Saeid T, Shen J, Assadi H. Microstructural characterization in dissimilar friction stir welding between 304 stainless steel and st37 steel, *MATERIALS CHARACTERIZATION* (2012) 74, 28–41.
14. Theodoro MC, Pereira VF, Mei PR. et al. Dissimilar Friction Stir Welding Between UNS S31603 Austenitic Stainless Steel and UNS S32750 Superduplex Stainless Steel. *Metall Mater Trans B* 46, 1440–1447 (2015).
15. Wang W, Hu Y, Zhang M, Zhao H. Microstructure and mechanical properties of dissimilar friction stir welds in austenitic–duplex stainless steels. *Materials Science and Engineering: A*, (2020), 787, 139499.
16. Sato Y S, Kokawa H, Fujii HT, Yano Y, Sekio Y. Mechanical properties and microstructure of dissimilar friction stir welds of 11Cr–Ferritic/Martensitic steel to 316 stainless steel. *Metallurgical and Materials Transactions A*, (2015), 46, 5789–5800
17. Mondal M, Das H, Ahn E Y, Hong S T, Kim MJ, Han HN, Pal TK. Characterization of friction stir welded joint of low nickel austenitic stainless steel and modified ferritic stainless steel. *Metals and Materials International* (2017), 23, 948–957.

18. Bin Matlan MJ, Mohebhi H, Pedapati SR. et al. Dissimilar Friction Stir Welding of Carbon Steel and Stainless Steel: Some Observation on Microstructural Evolution and Stress Corrosion Cracking Performance. *Trans Indian Inst Met.*(2018) 71, 2553–2564.
19. Guo G, Shen Y, Wu K, Yan Y. Effect of material position on microstructure and mechanical properties of friction stir welded dissimilar austenite–ferrite stainless steels joints. *Journal of Adhesion Science and Technology* (2021), 35(12), 1320–1336.
20. He B, Cui L, Wang D, Liu Y, Liu C, Li H. The metallurgical bonding and high temperature tensile behaviors of 9Cr–1W steel and 316L steel dissimilar joint by friction stir welding. *Journal of Manufacturing Processes*, (2019), 44, 241–251.
21. Alghazalah SAS, Ali SMJM. Effect of Friction Time on Mechanical Properties of Two Dissimilar Welded Joints of Austenitic Stainless Steel AISI304 and Low Carbon Steel ST–37 Using Rotary Friction Welding Techniques. *International Research Journal of Innovations in Engineering and Technology*, (2022), 6(9), 121.
22. Ma H, Qin G, Geng P, Li F, Fu B, Meng X. Microstructure characterization and properties of carbon steel to stainless steel dissimilar metal joint made by friction welding. *Materials & Design* (2015), 86, 587–597.
23. Salas Reyes AE, Lara Rodriguez GÁ, González Parra J.R, Mercado Lemus VH. Microstructural Characterization and Corrosion Behavior of Similar and Dissimilar Welded Advanced High–Strength Steels (AHSS) by Rotary Friction Welding. *Materials* (2024), 17, 918.
24. Banerjee A, da Silva L, Rahimi S. Finite element modelling of transient behaviours and microstructural evolution during dissimilar rotary friction welding of 316 austenitic stainless steel to A516 ferritic steel. *Journal of Advanced Joining Processes*(2023), 8, 100167.
25. Gambu ZV. An investigation of welded 304 and 316l stainless steel rods through rotary friction welding process (Doctoral dissertation, (2020), University of Johannesburg.
26. Kumar AS, Khadeer SA, Rajinikanth V, Pahari S, Kumar BR. Evaluation of bond interface characteristics of rotary friction welded carbon steel to low alloy steel pipe joints. *Materials Science and Engineering: A*, (2021), 824, 141844.
27. Kulkarni VV, Kulkarni PC. Experimental Study and Investigation of Mechanical Properties of Material SS304/SS316 Using Rotary Friction Welding Technique. (2022, June). In *Proceedings of Second International Conference in Mechanical and Energy Technology: ICMET 2021, India* (pp. 109–120). Singapore: Springer Nature Singapore.
28. Wang Y, Sebeck K, Tess M, Gingrich E, Feng Z, Haynes JA., Pierce D. Interfacial microstructure and mechanical properties of rotary inertia friction welded dissimilar 422 martensitic stainless steel to 4140 low alloy steel joints. *Materials Science and Engineering: A*, (2023), 885, 145607.
29. Thien N D, Le Quang D, Van TP, Anh T T. A welding temperature determination method of low carbon steel and stainless steel welded joint by Rotary friction welding process. (2016, November). In *2016 3rd International Conference on Green Technology and Sustainable Development (GTSD)* (pp. 206–211). IEEE.
30. Khamar S, Vyas V, Tamakuwala P., Badheka VJ. Mechanical and Metallurgical Analysis of Rotary Friction Welded Low Carbon Steel and Stainless Steel. In *International Conference on Futuristic Advancements in Materials, Manufacturing and Thermal Sciences* (2024, January). (pp. 203–214). Singapore: Springer Nature Singapore.
31. Alghazalah, S. A. S., & Ali, S. M. J. M. Effect of Forging Pressure on Mechanical Properties of Two Dissimilar Welded Joints of Austenitic Stainless Steel AISI304 and Low Carbon Steel ST–

- 37 Using Rotary Friction Welding Techniques. *Universal Journal of Mechanical Engineering*, (2023). 11(1), 12.
32. Mishra A, Gangil N, Siddiquee A N, Khan YS, Bhardwaj T, Singh, D K. Microstructural investigation on linear friction welded stainless steel and medium carbon steel. *Materials Today: Proceedings*. (2023).
33. Su Y, Li W, Wang X, Ma T, Li Y, Liu Y, Vairi A. On the process variables and weld quality of a linear friction welded dissimilar joint between S31042 and S34700 austenitic steels. *Advanced Engineering Materials*(2019), 21(7), 1801354.
34. Zambrano O A, Gholipour J, Wanjara P, Jiang J. Linear friction welding of abrasion resistant CPM 15V tool steel to an alloyed carbon shovel-tooth steel. *Journal of Manufacturing and Materials Processing*, (2023), 7(2), 51.
35. Rostamiyan Y, Zaferani M. Fabrication of polyethylene-based surface composite reinforced by carbon nano-tube and nano-clay through friction stir processing, *J. Mater. Process. Technol.*(2014), 233(4): 580-587.
36. R. Cazes; *Procédés de soudage: Principes généraux et critères de choix. Techniques de l'ingénieur. Génie mécanique.* (1995) B7700:1-6
37. Kautz DD. *Fundamentals of Friction Welding, Welding Fundamentals and Processes.*(2011), 06A, ASM Handbook, ASM International: 179-185.
38. Maalekian M. Friction welding-Critical assessment of literature, *Science and Technology of Welding and Joining.* (2007), 12:738-759.
39. Rombaut P, Wim DW, Koenraad F. Friction welding of Steel to ceramic. *Sustainable Construction and Design.* (2011) 2(3): 448-457.
40. Dawood AB, Butt SI, Hussain G, Siddiqui MA, Maqsood A, Zhang F. Thermal model of rotary friction welding for similar and dissimilar metals. *Metals.* (2017), 7(6): 224.

Rare Earth Fluorescent Nanomaterials for Enhanced Development of Latent Fingerprints in Forensic Sciences

Hanen DOUIRI

*Laboratory of Dielectric and Photonic Materials, Faculty of Sciences of Sfax, Sfax University,
Sfax 3018, Tunisia;
hanen.douiri.etud@fss.usf.tn
ORCID 0000-0002-5542-2281*

Ramzi MAALEJ

*Laboratory of Dielectric and Photonic Materials, Faculty of Sciences of Sfax, Sfax University,
Sfax 3018, Tunisia;
ramzi.maalej@fss.usf.tn
ORCID 0000-0002-6722-1882*

Abstract. Currently, effective fingerprint detection is crucial to criminal investigations. Fluorescent phosphors can be used to visualize fingerprints with high resolution and high contrast without interference of the background surface, which is ideal for its collection and registration. In this work, we investigated the potential rare earth fluorescent phosphors to visualize latent fingerprints. We prepared phosphor powders with various doping rare earth elements (Eu, Dy, Er, Yb and La) by various methods of synthesis. Morphology and luminescence properties of the synthesized powders were studied scanning Emission Electron Microscopy (SEM) and Photoluminescence (PL) spectroscopy, respectively. Various surfaces, including difficult ones (wood and ceramic), were successfully tested for latent fingerprint development with the prepared phosphor powders. Thanks to the high contrast obtained, fingerprint ridge patterns at all three levels were highlighted: core (level 1) islands, bifurcation, and enclosure (level 2), and even sweat pores (level 3). Thus, our results demonstrate that the different kinds of rare earth fluorescent nanomaterials hold great promise for latent fingerprint imaging applications in forensic sciences.

Keywords: Rare earth, Phosphors, luminescence, Fingerprints

1. Introduction

Due to their distinctiveness, latent fingerprints play a crucial role in identifying individuals at crime scenes. Thanks to this, the extraction of latent fingerprints is one of the first actions to take in a crime scene. Perspiration continually produces sebum and sweat, which can leave detectable marks when fingers come into contact with various surfaces [1,2]. Fingerprints at crime scenes are often not visible to the naked eye, particularly those left on smooth surfaces, which are especially challenging to detect. Typically, only level 1 and level 2 ridge features are discernible, though a few individuals may be able to observe level 3 ridge details or sweat pores [3,4]. Level 1 details encompass general morphological features, such as the overall ridge pattern and ridge flow of the fingerprint. Level 2 details provide information on the alignment and pattern of individual ridges. Level 3 details include finer elements like sweat

pores, ridge curvature, spots, and dimensional aspects of the fingerprint ridges. Therefore, it is crucial to enhance the efficiency of the powder dusting method, as it is the simplest and most commonly used technique for fingerprint visualization compared to other methods. In order to improve the resolution of latent fingerprints on both porous and non-porous surfaces, research groups have explored the use of luminescent rare earth nanoparticle powders [5-9]. Rare earth (RE) elements are considered significant as potential activators for fluorescent materials across various wavelengths due to their unique electronic structures. Their luminescent properties are determined by the positioning of the lanthanide (Ln) dopants' 4f energy levels relative to the valence band (VB) and conduction band (CB) of the host material [10,11].

In this work, we report the successful preparation of non-toxic luminescent $Y_2Sn_2O_7:Eu^{3+}$, Dy^{3+} YTO: Er^{3+} , Yb^{3+} and $La_2O_3:Bi^{3+}$ nanophosphors at various doping concentrations via different methods of

synthesis. These powders were characterized using different techniques and then used to detect even the third level of detail in fingerprints.

2. Sample preparation

$Y_2Sn_2O_7:Eu^{3+}$, Dy^{3+} nanopowders were synthesized via coprecipitation method. Stoichiometric amounts of $SnCl_2 \cdot 2H_2O$, Eu_2O_3 , and Y_2O_3 were dissolved in 1M HCl solution and stirred for 2 h. Then, 40 mL of ethylene glycol was added and the solution was slowly heated up to $100^\circ C$. Afterwards, 2 g of urea was added and the solution was stirred 2 h at $150^\circ C$. After being cooled to room temperature, the precipitate was collected by centrifugation, washed two times with acetone, and dried at room temperature. The samples thus prepared were finally calcined at $1300^\circ C$ in air at a heating rate of $10^\circ C$ per minute for 5 h.

YTO: Er^{3+} , Yb^{3+} nanopowders, different oxides (Y_2O_3 , TiO_2 , Yb_2O_3 and Er_2O_3) were prepared by grinding the corresponding stoichiometric composition with some drops of acetone in a ball mill agate mortar for 3 h, until they were ground homogeneously. The materials were pre-sintered under air atmosphere at $800^\circ C$ for 4 h and then sintered at $1200^\circ C$ for 5 h. The mixture was pelletized and heated repeatedly at $1500^\circ C$ for 5 h. For $La_2O_3:Bi^{3+}$, a quantity of 50 mL of distilled water was used to thoroughly dissolve 5 g of citric acid monohydrate and 5 g of lanthanum nitrate ($La(NO_3)_3 \cdot 6H_2O$). After that, an appropriate amount of bismuth nitrate ($Bi(NO_3)_3 \cdot 5H_2O$) was added to the previously stated solution dropwise after being separately dissolved in 10 mL of distilled water and 0.5 mL of 70 % concentrated nitric acid. After three hours of intense stirring at $85^\circ C$, this was placed in a $200^\circ C$ furnace and burned with a white flame for 2 h. Brown powder was the end outcome. In order to improve the crystallinity and to reduce the $1200^\circ C$, maintained for 2 h.

3. Results and discussion

Figure 1 shows SEM images of different compounds. Small particles have an irregular shape, with each particle consisting of multiple crystallites.

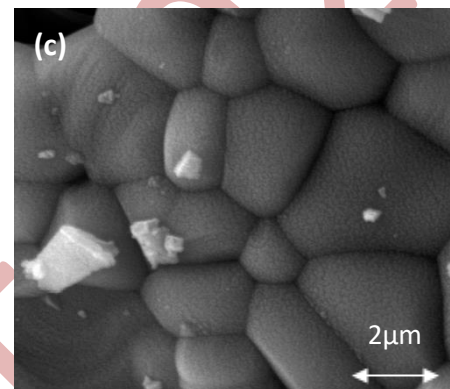
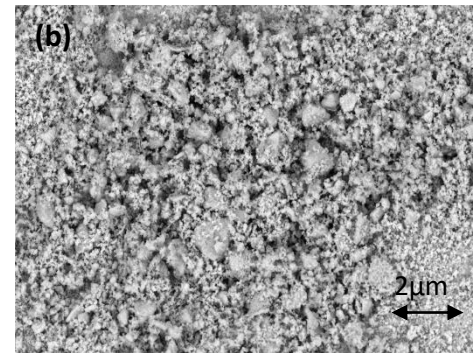
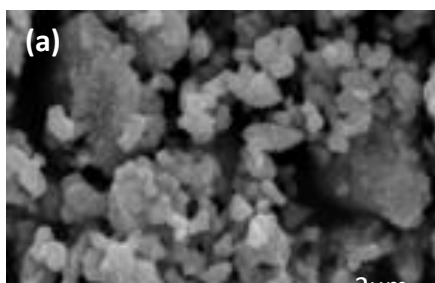
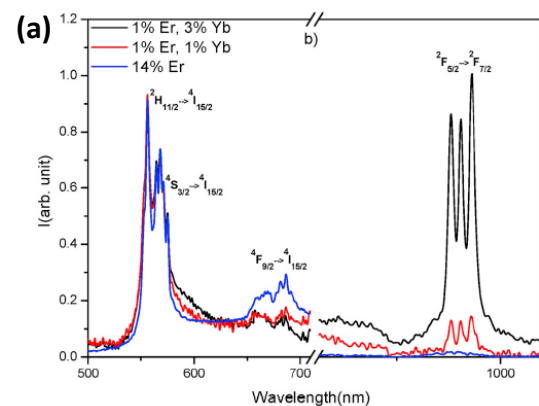


Figure 1. SEM images of (a) $Y_2Sn_2O_7:Eu^{3+}$, Dy^{3+} , (b) YTO: Er^{3+} , Yb^{3+} and (c) $La_2O_3:Bi^{3+}$ phosphors

Figure 2 shows photoluminescence spectra of the different synthesized powders with different amounts of dopant concentrations.



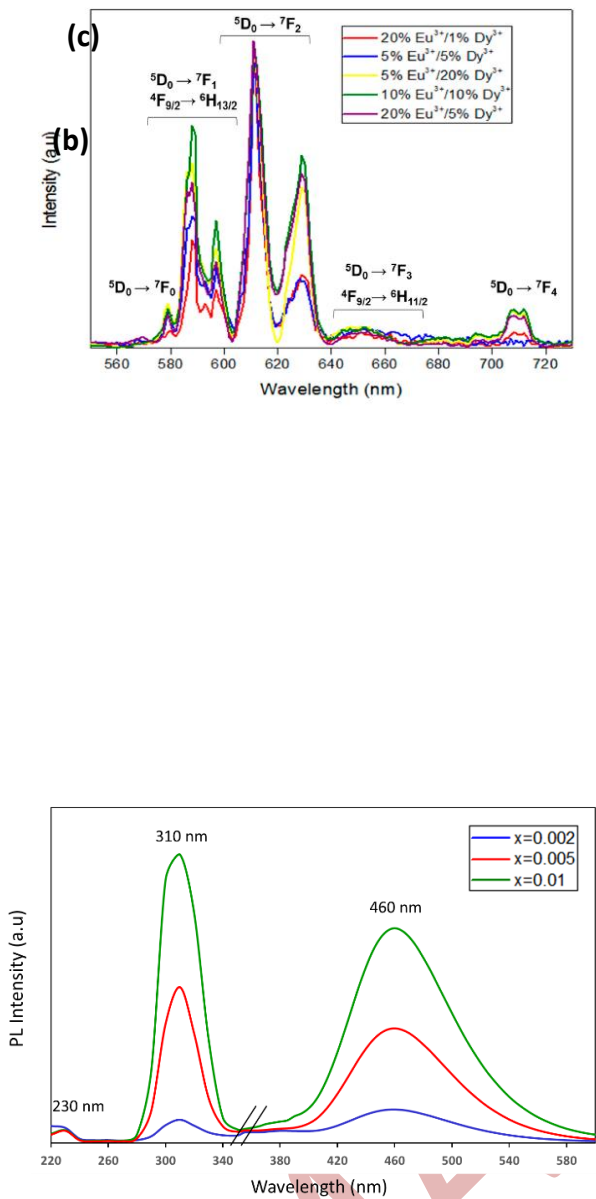


Figure 2. Emission spectra of (a) $Y_2Sn_2O_7:Eu^{3+}, Dy^{3+}$ and (b) $YTO:Er^{3+}, Yb^{3+}$; (c) Excitation and emission spectra of $La_{2-x}O_3:Bi_x$ phosphors

$Y_2Sn_2O_7:Eu^{3+}, Dy^{3+}$ phosphors present an intense $^5D_0 \rightarrow ^7F_2$ emission peak at 611 and 626 nm [7]. For $YTO:Er^{3+}, Yb^{3+}$ powders, the intense emission is located at 550-600 nm and corresponds to $^2H_{11/2} \rightarrow ^4I_{15/2}$ transition [7]. For $La_{2-x}O_3:Bi_x$ the intense emission is located at 420 nm and is attributed to radiative transitions from the 3P_1 excited state back to the 1S_0 ground state [8].

Figure 3 illustrates the fingerprint images under UV illumination for the three synthesized fluorescent nanopowders on aluminum foil. The quality of the latent fingerprint based on visual assessment was excellent. Moreover, from Fig.3 (d), all three levels of fingerprint ridge patterns are clearly visualized:

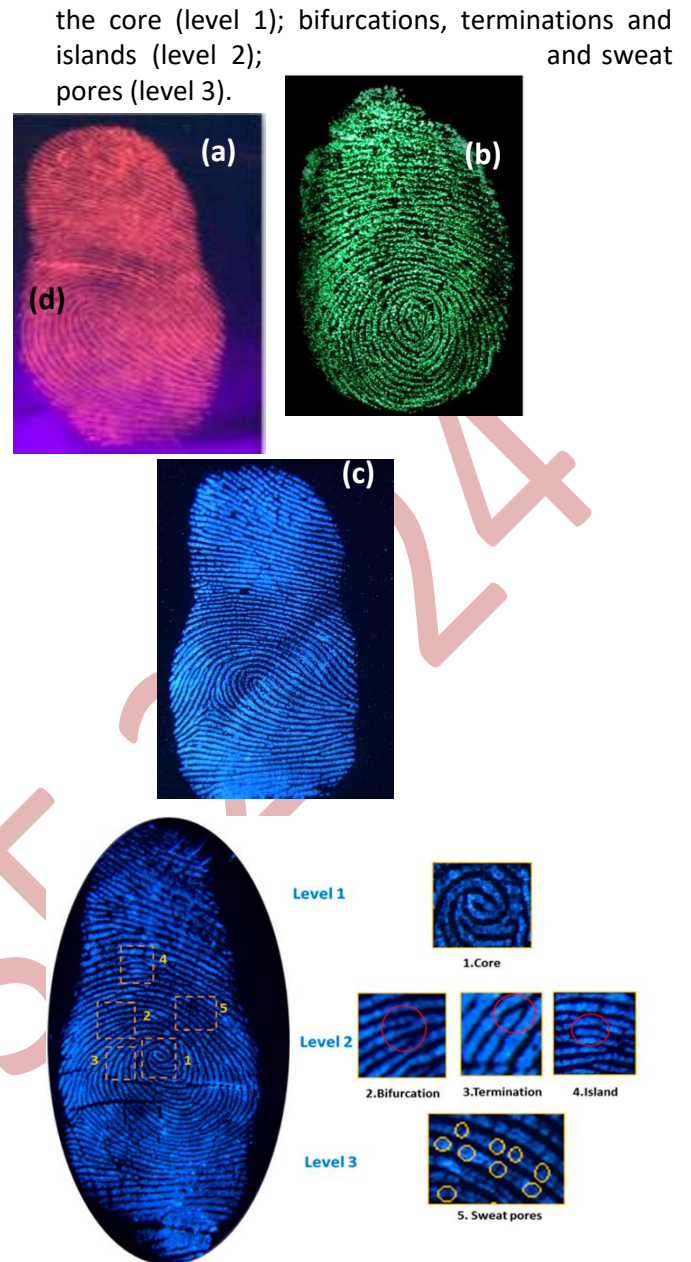


Figure 3. Developed fingerprint images obtained with $Y_2Sn_2O_7:Eu^{3+}, Dy^{3+}$, (b) $YTO:Er^{3+}, Yb^{3+}$; (c) $La_2O_3:Bi^{3+}$ phosphors on aluminium foil; (d) Enlarged fingerprint image visualization on aluminium foil

4. Conclusion

Different fluorescent nanopowders were successfully synthesized in order to be used in the detection of latent fingerprints in the scene of

crime. Morphological and optical properties of these powders were characterized via SEM and PL techniques. When exposed to UV light, all phosphors demonstrated significant promise for the viewing of latent fingerprints by generating

latent fingerprint images with excellent contrast and recognition of all three levels. This demonstrates that they are promising fluorescent agents for forensic applications.

References

- [1] Y. Yang, X. Liu, Y. Lu, L. Tang, J. Zhang, L. Ge, F. Li, Visualization of latent fingerprints using a simple “silver imaging ink. *Anal. Methods*. 8 (2016) pp 6293.
- [2] C. Wang, J. Zhou, L. Lulu, Q. Song, Rapid Visualization of Latent Fingerprints with Color-Tunable Solid Fluorescent Carbon Dots. *Part. Part. Syst. Charact.* 35 (2018), pp1700387.
- [3] R.B. Basavaraj, G.P. Darshan, B.D. Prasad, S.C. Sharma, H. J. Nagabhushana, Rapid visualization of latent fingerprints using novel $\text{CaSiO}_3:\text{Sm}^{3+}$ nanophosphors fabricated via ultrasound route. *Rare Earths* 37 (2019), pp 32–44.
- [4] B. Marappa, M.S. Rudresha, R.B Basavaraj, G.P. Darshan, B.Daruka Prasad, S.C. Sharma; S. Sivakumari, P. Amudha, H. EGCG Nagabhushana, *Sens. Actuators B Chem.* 264 (2018), pp 426–439.
- [5] M.Gouiaa, I. Bennour , L.Rzouga Haddada, A. Toncelli , J. Xu, A. Mbarek, A. Moscardini, N. Essoukri Ben Amara, R. Maalej, Spectroscopic characterization of Er, Yb: $\text{Y}_2\text{Ti}_2\text{O}_7$ phosphor for latent fingerprint detection. *Physica B* 582 (2020) pp 412009, doi.org/10.1016/j.physb.2020.412009
- [6] L. Brini, I.Bennour , A.Toncelli, R. Maalej, M.Abdelhedi, Eu-Doped Pyrochlore Crystal Nano-Powders as Fluorescent Solid for Fingerprint Visualization and for Anti-Counterfeiting Applications *Materials* 15 (2022) pp 2423, doi.org/10.3390/ma15072423
- [7] L. Brini, H. Douiri , M.Abid , A.Toncelli, M. Qasymeh, R. Maalej, M.Abdelhedi, *Crystals* 14 (2024), pp 300, doi.org/10.3390/cryst14040300
- [8] H. Douiri, M. Abid, L. Rzouga Haddada, L. Brini, A. Toncelli, N. Essoukri Ben Amara, R. Maalej, Strongly Fluorescent Blue-Emitting $\text{La}_2\text{O}_3:\text{Bi}^{3+}$ Phosphor for Latent Fingerprint Detection, *Materials* 17(2024),pp 4217. doi.org/10.3390/ma17174217
- [9] N.M. Maalej, A. Qurashi, , I. Bennour, L.R. Haddada, M.N. Shaikh, M. Ilyas, N.E.B. Amara, R. Maalej, M.A. Gondal, Green emitting rare earth Gd_2O_3 . Green Emitting Rare Earth $\text{Gd}_2\text{O}_3:\text{Tb}^{3+}$ Nanoparticles for Rapid Imaging of Latent Fingerprint Methods *Appl. Fluores.* 9(2021), pp 025002.
- [10] J. Zhong, W. Zhao, Y. Zhuo, C. Yan, J. Wen, J. Brgoch, Understanding the blue-emitting orthoborate phosphor $\text{NaBaBO}_3:\text{Ce}^{3+}$ through experiment and computation. *J. Mater. Chem. C* 7 (2019), pp 654–662.
- [11] P. Guss, M.E. Foster, B.M. Wong, F.P. Doty, K. Shah, M.R. Squillante, U. Shirwadkar, R. Hawrami, J. Tower, D. Yuan, Results for aliovalent doping of CeBr_3 with Ce^{2+} , *J. Appl. Phys.* 115 (2014), pp 034908.

Towards High Temperature Thermoelectrics: Effect of simultaneous doping and defect chemistry engineering on perovskite materials

Shahed Rasekh

University of Aveiro- Department of Materials and Ceramic Engineering, CICECO-Aveiro Institute of Materials, 3810-193, Aveiro, Portugal,
shahedvrm@ua.pt
ORCID: 0000-0003-3466-9952

Parisa Amirkhizi

Department of Materials and Ceramic Engineering, CICECO-Aveiro Institute of Materials, University of Aveiro, 3810-193 Aveiro, Portugal,
parisa.amirkhizi@ua.pt
ORCID: 0000-0003-2764-4108

Mehdi Hedayati

University of Aveiro- Department of Materials and Ceramic Engineering, CICECO-Aveiro Institute of Materials, 3810-193, Aveiro, Portugal,
mehdi.hedayati@ua.pt
ORCID: 0009-0003-0289-3439

Maria A. Madre

INMA (CSIC-Universidad de Zaragoza) Department of Materials Science, 50059, Zaragoza, Spain,
amadre@unizar.es
ORCID: 0000-0002-0794-3998

Andres Sotelo

INMA (CSIC-Universidad de Zaragoza) Department of Materials Science, 50059, Zaragoza, Spain,
asotelo@unizar.es
ORCID: 0000-0001-7056-0546

Miguel A. Torres

INMA (CSIC-Universidad de Zaragoza) Department of Materials Science, 50059, Zaragoza, Spain,
matorres@unizar.es
ORCID: 0000-0003-3995-5763

Andrei Kovalevsky

Department of Materials and Ceramic Engineering, CICECO-Aveiro Institute of Materials, University of Aveiro, 3810-193 Aveiro, Portugal,
akavaleuski@ua.pt
ORCID: 0000-0001-5814-9797

Cite this paper as: Rasekh, Sh., Amirkhizi, P., Hedayati, M., Madre, MA, Sotelo, A., Torres, MA, Kovalevsky, A., Towards High Temperature Thermoelectrics: Effect of simultaneous doping and defect chemistry engineering on perovskite materials .Int. Conf. Advanced. Mater. Sci.& Eng. HiTech.and Device Appl.Oct. 24-26 2024, Ankara, Turkiye

Abstract. The global energy crisis demands innovative solutions to recover wasted heat from industrial processes, especially in energy-intensive sectors like ceramics, glass, and automotive manufacturing. Thermoelectric power generation, which directly converts heat into electricity using solid-state devices, has emerged as a promising approach for enhancing energy efficiency and reducing carbon emissions. With rising interest in high-temperature applications, oxide materials have gotten huge attention due to their superior thermal stability, natural abundance, and non-toxic properties.

This research focuses on developing ceramic composites with optimized thermoelectric properties. These are achieved through material engineering approaches, including structural modifications, e.g. doping and defect engineering. This work focuses on enhancement of thermoelectric properties simultaneous doping and defect chemistry engineering on perovskite materials, namely BaTiO. It was found that doping in B site led to formation of cubic structure favouring thermoelectric properties, while existence of defect reduced thermal conductivity. As a consequence of these modification, an interesting ZT of 0.25 at 900°C were obtained for these materials.

Keywords: Thermoelectric, Composite, waste heat recovery, Energy Conversion, synthesis
© 2024 Published by ICMATSE

Among the emerging technologies for alternative green power generation, thermoelectric (TE) materials gain large attention due to their ability of direct electrical energy production from heat and vice versa based on Seebeck and Peltier effects, to be used as power generator and cooling system, respectively [1,2]. A basic TE power generator circuit is just composed of two different semiconductor-type materials, i.e. n- and p- type, with similar properties, known as TE pair, without any additional components and/or moving parts. Great efforts have been made to increase the performance of these materials, measured by Figure of merit $ZT=TS^2/\rho\kappa$ (in which the electrical part S^2/ρ is also called power factor, PF), where S is the Seebeck coefficient, ρ the electrical resistivity, κ the thermal conductivity, and T is the absolute temperature. The demand of performing TE materials ($ZT\sim 1$) for low- and intermediate temperature applications is covered by "traditional", e.g. Bi₂Te₃-based thermoelectric [3]. Existing alternatives with promising peak ZT's of 0.7-1.2 (Half-Heusler and SiGe-based alloys...) [4] still lack the thermal or chemical stability at ~500-600°C or require a protective packing to operate at high temperatures or expensive and time-consuming production methods, like Arc-Melting [5]. Nowadays, by following the discovery of relatively high thermopower on NaCo₂O₄ [6], the efforts is focused on designing thermoelectric materials based on transition metal oxides [7]. Their main advantages are low toxicity, high natural abundance and reasonable stability at high temperatures and their ability of properties enhancing using different physical or chemical methods. Studies on layered cobalt oxides e.g. Ca₃C₄O₉, as representatives of p-type TE oxides, resulted in extraordinary TE properties enhancement, surpassing Single Crystal values, using different synthesis, sintering, and fabrication of bulk sample [8]. Moreover, the best performance values obtained for n-type materials are based on perovskites, e.g. SrTiO₃ [9], which are still too low for practical applications [10], mainly due to their complex structure (cubic/orthorhombic perovskite or hexagonal wurtzite, etc.). In both

cases, the achieved enhancement involved modifying band gap and charge carrier concentration [11]. This modification can be originated from structural modifications, synthesis process, and/or during their sintering and fabrications.

Table 1. *Samples composition and corresponding ID*

Sample	Composition
E1	BaTiO ₃
E2	Ba _{0.975} TiO ₃
E3	Ba _{0.95} TiO ₃
E4	BaTi _{0.95} Ta _{0.05} O ₃
E5	Ba _{0.975} Ti _{0.95} Ta _{0.05} O ₃
E6	Ba _{0.95} Ti _{0.95} Ta _{0.05} O ₃
E7	BaTi _{0.9} Ta _{0.1} O ₃
E8	Ba _{0.975} Ti _{0.9} Ta _{0.1} O ₃
E9	Ba _{0.95} Ti _{0.9} Ta _{0.1} O ₃

This work studies the effects of various grade of chemical defect and doping in BaTiO on thermoelectric properties. In this work the compounds (Ba_(1-x)Ti_(1-y)Ta_yO₃ (where x= 0, 0.025 and 0.05 and y= 0, 0.05 and 0.1) prepared using classical solid state rout. The samples were identified using E1 through E9 as described in Table 1.

Powder X-ray diffraction (XRD) has been performed in a PHILIPS X'PERT between 10 and 80 ° to identify the phases in the samples. Microstructural observations were performed on samples surfaces after sintering in a SEM, Hitachi SU-70 instrument fitted with an energy dispersive spectrometer (EDS) used to determine the elemental composition of each phase. Electrical conductivity was measured using the four-point probe DC homemade equipment (Aveiro, Portugal) and Seebeck coefficient was simultaneously measured in the same system in a steady-state mode under H₂ atmosphere from 900°C to 250°C. The thermal conductivity was calculated using data recorded from thermal diffusivity utilizing a laser-flash system (Linseis LFA 1000) and Specific heat employing the Dulong-Petit law.

Results and discussion

Figure 1 shows XRD data for undoped samples while Figure 2 shows the doped ones. For undoped samples secondary phase were identified as BaTaO compound. However, all the doped samples show very similar and single phase pattern, demonstrating Ta doping effectively favoured the formation of cubic.

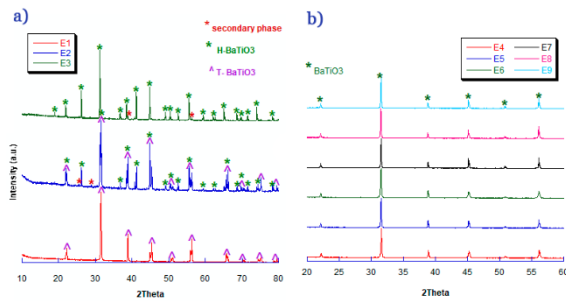


Figure 1. XRD patterns of a) $Ba_{(1-x)}O_3$ (where $x=0, 0.025$ and 0.05) and b) $Ba_{(1-x)}Ti_{(1-y)}Ta_yO_3$ (where $x=0, 0.025$ and 0.05 and $y=0, 0.05$ and 0.1)

Representative SEM images shown in Figure 3, indicate that the n-type compound is formed by large polygonal grains with clear porosities between the grains. EDS image shows that all the elements were homogeneously dispersed in all the samples. Density measurement revealed ca. 85% relative density for all samples in agreement with SEM observation. The porosity produced is mainly due to the lower sintering temperature (ca. 1400°C) competing with melting point (ca. 1600°C).

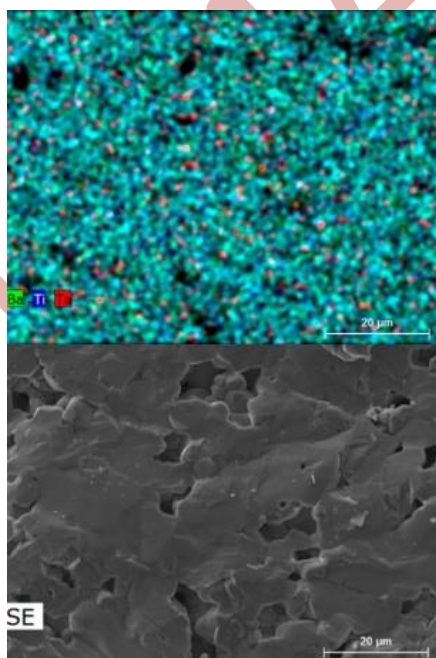


Figure 3. Representative SEM (down) and EDS mapping (up) of the n-type compound.

The effect of simultaneous doping and defect chemistry engineering on electrical conductivity in different temperature is illustrated in Figure 4.

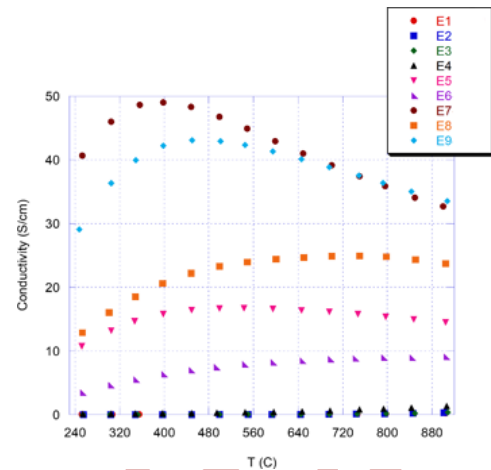


Figure 4. Samples electrical conductivity variation with temperature

As it can be observed doping the samples with Ta greatly enhanced the conductivity of the samples. The maximum conductivity measured for samples E7 and E9 (32 S/cm) more than 30 times of undoped samples (ca. 1 S/cm). this large difference can be associated to charge carrier modification in doped samples originated from different oxidation state to Ta (+5) and Ti (+3) as well as formation of cubic structure in doped samples in compared to tetragonal ones in undoped samples. All samples showed a semiconductor like behaviour with exception of E7 and E9 which have higher Ta doping amount and higher charge carrier concentration.

S variation with temperature, shown in Figure 5 displays negative values confirming n-type thermoelectric behaviour. A drastically changes observed from undoped sample in compare with doped ones in agreement with observation in electrical conductivity. The Seebeck values of all doped samples increased with temperature reaching interesting values of 350 $\mu V/K$ for E5 and E6 which associated with lower charge carrier concentration in these samples.

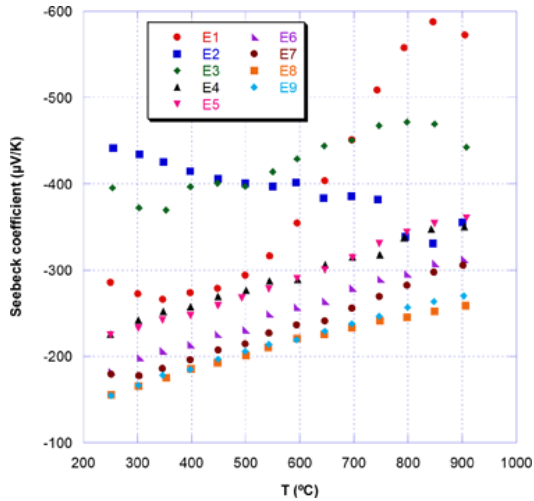


Figure 5. Seebeck coefficient variation with temperature for both compounds

The thermoelectric performances of these samples were determined through their PF, calculated from electrical conductivity and Seebeck values, and its variation with temperature is illustrated in Figure 5.

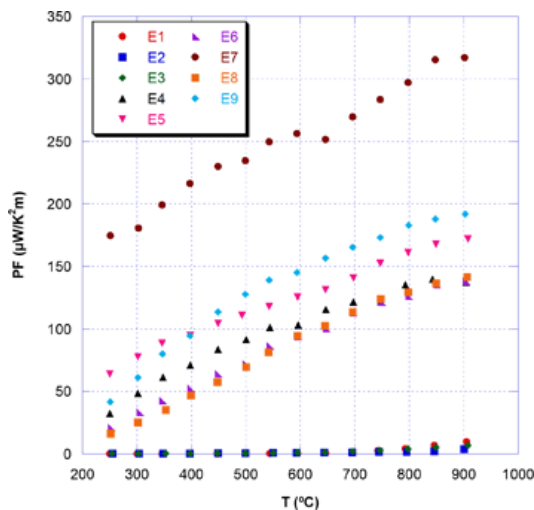


Figure 5. PF variation with temperature

The highest values at 900 °C was obtained for E7 sample with reaching 320 $\mu\text{W}/\text{K}^2\text{m}$, mainly due to higher electrical conductivity together with moderate Seebeck value.

The calculated thermal conductivity of samples presented in Figure 6. In all the samples a decrease in the thermal conductivity values observed as the temperature increases. The reduction in thermal conductivity in Ta-doped samples can be attributed to the mass contrast between Ta and Ti, which increases phonon scattering and reduces thermal transport. Additionally, the presence of oxygen and A-site vacancies further disrupts the lattice, contributing to lower thermal conductivity.

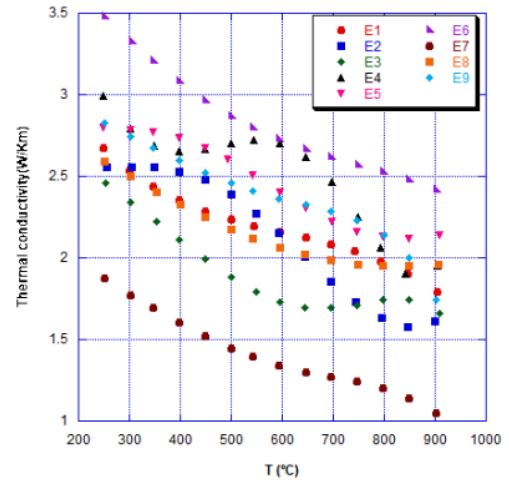


Figure 6. Thermal conductivity variation with temperature

The thermoelectric figure of merit (ZT) of the BaTiO₃ samples as a function of temperature is shown in Figure 7. An important enhancement on ZT values is clear when samples doped with Ta. Moreover, the ZT values increased with temperature for all the samples. As expected from Seebeck and electrical conductivity, samples with higher Ta amount shows higher ZT. Furthermore, the Ba deficiency effectively reduces thermal transport, likely due to increased phonon scattering from oxygen vacancies. Therefore, samples with combine Ta doping and Ba deficiency shower higher ZT values reaching a significant value of 0.4 for E7 sample at 900°C.

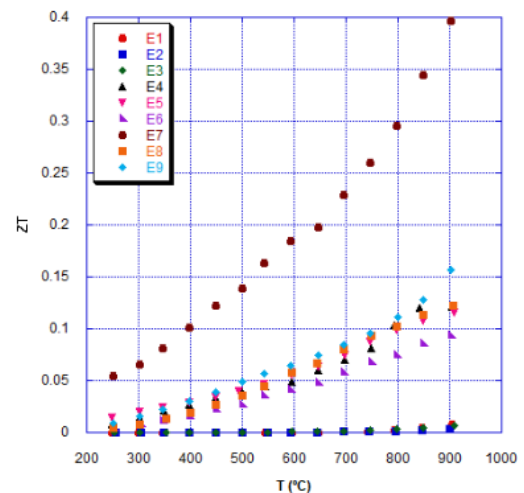


Figure 7. Figure of merit (ZT) variation with temperature

Conclusions

In this work, Ba_(1-x)Ti_(1-y)Ta_yO₃ (where x= 0, 0.025 and 0.05 and y= 0, 0.05 and 0.1) compounds have been successfully prepared through the solid state method. XRD patterns showed that the doped samples were nearly single phase. SEM/EDX

observation agreed with these data while showing that the compounds possessed porosity. The Ta doped samples shows a great improvement Electrical conductivity value, but lower $|S|$ values. Nevertheless, Ta doped samples Power Factor and ZT are much higher than undoped ones. Among them, samples with moderate Ba deficiency

demonstrate higher thermoelectric performance, ZT. These results establish the BaTiO compound can effectively engineering through doping and defect engineering with promising values suitable for practical applications.

References

1. D.M. Rowe, in: D.M. Rowe (Ed.), *Thermoelectrics Handbook: Macro to Nano*, 1st edn, CRC Press, Boca Raton, FL, 2006, pp. 1-3-1-7.
2. G.J. Snyder, E.S. Toberer. Complex thermoelectric materials. *Nat Mater*, 7 (2008) pp105-14. 10.1038/nmat2090.
3. M. S. Dresselhaus, G. Chen, M. Y. Tang, R. G. Yang, H. Lee, D. Z. Wang, Z. F. Ren, J.-P. Fleurial, P. Gogna. *New Directions for Low-Dimensional Thermoelectric Materials*, *Adv Mater*, 19 (2007) PP 1043–1053. 10.1002/adma.200600527
4. L. Huang, Q. Zhang, B. Yuan, X. Lai, X. Yan, and Z. Ren, Recent progress in half-Heusler thermoelectric materials, *Materials Research Bulletin*, 76 (2016) pp. 107–112 10.1016/j.materresbull.2015.11.032
5. M. Gharsallah, F. Serrano-Sánchez, J. Bermúdez, N. M. Nemes, J. L. Martínez, F. Elhalouani & J. A. Alonso, Nanostructured Bi₂Te₃ Prepared by a Straightforward Arc-Melting Method *Nanoscale research letters* 11 (2016) pp. 142-148 10.1186/s11671-016-1345-5
6. I. Terasaki, Y. Sasago, and K. Uchinokura, Large thermoelectric power in NaCo₂O₄ single crystals *Phys. Rev. B* 56 (1997) R12685 10.1103/PhysRevB.56.R12685
7. A. Sotelo, S. Rasekh, M.A. Torres, P. Bosque, M.A. Madre, J.C. Diez, Improved thermoelectric performances in textured Bi_{1.6}Pb_{0.4}Ba₂Co₂O_y/Ag composites *Ceram. Int.* 42 (2016) pp 18592-18596 10.1016/j.ceramint.2016.08.202
8. M. A. Madre, Sh. Rasekh, M. A. Torres, P. Bosque, J. C. Diez & A. Sotelo Enhanced electrical and thermoelectric properties from textured Bi_{1.6}Pb_{0.4}Ba₂Co₂O_y/Ag composites *J. Mater. Sci.* 52 (2017) pp 4833 –4839 0.1007/s10853-016-0718-6
9. Y. Yin, B. Tudu, A. Tiwari, Recent advances in oxide thermoelectric materials and modules *Vacuum* 146 (2017) pp 356-374 10.1016/j.vacuum.2017.04.015
10. L. Bocher, M. H. Aguirre, D. Logvinovich, A. Shkabko, R. Robert, M. Trottmann, and A. Weidenkaff, CaMn_{1-x}Nb_xO₃ ($x \leq 0.08$) Perovskite-Type Phases As Promising New High-Temperature n-Type Thermoelectric Materials. *Inorg. Chem.* 47 (2008) pp 8077 -8085 10.1021/ic800463s
11. E. Li, N. Wang, H. He, and H. Chen, Improved Thermoelectric Performances of SrTiO₃ Ceramic Doped with Nb by Surface Modification of Nanosized Titania *Nanoscale Res. Lett.* 11 (2016) 188 10.1186/s11671-016-1407-8.

Acknowledgements

The authors wish to thank the Gobierno de Aragón (Grupo de Investigación T54_23R) and Universidad de Zaragoza (UZ2022-IAR-09) for financial support. Sh. Rasekh acknowledges the support of the Research Employment Contract FCT–CEECIND/02608/2017. This work was also developed within the scope of the PhD project of P. Amirkhizi (grant 2020.08051.BD funded by FCT) and the project CICECO-Aveiro Institute of Materials, UIDB/50011/2020, UIDP/50011/2020 & LA/P/0006/2020, financed by national funds through the FCT/MCTES (PIDDAC). Authors would like to acknowledge the use of Servicio General de Apoyo a la Investigación-SAI, Universidad de Zaragoza.

Photocatalytic activity under sunlight by copper Oxide Thin Films

Nour elhouda Redjough

Laboratory of Thin Film Physics and Applications LPCMA, University Mohamed Khider-Biskra, Algeria,
 nourelhouda.redjough@univ-biskra.dz
 ORCID: 0009-0001-1496-8237

Nedjette Belhamra

Laboratory of Thin Film Physics and Applications LPCMA, University Mohamed Khider-Biskra, Algeria,
 n.belhamra@univ-biskra.dz
 ORCID: 0009-0000-4855-5708

Abstract. Copper oxide is a P-type semiconductor material that is black in color with a slight transparency. It is an interesting material for various applications due to the abundance of its components in nature, its good thermal stability and its structural and optical properties. This property allows it to be almost excellent in many applications such as catalysts, solar cells and batteries... In this work-in-progress, the solution was prepared by the Sol-Gel method and thin films of CuO were deposited on glass substrates by Dip Coating technique, this study focused on different film thicknesses by varying the frequent number of layers deposited. The structural analysis by X- ray diffraction (XRD) shows that all the samples are polycrystalline with monoclinic crystal structure. The optical properties of the films were characterized by UV-Visible spectrophotometry, which shows that the films show high absorbance in the visible region. Their optical band gap decreases from 2.10 to 1.80 eV when varying the frequent number of layers deposited increases from 2 to 5 layers. The photocatalytic performance of nanocomposites synthesized under sunlight was studied in the degradation of crystal violet (CV) dye as a target pollutant for 150 min.

Keywords: Sol-Gel, Dip-Coating, Copper Oxide, Thin Films, photocatalytic
 © 2024 Published by ICMATSE

Dip-coating or soaking: less used method, it consists in soaking the substrate in the solution to be deposited and then removing it with a constant speed which conditions the thickness of the deposit (Figure 1).

Table 1. Some chemical properties of CuO [2]

property	value
molecular formula	CuO
appearance	black powder
water solubility	insoluble

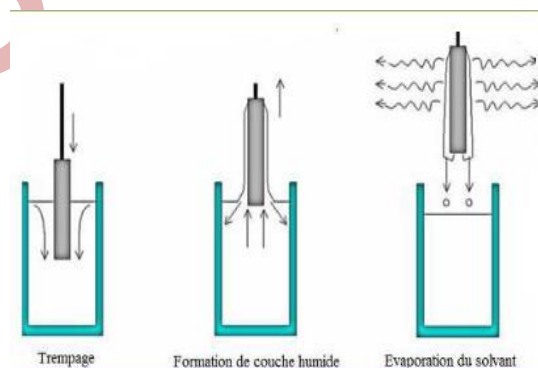


Figure 1. Deposition of thin films by dipping-pulling [1].

Copper oxide (II) in mineral form known as tenority in its natural state, with the CuO formula, it also comes in the form of a dark grey or dark black powder. Table 1 groups some chemical properties of copper oxide (CuO).

1. S. Chelouche, Propriétés des fenêtres optiques ZnO:Al pour cellules solaires en couches minces à base de CIGS, Mémoire de magister, Université Ferhat Abbas-Setif-Algérie (2012).
2. A. Altaweel, Synthèse de nanostructure d'oxyde de cuivre par microo-post- décharge microonde à pression atmosphérique, Thèse de doctorat, Université de lorraine (2014).

Research and Development of Gd-doped Al/Gd/Y₂O₃/Si/Al MOS-based Nuclear Radiation Detectors

Canan Kaliber

Erciyes University-Department of Physics, 38030, Kayseri, Türkiye,
nejdetparan@erciyes.edu.tr
ORCID: 0000-000X-0XXX-0XXX

Saleh Abubakar

Erciyes University-Department of Physics, 38030, Kayseri, Türkiye,
salehbinabubakar@gmail.com
ORCID: 0000-0003-1511-2219

Emrah Tiras

Erciyes University-Department of Physics, 38030, Kayseri, Türkiye,
University of Iowa-Department of Physics & Astronomy, 52242, Iowa City, IA, USA,
etiras@fnal.gov
ORCID: 0000-0002-5628-7464

Cite this paper as: Abubakar, S., Kaliber, C., Tiras, E., Research and Development of Gd-doped Al/Gd/Y₂O₃/Si/Al MOS-based Nuclear Radiation Detectors. Int. Conf. Advanced. Mater. Sci. & Eng. HiTech. and Device Appl. Oct. 24-26 2024, Ankara, Türkiye

Abstract. Optimizing the gate dielectric's radiation response is critical for enhancing the sensitivity and performance of radiation sensors. This study explores the effects of gamma irradiation on the electrical characteristics of Al/Gd/Y₂O₃/n-Si/Al MOS capacitors. These capacitors are fabricated with a stacked gate oxide layer containing Gadolinium (Gd) and Yttrium Oxide (Y₂O₃), grown on an n-type Silicon(n-Si) substrate via thermal oxidation and electron beam evaporation techniques. The aluminum gate and back contacts were deposited using thermal evaporation. The impact of gamma irradiation was assessed through Capacitance-Voltage (C-V), Conductance-Voltage (G-V), and Current Density-Voltage (J-V) measurements. Additionally, the interface state and oxide trap charge densities were evaluated from mid-gap to flat-band points based on the C-V curves for in-depth analysis. The results indicate that interfacial layers, likely responsible for forming interfacial dipoles, play a key role in reducing interface trap and oxide trap charge densities, enhancing the device's charge storage capacity. These improvements significantly enhanced the radiation sensitivities of the devices.

Keywords: Gd, MOS Capacitors, Nuclear Radiation, Si, Y₂O₃.

© 2024 Published by ICMATSE

1. INTRODUCTION

The optimization of gate dielectric oxides is critical for enhancing the performance and sensitivity of radiation sensors, particularly in environments with high levels of ionizing radiation. Radiation detectors play a vital role in various fields such as nuclear physics, space applications, medical imaging, and radiation dosimetry, where precise detection of ionizing particles is necessary. One of the promising approaches to achieving high sensitivity and improved performance in these detectors is the integration of advanced dielectric oxide materials within Metal-Oxide-

Semiconductor (MOS) capacitor structures. Among these materials, Gadolinium (Gd)-doped Yttrium Oxide (Y₂O₃) has garnered considerable interest due to its unique dielectric properties, high radiation resistance, and potential to enhance charge storage capabilities [1,2]. This study focuses on the research and development of Gd-doped Al/Gd/Y₂O₃/Si/Al MOS-based nuclear radiation detectors, aiming to achieve superior sensitivity to ionizing radiation. By leveraging the properties of Gadolinium, known for its high neutron capture cross-section, and Y₂O₃, valued for its robust dielectric constant and thermal stability, the designed MOS structure seeks to address the

challenges of detecting low-energy gamma radiation. The stacked gate dielectric structure, consisting of a thin Gd-doped Y_2O_3 layer deposited on a silicon (Si) substrate, serves as the core of the MOS capacitor design. The integration of these materials is expected to not only improve the overall dielectric performance but also to enhance the detection sensitivity in gamma-irradiated environments of the Gd-doped Al/Gd/ Y_2O_3 /Si/Al MOS-based capacitors carried out on an n-type silicon (n-Si) substrate using advanced electron beam evaporation and thermal oxidation techniques, ensuring precise control over thin film thickness and uniformity. These techniques were chosen for their ability to produce high-quality, defect-free dielectric layers that are essential for maintaining the integrity and functionality of the MOS capacitors under radiation exposure. The resulting thin films, composed of Al, Gd, and Y_2O_3 , were subjected to comprehensive structural and morphological analysis using Scanning Electron Microscopy (SEM) and X-ray diffraction (XRD) measurements. SEM was employed to investigate the surface morphology and homogeneity of the deposited films, while XRD provided insight into the crystalline structure and phase composition of the Gd-doped Y_2O_3 layer. The development of Gd-doped Al/Gd/ Y_2O_3 /Si/Al MOS-based capacitors offers a promising avenue for advancing the next generation of radiation detectors with improved sensitivity, stability, and accuracy.

2. EXPERIMENTAL DETAILS

The fabrication of Gd-doped Al/Gd/ Y_2O_3 /Si/Al MOS-based capacitors was performed on an n-type silicon (n-Si) substrate, utilizing advanced electron beam evaporation and thermal oxidation techniques. These methods were selected for their ability to achieve precise control over thin film thickness and uniformity, which is crucial for ensuring the high-quality, defect-free dielectric layers required for optimal MOS capacitor performance. To explore the effects of different Gadolinium (Gd) layer thicknesses on the device properties, three variations were fabricated, with Gd thicknesses of 10 nm, 100 nm, and 150 nm. For the Y_2O_3 oxide layer, a consistent thickness of 150 nm was deposited on the n-Si wafer to maintain a stable dielectric interface.

The structural and optical characteristics of the resulting thin films were thoroughly analyzed using Scanning Electron Microscopy (SEM) and X-ray

diffraction (XRD) techniques. SEM provided detailed insights into the surface morphology, uniformity, and homogeneity of the deposited films, while XRD was employed to determine the crystalline structure, phase composition, and potential changes in the material's lattice structure due to the incorporation of Gd. These analyses are critical for understanding the influence of film thickness and material properties on the overall performance of the MOS capacitors in radiation detection applications. The fabricated Gd-doped Al/Gd/ Y_2O_3 /Si/Al MOS-based capacitors are shown in Figure 1.

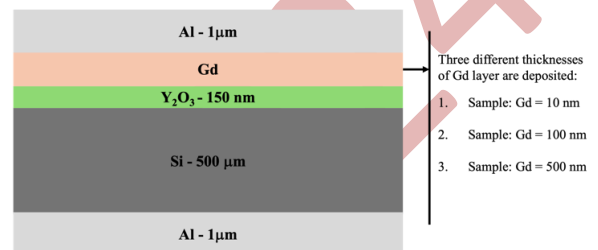


Figure 1. Schematic image of the fabricated Gd-doped Al/Gd/ Y_2O_3 /Si/Al MOS-based capacitors.

3. RESULTS AND DISCUSSION

Scanning Electron Microscopy (SEM) was used to look at the surface details and very small structures of the 100 nm and 500 nm thick Gd thin films that were made, along with the Gd-doped Gd/ Y_2O_3 /n-Si structures. The resulting SEM images, provided in Figure 2, offer detailed insights into the surface texture, uniformity, and grain structures of the thin films. These observations are critical for assessing the quality and consistency of the deposition process and understanding the role of Gd doping in modifying surface features. We also used X-ray Diffraction (XRD) to study the crystalline structures and phase compositions of the thin films made from Y_2O_3 , Gd, and Gd-doped Gd/ Y_2O_3 /n-Si. The XRD spectra in Figures 3, 4, and 5 show what crystallographic phases were present in each sample. This helped us figure out how adding Gd changed the structural properties of the thin films. We need these tests to understand the material properties and their potential impact on the electrical performance of MOS capacitors, particularly in radiation detection applications.

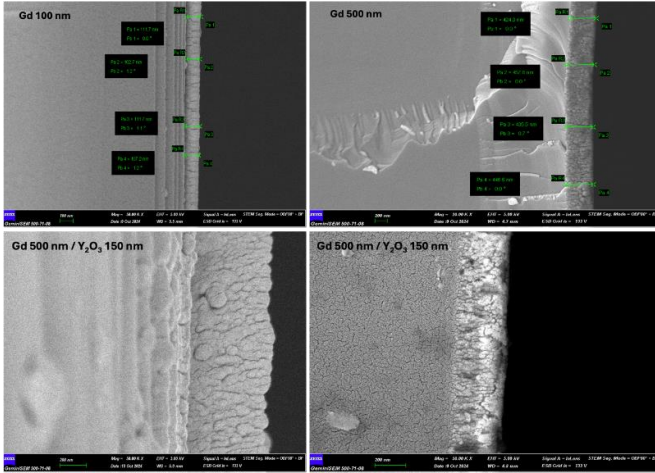


Figure 2. SEM Images of the films; Gd 100nm, Gd 500nm, Gd 100nm/Y₂O₃ 150, and Gd 500nm/Y₂O₃ 150nm.

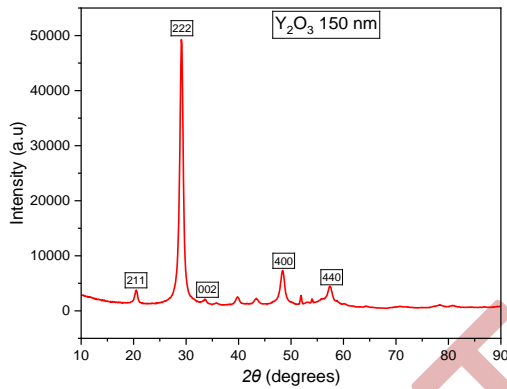


Figure 3. X-ray Diffraction (XRD) Patterns of the fabricated Y₂O₃/n-Silicon.

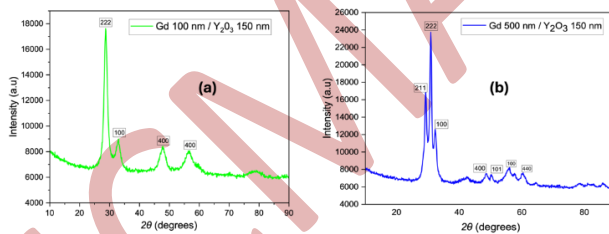


Figure 4. X-ray Diffraction (XRD) Patterns of the fabricated **a)** Gd-100 nm/n-Silicon, and **b)** Gd-500 nm/n-Silicon.

References

1. V.H. Mudavakkat, V.V. Atuchin, V.N. Kruchinin, A. Kayani, C.V. Ramana, Structure, morphology and optical properties of nanocrystalline yttrium oxide (Y₂O₃) thin films, *Opt. Mater.* 34 (2012) 893–900.
2. G.F. Knoll, Radiation Detection and Measurement, *Proceedings of the IEEE* 69 (2010) 830.
3. W.J. Price, Nuclear radiation detection, (1958).
4. J. Dumazert, R. Coulon, Q. Lecomte, G.H.V. Bertrand, M. Hamel; Gadolinium for neutron detection in current nuclear instrumentation research: A review, *Nuclear Inst. and Methods in Physics Research, A* 882 (2018) 53–68.
5. Saleh Abubakar; Senol Kaya; Huseyin Karacali; Ercan Yilmaz; The gamma irradiation responses of yttrium oxide capacitors and first assessment usage in radiation sensors, *Sensors and Actuators A* 258 (2017) 44–48

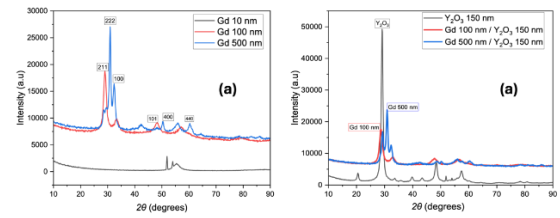


Figure 5. X-ray Diffraction (XRD) Patterns of Gd-10 nm, Gd-100 nm, and Gd-500 nm on n-Silicon Substrates.

4. CONCLUSION

In this study, we have fabricated Al/Gd/Y₂O₃/Si/Al MOS-based capacitors. A thorough study of the thin films' structure and optical properties was carried out using scanning electron microscopy (SEM) and X-ray diffraction (XRD) methods. The use of SEM yielded comprehensive insights into the surface morphology, uniformity, and homogeneity of the deposited films. We utilized XRD to analyze the crystalline structure, phase composition, and any potential alterations in the material's lattice structure due to the incorporation of Gd. The studies were necessary to understand how film thickness and material properties affect how well MOS capacitors work in radiation detection applications as a whole.

CONFLICTS OF INTEREST

The authors declared no conflict of interest.

ACKNOWLEDGEMENT

This work was supported by the Erciyes University Scientific Research Projects Coordination Unit (BAP) through the projects coded FBA-2022-12207, FBG-2022-11499, and FDS-2021-11525, as well as by a project awarded to Associate Professor Dr. Emrah TIRAŞ within the scope of the Outstanding Young Scientists Award Program (GEBİP) of the Turkish Academy of Sciences (TÜBA). We thank the Erciyes University BAP unit and TÜBA for their support.

Ni-Co based metallic foams for hydrogen production via electrochemical water splitting

Sadia Ata

School of Chemistry, University of the Punjab, P.O. Box No. 54590, Lahore, Pakistan,
sadia.chem@pu.edu.pk
ORCID: 0000-0003-0990-8587

Anila Tabassum

School of Chemistry, University of the Punjab, P.O. Box No. 54590, Lahore, Pakistan,
anila.shahzadi@gmail.com
ORCID: 0009-0000-6295-1897

Cite this paper as: Ata S. , Tabassum A. Ni-Co based metallic foams for hydrogen production via electrochemical water splitting. Int. Conf. Advanced. Mater. Sci.& Eng. HiTech.and Device Appl. Oct. 24-26 2024, Ankara, Turkiye

Abstract. The dwindling supply of fossil fuels has diverted intentions towards the production of hydrogen which is considered as a green and sustainable fuel for future generations. Electrochemical water splitting is extensively employed for hydrogen production. However, over voltage required for the process demands an active, cost effective and eco friendly catalysts. So in this work, we have prepared Ni-Co oxides over nickel foam. The hydrothermal method was used as one step coating and synthesis method. In first step, morphological changes were induced by varying surface-directing agents. We used cetyltrimethylammonium bromide (CTAB) and L-lysine (an amino acid). The fabricated Ni-Co oxides exhibited an onset potential for OER at 320 mV with L-lysine, surpassing the overpotential values obtained using CTAB (380 mV). In second step, to enhance the activity of Ni-Co oxides, they were co-doped with Boron and Fluorine heteroatoms. The prepared material exhibited lower potential of 310 mV at current density of 50 mA/cm², ensuring their capability to induct water splitting reaction at moderate conditions. Durability tests conducted over 1000 CV cycles demonstrated their ability to withstand drastic conditions. These findings ensure that the prepared catalyst has great potential for OER (very crucial step for hydrogen generation).

Keywords: Ni-Co oxides, hetero-atoms doping, hydrothermal synthesis, electrochemical water splitting process, self-standing structures

© 2024 Published by ICMATSE

The excessive usage of fossil fuels and their harmful effects on the environment have prompted scientists to search alternative sustainable fuel. In this regard, hydrogen is recognized as an ideal green fuel. It has the highest mass energy density among all the fuels, ranging from 120 to 142 MJ/kg. It also has zero carbon emissions. Electrochemical water splitting is a key method for hydrogen generation. Metal oxides are the materials which have affordability, abundance, ease of manufacturing, and environmental friendliness. Their tunable electronic states makes them exceptional. The researchers have found that bi/tri-metallics oxides are more active towards electrochemical water splitting owing to metals synergistic relation. Various tactics like nanosizing, doping, morphological optimization, binder-free synthesis and hybrid materials have been employed to enhance the electrochemical activity [1-7].

Herein, NiCo oxides have been fabricated directly on nickel foam using typical hydrothermal synthesis process.

First, the nickel foam is cut into pieces and cleaned ultrasonically with 3M HCl, acetone, ethanol, and deionized water. Next, nickel and cobalt in equal molar ratios are mixed with urea. The surfatants were added (First method). For doping ammonium fluoride (fluorine source) and boric acid (boron source) were added (Second method). The mixture is stirred and poured into a 100 ml Teflon-lined stainless steel autoclave containing the nickel foam pieces. After completion of reaction, the product is obtained and calcined in a muffle furnace.

The electrochemical performance was evaluated using a potentiostat with a three-electrode setup (1M KOH). The working electrode was our fabricated material. While the reference electrode was Hg/HgO, and the counter electrode was a graphite rod. The fabricated Ni-Co oxides showed an onset potential for OER at 320 mV when using L-lysine as a surfactant. These results surpassed the overpotential values obtained when using CTAB (380 mV) (Fig.2). The B/F co-doped material exhibited a lower

potential of 310 mV at a current density of 50 mA/cm² (Fig.2). The observed activity was attributed to the morphological evolution induced by adding surfactants, and also by doping which modulate adsorption/desorption energies of intermediates, thereby allowing gas production at a reasonable rate (table 1).

Table 1. Overpotential values

Material	Overpotential at 50 mAcm ⁻²
NiCo	450
NiCo CTAB	430
NiCo L-Lysine	420
NiCo pure	350
B-NiCo	330
F-NiCo	320
B/F NiCo	310

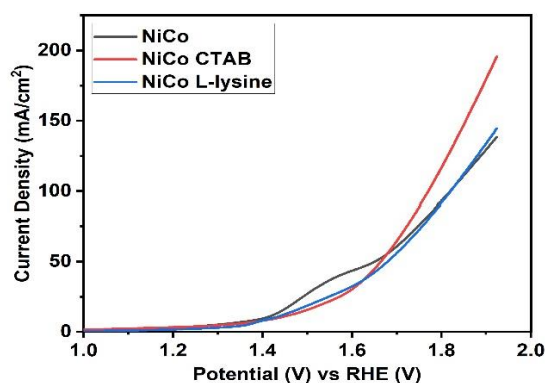


Figure 1. LSV curves for Surfactants assisted NiCo

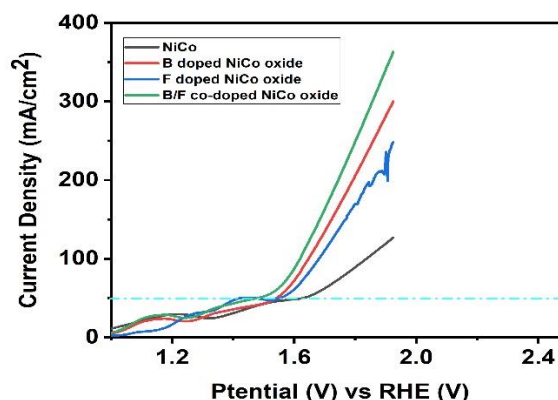


Figure 2. LSV curves for Doped NiCo

References:

[1]. Morales, D. M., Kazakova, M. A., Dieckhöfer, S., Selyutin, A. G., Golubtsov, G. V., Schuhmann, W., & Masa, J. (2020). Trimetallic Mn-Fe-Ni oxide nanoparticles supported on multi-walled carbon nanotubes as high-performance bifunctional ORR/OER electrocatalyst in alkaline media. *Advanced Functional Materials*, 30(6), 1905992.

[2]. Zeng, M., & Li, Y. (2015). Recent advances in heterogeneous electrocatalysts for the hydrogen evolution reaction. *Journal of Materials Chemistry A*, 3(29), 14942-14962.

[3]. Yuan, N., Jiang, Q., Li, J., & Tang, J. (2020). A review on non-noble metal based electrocatalysis for the oxygen evolution reaction. *Arabian Journal of Chemistry*, 13(2), 4294-4309.

[4]. Shit, S., Bolar, S., Murmu, N. C., & Kuila, T. (2020). An account of the strategies to enhance the water splitting efficiency of noble-metal-free electrocatalysts. *Journal of Energy Chemistry*.

[5]. Zhu, Y., Lin, Q., Zhong, Y., Tahini, H. A., Shao, Z., & Wang, H. (2020). Metal oxide-based materials as an emerging family of hydrogen evolution electrocatalysts. *Energy & Environmental Science*, 13(10), 3361-3392.

[6]. Lu, F., Zhou, M., Zhou, Y., & Zeng, X. (2017). First-row transition metal based catalysts for the oxygen evolution reaction under alkaline conditions: basic principles and recent advances. *Small*, 13(45), 1701931.

[7]. Bai, L., Wen, X., & Guan, J. (2019). Amorphous FeCoNi oxide for oxygen evolution reaction. *Materials Today Energy*, 12, 311-317.

Advances and Challenges in Solid State Electrolytes and Processing Technology for Energy Storage Devices

Sajid Hussain Siyal

¹*Department of Metallurgy and Materials Engineeirn, Dawood University of Engineering and Technology, Karachi, Sindh, PAKISTAN
sajid.hussain@duet.edu.pk
ORCID: 0000-0002-9041-0649*

Cite this paper as Siyal H.. Advances and Challenges in Solid State Electrolytes and Processing Technology for Energy Storage Devices, Int. Conf. Advanced. Mater. Sci.& Eng. HiTech.and Device Appl.Oct. 24-26 2024,Ankara, Turkey

Abstract. The huge capacity and low negative electrochemical potential of lithium-metal batteries (LMBs) make them promising energy storage technologies. Nevertheless, their high risk, constrained electrochemical window, and imbalanced electrolyte-electrode interfaces continue to interfere with their practical uses. Here is a revolutionary method for creating dual ceramic-based electrolytes, which have higher energy densities in LMBs and so have enormous potential for energy storage. In order to combine the two ceramic structures with polyethylene oxide and create a free-standing electrolyte film for improved battery safety and the required interfacial stability, the electrolyte film generated using the curable technique had to be prepared as a flexible Li⁺ interpenetrating network film. The films presented a satisfactory electrochemical performance, including, good ionic conductivity, large transference number, and wide electrochemical stability window (ESW) at room temperature. Most importantly, the fundamental function of fillers is to support building a stable solid-electrolyte-interphase (SEI) and limits the growth of dendrites. Thus, prepared dual ceramic-based electrolytes effectively renders to inhibit lithium dendrite growth in a symmetrical cell test during charge/discharge with long hours without short-circuiting occurrence at RT. Additionally, the battery assembly has exceptional cycle stability and great columbic efficiency. According to this study, a primary solution of a promising electrolyte for high-performance LMB applications can be designed with the aid of the binary network architectures of Li-ion conductors.

Keywords: film, lithium-metal batteries, Li-dendrites
© 2024 Published by ICMATSE

Introduction

Rechargeable lithium-metallic batteries (LMBs) with high energies and maximum power densities are the most promising power sources to meet the demand for electronic portables and hybrid vehicles [1-3]. However, the use of LMBs possess a great challenge owing to the safety issues such as liquid leakage, flammability, poor interfacial compatibility and side reactions of electrodes and electrolytes [4-7]. Another major challenge associated with the uncontrolled enhancement of Li-dendrite, which may penetrate easily and cause an internal short circuit [8-12]. In order to overcome these problems, various composite gel polymer electrolytes for safe and substantial stable cycling of LMBs were suggested [13].

An immediate alternative solution among conventional liquid and solid electrolyte is composite gel polymer electrolytes [14]. Composite electrolyte is composed of polymer matrix and inorganic fillers show unique advantages such as battery safety, good mechanical property, better electrochemical stability and high ionic conductivity [15-16]. Commonly, used polymers such as polyethylene oxide (POLYMER) [17-18], polyacrylonitrile (PAN) [19], polyvinylidene fluoride (PVDF) [20], polyvinylidene fluoride hexa fluoropropylene (PVDF-HFP) [21], and poly-methylmethacrylate (PMMA) [22-23]. Among them, POLYMER has been widely investigated as the matrix of composite electrolytes on the account of its good compatibility, efficiency in coordinating metal ions, excellent liquid absorption and good shape flexibility [24-25]. However, polymer types suffers from poor ionic conductivity due to its semi crystalline nature which may reduce its

performance [26]. To overcome these issues, inorganic active fillers have been introduced, different nanofillers [27-33]. Among the explored fillers, CERAMIC nanofillers is dominant due to its Al-doped higher ionic conductivity, lower cost and a better chemical stability in contact with Li metal [34-35]. Great progress has been made to develop the composite electrolyte from the interaction between inorganic fillers ceramic nanofillers, polymer POLYMER [36-38], and LiTFSI as liquid plasticizer in recent years [39]. However, the addition of ceramics fillers can effectively reduce the crystalline nature of polymer with an improved ionic conductivity of composite electrolyte, but there are still some critical challenges, such as narrow electrochemical window, poor mechanical strength and poor electrochemical performance [13, 40-42]. It is still need to improve the synthesis process of composite electrolytes for enhancement of mechanical properties along with electrochemical performance. Irradiation is a viable and fundamental strategy in facilitating the design and control of polymer networks by the free radical polymerization [43-45]. Recently, curing emerged as a very efficient route to obtain an easily and reliable electrolyte with high performances and utilized for surface modifications [46-47]. Several studies have reported that benzophenone (Bp) photo-initiator, exposed in POLYMER solution under irradiation can form free radicals which are grafted onto polymer molecular chains through insertion regular pattern, causing the cross-linking of the polymer [48-49]. Such interpenetrating polymer networks formed by high-power light irradiation can provide excellent

thermal stability and effectively improved wettability [50-53].

In this research, a free-standing membrane composed of polymer and ceramic was prepared via curing in the presence of photo initiator to achieve the high mechanical strength and improved electrochemical performance of LMBs. The as-prepared irradiated composite electrolytes not only exhibit flexibility, good ionic conductivity, and large electrochemical window but also prevent the formation of Li dendrites. Irradiated curing process takes less time. Therefore, this work opens a new window towards the highly efficient preparation of membrane for high performance LMBs.

In summary, the membranes composed of polymer and different ratio of nanofillers have been successfully prepared using Ultraviolet Light of. The appropriate ratio of ceramics shows the high ionic conductivity room temperature and high UTS were observed. The curing on mix membrane showed an excellent window and extraordinary transference number. Additionally, the polymer mix with ceramics contributes to the wide cyclic stability and reasonable rate capacity during cell process due to its capability of effectively suppress dendritic of Lithium growth. It can be summarized that, this technique provides a novel implementation for the preparation of an effective composite electrolyte and perspective membrane is a promising electrolyte for high-performance quasi solid-state of energy storage.

References

1. Siyal, S. H., Javed, M. S., Jatoi, A. H., Lan, J. L., Yu, Y., Saleem, M., & Yang, X. (2020). In situ curing technology for dual ceramic composed by organic-inorganic functional polymer gel electrolyte for dendritic-free and robust lithium-metal batteries. *Advanced Materials Interfaces*, 7(20), 2000830.
2. Siyal, S. H., Li, M., Li, H., Lan, J. L., Yu, Y., & Yang, X. (2019). Ultraviolet irradiated POLYMER/CERAMIC NANOFILLERS composite gel polymer electrolytes for lithium-metallic batteries (LMBs). *Applied Surface Science*, 494, 1119-1126.

Synthesis, Structure and Magnetic Properties of (Co/Ce) co-doped ZnO Nanoparticles

Merve Mine Seker Perez

*Marmara University - Graduate School of Science and Engineering, 34840, Istanbul, Türkiye,
mervemineseker@gmail.com
ORCID: 0000-0001-9681-8031*

Cihat Boyraz

*Marmara University - Department of Mechanical Engineering, 34854, Istanbul, Türkiye,
cboyraz@marmara.edu.tr
ORCID: 0000-0002-3508-7703*

Lutfi Arda

*Bahcesehir University - Department of Mechatronic Engineering, 34349, Istanbul, Türkiye,
lutfi.arda@eng.bau.edu.tr
ORCID: 0000-0003-0722-3891*

Abstract. Zn_{0.95-x}Ce_xCo_{0.05}O (x=0.00, 0.01, 0.02, 0.03, 0.04, and 0.05) nanoparticles obtained by the sol-gel method was used to create in order to investigate the impact of the Co/Ce co-doping on magnetic properties. By changing the doping levels (x=0.00, 0.01, 0.02, 0.03, 0.04, and 0.05), the stoichiometry was corrected. The structural properties of all Co/Ce co-doped ZnO nanoparticles were examined using X-ray diffraction, and the c/a ratios were used to demonstrate the presence of a hexagonal Wurtzite structure. Scanning electron microscopy (SEM) examination was used to assess the surface morphology, crystallite size, and nanoparticle morphologies. Electron Dispersive Spectroscopy (EDAX) was utilized to ascertain the elemental compositions. Magnetic characterizations were performed using the Quantum Design Vibrating Sample Magnetometer (QDVS) instrument for all samples. Up to 10 kOe of magnetic field was used for the magnetization measurements as a function of magnetic field (M-H). Magnetization-temperature dependence measurements (M-T) were conducted in the 10-300 K temperature range.

Keywords: Co/Ce co-doped ZnO; Sol-gel method; Nanoparticles; Magnetic properties

© 2024 Published by ICMATSE

1. Introduction

ZnO-based nanomaterials are attracting attention due to their wide range of applications in many fields [1]. Despite the superior properties of ZnO, researchers have been working to enhance its structural, electrical, magnetic, and optical properties by doping it with various elements, such as transition metals (Ni, Co, Fe, Mn...) and rare earth elements (Y, Ce, Yb, Eu...) to improve its performance in specific applications [2]. Additionally, ZnO nanomaterials (nanoparticles, nanorods, thin films, etc.) are synthesized using different physical and chemical methods, such as sol-gel, hydrothermal, co-precipitation, solid-state reaction, pulsed laser deposition, and DC sputtering, to improve their properties. One of the main points

to consider during both doping and the synthesis of ZnO via different methods is the investigation of defects that arise during doping and synthesis [3]. In this study, Zn_{0.95-x}Co_{0.05}Ce_xO NPs (x=0.00-0.05) were synthesized for the first time using the sol-gel method. The effects of intrinsic defects such as zinc interstitials (Zni), zinc vacancies (Vzn), and oxygen vacancies (Vo) in Zn_{0.95-x}Co_{0.05}Ce_xO NPs were investigated using photoluminescence (PL) and electron spin resonance (ESR). Additionally, the impact of Co/Ce co-doping on the magnetic and structural properties of ZnO NPs at room temperature (RT) was explored.

2. Experimental methods

While synthesizing Co/Ce-doped ZnO nanoparticles via the sol-gel method, Zinc acetate dihydrate

(ZnAc), Cobalt acetate tetrahydrate (CoAc), and Cerium acetate tetrahydrate (CeAc) were used as precursor materials. Additionally, methanol (ME) and monoethanolamine (MEA) were used as stabilizers. The starting materials were dissolved in ME at a concentration of 0.25M. To obtain a transparent solution, the final solution was continuously stirred at room temperature using a magnetic stirrer. The viscosity of the solutions was controlled by adding ME, and a transparent solution was obtained. For synthesis details, refer to [7, 12, 21]. Afterward, the lid of the beaker containing the transparent solution was opened, and the solution was stirred for 12 hours using a magnetic stirrer to allow the solvents to evaporate at room temperature. The resulting gels were subjected to a pre-heating process at 400°C for 10 minutes. The synthesized $Zn_{0.95-x}Co_{0.05}Ce_xO$ ($x=0.0-0.05$) powders were then subjected to calcination at 600°C to obtain homogeneous nanoparticles. In order to determine the structural characteristics of the powders, monochromated Cu K α (1.5418Å) was scanned in the 2θ scan range between 10° and 70° at room temperature, with a step increase of 0.02. Using the Jeol-6390-LV scanning electron microscopy (SEM-EDX) instrument, the surface morphologies of the materials were analysed. Photoluminescence qualities were discovered using the Agilent Cary Eclipse Fluorescence Spectrophotometer. Room temperature ESR spectra of Zn $_{1-x}$ Mn $_x$ O samples were obtained using a Bruker EMX model X-band spectrometer operating at 9.71 GHz.

3. Results and discussions

Using the XRD technique, the structural phase behavior of $Zn_{0.95-x}Co_{0.05}Ce_xO$ NPs was examined in the $20^\circ \leq 2\theta \leq 80^\circ$ range. Up to a Ce doping level of $x=0.02$, as illustrated in Figure 1, all peak positions were indexed, and a single phase was found in the XRD patterns. Following this ratio of doping, the CeO phase was detected.

References

1. L. Arda, The effects of Tb doped ZnO nanorod: An EPR study, *Journal of Magnetism and Magnetic Materials*, Volume 475, 2019, Pages 493-501,
2. A. Guler, L. Arda, N. Dogan, C. Boyraz, E. Ozugurlu, The annealing effect on microstructure and ESR properties of (Cu/Ni) co-doped ZnO nanoparticles, *Ceramics International*, Volume 45, Issue 2, Part A, 2019, Pages 1737-1745
3. L. Arda, O. Karatas, M. C. Alphan, E. Ozugurlu, Electron spin resonance and photoluminescence studies of Co/Mg co-doped ZnO nanoparticles, *International Journal of Applied Ceramic Technology*. 21 (2024) 2458 – 2473.

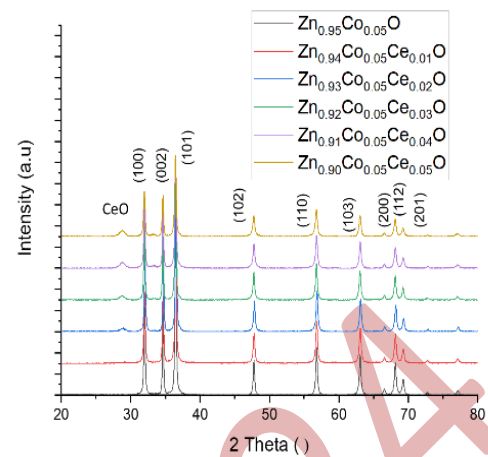


Figure 1. The X-ray diffraction patterns of $Zn_{0.95-x}Co_{0.05}Ce_xO$ NPs.

We used photoluminescence (PL) analysis to investigate the effects of Co/Ce doping on the crystalline characteristics, defect types, and defect densities of ZnO nanoparticles.

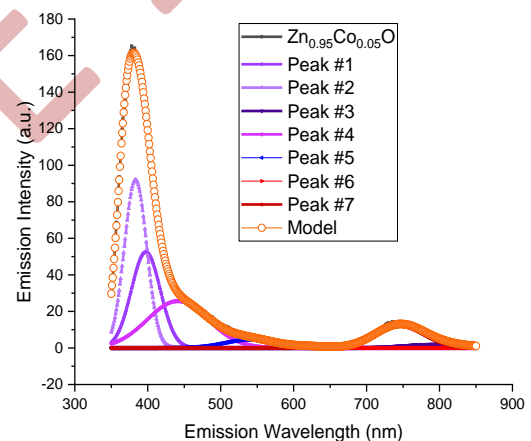


Figure 2. Gaussian decompositions of PL spectra of $Zn_{0.95-x}Co_{0.05}Ce_xO$ NPs. using the Fityk software

Investigation Of The Springback Behavior Of Double-Phase Steel Sheets In The V Bending Process

Eda Nur Düzenli

*Gazi University- Department of Manufacturing Engineering, 06500, Ankara, Turkey,
edanurduzenli1@gmail.com
ORCID: 0000-0002-5751-2205*

Hakan Gürün

*Gazi University- Department of Manufacturing Engineering, 06500, Ankara, Turkey,
hgurun@gazi.edu.tr
ORCID: 0000-0001-6189-6830*

Cite this paper as: Duzenli, EN, Gurun, H. Investigation of the Springback Behavior of Double-Phase Steel Sheets in the V Bending Process Int. Conf. Advanced. Mater. Sci.& Eng. HiTech.and Device Appl.Oct. 24-26 2024, Ankara, Turkey

Abstract. The high strength of dual-phase steel sheets has led to their widespread use in the automotive industry. However, the elastic springback behavior of these materials during the forming process is an issue that needs to be carefully investigated to ensure that the manufactured parts meet precise dimensional and tolerance requirements. Computer-aided deformation analysis is nowadays a widely preferred method for the detailed investigation of the behavior of materials and structures under load. In this study, computer-aided deformation analyses were performed using Deform 2D software to predict the springback behavior of DP600, DP800 and DP1000 materials in V-bending operations. Two different models, 60° and 90° V-bending, were used in the analysis. Bending analyses were repeated for different bending radius values (3, 4, 5 mm) and different sheet thicknesses (1, 1.5, 2 mm). In the study, the effects of bending process parameters on the amount of elastic springback of the materials after forming were investigated. It was found that as the bending radius and sheet thickness increased, the elastic springback values decreased significantly.

Translated with DeepL.com (free version)

Keywords: Springback, V-bending, dual-phase steels
© 2024 Published by ICMATSE

1. Introduction

Sheet metal molding is a type of technology that is widely applied in many industries. Sheet metal molds are widely used in many sectors from the automotive industry to white goods production, from aerospace and aviation to electrical electronics. One of the most common application areas of sheet metal molding is bending molding. Especially in processes where sheet metal or metal plates are used, springback is inevitable. The springback is caused by the elastic behavior of the metal. With the demand for lightweight and high-strength materials, dual-phase steels have become a preferred alternative in engineering applications. The increase in the strength properties of the materials and the pre-design of sheet products have the effect of increasing the amount of elastic springback that occurs as a result of forming operations. Experimental determination of

the amount of elastic springback leads to unpredictable errors in the production processes and therefore cost increases. Finite element analysis has been widely used for the estimation and compensation of elastic springback in forming processes. The problem of springback in bending processes has been extensively studied in the literature and there are many researches on this subject.

Cinar et al. investigated the springback of A6061 aluminum alloy used in automotive in different forming processes (V-bending, U-bending, deep drawing, etc.). They concluded that bending angle and sheet thickness are the parameters that affect springback the most [1]. Chikalthankar et al. investigated many factors (punch angle, grain orientation, die properties, sheet thickness, etc.) affecting springback in sheet metal bending

processes. They concluded that punch angle has a significant effect on springback and different grain orientations also affect springback [2]. Chikalthankar et al. determined that punch angle is the most important parameter among the factors affecting springback. They also observed that the grain orientation of the sheet material also affects springback due to different yield strengths [3].

Hekim investigated the springback behavior, which is one of the most common problems in V-bending process, one of the sheet metals forming methods. In the study, it was observed that springback decreases with increasing compression force in both experimental and finite element analysis. According to the rolling direction of the sheet, the minimum springback was realized at 45° and the maximum springback was realized at 90° rolling direction [4]. Gürün et al. carried out experimental and analytical studies to determine the springback behavior of AA 2024 material in bending process. When they compared the obtained values, they observed that the effect of material thickness, punch tip radius and bending angle on springback is quite high [5].

Tekaslan et al. designed a modular V-bending mold and measured the springback of sheet metals at different bending angles. It was observed that the springback values varied between 0.5° and 5° [6]. Wasif et al. prepared an experimental setup to investigate the effects of thickness, width, bending angle and machine tool parameters on springback during V-bending of JSC440 and JSC590 high strength steels. They analyzed the relationships between springback and parameters using graphs [7].

Uslu and Tosun experimentally investigated the springback behavior of DC series sheet metals formed by V bending over process parameters such as material quality, thickness, rolling direction and die angle. They predicted that the springback problem in the V-die bending process can be compensated by fixing the dies in the opposite direction by the springback value determined during design [8]. Özdemir performed V-bending operations using different thicknesses and punch radii for Dp600 sheet material with Taguchi method and obtained experimental results. As a result of Taguchi analysis, it was determined that the most effective parameter on springback was sheet thickness [9]. In their study, Aslan and Karağaçaç performed experimental and computer-aided analysis with finite element method by considering material, process and mold parameters (material type, thickness, yield strength,

bending force, bending angle, etc.) which are effective in V-bending. The studies showed that sheet material thickness and bending angle increased the springback, while ironing time decreased the springback. It was also found that although the effect of friction is small, it increases the springback for 6022 T4 material, while the decrease in bending radius decreases the springback. The increase in yield strength and consolidation increased the springback, while bending force decreased the springback [10].

Şen et al. determined the optimum bending radii (R) to compensate the springback of DP600 sheet metal parts of different thicknesses depending on the sheet thickness (T) by Finite Element Analysis (FEA). After the analysis, it was concluded that the springback values decreased with increasing sheet thickness [11]. Kılıç et al. investigated the effect of deformation rate and sheet width on the springback of DP800 steels, which are frequently used in automotive industry. As a result, it was found that the springback decreased slightly with increasing deformation rate, but sheet width did not have a significant effect [12]. Yıldırım et al. investigated the effect of corner crushing on U bending of DP600 and DP1000 steels. The corner crushing process significantly reduced the springback as a result of bending [13].

In this study, the springback rates of dual phase steel materials (DP600, DP800 and DP1000) at different sheet thicknesses ($t:1$, $t:1.5$ and $t:2$) at 60° and 90° in V-bending process were investigated. Sheet material thickness, material type, bending angle and bending radius were taken as variables. Although there are many studies in the literature investigating the springback behavior of various materials, there is no comparative study on the springback values of three different materials such as DP600, DP800 and DP1000 in V-bending processes. The aim of this study is to experimentally investigate the springback behavior of DP600, DP800 and DP1000 steels in V-bending processes and to reveal the reasons for the differences in these behaviors.

2. Bending Analyzes

In this study, V-bending analyses were performed using three different dual-phase steel materials (DP600, DP800 and DP1000). Two different models for 60° and 90° were created for the analyses and are given in Figure 1.

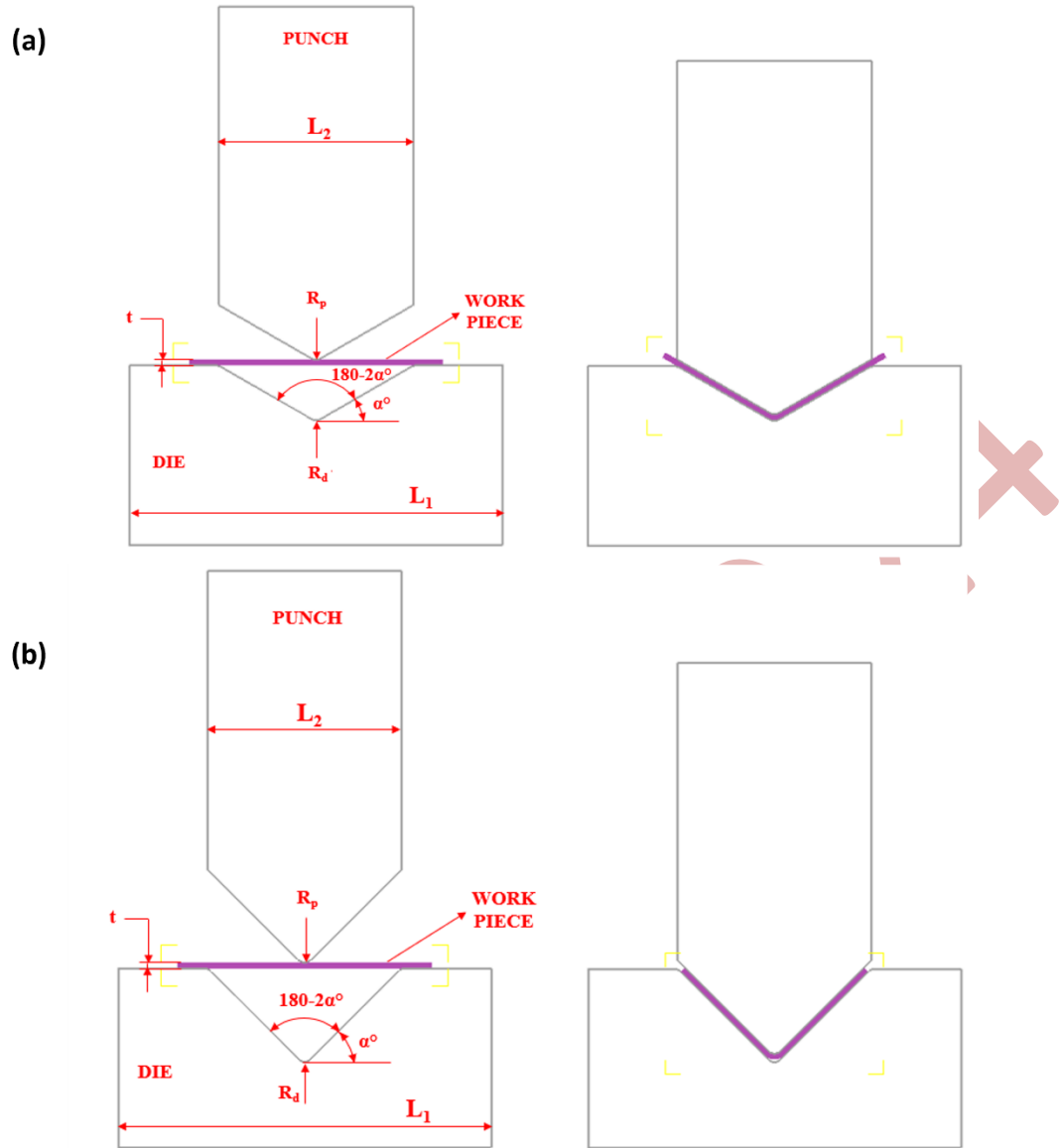


Figure 1. Analysis of dual phase steel materials (DP600, DP800 and DP1000), (a) 60° V-bending and (b) 90° V-bending

In the analysis, the mold was moved along the vertical axis and the sheet material was shaped. The analysis studies were repeated for sheet materials with 1mm, 1.5mm and 2mm thickness. Different models were prepared by changing the bending radius dimensions (R3, R4 and R5) for each sheet material thickness. Mold width (L_1) and punch width (L_2) were kept constant. Analyses were carried out in DEFORM 2D program to determine the springback values on the sheet material. Within the scope of the study, the deformation behavior, stress state, thickness variations and springback tendencies of the materials were examined. The dimensions and variables used for both models are given in Table 1.

Table 1. Used measures and variables

Parameters	Symbol	Value
Die width	L_1	125mm
Punch width	L_2	65mm
Die corner radius	R_d (R3, R4 and R5)	Variable
Punch corner radius	R_p (R3, R4 and R5)	Variable
Punch feed rate	V	10mm/sc
Sheet material	DP600, DP800 and DP1000	Variable
Sheet material thickness	t (1mm, 1.5mm and 2mm)	Variable

After the forming analysis, the forces applied to the sheet material were removed and the springback analysis was performed. The unit deformation,

stresses, wall thickness, changes and springbacks on the sheet material were measured in the DEFORM 2D program. In order to transfer the material data to the DEFORM program, tensile tests were performed on sheet materials. Depending on the engineering curves obtained from the tensile tests, true stress / strain curves were generated. Engineering and actual stress / strain curves for DP600, DP800 and DP1000 materials are given in Figure 2.

Deformation analyses were first performed on the sheet materials and then the springback behavior was analyzed. The change of part forms after forming and after springback in 60° and 90° V-bending process is given in Figure 3.

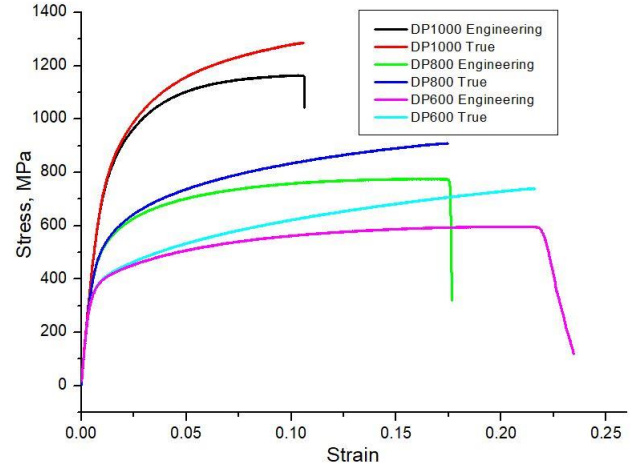


Figure 2. Engineering and true stress/strain curves for DP600, DP800 and DP1000 materials

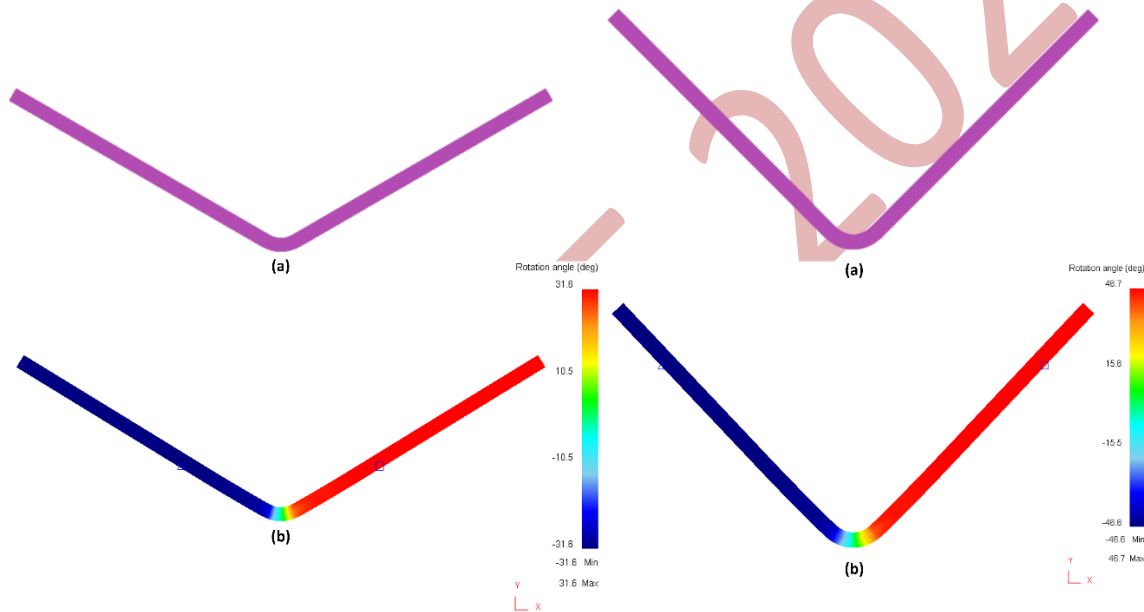


Figure 3. Part form before and after back bending in V-bending process (Left a: part form after 60° forming, left b: part form after 60° back bending) (Right a: part form after 90° forming, right b: part form after 90° back stretching)

3. Results and Discussion

As a result of the analysis, it was observed that when the properties such as the type of material, thickness of the sheet, bending angle and bending radius changed, the amount of springback also varied. This shows that the springback is not due to a single cause, but is under the influence of multiple factors. The springback values obtained for the values of R3, R4 and R5 for 60° and 90° bends are given in Figure 4 for all three materials (DP600, DP800 and DP1000).

(a)		60°				60°				60°							
		DP600			Bend Radius (R)			DP800			Bend Radius (R)			DP1000			Bend Radius (R)
		R:3	R:4	R:5	R:3	R:4	R:5	R:3	R:4	R:5	R:3	R:4	R:5				
Sheet Thickness (t)	t:1	6.5°	6.2°	5.7°	6.9°	6.6°	5.9°	9.2°	8.6°	7.9°							
	t:1.5	5°	4.2°	3.4°	5.2°	4.6°	4°	7.6°	7.4°	6°							
	t:2	3.2°	2.8°	2.6°	4°	3.4°	3°	6.6°	5.4°	5.1°							

(b)		90°				90°				90°							
		DP600			Bend Radius (R)			DP800			Bend Radius (R)			DP1000			Bend Radius (R)
		R:3	R:4	R:5	R:3	R:4	R:5	R:3	R:4	R:5	R:3	R:4	R:5				
Sheet Thickness (t)	t:1	7.7°	6.7°	5.8°	8°	7.3°	6°	12°	9.7°	7.8°							
	t:1.5	5.3°	4.5°	3.9°	5.6°	4.7°	4°	9.1°	7.5°	5.7°							
	t:2	3.3°	2.7°	2.6°	4.1°	3.3°	2.7°	6.8°	5.9°	4.1°							

Figure 4. V-bending springback values for dual-phase steel materials (DP600, DP800 and DP1000) with bend radii R3, R4 and R5 (a) 60° v-bend and (b) 90°

3.1. Effect of material and sheet thickness on springback

The springback values obtained for the bending radius R3 values at 60° and 90° bends are given in Figure 6a/6b for all three materials (DP600, DP800 and DP1000). When Figure 5 is examined, it is seen that for both angle values (60° and 90°), when the strength of the material increases, the springback value also increases. The DP600 has the lowest, DP800 has the highest and DP1000 has the highest springback values. Almedia et al. compared the springback between DP600 and DP800 steel grades and obtained higher springback value in DP800 steel [14].

When the obtained springback graphs were analyzed, it was determined that the increase in sheet thickness decreased the springback values. In 60° V-bending, with the increase in sheet thickness from 1mm to 2mm, the springback value decreased by approximately 50% for DP600, 42% for DP800 and 28% for DP1000, while in 90° V-bending, it decreased by approximately 57% for DP600, 48% for DP800 and 43% for DP1000. It can be seen that the increase in sheet thickness reduces the springback. In their study, Dametew and Gebresenbent applied mathematical methods to the effects of springback on sheet metal bending and found that springback decreases with increasing sheet thickness. Similar results were obtained in the literature [15].

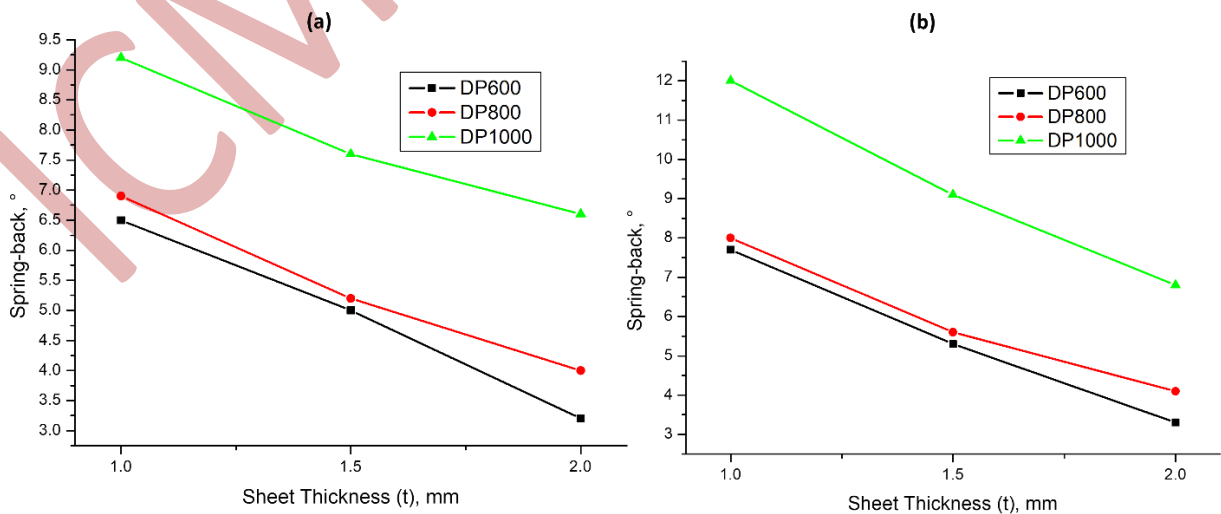


Figure 5. (a) 60° V-bending, (b) 90° V-bending

3.2. Effect of bending angle on springback

The springback values obtained for DP600 material with bending radius R3 at 60° and 90° bends are given in Figure 6. The experiments showed that the amount

of springback increases linearly with increasing bending angle. In the Karağağ study, it was determined that the increase in the mold angle increases the stresses in the material and as a result, the amount of springback increases [16].

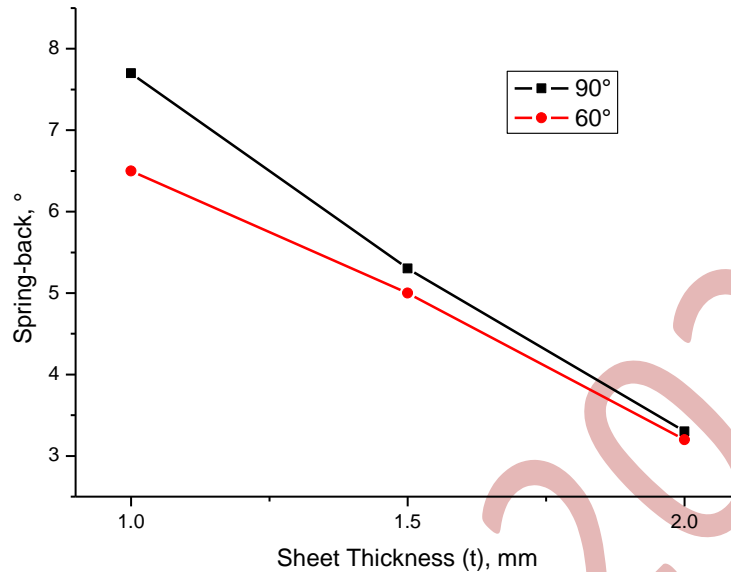


Figure 6. Springback values at 60° and 90° bending angles

3.3. Effect of bend radius on springback

The springback values obtained for DP600 material bend radius R3, R4 and R5 for 60° and 90° bends are given in Figure 7. Small mold radius causes more plastic deformation in the material and increases the springback. On the other hand, large mold radius

decreases the plastic deformation and decreases the springback. It was found that the springback decreases with increasing mold radius. In the literature, Osman et al. observed that for a given sheet thickness t in V-die bending, increasing the bending radius (Rp) decreases the springback rate [17].

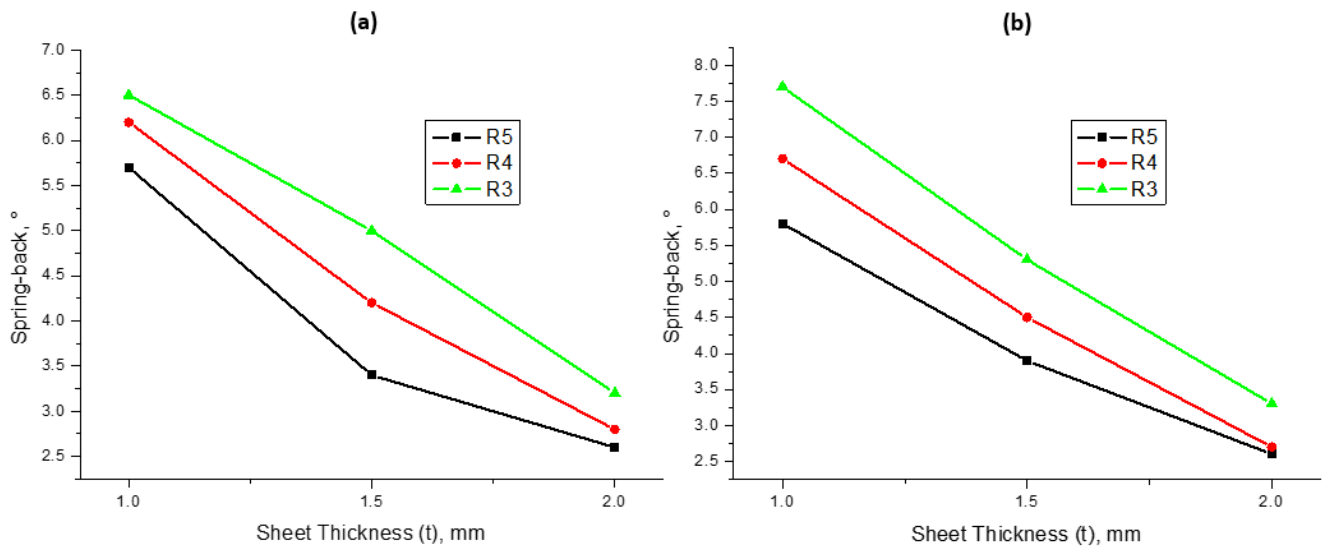


Figure 7. (a) 60° (R3, R4 and R5) V-bending, (b) 90° (R3, R4 and R5) V-bending

4. Conclusion

In this study, V-bending analyses were performed using DP600, DP800 and DP1000 materials. The curvature values were determined as R1:3, R2:4, R3:5 mm for all sheet thicknesses for all three sheet materials used (DP600, DP800 and DP1000). As a result of the forming analyzes, the following results were obtained:

1. The results of the analysis were found to be consistent with the literature.

2. As the yield strength of the material increased, the springback values also increased.

3. It was observed that the springback decreased as the sheet thickness increased.

4. As the bending radius increased, the springback decreased.

5. The lowest springback value was 2.6° for DP600 material, 2 mm sheet thickness, and R=5 mm punch radius.

6. The highest springback value was 12° for DP1000 material, 1mm sheet thickness, and R=3 mm punch radius.

5. References

- Cinar, Z., Asmael, M., Zeeshan, Q., & Safaei, B. (2021). Effect of springback on A6061 sheet metal bending: a review. *Jurnal Kejuruteraan*, 33(1), 13-26.
- Chikalthankar, S. B., Belurkar, G. D., & Nandedkar, V. M. (2014). Factors affecting on springback in sheet metal bending: a review. *International Journal of Engineering and Advanced Technology*, 3(4), 247-251.
- Chikalthankar, S. B., Belurkar, G. D., & Nandedkar, V. M. (2014). Factors affecting on springback in sheet metal bending: a review. *International Journal of Engineering and Advanced Technology*, 3(4), 247-251.
- Hekim, A. (2016). *Investigation of springback in sheet metal bending by finite element method (Master's thesis, Hitit University Institute of Science and Technology)*.
- Gürün, H., Çavuşoğlu, O., Çaydaş, U., Özek, C., & Çelik, M. (2018). Investigation of springback behavior of AA2024 alloy after V-bending process. *Firat University Journal of Engineering Sciences*, 30(1), 1-8.
- Tekaslan, Ö., Gerger, N., & Şeker, U. (2008). Determination of spring-back of stainless steel sheet metal in "V" bending dies. *Materials & design*, 29(5), 1043-1050.
- Wasif, M., Iqbal, S. A., Tufail, M., & Karim, H. (2020). Experimental analysis and prediction of springback in V-bending process of high-tensile strength steels. *Transactions of the Indian institute of metals*, 73, 285-300.
- Uslu, E., & Tosun, N. (2019). Experimental investigation of springback of DC series steel sheet in V-bending process. *Bayburt Üniversitesi Fen Bilimleri Dergisi*, 2(2), 300-306.
- ÖZDEMİR, M. (2020). Optimization of spring back in air v bending processing using Taguchi and RSM method. *Mechanics*, 26(1), 73-81.
- Aslan, Y., & Karaağaç, İ. (2014). SPRINGBACK BEHAVIOR IN V BENDING. *Gazi University Journal of Science Part C: Design and Technology*, 2(3), 255-263.
- Şen, M., Yıldırım, E., Çebi, H., & Özdemir, C. (2015). Determination of bending radii depending on sheet thickness to optimize springback in the design of automotive sheet metal parts made of dual phase steels. *Electronic Journal of Machine Technologies*, 12(2), 75-95.
- Kılıç, S., Öztürk, F., & Toros, S. (2009). Investigation of Mechanical Properties and Back Stretching Behavior of DP 800 steel. *Journal of Machine Design and Manufacturing*, 11(1), 40-45.
- Yildirim, S., Gürün, H., Dilipak, H., Küçüktürk, G., & Ersöz, C. The Effect of Corner Crushing on Back Flexing in U-Bending of DP600 and DP1000 Dual Phase Steel Materials, 1st National Congress of Scientific and Professional Studies in Engineering, Nevşehir, Turkey, June 2019, 21-25
- Almeida, C. O. L., Lima, L. H. L., & dos Santos Pereira, M. (2020). Springback comparison between DP600 and DP800 steel grades. *Materials Research Express*, 7(1), 016598.
- Dametew, A. W., & Gebresenbet, T. (2017). Study the effects of spring back on sheet metal bending using mathematical methods. *J Material Sci Eng*, 6(382), 22-2169.
- Karaağaç, İ. (2017). The experimental investigation of springback in V-bending using the flexforming process. *Arabian Journal for Science and Engineering*, 42, 1853-1864.
- Osman, M. A., Shazly, M., El-Mokaddem, A., & Wifi, A. S. (2010). Springback prediction in V-die bending: modelling and experimentation. *Journal of achievements in Materials and Manufacturing Engineering*, 38(2), 179-186.

Quality Control Analysis in the Steel Industry with Simulation Techniques

İsmail Taşcı

Zonguldak Bülent Ecevit University- Devrek Vocational School, 67800, Zonguldak, Turkey,
ismail.tasci@beun.edu.tr

ORCID: 0000-0001-7233-0330

İlhami Muharrem Orak

Karabük University-Computer Engineering Department, 78050, Karabük, Turkey,
imorak@karabuk.edu.tr

ORCID: 0000-0002-7219-4209

Cite this paper as: Orak, İM., Taşcı, İ. Quality Control Analysis in the Iron and Steel Industry with Simulation Techniques. Int. Conf. Advanced. Mater. Sci. & Eng. HiTech. and Device Appl. Oct. 24-26 2024, Ankara, Türkiye

Abstract. In steel plate production processes, deformations and residual stresses in products significantly reduce material quality, while increasing scrap amount and product cost. Roller Leveling process, which consists of passing the plates through a series of rollers, is one of the most effective methods used to eliminate production-related defects in steel plates. In this process, in order to obtain high quality products, the operating parameters of Leveler devices must be determined precisely according to the defects and properties of the plate. However, in the current situation, the parameters of the device are determined by the operators by trial-and-error method. In this study, it is aimed to determine the parameters of the Leveler device more precisely by using advanced simulation techniques. The data obtained from the simulation designed by taking into account the operating principle of the Leveler device and the steel plate properties and the operating data of the real device are compared to confirm the accuracy of the simulation system. After this process, it is observed how the device affects product quality at different parameter values for steel plates with different properties and different error rates with the simulation. The obtained results show that the appropriate operating parameters of the device can be determined with the simulation designed without trial and error with the real device to eliminate defects in the product.

Keywords: steel plate, roller leveler, simulation

© 2024 Published by ICMATSE

INTRODUCTION

Today, in the iron and steel industry, companies' survival in conditions of decreasing resources and increasing competition depends on developing quality control, error control and error correction technologies to produce high quality and low-cost production with fewer errors. Various product defects are encountered in iron and steel plate production processes and it is of great importance to detect these errors and correct them if possible (Fig. 1).

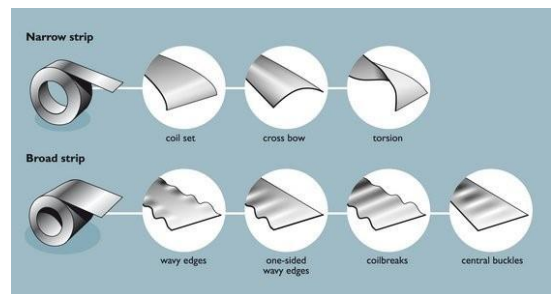


Figure 1. Examples of deformation in steel sheet products [1]

In the stage where steel sheet products reach the end user, the product is unwrapped from the coils, cut lengthwise and widthwise according to the desired dimensions and packaged. During this process, deformation defects and internal stresses originating from production and storage in the products must be corrected (Fig. 2). Today, one of the most

preferred methods for correcting deformation defects and internal stresses in steel sheets is the Roller Leveling process.

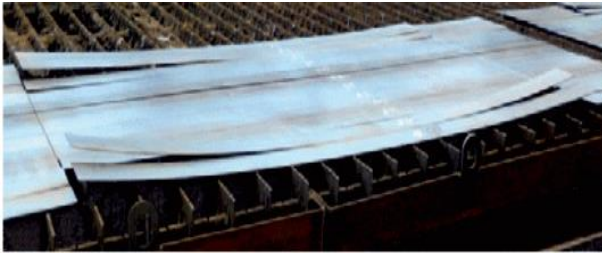


Figure 2. Curvature caused by the release of residual stresses in steel sheets after laser cutting [2].

In the leveler system, it essentially performs a bending operation. The non-flat part or plate is subjected to plastic deformation by a series of consecutive bends. These consecutive bending operations are created by passing the steel plate between the upper and lower leveling roller sets in the system. The leveling rollers are moved in the direction of the moving material. As a result, the plate takes a wave-like path through the system (Fig. 3). This wave is largest at the entrance to the system and smallest at the exit. Thanks to these operations, smooth and internally stress-free plates can be obtained.

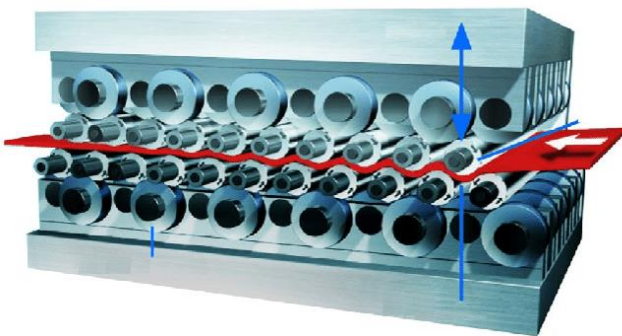


Figure 3. Roller Leveling process on steel plate products [3]

In the use of Rolling Leveler systems, the reference parameters specified by the manufacturers are often insufficient to obtain the desired result. In order to obtain better efficiency from the Leveler system in businesses, operators try to determine the parameters that provide flatter material output based on their observations and trial and error methods. The basis of this problem is that the manufacturers cannot conduct sufficient R&D and testing processes to avoid

high costs. In order to test the system produced, the flatness of the output products with different properties and sizes must be measured, and the products must be sent to test centers or subjected to laser cutting processes to measure their residual internal stresses.

Simulation is recommended as a more comprehensive method that can contribute to product design in reducing the costs of R&D and testing operations. Simulation is the process of designing a model of a system and conducting experiments with this model to test the operation of the system or to evaluate different designs for the operation of the system [4]. Simulation can be used to create models of planned changes and to gain insight into possible behaviors of the system. The reason for using simulation in production systems is that it can analyze the system from many perspectives, thus avoiding the costly and risky implementation of real production and determining which combinations of production system components will dynamically fit the current and strategic business needs [5]. Simulation has many areas of application in production systems, such as determining machine and personnel needs, determining requirements, performance evaluation and efficiency analysis, time analysis for the system, and production planning [6].

MATERIALS AND METHODS

In scientific studies and industrial production processes, finite element based simulation software produces effective solutions. For this reason, it is aimed to use SIMULIA ABAQUS simulation software, which visualizes the finite element analysis results, for both modeling and analysis of mechanical components in the test processes of the Rolling Leveler system (Fig. 4). In addition, thanks to its open source code, it offers users the opportunity to produce application-oriented solutions with the help of the Python programming language.

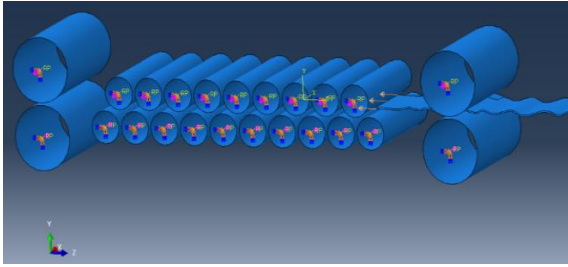


Figure 4. Developed Roller Leveler system simulation

In order to obtain correct results in the system simulation, it is important to use the same parameters as the real system (Fig. 5). In the simulation, the distance ratios between the rollers used in the real system are 2.98 mm for the first roller pressing 2 mm thick steel plate material, while it is 5.97 mm for the 4 mm thick material. The final exit roller pressure is considered as 0 mm and the other roller positions are calculated linearly.

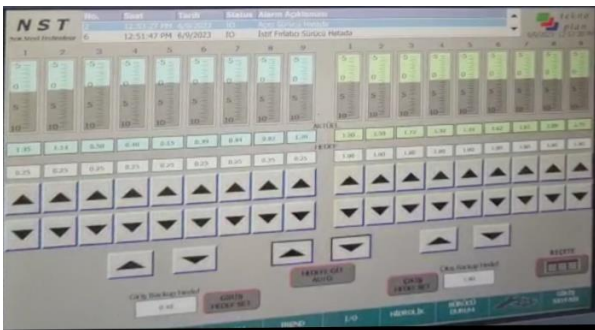


Figure 5. Leveler device system system parameters

In order to calculate correctly the responses of the s355 standard steel plate used in the real system in elastic and plastic deformation in the simulation, its mechanical properties should be defined in the same way in the system simulation (Fig. 6).

Steel plate When the material is subjected to plastic deformation by applying force and then the applied force is removed, structural differences occur together with the shape change in the material. The structure of the material that has undergone plastic deformation is compressed and the yield point increases slightly. When the same material is subjected to plastic deformation again, more force must be applied since the yield point increases. In order to account for this hardening caused by the bending of the steel plate in the opposite direction between the rolls in the simulation model, it is

recommended that the Bauschinger effect be applied [7, 8].

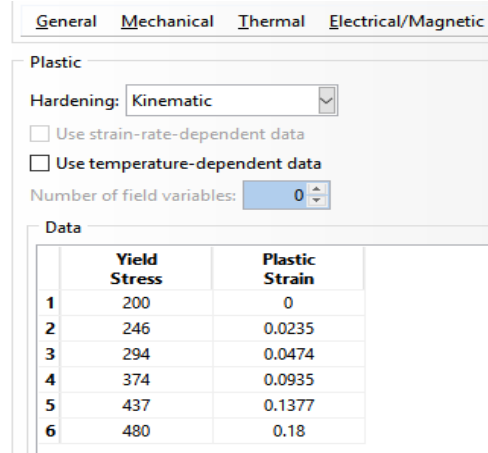


Figure 6. Defining material mechanical properties in leveler simulation

SIMULATION RESULTS

When the simulation study is successfully completed, it is possible to visualize the analysis results and access the desired detailed data using the analysis file created as a result of the simulation. Using this data, graphs and reports can be created for the desired type of analysis results from the program interface.

In the prepared system simulation; parameters such as the distance between the rollers, roller pressure ratio and the operating speed of the system were tested and their effects on the result were analyzed. In the Leveler system simulation, simulations were prepared at different pressure ratios to observe the effect of the roller pressure ratio parameter. As a result of the simulation outputs, it was observed that the increase in roller pressure ratios increased the plastic deformation values in the material. However, when excessive pressure was applied, it was determined that the material was squeezed between the rollers and caused undesirable excessive deformations. In cases where the roller pressure ratio was insufficient, the plastic deformation rates formed in the material were insufficient (Fig. 7). At the same time, the increase in the roller pressure ratio increased the force applied by the rollers to the material in direct proportion. It was observed that the effect of this roller pressure ratio parameter obtained from the

simulation was compatible with the real system data.

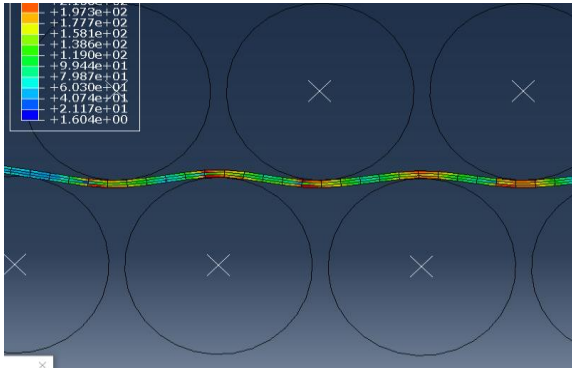


Figure 7. *The material does not undergo sufficient deformation due to insufficient roller pressure ratio in the Leveler simulation*

In order to observe the effect of the distance ratios between the rollers in the leveler system simulation, simulations were prepared with different roller distance ratios. As a result of the simulation outputs, it was observed that the increase in the distance ratios between the rollers reduced the plastic deformation values in the material. It was observed that in cases where the distance between the rollers was too much, the pressure ratio was insufficient and in cases where the distance between the rollers was reduced, excessive pressure was applied to the material and the material was squeezed between the rollers, causing undesirable excessive deformations (Fig. 8). The increase in the distance ratio between the rollers inversely affects the force applied by the rollers to the material. It was observed that the effect of this distance parameter between the rollers obtained from the simulation was consistent with the real system data.

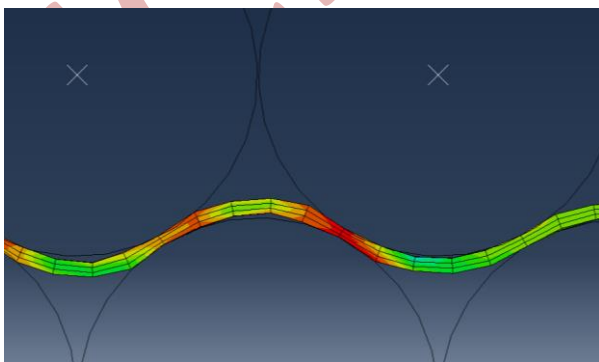


Figure 8. *When the distance between the rollers decreases in the Leveler simulation, the material undergoes excessive deformation*

In the prepared simulation, initial stress values were also defined for the material in order to examine the amount of smoothness and residual stress effect that occurred in the material as a result of the process. As a result of the stress applied to the material, it was observed that the material had internal stress-induced deformation (Fig. 9,10). As a result of the simulation, the smoothness and residual stress data that occurred in the material were compared with the simulation initial values and examined (Fig. 11,12).

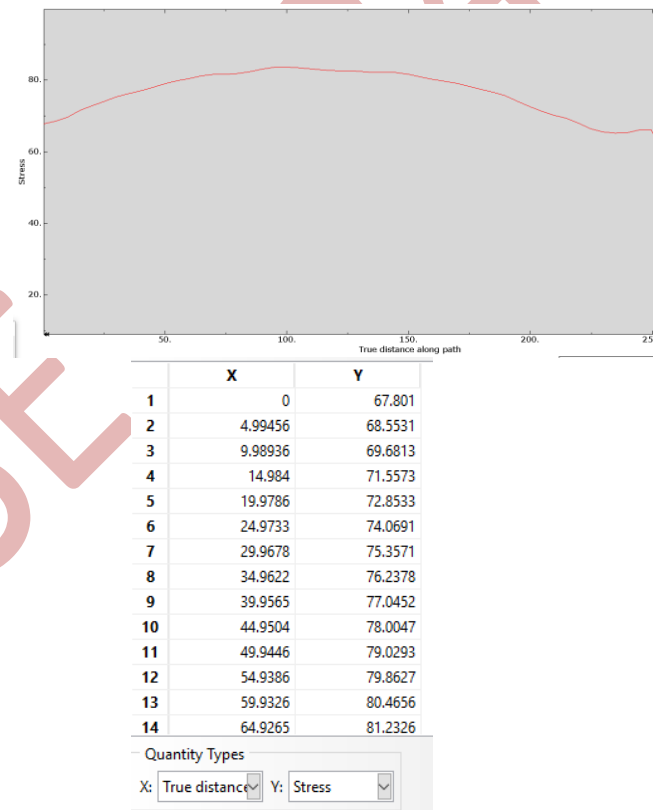


Figure 9. *Residual stress graph and data of the material at the beginning of the Leveler simulation*

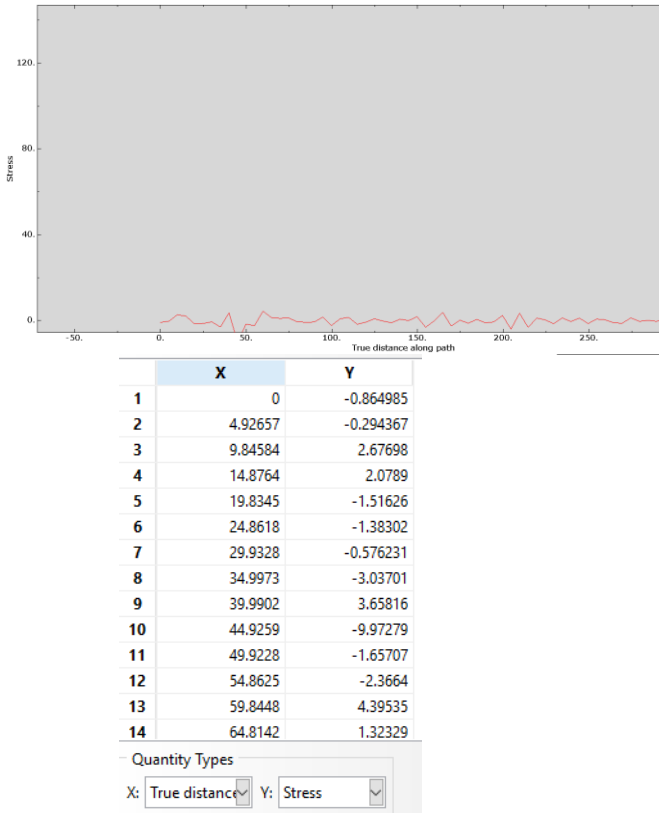


Figure 10. Residual stress graph and data of the material as a result of leveler simulation

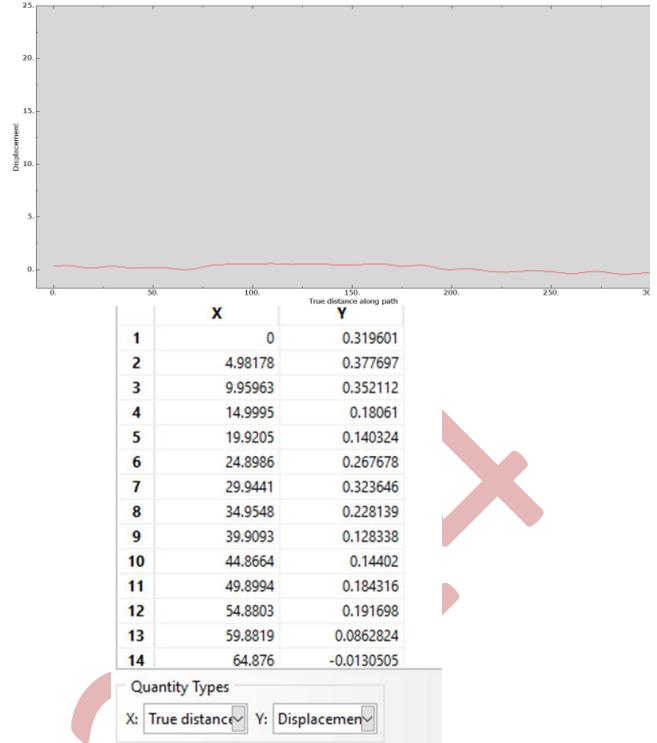


Figure 12. Material flatness graph and data as a result of leveler simulation

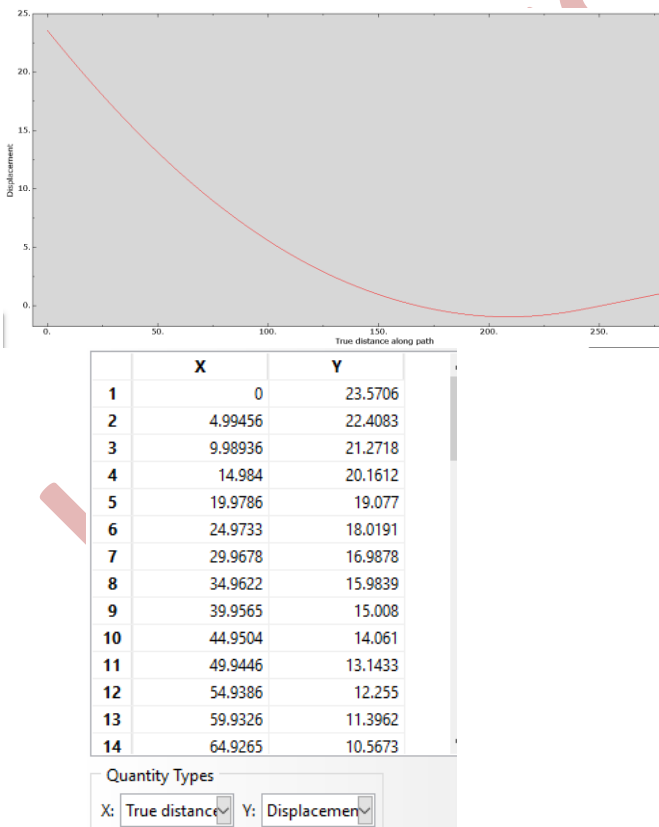


Figure 11. Flatness graph and data of the material at the beginning of the Leveler simulation

DISCUSSION

In the simulation phase of the system, Mesh (solution network), which also affects the precision in the calculation processes for materials, is created and defined in small pieces. It has been concluded that while the solution network defined for materials is in small units, it positively affects the result accuracy in cases requiring process precision, while it increases the calculation cost. The operating speed of the simulation system must first accelerate from a stationary state to reach the desired speed and then slow down and stop, as in the real system. Otherwise, material jamming between the rollers, excessive deformation in the materials or calculation errors occur during the simulation. Although similar results are obtained in the same parameters when the real system and the simulation are

compared, the simulation needs more accuracy tests to calculate the net accuracy rate. After the simulation accuracy rates are clarified, the system parameters will be tested before being applied to the real system and the simulation system will provide the opportunity to observe the

possible results on the material. In subsequent studies, it is aimed to use the parameter and material results obtained from the simulation system in training an artificial intelligence system to be developed for system parameter estimation.

REFERENCES

1. Why roller leveling. (2021, June 20). [Illustration]. <https://www.arku.com/en/why-roller-leveling/>
2. Kotov, K. A., Bolobanova, N. L., & Nushtaev, D. V. (2020). Modeling the Stress State of a Steel Strip with a Roller Leveling Machine under Cyclic Alternating Deformations. *Steel in Translation*, 50(11), 750-755.
3. Ulibarri Hernández, U., Mendiguren, J., Sáenz de Argandoña, E., Galdos, L., Silvestre, E., & Gil, I. (2016). Friction characterisation in levelling processes. *Advances in Materials and Processing Technologies*, 2(4), 503-513.
4. Shannon, R. E. (1975). *Systems simulation; the art and science* (No. 04; T57. 62, S4.).
5. Li, M., & Shurrab, H. (2015). SIMULATION OF PRODUCTION SYSTEMS SIM'S COFFEE CUPS-PROJECT REPORT
6. Ulibarri Hernández, U., Mendiguren, J., Sáenz de Argandoña, E., Galdos, L., Silvestre, E., & Gil, I. (2016). Friction characterisation in levelling processes. *Advances in Materials and Processing Technologies*, 2(4), 503-513.
7. Madej, L., Muszka, K., Perzyński, K., Majta, J., & Pietrzyk, M. (2011). Computer aided development of the levelling technology for flat products. *CIRP annals*, 60(1), 291-294.
8. Lemoine, X., & Aouafi, A. (2008). Bauschinger effect correspondence of experimental tests. *International Journal of Material Forming*, 1(1), 241-244.

4D Printing of Shape Memory Polymer with Digital Light Processing

Nurdan TATLISU

Gazi Universit, Graduate School of Natural and Applied Sciences, 06500, Ankara, Turkey
nurdan.tatlisu1@gmail.com
ORCID: 0000-0002-7069-260X

Oğuzhan YILMAZ

Advanced Manufacturing Technologies Research Group, Faculty of Engineering, Gazi University, 06570, Ankara, Turkiye, oguzhanyilmaz@gazi.edu.tr
ORCID: 0000-0002-2641-2324

Tatlisu, N., Yilmaz, O. 4D Printing of Shape Memory Polymer with DLP .Int. Conf. Advanced. Mater. Sci.& Eng. HiTech.and Device Appl.Oct. 24-26 2024, Ankara, Turkiye

Abstract. Digital Light Process (DLP) is one of the frequently preferred additive manufacturing methods due to its easy availability, high dimensional accuracy and surface quality. In the DLP method, the photopolymer resin in the liquid phase placed in the printer tank is used to run the model by hardening a light source to harden the relevant depth surface specified in the stl file. Unlike other additive manufacturing methods, the 4D printing method is an additive manufacturing method in which the shape, size or color change of the object is transformed into a different form as a function of the time as a result of the effect of external factors such as heat, humidity, magnetic or light on the material. This work aims to to examine the applicability of the DLP process in 4D printing method. The symbol memory feature of phosphine oxide-based methyl methacrylate oligomer resin was examined. Two samples with this ability of 0.1 mm and 0.35 mm were taken and subjected to the same conditions bending test. Using the data obtained as a result of the bending test, the shape re-recordability ratio (Rr) and shape ratio (Rf) were calculated and the results were compared. As a result of the research, DLP, which is widely preferred in additive manufacturing, has been shown to be an accepted technology in this field thanks to the high Rr values it has shown in the 4D printing method.

Keywords: DLP, 4D Printing, Shape memory polymer, Rr, Rf, heat initiated
© 2024 Published by ICMATSE

1. INTRODUCTION

4D printing is a novel applications in additive manufacturing and involves the actuation of smart materials, including Shape Memory Polymers (SMPs), Shape Memory Composites, Shape Memory Alloys (SMA's), and many others.[1] Currently, shape memory polymers (SMPs) are applied in various fields such as aerospace [10], additive manufacturing [1], textile industry [11], and biomedical sciences [12]. The excellent performance of SMPs makes them particularly useful in biomedical applications, such as SMP dental tools, and SMP vascular stent.[6] Compared to other soft active materials applicable in 4D printing, shape memory polymers have higher hardness.[6-7] Among them, UV-curable SMPs are compatible with Digital Light Processing (DLP) 3D printing to produce complex structures and produce SMP structures with high surface quality.[9] In addition, they can be used with many 3D printing technologies.[6-7] Shape memory polymers promising bio-resorbable

and environment-friendly. SMPs change their function dynamically over time when they receive stimuli from outside the material, such as humidity, temperature, light, and magnetic fields. [1] Moreover, SMPs also has low density and activated temperature, high elastic deformation. [2] SMPs can be applied in many areas because of their affordable price and easy formability. [3] SMPs remain popular for use in wearable technologies and biomedical materials due to their excellent bio-resorbable. [3] In this research, the shape recovery and shape fixity ability was tested according to the sample thickness. At the same time, the applicability of the DLP production method for 4D printing was also examined. Bending test was used to testing shape recovery and shape stability rate. All the samples were fabricated using an Zortrax Inkspire DLP printer.

2. MATERIALS AND METHOD

2.1. Digital Light Processing

In this research, the manufacturability of shape memory polymer structures with the DLP method and their usability in 4D printing were investigated. For this purpose, three samples with different thicknesses of 0.35 mm and 0.1 mm were produced using a digital light process (DLP) 3D printer. Zortrax Inkspire DLP printer was used to printing test samples the photosensitive resin cured under a projection UV light. The printer has wavelength of the UV light is 405 nm. Alias model basic transparent photopolymer resin was used. To get stl file all of samples, we were used Z-SUIT which is a slicing software bundle of zortrax inkspire. Resin parameters were obtained by repeating the recommendations given by the company until the optimum result was achieved.[8] The printing parameters obtained for the Alias brand resin used as the external setting are given in the Table 1.

Table 1. Z-SUIT printing parameters for Zortrax Inkspire 3D printer

Printing Parameters	Parameter Values
Layer Thickness	0.05 mm
Layer Exposure Time	9.00 s
Bottom Layer Exposure Time	33.00 s
Bottom Layers	10 pcs
Exposure Off Time	3.00s
Platform Lift Speed	240 mm/m

Also, the relationship between the DLP process and printing parameters is shown schematically in Fig 1.

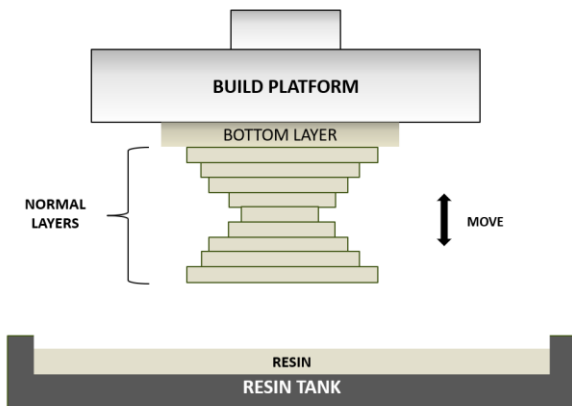


Figure 1. Scheme diagram of DLP printing

After all samples were printed, the samples were washed with isopropyl alcohol in the Anycubic Washing and Curing device for 15 minutes. Then, they were dried and the curing stage was completed

in 20 minutes as recommended by the resin company.

2.2. Differential Scanning Calorimetry (DSC)

DSC thermal analysis method was used to determine the glass transition temperature of the shape memory polymer sample. The analysis was carried out on DSC7020 HITACHI thermal analyzer. The samples were gradually heated up to 200 °C starting from 30 °C in a nitrogen protective atmosphere with a heating rate of 10 °C/min.

2.3. Shape Memory Test

Bending test was used to determine the shape memory properties of the polymer samples. There are two important parameters in determining shape memory properties. [4] One of them is shape recovery ratio which is known as recovery ratio (Rr) defined as the capability of the SMP to regain its initial shape. It could be between 0 and 100% according to polymers microstructural ability. 100% means recovered shape is uniform with initial shape.[5] Shape fixity ratio (Rf) is meaning have the ability to maintaining the temporary shape after the removal of stimulus (in this study used external force). [5] The shape recovery ratio (Rr), and the shape fixity ratio (Rf) could be calculated by the following formulas (1-2): [3]

$$\text{Shape fixity ratio: } \frac{\theta_{fixed}}{\theta_{max}} \times 100 \quad (1)$$

$$\text{Shape recovery ratio: } \frac{\theta_{max} - \theta_t}{\theta_{max}} \times 100 \quad (2)$$

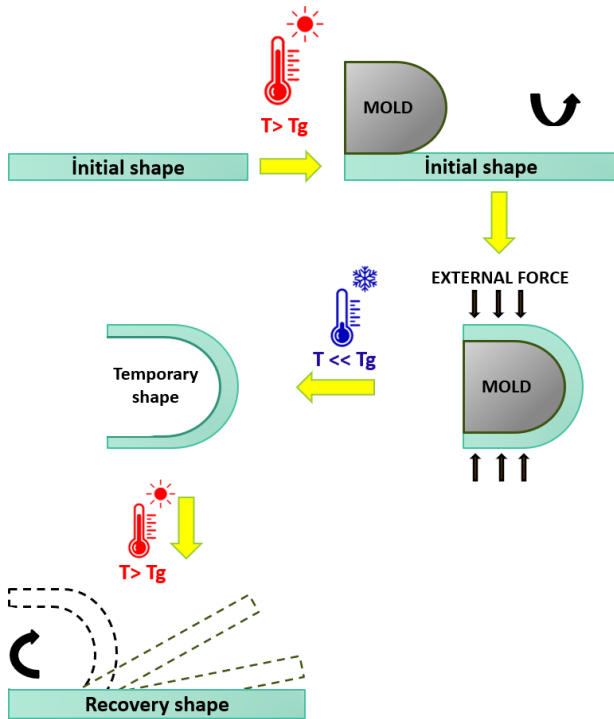


Figure 2. Scheme diagram of bending shape memory testing with recovery and temporary shape.

The dimensions of one of the samples prepared in two different sizes are "30mm x 10mm x 0.1mm" while the dimensions of the other are "30mm x 10mm x 0.35mm". Both of the different thickness samples were heated to above glass transition temperature which is about 120 °C and then try to fixed to fit a 10 mm thick mold by applying an external force. After cooling in cold water (nearly by 15°C) the maximum bending angle recorded was θ_{max} . The sample was shaped based on the mold, by external force applied along 10s. Then external force were removed. The temporary shaped sample hold on room temperature until it was fully dry and fixed. The sample with temporary shape memory expands by stretching a little. The angle at which this expansion is measured is θ_{fixed} . In the last stage, we gradually heated the temporary shape from 95 °C to 120 °C. We recorded the bending angle (θ_t) of the samples when they reached the glass transition temperature of 120 °C. All the processes described above are shown schematically in Figure 2.

3. RESULTS AND DISCUSSIONS

In this research, wo samples with different thicknesses were used to measure shape memory properties. The bending test applied to the samples to determine the shape memory performances revealed that all the samples produced had significant shape memory effects together with their shape stability and shape memory rates. The shape

memory test of the samples with two different thicknesses was observed by bending test.

3.1. Differential Scanning Calorimetry (DSC)

According to the DSC analysis results shown in Figure 5. As DSC analysis results, the glass transition temperature was determined as 110.423°C.

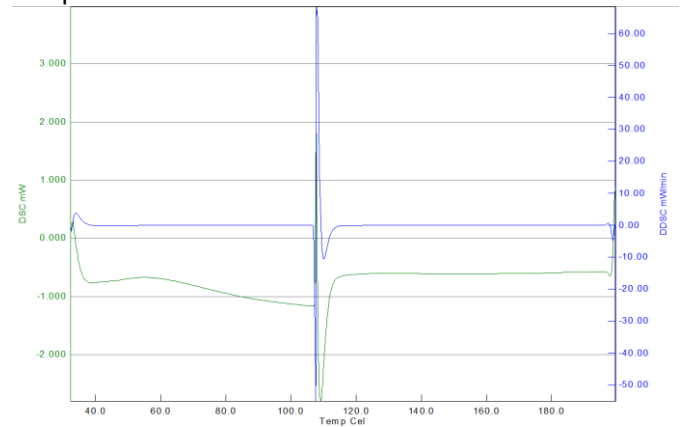


Figure 4. DSC analys of photopolymer resin

3.2. Shape Memory Effect

The graphs of recovery ratio and fixity ratio data resulting from thermal analysis are shown in this section. The Rf and Rr values obtained by performing analyses on 3 samples for each thickness are given in a tabular form in Tables 2-3-4-5. The temporarily shaped sample and the mold with a width of 0.35mm are shown in Fig 3.

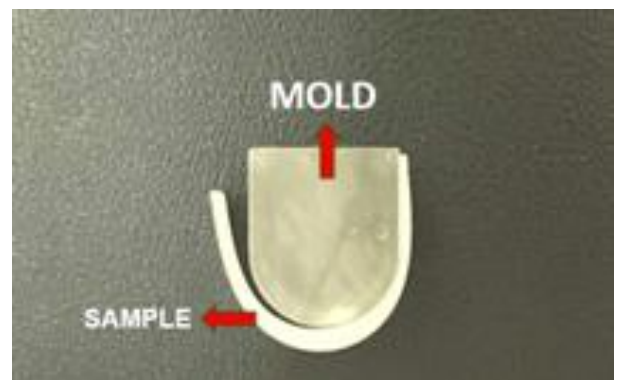


Figure 3. Temporarily shaped sample with a thickness of 0.35 mm

As seen the figure when sample met with cold water it was unable to maintain its mold shape and started to diverge at the ends. This deviation was measured and designated as Rf. Then the temporarily shaped sample was then gradually raised above the glass transition temperature (~120°C) in the oven at 95°C. Analysis results of samples measuring 30 x 10 x 0.1

mm³ are given below. Table 2-3. In addition, the standard deviation values of the data obtained as a result of the shape memory test applied 3 times and the relative error rates of the analysis results were also calculated in these tables. As the standard deviation and relative error decrease, the reliability of the results increases. Therefore, it is important to know these parameters in order to make the estimates of shape memory performance more reliable.

Table 2. *Rf values of the 0.1mm thickness samples*

Samples	Rf	Relative Error (Rf)
1	92,223	-

2	91,667	0.006
3	88,334	0.03635
Avarage	90.74	
Standard deviation	2.103	

Table 3. *Rr values of the 0.1mm thickness samples*

Samples	Rr	Relative Error (Rr)
1	82,223	-
2	82,223	0.00
3	85,556	0.04053
Avarage	83.34	
Standard deviation	1.924	

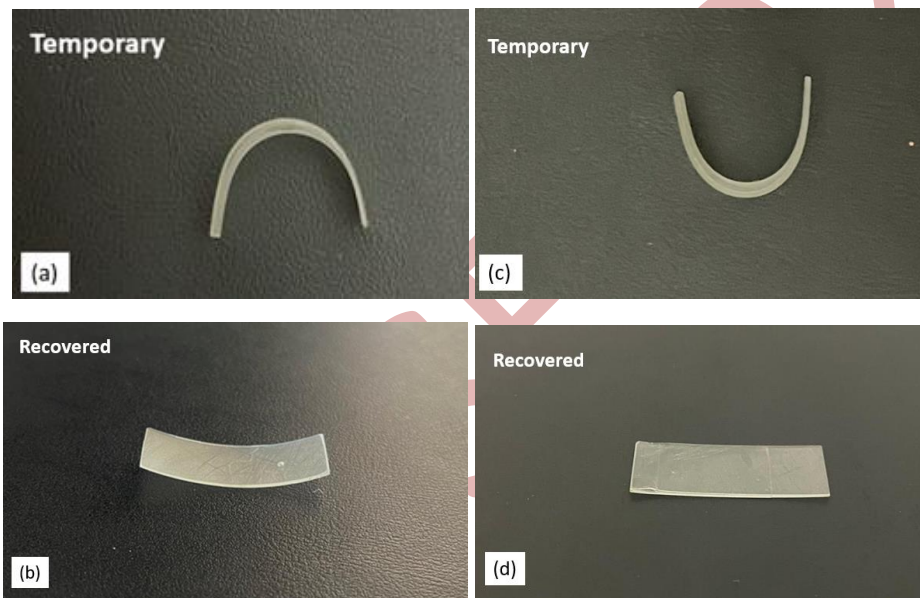


Figure 5. Thermal analysis stages of polymer resin samples. (a) 0.1mm with a transition temperature of ± 120 °C after having temporary shape; and (b) after recovery 0.1mm thickness of sample. (c) Temporary shape of 0.35 mm thickness of sample (d) after recovery 0.35mm thickness of sample

The recycling process of the 0.35 mm thick sample was measured as 1.57 seconds, while the 0.1 mm thick sample was recorded as 1.04 seconds. The resulting recycling process was then examined. Fig 5. (b and d) show the recycling process of samples with thickness values of 0.1 mm and 0.35 mm. It has been understood that 0.35mm thickness of sample is more successful in recycling and shows an almost perfect result. (Fig. 5 (d)). As for the temporary form, the results were found to be relatively close to each other. Secondly, the analysis continued with 30 x 10 x 0.35 mm³ first sample. and the resulting graphs are shown in Table 4-5.

Table 4. *Rf values of the 0.35mm thickness samples*

Samples	Rf	Relative Error (Rf)
1	94,44	-
2	96,112	0.0178
3	97,22	0.01152
Avarage	95.92	
Standard deviation	1.4	

Table 5. *Rr values of the 0.35mm thickness samples*

Samples	Rr	Relative Error (Rr)
1	94,44	-
2	96,84	0.0254
3	97,22	0.00392
Avarage	93.69	

Standard deviation	1.507
---------------------------	-------

According to the shape memory test results, shape fixity (Rf) and shape recovery (Rr) rates for photopolymer resin varied depending on the sample thickness. The shape memory test, when evaluated alongside the bending tests conducted on three samples each, indicates that samples with a thickness of 0.35 mm exhibit superior shape memory performance compared to those with a thickness of 0.1 mm. Among these samples, the material with the highest average shape stability (Rf) rate of 95.92% was determined to be the 0.35 mm thick sample. Similarly, the sample with the highest average shape memory (Rf) rate of 93.69% was determined to be the 0.35 mm thick sample.

As a result, it has been revealed that the use of 0.35 mm thick polymer sample with shape stability and

shape memory rate of over 90% is more efficient with higher Rr and Rf ratios in the production of shape memory parts. In addition, it has been understood that the digital light process, one of the additive manufacturing methods, is extremely suitable for 4D printing applications due to its high surface quality and time saving.

As a consequence, it is thought that this study may be a guide for the development of shape memory polymer materials manufacturing with DLP, the use of shape memory polymers that can be used in 4D printing applications in areas such as technology, robotics, biomedicine, and biomedical industry.

References

- [1] Zhang R, Wang S, Tian J, Chen K, Xue P, Wu Y, Chou W. Effect of PEW and CS on the Thermal, Mechanical, and Shape Memory Properties of UHMWPE. *Polymers*. 2020; 12(2):483. <https://doi.org/10.3390/polym12020483>
- [2] PISANI, Silvia, et al. Shape-memory polymers hallmarks and their biomedical applications in the form of nanofibers. *International Journal of Molecular Sciences*, 2022, 23.3: 1290.
- [3] Kim, Mijeong, Seongeun Jang, Sungwoong Choi, Junghoon Yang, Jungpil Kim, and Duyoung Choi. 2021. "Analysis of Shape Memory Behavior and Mechanical Properties of Shape Memory Polymer Composites Using Thermal Conductive Fillers" *Micromachines* 12, no. 9: 1107. <https://doi.org/10.3390/mi12091107>
- [4] MONZÓN, M. D., et al. 4D printing: processability and measurement of recovery force in shape memory polymers. *The International Journal of Advanced Manufacturing Technology*, 2017, 89: 1827-1836.
- [5] RASTOGI, Prasansha; KANDASUBRAMANIAN, Balasubramanian. Breakthrough in the printing tactics for stimuli-responsive materials: 4D printing. *Chemical Engineering Journal*, 2019, 366: 264-304.
- [6] ZHANG, Biao, et al. Mechanically robust and UV-curable shape-memory polymers for digital light processing based 4D printing. *Advanced Materials*, 2021, 33.27: 2101298.
- [7] CORTÉS, Alejandro, et al. DLP 4D-printing of remotely, modularly, and selectively controllable shape memory polymer nanocomposites embedding carbon nanotubes. *Advanced Functional Materials*, 2021, 31.50: 2106774.
- [8] <https://www.dokuzkimya.com/blogs/news/3d-printer-pozlama-suresi-bulma>(Accessed on 28.09.2024)
- [9] COSOLA, Andrea, et al. DLP 3D-printing of shape memory polymers stabilized by thermoreversible hydrogen bonding interactions. *Applied Materials Today*, 2021, 23: 101060
- [10] Li Y J, Zhang F H, Liu Y J, et al. 4D printed shape memory polymers and their structures for biomedical applications. *Sci China Tech Sci*, 2020, 63: 545–560
- [11] Li S. Review on development and application of 4D-printing technology in smart textiles. *Journal of Engineered Fibers and Fabrics*. 2023;18.
- [12] LI, YueJia, et al. 4D printed shape memory polymers and their structures for biomedical applications. *Science China Technological Sciences*, 2020, 63.4: 545-560.

A Study on Production and Characterization of AlSi10Mg Alloy Using SLM Technique

Zehra TEKKAYA

Gazi University- Department of Metallurgical and Materials Engineering, 06560, Ankara, Turkiye,
zehrtekkaya26@gmail.com
ORCID: 0009-0006-8652-8050

Alpay OZER

Gazi University, Department of Metallurgical and Materials Engineering, 06500, Ankara, Turkiye Gazi University
Welding and Joining Technologies Research and Application Center 06500, Ankara Turkiye
aozer@gazi.edu.tr
ORCID: 0000-0001-8496-0305

Hakan ATES

Gazi University, Department of Metallurgical and Materials Engineering, 06500, Ankara, Turkiye Gazi University
Welding and Joining Technologies Research and Application Center 06500, Ankara Turkiye
hates@gazi.edu.tr
ORCID: 0000-0002-5132-4107

Cite this paper as: Tekkaya Z., Ozer A., Ates H., production and characterization of AlSi10Mg material using slm technique, Int. Conf. Advanced. Mater. Sci. & Eng. HiTech. and Device Appl. Oct. 24-26 2024, Ankara, Turkey

Abstract. With the development of additive manufacturing technology, the use of parts produced with this technology has rapidly become established in human life. In this study, powder additive manufacturing and its applications, which are very much in our lives today, are examined and interpreted. SLM method is a powder additive manufacturing technology in which parts are produced by laser scanning the platform on which a thin layer of powder is laid. When selected areas are scanned with laser scanning, the powders melt and form parts layer by layer, and they have higher density and better performance than traditional manufacturing methods. The AlSi10Mg sample produced by the SLM method was used in the experimental study. The parameters affecting the production of the AlSi10Mg sample were compared using other studies. Bending tests of this sample were carried out at room temperature; microscope examinations were carried out after standard sanding and polishing processes; they were etched, and images were taken in the optical microscope and SEM. Structural characterization studies were carried out in the XRD laboratory on a Bruker D8 advance (Lynxeye detector) brand device. According to the data we obtained from all these studies, the advantages and disadvantages of the SLM method were discussed.

Keywords: Additive Manufacturing, AlSi10Mg, SLM, XRD
© 2024 Published by ICMATSE

The difference between the additive manufacturing method and conventional machining methods is that the layers are manufactured in the desired shape by stacking them on top of each other. *Additive manufacturing* is a general term encompassing all manufacturing technologies that automatically produce modules by combining volume elements called voxels (the 3D equivalent of a pixel). With additive manufacturing, the part prototype, which is created employing computer-aided graphic design (CAD), is transformed into a prototype with a three-gene lattice, another kind of prototype [1, 2]. After

the prototype is separated into layers with special software, it is turned into a part layer by layer with the help of a three-dimensional printer. With additive manufacturing, it is straightforward to design the product, and parts that are difficult to manufacture can be manufactured easily and quickly [1-5].

The selective laser melting (SLM) method is a method that produces parts by scanning the platform on which a thin layer of powder is laid with a laser. When selected areas are scanned by laser scanning, the powders melt and form parts layer by layer. After scanning a layer, the moving platform goes down to the following layer thickness. The new powder is laid

on top with the help of a roller, and the scanning continues. After the part production is finished, the residual powder is cleaned manually or with the help of a vacuum. Since the layers formed by the SLM method cool rapidly, the part microstructure is fine-grained. This rapid cooling refers to the part's mechanical properties being good [6, 7].

This study performed by AlSi10Mg samples produced by SLM for characterizations such as optical microscopy, X-ray diffraction (XRD), and microhardness. The obtained results were discussed by comparing the literature. The microstructural analysis using optical microscopy revealed a fine cellular dendritic structure, which is consistent with previous studies on SLM-processed AlSi10Mg alloys [8]. XRD analysis confirmed the presence of primary α -Al and Si phases, aligning with the findings of other researchers [9]. The microhardness measurements showed an average value of approximately 115-125 HV, which is in agreement with the reported values in the literature for SLM-fabricated AlSi10Mg [10]. These results demonstrate the reproducibility and reliability of the SLM process for producing high-quality AlSi10Mg components. AlSi10Mg specimens showed good bending strength properties. The results are in close agreement with the results of studies in the literature. This alloy containing silicon

and magnesium exhibits a good balance of strength and ductility, making it suitable for applications requiring significant deformation without fracture. The bending properties of AlSi10Mg can be further improved by heat treatments such as T6, which improves its elongation and reduces anisotropy, resulting in more uniform mechanical behavior in different directions. These treatments will eventually make AlSi10Mg an ideal choice for complex geometries and high load applications in industries such as aerospace and automotive [8-10].

The microstructures of AlSi10Mg samples typically consist of a primary α -Al matrix with a fine dispersion of eutectic silicon particles and Mg₂Si precipitates. This microstructure is known to be achieved by processes such as selective laser melting (SLM), which promotes rapid solidification, providing a refined grain structure and improved mechanical properties. The presence of silicon improves the alloy's wear resistance and reduces thermal expansion, while magnesium contributes to its strength and hardness. Heat treatments can further alter the microstructure and improve properties such as ductility and tensile strength, making AlSi10Mg suitable for high-performance applications in the aerospace and automotive industries [8-10].

References

- [1] A. B. Badiru, V. V. Valencia, D. Liu, Additive Manufacturing Handbook. New York: CRC Press, 2017.
- [2] I. Gibson, D. Rosen, and B. Stucker, Additive Manufacturing Technologies, 3D Printing, Rapid Prototyping and Direct Digital Manufacturing. Oxford: Springer, 2015.
- [3] M. Brandt, Laser Additive Manufacturing, Materials, Design, Technologies and Applications. Duxford: Woodhead Publishing, 2017.
- [4] J. O. Milewski, Additive Manufacturing of Metals, From Fundamentals Technology to Rocket Nozzles, Medical Implants and Custom Jewelry. Cham: Springer Series in Materials Science, 2017.
- [5] T. S. Srivatsan, and T. S. Sudarsan, Additive Manufacturing, Innovations, Advances and Applications. New York: CRC Press, 2016.
- [6] Siyambaş, Y., & Turgut, Y. (2022). Defects, mechanical properties and surface roughness of AlSi10Mg alloy parts produced by selective laser melting (SLM) Method-A review. Gazi Üniversitesi Fen Bilimleri Dergisi Part C: Tasarım ve Teknoloji. <https://doi.org/10.29109/gujsc.1130098>
- [7] Bozkurt, Y., Gülsoy, H., & Karayel, E. (2021). Eklemeli İmalat Teknolojilerinin Tıbbi Ekipmanların Üretiminde Kullanımı. El-Cezeri Fen ve Mühendislik Dergisi. <https://doi.org/10.31202/ecjse.902023> in Turkish
- [8] Dong, S., Zhang, X., Ma, F. et al. Research on deposited tracks and microstructures of AlSi10Mg alloy produced by selective laser melting. Appl. Phys. A 126, 643 (2020). <https://doi.org/10.1007/s00339-020-03826-6>
- [9] Hyer, H., Zhou, L., Park, S. et al. Understanding the Laser Powder Bed Fusion of AlSi10Mg Alloy. Metallogr. Microstruct. Anal. 9, 484–502 (2020). <https://doi.org/10.1007/s13632-020-00659-w>
- [10] Xiao, Y., Yang, Y., Wu, S. et al. Microstructure and Mechanical Properties of AlSi10Mg Alloy Manufactured by Laser Powder Bed Fusion Under Nitrogen and Argon Atmosphere. Acta Metall. Sin. (Engl. Lett.) 35, 486–500 (2022). <https://doi.org/10.1007/s40195-021-01354-7>

Zinc foams made by a cold sintering process

Thalmaier Gyorgy

*Technical University of Cluj-Napoca, Materials Science and Engineering Department, 400641, Cluj-Napoca, Romania,
ORCID: 0000-0003-2762-6110*

Sechel Niculina Argentina

*Technical University of Cluj-Napoca, Materials Science and Engineering Department, 400641, Cluj-Napoca, Romania,
ORCID: 0009-0004-5941-3843*

Nasui Mircea

*Technical University of Cluj-Napoca, Physics and Chemistry Department, 400641, Cluj-Napoca, Romania,
ORCID: 0000-0002-4792-2032*

Simon Alexandra

*Technical University of Cluj-Napoca, Materials Science and Engineering Department, 400641, Cluj-Napoca, Romania,
ORCID: 0009-0001-4203-4220*

Constantinescu Horia

*Technical University of Cluj-Napoca, Physics and Chemistry Department, 400641, Cluj-Napoca, Romania,
ORCID: 0000-0003-3290-3290*

Ioan Vida-Simiti

*Technical University of Cluj-Napoca, Materials Science and Engineering Department, 400641, Cluj-Napoca, Romania,
ORCID: 0000-0002-4663-0652*

Cite this paper as: Thalmaier Gy., Sechel N.A. Nasui M., Simon A., Constantinescu H., Vida-Simiti I., Zinc foams made by a cold sintering process. Int. Conf. Advanced. Mater. Sci. & Eng. HiTech. and Device Appl. Oct. 24-26 2024, Ankara, Turkiye

Abstract. This study demonstrates an innovative approach to sintering zinc powder through a cold/chemical sintering process. The technique involves densifying zinc at low to room temperatures by simultaneously applying uniaxial pressure and utilizing an acetic acid based solvent. This method offers an environmentally sustainable production pathway, leading to significant reductions in energy consumption and emissions.

The study focuses on the sintering of zinc powder while utilizing the zinc oxide surface layer. Sintering was performed at temperatures approximate to room temperature, under a pressure of 200 MPa at different temperatures. Different concentrations of NaCl (40%, and 60% with particle size ranges 0.3-0.4 mm and 0.8-1 mm) were employed to enhance porosity.

The cold sintering process investigated key processing parameters, encompassing the temperature, the porosity and the space holder size. These factors exert critical influence over zinc densification. Consequently, the study employed electron microscopy to explore their impacts on the final porous structure. These samples also presented good compression strength.

Keywords: Zinc foam, Cold sintering, Space holder

© 2024 Published by ICMATSE

1. Introduction

Cold sintering is a novel sintering technique that bonds the powder particles at temperatures well below the classical sintering temperatures. This type of sintering necessitates an applied external pressure to increase the driving force for mass transport [1]. This method can be applied to a limited number of materials, the majority being of a ceramic nature [2]. For the cold sintering of metallic materials the bibliographic data shows that the needed pressure for the mass transport enhancement is in the GPa's area, and is too high for current, day to day operation [3]. Unlike classical sintering, cold sintering uses temperatures lower than 250°C, and, to accelerate the diffusion of atoms a liquid phase is used as a pathway for mass transport [4].

One of the most studied cold sintered compounds is ZnO. Due to its abundance, low price, tunable surface chemistry, interesting physical properties for a wide range of applications [5]. This ceramic material has a high melting temperature (1975 °C) however it can be sintered at temperatures as low as 150°C [6-7]

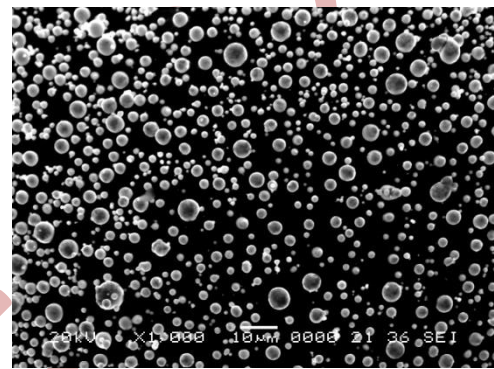
In the present work we studied the cold sintering of some zinc foams by using the powder's native oxide layer as a means of cold sintering them [8]. These porous materials had a limited porosity, however they have the potential to be used as electrodes for Zn-Air batteries. The present paper is aiming to demonstrate the possibility of extending this sintering method to the sintering and dissolution process (SDP) that is widely used in manufacturing porous materials using powder metallurgy.

2. Experimental

In the case of the samples obtained in this work, spherical zinc powder (particle size < 10 µm, fig.1 a.) was mixed with sodium chloride (size range 0.3-0.4 mm and 0.8-1 mm, angular shape, fig.1 b.) to obtain samples with 40% and 60% porosities in the final samples. The zinc powder used in this work is characterized by a very small particle size, which results in a consistent layer of zinc oxide on their surface that can be used for the cold sintering process. The selected space holder does not interact consistently under the envisioned experimental condition with the used materials and does not impede the cold sintering process as will be evidenced in the following sections. The mixture was

placed in a 1 cm² surface area cylindrical mold, over which was added ~6 wt% of the liquid phase, (a mixture of 25% acetic acid, 25% water, and 50% ethyl alcohol) for the cold sintering process.

A pressure of 200 MPa at different temperatures (25, 250 and 300 °C) for 30 seconds was maintained for the dissolution and precipitation of the Zn atoms to take place and for the cold sintering process to take place. After evaporation of the liquid phase the sample was maintained at room temperature for 24 h and followed by a space holder dissolution in flowing water for 24 h. By dissolving the NaCl a metallic zinc foam was obtained.



a).



b).

Figure 1. Images of the used powders Zn (a) and NaCl (b)

The powder and sintered samples were analysed by scanning electron microscopy. The samples density was calculated by dividing weight to the volume calculated from the sample's dimensions.

Compression test of samples was performed on a universal testing machine with a crosshead velocity of 0.5 mm/min.

3. Results and discussions

After the space holder dissolution, the samples presented somewhat higher porosities than the prescribed ones, since in the structures an interparticle porosity was present alongside the pore former particles, this increase was in the range of 2-4 %, more at the lower porosity sample and less for the 60% porosity samples. The top side of typical samples before and after the dissolution process are presented in figure 2. The angular shape of the pores that resembles the used NaCl particles is evident.

As usually observed in the SDP process a small part of the space holder was not eliminated. This usually is caused by the closure of some pores during the forming process and by the reprecipitation of the saline solution remained in certain areas where the water used for the dissolution of the NaCl particles has a difficult access. No significant shrinkage was observed during the cold sintering process.

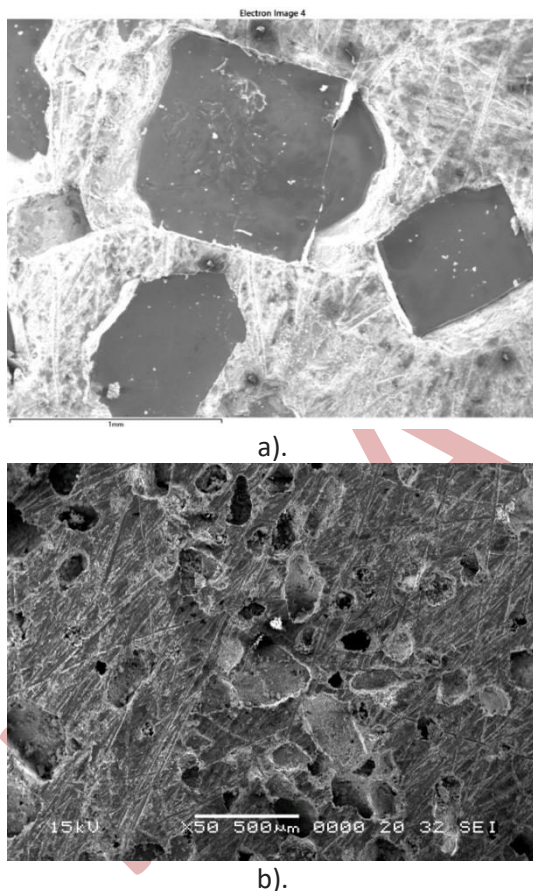


Figure 2. Appearance of the samples before (a) and after (b) the removal of the pore former

Figure 3 presents a typical image observed during the SEM analysis. In the pores wall one can clearly observe the sintering of the particles. The sintering degree calculated as the ratio of the sintering necks width divided by the particle diameter is around 0.6 which corresponds to a good sintering. The sintering

degree is uniform in the cross section of the samples, suggesting a good distribution of the liquid phase during the sintering stage. Between the particles in the pore wall certain small pores in the micron and submicron range are present that can act as weak points during the compression tests. This weak link behavior is pronounced by the brittle nature of the ZnO phase present.

The compression tests obtained on these samples presents a reasonable ductility. The reduced ductility is caused by the Zn hexagonal crystalline structure that has lower deformability than the cubic one and the presence of a significant amount of oxide phase especially in the sintering necks that also reduces the ductility.

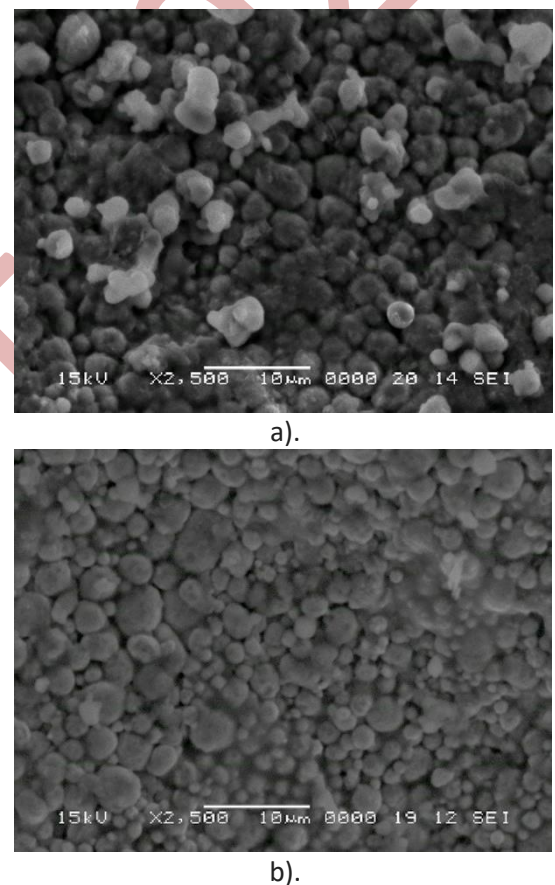


Figure 3. Typical SEM image of the pores wall a). P=40 % T=250°C, b). P=60 % T=250°C

Zinc has a compressive strength of 75-160 MPa [9], being influenced by several factors such as purity, temperature and, heat treatments. The lower strength for samples sintered at 25°C is due to zinc acetate present in the samples at this temperature [8]. At temperatures close to 300°C zinc acetate decomposes into zinc oxide, acetone and carbon dioxide [10].

Table 1. Compressive strength versus the NaCl particle size and cold sintering temperature

Porosity [%]	NaCl size [mm]	Temperature [°C]	Compr. strength [MPa]
40%	0,3-0,4	25	38
		250	81
		300	70
	0,8-1,0	25	6,5
		250	77
		300	24
60%	0,3-0,4	25	7
		250	83
		300	76
	0,8-1,0	25	8
		250	81
		300	8,6

The highest value of compressive strength was measured for the samples sintered at a temperature of 250 °C, all of them over 75 MPa (Tab. 1). By increasing the temperature to 300 °C a sharp drop in the compression strength of the samples with the 0.8-1 mm pores, sign that the stress concentrator effect of the pores became of great importance.

The results obtained for the samples sintered at 250°C and 300°C are satisfactory. Therefore, the

References

1. C. Vakifahmetoglu, L. Karacasulu, Cold sintering of ceramics and glasses: A review *Current Opinion in Solid State & Materials Science* 24 (2020) 10080, <https://doi.org/10.1016/j.cossms.2020.100807>
2. A. Ndayishimiye, M. Y. Sengul, T. Sada, S. Dursun, S. H. Bang, Z. A. Grady, K. Tsuji, S. Funahashi, A. C.T. van Duin, C. A. Randall, Roadmap for densification in cold sintering: Chemical pathways, *Open Ceramics* 2 (2020) <https://doi.org/10.1016/j.oceram.2020.100019>
3. E. Gutmanas, A. Rabinkin, M. Roitberg, Cold sintering under high pressure, *Scr. Mater.*, 13 (1979), pp. 11-15, [https://doi.org/10.1016/0036-9748\(79\)90380-6](https://doi.org/10.1016/0036-9748(79)90380-6)
4. Y. K. Lee, J. Kim, Y. Kim, J. W. Kwak, Y. Yoon, J. A. Rogers, Room Temperature Electrochemical Sintering of Zn Microparticles and Its Use in Printable Conducting Inks for Bioresorbable Electronics, *Adv. Mater.* 2017, 29, 1702665, <https://doi.org/10.1002/adma.201702665>
5. Ü. Özgür, Y.I. Alivov, C. Liu, A. Teke, M.A. Reshchikov, S. Do, V. Avrutin, A comprehensive review of ZnO materials and devices, *J. Appl. Phys.* 98 (2005) 041301, <https://doi.org/10.1063/1.1992666>.
6. S.H. Bang, M.Y. Sengul, Z. Fan, A. Ndayishimiye, A.C.T. van Duin, C.A. Randall, Morphological and chemical evolution of transient interfaces during zinc oxide cold sintering process, *Materials Today Chemistry* 24 (2022) 100925, <https://doi.org/10.1016/j.mtchem.2022.100925>
7. A. Ndayishimiye, M. Y. Sengul, S. H. Bang, K. Tsuji., K. Takashima, T. Hérisson de Beauvoird, D. Denuxe, J.-M. Thibaude, A. C.T. van Duin, C. Elissalde, G. Goglio, C. A. Randall, Comparing hydrothermal sintering and cold sintering process: Mechanisms, microstructure, kinetics and chemistry, *Journal of the European Ceramic Society* 40 (2020) 1312–1324, <https://doi.org/10.1016/j.jeurceramsoc.2019.11.049>
8. K. Jayasayee, S. Clark, C. King, P. I. Dahl, J. Richard Tolchard, M. Juel, Cold Sintering as a Cost-Effective Process to Manufacture Porous Zinc Electrodes for Rechargeable Zinc-Air Batteries, *Processes* 2020, 8, 592, <https://doi.org/10.3390/pr8050592>
9. <https://www.azom.com/properties.aspx?ArticleID=749>

samples obtained by cold sintering of zinc powder can be used for applications that do not require very high resistance, such as anodes for zinc air batteries.

4. Conclusions

The present work main findings can be summarized as follow:

- Cold sintering of zinc foams is possible, supported by SEM and compressive strength results.
- The sintering degree is between 60-65%, indicating a good sintering
- Compressive strength is excellent for samples sintered at 250°C and 300°C, indicating the possibility of using cold sintered zinc foams for applications that do require mechanical characteristics.

The highest value of the compressive strength was recorded for the samples cold sintered at 250°C, with a value over 81 MP for a NaCl particle size range of 0.3- 0.4 mm.

10. R.A. Mereu, A. Mesaros, T. Jr. Petrisor, M. Gabor, M. Popa, L. Ciontea, T. Petrisor, Synthesis, characterization and thermal decomposition study of zinc propionate as a precursor for ZnO nanopowders and thin films. *J Anal Appl Pyrolysis*. 104 (2013) 653–659. <https://doi.org/10.1016/j.jaap.2013.05.001>

ICMATSE 2024

Development of Nickel-Based Bimetallic Anode Catalysts for Direct Ethanol Fuel Cells

Fatma Nur Tiren

Gazi University, Chemical Engineering Department, Ankara, Turkey,
fatmanur.tiren@gazi.edu.tr
ORCID: 0009-0005-2514-1306

Yavuz Yağızatlı

Gazi University, Chemical Engineering Department, Ankara, Turkey,
yavuzyagizatli@gazi.edu.tr
ORCID: 0000-0003-4926-3621

İrfan Ar

Gazi University, Chemical Engineering Department, Ankara, Turkey,
irfanar@gazi.edu.tr
ORCID: 0000-0002-6473-9205

Cite this paper as: Tiren, FN., Yağızatlı, Y., Ar, İ., "Development of Ni-based Bimetallic in Direct Ethanol Fuel Cells". Int. Conf. Advanced. Mater. Sci. & Eng. HiTech. and Device Appl. Oct. 24-26 2024, Ankara, Turkiye

Abstract. Fuel cells are of great importance in terms of clean energy production and reducing energy dependency on foreign countries. Direct liquid fuel cells provide fuels with higher energy density and easier fuel management compared to other types. Ethanol offers high energy efficiency, easy storage and distribution, and renewability advantages in these systems. Despite the high electrochemical behaviors of platinum and palladium-based catalysts, their high costs prevent the widespread use of fuel cells, therefore, the search for low-cost and high-efficiency catalysts continues [1]. In this study, catalysts were synthesized by binary metal co-participation method in various molar ratios (Ni₉₀Cu₁₀, Ni₈₀Cu₂₀, Ni₇₀Cu₃₀, Ni₉₀Co₁₀, Ni₈₀Co₂₀, Ni₇₀Co₃₀, and Ni₅₀Co₅₀) to observe their electrochemical behaviors. The synthesized catalysts were subjected to Cyclic Voltammetry (CV), Chronoamperometry (CA), and Electrochemical Impedance Spectroscopy (EIS) analyses and Linear Sweep Voltammetry (LCV) in a basic electrolyte medium (1 M NaOH with 0.2 M EtOH), along with some characterization methods, FTIR, N₂ adsorption-desorption, SEM-EDx and XRD.

Keywords: Nickel, Copper, Cobalt, Direct Ethanol Fuel Cell, Anode catalysts
© 2024 Published by ICMATSE

1. Introduction

The global demand for energy continues to rise, leading to the need for new energy sources as fossil resources are depleting. Fuel cells represent a significant advancement in the search for sustainable and efficient energy conversion technologies. Among the various types, direct ethanol fuel cells (DEFC) have garnered considerable interest due to their high energy densities, low operating temperatures, and ability to use ethanol, a renewable and less toxic fuel compared to methanol. At the core of DEFC performance lies the catalytic activity of the anode material, which

facilitates the electrooxidation of ethanol [2]. This study focuses on the synthesis and characterization of Ni-Co, Ni-Cu, and pure Ni catalysts for ethanol electrooxidation in alkaline media. By extensively studying the electrooxidation of ethanol on transition metal catalysts, nickel-based catalysts show promise due to their excellent catalytic properties and cost-effectiveness. However, pure nickel catalysts often suffer from poor stability and low catalytic activity due to issues such as poisoning and surface degradation [3]. Alloying nickel (Ni) with other metals such as copper (Cu) and cobalt (Co) can potentially enhance catalytic performance by modifying the electronic structure and increasing

resistance to poisoning. Ni-Cu alloys are known for their improved conductivity and resistance to oxidation, while Ni-Co alloys exhibit enhanced catalytic activity and stability due to the synergistic effects between nickel and cobalt. Despite the promising potential of Ni-Cu and Ni-Co catalysts, systematic studies are still needed to investigate the optimal composition and synthesis methods to maximize their catalytic performance in ethanol electrooxidation [4]. This study involves the synthesis and characterization of Ni-Co and Ni-Cu catalysts with different compositions to determine their efficiency in ethanol electrooxidation. The molar compositions of the synthesized Ni-Cu and Ni-Co catalysts were Ni:Cu (90:10), Ni:Cu (80:20), Ni:Cu (70:30), Ni:Co (90:10), Ni:Co (80:20), Ni:Co (70:30), Ni:Co (50:50) and pure Ni. Their catalytic activities in 1 M NaOH and 0.2 M EtOH solutions were evaluated using cyclic voltammetry (CV), chronoamperometry (CA), and electrochemical impedance spectroscopy (EIS). The synthesized catalysts were characterized using X-ray diffraction (XRD), scanning electron microscopy (SEM-EDS), and N₂ adsorption-desorption isotherms to gain insights into the structural and morphological properties, crystallographic phases, surface morphology, elemental composition, and specific surface areas of the catalysts.

2. Material and Methods

In this study, firstly, (Nickel-Cobalt and Nickel-Copper) alloys were synthesized by coprecipitation synthesis method in different ratios (Ni₉₀Cu₁₀, Ni₈₀Cu₂₀, Ni₇₀Cu₃₀ and Ni₉₀Co₁₀, Ni₈₀Co₂₀, Ni₇₀Co₃₀, Ni₅₀Co₅₀ and pure Ni) from their nitrate salts to determine the optimum result. The synthesized precipitate was subjected to 600 °C for 8 hours by calcination method to remove the salts and the structure was fixed. 150 mL of Nafion solution, 850 mL of ethanol and 4 mg of the obtained bimetallics were taken to form the catalyst slurry. The slurry was made homogeneous by vortex and prepared for electrochemical measurements and characterization methods. For electrochemical measurements, the catalysts coated on glassy carbon electrode were carried out in 1 M NaOH+0.2 M EtOH solution medium. In order to observe the catalytic activity, nickel-copper and nickel-cobalt catalysts prepared at 90:10, 80:20, 70:30 and 50:50 mole ratios were subjected to cyclic voltammetry method at 50 mV/s scanning rate and in the range of -1.0 to 1.0. In order to provide information about the resistance

and capacitive behaviors of the catalysts, they were investigated by EIS (Electrochemical Impedance Spectroscopy) method in the frequency range of 9.5, 0.01 V EAC and 1.0 Hz - 1,000,000 Hz scanning range. In order to evaluate the stability and durability of the catalysts over time, the prepared nickel-copper, nickel-cobalt and pure nickel catalysts were examined by chronoamperometry method at 0.7 V/1000 s scanning rate. As a result of electrochemical measurements, 90-10% Ni-Cu catalyst shows the highest activity among the catalysts at various ratios. For this reason, the characterization methods were continued with 90-10% Ni-Cu catalyst and the structure was tried to be understood. XRD analyzes of the catalysts were carried out in the 2-90° scanning range and 5°/min scanning rate. XRD is used to determine the crystal structure and phase composition of the catalysts. In order to identify functional groups and chemical bonds in catalyst materials, Fourier Transform Infrared Spectroscopy (FTIR) method was analyzed in the wavenumber range of 400 to 4000 cm⁻¹ on an instrument with single reflection diamond crystal ATR accessory, KBr beam splitter and air-cooled light source. Scanning Electron Microscopy/Energy Dispersive X-ray Spectroscopy (SEM/EDX) Analysis was used to analyze the surface morphology and particle size of the catalysts, while EDX helps to determine the elemental composition. Scanning Electron Microscopy (SEM) images of the catalyst at 500 nm, 200 nm, and 2 μm are available at 15.00 kV accelerating voltage and 10,000x, 20,000x and 50,000x magnifications. N₂ Adsorption - Desorption provides information about the surface area, pore volume and pore size distribution of the catalysts. Nitrogen gas was used as the analysis gas in these measurements. The X cross-sectional area was taken as 16.2 Å²/molec, non-ideality as 6.58e-05, bath temperature as 77.40 °C, gas outlet temperature as 200.0 °C, gas outlet time as 3.0 hours and P/Po tolerance as 3.

3. Result and Discussion

Ethanol electrooxidation activities of catalysts synthesized at different ratios are given in Figure 1. As a result of CV analyses, it was observed that Ni₉₀Cu₁₀ catalyst showed higher electrochemical activity compared to other catalysts with a value of 3.044 mA/cm². In addition, it was observed that the activity of the catalyst increased as the Co ratio increased (Ni₉₀Co₁₀: 0.283 mA/cm², Ni₈₀Co₂₀: 0.537 mA/cm² and Ni₇₀Co₃₀: 1.557 mA/cm²). Therefore, the study was continued by further

increasing the Co:Ni molar ratio. However, the expected activity could not be reached by increasing only the Co ratio (Ni50Co50: 0.40 mA/cm²). No electrochemical activity was observed in the absence of a catalyst, indicating that there was no catalytic activity at the electrodes.

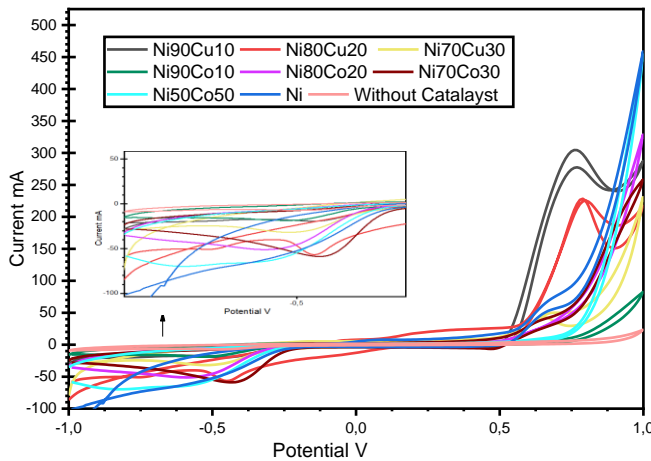


Figure 1. Cyclic voltammogram for all catalysts. (Ni-Cu catalysts, Ni-Co catalysts, Pure Ni catalyst and without catalyst) (0.2 M EtOH and 1 M NaOH)

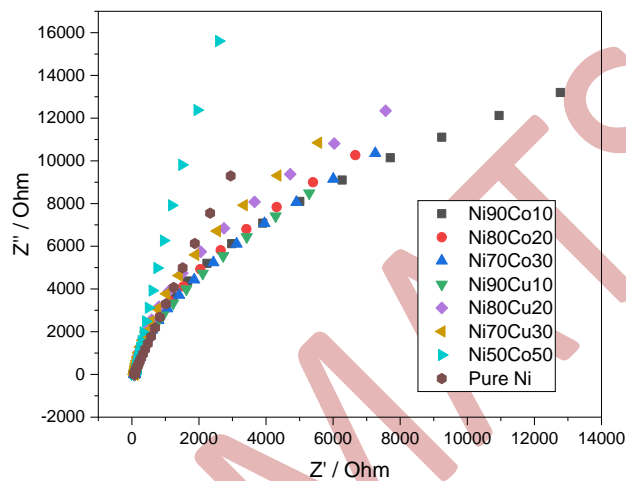


Figure 2. Nyquist diagram for Ni-Co, Ni-Cu and Pure Ni catalysts. (0.2 M EtOH and 1 M NaOH) simi

In Fig. 2, Z' (Real Resistance) and Z'' (Virtual Resistance) values are given in Ohm, and the electrochemical performances of different Ni-Cu and Ni-Co ratios (90:10, 80:20, 70:30) are evaluated. In the Nyquist diagram (Z' vs Z''), all samples show similar trends and have a semicircular form. This semicircular form indicates a process with a single time constant in the system and generally represents a charge transfer resistance and double layer capacitance. The real and imaginary parts of the impedance show a similar trend for all alloys. It can be said that Ni90Cu10 catalyst has the best catalytic activity for ethanol electrooxidation compared to the others.

In general, catalysts with 90:10 ratio show the lowest impedance, indicating that they have the best electrochemical performance. Low impedances indicate that the charge transfer resistance is lower and therefore the catalyst is more effective. The impedance results support the cyclic voltammetry results. XRD analysis was performed to determine the crystal properties of the catalyst (Ni90Cu10) and the phases it contains. The XRD pattern of the Ni90Cu10 catalyst is given in Figure 3. In the XRD pattern of the catalyst in Figure 3, 5 peaks centered at $2\theta = 37.25^\circ, 43.29^\circ, 62.86^\circ, 75.4^\circ, 79.36^\circ$ were observed. The observed peaks belong to the 003, 012, 104, 113 and 006 [6] surfaces, respectively. When the nickel mole ratio in the bimetallic Ni-Cu sample was high, metallic Ni nanoparticles were formed in addition to the Ni-Cu alloy. In addition, the sharp and high intensity peaks in the XRD pattern indicate that the catalyst has a highly crystalline structure and a large surface area. This is a critical feature that increases the efficiency of the catalyst and provides the desired reactivity [5]. These diffraction peaks belonging to the crystal plane are nickel oxide peaks [6]. The formation of nickel oxide peaks is common compared to the mole fraction of the catalyst.

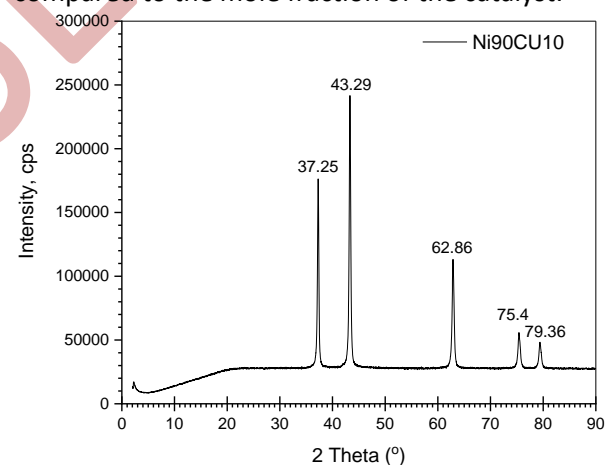


Figure 3. XRD patterns of Ni₉₀Cu₁₀ catalyst

4. Conclusion

This study focused on finding the optimum ratios of Ni-Cu and Ni-Co catalysts by studying their performance in alkaline media. Cyclic voltammetry experiments revealed that both Ni-Cu and Ni-Co catalysts exhibited high current densities, indicating significant electrochemical activity for ethanol oxidation.

The highest current density for Ni-Cu catalysts was observed as 3.044 mA/cm² for the Ni90Cu10 composition, demonstrating the potential of this particular ratio to reach optimum performance.

Chronoamperometry (CA) measurements show that there are significant differences between the initial current densities, and the current density stabilities at the end of 1000 seconds show the stability performances. These results support other values obtained in other electrochemical analysis. Ni-Co catalysts also showed promising results; the Ni70Co30 composition provided the highest current density among the tested ratios.

References

1. Kivrak, H., & Ulaş, B. (2017). Doğrudan metanol yakıt pili karbon destekli Pt-Ru anot katalizörlerinin sıralı indirgeme yöntemi ile sentezi ve geliştirilmesi. *Yüzüncü Yıl Üniversitesi Fen Bilimleri Enstitüsü Dergisi / Journal of the Institute of Natural & Applied Sciences*, 22(1), 21-32.
2. Chang, J., Wang, G., Chang, X., Yang, Z., Wang, H., Li, B., Zhang, W., Kovarik, L., Du, Y., Orlovskaya, N., Xu, B., Wang, G., & Yang, Y. (2023). Interface synergism and engineering of Pd/Co@N-C for direct ethanol fuel cells. *Nature Communications*, 14, Article 1346.
3. Xu, C., Hu, Y., Rong, J., Jiang, S. P., & Liu, Y. (2007). Ni hollow spheres as catalysts for methanol and ethanol electrooxidation. *Journal of Power Sources*, 171(2), 638-645.
4. Hassanzadeh, V., Sheikh-Mohseni, M. A., & Habibi, B. (2019). sCatalytic oxidation of ethanol by a nanostructured Ni-Co/RGO composite: Electrochemical construction and investigation. *Journal of Electroanalytical Chemistry*, 113200.
5. X-ray diffraction patterns of 90-10 Cu-Ni and Cu-Ni-Mt nanocomposite coatings run from 40–100° 2θ at a step size of 0.05° and dwell time of 1 sec (ss: steel substrate) by A.A. El-Shafei et al. in *Materials Science and Engineering*
6. Richardson, J. (2003). X-ray diffraction study of nickel oxide reduction by hydrogen. *Applied Catalysis A: General*, 246(1), 137–150.

Further increase in cobalt content leads to increase in activity of the catalyst. Therefore, Ni50Co50 catalyst was synthesized and subjected to electrochemical tests in order to find the optimum Ni:Co ratio. However, the result was not as expected and only current density of 0.40 mA/cm² could be obtained.

The Effect of Temperature on the Tensile Behavior of Additively Manufactured IN 718 for As-Built and Direct-Aged Conditions

Tuğçe Kaleli Alay

Welding Technology and NDT Center, METU, Ankara, Türkiye, tkaleli@metu.edu.tr
ORCID: 0000-0003-1109-8958

Cemil Hakan Gür

Department of Metallurgical and Materials Engineering, METU, Ankara, Türkiye, chgur@metu.edu.tr
ORCID: 0000-0002-4884-9818

Cite this paper as: Kaleli Alay, T., Gür, C.H. The Effects of Deformation Temperature on Deformation Kinetics in Additively Manufactured IN 718. Int. Conf. Advanced. Mater. Sci. & Eng. HiTech. and Device Appl. Oct. 24-26 2024, Ankara, Türkiye

Abstract. This study explores the effect of temperature on the tensile behavior of IN 718 specimens produced via Selective Laser Melting (SLM). Tensile tests were conducted at 550°C, and 650°C on as-built and direct-aged (DA) specimens. In all specimens, Dynamic Strain Aging (DSA) was observed at 550°C, contributing to serrations in the stress-strain curves. At 650°C, anomalies in yield strength and temperature-induced brittleness were noted, likely linked to the dissolution of carbides at grain boundaries. The results revealed distinct differences in temperature-dependent tensile behavior between the as-built and direct-aged conditions. These effects provide key insights into optimizing SLMed IN 718 for high-temperature applications, emphasizing the complex interplay between temperature, microstructure, and mechanical properties.

Keywords: IN 718, Selective Laser Melting, Direct Aging, High-Temperature Tensile Test, Dynamic Strain Aging

© 2024 Published by ICMATSE

1. Introduction

Nickel-based superalloys, such as Inconel 718 (IN718), are widely used in high-temperature environments because of their excellent mechanical properties, corrosion resistance, and ability to retain strength at elevated temperatures, making them a popular choice for aerospace, power generation, and other high-temperature applications. Given the increasing demand for high-temperature applications, understanding how temperature affects the tensile behavior and deformation mechanisms in both as-built and heat-treated IN 718 conditions is critical.

Additionally, the occurrence of phenomena such as Dynamic Strain Aging (DSA), carbide dissolution, and changes in dislocation dynamics can significantly influence the material's yield strength, ductility, and overall structural integrity at elevated temperatures. Dynamic strain aging (DSA) has been observed in various nickel-based superalloys across different microstructures, temperature ranges, and strain rates.

Numerous studies have documented the occurrence of this effect [1]–[5]. For example, research by Chen and Chaturvedi on DA-treated IN718 within the 300–577°C range concluded that the serrated flow behavior is primarily driven by interstitial carbon atoms, independent of interactions between dislocations and precipitates [1], [3]. Similarly, Hale et al. noted that serrations arise from the diffusion of interstitial carbon atoms at lower temperatures (127–427 °C) and substitutional chromium atoms at higher temperatures (477–627 °C) [3]. Nalawade et al. also found that serrated flow was associated with the movement of interstitial carbon atoms at temperatures below half the melting point, while both interstitial and substitutional solutes influenced the behavior at higher temperatures [4].

This study aims to investigate the tensile behavior of SLM-produced IN 718 specimens under varying thermal conditions, focusing on the effects of deformation temperature and heat treatment. By comparing the tensile properties of as-built and direct-aged samples at 550 °C and 650 °C, this work provides crucial insights into the microstructural factors driving temperature-dependent mechanical

performance. The findings of this study are instrumental for optimizing the use of SLMed IN 718 in demanding high-temperature environments.

2. Results and Discussion

The specimens were produced via the SLM process using gas-atomized IN 718 powders within the range of 20-55 μm . The process was optimized to obtain a volumetric energy input of 52 J/mm^3 . Cylindrical samples were built with vertical build direction and stripe scanning model, as shown in Figure 1. Then, the direct aging treatment was applied to some specimens (heating at 720°C for 8 hours, furnace cooling to 620°C and holding for 10 hours, and then air cooling).

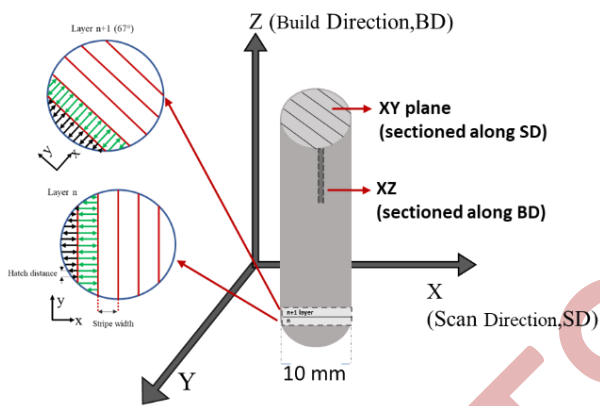


Figure 21 Schematic demonstration of scanning strategy and build orientation of SLM samples

As-processed specimens were analyzed by OM, SEM, and XRD for microstructural analysis. The microstructures of as-built and DA-treated samples are shown in Figure 1. After DA treatment, Laves phases were not dissolved; however, strengthening precipitates (γ' and γ'') were formed. The presence of precipitated phases hinders dislocation motion, leading to an increase in dislocation density. As a result, a greater applied force is necessary to overcome the accumulated dislocations, resulting in enhanced yield and tensile strength.

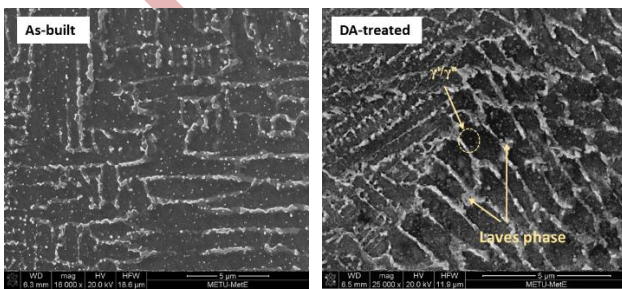


Figure 22 SEM images of as-built and DA-treated samples

In the tensile test of as-built specimens, the yield strength exhibited an unusual increase as the temperature rose from 550°C to 650°C, accompanied by a decreased elongation, as shown in Table 1.

Table 1. Mechanical test results (Elongation % and Yield Strength) of as-built and DA-treated specimens

ID	550°C		650°C	
	El. (%)	YS(MPa)	El.(%)	YS(MPa)
As-built	32,1	486	27,3	650
DA	11,8	1125	11,5	970

Conversely, the DA samples displayed a variety in yield strength with no significant change in elongation over the same temperature range. Moreover, serrations were observed in the stress-strain curves of IN 718 specimens deformed at 550°C (Figure 2).

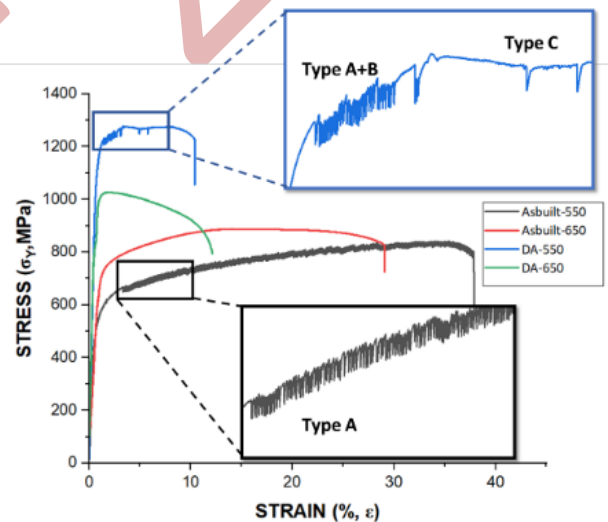


Figure 23 Stress-Strain Curve of As-built and DA specimens at 550 °C and 650 °C, demonstrated DSA Regime Type

Previous studies by Chen and Chaturdevi [1] and McLouth et al. [5] reported serrated stress-strain behavior in IN 718 at elevated temperatures due to the segregation and depletion of interstitial elements at dislocation cores. The findings of this study are consistent with these observations. The as-built specimens exhibited Type B serrations in their stress-strain curves. Moreover, DA specimens initially displayed a mixed Type A+B serration regime, transitioning to Type C, signaling a shift from dislocation-dominated deformation to stacking fault

mechanisms. At temperatures above 650°C, serrated flow behavior was not observed, likely due to the enhanced mobility of solute atoms that allowed them to follow dislocations without impeding their motion. Previous investigations have established that prior deformation facilitates the transformation of the γ'' phase to the δ phase in the IN718 alloy, with planar defects in the γ'' phase acting as effective nucleation sites for the precipitation of the stable δ phase. In this study, the internal strains were correlated to the Geometrically Necessary Dislocations (GNDs) values. The GND value of as-built samples was calculated from EBSD maps of samples as $4.224 \times 10^{13} \text{ m}^{-2}$. This higher internal strain in the as-built samples contributed to earlier precipitation or precipitation occurring at reduced temperatures. In order to observe this phenomenon, fracture surface analysis were applied after deformation. The induced strengthening phases were observed on the SEM images of the lateral section of fracture surfaces of as-built samples (Figure 4). During tensile testing at elevated temperatures, additional strains were imposed, resulting in the emergence of secondary γ' , γ'' , and δ phases. SEM images of the lateral fracture surfaces of as-built samples validated the presence of secondary γ' and γ'' .

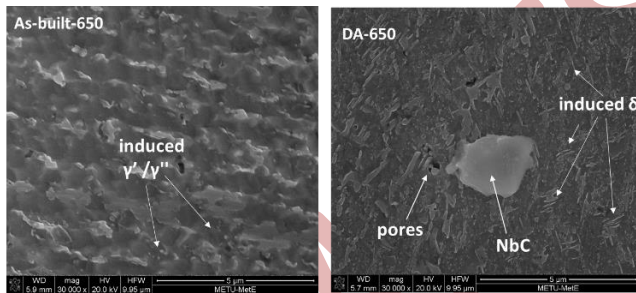


Figure 24 SEM images of lateral sections of fracture surfaces of as-built and DA-treated samples deformed at 650 °C

Moreover, the DA sample tested at 550°C displayed secondary γ' (see Figure 5), while the DA-SP sample tested at 650 °C demonstrated a notable increase in δ phase formation (Figure 4) .

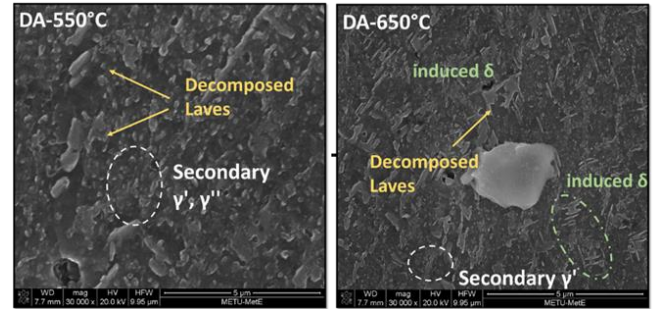


Figure 25 SEM images of lateral sections of fracture surfaces of DA-treated samples deformed at 550 °C and 650 °C

The elongated chain-like morphology of the Laves phase negatively impacts the mechanical properties at elevated temperatures. Figure 5 illustrates the fragmentation of the Laves phase following testing at 650 °C. Additionally, newly formed γ''/γ' phases and chromium-rich carbides were identified. Moreover, the presence of microvoids, along with specific phases, suggests complex fracture mechanisms and the interactions of various microstructural features during the deformation and fracture processes of the material at high temperatures. The existence of secondary γ' and γ'' phases can substantially affect the mechanical properties of the material, contributing to strengthening and enhancing resistance to deformation. Furthermore, the fragmentation of Laves phases and the development of δ phases at elevated temperatures may also impact the material's performance and fracture response.

3. Conclusion

These findings shed light on the complex interplay between microstructure, temperature, and deformation mechanisms in additively manufactured IN 718, culminating in the following conclusions:

- At 550°C, the phenomenon of DSA was detected, stemming from the interactions between solute atoms and dislocations.
- The higher GND values observed in the as-built samples led to the earlier formation of secondary phases during deformation.
- At 650°C, unusual behavior in yield strength and temperature-related brittleness was identified. Consequently, raising the test temperature resulted in diminished elongation values while increasing yield strength, which can be attributed to the dissolution of carbides at the grain boundaries.

4. References

1. W. Chen and M. C. Chaturvedi, "On the mechanism of serrated deformation in aged IN718," *Materials Science and Engineering: A*, vol. 229, no. 1, pp. 163–168, 1997, doi: [https://doi.org/10.1016/S0921-5093\(97\)00005-1](https://doi.org/10.1016/S0921-5093(97)00005-1).
2. S. Ozer, G. M. Bilgin, K. Davut, Z. Esen, and A. F. Dericioglu, "Effect of post fabrication aging treatment on the microstructure, crystallographic texture and elevated temperature mechanical properties of IN718 alloy fabricated by selective laser melting," *J Mater Process Technol*, vol. 306, p. 117622, 2022, doi: <https://doi.org/10.1016/j.jmatprotec.2022.117622>.
3. C. L. Hale, W. S. Rollings, and M. L. Weaver, "Activation energy calculations for discontinuous yielding in IN718SPF," *Materials Science and Engineering: A*, vol. 300, no. 1, pp. 153–164, 2001, doi: [https://doi.org/10.1016/S0921-5093\(00\)01470-2](https://doi.org/10.1016/S0921-5093(00)01470-2).
4. S. A. Nalawade, M. Sundararaman, R. Kishore, and J. G. Shah, "The influence of aging on the serrated yielding phenomena in a nickel-base superalloy," *Scr Mater*, vol. 59, no. 9, pp. 991–994, 2008, doi: <https://doi.org/10.1016/j.scriptamat.2008.07.004>.
5. T. D. McLouth *et al.*, "Influence of reduced carbon content on microstructure and mechanical behavior of IN718 prepared by laser powder bed fusion," *Additive Manufacturing Letters*, vol. 3, p. 100037, 2022, doi: <https://doi.org/10.1016/j.addlet.2022.100037>.

Next generation drug delivery nanosystems

Tanveer Tabish

*Company name- Radcliffe Department of Medicine, University of Oxford, OX3 7BN, Oxford, United Kingdom,
tanveer.tabish@cardiov.ox.ac.uk
ORCID: 0000-0001-5578-076X*

Cite this paper as Tabish T. Next generation drug delivery nanosystems Int. Conf. Advanced. Mater. Sci.& Eng. HiTech.and Device Appl.Oct. 24-26 2024,Ankara, Turkey

Abstract. For more than a century, nitric oxide (NO) donating formulations have been a mainstay treatment for the management of cardiovascular diseases. These donors primarily produce NO in the circulation and are not targeted to specific cellular sites of action. However, it would be desirable to deliver the right amount of NO to a precise location at the right time. To achieve these aims, we have recently developed several strategies aimed at therapeutically generating or releasing NO in living systems showing that graphene could either generate NO endogenously by the catalytic decomposition of endogenous NO substrates or can store and release therapeutically relevant amounts of NO gas or other NO sources. For example, acidified nitrite conjugated graphene as NO carrier showed a dose-dependent effect to promote proliferation in endothelial cells and to inhibit growth in smooth muscle cells (SMCs), which was associated with cGMP release indicating intracellular activation of canonical NO signalling. This talk will present our recent proof-of-principle data on the utility of porous graphene as a NO delivery vehicle to release physiologically relevant amounts of NO *in vitro*, thereby highlighting the potential of these formulations as a strategy for the treatment of cardiovascular diseases.

Keywords: nitric oxide, cardiovascular nanomedicine, graphene nanoparticles, drug delivery

© 2024 Published by ICMATSE

For more than a century, nitric oxide (NO) donating formulations such as organic nitrates and nitrites have been a cornerstone for the treatment of cardiovascular diseases. These donors primarily produce NO systemically, however it would be desirable to deliver the right amount of NO to a precise location at the right time. To address this need, we hypothesised that graphene-based nanomaterials can be developed to store and release therapeutic amounts of NO in a controlled fashion. **Methodology & results:** we describe the design and characterisation of a novel NO delivery system via the incorporation of sodium nitrite as a NO source into porous graphene oxide nanosheets (termed NO@Th-PGO) (**Figure**). The exchange between functional groups and the corresponding morphologies were confirmed by X-ray diffraction (XRD), Fourier transform infrared spectroscopy (FTIR), Raman spectroscopy and scanning electron microscopy (SEM). The real-time release of NO from NO@Th-PGO was measured using a free radical analyser equipped with NO electrode and the total capacity for NO production

by ozone-chemiluminescence. The NO release was sustained at $>5 \times 10^{-10}$ mol cm⁻² min⁻¹ for at least 3 hours, which is comparable to production by healthy endothelium (cf, 0.5 – 4 $\times 10^{-10}$ mol cm⁻² min⁻¹). The underlying mechanism of NO release likely involves a role for thiols as a reducing agent, thereby converting graphene-conjugated nitrite into NO. To test whether NO released from NO@Th-PGO is localised intracellularly, we used a fluorescent NO-specific probe, 4-amino-5-methylamino-2',7'-difluorofluorescein (DAF-FM DA) for real-time imaging. This detected the release of NO from NO@Th-PGO in both vascular endothelial and smooth muscle cells. Furthermore, exposure of vascular cells to NO@Th-PGO *in vitro* increased endothelial cell proliferation and inhibited smooth muscle cell growth. **Conclusions:** here we demonstrate the utility of porous graphene as a NO delivery vehicle to release physiologically relevant amounts of NO in culture. This work highlights the potential of these formulations as a promising strategy for the treatment of cardiovascular diseases.

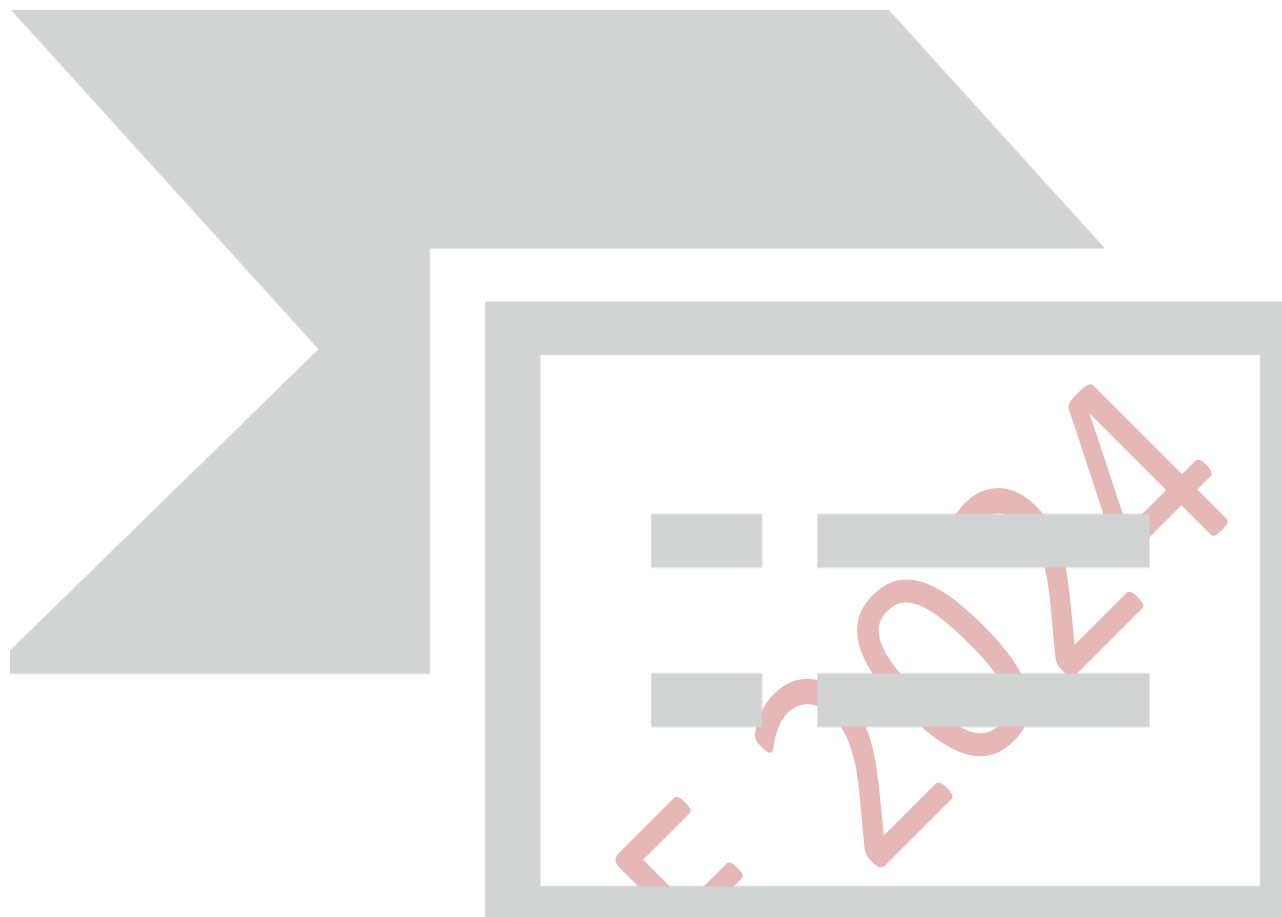


Figure: A schematic illustration of the crosslinking of cysteamine to porous graphene oxide (PGO) followed by the S-nitrosation of cysteamine-functionalised PGO to form S-nitrosocysteamine-functionalised PGO (termed SNO-Cys@PGO).

References

1. Tabish, T. A., Hussain, M. Z., Zervou, S., Myers, W. K., Tu, W., Xu, J., ... & Lygate, C. A. (2024). S-nitrosocysteamine-functionalised porous graphene oxide nanosheets as nitric oxide delivery vehicles for cardiovascular applications. *Redox Biology*, 72, 103144.
2. Tabish, T. A., Crabtree, M. J., Townley, H. E., Winyard, P. G., & Lygate, C. A. (2023). Nitric oxide releasing nanomaterials for cardiovascular applications. *JACC: Basic to Translational Science*.
3. Tabish, T. A., Zhu, Y., Shukla, S., Kadian, S., Sangha, G. S., Lygate, C. A., & Narayan, R. J. (2023). Graphene nanocomposites for real-time electrochemical sensing of nitric oxide in biological systems. *Applied Physics Reviews*, 10(4).
4. Tabish, T. A., & Lygate, C. A. (2023). Mitochondria-targeted nanomedicines for cardiovascular applications. *Nanomedicine*.

Open Hole Tension Test And Finite Element Method Simulation In Polymer Matrix Composite Materials: Experimental And Analytical Comparison

Mete Bakir

TAI/Ankara Yildirim Beyazit University- Materials Engineering/Assist. Prof., 06000, Ankara, Türkiye,
mete.bakir@tai.com.tr/mete.bakir@aybu.edu.tr
ORCID: 0000-0002-5044-3104

Utku Dogan

Ankara Yildirim Beyazit University - Mechanical Engineering, 06000, Ankara, Türkiye,
utkuu.dgn@gmail.com
ORCID: 0009-0001-5610-8999

Sefa Sahin

Ankara Yildirim Beyazit University - Mechanical Engineering, 06000, Ankara, Türkiye,
sahinsefa1234@gmail.com
ORCID: 0009-0003-0952-5671

Enes Karakus

Ankara Yildirim Beyazit University - Mechanical Engineering, 06000, Ankara, Türkiye,
eneskarakus.5555@gmail.com
ORCID: 0009-0009-9241-3104

Cite this paper as: Bakir, M, Dogan, U, Sahin, S, Karakus, E. Open Hole Tension Test And Finite Element Method Simulation In Polymer Matrix Composite Materials: Experimental And Analytical Comparison. Int. Conf. Advanced. Mater. Sci. & Eng. HiTech. and Device Appl. Oct. 24-26 2024, Ankara, Turkiye

Abstract. This study focuses on tensile strength of composite materials which has a hole at its center. Main parameters are orientation and hole diameters that affect test results dramatically. Open Hole Tensile (OHT) tests are important for aerospace applications since there are thousands of fasteners on an aircraft. This research includes open hole tensile (OHT) tests results which specimens that geometry and orientations are different. Additionally, study works on finite element analysis of OHT in failure mode, test results and prediction. Finite Element Numerical Simulations which done on LS Dyna were validated by experimental test results with small differences. Also orientation effect on results investigated that not worked much in literature. This paper details test method and analysis method for OHT test. Further discuss simulation results and experimental test results. Findings provide some insights for future research and developments in composite open hole tensile test.

Keywords: Composite, Open Hole Tensile Test (OHT), Simulation
© 2024 Published by ICMATSE

1 Introduction

Composite materials that can be connected to other elements in aircraft structures must pass open-hole tension tests as part of the qualifying procedure. A new pair of testing is needed for every new set of materials. The development of analysis tools for the prediction of failure and damage in these tests is desirable in order to minimize costs. Based on open hole tensile tests on the same composite laminates, it was found that changes in hole radius lead to differences in

the stress levels and damage behavior of the composite laminates. In a study, transverse cracks developed in the upper layer of all specimens, firstly at the notch surroundings and at the free edges at higher applied strains. Also on this article, open hole tensile tests of each laminate showed that strength decreased with size [1]. Another open hole tensile test experiment compares the material differences on the test results. In this study [2] they proves CFRP material has a greater strength and stiffness than GFRP material. But there is a similar point between these two material which is damage progression. Another parameter that affect the test results is hole

diameter [3]. When the diameter of the hole increases, strength reduces. For example, if the hole size is small, failure is delamination through the width. If size of the hole is large, failure firstly occurs at the fiber.

1.1 Material and Specimens

CFREP specimens were fabricated using IM7-12K carbon fibre reinforced epoxy matrix (Hexcel, United States). The IM7-12K/Epoxy prepregs were subjected to autoclave and hot press processes to bond them. Three sets of six specimens with different stacking sequences were formed. Table 1 shows the dimensions and stacking sequences of the specimens.

Table 1 Stacking sequence and specimen dimensions

Stacking Sequence	Width (mm)	Thickness (mm)	Hole diameter (mm)	
[45/0/-45/90] _{2s}	38,08	2,944	6,44	305
[0/45/0/90/0/-45/0/45/0/-45] _s	38,08	3,68	6,44	305
[45/-45/0/45/-45/90/45/-45/45/-45] _s	38,08	3,68	6,44	305

Open Hole Tension (OHT)

A 250 kN loading cell on an Instron 5985 tensile testing apparatus was used to test open-hole specimens. The test standard utilized was ASTM D5766-02a [4]. The calculated crosshead speed was 1.27 mm/min. By dividing the force applied in the loading direction by the specimens' cross-sectional area, stress values were calculated. To gain a deeper understanding of the stress distributions and damage patterns of the specimens at failure, Digital Image Correlation (DIC) was employed.

Numerical Simulation

The models for plastic deformation, delamination, multiple interlaminar cracks, and fiber breaking failure were considered based on the experimental observation. Because the observed out-of-plane deformations before to peak load were minimal in the layup, the geometrical nonlinearity was disregarded. Three distinct orientations were included in this investigation. These are [45/0/-45/90]_{2s} (QIS), [0/45/0/90/0/-45/0/45/0/-45]_s (HRD) and [45/-45/0/45/45/-45/90/45/-45/45/45/-45]_s (SFT), respectively. Using the finite element method and LS-Dyna software, the open

hole tension behavior of carbon fiber reinforced epoxy plastic (CFREP) specimens was examined. Using the HyperMesh program, the specimens' geometrical models were produced. Every layer has a thickness of 0.184 mm. The specimens' length was 305 mm, width was 38.08 mm, and hole diameter was 6.44 mm. Using data from experiments, the MAT054/55 material model developed by LS-Dyna defined the material properties. The mechanical properties of the laminates are reported in Table 2. The failure criterion chosen was the Tsai-Wu one. In the model, shell elements are used in accordance with the suitability determined by convergence analysis. Only quadrilateral mesh was used for each model. One of the specimens' short edges was fixed, and a force was applied to the other short edge in a longitudinal direction to create boundary conditions. Since the experiments were carried out at room temperature, thermal effects were neglected. Implicit solver type was used in the simulations because of the fact that the crosshead speed is sufficiently low to be treated as quasistatic. The accuracy and validity of the model are assessed by comparing the derived findings with the experimental data.

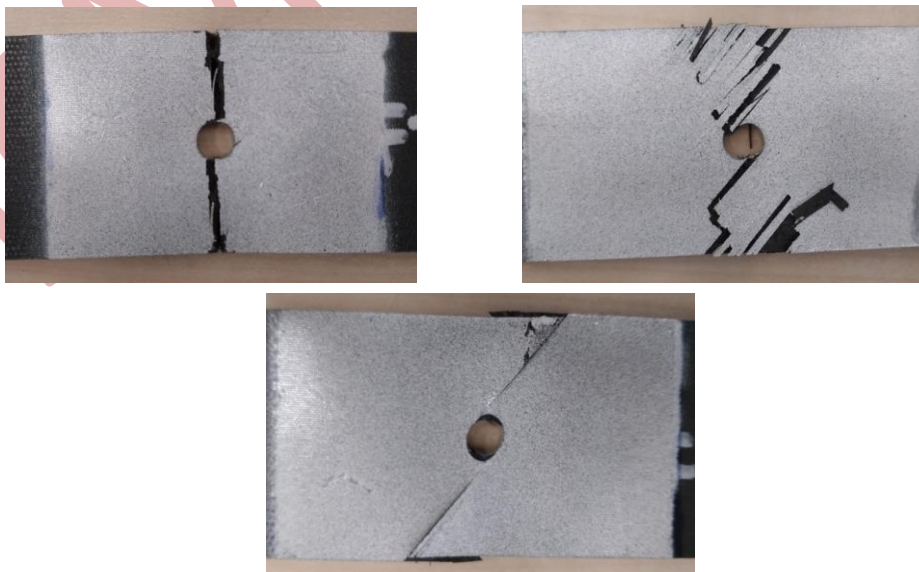
Table 2 Mechanical properties of QIS, HRD and, SFT laminates

Stacking Sequence	QIS	HRD	SFT
E_1 (GPa)	165	313	115
E_2 (GPa)	8,5	10,5	8,5
ν_{12}	0.033	0,033	0,033
$\nu_{13} = \nu_{23}$	0.033	0.033	0.033
G_{12} (GPa)	4,6	4,6	4,6
$G_{13} = G_{23}$ (GPa)	4,6	4,6	4,6
X_T (MPa)	2980	6826	2106
Y_T (MPa)	80	80	80
X_C (MPa)	1860	1880	1860
Y_C (MPa)	250	250	250
S_C (MPa)	80	80	110

Experimental Results

There were six through-hole tension tests conducted for every orientation of lay-up. The speed at which each test was conducted was 1.27 mm/min. The post-failure fracture circumstances for each lay-up orientation are depicted in Figure 1. Every specimen failed in line with the

through-hole tensile failure modes after being checked for the failure modes listed in the ASTM D5766-02a standard. This standard states that soft (SFT) and quasi-isotropic (QIS) specimens failed in the AGM (Angled Gage Middle) mode. During the LGM (Lateral Gage Middle) mode, Hard (HRD) specimens failed.


Figure 1 Post-failure fracture for a) HRD, b) QIS, and c) SFT

Comparison of Experimental Results with Simulation Results

Graphs show the force versus displacement graphs for QIS, HRD and SFT, respectively. It is understood that the experimental and numerical results for each lay-up orientation are in good agreement.

Nevertheless, there are acceptable error rates between our experimental and numerical data. This rate was calculated as 8.84% for QIS, 5.79% for HRD and 0.048% for SFT. The different error rates for different lay-up orientations can be explained by fibre aspects. QIS has a structure in which the fibres are placed at different angles.

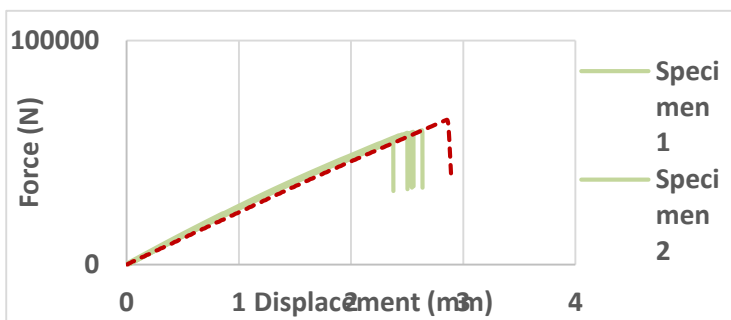


Figure 2 Force – displacement graph for QIS orientation.

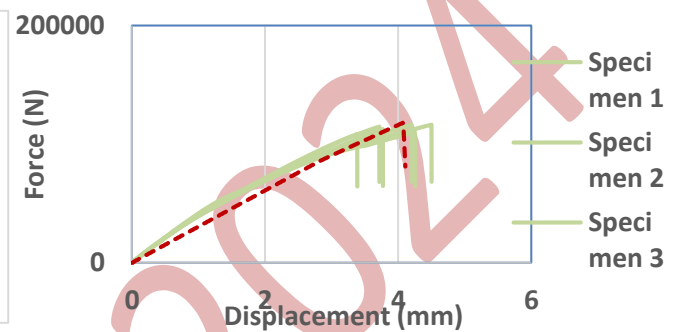


Figure 3 Force – displacement graph for HRD orientation.

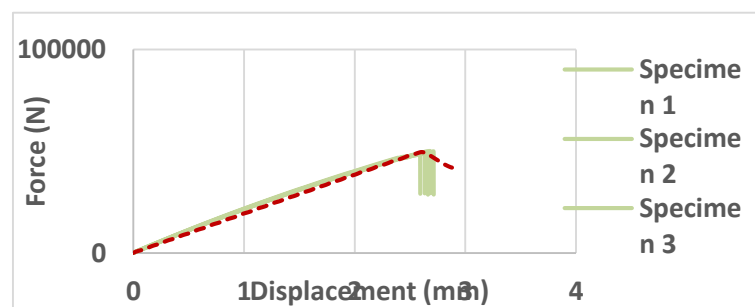


Figure 4 Force – displacement graph for SFT orientation.

Conclusion

This study used experimental, computational, and visual methods to thoroughly evaluate the open hole stress behavior of composite specimens with three alternative stacking sequences. It was discovered that there was strong agreement between the simulations carried out using the finite element method and the experimentally obtained open hole tension test findings. This agreement shows how trustworthy and realistic

the generated finite element model is. To sum up, this research constitutes a significant advancement in comprehending and simulating the behavior of open-hole stress in composite materials. The results yielded provide light on future directions for research and offer useful information for the design and analysis of composite materials. This work will be a valuable reference, particularly in industries like aerospace and automotive where composite materials are employed extensively

References

1. Size effects on the tensile and compressive failure of notched composite laminates G.H. Erçin a , P.P. Camanho b,† , J. Xavier c , G. Catalanotti b , S. Mahdi d , P. Linde e 96 (2013) 736-744. DOI:10.1016/j.compstruct.2012.10.004
2. O'Higgins, Ronan M., Michael A. McCarthy, and Conor T. McCarthy. "Comparison of open hole tension characteristics of high strength glass and carbon fibre-reinforced composite materials." *Composites Science and Technology* 68.13 (2008): 2770-2778.
3. Wisnom, Michael R., and Stephen R. Hallett. "The role of delamination in strength, failure mechanism and hole size effect in open hole tensile tests on quasi-isotropic laminates." *Composites Part A: Applied Science and Manufacturing* 40.4 (2009): 335-342.
4. Standard Test Method for Open Hole Tensile Strength of Polymer Matrix Composite Laminates

ICMATSE 2024

Residual Stresses and Distortion in WAAM

Ahmet İrfan YÜKLER

*Nişantaşı University- Mechanical Engineering Department, 34398, İstanbul, Türkiye,
irfan.yukler@nisantasi.edu.tr
ORCID: 0000-0001-8146-8665*

Cite this paper as: Yukler, Al. Residual Stresses and Distortion in WAAM. Int. Conf. Advanced. Mater. Sci.& Eng. HiTech.and Device Appl.Oct. 24-26 2024, Ankara, Turkiye

Abstract. The Wire Arc Additive Manufacturing (WAAM) process is a new additive manufacturing technique that offers economical benefits. In this method, the wire and a part of the substrate are melted by an electric arc from the power source, allowing the material to be deposited on top of the substrate layer by layer to create the desired preform. Thermal shrinkage of the added material can distort the manufactured part and generate residual stresses. Materials temperature-dependent properties, welding parameters and structure geometry determine the magnitude of the stresses and distortions. The residual stress and distortion formation in WAAM and the factors affecting them are explained in this paper.

Keywords: Wire arc additive manufacturing, Residual stresses, Distortions
© 2024 Published by ICMATSE

1.Introduction

Wire Arc Additive Manufacturing (WAAM) is an additive manufacturing method. In WAAM, the metallic wire is melt using an electric arc energy. The melt is deposited on a substrate in a layer-by-layer fashion using a 3D CAD model data as illustrated in Figure 1 [1]. A robotic system is utilized in production of the 3D metal component. Conventional Gas Metal Arc Welding (GMAW), Gas Tungsten Arc Welding (GTAW), and Plasma Arc Welding (PAW) can used in the WAAM process [1]. WAAM has gained increasing popularity in aerospace, automotive, military, marine and construction industries in the last decade [2]. Design flexibility, reduced manufacturing time and low buy-to-fly ratio [3] make the WAAM process attractive for steel [2,4], aluminium [5], titanium [6], and nickel [7] part fabrications. The parts fabricated by WAAM require post production machining to obtain the required surface finish and dimensional tolerances [1].

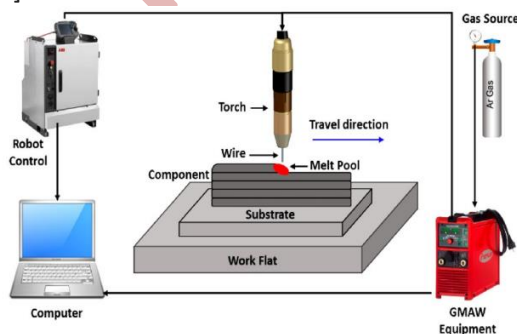


Figure 1. Illustration of GMAW-WAAM process [1].

2.Results & Discussions

2.1.Temperature Distribution in WAAM Parts

Xiong et al produced a ten-layer mild steel thin-walled structures [9]. They measured thermal cycles on the substrate. Figure 2 shows the thermal profiles measured by thermocouples during the metal deposition process. The temperature increases rapidly until a peak temperature is achieved. After completing the deposition of each layer, the temperature gradually decreases with cooling. The surface of the substrate melted in the first pass and then it solidified. Uneven heating and cooling in the deposited metal and the substrate causes thermal gradient in the welding zone. The axial maximum temperature gradient in the molten pool declines gradually as the deposition height increases.

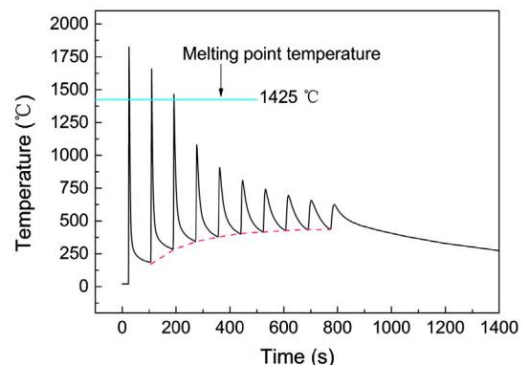


Figure 2. (a)Thermal cycle curves of the substrate [9].

2.2. Residual Stress and Distortion Formation in WAAM

The uneven heating-cooling thermal cycles of the WAAM lead to thermal stress formation [10]. Temperature gradient mechanism (TGM) model (Figure 3) explains the residual stress formation mechanism in WAAM [10]. During the heating stage, the welding energy heats up the feed material rapidly.

The heated material tends to expand but this thermal expansion is restrained by the colder surrounding metal. Thus, a compressive stress state is formed located at the heated zone. During the cooling stage when the heat source is removed, the previously formed heated zone begins to cool down and a shrinkage of materials in this zone tend to occur. The shrinkage is partially restrained by the plastic strain formed during the heating stage. Finally, tensile residual stress is formed in the heated zone which is balanced by a compressive zone.

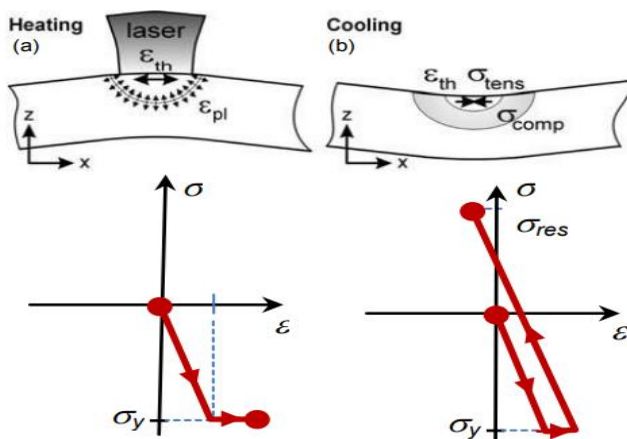


Figure 3. Temperature gradient mechanism (TGM) model. (a) Localized deformation during the heating-phase and (b) cooling-phase in the heat-applied zone; red arrows show the direction of residual stress formed during heating phase (compressive RS) and cooling-phase (tensile RS) [10].

Transverse shrinkage, longitudinal shrinkage and, through-thickness (axial or normal) shrinkage occur in the work piece which cause angular distortion, longitudinal bending, and rotational distortion [11]. The magnitude of transversal and axial residual stresses are low and they are mostly compressive (See Figure 4) [11]. The longitudinal residual stress is tensile and maximum at the mid-length of a layer while the transverse and normal stresses are found negligible for typical thin wall builds of mild steel, which was expected due to small transverse cross-section and multiple thermal cycles [12].

The longitudinal residual stress exhibits a steep gradient at the both ends of the deposit that makes the parts susceptible to buckling and warping. The longitudinal residual stresses are apparently bigger than the transversal and axial residual stresses. The longitudinal stress decrease with the the height of the wall. Mainly angular distortion and bending distortion occur in WAAM parts (Figure 5) [13].

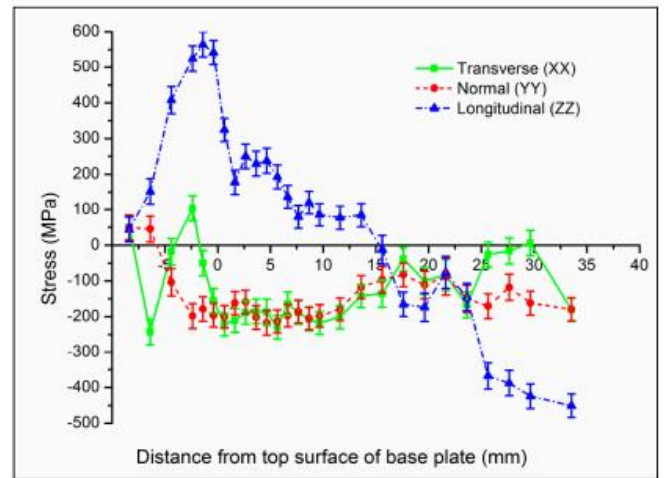


Figure 4. Residual stress measurements in wire-fed additive manufacturing of Ti-6Al-4V wall [11].

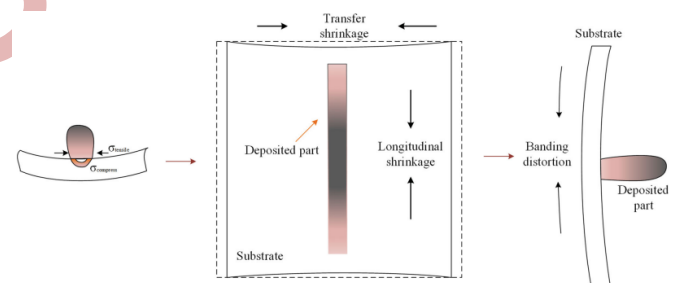


Figure 5. Angular distortion and bending distortion of a WAAM part [13].

2.3. Factors Affecting Residual Stresses and Distortions

The major influencing factors of distortion and residual stress can be classified into three aspects including structure geometry, material properties, and processing [14]. More stress and distortion occurs with high metal thermal expansion coefficient, high Young modulus, and high welding heat input. The thermal stress and distortion decreases with high preheating, short bead length and an increase of the substrate thickness. Clamping of the substrate and the layers number lowers defect formation.

Conclusions

The below results were obtained from literature survey of mild steel WAAM parts:

1. Residual stress formation in WAAM can be described by the temperature gradient mechanism (TGM) model.

2. The largest magnitudes of residual stresses are observed in the direction of the welding line.

3. The heat input of welding, thickness of the substrate, thermal expansion coefficient of the deposited metal enhance distortion formation.

4. Preheating, dwell time, active cooling and clamping lower the distortion formation.

References

1. M.R. Zahidin, et al., Research challenges, quality control and monitoring strategy for Wire Arc Additive Manufacturing, *J Mat Res Tech*, 24 (2023), pp. 2769-2794, 10.1016/j.jmrt.2023.03.200.
2. T. Tankova, et al., Characterization of robotized CMT-WAAM carbon steel, *Journal of Constructional Steel Research*, *J Const St Res*, 199(2022), pp. 107624, 10.1016/j.jcsr.2022.107624.199.
3. S. Kokarea, J.P. Oliveira, R. Godin, Modelling of Wire Arc Additive Manufactured Product Cost, *Proc Comp Sci*, 217(2023) pp. 1513–1521, 10.1016/j.procs.2022.12.351
4. S.K. Sharma, et al., Processing Techniques, Microstructural and Mechanical Properties of Wire Arc Additive Manufactured Stainless Steel: A Review, *J Inst Eng India Ser C*, 103(2022), pp. 1325–1339, 10.1007/s40032-022-00853-5.
5. G. Çam, Prospects of producing aluminum parts by wire arc additive manufacturing (WAAM), *Mats Today: Proc*, 62(2022), pp. 77-85, 10.1016/j.matpr.2022.02.137.
6. Z. Lin, K Song, X. Yu, A review on wire and arc additive manufacturing of titanium alloy, *J Manf Proc*, 70(2021), pp. 24-45, 10.1016/j.jmapro.2021.08.018.
7. V. Dhinakaran, et al., Wire Arc Additive Manufacturing (WAAM) process of nickel-based superalloys – A review, *Mats Today: Proc*, 21(2020), pp. 9020-9025, 10.1016/j.matpr.2019.08.159.
8. N. Bastola, et al., A Review of the Residual Stress Generation in Metal Additive Manufacturing: Analysis of Cause, Measurement, Effects, and Prevention, *Micromach*, 14,(2023), pp. 1480, 10.3390/mi14071480.
9. J. Xiong, Y.Lei, R. Li, Finite element analysis and experimental validation of thermal behavior for thin-walled parts in GMAW-based additive manufacturing with various substrate preheating temperatures, *App Therm Eng*, 126(2017), pp. 43-52, 10.1016/j.applthermaleng.2017.07.168.
10. C. Li, et al., Residual Stress in Metal Additive Manufacturing, *Proc CIRP*, 71(2018), pp. 348–353, 10.1016/j.procir.2018.05.039.
11. P. Michaleris, *Minimization of Welding Distortion and Buckling: Modeling and Implementation*, Woodhead Publishing Limited, Cambridge UK, 2011.
12. T. DebRoy, et al., Additive manufacturing of metallic components – Process, structure and properties, *Prog Mats Sci*, 92(2018), pp. 112-224, 10.1016/j.pmatsci.2017.10.001.
13. B. Wu, et al., Mitigation of thermal distortion in wire arc additively manufactured Ti6Al4V part using active interpass cooling, *Sci Tech Weld Join*, 24(2019), pp. 484-494, 10.1080/13621718.2019.1580439.
14. D. Xie, et al., A Review on Distortion and Residual Stress in Additive Manufacturing, *Chi J Mech Eng: AM Frnt*, 1(2022), pp. 100039, 10.1016/j.cjmeam.2022.100039.



ICMATSE

2024

**INTERNATIONAL CONFERENCE ON
ADVANCED MATERIALS SCIENCE &
ENGINEERING AND
HIGH TECH DEVICE APPLICATIONS**

ISBN: 978-625-97601-1-7

October 24 - 26 2024

Gazi University Ankara / TURKEY

icmatse.org

